MAGMA EMPLACEMENT AND DEFORMATION IN RHYOLITIC DYKES: INSIGHT INTO MAGMATIC OUTGASSING

Presented for the degree of Ph.D. by

Ellen Marie McGowan
MGeol (The University of Leicester, 2011)

Initial submission January 2016
Final submission September 2016

Lancaster Environment Centre,
Lancaster University

Declaration

I, Ellen Marie McGowan, hereby declare that the content of this thesis is the result of my own work, and that no part of the work has been submitted in substantially the same form for the award of a higher degree elsewhere.

This thesis is dedicated to Nan-Nar, who sadly passed away in 2015.
Nan, you taught our family the importance and meaning of love, we love you.

Abstract

Exposed rhyolitic dykes at eroded volcanoes arguably provide in situ records of conduit processes during rhyolitic eruptions, thus bridging the gap between surface and sub-surface processes. This study involved micro- to macro-scale analysis of the textures and water content within shallow (emplacement depths <500 m) rhyolitic dykes at two Icelandic central volcanoes.

It is demonstrated that dyke propagation commenced with the intrusion of gas-charged currents that were laden with particles, and that the distribution of intruded particles and degree of magmatic overpressure required for dyke propagation were governed by the country rock permeability and strength, with pre-existing fractures playing a pivotal governing role. During this stage of dyke evolution significant amounts of exsolved gas may have escaped. Furthermore, during later magma emplacement within the dyke interiors, particles that were intruded and deposited during the initial phase were sometimes preserved at the dyke margins, forming dyke-marginal external tuffisite veins, which would have been capable of facilitating persistent outgassing during dyke growth.

It is further demonstrated that following initial dyke-opening, geochemically homogenous dykes grew via the incremental emplacement of magma, with fluctuations in the shallow-dyke permeability occurring via bubble collapse, and this is deemed to have been critical in dictating pressure within the deeper magma source region and fragmentation. Of further significance, it is also shown that shear deformation was localised during magma emplacement, with localised vesiculation occurring along emplacement boundary layers via viscous heating, which temporarily promoted magma ascent, but with later bubble collapse culminating in brittle failure of bubble-free magma, after shear zone migration. However, in some instances high

strain rates during viscous bubble deformation resulted in ductile-brittle transitions, with resultant slip triggering micro-tensile failure of bubbly magma, as the slipped magmatic plug experienced decompression. This tensile failure probably occurred distal to shear zones, where bubbles where relatively isolated. Interlinking of the micro-cracks formed extensive internal tuffisite vein networks, which acted as efficient outgassing pathways, given their access to significant quantities of pre-exsolved volatiles.

The models presented in this thesis are relevant to the conduit processes that take place during rhyolitic eruptions; insight is provided into how rhyolitic magma ascends through the shallow (<500 m deep) crust and also into how the magma deforms during its ascent and into the processes that govern magmatic outgassing.

Acknowledgments

Thank you to my supervisors, Hugh Tuffen, Mike James and Peter Wynn. Peter, thank you for your advice, guidance and input during the first year of my PhD. Hugh and Mike, thank you for your advice, guidance and input throughout; I can't thank you both enough for proving comments on numerous iterations of my chapters. You all certainly gave me proficient training in how to be a researcher.

Thank you to Hugh Tuffen, Debbie Hurst, Jacqui Owen and staff at the Diamond Light Source Facility in Oxfordshire, who all assisted with FTIR analysis. Thanks also to Hugh, Mike, Jacqui and Hjalti Franzson for field assistance, and to Kristján Sæmundsson for advice on where to find some splendid rhyolitic dykes in Húsafell.

Thank you to everyone in the Geology Department at Leicester University, as this is where my passion for geology was forged and where my path into academia really began. Specific thanks to Mike Branney, who was my Masters project supervisor. Branney, thanks for introducing me to volcanology, for inspiring me to try my hand at volcanological research, for encouraging me to spread my wings, and for introducing me to the fantastic geology of The Lake District. Thank you to the technician staff, Rob Wilson, Lyn Marvin and Nick Marsh, who assisted with SEM and XRF analysis, and who always made me feel welcome.

Thank you to my family, Mum, Dad, Claire, Phil, Nan-Nar, Gan-Gan, Aunty Christine, Charlie, Rebecca, Darcy, Maddie, Elise, and Aryanna, for your unyielding love and support.

Last, *but by no means least*, thanks to Meg, for being the perfect companion on camping and hiking trips, and for being a girl's best friend – WOOF!

Contents

Figure list

PAGE

Chapter 1

Chapter 2

Chapter 3

Chapter 4

Table list

PAGE

Chapter 1

Chapter 2

Chapter 3

Chapter 4

Terminology

In this thesis, tuffisite veins, dykes and conduits are frequently referred to; the definitions of these terms are provided in this section.

Tuffisite veins are fractures in magma or country rock that act as pathways for the transport of particles carried by a gas phase. The final preserved fracture is propped open by clastic particles and is typically millimetres to centimetres wide. Magma-hosted tuffisite veins are referred to as internal tuffisite veins and are generally filled by juvenile clasts, with lithic clasts either lacking, or constituting a minor proportion of the vein-filling material. In comparison, external tuffisite veins may be housed wholly within the country rock or form the marginal layer of a dyke or conduit and thus the contact between a dyke or conduit and the country rock. These tuffisite veins also contain juvenile clasts, and a high proportion of lithic clasts relative to internal tuffisite veins.

The name tuffisite vein derives from the fact that they dominantly contain ash-sized volcanic particles and they often have vein-like geometries, but more complex irregular geometries exist, with individual veins varying in shape and thickness. In addition, many tuffisite veins have branching forms, with connected branches having different orientations. Tuffisite veins are associated with rhyolitic (e.g., Heiken et al., 1988; Stasiuk et al., 1996; Tuffen and Dingwell, 2005; this study) and andesitic (Plail et al., 2014) rocks, with proven examples from basaltic rocks currently lacking.

It is necessary to distinguish between magmatic shear zones and tuffisite veins. Here a magmatic shear zone is defined as a damage zone, which can involve localised cataclasis and magma failure, whereas tuffisite veins involve the transport of particles through fractures by a supporting fluid (e.g., magmatic or hydrothermal fluids). Tuffisite veins can sometimes evolve into magmatic shear zones (e.g., Tuffen et al.,

2003; Tuffen and Dingwell, 2005), with shear deformation sometimes destroying earlier-formed sedimentary structures that formed during the life-cycle of the tuffisite vein (Tuffen and Dingwell, 2005).

Dykes are defined as sheet-like igneous intrusions that are discordant with the orientation of country rock bedding. They differ from tuffisite veins because they are composed of intact lava or intact lava and clastic zones, with clastic zones being tuffisite veins or magmatic shear zones. The dykes that were studied for this research are ~2-10 m wide, with exposure lengths generally greater than ten meters. Some steeply dipping dykes change orientation along strike causing them to locally turn into near-horizontal sills i.e., they are concordant with the orientation of country rock bedding.

No conduits were studied for this research, but they are discussed throughout this thesis because they share textural similarities with the studied dykes. Conduits are defined as pipe-like intrusive igneous bodies, but their upper parts may flare outwards, giving them a funnel-like shape. They are generally wider than dykes (>10 m wide), but similarly to dykes they can be texturally diverse, consisting of intact lava and clastic zones. Conduits typically extend to depths of a few hundred meters, overlying and connecting with dykes at depths greater than this. Traditionally, conduits have been viewed as zones of wholescale magma fragmentation, but recent discoveries demonstrate that fragmentation within conduits may be more localised (e.g., Castro et al., 2012; Schipper et al., 2013) and similar to that with dykes (e.g., Tuffen et al., 2003; Tuffen and Dingwell 2005).

Chapter 1: Introduction

1.1. Rhyolitic volcanoes

Rhyolitic volcanoes have produced some of Earth's largest and most catastrophic eruptions, with Yellowstone being perhaps the prime example. Many other large and catastrophic eruptions have involved rhyolite. For instance, the 1912 rhyo-andesitic eruption of Novarupta-Katmai in Alaska was the largest eruption of the 20th century, with the volume of subaerial pyroclastic deposits totalling ~30 km^3 (Hildreth and Fierstein, 2012). However, this eruption was relatively small when compared with the predominantly rhyolitic eruptions from Taupo volcano, on New Zealand's North Island; the ~1.8 ka Taupo eruption (Wilson and Walker, 1985; Houghton et al., 2010) produced deposits with a volume >105 km^3 (~35 km^3 DRE), and the ~26.5 ka Oruanui eruption (Wilson, 2001; Wilson et al., 2006) produced deposits with a volume >1000 km^3 (~530 km^3 DRE). The major hazards associated with such eruptions include pyroclastic density currents, block and ash flows, ash falls, lahars, and tsunamis, all of which pose a threat to nearby communities. Indeed, the rhyodacitic eruption of Thera around 1400 BC may have wiped out the Minoan civilisation (Bond and Sparks, 1976; Heiken and McCoy, 1984).

The recent rhyolitic eruptions in Chile (**Fig. 1.1.**), of Chaitén (2008-2009) and Cordón Caulle (2011-2012) caused thousands of people to be evacuated from their homes, with crops destroyed, water contaminated, and flights disrupted, whilst ash deposition in rivers resulted in floods (Carn et al., 2009; Lara, 2009). More broadly, ash and volatiles released during eruptions can influence Earth's climate. For instance, it is debated as whether or not the several centuries of climate cooling, which followed the predominantly rhyolitic eruption (Ninkovich et al., 1978) of Toba volcano in

Indonesia ~75,000 years ago caused a bottleneck in the human population (Ambrose, 2003; Gathorne-Hardy and Harcourt-Smith, 2003). However, volcanoes also provide benefits, as volcanic ash is nutrient-rich, and thus a key ingredient of successful agriculture; they are also important for the tourist industry, and geothermal energy provides an environmentally friendly power source.

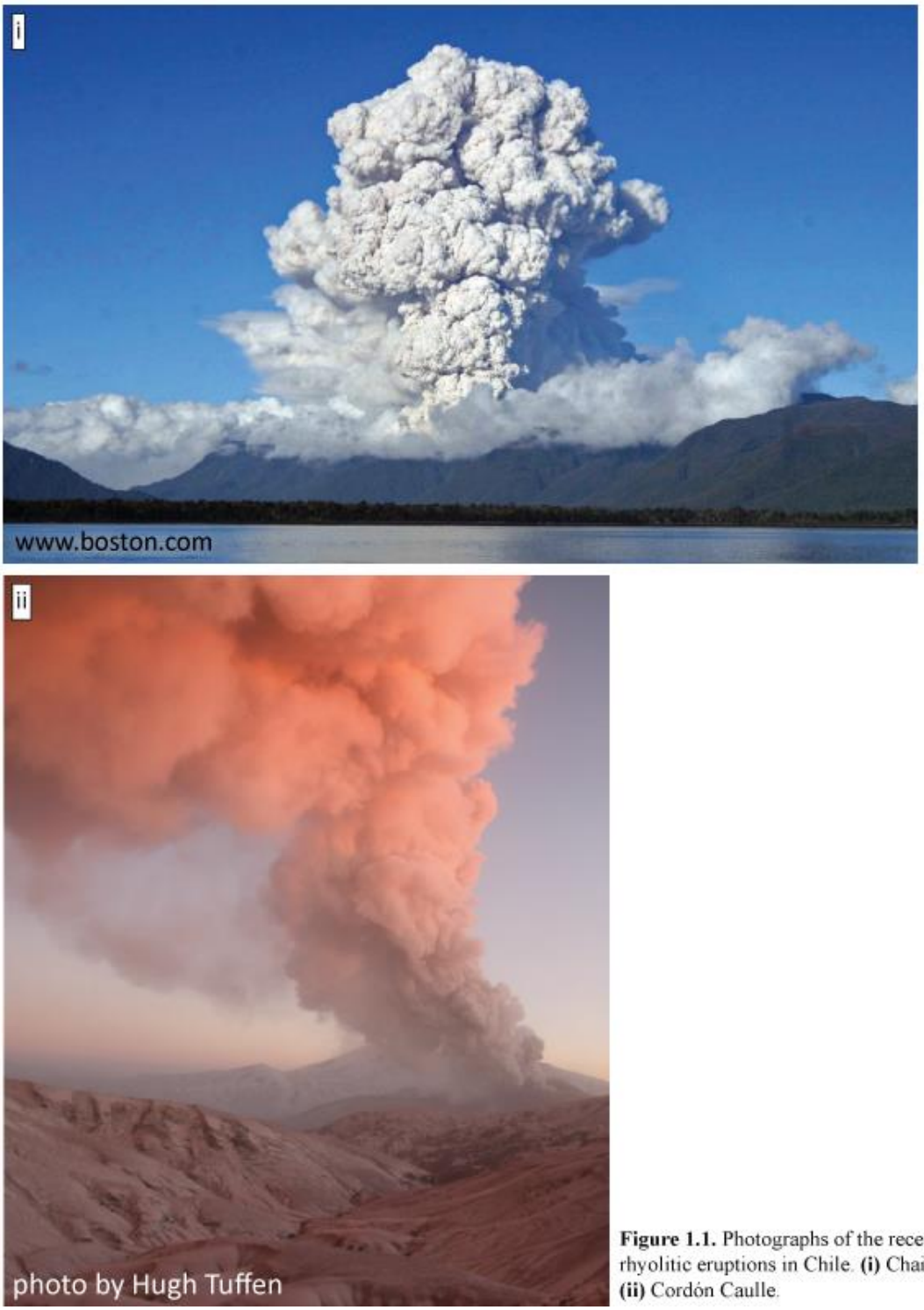

Figure 1.1. Photographs of the recent rhyolitic eruptions in Chile. **(i)** Chaitén. **(ii)** Cordón Caulle.

1.2. Poorly understood rhyolitic dyke and conduit processes

The loss of magmatic gases from rhyolitic magma (magmatic outgassing) strongly influences the duration and style of eruptions. It is thought that magma loses gas as it ascends along volcanic conduits and dykes, with tuffisite veins (Heiken et al., 1988; Stasiuk et al., 1996; Tuffen et al., 2003; Tuffen and Dingwell, 2005; Tuffen et al., 2008; Castro et al., 2012b; Berlo et al., 2013; Schipper et al., 2013; Castro et al., 2014; Cabrera et al., 2015) and permeable bubble networks (Taylor et al., 1983; Eichelberger et al., 1986; Westrich and Eichelberger, 1994; Stasiuk et al., 1996; Okumura et al., 2009; Schipper et al., 2013) considered important outgassing pathways.

The formation and evolution of internal tuffisite veins is reasonably well constrained (e.g., Tuffen et al. 2003; Tuffen et al. 2005), but their outgassing capability is poorly constrained. By themselves, internal tuffisite veins may be ineffective outgassing pathways because water diffusion in rhyolitic melts is relatively sluggish (Yoshimura and Nakamura, 2008), and because the diffusive loss of water into tuffisite veins is localised and transient (Castro et al., 2012b). Therefore, the outgassing ability of internal tuffisite veins is probably most effective when they intersect bubbles (Castro et al., 2012b; Castro et al., 2014; Cabrera et al., 2015), but it is still unclear as to how internal tuffisite veins and bubbles relate to one another during intrusive magma emplacement within dykes and conduits.

Documented examples of external tuffisite veins exist (e.g., Heiken et al. 1988; Stasiuk et al. 1996), but the formation and evolution of these tuffisite veins remains poorly constrained. For instance, it is unclear how the formation of these veins is influenced by the nature of the country rock, or how their permeability evolves through time.

The formation and evolution of tuffisite veins and permeable bubble networks are not just important to consider in terms of eruption duration and style, but also in terms of short-term eruption forecasting, as these outgassing pathways are probable triggers for conduit-originating low-frequency earthquakes, which occur during eruptions, often accompanying or preceding vent activity (Miller et al., 1998; White et al., 1998; Voight et al., 1999). More specifically, some volcanic earthquakes may reflect migration of magmatic gas from bubbles into fractures (Gil Cruz and Chouet, 1997; Waite et al., 2008), and the formation and lifecycle of internal tuffisite veins (Tuffen et al., 2003; Tuffen and Dingwell, 2005).

1.3. Field studies of dykes and conduits

Previous studies of rhyolitic dykes (Walker, 1969; Almond, 1971; Ekren and Byers, 1976; Tuffen et al., 2003; Tuffen and Dingwell, 2005; Tuffen and Castro, 2009) and conduits (Reedman et al., 1987; Stasiuk et al., 1996; Kano et al., 1997), and a rhyodacitic dyke and conduit (Eichelberger et al. 1986; Heiken et al. 1988) provided insight into magmatic outgassing (**section 1.3.1.; Table 1.1.**) and welding (**section 1.3.2.; Table 1.1.**), with evidence built on textural analysis (Walker, 1969; Almond, 1971; Reedman et al., 1987; Heiken et al., 1988; Kano et al., 1997; Tuffen et al., 2003; Tuffen and Dingwell, 2005), or textural analysis and water measurements (Eichelberger et al., 1986; Stasiuk et al., 1996; Tuffen and Castro, 2009). In addition, studies of composite dykes (Guppy and Hawkes, 1925; Gibson and Walker, 1963; Walker and Skelhorn, 1966) and conduits (Eichelberger et al., 1988; Eichelberger, 1989) provided insight into intrusive magma emplacement (**section 1.3.3.**).

Table 1.1. Summary of the previous field studies of rhyolitic and rhyo-dacitic dykes and conduits.

name / location	conduit or dyke	erupted material	eruption environment	date of activity	composition	width	emplacement depth	main contribution of study	reference
n/a / Oregon, USA	dykes	pyroclastic density currents	subaerial	~5-2 Ma	rhyolite	not provided	<150 m	identified source of subaerial deposits, provided insight into regional geology, proposed that fragmented dyke-filling material welds during late effusive phases of eruptions	Walker (1969)
Sabaloka cauldron / Sudan	dykes	pyroclastic density currents	subaerial	~160 Ma	rhyolite	~50-100 m	<~1000 m	identified source of subaerial deposits, provided insight into regional geology, suggested that fragmented dyke-filling material welds via country rock relaxation	Almond (1971)
n/a / Nevada, USA	dyke	pyroclastic density currents	subaerial	25 Ma	rhyolite	60-460 m	~500 m	identified source of deposits, provided insight into regional geology	Ekren & Byers (1976)
Obsidian Dome / California, USA	conduit and dyke	pyroclastic material, followed by dome	subaerial	600 yrs ago	rhyodacite	~50 m	~400-500 m	suggested that permeable bubble networks and permeable wall rock permit lateral outgassing	Eichelberger et al. (1986)
Weolseong vent / Republic of Korea	conduit	pyroclastic density currents	subaerial	~100-70 Ma	rhyolite	400-700 m	possibly 200-400 m	proposed that conduit-filling material was deposited via agglutination with zones of shear and welding migrating towards the conduit centre with time	Reedman et al. (1987)
Obsidian Dome / California, USA	conduit and dyke	pyroclastic material, followed by dome	subaerial	600 yrs ago	rhyodacite	~50 m	~300-500 m	provided insight into the formation of external tuffisite veins	Heiken et al. (1988)
n/a / Shiotani,	conduit	pyroclastic	subaqueous	~15 Ma	rhyolite	~500-1000 m	200-1500 m	suggested that conduit-filling	Kano et al.

SW Japan		material					(water depth above vent), exposed to a depth of ~200 m below vent-top	material welds due to shedding back of hot erupted pyroclasts	(1997)
Mule Creek vent / New Mexico, USA	conduit	pyroclastic material, followed by dome	subaerial	~20 Ma	rhyolite	50-800 m	~50-350 m	suggested that shear-induced bubble coalescence may form permeable bubble networks at conduit margins and that these along with internal and external tuffisite veins permit vertical and lateral outgassing	Stasiuk et al. (1996)
Thumall / Iceland	dyke	lava	subglacial to subaerial	~70 ka	rhyolite	~10 m	~10-50 m	demonstrated that magma may repeatedly fracture and heal, and proposed that such deformation may be the trigger mechanism for hybrid earthquakes	Tuffen et al. (2003)
Thumall and Skriðugil / Iceland	dykes	lava	subglacial to subaerial	~70 ka	rhyolite	~10-20 m	~10-50 m	s.a.a. and presented a model regarding the formation and evolution of internal tuffisite veins	Tuffen & Dingell (2005)
Hrafntinnuhryggur (Obsidian Ridge) / Iceland	dyke	minor amount of pyroclastic material, followed by lava	subglacial to subaerial	~24 ka	rhyolite	~2-15 m	30-50 m (ice thickness above lava lobes), exposed to a depth of <50 m beneath lava lobes	first documented example of a rhyolitic fissure eruption beneath thin ice/firn, provided details of textures within the dyke-fed lava lobes, and estimated emplacement pressure from the dissolved water content	Tuffen & Castro (2009)

1.3.1. Outgassing pathways

Some previous field studies of dykes and conduits provided insight into magmatic outgassing; the contributions made by these studies are summarised in this section.

Eichelberger et al. (1986) measured the porosity and permeability of a dome and conduit using borehole cores from Obsidian Dome in California, and found that the dome porosity increases towards the vent, with permeability dramatically increasing at a porosity of 60 vol. %, and the conduit porosity to be ~10-20 vol. %. Based on the hornblende stability field the initial water content was estimated as being >3 wt. %. The dissolved water content was also measured and found to be ~1 and 0.1 wt. % in the conduit and dome respectively. Considering the initial and dissolved water content, the porosity, and the overburden pressure, the obsidian should be more vesicular, considering closed-system degassing under equilibrium conditions. The permeability increase at a porosity of 60 vol. % was inferred as the critical porosity at which the percolation threshold is exceeded. Eichelberger et al. envisaged that outgassing occurred during the last 500 m of ascent, with the permeable magmatic foam losing gas laterally through permeable fall-back tephra that lines the conduit margins, followed by extrusion of highly inflated and volatile-poor magma that collapsed post-extrusion.

This permeable foam model was questioned due to the lack of textural evidence for foam collapse (Friedman, 1989), but experiments later demonstrated that bubbles may collapse and leave no trace (Westrich and Eichelberger, 1994). However, textural evidence of bubble collapse in the form of microlite trains exists in subaerial rhyolitic lava flows and welded pyroclastic deposits (**Fig. 1.2.i**; Iddings, 1888; Ross and Smith, 1961; Manley, 1995; Manley, 1996; Kano et al., 1997; Tuffen and Castro, 2008; Tuffen and Castro, 2009). In addition, collapsed bubbles in subaerial rhyolitic

lava may be preserved as pale domains extending from vesicles (**Fig. 1.2.ii**; Owen et al. 2012).

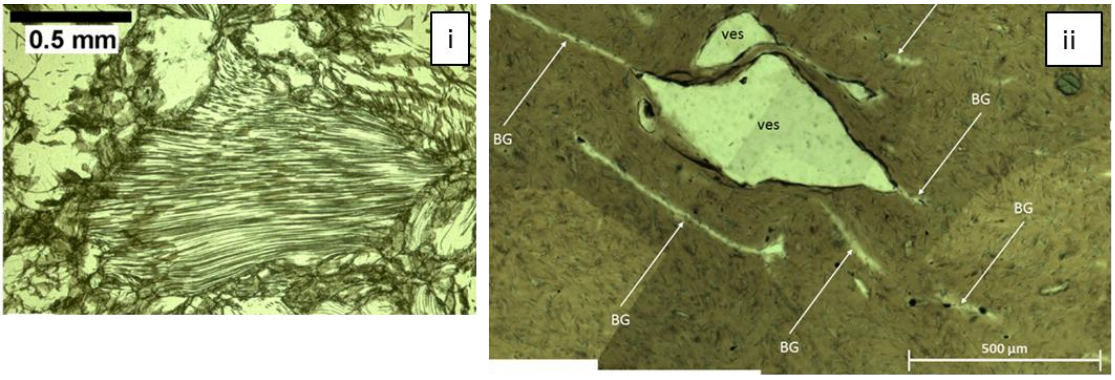

Figure 1.2. (i) Collapsed obsidian foam from Hrafntinnuhryggur, Krafla volcano, Iceland. From Tuffen and Castro (2009). **(ii)** Collapsed bubbles (labelled BG) in obsidian from Bláhnúkur, Torfajökull volcano, Iceland, note how some of the collapsed bubbles extend from the vesicles (labelled ves). From Owen et al. (2012).

A limitation of the permeable foam model is its failure to explain heterogeneous vesicle distributions within obsidian flows (Fink et al., 1992). This considered, Fink et al. suggested that bubble collapse may precede extrusion, with the magma being largely degassed and vesicle-free upon extrusion, but with post-extrusion vesiculation occurring via second boiling. In this framework, it is expected that evidence of bubble collapse may exist within dykes and conduits.

Stasiuk et al. (1996) conducted macroscopic analysis of the textures and water content within a dissected rhyolitic conduit in Mule Creek, New Mexico. This conduit consists of pyroclastic breccia next to the country rock, with the breccia being inwardly bordered by an obsidian breccia, which becomes more viscously deformed and welded inwards, and surrounds vesicle-free, intact obsidian (**Fig. 1.3.i**). The intact obsidian varies in thickness from 1 to 7 m (locally thickening into embayments), and has a gradational contact with microcrystalline rhyolite, which forms the conduit centre. The conduit contains irregular vesicles with pinch-and-swell forms towards its margins, whereas vesicles near the conduit centre are more spherical. Stasiuk et al. described interior vertical tuffisite veins within the microcrystalline rhyolite, and sub-

horizontal external tuffisite veins. The external veins are truncated by the intact obsidian and weave through the obsidian and pyroclastic breccias, and they intrude the country rock (**Fig. 1.3.i and ii**), with their position not having been influenced by pre-existing country rock fractures.

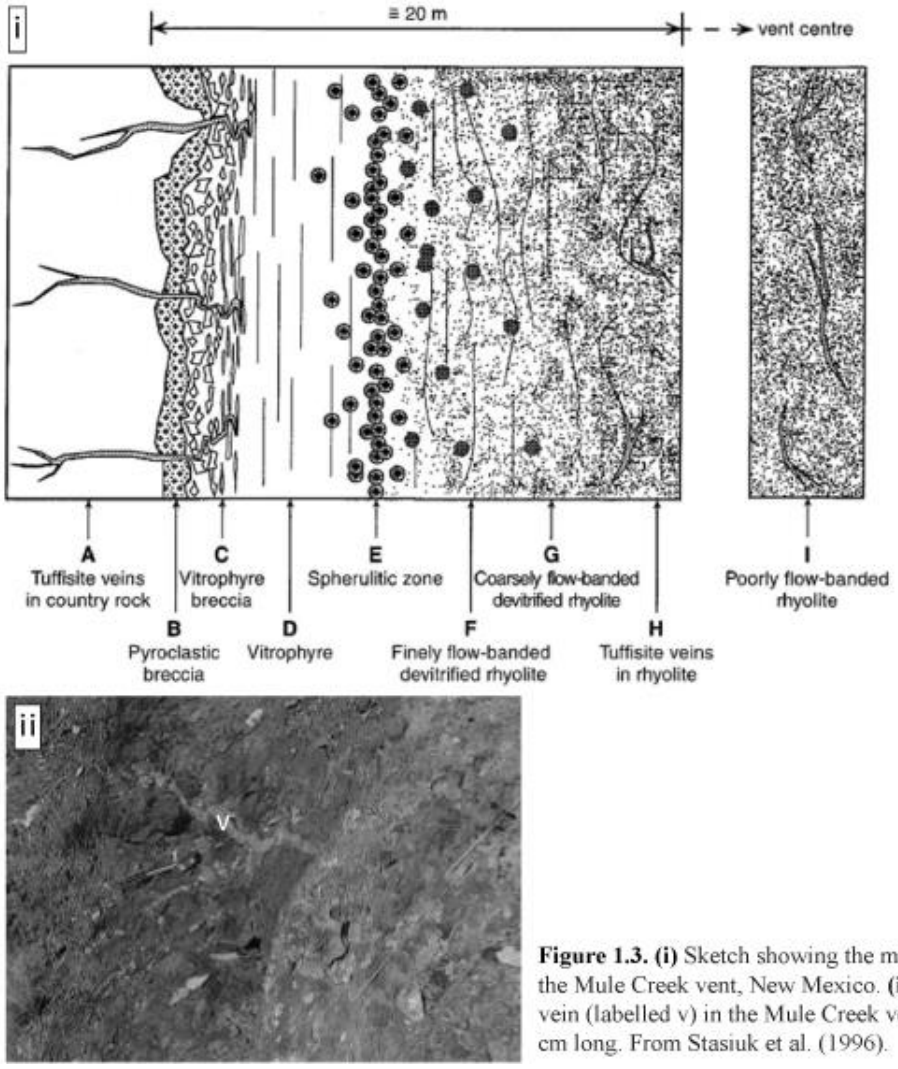

Figure 1.3. (i) Sketch showing the main textural zones in the Mule Creek vent, New Mexico. **(ii)** External tuffisite vein (labelled v) in the Mule Creek vent, hammer is 60 cm long. From Stasiuk et al. (1996).

Stasiuk et al. (1996) infer that the pyroclastic breccia formed during the explosive phase of the eruption, with the mode of deposition not described, but presumably this material was deposited from particle-laden gas currents. In contrast, the obsidian breccia is thought by the authors to have formed via autobrecciation of lava during a later effusive phase of the eruption. As the external veins weave through the obsidian autobreccia and pyroclastic breccia they must have formed after the

breccias, and were then truncated by magma that later flowed along the conduit centre (Stasiuk et al., 1996). The pre-eruptive water content of the obsidian spans ~2.5-3 wt. % (determined from melt inclusions). Considering the initial water content, the porosity of the rhyolite (~20-40 %), and the overburden pressure, Stasiuk et al. proposed that the rhyolite should be more vesicular considering closed-system degassing under equilibrium conditions. They therefore inferred that water was able to escape from the magma, and that the vesicle-free obsidian formed via bubble collapse, but no micro-textural evidence for collapse was presented. Indeed, no previous studies have documented micro-textural evidence in support of bubble collapse during magma intrusion.

Stasiuk et al. (1996) also proposed that bubble networks are important outgassing pathways, but with bubble shear at conduit margins enabling the percolation threshold to be exceeded at porosities of <<60 % - far lower than proposed by Eichelberger et al., (1986). Eichelberger et al. proposed that gas escapes from bubble networks laterally, through permeable fall-back tephra at shallow depths (<500 m), with Stasiuk et al. suggesting that tuffisite veins create localised permeability and that they are important in facilitating lateral and vertical outgassing from depths >400 m. Indeed, after the study of Eichelberger et al., Heiken et al. (1988) described external tuffisite veins at Obsidian Dome which exist at depths of ~300-500 m, forming part of the feeder dyke and conduit. In addition, internal tuffisite veins occur within shallowly (<50 m deep) dissected rhyolitic dykes (**Fig. 1.4.**), and these are thought to have been important outgassing pathways (Tuffen et al., 2003; Tuffen and Dingwell, 2005). Based on the field studies of rhyolitic dykes and conduits, both bubble networks and tuffisite veins are deemed important outgassing pathways, with internal and external veins both being important.

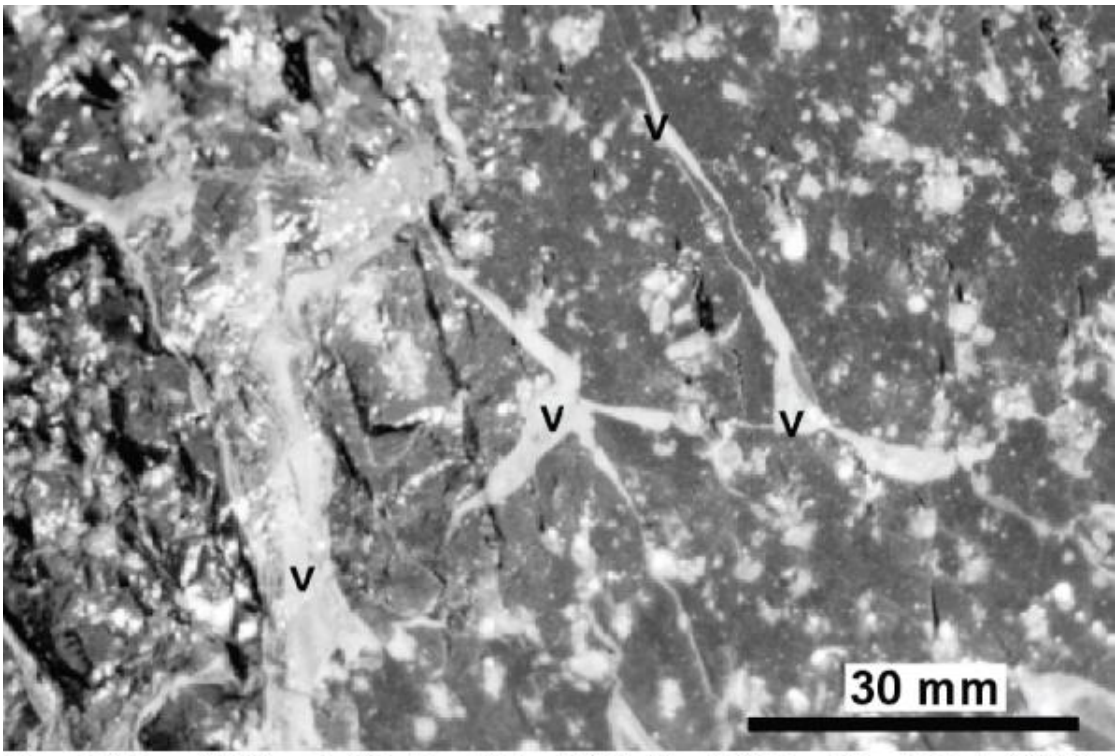

Figure 1.4. Internal tuffisite veins (v) in Thumall dyke at SE Rauðfossafjöll, Iceland. From Tuffen et al. (2003).

1.3.2. Welded rhyolitic dykes

Previous field studies of dykes and conduits have provided insight into dyke and conduit welding; the contributions made by these studies are summarised in this section.

Welding (healing) involves sintering at contact points and porosity reduction through compaction (Smith, 1960). Some early studies addressing welding of rhyolitic dykes and conduits envisaged that viscous deformation and welding occurred in the latter stages of emplacement, with near-contemporaneous welding of the whole dyke or conduit (Walker, 1969; Almond, 1971; Wolff, 1986; Kano et al., 1997). There is disagreement as to whether country rock relaxation (i.e., compression of the magma via the lateral movement of the country rock bordering the intrusion as the pressure within the intrusion decreases) plays a minor role in welding (Walker, 1969) or a more dominant role (Almond, 1971; Wolff, 1986). Reedman et al. (1987) envisaged

welding as a more progressive process, with welding migrating towards the dyke centre with time. More recently, Tuffen et al. (2003) and Tuffen and Dingwell (2005) described multiple generations of tuffisite veins in shallowly (<50 m deep) dissected welded dykes (**Fig. 1.5.**), which are interpreted as evidence for localised fracturing and healing of magma during ascent.

Figure 1.5. (i) Welded rhyolitic dyke at SE Rauðfossafjöll, Iceland. Obsidian margins (o) surround a devitrified interior, which contains vertical flow bands (arrow). From Tuffen et al. (2003). **(ii)** Microphotograph showing evidence of repeated fracture and healing of magma, sample from dyke shown in **(i)**, earlier generations of viscously deformed tuffisite veins (p3 and p4c) are truncated by a vein that formed later (p2). From Tuffen and Dingwell (2005).

1.3.3. Composite dykes

Previous field studies of compositionally zoned dykes and conduits have provided insight into the intrusive emplacement of magma; the contributions made by these studies are summarised in this section.

The Streitishvarf dyke in Eastern Iceland has mafic margins and a more silicic core, with silicic fingers enclosed within the mafic margins, thought to record multi-staged emplacement of mafic magma, closely followed by emplacement of more silicic magma (**Fig. 1.6.**; Guppy and Hawkes, 1925). Gibson and Walker (1963) and Walker and Skelhorn (1966) provided comprehensive descriptions of composite dykes, which have mafic cores and more silicic margins, with the different

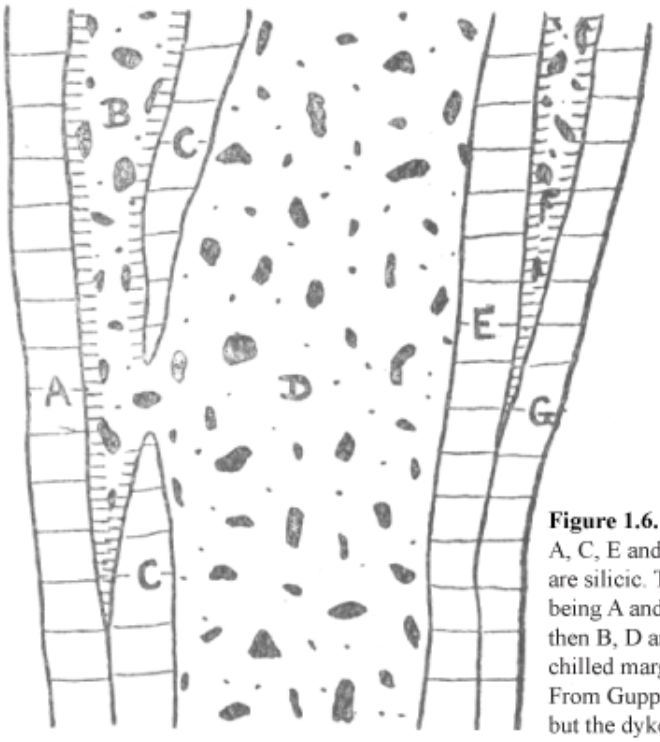

Figure 1.6. Drawing of the Streitishvarf dyke, units A, C, E and G are mafic, whereas units B, D and F are silicic. The order of intrusion is interpreted as being A and G (separately), followed by C and E, and then B, D and F. Closely spaced dashed lines indicate chilled margins, the black shapes are mafic enclaves. From Guppy and Hawkes (1925). No scale provided, but the dyke is 15-25 m wide.

compositional zones being nearly symmetrical about the dyke centres. These authors proposed that emplacement of mafic magma was closely followed by emplacement of silicic magma in the dyke centres, presenting evidence for little delay between emplacement events, including fluidal mafic enclaves in the silicic lava (**Fig. 1.7.i**),

fluidal contacts between the two lava types (**Fig. 1.7.ii**), and the general absence of chilled margins on the silicic lava, except where the mafic lava is absent. Interestingly, Walker and Skelhorn (1966) further inferred that in most instances the silicic magma was less viscous than the mafic magma, and they proposed that the water content or temperature of the silicic magma was high, accounting for why its viscosity was lower than expected. This may further indicate that there was little delay between emplacement events because the silicic magma may have been heated by the mafic magma. Some of the dykes described by Walker and Skelhorn (1966) are thought to have grown via three stages of emplacement, with the sequence of intrusion being mafic-silicic-mafic (**Fig. 1.7.iii**); again each side of the dyke is a near-mirror image of the other, with intrusive events focused in the dyke centres. The studies of composite dykes demonstrate that they can form via multi-staged emplacement, with negligible cooling occurring between emplacement events.

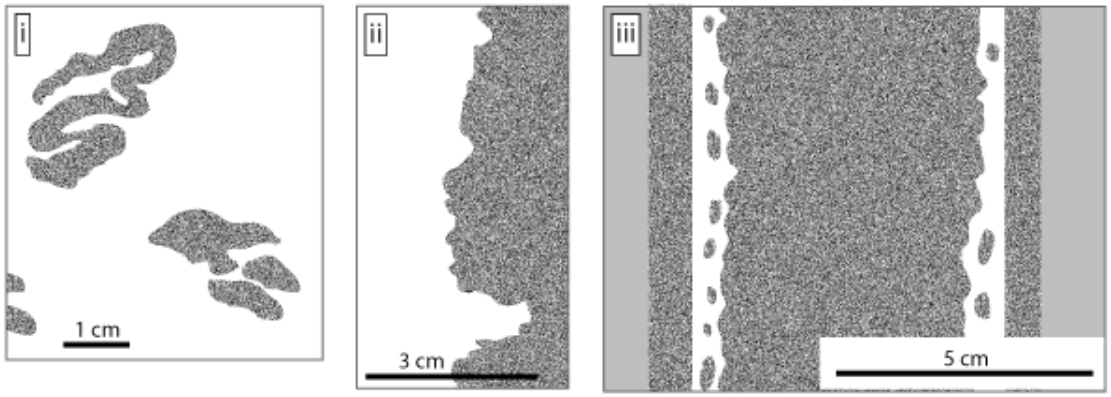

Figure 1.7. Sketches of textures within composite dykes (see main text for description), stippled, white and grey represent mafic lava, silicic lava and country rock respectively. Redrawn from Walker and Skelhorn (1966).

1.4. Explosivity of rhyolitic eruptions

The explosivity of rhyolitic volcanoes is controlled by bubble growth and the loss of magmatic water via permeable pathways (Gonnermann and Manga, 2007). In this

section, previous studies that have investigated how the loss of magmatic water influences eruption style are summarised, together with a variety of models that consider how magmatic water is lost during eruptions.

1.4.1. Influence of magmatic water loss: insight from water and hydrogen isotope measurements

Eichelberger and Westrich (1981) measured the water content in explosive and effusive material (i.e., pyroclasts and dome samples, respectively) produced during single rhyolitic eruptions, and that were thought to have undergone explosive to effusive transitions. The explosive material was found to contain more water than the effusive material, it was therefore postulated that the transitions resulted from stratification of the dissolved water content, with water-rich magma sitting above water-poor magma, and with deeper magma being erupted through time. However, shortly after this study it became apparent that explosive and effusive material from individual rhyolitic eruptions can have the same pre-eruptive water content, with different eruption styles representing different degrees of water loss, rather than volatile stratification (Taylor et al., 1983). Taylor et al. measured hydrogen to deuterium ratios (D/H) and total dissolved water concentrations (H_2O_t) in the eruptive products from rhyolitic volcanoes which were thought to have undergone explosive to effusive transitions. Deuterium enters the gas phase more readily than hydrogen, water exsolution will thus reduce D/H (Taylor et al., 1983). Taylor et al. presented two end member degassing models, named the closed- and open-system degassing models; in a closed-system exsolved magmatic gases do not escape from the system, whereas in an open-system they do escape. Assuming equilibrium conditions a closed-system will produce a subtle decrease in D/H, as the water content of the melt decreases (i.e., as bubbles grow during ascent). In contrast, the open-system model assumes continued

escape of exsolved water, producing a more substantial decrease in D/H. Taylor et al. found H_2O_t and D/H to be higher in the explosive material, relative to the effusive material, which was best described by open-system degassing. It was therefore proposed that bubble coalescence occurred during ascent, creating permeable bubble networks, from which water escaped, and that following gas loss the bubbles collapsed.

Newman et al. (1988) refined the work of Taylor et al. by recognising that isotopic fractionation of magmatic water is speciation-dependent, and that this must be considered when modelling degassing. Newman et al. measured the concentration of dissolved CO_2, molecular H_2O, and H_2O in the form of hydroxyl groups, as well as D/H, in near-vesicle-free obsidian from the ~1340 A.D. eruption of the Mono Craters in California. This eruption is thought to have progressed from a Plinian phase to a dome growth phase. As H_2O_t and D/H decrease throughout the eruptive sequence, Newman et al. proposed that the explosive phase could have consisted of open- or closed-system behaviour, with the effusive phase characterised by open-system behaviour (**Fig. 1.8.i and ii**). However, the explosive material has relatively high CO_2-H_2O_t ratios, which is indicative of closed-system behaviour, as CO_2 is less soluble than H_2O at any given depth (i.e., pressure), and so open-system degassing should have resulted in lower CO_2/H_2O_t (**Fig. 1.8.iii**). To explain the H_2O_t decrease throughout the explosive phase Newman et al. suggested that the fragmentation surface migrated upwards with time, with quenched fragments scavenged from the conduit walls, and that the H_2O_t content records depth (i.e., pressure) in the conduit.

Rust et al. (2004) challenged the Newman et al. model after modelling CO_2-H_2O degassing systematics using the Newman et al. data, together with further H_2O_t and CO_2 measurements, and micro-textural analyses of Mono Crater samples, stating

that the closed-system model requires unreasonably high (>1 wt. %) CO_2 concentrations in the parent melt. Instead, Rust et al. proposed that autobrecciation at the conduit margins formed permeable zones, enabling open-system degassing and the influx of deep-sourced CO_2-rich vapour. The Rust et al. model depicts a switch from open-system degassing with CO_2-buffering (explosive phase), to open-system degassing (effusive phase), explaining the decrease in D/H and H_2O_t throughout the eruption sequence, and relatively high CO_2/H_2O_t of the explosive phase.

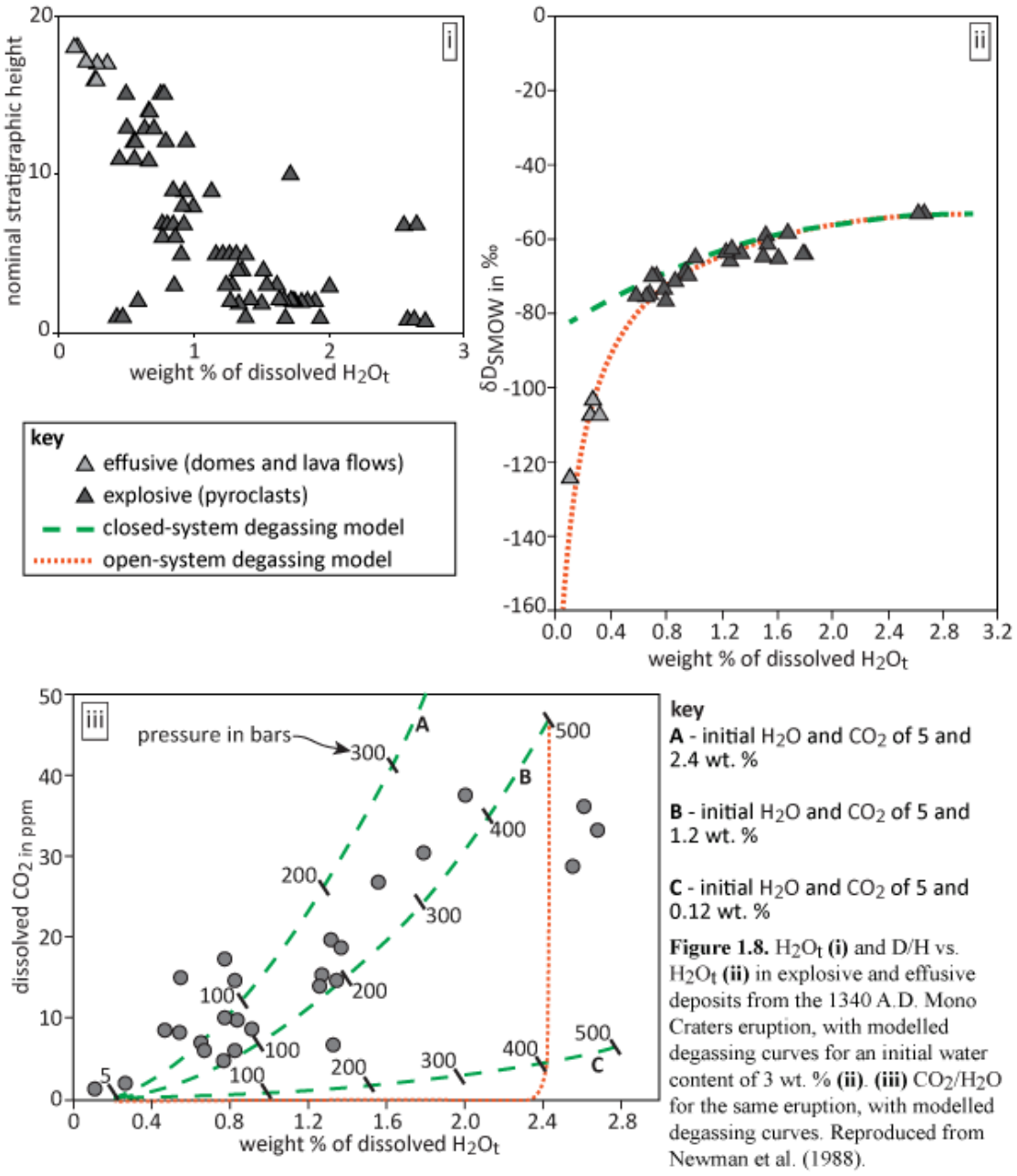

Figure 1.8. H_2O_t **(i)** and D/H vs. H_2O_t **(ii)** in explosive and effusive deposits from the 1340 A.D. Mono Craters eruption, with modelled degassing curves for an initial water content of 3 wt. % **(ii)**. **(iii)** CO_2/H_2O for the same eruption, with modelled degassing curves. Reproduced from Newman et al. (1988).

Prior to the study of Rust et al., Taylor et al. (1991) measured D/H and H_2O_t in samples from the ~600 year B.P. explosive-effusive Obsidian Dome eruption, with samples including pyroclasts, dome lava, and borehole cores from the unexposed conduit. The D/H-H_2O_t trends were best-fit by a degassing model intermediate to the closed- and open-system models, namely the multi-step degassing model. The multi-step model involves multiple open-system phases that are interspersed with periods of gas retention in a closed-system.

Recently, Castro et al. (2014) measured H_2O_t and D/H in a suite of texturally diverse rhyolitic samples from the 2008 rhyolitic eruption of Chaitén. The D/H-H_2O relations were similarly best-fit by a multi-step degassing model (**Fig. 1.9.**), and comparison of H_2O_t and D/H between clasts housed in tuffisite veins and their host obsidian indicate a variety of degassing histories (**Table 1.2.**), adding to the broader picture of multi-step degassing. Castro et al. (2012b; 2014) infer that degassing is most efficient when tuffisite veins intersect exsolved batches of volatiles, i.e., pre-existing bubbles in magma.

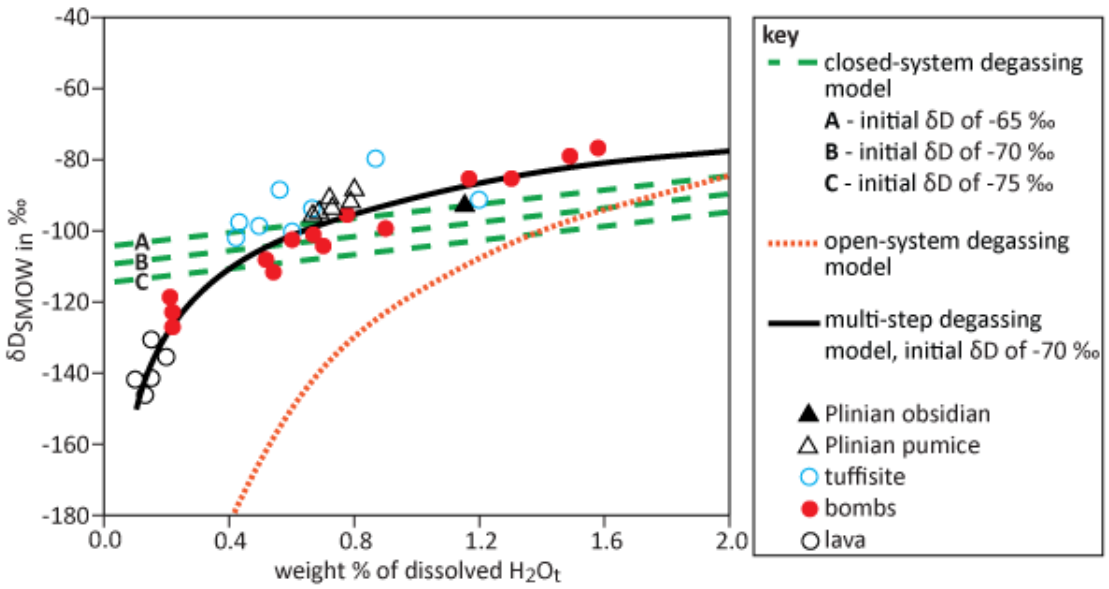

Figure 1.9. D/H vs. H_2O_t for samples from Chaitén, with modelled degassing curves for a pre-eruptive water content of 4 wt. %. Reproduced from Castro et al. (2014).

Table 1.2. Findings and interpretations summarised from Castro et al. (2014) regarding H_2O_t and D/H measurements made in clasts within tuffisite veins from Chaitén and their host obsidian. Pressure estimates assume equilibrium conditions (Newman and Lowenstern 2002).

findings	interpretations
clasts in tuffisite vein are depleted in H_2O_t relative to host	transient pressure drop of ~3 MPa during vein opening
clasts in tuffisite vein are enriched in H_2O_t relative to host	overpressure in vein due to blockage
	clasts transported upwards in vein from a depth of ~500 m
clasts in tuffisite vein have similar H_2O_t and D/H to host	consistent with closed-system degassing model, clasts had similar degassing history to host
clasts in tuffisite vein are depleted in H_2O_t relative to host and have higher D/H than host	transient pressure drop in vein enabled water loss from clasts, buffered by influx of a D-rich vapour (sourced from less degassed deeper magma batch, or from hydrous host magma)

1.4.2. Influence of magmatic water loss: insight from observations of eruptions

Conceptual models of rhyolitic eruptions that are based on ancient deposits involve discrete explosive and effusive phases, driven by water retention and loss respectively (Taylor et al., 1983; Eichelberger et al., 1986; Newman et al., 1988; Dobson et al., 1989; Taylor et al., 1991; Rust et al., 2004). However, recent observations of rhyolitic eruptions demonstrate that the outgassing process needed to create water-poor, effusive lava is itself explosive, leading to simultaneous explosive and effusive activity (Lara, 2009; Carn et al., 2009; Castro et al., 2012b; Castro et al., 2013; Schipper et al., 2013; Castro et al., 2014; **Fig. 1.10.**).

The Chaitén (Castro and Dingwell, 2009; Lara, 2009; Carn et al., 2009) and Cordón Caulle eruptions (Schipper et al., 2013) both commenced with Plinian activity, followed by hybrid behaviour; lava effusion, coupled with the explosive ejection of pyroclasts. Based on observations of the Cordón Caulle eruption, and the textures, water content, porosity and permeability of pyroclasts, Schipper et al. (2013) link discrete types of vent activity to different conduit processes (**Fig. 1.11.i**). These authors suggested that gas venting was fed by permeable bubble networks, which formed via shear-induced bubble coalescence, with network porosity reaching 30 vol.

% at a depth of 1-2 km (**Fig. 1.11.ii**), which is now thought to be the critical porosity required to exceed the percolation threshold (Saar and Manga, 1999; Blower, 2001; Okumura et al., 2009). Schipper et al. also inferred that pulsatory jets of particles and

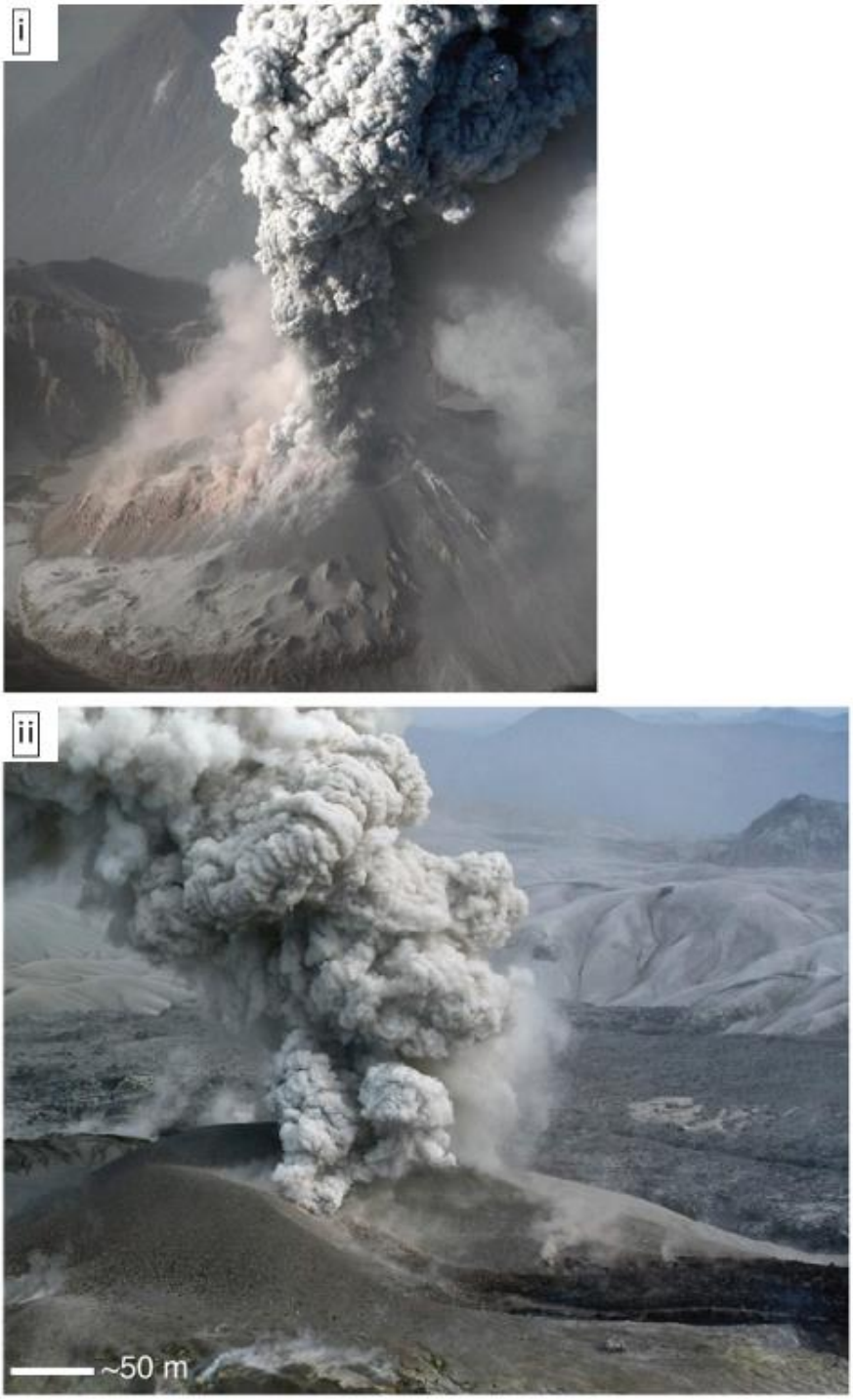

Figure 1.10. Simultaneous explosive and effusive eruption behaviour during the rhyolitic eruptions of Chaitén **(i)** and Cordón Caulle **(ii)**. The lava in **(i)** is the red material on the left and in **(ii)** the lava is the black material in the foreground and black landscape in the background. The lava in **(i)** is ~300 m long. **(i)** Photo by Jeffrey Marso, USGS. **(ii)** Photo by Alejandro Sotomayer. Both images are from Castro et al. (2014).

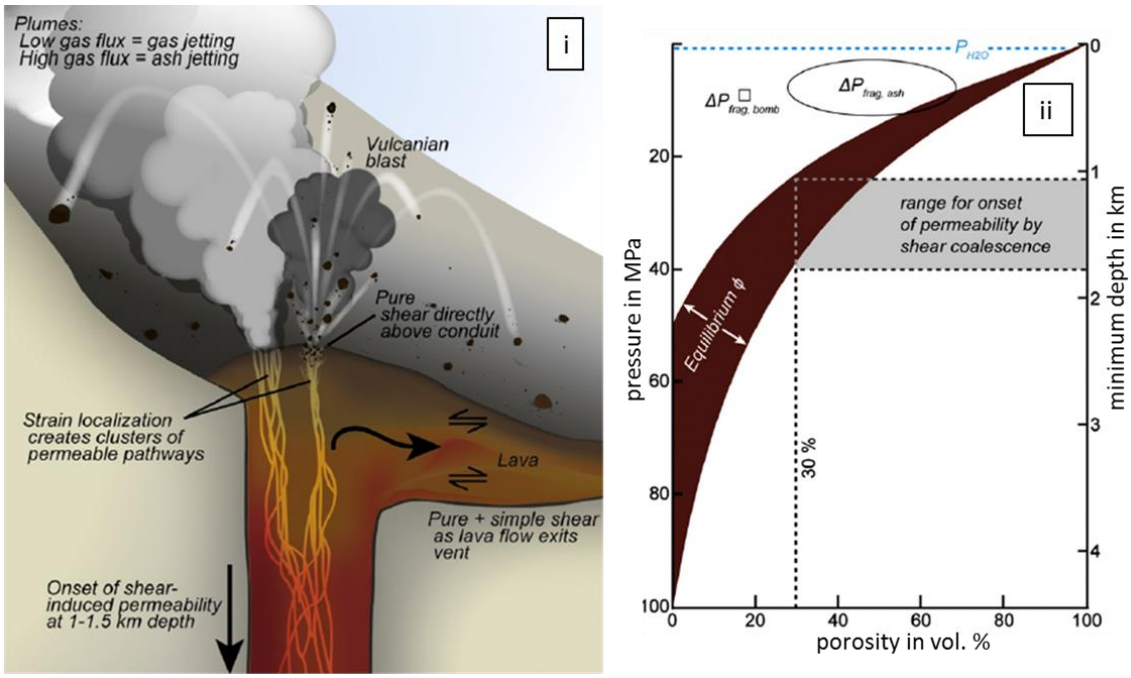

Figure 1.11. (i) Schematic cross section through the Cordón Caulle vent and shallow conduit, during hybrid explosive-effusive behaviour. **(ii)** Estimated depth at which permeable bubble networks reached a porosity of 30 vol. % and exceeded the percolation threshold, during ascent of the Cordón Caulle magma, see Schipper et al., (2013) for further details. Both images are from Schipper et al., (2013).

gas (the surface expression of tuffisite veins) occurred when bubbles networks could not keep pace with volatile exsolution, with brittle failure resulting from shear localisation and increases in the strain rate. Lastly, Schipper et al. proposed that Vulcanian explosions occurred when neither the tuffisite veins nor bubble networks could keep pace with the supply of volatiles from deeper in the conduit. Hiatuses between particle-gas venting from individual sub-vents spanned seconds to minutes, providing an approximation for the reactivation time of individual tuffisite veins.

Based on the low water content (0.14-0.25 wt. %) of the pyroclasts, and the solubility-pressure relationship of water (Newman and Lowenstern, 2002), Schipper et al. (2013) proposed that brittle failure was confined to depths of 10-20 m. The authors further proposed that the lava cap played a key role in restricting upper-conduit permeability, enabling gas pressure to build, with influxes of volatile-rich magma from depth also contributing to pressurisation. The Cordón Caulle eruption further

highlights the instrumental role played by bubble networks and tuffisite veins in the loss of magmatic water and eruption behaviour of rhyolitic volcanoes.

1.4.3. Influence of the ascent rate and estimates of ascent rates

The relationship between magma ascent rate and explosivity is not trivial. When magma ascends slowly there may be sufficient time for bubble growth and coalescence, with resultant permeable bubble networks permitting outgassing, making explosive behaviour less likely (Gonnermann and Manga, 2007). In contrast, higher ascent rates may favour explosive behaviour due to insufficient time for significant outgassing via bubble networks, resulting in greater gas overpressure within bubbles and magma fragmentation (Gonnermann and Manga, 2007). However, higher ascent rates will favour brittle failure because strain rates will be higher (Goto, 1999), with resultant internal tuffisite veins permitting outgassing (Stasiuk et al., 1996; Tuffen et al., 2003; Tuffen and Dingwell, 2005; Schipper et al., 2013) and potentially relieving overpressure (Gonnermann and Manga, 2003).

The ascent rate of magma may be assessed using the thicknesses of microlite overgrowth rims (e.g., Castro and Dingwell, 2009), or by comparing the number density and size of microlites produced during decompression experiments with natural pyroclast textures (e.g. Castro and Gardner, 2008). In addition, a relative ascent rate may be established for deposits produced during a single eruption by determining microlite number densities, as decompression experiments on rhyolitic (Martel and Schmidt, 2003; Martel, 2012) and rhyodacitic melts (Brugger and Hammer, 2010) have demonstrated a positive correlation between microlite number density and decompression rate.

Because internal tuffisite veins are considered important outgassing pathways it is important to assess the conditions under which magma will fracture; this is possible when assuming shear failure by using the following brittle failure criterion, $\eta_s \times \dot{\gamma} > \sigma_m$, where η_s is the shear viscosity, $\dot{\gamma}$ is the strain rate, and σ_m is the melt's strength (Tuffen et al. 2003; see **section 1.5.1.** for the origin of this criterion). The ascent rate of magma during the 2008 rhyolitic eruption of Chaitén is well constrained (~1 m s^{-1}; Castro and Dingwell, 2009), and thus, the strain rate within the conduit may be estimated (strain rate = ascent rate / conduit radius), giving a strain rate of 0.1 s^{-1} for a 10 m conduit radius (Castro et al., 2005; Castro and Dingwell, 2009). Okumura et al. (2013) proposed that brittle failure of the Chaitén magma occurred at a depth of 1 km (**Fig. 1.12.i**), determined using the strain rate of 0.1 s^{-1}, the brittle failure criterion given above, the shear strength of bubbly rhyolite (0.3 MPa; determined in their torsional shear experiments), and by determining the shear viscosity of the Chaitén magma. Furthermore, based on the ideal gas law and the pre-eruptive water content (3-5 wt. %) Okumura et al. (2009) also suggested that rhyolitic magma may attain a porosity of 30 vol. % at a depth of ~2.5-1 km and thus exceed the percolation threshold (**Fig. 1.12.ii**). Therefore, at ascent rates of >1 m s^{-1} brittle failure may precede effective outgassing through bubble networks, resulting in the rapid ascent of undegassed magma in the conduit interior, and consequently, explosive activity, whereas at ascent rates of <0.01 m s^{-1} effective outgassing through bubble networks may precede brittle failure, with brittle failure playing a negligible role in abating explosive activity in comparison to bubble networks (Okumura et al. 2013; **Fig. 1.12.i**).

Castro and Gardner (2008) used experimentally determined microlite growth rates to determine the ascent rate of magma that produced pumice clasts during sub-

Plinian eruptions of the Inyo Domes, and found that the magma ascended slowly (a few cm per second), with the ascent rate comparable to that in the effusive latter

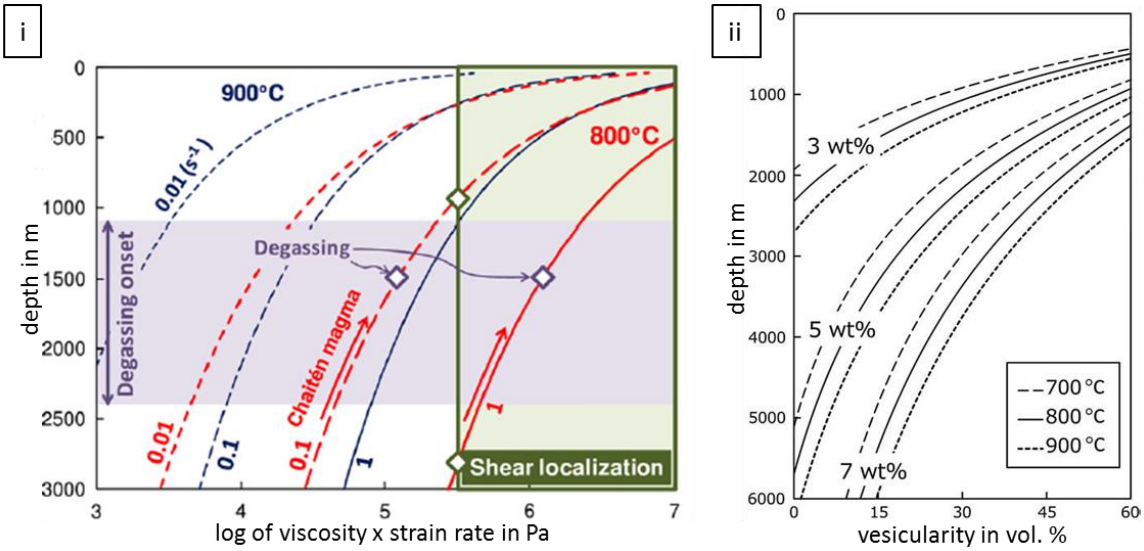

Figure 1.12. (i) Onset depths of magma degassing and shear localisation for rhyolitic magma. The solid, long-dashed and short-dashed curves represent strain rates of 1, 0.1, and 0.01 s^{-1} respectively. See main text and Okumura et al., (2013) for further details. **(ii)** Vesicularity vs. depth for rhyolitic magma with different water concentrations and temperatures. See main text and Okumura et al., (2009) for further details. **(i)** From Okumura et al., (2013). **(ii)** From Okumura et al., (2009).

stages of the eruptions. This contradicts the relationship between ascent rate and explosivity proposed by Okumura et al. (2013). Castro and Gardner (2008) suggested that the rapid unloading of a pressurised magma-filled dyke could have triggered the explosive phases of the Inyo eruptions, with explosivity decreasing because outgassing increased with time. At such sluggish ascent rates, strain rates would have been too low for brittle failure and the formation of permeable outgassing pathways via shear failure. The influence of ascent rate on explosivity will be unique to each eruption, with the study of Castro and Gardner (2008) highlighting that sluggish ascent will not always guarantee effusive activity if outgassing is prohibited.

1.5. Rheology of rhyolitic magma

The rheology of magma dictates its deformational and flow response to an applied stress. Rheology is dependent on melt temperature, geochemical composition,

pressure, the content of crystals and bubbles, the amount of stress and the strain rate, with the rheological framework defining the influence of these parameters built from experimental and field studies (Spera, 2000). Magma rheology is important because it will influence the ascent rate and whether magma experiences ductile or brittle deformation, and is thus intertwined with outgassing. For fluids, rheology is described in terms of the relationship between the applied shear stress and the resultant strain rate (**Fig. 1.13.**; Parfitt and Wilson, 2009). For a Newtonian fluid, a proportional relationship exists between the applied shear stress and the resultant strain rate, with water being a common example of a Newtonian fluid. If a fluid exhibits any deviation from this relationship it is a non-Newtonian fluid (e.g., thixotropic, dilatant or Bingham). Thixotropic and dilatant fluids are characterised by shear-thinning and shear-thickening behaviour, i.e., when stress is applied, the apparent viscosity will decrease or increase, respectively, whereas Bingham plastics possess yield strength and deformation will only occur when the applied stress exceeds this.

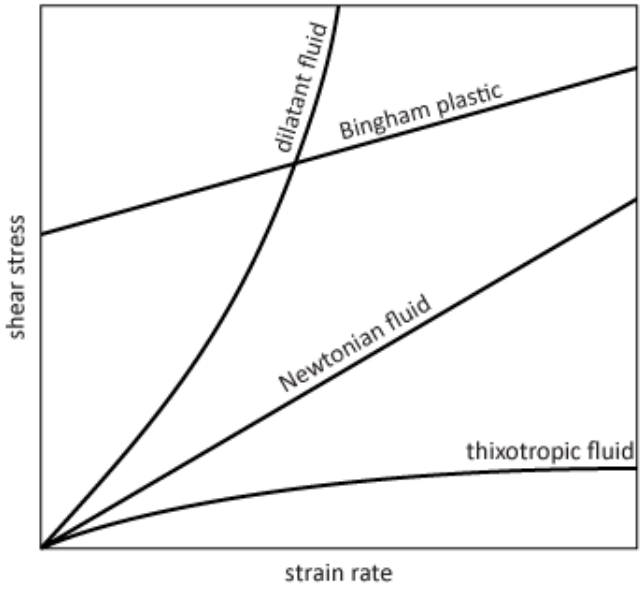

Figure 1.13. Relationship between shear stress and strain rate for fluids with different rheologies. Reproduced from Parfitt and Wilson (2009).

1.5.1. Single-phase magma

Single-phase rhyolitic magma (i.e., melt) may respond to stress in a Newtonian or non-Newtonian manner (Dingwell and Webb, 1989). During Newtonian behaviour stress will not accumulate during shear deformation, due to the proportional applied stress to resultant strain rate relationship. However, if a melt cannot respond fast enough to an applied stress, stress may accumulate, as demonstrated by deformation experiments in which silicic melts behaved as Newtonian fluids at low stresses, and non-Newtonian fluids at high stresses (Dingwell and Webb, 1989; Webb and Dingwell, 1990a; Webb and Dingwell, 1990b), with the latter characterised by shear-thinning behaviour. These authors found the structural relaxation time of a melt (r) which is exhibiting non-Newtonian viscoelastic behaviour to be in agreement with the Maxwell relation: $r = \eta_s / G$, where η_s is shear viscosity of the melt and G is the shear modulus.

Using the fibre elongation method Webb and Dingwell (1990) found that brittle failure occurred when the deformation timescale was 2 orders of magnitude less than the relaxation timescale. Therefore, assuming a shear modulus of 10 GPa (Dingwell and Webb, 1989) and considering the Maxwell relation, brittle failure will occur when $\eta_s \times \dot{\gamma} > 10^8$ Pa (Goto, 1999), where $\dot{\gamma}$ is the strain rate. This brittle failure criterion may be modified to $\eta_s \times \dot{\gamma} > \sigma_m$, where σ_m is the melt's strength (Tuffen et al., 2003). The shear modulus is relatively insensitive to melt composition (Dingwell and Webb, 1989) and the criterion is therefore applicable to all silicic melts.

The deformational response of a melt is temperature- and strain rate-dependent, and may be explained by considering the glass transition, which defines a transition from liquid to solid-like behaviour (Dingwell and Webb, 1989; Dingwell, 1996). The transition is often described as a single temperature, named the glass

transition temperature (Tg). Below Tg a melt behaves in a solid-like manner, and above Tg a melt behaves like a liquid. Considering the glass transition as a single temperature is appropriate for experiments, such as scanning calorimetry, because the timescales of such experiments are short enough for the structural relaxation timescale to be considered constant (Dingwell and Webb, 1989). However, when considering magma deformation within a conduit or dyke it is appropriate to view the transition as a curved interval in temperature-strain rate space, because long timescales are involved and structural relaxation becomes important (Dingwell and Webb, 1989; Dingwell, 1996). The glass transition interval separates liquid and solid-like fields, with the liquid field represented by high temperatures and low strain rates, and the solid-like field represented by low temperatures and high strain rates (**Fig. 1.14.**).

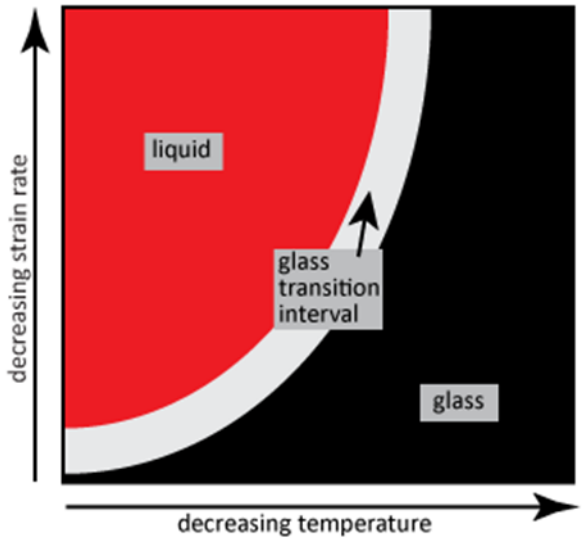

Figure 1.14. The glass transition interval in temperature-strain rate space. Reproduced from Dingwell (1996).

Dingwell (1996) hypothesised that during the formation of volcanic glasses the glass transition interval may be crossed numerous times. Multiple generations of tuffisite veins in shallowly dissected (depth <50 m) rhyolitic dykes at SE Rauðfossafjöll in Iceland (**Fig. 1.4.**) provide evidence for repeated crossing of Tg, because early-formed veins have undergone high viscous strain and are truncated by later generations of veins, indicating repeated crossing of Tg during cycles of

fracturing and healing in the shallow conduit (Tuffen et al., 2003; Tuffen and Dingwell, 2005). Gonnermann and Manga (2003, 2005) similarly described brecciated and flow banded obsidian from Big Glass Mountain Dome in California, recognising that the flow bands are brecciated clasts which experienced high viscous strain (**Fig. 1.15.**). Indeed, it was recognised some time ago that obsidian is capable of near-contemporaneous brittle and ductile behaviour (Fenner, 1920), with brittle-ductile transitions being ascribed to decreases in viscosity (Fuller, 1927). Tuffen et al. (2003) proposed that increases in the strain rate caused brittle failure in the SE Rauðfossafjöll dykes, and that brittle-ductile transitions were caused by decreases in the strain rate, or a reduction in the viscosity due to frictional heating.

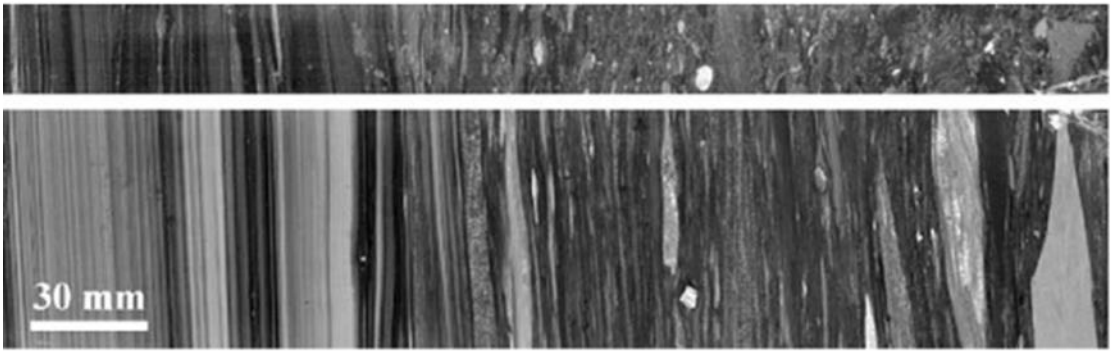

Figure 1.15. Evidence of brittle-ductile transitions in rhyolite. Two perpendicularly orientated images of an obsidian sample, the sample gradationally changes from angular clasts (right) to deformed fragments to planar flow banding (left). From Gonnermann and Manga (2005)

1.5.2. Multi-phase magma

Magma commonly consists of three phases, i.e., crystals and gas bubbles enclosed in a melt. Crystals and bubbles influence magma rheology and can result in non-Newtonian behaviour.

i) Effect of bubbles

The effect of bubbles on magma rheology depends on the gas volume fraction ($ø_b$) and the capillary number ($Ca = r \times \dot{\gamma} \times \eta_s / \Gamma$, where r is the radius of the relaxed,

undeformed bubble, $\dot{\gamma}$ is the strain rate, η_s is the melt viscosity, and Γ is surface tension). The capillary number is a ratio between the forces acting to deform a bubble, and the forces resisting deformation. Stein and Spera (2002) measured the viscosity of a bubbly rhyolitic melt during high temperature shear deformation experiments. Three flow regimes were identified, described in terms of the relative viscosity ($\eta_r = \eta_e / \eta_s$, where η_r is the relative viscosity and η_e is the bulk viscosity). When Ca was <0.1 (small spherical bubbles, low strain rates), η_r increased as $ø_b$ increased; when 0.1<Ca<10 η_r depended on Ca and $ø_b$, and when Ca was >10 (large elongate bubbles, high strain rates) η_r decreased as $ø_b$ increased. These three flow regimes are often simplified into end member regimes characterised by Ca <<1 and Ca >>1 (Llewellin et al., 2002; Llewellin and Manga, 2005, and references therein). The reason that these flow regimes exist is because bubbles distort (deflect) flow lines in the melt, and elongate bubbles will cause less distortion than spherical bubbles (Llewellin et al., 2002). In summary, bubbles are capable of inducing shear thickening, or shear-thinning behaviour, and deformed bubbles are capable of reducing magma viscosity by a factor of five (Stein and Spera, 2002). The orientation of deformed bubbles will also be important, as elongate bubbles that are aligned with the flow direction will cause a decrease in the relative viscosity in comparison to elongate bubbles of a similar size that are at an angle to the flow direction.

ii) Effect of crystals

Crystals may be considered as rigid inclusions in magma (Llewellin, 2002) and their effect on η_r depends on the crystal fraction ($ø_c$) and crystal shape. Lejeune and Richet (1995) used uniaxial compression experiments to measure the viscosity of silicic melts containing varying amounts of spherical crystals. When $ø_c$ was <0.40 the magma

behaved as a Newtonian fluid and η_r could be estimated by using the Einstein-Roscoe equation: $\eta_r = \eta_s (1 - \phi_c / \phi_m)^{-n}$, where ϕ_m and n are constants with values of 0.6 and 2.5 respectively. However, at ϕ_c >0.40 the magma behaved as a Bingham plastic, with η_r increasing as ϕ_c increased. Non-Newtonian behaviour at high crystal fractions is thought to result from crystal-crystal interactions (Lejeune and Richet 1995, and references therein). If crystals are unaligned, with high aspect ratios, the onset of non-Newtonian behaviour may occur when ϕ_c is <0.40 (Cashman and Sparks, 2013 and references therein).

1.5.3. Strength, strain rate and viscosity

The brittle failure of magma is influenced by the magma's strength and viscosity, and the strain rate. It is therefore important to constrain these parameters before attempting to determine the mechanism of brittle failure in volcanic conduits and dykes.

i) Strength

By using high temperature fibre elongation experiments the tensile strengths of bubble-free silicic melts have been estimated to be of the order of 100 MPa, and almost independent of sample composition (Webb and Dingwell, 1990a). In contrast, the tensile strength of bubbly magma was found to be only ~1 MPa, by using high temperature decrepitation experiments (Romano et al., 1996). The latter authors suggest that the lower strength of bubbly magma may be due to the presence of dehydration-related micro-cracks around bubbles.

Okumura et al. (2010) conducted high temperature shear deformation experiments on rhyolitic melts, and during deformation their samples developed bubble-free borders and bubbly cores. The authors were able to constrain the strain

rate at which their samples fractured, and also determine sample viscosity. Based on the brittle failure criterion of Tuffen et al. (2003) the authors calculated shear strengths to be 10-100 MPa and 1 MPa for bubble-free and bubbly magma respectively. In similar experiments Okumura et al. (2013) found bubbly rhyolitic magma to have a shear strength of 0.3 MPa.

High temperature deformation experiments have demonstrated that the compressive strength of bubble-free rhyolitic magma is >300 MPa (Tuffen et al., 2008). The decompressive strength of magma was investigated by Spieler et al. (2004) and Mueller et al. (2008), who conducted high temperature decompression experiments with the objective of identifying the minimum gas overpressure (internal bubble gas pressure minus the ambient pressure, i.e., the fragmentation threshold) to cause macroscopic tensile failure. Spieler et al. (2004) demonstrated that there is not a critical bubble content at which failure occurs, but instead demonstrated that near-vesicle-free samples may macroscopically fragment, with the fragmentation threshold (ΔP_{fr}) decreasing with increased porosity (**Fig. 1.16.i**). Based on their experimental results Spieler et al. proposed the following fragmentation criterion $\Delta P_{fr} = \sigma_m / ø$, where σ_m is the melt's tensile strength with a constant value of 1 MPa and ø is porosity. However, Mueller et al. (2008) found that ΔP_{fr} increases as the permeability increases (**Fig. 1.16.ii**) and proposed another fragmentation criterion, which considers porosity and permeability and is as follows $\Delta P_{fr} = \frac{a\sqrt{k} + \sigma_m}{ø}$, where k is the permeability, σ_m is given a constant value of 1.54 MPa, and a is also a constant with a value of 8.21×10^5 MPa m^{-1}. Mueller et al. state that crystallinity, bulk geochemistry and pore geometry have a negligible effect on the fragmentation threshold, with permeability being the overriding influence.

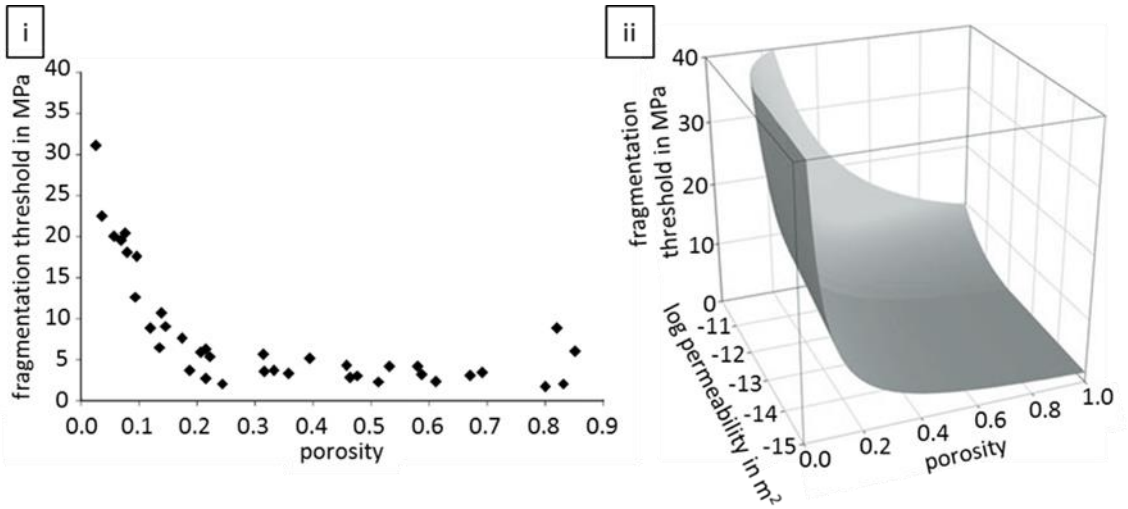

Figure 1.16. Relationship between porosity and permeability with the fragmentation threshold. **(i)** From Spieler et al. (2004). **(ii)** From Mueller et al. (2008). See main text for description.

i) Strain rate

Strain rates within rhyolitic lava flows have been estimated using three methods; one considers the inferred flow rate and ogive spacing (Fink, 1980), another considers the inferred flow rate and lava volume (Castro et al., 2002b), and the third uses the geometry of deformed vesicles (Rust et al., 2003). The latter method has also been used to estimate the strain rate within rhyolitic conduits (Rust et al., 2003), and this method requires bubbles to have been quenched during steady-state deformation. Strain rates within conduits have been independently estimated by using the ascent rate and conduit diameter (Goto, 1999; Okumura et al., 2013). These methods yielded strain rate estimates within obsidian lava flows spanning 10^{-8} - 10^{-4} s^{-1}, whereas estimates for magmas in conduits of differing compositions span 10^{-8} - 10^{-1} s^{-1} (**Table 1.3.**).

Table 1.3. Estimates of strain rates within lava flows and conduits.

lava flow or lava-filled conduit	composition	reference	methodology	strain rate (s^{-1})
flow	rhyolite	Fink (1980)	ridge spacing and emplacement rate	10^{-4} - 10^{-7}
flow	rhyolite	Castro et al. (2002)	flow rate and dome volume (data from Fink and Griffiths (1998))	10^{-8}
flow	rhyolite	Rust et al. (2003)	3D geometry of deformed vesicles	10^{-7}

spatter-fed flow	rhyolite	Rust et al. (2003)	3D geometry of deformed vesicles	10^{-6}
1 m from conduit centre	dacite	Goto et al. (1999)	conduit dimensions and ascent rate	10^{-5}
1 m from conduit centre	andesite	calculated from data provided in Voight et al. (1999) and methodology of Goto (1999)		10^{-8}-10^{-7}
conduit margin	andesite	calculated from data provided in Voight et al. (1999) and methodology of Goto (1999)		10^{-7}-10^{-6}
conduit	rhyolite	Rust et al. (2003)	3D geometry of deformed vesicles	10^{-2}
conduit	rhyolite	Tuffen et al. (2003)	used to estimate conditions of brittle failure (see references therein for source of strain rates, estimates not based on rhyolitic conduits)	10^{-2}-10^{-6}
conduit	rhyolite	Okumura et al. (2013)	conduit dimensions and ascent rate (Castro and Dingwell 2009)	10^{-1}

iii) Viscosity

Viscosity is the measure of melt resistance to stress and it partly depends on the silica content, as melt polymerisation increases with the number of Si-O-Si bonds. Rhyolitic melts are silica-rich (>69 wt. %) relative to basaltic (<52 wt. %) melts, and because of this rhyolitic melts have higher viscosities due to greater polymerisation. Melt viscosity is also strongly dependent on the water content and temperature (**Fig. 1.17.**); increases in either will act to depolymerise the melt, decreasing melt viscosity. Conversely, decreases in the water content and temperature will increase melt

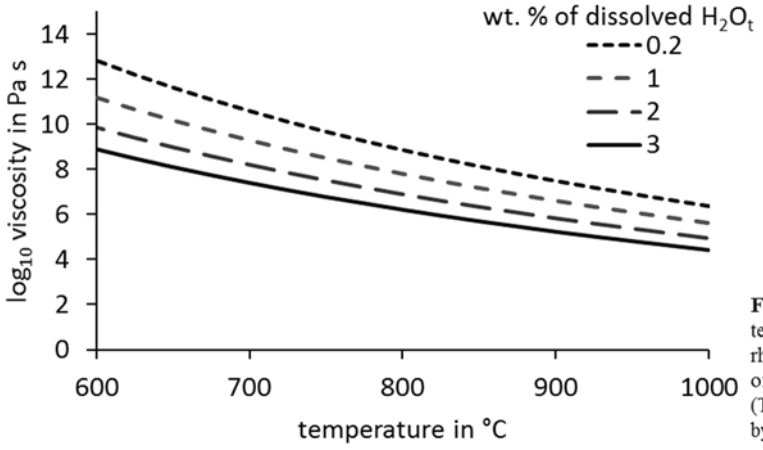

Figure 1.17. Effect of water and temperature on the viscosity of a rhyolitic melt. Based on the composition of a dyke at SE Rauðfossafjöll, Iceland (Tuffen 2001) and the model presented by Giordano et al. (2008).

viscosity. Water dissolved as hydroxyl groups acts to depolymerise the melt, and because there is a limited number of reaction sites (Doremus, 2000) the effect of water on viscosity becomes less pronounced as the water content increases (Stolper, 1982b).

The compositional and temperature dependence of melt viscosity has long been recognised (Shaw, 1963; Friedman et al., 1963; Shaw, 1972). These early studies enabled calibration of a unique method of determining lava flow viscosities, which involved determining viscosity based on the geometry of surface folds (Fink, 1980). Internal folds within obsidian lava flows have also been used to constrain flow viscosity (Castro and Cashman, 1999), with buckle fold thickness and wavelength used to calculate the relative viscosity of vesicle-free and vesicular layers. This demonstrated that obsidian flows are stratified in terms of viscosity, with vesicular layers less viscous than vesicle-free layers. The vesicular layers exhibited non-Newtonian shear thinning behaviour, whereas adjacent vesicle-free layers behaved like a Newtonian fluid.

Friedman et al. (1963) provided viscosity estimates for rhyolitic melts that spanned 10^{10} - 10^{14} Pa s (<1 wt. % dissolved H_2O_t, temperature 600-800 °C), but these temperature estimates are rather low, as temperature estimates for rhyolite include ~750-800 °C (Torfajökull volcano, Iceland; Gunnarsson et al., 1998), 800 °C (Chaitén volcano, Chile; Castro and Dingwell, 2009), 900 °C (Krafla volcano, Iceland; Elders et al., 2011, and Cordón Caulle volcano, Chile; Farquharson et al., 2015). Three viscosity models have been developed (Hess and Dingwell, 1996; Zhang et al., 2003; Giordano et al., 2008b), which are rooted in laboratory studies of viscosity. The models of Zhang et al. and Hess and Dingwell require the user to input the magmatic temperature and concentration of dissolved H_2O_t, but Giordanio's model is perhaps the most robust, as it requires the user to input the major element composition

(including the concentration of dissolved H_2O_t) and magmatic temperature. Nevertheless, a good correlation exists between viscosity estimates for the Cordón Caulle lava flow using the three different models, with estimates for the melt spanning ~10^7 - 10^{12} Pa s, and melt+crystals spanning ~10^9 - 10^{14} Pa s (**Fig. 1.18.**; Farquharson et al., 2015). The latter estimates were obtained using the melt viscosity determined from each viscosity model and a modified version of the Einstein-Roscoe equation (Pinkerton and Stevenson, 1992). Farquharson et al. further demonstrated that the estimates encompass the flow viscosity (1.21×10^{10} - 4.03×10^{10} Pa s) determined with Jeffrey's (1925) equation (**Fig. 1.18.**), which requires knowledge of flow velocity and depth, determined using a unique method of 3D imaging.

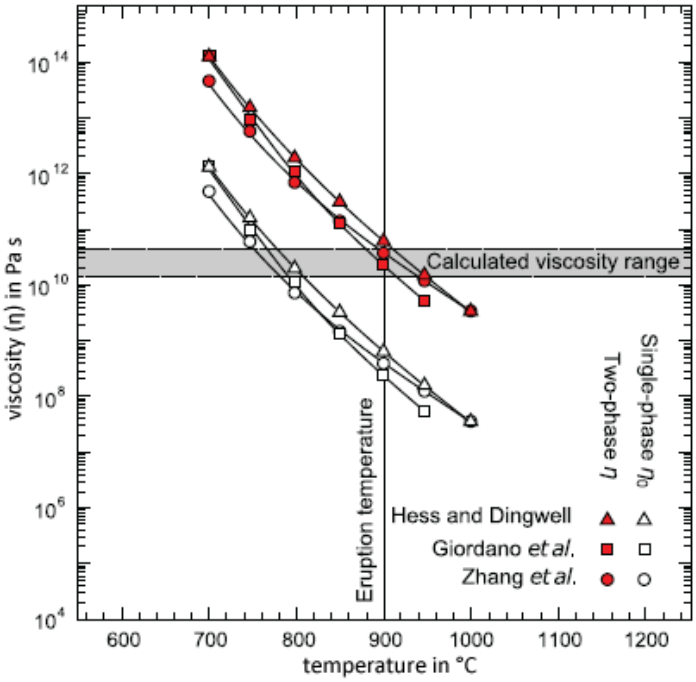

Figure 1.18. Calculated viscosity for the Cordón Caulle lava flow, from Farquharson et al., (2015). The authors made the calculations using three different viscosity models (see key) and the Jeffery (1925) equation (grey band).

1.6. Water dissolved in rhyolitic magma

Water is the principal volatile species in rhyolitic magma, and its behaviour is important to constrain because it controls vesiculation, pressurisation and explosivity, and strongly affects melt viscosity.

1.6.1. Speciation

In a rhyolitic melt water is dissolved in the form of two main species, molecular water (H_2O_m) and hydroxyl (OH^-) groups (associated with Al, Si, or other cations), with the combined concentration of these two species giving the total water content (H_2O_t; Stolper 1982a). H_2O_m is not bound to the melt's silicate polymer framework, unlike OH^- (Stolper, 1982a). Based on the following equilibrium equation $H_2O_m + O \rightleftharpoons 2OH^-$ it is thought that H_2O_m reacts with bridging anhydrous oxygen atoms (O) in the network, forming two OH^- groups (Stolper, 1982a, 1982b; Zhang et al., 1995). Because OH^- groups are bound to the melt network H_2O_m is the dominant diffusive species, and following H_2O_m diffusion OH^- concentration gradients form as OH^- reconverts to H_2O_m, re-establishing species equilibrium (Stolper, 1982b; McIntosh et al., 2014b). The species interconversion rate is temperature-dependant, as network bonds are broken more easily at higher temperatures (Mott, 1987). For example, Zhang et al. (1995) experimentally studied the kinetics of water species interconversion finding that the time taken to reach species equilibrium is dependent on the temperature and water content. In these experiments rhyolitic melts containing ~0.5-2 wt. % H_2O_t reached species-equilibrium after ~20 seconds to 6 minutes at 600 °C, and ~2 hours at 500 °C, with equilibrium not reached at temperatures <500 °C. Zhang et al. (2000) found that the interconversion rate is insensitive to pressure when the pressure is <500 MPa.

Stolper (1982a) measured water speciation in a range of natural and synthetic samples which had experienced different quenching histories, and demonstrated that the concentrations of H_2O_m and OH^- are dependent on H_2O_t. For instance, when the H_2O_t content is low OH^- is the dominant species, whereas at high H_2O_t concentrations H_2O_m is dominant (**Fig. 1.19.i**); the OH^- content plateaus at high H_2O_t concentrations

because of the limited number of available reaction sites (Doremus, 2000). The relative concentrations of H_2O_m and OH^- are near-independent of sample composition for silicate melts, as demonstrated by speciation measurements for samples of different compositions (**Fig. 1.19.i**; Stolper, 1982a). The samples used by Stolper (1982a) had probably achieved species equilibrium because of the rapidity of species interconversion at high temperatures, unless quenching rates were shorter than a few seconds. Nowak and Behrens (2001) conducted high temperature measurements of OH^- and H_2O_t concentrations in rhyolitic melts, and showed OH^- concentrations to be temperature-dependent (**Fig. 1.19.ii**).

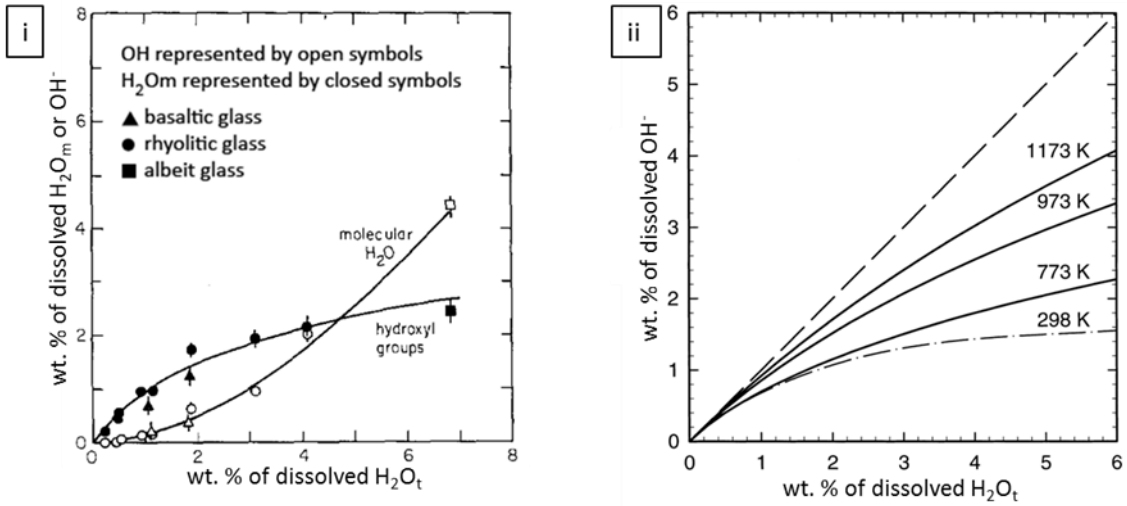

Figure 1.19. Speciation models. **(i)** From Stolper (1982a). **(ii)** From Nowak and Behrens (2001).

Volcanic glasses can become hydrated during post-magmatic alteration (Roulia et al., 2006; Denton et al., 2009; Denton et al., 2012), with water being added as H_2O_m, resulting in hydrated glasses having higher H_2O_m-H_2O_t ratios than non-hydrated glasses (Stolper, 1982b; see figure 5 in Owen et al., 2012). The temperature during post-magmatic hydration is probably low enough to preclude any species interconversion (Stolper, 1982b). The concentration of OH^- may thus be used in conjunction with speciation models (Stopler, 1982a; Nowak and Behrens, 2001; **Fig. 1.19.**) to determine the magmatic H_2O_t concentration. The Nowak and Behrens (2001)

speciation model (**Fig. 1.19.ii**) represents speciation values at magmatic temperatures and should therefore only be used for samples that quenched in less than a few seconds, i.e., in samples in which high temperature species equilibrium was preserved. In contrast, Stopler's (1982a) model (**Fig. 1.19.i**) probably provides the species equilibrium values at ~Tg, i.e., when species interconversion stopped (the exact temperature at which interconversion stops is currently unresolved), and is thus more applicable to slowly-cooled dissected dykes and conduits.

1.6.2. Solubility and solubility models

It has long been understood that water solubility is pressure- and temperature-dependant (Goranson, 1931), with solubility decreasing as the temperature increases and as the pressure decreases (**Fig. 1.20.**). In recent years, numerous models have been presented to model water solubility as a function of pressure and temperature (see Moore, 2008 for a review).

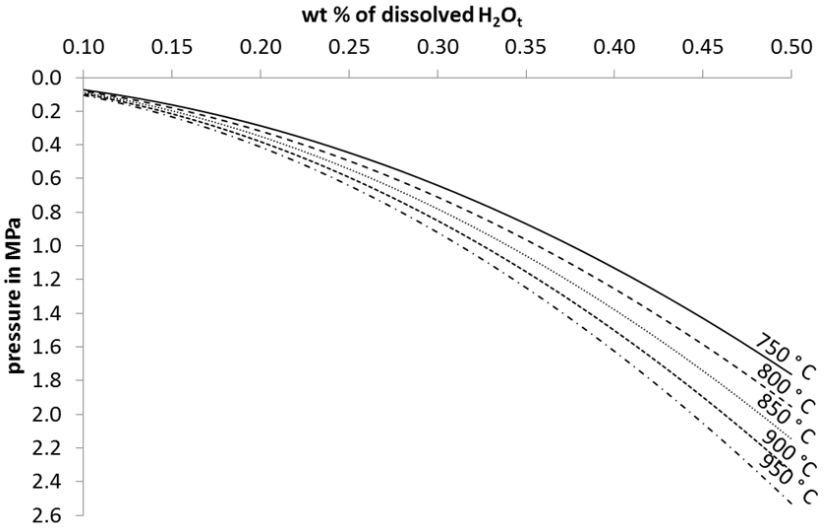

Figure 1.20. Water solubility as a function of pressure and temperature for a generic rhyolite, produced using VolatileCalc (Newman and Lowenstern 2002).

Moore et al. (1998) presented a solubility model, but this does not account for the influence of CO_2 on water solubility, which leads to an apparent decrease in water solubility at a given pressure (Newman and Lowenstern, 2002). Even small amounts

(several to tens of ppm) of CO_2 will affect H_2O solubility (Tuffen et al., 2010). Papale (1999) presented a solubility model which requires the user to input the melt's major element composition, as different elements will influence water solubility. For instance, H_2O solubility will decrease as the K_2O content increases (Papale et al., 2006). However, Newman and Lowenstern (2002) presented a solubility model (VolatileCalc) that was intentionally limited to a generic rhyolite because the effect of different elements on water solubility remains poorly understood. However, VolatileCalc can calculate water solubility for a range of basaltic compositions because more is known about the effect of major elements on water solubility for basalts (Dixon and Stopler, 1995; Dixon et al., 1995; Dixon, 1997)..

For rhyolite, VolatileCalc is rooted in a thermodynamic model for hydrous silicate melts (Silver and Stolper, 1985; Silver, 1988). The robustness of VolatileCalc to model H_2O-CO_2-systems over a broad range of pressures and temperatures was demonstrated by Newman and Lowenstern (2002). For instance, the model closely matches experimental studies for pressures between ~0 and 2000 bars (**Fig. 1.21.i**), and below 3000 bars there is good agreement between Moore et al.'s (1998) model and VolatileCalc for CO_2-free rhyolitic melts (**Fig. 1.21.ii**). VolatileCalc is the most

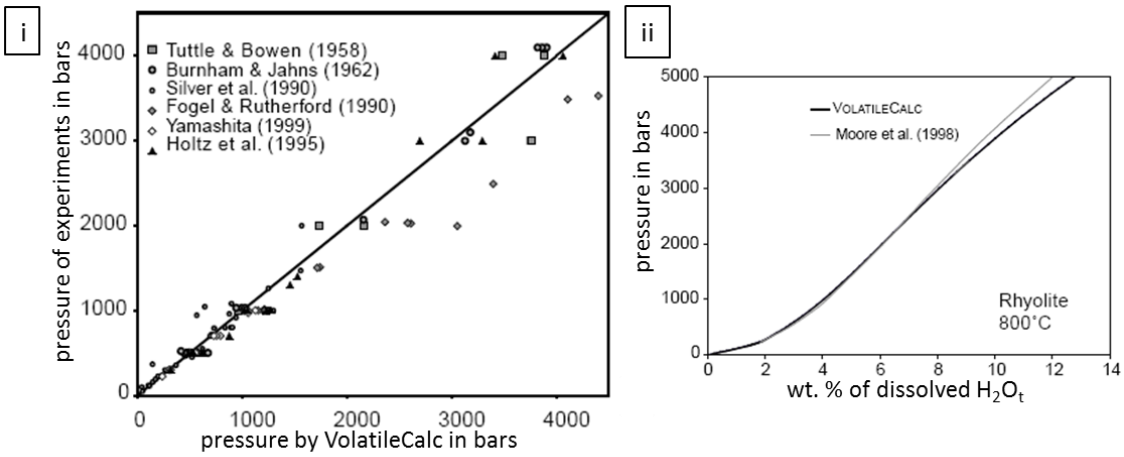

Figure 1.21. (i) Comparison of pressure calculations using VolatileCalc for reported dissolved H_2O_t concentrations of experimental run products and temperatures, Fogel and Rutherford (1990) experiments were for a H_2O-CO_2-system, all other experiments were CO_2-free. **(ii)** H_2O solubility as a function of pressure in rhyolite containing no CO_2, comparison between model of Moore et al. (1998) and VolatileCalc (Newman and Lowenstern 2002). Both graphs are from Newman and Lowenstern (2002).

commonly used solubility model because of its capability to deal with H_2O-CO_2-systems and because it is straightforward to use (Tuffen et al., 2010). Some recent studies have used VolatileCalc to reconstruct the paleo-ice thicknesses and degassing histories of subglacial rhyolitic eruptions (Tuffen et al., 2010; Owen et al., 2012; Owen et al., 2013b), to determine the degassing history of recent rhyolitic eruptions (Castro et al., 2012b; Schipper et al., 2013; Castro et al., 2014), to constrain the degassing history of an Ocean Island Basalt (Kendrick et al., 2015), and to determine the composition of fluids released from a subducted tectonic plate (Ribeiro et al., 2015).

1.6.3. Diffusivity and concentration gradients in pyroclasts

Water diffusion is required for water to escape from magma, regardless of whether the water escapes via bubble networks or tuffisite veins. For this reason it is important to understand the diffusive behaviour of water in rhyolitic melts.

For a comprehensive review regarding the diffusion of water in rhyolitic melts see Zhang and Ni (2010). Ni and Zhang (2008) conducted high-T-P-experiments to constrain the diffusivity of water in rhyolitic melts, and they found that for a rhyolitic melt containing ≤2 wt. % total water (H_2O_t), water diffusivity ($D_{H_2O_t}$) is well described by the equation below, where C is the H_2O_t content in wt. %, C_0 is 1 wt. %, P is pressure in GPa, and T is temperature in Kelvin.

$$D_{H_2O_t} = \frac{C}{C_0} \exp\left(9.5279 + 1.8875P - \frac{9698.5 + 3625.6P}{T}\right)$$

Alternatively, the equation below may be used if the pressure is unknown (Zhang et al., 1991; Zhang, 1999), and is also applicable to rhyolitic melts containing ≤2 wt. % H_2O_t.

$$D_{H_2O_t} = \frac{C}{C_0} \exp\left(-16.83 - \frac{10992}{T}\right)$$

In these formulations H_2O_m is assumed as the only diffusive species, with species equilibrium also assumed. The former assumption may be incorrect, as Behrens and Nowak (1997) suggest that OH^- may contribute to H_2O_t diffusion, but Zhang et al. (2000) state that this contribution is unresolvable from concentration gradients formed via diffusion. The latter assumption is valid because Ni and Zhang (2008) ensured that quenching times were rapid enough to preserve species equilibrium.

Water concentration gradients proximal to bubbles, spherulites, fractures and tuffisite veins in obsidian have been used to estimate the timescale of bubble growth (Castro et al., 2005) and resorption (Watkins et al., 2012; McIntosh et al., 2014a), crystal growth (Castro et al., 2008), fracturing and healing of magma (Cabrera et al., 2011) and the lifespan of tuffisite veins (Castro et al., 2012b; Berlo et al., 2013; **Fig. 1.22.; Table 1.4.**). A relatively straightforward method of calculating the time (t) taken for a concentration gradient to form over a particular length (d) is given by $t = d^2 \times D_{H_2O_t}$(Watkins et al., 2012; McIntosh et al., 2014a), and is based on Fick's first law of diffusion. This calculation assumes constant boundary conditions, and therefore does not model $D_{H_2O_t}$ changes with time (i.e., changes in *C*, *T* and *P*), which is possible with more complex diffusion models (e.g., Castro et al., 2005; Humphreys et al., 2008; Cabrera et al., 2011; Castro et al., 2012b).

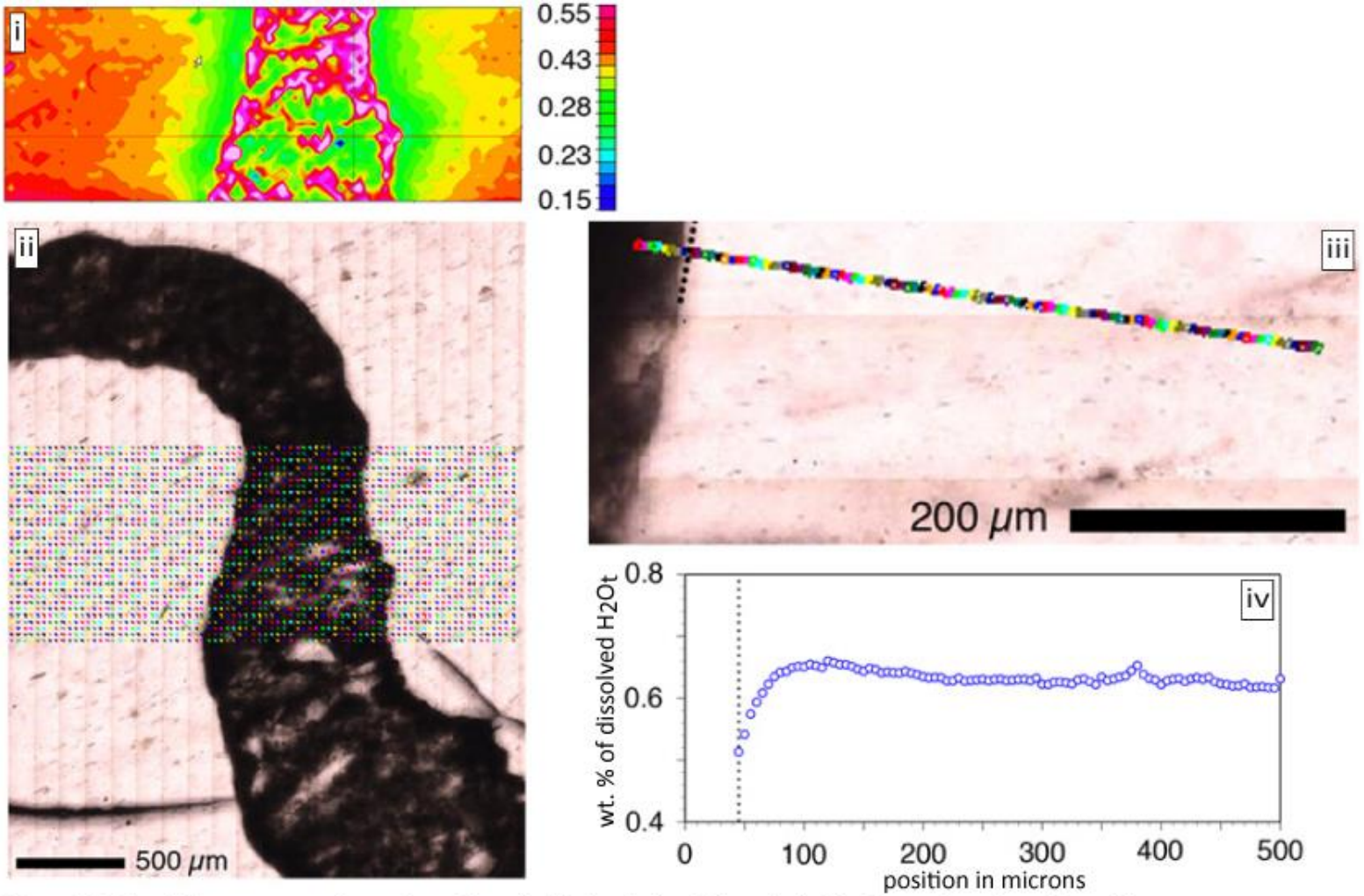

Figure 1.22. (i and iv) H_2O_t concentration gradients in host obsidian bordering tuffisite veins in Chaitén pyroclasts, the position of the measurements are shown in **ii** and **iii** respectively. These formed due the pressure being lower in the tuffisite veins than the surrounding magma, and were used by Castro et al., (2012b) to calculate the lifespan of tuffisite veins. All images are from Castro et al., (2012b); some additional labels have been added.

Table 1.4. Summary of studies that have found H_2O concentration gradients in obsidian.

sample	approx. length of concentration gradients	approx. far-field water content in wt. %	approx. variation in water content in wt. % relative to far-field content	location of concentration gradient	temperature used in diffusion model	interpretation provided by authors	reference
interlayered obsidian-pumice from lava flows	300-1000 µm	0.2 (host distal to vesicles)	-0.1	next to vesicles (water content decreases towards vesicles)	850 °C	bubble growth took 10 hrs to 15 days, with bubble growth starting after the lava flows stopped moving	Castro et al. (2005)
obsidian lava	500 µm	0.15	+0.04	next to spherulites (water content increases towards spherulites)	650 - 850 °C	water rejected during spherulite growth, with growth taking ~1 day to 2 weeks and being size- and temperature-dependant	Castro et al. (2008)
obsidian pyroclast	200-400 µm	0.6-0.8 (host distal to faults)	-0.04-0.1	next to healed faults (water content decreases towards faults)	850 °C	diffusion from fault surfaces took 10-30 mins	Cabrera et. al. (2011)
obsidian pyroclast	50-300 µm	0.75-0.95 (host distal to vein)	+0.2-0.3 (host-vein contacts)	next to partially welded tuffisite veins (water content decreases towards veins)	625 and 825 °C	transient low pressure (hydrostatic pressure) during tuffisite vein formation, with vein lifespans of 20 hrs to 10 days	Castro et al. (2012b)
obsidian pyroclast	800 µm	1.7 (host distal to vesicles)	+0.5-0.7 (host-vesicle contacts)	next to vesicles (water content increases towards vesicles)	700 °C and 850 °C	resorption over 2-7 hrs at 700 °C or 30 mins to 1.5 hrs at 850 °C caused by a pressure increase of ~10 MPa in conduit just prior to eruption, secondary bubble population around vesicle observed and thought to also be evidence for resorption	Watkins et al. (2012)

obsidian from lava-filled conduit	500 µm	1.0 (clast centre)	-0.5 (clast edge)	pumice clast in highly welded tuffisite vein (water content decreases towards clast edge)	800 °C	water decrease towards clast edge reflects diffusion from relatively water enriched and deep sourced clast, difference between the water content of clast centre and vein indicates that the clast was transported for a vertical distance of 160 m in the vein (pressure change of 40 bars)	Berlo et al. (2013)
	n/a	0.58 (host next to vein)	+0.42 (clast centre)	centre of pumice clast in highly welded vein has higher water content than the host			

1.7. Redox state of obsidian

Redox state or oxygen fugacity (fO_2) can be determined by measuring the FeO-Fe_2O_3 ratio, with a glass (or melt) being relatively reduced or oxidised if there is a greater or lower ratio respectively (Gaillard et al., 2002). Obsidian colour can be a function of the redox state, as it is widely established that green and blue obsidian are relatively reduced, compared with brown and black obsidian, with red obsidian being even more oxidised than brown and black obsidian (Fuller, 1927; Gaillard et al., 2002; Donald et al., 2006; Moriizumi et al., 2009). Obsidian can be dark or light brown, with lighter shades being relatively reduced in contrast to darker shades (Castro et al., 2009).

Early studies considering the origin of coloured flow bands in obsidian proposed that they formed via volatile diffusion during deformation. For instance, in considering red flow bands Fuller (1927) suggested that transient pressure drops form during tensional fracturing, causing volatiles to diffuse into the fractures, with volatile enrichments causing oxidation of fine particles within the fractures, but he did not specify the oxidising agent. Nelson (1981) proposed that red flow bands formed due to viscous heating along localised shear planes. This link between temperature and oxidation was previously made by Sato and Wright (1966) who measured the temperature and fO_2 of cooling lavas and suggested that oxidation occurred during cooling, as H_2 has a higher diffusivity than O_2 and H_2O, and preferential escape of H_2 will increase fO_2.

More recently, experiments on silicic melts have been used to investigate oxidation and reduction kinetics, and quantify how decreases in H_2 fugacity (fH_2) increase fO_2 (Gaillard et al., 2002), demonstrating that following H_2 loss it may take tens of hours to reach redox-equilibrium because the diffusive loss of H_2 is much faster than $Fe^{2+} \leftrightarrow Fe^{3+}$ transformations, with the transformation time positively

correlated with melt viscosity. The influence of fH_2 on fO_2 is further demonstrated by reduction haloes surrounding spherulites (**Fig. 1.23.**), which reflect H_2 liberation and rejection during growth of the anhydrous mineral assemblage that constitutes the spherulite (Castro et al., 2009).

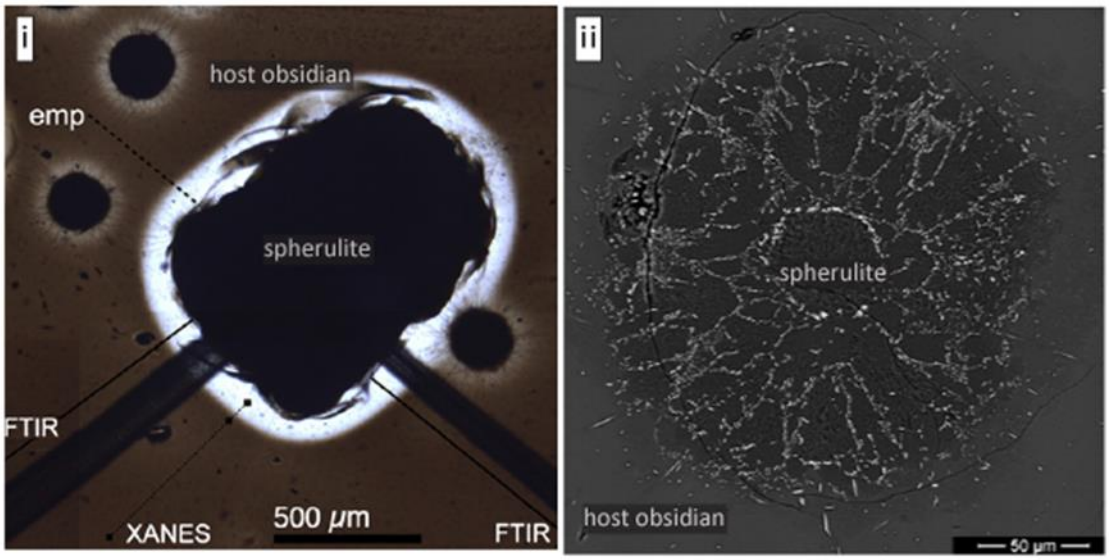

Figure 1.23. (i) Microphotograph of a spherulite with a reduction halo, from Hrafntinnuhryggur ridge, Krafla volcano, Iceland. Black dashed lines, diamonds and broad dark swaths mark the position of various analytical measurements, see Castro et al., (2009) for further details. **(ii)** Backscattered electron image of a spherulite. Images are from Castro et al., (2009).

Another method of increasing fO_2 involves the interaction between unquenched magma and atmospheric oxygen. This may be recorded by small pumice clasts and rinds of large pumice clasts that are relatively reduced, in contrast to the cores of the large pumice clasts, which is attributed to oxidation of the cores by entry of air into hot clast interiors, whilst more rapid cooling prevented oxidation of the small clasts and large clast rims (Tait et al., 1998). I suggest an alternative explanation: perhaps H_2 was lost from the small clasts and the rims of large clasts via diffusion, but not from the interiors of large clasts.

The oxidation state of lava-filled dykes could be represented by the colour of obsidian, with the colour potentially recording important information about the loss

and migration of magmatic gas and possible influx of the atmosphere during magma ascent and emplacement.

1.8. Conduit processes of rhyolitic eruptions and some consideration of more mafic eruptions

1.8.1. Magma chamber to conduit, bubble nucleation and growth

The initial ascent of magma towards Earth's surface requires a connected magmatic system in which a pressure differential exists between the deepest (i.e., the magma chamber or source region at a depth of tens of km) and shallowest (surface to depths of a few hundred meters) parts of the system, with the pressure being greatest in the deeper part. Pressure differentials may become established via shallow- or deeply-seated processes; the triggers for magma ascent may thus be referred to as top-down or bottom-up triggers respectively (Girona et al., 2015). Top-down triggers involve decompression, with possible causes including removal of a surface load e.g., partial collapse of an edifice or lava-dome (Lipman and Mullineaux, 1981; Voight et al., 2006) or degassing of shallow-seated magma (Girona et al., 2015). Bottom-up triggers involve a pressure increase within the source region, which may occur when a critical volume of magma is exceeded in a magma chamber due to the influx of fresh magma (Blake, 1981), or due to bubble nucleation and growth, with the latter triggered by the injection of relatively mafic magma into a more silicic magma body (Sparks et al., 1977; McGarvie, 1984; Blake, 1984; Mørk, 1984; McGarvie, 1985) or by crystallisation (Tait et al., 1989).

Bubble nucleation requires the melt to be supersaturated in volatiles, such as H_2O, CO_2 and SO_2 (Sparks, 1978; Navon and Lyakhovsky, 1998), and nucleation will be enhanced if crystals are present in the melt because these can act as nucleation sites

(Hurwitz and Navon, 1994; Navon and Lyakhovsky, 1998). Bubble nucleation in the presence of crystals will be heterogeneous (Hurwitz and Navon, 1994; Navon and Lyakhovsky, 1998), but if the number density of crystals is $<10^4$ per cm^3 nucleation may be homogenous, which requires greater volatile-supersaturation (Mangan and Sisson, 2000). Once nucleation has commenced bubbles will grow as volatiles diffuse through the melt and exsolve at bubble walls, which requires the melt to be volatile-saturated. Bubbly magma will be less dense than the surrounding country rock. Therefore, as magma ascends and decompresses, buoyancy may become increasingly important in promoting ascent. During decompression bubbles may also grow via gas expansion or shear-induced bubble coalescence (Burgisser and Gardner, 2004; Okumura et al., 2008), with growth being dictated by the volatile content, melt viscosity, surface tension, shear stress, and ascent rate. Equilibrium degassing is characterised by negligible volatile oversaturation, with non-equilibrium degassing occurring when bubble growth is ineffective at preventing oversaturation (Gonnermann and Manga, 2007). If magma ascent is sluggish, bubble growth is limited by decompression, whereas if ascent is rapid, diffusion is the limiting factor (Proussevitch and Sahagian, 1996).

1.8.2. Ductile deformation and the formation of permeable bubble networks

For bubble coalescence to occur a critical bubble wall thickness must be achieved, allowing bubble walls to rupture. Based on the thickness of intact and broken bubble walls in pumice clasts it has been proposed that the critical thickness for rhyolite is 1 μm (Klug and Cashman, 1996), or 0.2-1 μm (Navon and Lyakhovsky, 1998), and observations of experimentally vesiculated rhyolite have been used to suggest that the critical thickness is ~0.5 μm (Castro et al., 2012a). Three mechanisms may cause

bubble walls to become thinner, namely melt drainage, dimpling and stretching (Castro et al., 2012a). Melt drainage involves two similarly-sized adjacent bubbles deforming against one another, with capillary forces causing the inter-bubble melt to drain away (Proussevitch et al., 1993). Castro et al. (2012a) calculated that melt drainage will take ~2 days to >100 days for rhyolite, because of the long timescales involved melt drainage is not considered important during rhyolitic eruptions (Murase and McBirney, 1973; Sparks, 1978; Navon and Lyakhovsky, 1998; Castro et al., 2012a). However, dimpling and stretching are more rapid ways to thin bubble walls (Castro et al., 2012a). Dimpling may occur when differently sized bubbles are proximal to one another, because the surface tension pressure will be greater for the smaller of the two bubbles the smaller bubble may protrude into the larger bubble (Proussevitch et al., 1993; Okumura et al., 2008). Therefore, during dimpling, the inter-bubble film will be convex towards the larger bubble, with the film thinning towards its apex (Castro et al., 2012a; **Fig. 1.24.**). Stretching of inter-bubble films may occur during bubble growth and viscous deformation (Navon and Lyakhovsky, 1998). With this in mind, shear is likely to be important in promoting bubble coalescence.

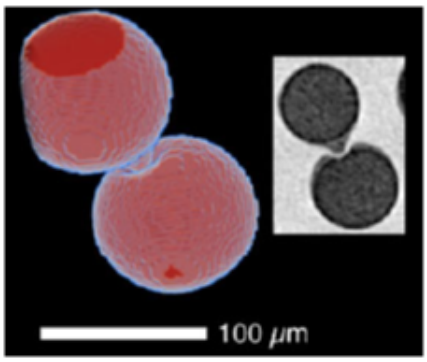

Figure 1.24. μ-CT renderings of experimentally vesiculated rhyolite. The slightly smaller upper bubble is protruding into the larger lower bubble, resulting in a dimpling texture. Note how the deformed bubble wall is thinnest at the apex. From Castro et al. (2012a).

Vesicles towards the margins of the Mule Creek dissected rhyolitic conduit have pinch-and-swell forms, whereas vesicles nearer the conduit centre are more spherical, attributed to shear stress being greater at the conduit margins, which promoted bubble coalescence (Stasiuk et al., 1996). Shear-induced bubble coalescence

in rhyolite has been observed during high-temperature decompression experiments (Burgisser and Gardner, 2004), with torsional deformation experiments on vesicular rhyolitic melts further demonstrating how shear promotes bubble coalescence (**Fig. 1.25.**; Okumura et al. 2008).

Okumura et al. (2009) built upon the experiments of Okumura et al. (2008) by measuring the permeability and porosity of quenched deformed samples. The percolation threshold for permeable gas flow was reached when the porosity obtained 30 % by volume. Based on the ideal gas law and the solubility-pressure relationship of

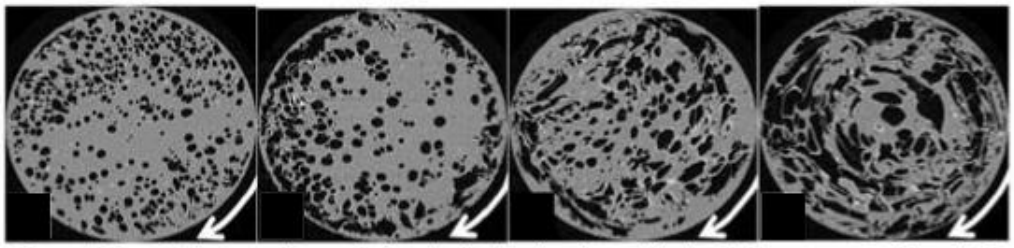

Figure 1.25. μ-CT images of quenched vesicular rhyolite, formed during high temperature shear deformation experiments, shear increases from left to right. Vesicles are black and host obsidian is grey. The image furthest to the right contains many large vesicles which formed via shear-induced bubble coalescence. See Okumura et al. (2008) for more details, this is where the images are from.

water this porosity could be attained at conduit margins at a depth of ~1-4 km for pre-eruptive water contents of 3-7 wt. % (**Fig. 1.12.ii**). Schipper et al. (2013) used a similar method to reconstruct the relationship between pressure (i.e., depth) and porosity for the Cordón Caulle 2011-12 magma, and estimated that the magma attained 30 vol. % porosity, and thus exceeded the percolation threshold, at a depth of ~1-2 km (**Fig. 1.11.ii**). Bubble networks may permit permeable gas flow at depths of a few kilometres, but what influences permeability at depths of a few hundred metres?

1.8.3. Tuffisite veins

When active, tuffisite veins facilitate the intrusive movement of gas-charged flows that are laden with particles. During vein activity clastic deposition of particles can occur (Heiken et al., 1988; Tuffen and Dingwell, 2005), which can progressively

block the vein whilst also propping it open. Tuffisite veins can feed subaerial jets of particles and gas (e.g., Schipper et al., 2013). During intrusive deposition similar structures to those in ignimbrites (e.g., Branney and Kokelaar, 2002) can form, but direct comparison between sedimentation of pyroclastic density currents and particles within fractures is complex and sometimes inappropriate, as both types of deposition will be influenced by different factors (**section 4.6.2.** provides discussion and models regarding particle deposition within fractures). Tuffisite veins are considered important outgassing pathways (Stasiuk et al., 1996; Tuffen et al., 2003; Tuffen and Dingwell, 2005; Tuffen et al., 2008; Castro et al., 2012b; Berlo et al., 2013; Castro et al., 2014; Cabrera et al., 2015), and they exist within the shallow (<500 m deep) parts of rhyolitic dykes and conduits (Heiken et al., 1988; Stasiuk et al., 1996; Tuffen et al., 2003; Tuffen and Dingwell, 2005). External tuffisite veins proximal to the Obsidian Dome dyke and conduit extend ~10 to >100 m into the country rock and are 7-40 cm wide (Heiken et al., 1988), and external veins within the dissected conduit at Mule Creek are ~1-5 cm wide and up to 40 m in length (Hugh Tuffen, pers. comm. 2012), with forking ends that are 0.1-1 cm wide (Stasiuk et al., 1996). Anastomosing networks of internal tuffisite veins in dissected Icelandic dykes are <1-80 mm wide, with some networks being ~5 m long (Tuffen and Dingwell, 2005). However, it is likely that the networks are much longer if their 3D geometry is considered. Indeed, tuffisite veins in the Chaitén conduit are thought to have extended from the surface to a depth of at least 500 m (Castro et al., 2014), and in considering a more mafic volcano, tuffisite veins within the Santiaguito conduit may extend from the surface to a depth of ~250 m (Holland et al., 2011).

Water concentration gradients in obsidian adjacent to tuffisite veins demonstrate that they can be localised and transient pressure valves, whereby

depletions (e.g., Castro et al., 2012) and enrichments (e.g., McGowan et al., 2015) in the water content record transient low and high pressures within tuffisite veins respectively, relative to the regional conduit pressure. The notion that tuffisite veins act as transient pressure valves during eruptions is supported by observations of the Cordón Caulle eruption (e.g., Schipper et al., 2013), where pulsating jets that consisted of particles and gas, or just gas were interpreted as being fed by tuffisite veins.

i) Formation of external tuffisite veins

External tuffisite veins may form via opening of new fractures in the country rock, or via opening of pre-existing fractures. For fracturing to occur, the magmatic pressure must exceed the confining pressure and the tensile strength of the country rock, whereas to prop open pre-existing fractures the magmatic pressure would just have to exceed the confining pressure. Heiken et al. (1988) analysed borehole cores obtained from depths of 300-500 m during the Obsidian Dome drilling project, and found external tuffisite veins containing similar ash shards to those formed during phreatomagmatic eruptions from Obsidian Dome. It was therefore proposed that the magma interacted with water, and that heating of groundwater created sufficiently high overpressure (5-9 MPa greater than overburden) to either fracture the country rock, or prop open pre-existing sheet fractures (i.e., sheet-like in 3D and vein-like in 2D). The external tuffisite veins at the dissected Mule Creek conduit (**Fig. 1.3.**) contain juvenile pumice clasts and are thought to have formed during the explosive phase of the eruption, and do not appear to follow pre-existing fractures in the country rock (Stasiuk et al. 1996).

ii) Formation of internal tuffisite veins via shear failure

The formation of internal tuffisite veins requires brittle failure of the melt. Assuming a shear modulus of 10 GPa (Dingwell and Webb 1989), and considering the Maxwell relation, brittle shear failure will occur when $\eta_s \times \dot{\gamma} > 10^8$ Pa where η_s and $\dot{\gamma}$ are the shear viscosity of the melt and the strain rate respectively. Goto (1999) proposed that this failure criterion may be met in volcanic conduits via increases in the ascent rate. Tuffen et al. (2003) employed a modified version of the brittle failure criterion ($\eta_s \times \dot{\gamma} > \sigma_m$, where σ_m is the magma's strength) to propose that shear failure was responsible for the formation of internal tuffisite veins, which exist in the shallow (<50 m deep) parts of dissected rhyolitic dykes (**Fig. 1.4. and 1.5.**). Gonnermann and Manga (2003) used a similar criterion to suggest that shear failure may occur at conduit margins during the last 1000 m of ascent. Evidence for shear failure of bubbly magma exists in rhyolitic pumice clasts, which contain localised zones of sheared vesicles and fractures (Marti et al., 1999; Wright and Weinberg, 2009; Schipper et al., 2013). Tuffisite veins inferred as existing at the margins of the dacitic Santiaguito conduit are also thought to have formed via shear failure (Bluth and Rose, 2004; Holland et al., 2011), with Holland et al. speculating that decompression within fracture networks caused them to evolve into tuffisite veins (**Fig. 1.26.**).

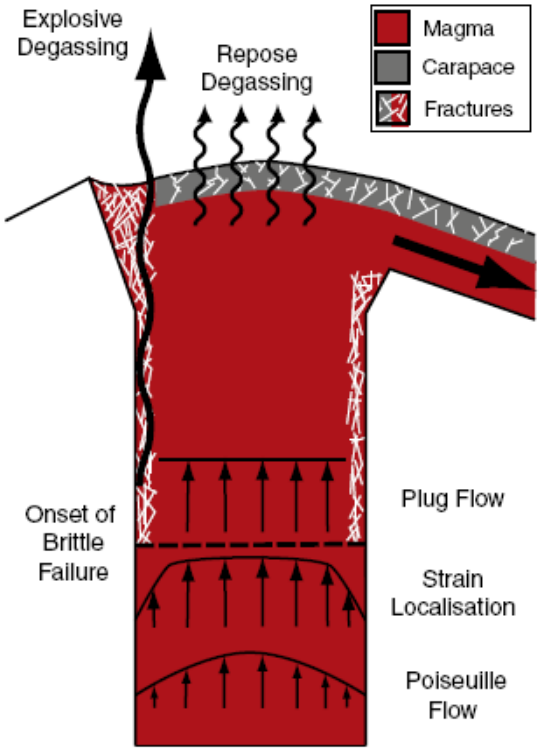

Figure 1.26. Schematic diagram depicting outgassing from the Santiaguito conduit. Image is from Holland et al. (2011). These authors propose that repose outgassing is fed by bubble networks, with more explosive outgassing being fed by tuffisite veins, which form via decompression of shear fractures at the conduit margins.

iii) Formation of internal tuffisite veins via tensile failure

McBirney and Murase (1970) inferred that tensile failure of bubble walls may occur if internal bubble pressures are sufficiently high. These authors inferred that when the bubble number density is low the melt's tensile strength will be most important in resisting failure, whereas at high number densities, surface tension will become more important. This is because the surface tension (σ) pressure of a bubble = 2σ / bubble radius, and is therefore negligible for large bubbles, only becoming significant for bubbles with a radius of <10 μm (Sparks, 1978).

Sparks (1978) noted that pumice clasts commonly have porosities of 75-85 vol. % and suggested that fragmentation will occur when the bubble content is >75 vol. %. However, he also emphasised that this does not take into account post-fragmentation bubble growth, which is now understood to occur (Thomas et al., 1994; Gardner et al., 1996). Klug and Cashman (1996; 2002) questioned the fragmentation

criterion of Sparks by highlighting that pumice clasts have porosities of ~30-95 vol. %; indeed, rhyolitic pumice porosities span ~30-80 vol. % (Wright et al., 2006; Degruyter et al., 2010b; Schipper et al., 2013). In support of the earlier questioning of the fragmentation criterion of Sparks, decompression experiments (**Fig. 1.16.**) have demonstrated that there is not a critical porosity at which failure occurs (Spieler et al., 2004; Mueller et al., 2008). Instead, failure has been shown to be a function of the difference between the internal bubble pressure and the ambient pressure (the fragmentation threshold), magma permeability and porosity (Mueller et al., 2008).

Alidibirov and Dingwell (1996) presented a conceptual model depicting the tensile failure of bubbly magma. This model envisages bubbly magma that is separated from the surface by an impervious cap rock, with bubble gas pressures in excess of atmospheric pressure. The cap rock is then rapidly removed, exposing the bubbles to atmospheric pressure, resulting in tensile failure of bubble walls. The disrupted and expanding magma is then propelled out of the conduit, and the fragmentation surface propagates downwards (**Fig. 1.27.**). However, at some depth,

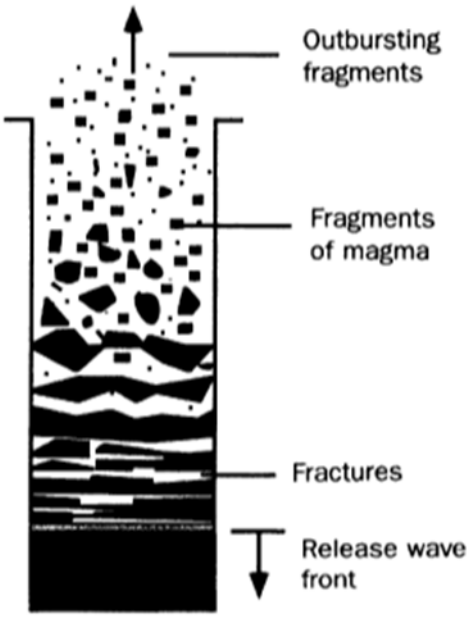

Figure 1.27. Schematic diagram of a volcanic conduit, depicting macroscopic tensile failure of magma via rapid decompression. See main text and Alidibirov and Dingwell. (1996) for further information. Image is from Alidibirov and Dingwell. (1996).

the bubble content and melt viscosity will be low enough for the melt to deform viscously, ending fragmentation.

Recently, numerical modelling has been used to suggest that microscopic tensile failure of bubble walls may occur below the fragmentation threshold (Heap et al., 2015). These authors suggest that microscopic cracks may nucleate at bubble walls and that such cracks may evolve into macroscopic cracks if they link together, intersect bubbles with high internal gas pressure, or if they cause instability and dome collapse (**Fig. 1.28.**).

The studies mentioned in this section, and in the preceding section, consider that magma failure is driven by shear or tension, with the latter occurring above or below the fragmentation threshold. Rather than ascribing fragmentation to one discrete mechanism, perhaps it is more appropriate to build a more complex model of fragmentation that allows for different trigger mechanisms.

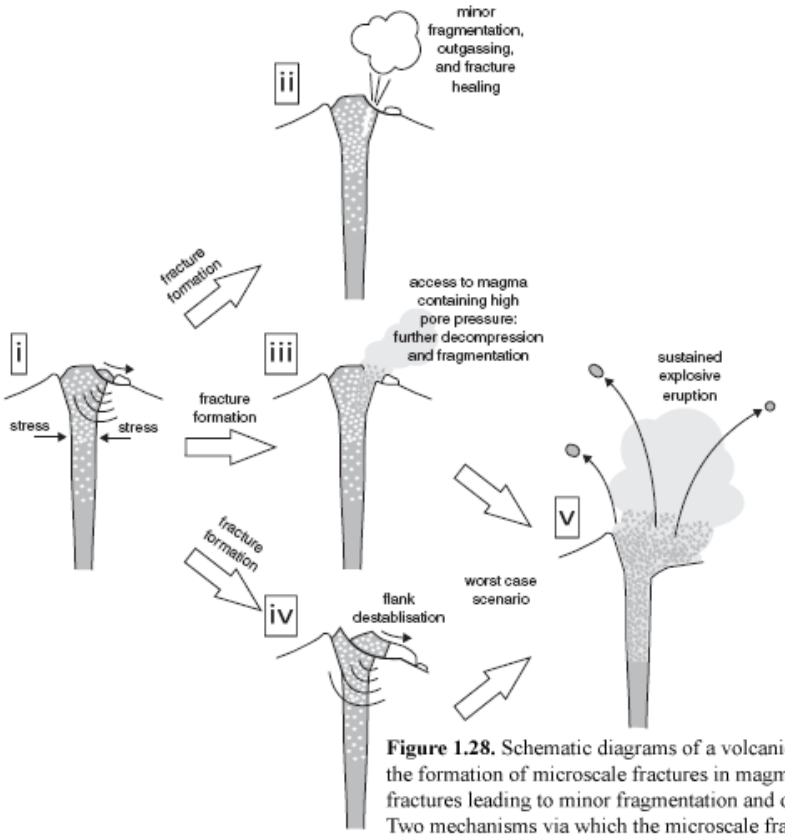

Figure 1.28. Schematic diagrams of a volcanic conduit depicting the formation of microscale fractures in magma **(i)**, with the fractures leading to minor fragmentation and outgassing **(ii)**. **(iii-iv)** Two mechanisms via which the microscale fractures may evolve into macroscopic fractures, which leads to an explosive eruption **(v)**. From Heap et al. (2015).

iv) Deposition and deformation

Particles within internal tuffisite veins are thought to be generated via abrasion of fracture walls during shear failure, and via spalling from the walls of extension fractures (Tuffen and Dingwell, 2005), with grains within some external veins inferred as having formed via magma-water interactions (e.g., Heiken et al. 1988). Internal and external tuffisite veins can contain poorly sorted, well sorted, planar, cross, graded (**Fig. 1.29.**) and truncated laminations, with the finest grains commonly occurring at vein margins (Heiken et al., 1988; Stasiuk et al., 1996; Tuffen and Dingwell, 2005). These features are thought to be sedimentary structures, recording fluidisation of particles by gas (Heiken et al., 1988; Stasiuk et al., 1996; Tuffen and Dingwell, 2005). The laminated nature of tuffisite vein-filling material is indicative of multiple depositional events, with truncated laminations recording erosive phases (Heiken et al., 1988). Variations in the size and sorting of grains within individual laminations arguably reflects temporal and spatial variations in the gas–particle ratio, and current velocity (Tuffen and Dingwell, 2005), with fracture geometry and wall roughness, clast to clast interactions, the size of clasts formed during initial fragmentation and later fragmentation during transport also likely to be important in influencing the characteristics of grains within individual laminations.

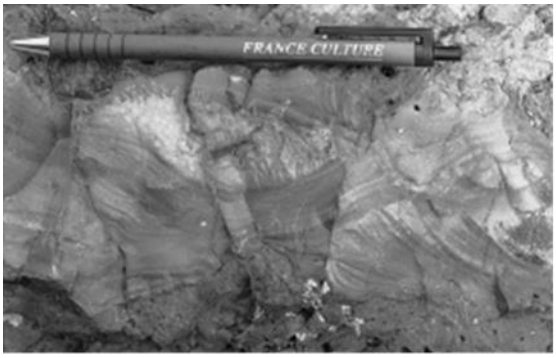

Figure 1.29. Cross and graded laminations in an external tuffisite vein at Mule Creek, New Mexico. From Stasiuk et al. (1996).

The evolution of internal tuffisite veins (**Fig. 1.30.**) has been reconstructed from macro- to micro-scale textures in dissected rhyolitic dykes (Tuffen and Dingwell 2005). Mosaic micro-structures, micro-fractures within clasts and trails of angular particles are all indicative of localised frictional stick-slip (phase 2, **Fig. 1.30.**). It is thought that following particle deposition localised shear zones develop within veins, potentially modifying and partially overprinting sedimentary structures. Indeed, rotary shear experiments have demonstrated that shear zones can cause the migration of ash particles resulting in grainsize segregation, whilst also creating localised dilatational zones with relatively high porosities (Lavallée et al., 2014). Furthermore, comminution will reduce the size of the coarsest (>10 µm) particles, with those smaller than this not being not significantly altered during slip (Kennedy and Russell, 2012). Following particle deposition and comminution the next phase (3) of tuffisite vein evolution involves stable sliding (i.e., viscous deformation) and folding of shear zones (**Fig. 1.30.**).

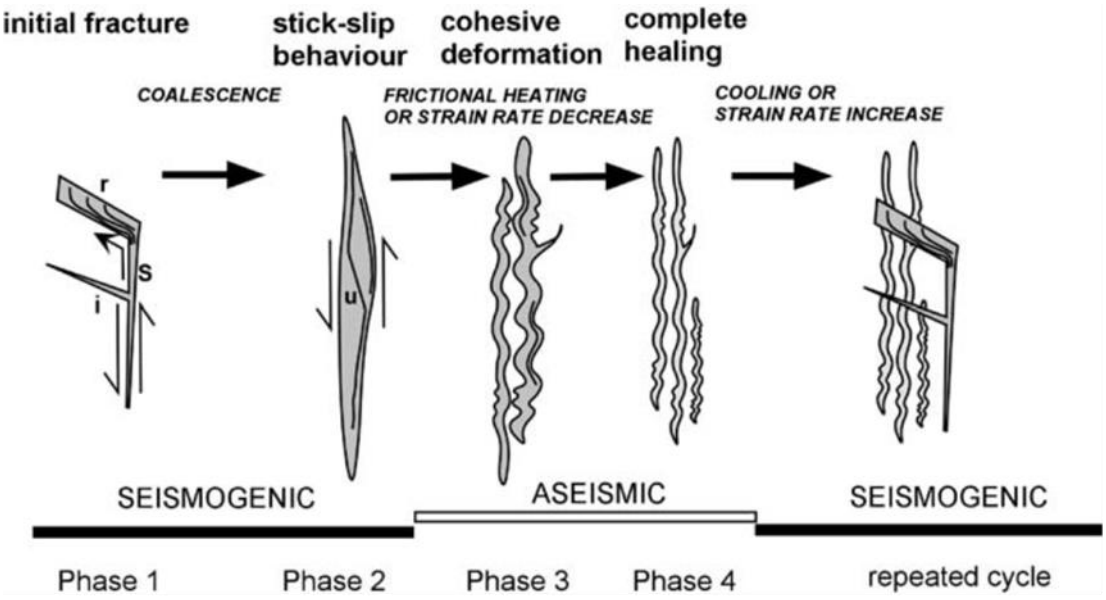

Figure 1.30. Phases of tuffisite vein evolution, S, I, R and U correspond to fault vein, injection vein, reservoir zone and ultracataclasite zone respectively. From Tuffen and Dingwell (2005).

Such brittle-ductile transitions may result from reduced strain rate or frictional heating, with frictional melting possibly promoting a return to viscous deformation. Indeed, frictional melts can act as lubricants on fault planes (Di Toro et al., 2006). In addition, stable frictional sliding may have been promoted by low-pressure dilatational zones within shear zones, which would encourage volatile exsolution, increase pore pressures, and therefore reduce frictional resistance (Lavallée et al., 2014). The viscously deformed tuffisite veins in the Icelandic dykes are cross cut by later generations of veins (Tuffen et al., 2003; Tuffen and Dingwell, 2005), indicating that if viscous heating did occur (Hess et al., 2008; Cordonnier et al., 2012b) it was ineffective at preventing ductile-brittle transitions (i.e., it was transitory). These transitions arguably result from increases in the strain rate, and represent the initiation of another cycle within the evolution of tuffisite veins (Tuffen and Dingwell, 2005).

1.8.4. Permeability reduction

i) Welding

Welding (healing) of melt particles involves sintering at contact points (**Fig. 1.31.**), and porosity reduction through compaction (Smith, 1960). Increases in the degree of

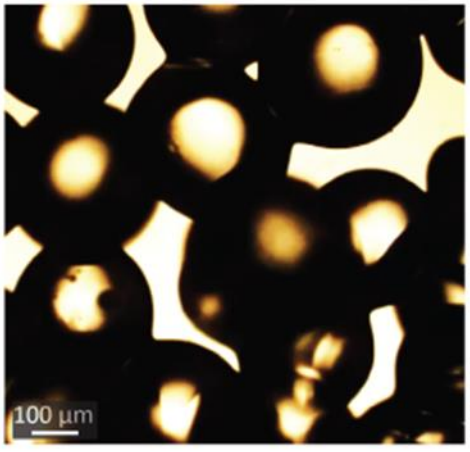

Figure 1.31. Microphotograph of hot stage experiment (taken at 870 °C). Borosilicate clasts (black) are sintering (image courtesy of Hugh Tuffen).

welding will cause decreases in the permeability and porosity, as clasts experience increasing amounts of viscous strain. Given that welding plays an important role in permeability reduction, especially in tuffisite veins, it is important to consider when evaluating how water escapes from magma.

Sintering is a diffusion related process (Sparks et al., 1999), and because of this, the structural relaxation time of a melt (r) provides a reasonable approximation of the sintering timescale (Tuffen et al., 2003); r is defined as η_s / G (Webb and Dingwell, 1990a), where η_s is the melt's shear viscosity and G is the shear modulus (10 GPa for silicic melts; Dingwell and Webb, 1989). Compaction timescales (t_v) may be approximated by dividing the shear strain (γ) by the shear strain rate ($\dot{\gamma}$; Tuffen et al., 2003). In this framework, the welding time (τ_w) is equal to r + (γ / $\dot{\gamma}$). High temperature deformation experiments have shown that the welding timescale provides a good approximation for the healing time of smooth-walled fractures (Yoshimura and Nakamura, 2010; Cordonnier et al., 2012a), but it underestimates the time required for healing of rough-walled fractures (Yoshimura and Nakamura, 2010). The relaxation time is partly dependent on melt viscosity, and because increased temperatures will decrease viscosity, τ_w will decrease with temperature. This has been demonstrated in high temperature deformation experiments in which magma porosity and permeability decreased with increased temperature (Chadderton et al., 2015). This has implications for the permeability of conduits and dykes because the temperature will be lowest nearest to the country rock, and thus, high permeability may be more sustainable here, in comparison to within conduit and dyke interiors.

Given that tuffisite veins are filled with fragments of obsidian, τ_w will partly be influenced by the timescale of particle sintering τ_s, which is related to the melt viscosity (η_s), particle size, and melt surface tension (Γ), $\tau_S = \frac{r\,\eta_s}{\Gamma}$ (Uhlmann et al.,

1975; Vasseur et al., 2013), where r is the radius of the undeformed particle. This considered, the welding timescale calculation can be modified to $\tau_w = \tau_s + (\gamma / \dot{\gamma})$, which would provide an approximation because it does not consider the effect of crystals (Vasseur et al., 2013), the presence of relatively cool or insoluble atmospheric gases (Sparks et al., 1999), or high pore pressure (Cordonnier et al., 2012a), all of which would increase τ_w. Furthermore, if water resorption occurred as a result of viscous compaction, i.e., due to a pressure increase (Friedman et al., 1963; Sparks et al., 1999), η_s would decrease, resulting in a decrease in τ_w. Bubbles may collapse following gas loss, or if volatiles are resorbed, with resorption occurring if the external pressure exceeds the internal bubble pressure (Westrich and Eichelberger, 1994) or via cooling (McIntosh et al., 2014a), because a pressure increase and temperature decrease will act to increase water solubility.

ii) Vapour phase precipitation

Any permeable pathway that facilitates the movement of magmatic gases may potentially become blocked or narrowed via vapour phase precipitation, if the conditions for precipitation are met. Cristobalite is a common precipitate associated with volcanoes and can be recognised by its characteristic 'fish-scale' cracks (**Fig. 1.32.i)**, and it forms via the corrosion of silica-rich glass (Horwell et al., 2013; Schipper et al., 2015), with corrosion being possible when Cl or F are present in the gas phase (Horwell et al., 2013). Schipper et al. (2015) describe cristobalite-filled vesicles in the 2011-12 Cordón Caulle lava flow, where cristobalite is common in relatively isolated vesicles, but rare in connected vesicles. This considered, Schipper et al. infer that a vapour may only corrode/deposit when the permeability of the pore space is sufficiently low.

Vapour phase precipitates in the form of silica polymorphs (including cristobalite), exist in voids and veins housed within explosively erupted country rock fragments and dome rocks from Soufrière Hills volcano, Montserrat (Boudon et al,. 1998; Horwell et al., 2013; **Fig. 1.32.i**), and are thought to have inhibited outgassing from the upper conduit (<500 m deep; **Fig. 1.32.ii**). Similar precipitates surrounded the Mt. St. Helens 1980 cryptodome (Komorowski et al., 1997), and exist within breccia erupted during the 1993 Galeras eruption (Stix et al., 1997), but it remains unclear as to how influential precipitates are in reducing outgassing from conduits and dykes.

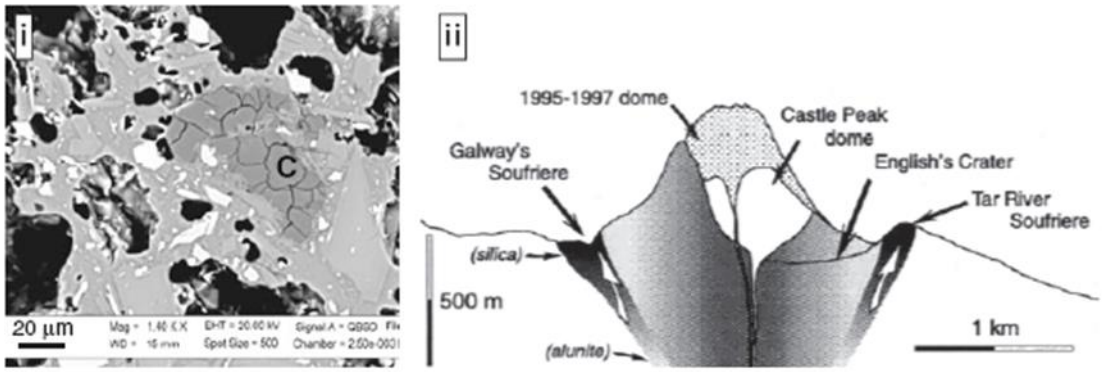

Figure 1.32. (i) Backscattered electron image of cristobalite in dome rock from Soufrière Hills volcano, Montserrat. From Horwell et al. (2013). **(ii)** Schematic cross section through Soufrière Hills volcano depicting the possible presence of silica precipitates to a depth of 500 m. From Boudon et al. (1998).

1.8.5. Volcanic earthquakes and geological signature

Volcanic earthquakes can provide important warning of forthcoming volcanic activity, and are sometimes indicative of the type of activity to come. Hence, many researchers have focused their attention on resolving the trigger mechanisms and mechanistic significance of volcanic earthquakes.

There are four main types of volcanic earthquakes, namely volcano-tectonic (VT), long-period (LP), hybrid, and tremor events. LP and hybrid events are sometimes collectively referred to as low-frequency (LF) events (Lahr et al., 1994;

Neuberg, 2000). VT events (**Fig. 1.33.i**) have relatively sharp, high frequency (>10 Hz) onsets, with relatively short, low frequency (<10 Hz) broadband codas (the trailing part on seismographs). In contrast, LP events (**Fig. 1.33.ii**) have gradational high frequency onsets, with relatively long, low frequency broadband codas (Chouet, 1996). Hybrid events (**Fig. 1.33.iii**) have characteristics of VT and LP events, as they have similar broadband codas to LP events, but sharp high frequency events can form part of their codas (Neuberg, 2000), and their onsets are similar to VT onsets (Chouet, 1996). Tremor events (**Fig. 1.33.iv**) have low frequencies, and are more sustained than the other types of events (Chouet, 1996). For instance, individual VT, LP and hybrid events typically last tens or hundreds of seconds, whereas individual tremor events typically last minutes to days, but they can last for more than a few months (Chouet, 1996; Neuberg, 2000). Tremor events probably represent overlapping LF events.

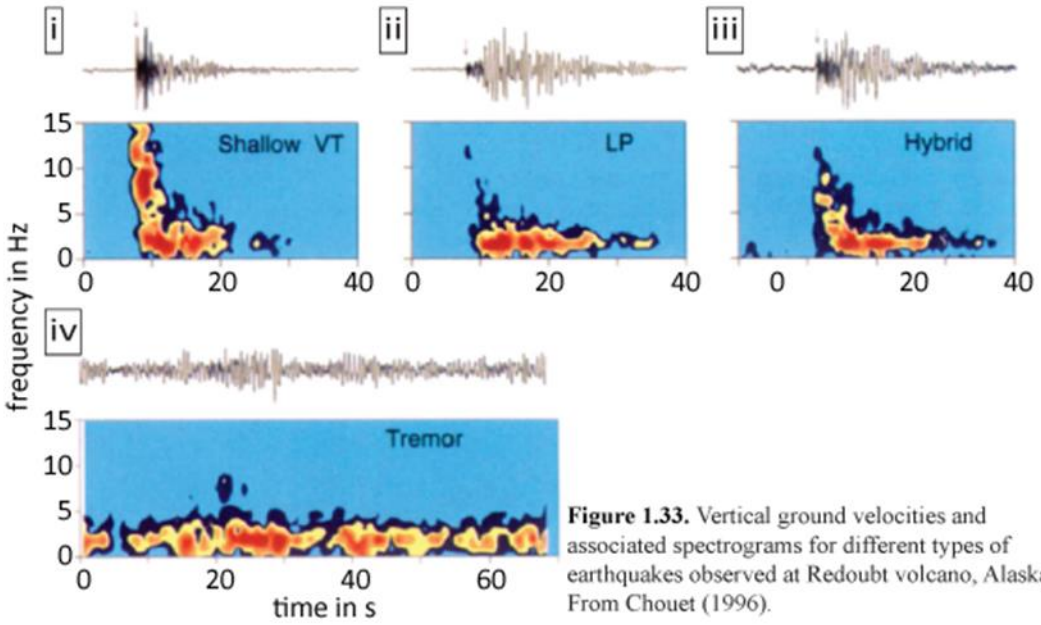

Figure 1.33. Vertical ground velocities and associated spectrograms for different types of earthquakes observed at Redoubt volcano, Alaska. From Chouet (1996).

The source region of VT events can be shallow (depth of a few km) or deep (depth of 5-10 km). VT events are usually the first sign of an awakening volcano (Lahr et al., 1994; Chouet, 1996) and may result from the brittle failure of solid rock (Chouet, 1996; Neuberg, 2000) or magma (Tuffen et al., 2008). Shallow VT events

have been inferred to form during the intrusive formation of cataclasite, which sometimes exists on spine exteriors (Nakada et al., 1999). LF events can also occur in the upper parts of conduits (Lahr et al., 1994; Chouet, 1996; Neuberg et al., 2006), or in a deeper part (>10 km deep) of the magmatic system (Chouet, 1996). The origin of deeper LF events is generally unclear, but 30 km-deep LP events that preceded the 1991 Pinatubo eruption are attributed to a basaltic intrusion (Chouet, 1996 and references therein).

Shallow LF events are important signals of forthcoming activity, with dome collapse events and Vulcanian explosions often following LF swarms (Miller et al., 1998; White et al., 1998; Voight et al., 1999), but such swarms do not guarantee an eruption (Neuberg et al., 2006). Hybrid events at Soufrière Hills volcano in Montserrat accompanied periods of inflation, linking them to pressure accumulation within the shallow (700-800 m deep) conduit (Voight et al., 1998). The similarity of individual LF waveforms that form LF swarms indicates that their source regions can remain stationary for several days, even persisting after dome collapse events and explosive activity, and being reactivated multiple times (Neuberg et al., 2006; Iverson et al., 2006).

The prolonged resonance of LF codas requires the presence of a fluid (Chouet, 1988). Shallow LP events may represent the excitation of pre-existing fractures by gas (Gil Cruz and Chouet, 1997; Waite et al., 2008), whereas shallow hybrid events may represent hydro-fracturing caused by magma-water interaction (Shepherd and Aspinall, 1982), stick-slip motion at the margins of a rising magma column (White et al., 1998; Iverson et al., 2006; Kendrick et al., 2012; Kendrick et al., 2014), or the shear failure of magma (Goto, 1999). Tuffen et al. (2003) argued that multiple generation of tuffisite veins (**Fig. 1.5.**) within a shallowly (<50 m deep) dissected

rhyolitic dyke provide evidence for the repeated fracturing and healing (RFH) of magma. The likely timescale of the RFH process (time required to accumulate enough stress for fracturing and for welding to occur) is tens of minutes to ~100 days, and broadly similar to the typical repeat time (tens of hours to a few days) of LF events (**Fig. 1.34.**). Considering this, along with the textural evidence, the RFH process may be responsible for LF swarms (Tuffen et al., 2003). This trigger mechanism is appealing because it unifies previous conceptions, as brittle magma failure would explain the high frequency component of hybrid earthquakes, whereas the low frequency coda of LF events may reflect gas, or particles and gas flowing through fractures. A swarm of pre-explosion LP events at Tungurahua Volcano in Ecuador may have resulted from the incremental filling of pre-existing fractures with ash (Molina et al., 2004). Indeed, ash-laden fluids flowing through tortuous fracture networks have been experimentally shown to produce LF-like acoustic signals (Benson et al., 2008). In addition, some of the signals produced during these experiments were similar to hybrid events, representing the coupled effect of the flowing fluid and fresh fracturing driven by high fluid pressure. The textures produced during these experiments were described as being akin to the fault rock within internal tuffisite veins in Icelandic rhyolitic dykes (e.g., Tuffen and Dingwell 2005).

In consideration of the studies mentioned in this section it is possible that VT events and high-frequency components of hybrid events result from the fracturing or comminution of cold rock or magma. In contrast, the low frequency codas of LP and hybrid events are probably linked with gas, or particles and gas flowing through fractures. Unfortunately, seismic data for rhyolitic volcanoes are relatively lacking (Carn et al., 2009) when compared with more mafic volcanoes such at Soufrière Hills volcano. Nevertheless, multiple generations of tuffisite veins within rhyolitic dykes

arguably shed light on seismic triggers, with the timescale of fracturing and healing comparable to the repeat time of hybrid earthquakes formed during more mafic eruptions (Tuffen et al. 2003; **Fig. 1.34.**). Following the eruption of Chaitén, the Chilean government developed a new real-time monitoring network (http://www.sernageomin.cl/volcanes.php), with the purpose of improving the monitoring of Chile's highest-risk volcanoes (Carn et al., 2009). Therefore, forging links between volcanic-earthquake triggers and vent activity at rhyolitic volcanoes will undoubtedly improve.

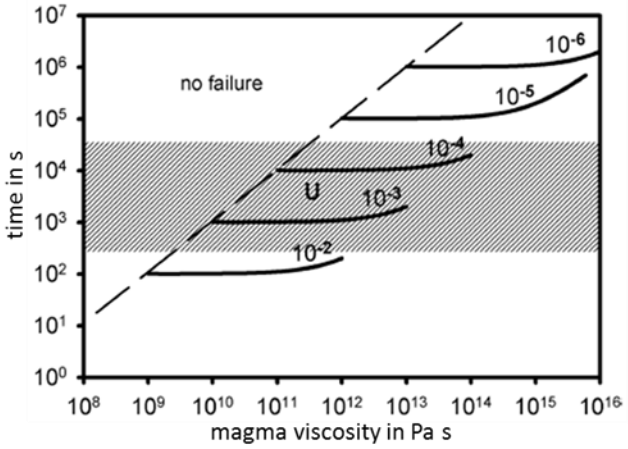

Figure 1.34. Solid black lines are RFH cycle timescales for different strain rates indicated in units of s^{-1}, shaded area represents the repeat time of LF earthquakes. From Tuffen et al. (2003).

1.9. The rationale, objective and approach of this research

Important insight has recently been obtained into rhyolitic eruptions via observations of the Chaitén and Cordón Caulle eruptions and via analysis of their deposits. However, the conduits of these volcanoes are unexposed, making it difficult to link the subsurface conduit processes with vent activity. Dissected rhyolitic dykes provide an in-situ record of the processes that took place during the intrusive emplacement of magma. These processes were probably very similar to the processes that took place in the shallow (<500 m deep) parts of the Chaitén and Cordón Caulle conduits during the

post-Plinian eruption phases. This thinking underscores the rationale behind this research.

The broad aim of this research was to gain insight into magma emplacement and deformation within shallow (emplacement depths <500 m) rhyolitic dykes, whilst assessing how these processes and the nature of the country rock influence magmatic outgassing. Bubbles are important to consider when evaluating magmatic outgassing. Therefore, the first objective of this study was to establish how bubbles formed and evolved throughout magma emplacement, and as tuffisite veins are considered important facilitators of magmatic outgassing the second objective involved assessing how external and internal tuffisite veins formed and evolved throughout magma emplacement. Because outgassing was the subject of interest it was also established as to whether magmatic water escaped from the dykes. The research questions included:

1. How did bubbles form and evolve throughout magma emplacement and what role did they play in magmatic outgassing?
2. How did the external and internal tuffisite veins form, how did their permeability evolve throughout magma emplacement, and what role did they play in magmatic outgassing?
3. Did water escape from the magma, and if so, how did it escape?
4. Are magmatic water concentration gradients modified during magma cooling and the reactivation of tuffisite veins, and if so what can they really tell us about magmatic outgassing?

The unique approach of this research involved a detailed micro- to macro-scale analysis of the textures and dissolved water content in rhyolitic dykes, focused on Icelandic dykes at two localities, namely SE Rauðfossafjöll and Húsafell. The former location was chosen because the dykes contain tuffisite veins (Tuffen, 2001; Tuffen et al., 2003; Tuffen and Dingwell, 2005), and because the pre-eruptive water content is known (Owen et al., 2013a). The latter locality was chosen because the dykes had not

been studied in detail, with only their locations marked on a geological map (Saemundsson and Noll, 1974), and their bulk geochemistry determined (Kristján Sæmundsson, pers. comm. 2012). The Húsafell dykes also offered an opportunity to conduct detailed observations of dyke-country rock contacts, which is not possible at SE Rauðfossafjöll. In addition, it was regarded as a possibility that the dykes may have had different emplacement depths; the emplacement depth of the SE Rauðfossafjöll dykes was ~10-50 m (Tuffen, 2001; Tuffen et al., 2003; Tuffen and Dingwell, 2005), whereas the emplacement depth of the Húsafell dykes had not been estimated prior to this study.

Field excursions were conducted in the summers of 2012 and 2013; during these excursions the dyke textures were studied and samples were collected. Petrological thin sections and wafers (~100-300 μm thick double polished obsidian sections) were made. Textures in the thin sections were analysed using a petrological microscope and a scanning electron microprobe. The macro-scale dissolved water content in the wafers was measured using a bench-top Fourier-transform infrared spectroscope, and the macro- to micro-scale dissolved water content was measured with a synchrotron-source Fourier-transform infrared spectroscope. Further details of the methodologies are provided in the following chapter.

Chapter 2: Methodology and errors

2.1. Recording sample elevations using a 3D model

2.1.1. Methodology

Sample elevations from one of the dykes (Thumall) at SE Rauðfossafjöll were determined by using a 3D model constructed from multiple photographs, using the method of James and Robson (2012). The model was used because it enables elevations to be determined at a high precision, compared to the precision of a handheld GPS. Samples were collected and their locations were marked with numbered yellow stickers. Multiple photos were then taken of the dyke using a digital Canon EOS 500D single-lens reflex camera. Image collection was completed on an overcast day in order to avoid shadows. Multiple (3-6) photos were taken at different positions encompassing the dyke; each position was ~5-20 m from the dyke, with a spacing of ~2 m (~800 images were collected in total).

To construct the 3D model, a freeware package (http://blog.neonascent.net/archives/bundler-photogrammetry-package/ by J. Harle) was used that uses a Structure From Motion application called Bundler (Snavely et al., 2006; Snavely et al., 2008b; Snavely et al., 2008a) and a Multiview Stereo dense matcher called Patch-based MultiView Stereo 2 (Furukawa and Ponce, 2010). Bundler matched distinctive features that are visible in multiple photos, and a sparse point-cloud was generated, representing the coordinates of the features in 3D-space. The Multiview Stereo dense matcher then also found distinctive features that are visible in multiple photos, but in contrast to Bundler, relatively dense patches of the features

were constructed, with the relative position of each patch previously computed by Bundler; together the patches form the 3D model of the dyke.

To orientate the 3D model a walking pole was secured in the snow near the dyke and placed as near to vertical as possible, prior to taking the photos. In addition, two meter rules were placed on the dyke that would be used later to apply a scale to the model. The model was orientated and a scale was added by using a Matlab® software tool called sfm_georef (James and Robson, 2012). This involved marking points at the ends of the walking pole and the meter rules in multiple photos. The model was orientated by defining the walking pole as vertical and as representing the z-axis on the model, and a scale was applied by assigning the distance between the points on individual meter rules a value of 1 m.

The elevation of a position near the top of the dyke was determined in the field by taking GPS readings, with three handheld GPS devices. The readings were 1177 m a.s.l., 1180 m a.s.l. and 1180 m a.s.l.; the average (1179 m a.s.l.) of these was used as the reference point, and sample elevations were calculated by measuring the distance along the z-axis on the 3D model between the reference point and the yellow stickers (sample locations). The measured distances were then subtracted or added (below or above 1179 m respectively) from or to 1179 m to give the elevation of each sample. All elevations were determined this way, excluding the lowest sample, which was estimated using a handheld GPS because it is not on the 3D model.

2.1.2. Error

Relative sample elevation errors mostly stem from the walking pole not being truly vertical. Therefore, to estimate the error associated with the sample elevations it was assumed that the walking pole was at an angle of 80°; this is thought to be the worst

case scenario, because care was taken to position the walking pole as close to 90° as possible. Trigonometry was then used to determine the error and was calculated as being 0.02 m over 1 m (e.g., **Fig. 2.1.**). Therefore, a sample with an elevation of 1170 m will have an error of 0.18 m (1179 m - 1170 m × 0.02 m) and a sample with an elevation of 1150 m will have an error of 0.58 m (1179 m - 1150 m × 0.02 m).

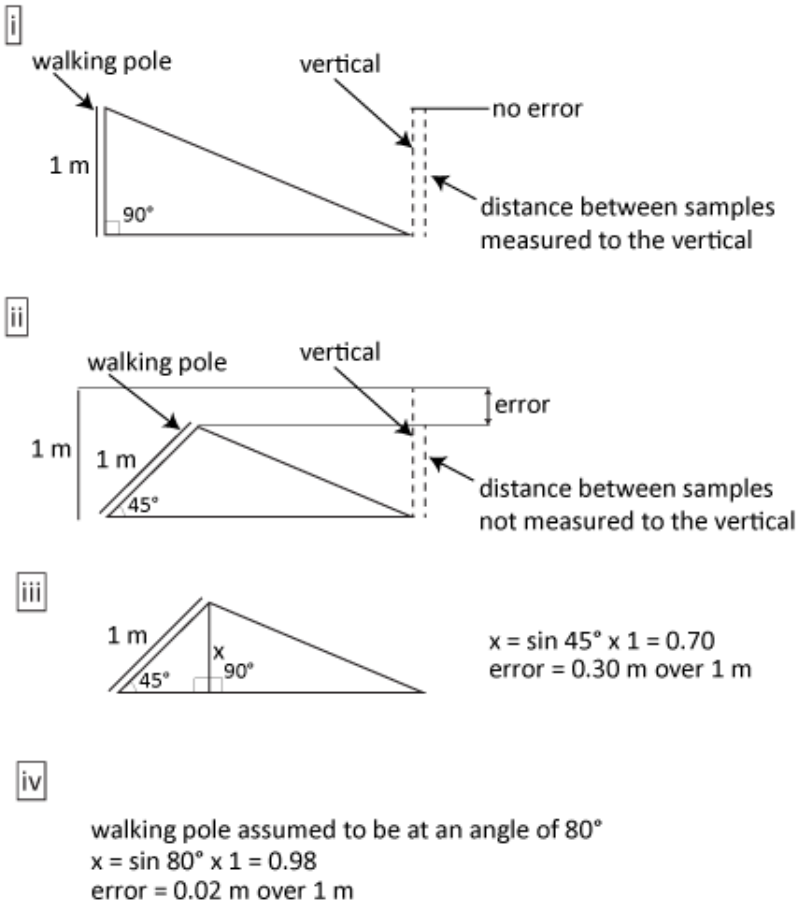

Figure 2.1. Example of how the error associated with the sample elevations was determined. See main text for further information.

2.2. Scanning electron microscopy

2.2.1. Principle

Scanning electron microprobes (SEMs) can be used to produce high resolution images of a sample, and also to determine the relative concentration of different elements within a sample. The main components of an SEM include an electron gun,

condensers, apertures, deflector coils, specimen stage, detectors, and a vacuum system. During SEM analysis a filament is heated to about 2400 °C (Reed, 2005) in the electron gun, resulting in the emission of electrons. Filaments are commonly made of tungsten, due to its high melting temperature (3422 °C), high tensile strength, low coefficient of thermal expansion and low vapour pressure. Once emitted, the elections pass through the condensers and apertures, resulting in a beam of electrons, with a minimum beam diameter of ~8 nm achievable with a tungsten source (Reed, 2005). The beam is directed by the deflector coils in a raster fashion across a sample. During the scan, the beam will penetrate the sample surface to a depth of ~2 orders of magnitude greater than the beam diameter (Wells, 1974). Analysis must be completed under vacuum conditions because the presence of atmospheric gas can cause the filament to burn out, whilst also causing electron scattering (Reed, 2005).

The raster scan area is a function of the magnification, with higher magnifications representing a smaller area; magnifications of ~10-10^6 are achievable with most SEMs (Reed, 2005). Image resolution is largely dependent on the working distance and beam diameter, with resolution being greater when the working distance and beam diameter are smaller. Some SEMs can achieve a resolution of <1 nm (http://www.nanotech-now.com/news.cgi?story_id=42612), but more generally, a resolution of ~1-100 nm should be expected (Keulen et al., 2007). Two types of images can be produced during SEM analysis, namely secondary electron (SE) and backscattered electron (BSE) images. SE images are used to analyse specimen topography, whereas BSE images are used for textural analysis and to reveal geochemical variations (Reed, 2005). Some SEMs also have X-ray spectrometers, allowing the relative amount of different elements to be determined.

SE images are produced via inelastic scattering interactions between incident electrons and atomic electrons. Basically, the incident electrons cause inner atomic electrons to be ejected (**Fig. 2.2.**), and these ejected secondary electrons are detected by secondary electron detectors (Echlin et al., 2013). In contrast to SE images, BSE

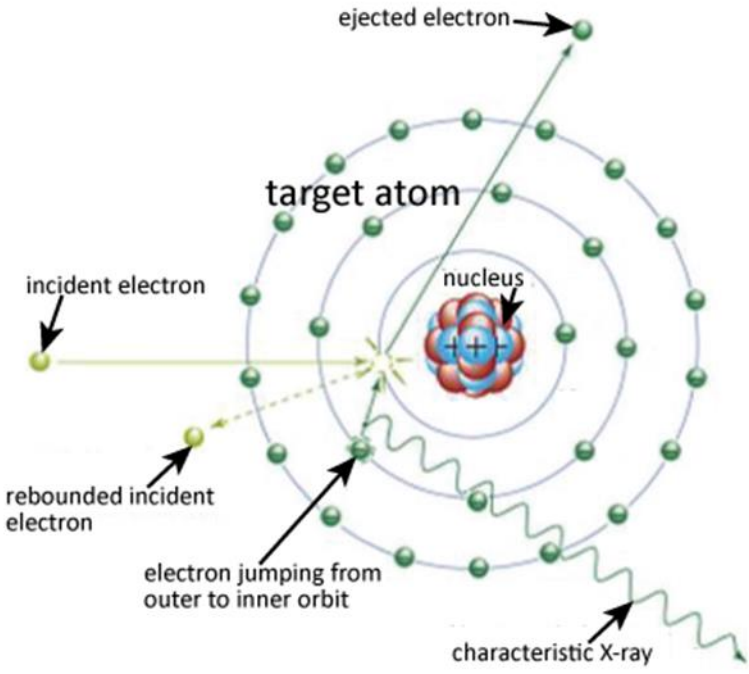

Figure 2.2. Schematic illustration showing an inelastic scattering interaction. Slightly modified from Bushberg et al. (2011).

images are produced via elastic interactions between incident electrons and atomic nuclei, with these interactions arising as incident electrons get deflected by the positive charge of the nucleus (**Fig. 2.3.**; Reed, 2005). The angle of deflection will be greater when the atomic mass is higher; electrons that are deflected by a large amount will not have travelled as far between emission and detection, relative to electrons that are slightly deflected (Reed, 2005). Because of the greater distance travelled, electrons that are deflected by a small amount will lose more energy before hitting the detector than those deflected by a large amount. The intensity of BSE images will therefore be stronger (lighter shade of grey) when the atomic mass is higher (Ginibre et al., 2002; Reed, 2005; Humphreys et al., 2008). BSE analysis requires using greater voltage and lower vacuum pressure than SE analysis because elastic interactions involve deeper

penetration of atoms than inelastic interactions. Distinguishing between secondary electrons and backscattered electrons is possible, as secondary electrons have much lower energies than backscattered electrons (Reed, 2005).

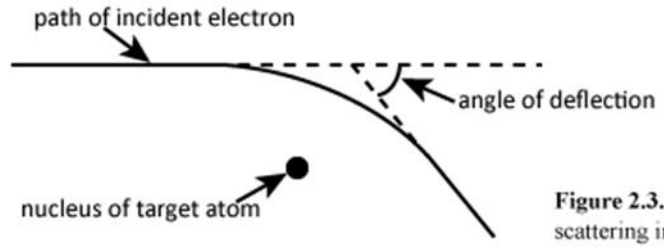

Figure 2.3. Schematic illustration showing an elastic scattering interaction. Redrawn from Reed, (2005).

Vesicle, fracture or sample edges may have strong intensities in BSE images, relative to the flat surface of a sample with the same composition because more electrons can escape from edges than from flat surfaces (**Fig. 2.4.**), producing a relatively enhanced signal. In addition, in BSE images regions that have high atomic

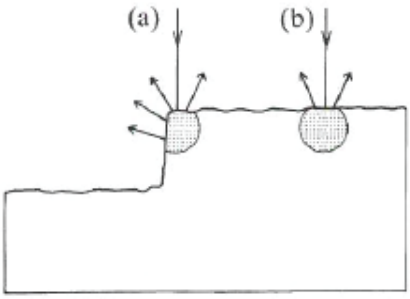

Figure 2.4. Schematic illustration showing why a greater signal is produced in a SEM scan from the edge of a sample (a), relative to a flat part of the sample (b). From Reed, (2005).

mass may be surrounded by haloes with relatively weak intensities. This is probably because the energy released from the region with a high atomic mass causes saturation of the detector, thus electrons released from the haloes are not detected.

During SEM analysis X-ray spectroscopic analysis may be completed, as X-rays are a by-product of secondary electron emissions (**Fig. 2.2.**); following the ejection of an inner atomic electron (secondary electron) an atom is left in an excited state, and an outer atomic electron will move to fill the space previously occupied by the inner electron, bringing the atom back to a ground (or unexcited) state, such

electron transitions release energy in the form of X-rays. Given that atomic structure is unique to individual elements the energy released during electron transitions will be characteristic of individual elements, and this is why X-ray spectroscopic analysis can be used to determine the relative amount of different elements.

2.2.2. Backscatter electron imaging and element mapping

For the purpose of this study, backscatter-electron analysis and X-ray spectroscopic analysis were completed. One of the reasons for using BSE imaging was because it allows textures to be analysed at much higher magnifications than possible with a petrological microscope. Textures from SE Rauðfossafjöll and Húsafell were analysed using BSE images. BSE imaging was also used to determine if variations in the mean atomic number exist around fractures, tuffisite veins and in different coloured obsidian. X-ray spectroscopy was used to determine the relative amount of some major elements within the Húsafell samples, to assess the extent and nature of post-magmatic alteration, and the cause of colour variations within obsidian.

i) Methodology

SEM analysis was completed with a Hitachi S-3600N SEM in Leicester University's Geology Department. Polished petrological thin sections were prepared at the CEPSAR Science Faculty of The Open University. Prior to SEM analysis the sections were coated in a thin (~2-20 nm thick) layer of carbon at Leicester University. This electrically conductive coating prevents charging (i.e., the build-up of a negative charge via the addition of electrons), whilst also increasing the amount of electrons that can be detected, thus increasing the signal to noise ratio. Samples were adhered to

the specimen stage with an alcohol-based silver paint, and SEM analysis was completed using high vacuum (1.5×10^{-3} Pa) conditions. BSE images were collected using a voltage of 15 kV, a working distance of ~13-15 mm, with each image composed of 80-200 scans. X-ray spectroscopic element mapping was completed in SE mode, using the same voltage and a working distance of 15 mm; points of interest were chosen using a software package called INCA.

2.3. Benchtop and Synchrotron-source Fourier-transform infrared spectroscopy

2.3.1. Principle

Fourier-transform infrared spectroscopy is a non-destructive micro-analytical technique that was used to measure the magmatic water concentration in glassy samples from SE Rauðfossafjöll and Húsafell. In the Benchtop Fourier-transform infrared spectroscope (BFTIR) infrared radiation is emitted at a range of wavelengths from a glowing black-body source, whereas the infrared radiation emitted in the Synchrotron-source FTIR (SFTIR) involves the acceleration of charged particles. Both techniques involve the transmission of an infrared beam through the sample, with the amount of beam absorption at specific wavelengths being displayed in a spectral output. Absorption at specific wavelengths will depend on the amount of water present in a sample, together with sample thickness and density. Thus, if the sample thickness and density are known the water concentration may be calculated. The radiation produced in the SFTIR has a much greater spectral flux and brilliance than that produced in the BFTIR (Willmott, 2011). Therefore, a smaller beam size and higher spatial resolution may be achieved with the SFTIR in comparison to the BFTIR.

2.3.2. Methodology

The water content was measured in double-polished obsidian wafers, ranging in thickness from ~60-350 μm. These wafers were made by hand, which first involved using a thin section saw to cut a 1 mm-thick slice of rock; if tuffisite veins were present the cut surface was orientated perpendicular to the vein margins. Then, the rock section was ground down with the aid of a little water by using a lapidary machine. Four different grades (320, 600, 800 and 3000) of diamond coated lapidary discs were used to achieve polished (scratch-free) surfaces. If rock sections were large enough, they were held on the lapidary disc with one finger. However, if samples were too small to be gripped in this way during the final stages of polishing, they were mounted on glass slides using Crystalbond adhesive. The samples were removed from glass slides via heating on a hot stage at 100 °C, which melted the Crystalbond. Any residual Crystalbond was removed from the wafers by rinsing them in acetone. Heating of the samples to 100 °C should not alter the water content. This is because analysis of hydrogen isotopes and the water content of obsidians has previously demonstrated that heating below 150 °C does not alter the water content of samples that contain ~0.13-0.17 wt. % water (Newman et al., 1986), which is similar to the water content of the SE Rauðfossafjöll samples. However, based on their findings, Newman et al. (1986) suggested that heating to <150 °C may release water from water-rich (>1 wt. % water) samples. The Húsafell samples contain ~4 wt. % water; therefore, to avoid affecting the water content, the Húsafell wafers were not mounted during wafer preparation, thus avoiding the need for heating. It was later realised that avoiding heating was probably unnecessary, because it is likely that only meteoric water would be released at temperatures <150 °C (Roulia et al., 2006; Denton et al.,

2009; Denton, 2010; Denton et al., 2012), and the magmatic water content is of interest here.

After making the wafers, photos were taken of them (e.g., **Fig. 2.5.**), by placing them on a light box below a digital Canon EOS 500D single-lens reflex camera, with a 80 mm macro lens, mounted on a tripod. The position of the SFTIR and BFTIR measurements were marked on the photographs. Wafer thicknesses were determined using a Mitutoyo digital displacement gauge.

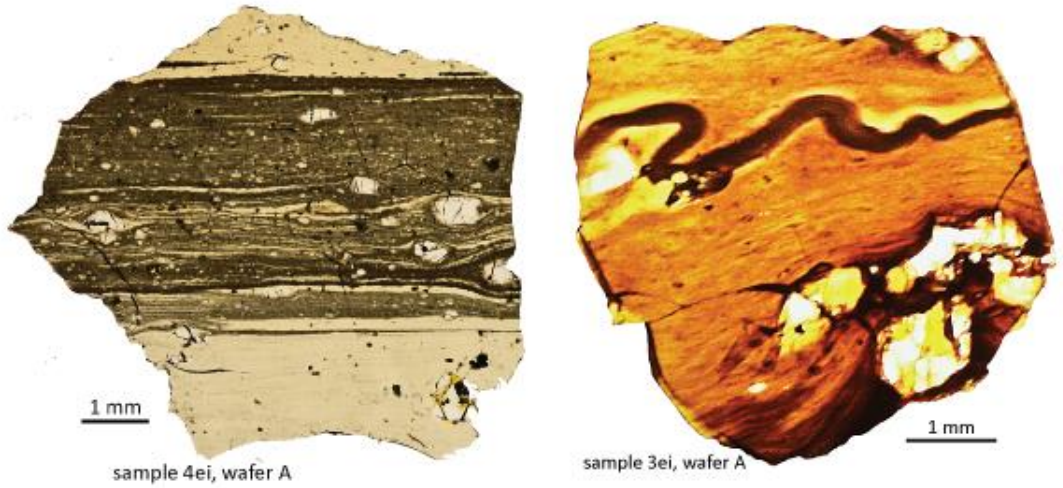

Figure 2.5. Some of the handmade obsidian wafers from Thumall (SE Rauðfossafjöll) that were analysed with the BFTIR and SFTIR.

Prior to taking water measurements, each sample was rinsed and wiped with acetone to remove any dirt or atmospheric water. The water content was measured in crystal-free and crack-free obsidian by using a Thermo Scientific Nicolet BFTIR at Lancaster University and the SFTIR at the Diamond Light Source Facility in Oxfordshire. Each measurement was obtained from 256 scans, with spectral resolutions of 4 cm^{-1} and 8 cm^{-1} for the BFTIR and SFTIR, respectively. The analytical area of each measurement was 100×100 μm and 8×8 μm for the BFTIR and SFTIR, respectively, and background spectrum were collected every hour, or after analytical runs if the runs took longer than an hour. Five measurements were made with the BFTIR along two transects (i.e., a total of ten measurements) in each wafer,

and 100 to >1000 measurements were made across multiple transects and maps within individual wafers using the SFTIR.

Once the measurements were completed a linear baseline correction was manually applied to individual spectrum (**Fig. 2.6.**), by using the Thermo Scientific OMNIC Software and Bruker OPUS 6.5 software for spectra from the BFTIR and SFTIR, respectively. A linear baseline correction was used because this baseline was found to cause the lowest deviation in the water content for repeated corrections of individual spectrum, relative to other types of baseline correction (**section 2.3.6.iv**). The dissolved water content in the SE Rauðfossafjöll samples was determined by using the 3570 cm^{-1} peak, which represents total water (H_2O_t) i.e., water dissolved as hydroxyl groups (OH^-) and molecular water (H_2O_m; Newman et al., 1986). Other peaks are related to individual water species; for instance, the 1600 cm^{-1}, 4500 cm^{-1} and 5200 cm^{-1} peaks relate to H_2O_m, OH^- and H_2O_m, respectively (Newman et al., 1986). However, the water content in the SE Rauðfossafjöll samples is too low for any measurable absorption at these peaks. In contrast, the 4500 cm^{-1} and 5200 cm^{-1} peaks were used to determine the water content in the Húsafell samples, because these samples contain more water. Due to the high water content of the Húsafell samples, the 3570 cm^{-1} peak is saturated, and thus unusable. Absorption values were converted into the weight fraction of H_2O_t by using the Beer-Lambert law, given below (Stolper, 1982; Newman et al., 1986; Owen 2013), where c is the weight fraction of H_2O_t, m is the molecular weight of water (18.02 g/mol), a is the absorbance, t is the sample thickness in cm, ρ is the sample density in g/L, and ε is the absorption coefficient in L/(mol·cm).

$$c = \frac{(m \times a)}{(t \times \rho \times \varepsilon)}$$

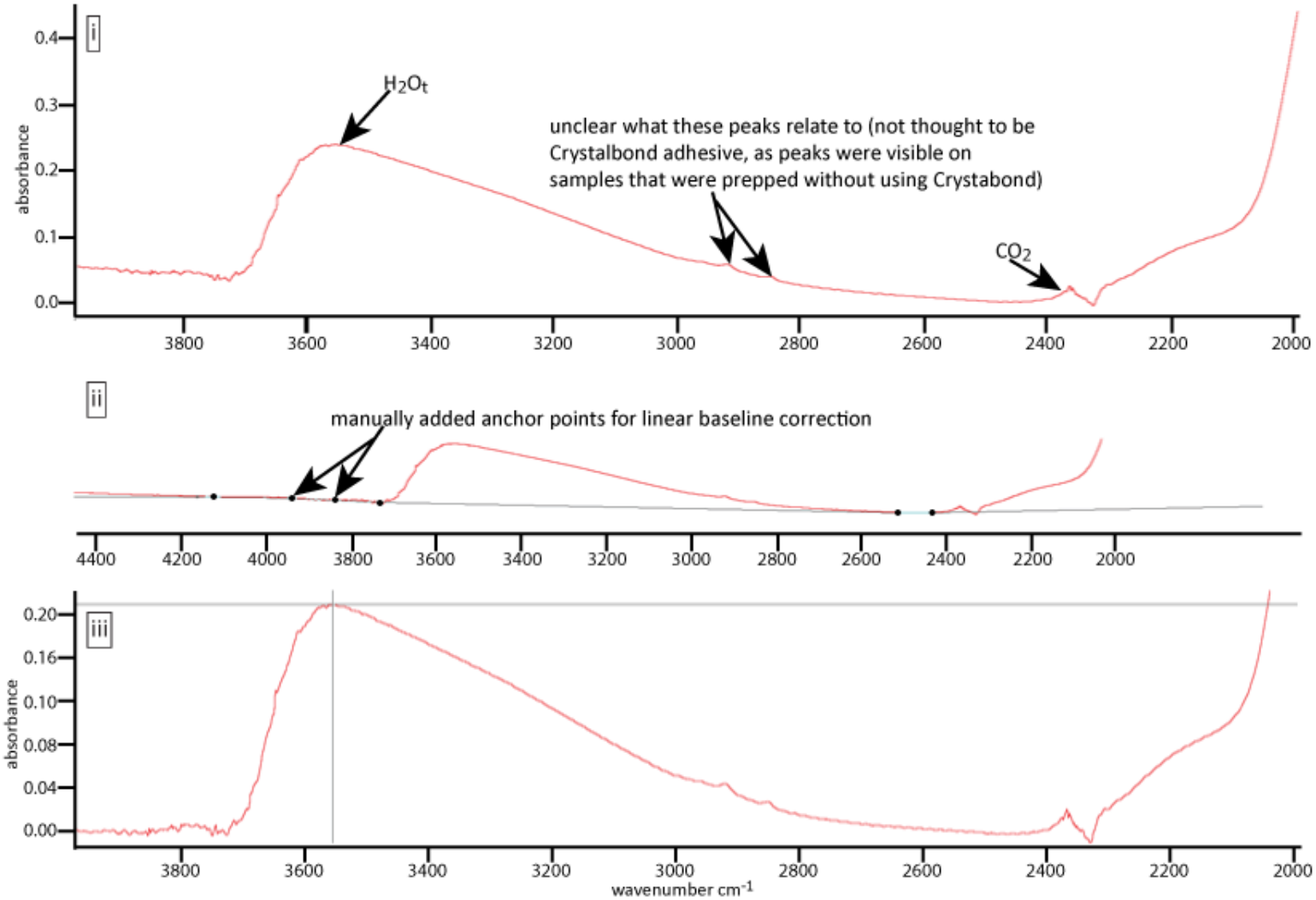

Figure 2.6. Example of how the FTIR spectra were baseline corrected. The spectrum is from wafer C of sample 1ei, transect 1_spectrum 3 and was collected on 09/11/12. **(i)** Original spectrum. **(ii)** Baseline added to spectrum. **(iii)** Spectrum after baseline correction.

2.3.3. Estimating sample density

Measurements of the dissolved water concentration were only made in vesicle-free samples. Sample densities were determined by measuring the mass and volume of each sample. The mass of each sample was determined by using a digital Fisherbrand PF-203 balance and values spanned 20-130 g. Sample volumes were determined by using the water displacement method, which involved filling a graduated cylinder with water, and recording the water volume. A sample was then submerged in the water, and the cylinder was tapped to free any air bubbles; the water volume was then recorded again. The initial water volume was subtracted from the water volume that contained the sample to give the sample volume. By dividing the mass (in g) by the volume (in ml) the density was determined in g cm^{-3}; the density was then converted into g/L for use in equation 1.

2.3.4. Choosing absorption coefficients

Absorption coefficients for rhyolitic glasses can vary with sample composition (Newman et al., 1986; Silver et al., 1990), temperature (Silver et al., 1990) and the total water content (Newman et al., 1986). It has been suggested that two absorption coefficients should be determined for the ~3570 cm^{-1} peak, one for OH^- and the other for H_2O_m (Newman et al., 1986; Silver et al., 1990). However, Leschik et al. (2004) suggested that composition has little effect on the absorption coefficient, and that using two absorption coefficients is unnecessary, with the use of one coefficient not changing the water content beyond analytical error. Also, samples with low concentrations (<0.2 wt. %) of water are likely to contain primarily OH^-, so one absorption coefficient should suffice (Stolper, 1982; Newman et al., 1988; Silver et al., 1990).

Due to the potential sensitivity of absorption coefficients, Newman et al. (1986) suggested that when determining the water content via infrared spectroscopy an absolute method should also be used to determine the water content, such as Karl–Fischer titration (KFT) or Nuclear reaction analysis (NRA), and in doing so, absorption coefficients can be determined for each sample of interest. Leschik et al. (2004) used five distinct analytical techniques (including BFTIR analysis) to determine H_2O_t in natural and synthetic rhyolitic glasses, and these authors found that for samples containing 0.1-6 wt. % H_2O_t, an absorption coefficient of 77.6 ±3.4 l mol^{-1} cm^{-1} could reproduce the water content within analytical error. They also found a systematic difference between the water content determined using KFT and NRA, and to account for this they calculated a mean absorption coefficient of 80 ±4.9 l mol^{-1} cm^{-1}, which they say is adequate to use for water-poor (<2 wt. %) rhyolitic glass. The 3570 cm^{-1} peak was used to determine H_2O_t in the SE Rauðfossafjöll samples, which all contain <2 wt. % H_2O_t. Therefore, an absorption coefficient of 80 $mol^{-1}cm^{-1}$ was used in this study. Using this value is in agreement with previous studies (e.g., Owen., 2013).

The water content of the Húsafell samples was determined by using the 4500 cm^{-1} and 5200 cm^{-1} peaks, which are unique to OH^- and H_2O_m respectively (Newman et al., 1986), and by using absorption coefficients of 1.73 l mol^{-1} cm^{-1} and 1.61 l mol^{-1} cm^{-1} respectively. These coefficients were validated by comparing H_2O_t determined by adding together the concentration of OH^- and H_2O_m determined using the 4500 cm^{-1} and 5200 cm^{-1} peaks respectively (Newman et al., 1986) with H_2O_t determined using the 3570 cm^{-1} peak. This was possible by using the data provided in Stolper, (1982a), which includes absorption at these peaks for five obsidian samples. Absorption coefficients of 1.73 l mol^{-1} cm^{-1} (Newman et al., 1986) 1.61 l mol^{-1} cm^{-1} (Newman et

al., 1986) and 80 l mol^{-1} cm^{-1} (Leschik et al., 2004) were used for the 4500 cm^{-1}, 5200 cm^{-1} and 3570 cm^{-1} peaks respectively. A good correlation exists between H_2O_t determined by using the two methods (**Fig. 2.7.**), which validates using absorption coefficients of 1.73 l mol^{-1} cm^{-1} and 1.61 l mol^{-1} cm^{-1}.

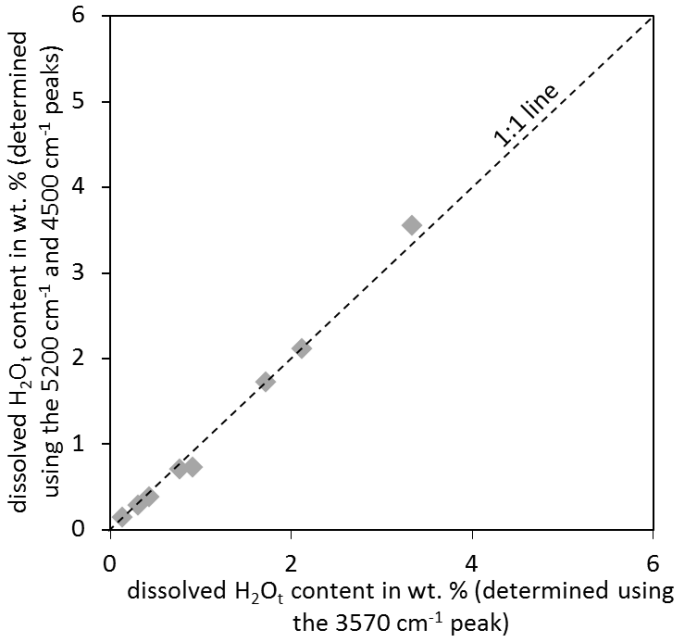

Figure 2.7. Comparison of the dissolved total water content, determined using different methods; see main text for further information. Data is from Stolper 1982a.

2.3.5. Constructing solubility pressure curves

To determine the pressure conditions within one of the SE Rauðfossafjöll dykes (Thumall) at the time of emplacement, solubility pressure curves were calculated and compared with the water content at different elevations within the dyke; a similar method has previously been used to reconstruct paleo-ice thicknesses (Tuffen et al., 2010; Owen et al., 2012; Owen, 2013). To calculate the curves, the saturation pressures for water concentrations of 0.1-0.4 wt. % were determined by using VolatileCalc (Newman and Lowenstern, 2002). In VolatileCalc the user can define the sample composition, magmatic temperature, and the concentration of CO_2; these were set as rhyolite, 800 °C, and 0 ppm respectively (reasons for these choices are provided

in **chapter 4 section 4.5.1.**). The VolatileCalc output provides the pressure (in bars) at which a given amount of water would be dissolved in the magma. This pressure was converted into Pa by multiplying it by 10^5, and then converted into depth by using the following equation,

$\text{depth} = \text{pressure} / (\text{density} \times \text{gravitational acceleration})$, where depth is in m, pressure is in Pa, density is in kg m^{-3}, and gravitational acceleration is in m s^{-2}. Multiple curves were constructed in this way, with each curve representing a different thickness and density of overburden. The overburden represents the lava filling the dyke and the eroded lava cap, which were assumed to have the same density. The thickness of the overburden was changed to represent different lava cap thicknesses. For example, today the highest part of the dyke is ~1180 m a.s.l., thus, a sample at 1165 m a.s.l. would have had an emplacement depth of 25 or 35 m, if the lava cap was 10 or 20 m thick, respectively (**Fig. 2.8.**).

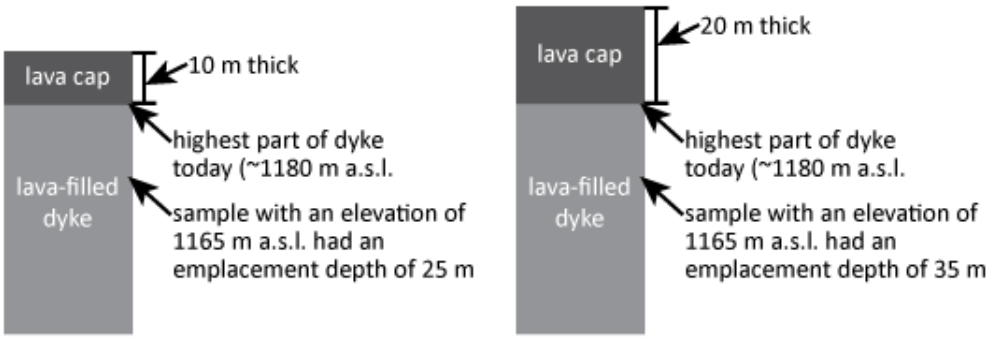

Figure 2.8. Schematic illustration explaining the conditions represented by the SPCs.

2.3.6. Errors

Errors associated with the dissolved water concentrations will stem from the choice of absorption coefficient, inaccuracies in sample density and thickness estimates, and inconsistencies in the manual baseline correction of spectra, and in reading the peak heights (amount of absorption). The errors associated with absorption coefficients and

density will cause the estimated water content to change by the same amount for each sample. In contrast, errors associated with thickness estimates are unique to individual measurements, because wafer thicknesses are variable. The error associated with the baseline correction and peak height may fluctuate with each sample, because subtle variations do exist between the forms of individual spectrum, but any fluctuations in this error are likely to be small, given that this error is small (**section 2.3.6.iv**).

i) Absorption coefficients

For the 3570 cm^{-1} peak Leschik et al. (2004) suggested the absorption coefficient of 80 ± 4.9 l mol^{-1} cm^{-1}. This considered, the water content was determined using coefficients of 75.1, 80 and 84.9 l mol^{-1} cm^{-1}. The positive error represents the difference between the water content determined using the former two coefficients, whereas the negative error represents the difference between the water content determined using the latter two coefficients. The positive and negative errors associated with the absorption coefficient for the 3570 cm^{-1} peak are 6.5 % and 5.8 %, respectively. These errors are relevant to the SE Rauðfossafjöll samples in which the 3570 cm^{-1} peak was used to determine the water content.

For the 4500 cm^{-1} peak Newman et al. (1986) suggested an absorption coefficient of 1.73 ± 0.02 l mol^{-1} cm^{-1}. This considered, the dissolved concentration of hydroxyl groups was determined using coefficients of 1.71, 1.73 and 1.75 l mol^{-1} cm^{-1}. Again, the positive error will represent the difference between the water content determined using the former two coefficients, whereas the negative error will represent the difference between the water content determined using the latter two coefficients. The positive and negative errors associated with the absorption coefficient for the 4500 cm^{-1} peak are 1.2 % and 1.1 %, respectively. These errors are

relevant to the Húsafell samples in which the 4500 cm^{-1} peak was used to determine the water content.

For the 5200 cm^{-1} peak Newman et al. (1986) suggested an absorption coefficient of 1.61 ± 0.05 l mol^{-1} cm^{-1}. This considered, the dissolved concentration of hydroxyl groups was determined using coefficients of 1.56, 1.61 and 1.66 l mol^{-1} cm^{-1}. The positive error will represent the difference between the water content determined using the former two coefficients, whereas the negative error will represent the difference between the water content determined using the latter two coefficients. The positive and negative errors associated with the absorption coefficient for the 5200 cm^{-1} peak are 3.2 % and 3.0 %, respectively. These errors are relevant to the Húsafell samples in which the 5200 cm^{-1} peak was used to determine the water content.

ii) Sample density

The density estimates of the glass are limited because they were made using bulk rock samples, and estimates therefore include phenocrysts; also some micro-cracks exist within the samples. However, the estimates are thought adequate because the density estimate for the SE Rauðfossafjöll samples is similar to the density estimate for other samples from Torfajökull volcano (Owen et al., 2012; Owen, 2013), and to the density estimated using the KWare Magma Software (Wohletz, 2002) and sample composition (Tuffen, 2001; **see section 4.5.1.**). The errors associated with density estimates will stem from limitations in determining the mass and volume of samples. Error associated with the measurements of mass will result from the accuracy and precision of the digital balance. No error is associated with the accuracy, as the balance is regularly calibrated by a K. E. Grisdale service engineer, and from ten repeat measurements of a sample with a mass of ~50 g the precision was found to be

<0.004 g. Considering that the sample masses span 20-130 g the error associated with mass is negligible.

To determine the error associated with volume estimates, Owen (2013) calculated the volume of obsidian cubes and compared these with volumes determined using the water displacement method and she found the volumes differed by <3 %. Therefore, the error associated with the density is taken as being 3 %. Even though the Húsafell and SE Rauðfossafjöll samples vary in composition, the average density estimate for obsidian samples from both locations was estimated as being 2400 kg m^{-3}. The positive and negative errors for both locations were thus determined by decreasing and increasing this density by 3 % giving densities of 2328 kg m^{-3} and 2472 kg m^{-3} respectively. The water concentration was then determined using these densities and it was established by how much the water concentration deviated from that determined using the density of 2400 kg m^{-3}. By using this method the positive and negative errors associated with density were found to be 3.0 and 2.9 %, respectively. These errors are relevant to the Húsafell and SE Rauðfossafjöll samples.

iii) Wafer thickness

Underestimates of wafer thicknesses will result in overestimates of the water content, with thickness overestimates resulting in underestimates of the water content. The thicknesses of the wafers were estimated by using a Mitutoyo digital micrometer. The precision of the micrometer was tested by repeatedly measuring the thickness of a wafer in two places ten times; the thicknesses at both locations (103 μm and 115 μm) was the same in both sets of ten measurements. This considered, the precision of micrometer is deemed as being high enough to neglect any precision-related errors. The micrometer has an accuracy of ± 3 μm (Owen, 2013). This forms the first part of

the error associated with measuring wafer thicknesses, with the second part occurring if the thickness is measured in a different position from the analysed area. This latter error is introduced because individual wafers are never a uniform thickness. For instance, wafers often thin towards their edges; the maximum variation in the thickness of an individual wafer was measured and found to be 40 μm, but commonly the maximum variation was found to be <20 μm. However, this maximum variation represents differences between the centres and edges of wafers, and is thus not representative of the difference between the thickness at the location of the thickness measurement and at the position in which the water content was analysed. In reality, thickness measurement positions are thought to have closely aligned with the positions at which the water concentrations were measured. The reason for this thinking is built from estimating variations in the alignment, which involved placing ten ~ 0.5 mm wide spots on white-tack; attempts were then made to hit the spots with the micrometer, and all spots were hit on the first attempt. The rod-tip of the digital micrometer has a diameter of 1 mm and because of this, it is likely to have always encompassed the areas in which the water measurements were made, as the areas were smaller than the area of the tip (~0.8 mm^2). It is possible that wafer thicknesses varied across this area, but such variations are thought to be negligible; thus, the error associated with thickness measurements will just be taken as that associated with the accuracy (±3 μm) of the micrometer. Each measured area has a unique thickness; the error associated with thickness is therefore unique to each measurement. For all measurements from Húsafell and SE Rauðfossafjöll the error associated with thickness caused the water concentration to deviate by a minimum and maximum amount of 0.90 % and 4.88 % respectively; individual error values for each measurement are provided in **A.3.8.** and **A.4.1.**.

iv) Baseline correction and peak heights

The software packages that were used to baseline-correct spectra allow three different types of baseline to be used, namely polynomial, linear and spline. To assess which baseline produced the most consistent results each baseline was repeatedly applied (ten times) to one spectrum from four samples, with the total number of corrections being 120. A linear baseline produced the smallest variation in peak height measurements (**Table 2.1.**) and was therefore chosen as the best baseline to use. The ten baseline corrections and peak height corrections that were done for the four samples with the linear baseline produced very consistent water concentrations, with the maximum percentage variation for the individual samples being 0.5 %, 1.2 %, 1.3 % and 1.7 % (**Table 2.1.**); the average of these four values is 1.2 %. Therefore, the positive and negative errors associated with the baseline correction and the peak heights are taken to be 1 %. This error is relevant to both the SE Rauðfossafjöll and Húsafell samples.

Table 2.1. Comparison of the amount of deviation in the water content by using different baseline corrections.

sample	baseline	mean water content (wt. %) of 10 corrections	max. difference in water content (wt. %) over 10 corrections	max. difference in water content as a percent of the mean water content	mean of percent difference linear	mean of percent difference polynomial	mean of percent difference spline
1ei (2012)	linear	0.100	0.001	1.2			
1ei (2012)	polynomial	0.103	0.001	1.2			
1ei (2012)	spline	0.099	0.002	2.4			
2e (2012)	linear	0.132	0.002	1.7			
2e (2012)	polynomial	0.147	0.064	43.6			
2e (2012)	spline	0.120	0.002	1.8			
3ei (2012)	linear	0.105	0.001	0.5			
3ei (2012)	polynomial	0.118	0.001	0.4			
3ei (2012)	spline	0.100	0.001	1.0			
4ei (2012)	linear	0.139	0.002	1.3			
4ei (2012)	polynomial	0.144	0.001	0.6			
4ei (2012)	spline	0.138	0.002	1.3			
					1.2	**11.5**	**1.6**

2.4. Bulk rock X-ray Fluorescence

2.4.1. Principle

The bulk rock major element composition of the Húsafell samples was determined by the technician staff at Leicester University using a PANalytical Axios-Advanced X-ray Fluorescence spectrometer (XRF). This technique involves generating a beam of X-rays within an X-ray tube and focusing the beam onto a sample. When a sample is bombarded with X-rays atomic electrons on inner orbits are ejected, which leaves the atom in an excited state and an outer atomic electron will move to fill the space previously occupied by the inner electron, bringing the atom back to a ground (or unexcited) state. Such electron transitions release energy in the form of X-rays. Given that atomic structure is unique to individual elements, the energy released during electron transitions will be characteristic of individual elements, and thus sample composition.

2.4.2. Methodology

The samples were prepared for XRF analysis at Lancaster University. This involved placing small chips (~1 cm in size) of a sample within an agate vessel that contained five agate balls; the vessel was then placed within a Retsch PM 100 Pulveriser machine for ~5-10 minutes at a speed of 400 rpm. This technique reduces the sample to fine dust, with a similar grade to talcum powder required for XRF analysis. The vessel and balls were thoroughly cleaned with acetone before and after sample pulverisation. The pulverised samples were then sent to Leicester University for analysis, where they were made into fused glass beads, with ~1 g of powder analysed per sample. Prior to analysis, beads were heated to a temperature of 1050 °C and held for 1 hour to release any volatiles, with the amount of weight loss equating to the loss

on ignition (LOI). Standard MRG-1 was analysed simultaneously with the samples. The major element composition of each sample was emailed to me in an Excel spreadsheet, with the LOI values also provided. The weight percent of each compound was recalculated to exclude LOI by adding together the weight percent of each compound and determining the weight percent of each compound as a percent of this total.

2.4.3. Errors

The error (**Table 2.2.**) was calculated by determining the difference between the measured values from standard MRG-1 and those provided in the GeoRem database (Jochum et al., 2005). The weight percent of each compound in sample MRG-1 was determined by Govindaraju (1994), except Fe_2O_3 which was determined by Bédard and Barnes (2002).

Table 2.2. Major element composition of standard MRG-1 as determined by XRF analysis at The University of Leicester and the composition of the standard listed on the GeoRem database. The difference between the values from Leicester and GeoRem represents the error.

	SiO_2	TiO_2	Al_2O_3	Fe_2O_3	MnO	MgO	CaO	Na_2O	K_2O	P_2O_5	K_2O+Na_2O
Leicester University (wt. % of compound)	39.121	3.830	8.587	17.950	0.156	13.597	14.729	0.790	0.204	0.060	
GeoRem (wt. % of compound)	39.120	3.770	8.470	17.940	0.170	13.550	14.700	0.740	0.180	0.080	
difference	0.001	0.060	0.117	0.010	0.014	0.047	0.029	0.050	0.024	0.020	
% error	0.002	1.595	1.382	0.053	8.037	0.344	0.199	6.772	13.595	25.269	20.368

2.5. Computerised axial tomographic scanning and sample porosity

2.5.1. Principle

Computerised axial tomographic (CAT) scanning is a non-destructive process that uses X-rays to create a 3D model of a sample, which can be dissected at any angle to view the samples internal structure. CAT scans are completed under vacuum conditions to minimise interaction between the X-rays and the atmosphere. During a CAT scan X-rays are generated within an X-ray tube, focused into a beam within an X-ray gun and then passed through the sample. The sample rotates 360° on a stage, so X-rays penetrate around the perimeter of the sample. As X-rays pass through the sample they are partially absorbed. An X-ray detector is situated behind the sample, and X-rays intersect this after passing through the sample. The amount of absorption (i.e., the reduction in X-ray intensity) is then computed by a software package called CT Pro, with the amount of absorption largely dependent on sample density. For instance, a particularly dense part of a sample (e.g., an iron-rich phenocryst) will result in more X-ray absorption relative to part of the sample that has a lower density. This technique is therefore particularly useful in determining the porosity and permeability of vesicular volcanic samples, due to the large density contrast between vesicles and the host rock. The resolution of CAT scan images is dependent on the position between the sample and the X-ray source. The industrial CAT scanner that was used for this study is capable of scanning samples with a volume similar to that of a soft drink can, and such images will have a resolution of ~50 μm. However, the resolution of a pea-sized sample would be much greater, with a resolution of a few microns being possible with most industrial CAT scanners. The quality of CAT scans is highly dependent on the number of frames captured per rotation, which can be

defined by the user. The user is also able to specify the hardness (in kV) of the X-rays and the amount (in μA) of X-rays produced, with the optimum scanning conditions being dependant on sample density, geometry and size. The optimum conditions are generally ascertained through trial and error. However, the aim when setting the scan conditions is to achieve the broadest range of greyscale values as possible in the final image, thereby encapsulating the density variability within a sample.

2.5.2. Methodology

The CAT scan was collected at Lancaster University by using an industrial Nikon XT H 160 scanner. Prior to scanning the vesicular obsidian sample (skri 2) from Skriðugil the sample was secured to the CAT scanner stage with white tack, to ensure it did not move during scanning. The X-ray hardness was set at 100 kV, the amount of generated X-rays was set at 75 μA, and the number of captured frames per rotation was set at 12064 (8 frames at 1508 positions around the sample). Once the scan was complete the CT Pro software automatically constructed the 3D model of the sample. The model was then processed using a software package called VG Studio Max. Processing involved applying greyscale thresholds to reduce noise and highlight the contrast between the vesicles and host rock.

Sample porosity was determined by manually tracing the vesicles in a CAT scan image (**Fig. 2.9.i**); the sample contains a tuffisite vein, which was also traced. The vesicles and tuffisite vein were then filled with a colour and the image was imported into ImageJ, where it was converted into a binary image (**Fig. 2.9.ii**). The Analyze Particles Tool within ImageJ was then used to determine the area of the vesicles, the tuffisite vein and the whole image. The area of the tuffisite vein was then subtracted from the total image area, with the remaining area representing the host

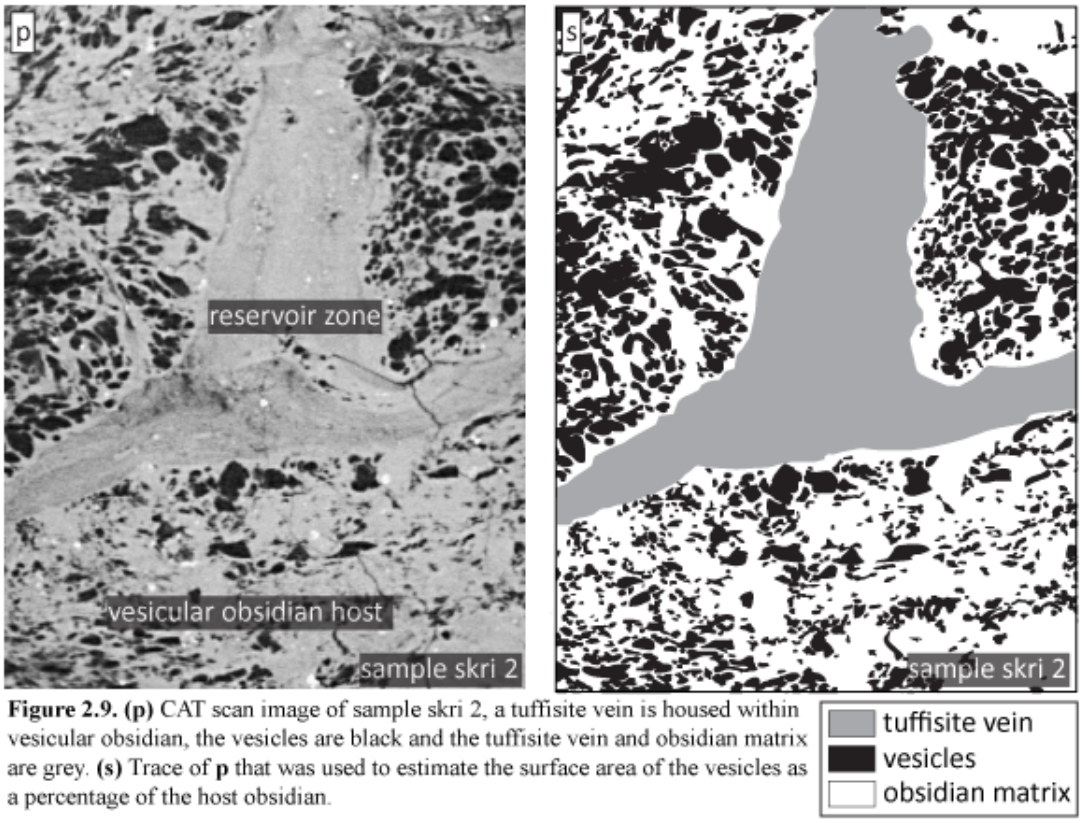

Figure 2.9. (p) CAT scan image of sample skri 2, a tuffisite vein is housed within vesicular obsidian, the vesicles are black and the tuffisite vein and obsidian matrix are grey. **(s)** Trace of **p** that was used to estimate the surface area of the vesicles as a percentage of the host obsidian.

obsidian and the vesicles; the area of the vesicles was then determined as a percentage of this remaining value. This method of determining sample porosity is straightforward, with more sophisticated techniques being possible (e.g., Wright et al., 2006; Degruyter et al., 2010b; Degruyter et al., 2010a; Schipper et al., 2013). However, the employed method was deemed adequate for the purpose of this study, and using the more sophisticated techniques would involve extracting the tuffisite vein from the 3D rock volume, which is problematic due to the similar density of the tuffisite vein and host rock. A simple way to alleviate this problem would be to scan a section of the rock that does not contain tuffisite veins, which may be completed in the future.

2.6. Grainsize measurements

2.6.1. Methodology

Obsidian clast sizes were determined using BSE images and photographs of petrological thin sections. In BSE images the obsidian clast surfaces are distinguishable from one another because microlites coat their surfaces, and the microlites have much stronger backscatter intensities relative to the clasts. However, because the microlites form an incomplete shell around the clasts, different clasts cannot be isolated via automated thresholding techniques. Similarly, the lack of colour contrast between clasts in the photographs meant that automated thresholding could not be used to isolate different clasts in these images either. Clast outlines were therefore traced by hand using Adobe Illustrator. The outlines were then filled with a colour, and scaled enlarged versions of the images were imported into ImageJ, where they were converted into binary images. The Analyze Particles tool within ImageJ was then used to measure grain areas. The radius (r in mm) of an equivalent sized circle was then calculated, using the following equation $r = \sqrt{A \div \pi}$, where A is the area. The grainsize was then determined as the weight percent of the total volume of the measured grains, following the methodology of Rust and Cashman (2011), and Lui et al. (2015). This involved four steps. Firstly, each clast was assumed to be a sphere, and sphere volumes (v in mm^3) were determined from the radius ($v = \frac{4}{3}\pi r^3$). Secondly, the clast volumes were added together, giving the total volume of all measured clasts. Thirdly, the proportional contribution of each clast (sphere) volume to the total volume was calculated (clast volume / total volume). Finally, the percentage contribution of clasts with a volume greater than a specific size was determined.

The percentage area of feldspar and pyroxene within binary versions of BSE images were determined by automatically applying thresholds using ImageJ. These thresholds were subjective, thus, a maximum and minimum threshold was applied. The Analyze Particles tool within ImageJ was then used to measure the surface area of the fragments as a percentage of the total image area.

2.6.2. Errors

The error associated with the obsidian clast measurements will stem from inaccuracies in tracing clast outlines manually, whereas those associated with the phenocryst percentage estimates will stem from subjectivity and limitations of applying thresholds. Both of these errors are deemed sufficiently small to be neglected, and are thus not considered further. The other source of error regarding the grainsize measurements will result from inaccuracies in measuring grain areas in ImageJ. This error was estimated by determining the area of shapes using ImageJ, for shapes that have calculable areas (i.e., circles, equilateral triangles, rectangles and squares). Ten different sizes of each shape were used, with the major axes of the shapes spanning 1-75 mm (6-45,000 pixels). The difference between the manually calculated areas and those calculated in ImageJ spans 0-50 %, with the percentage of error being greatest for the smallest shapes (**Table 2.3.**). The measured obsidian clasts from SE Rauðfossafjöll and Húsafell span ~1 μm - 1 cm, equating to 1- >100,000 pixels in the scaled enlarged images that were used in the measurements, but generally the clast areas are 100-10,000 pixels. If the maximum error of 50 % applies to the clast measurements this would cause the clast sizes to deviate by a minimum amount of 0.5 μm and a maximum of 0.5 mm, and because of this, the error associated with the clast sizes is thought to be negligible.

Table 2.3. Error associated with grainsize measurements.

circles (measurements are in mm)						
image No.	**clast No.**	**area**	**actual diameter (d)**	**actual area (pi*(d/2)^2)**	**error**	**% error**
3	1	4464.50	75	4417.86	46.63	1.04
3	2	1993.83	50	1963.50	30.33	1.52
2	1	983.09	35	962.11	20.97	2.13
2	2	723.74	30	706.86	16.88	2.33
2	3	505.74	25	490.87	14.87	2.94
2	4	326.37	20	314.16	12.21	3.74
2	5	185.36	15	176.71	8.64	4.66
1	1	84.71	10	78.54	6.17	7.28
1	2	68.76	9	63.62	5.14	7.48
1	3	54.69	8	50.27	4.42	8.08
1	4	42.35	7	38.48	3.87	9.13
1	5	31.52	6	28.27	3.24	10.28
1	6	22.42	5	19.63	2.79	12.43
1	7	14.95	4	12.57	2.38	15.93
1	8	8.84	3	7.07	1.78	20.08
1	9	4.36	2	3.14	1.22	27.94
1	10	1.49	1	0.79	0.71	47.46
equilateral triangle (measurements are in mm)						
image number	**clast number**	**area**	**length of sides (a)**	**actual area ($(\sqrt{3})/4*a^2$)**	**error**	**% error**
2	2	520.69	30	389.71	130.98	25.16
2	1	708.79	35	530.44	178.35	25.16
2	4	231.57	20	173.21	58.37	25.20
2	3	361.87	25	270.63	91.24	25.21
2	5	130.42	15	97.43	32.99	25.30
3	1	3262.05	75	2435.70	826.35	25.33
3	2	1452.33	50	1082.53	369.80	25.46
1	1	59.92	10	43.30	16.62	27.73
1	2	48.71	9	35.07	13.63	27.99
1	3	38.74	8	27.71	11.03	28.47
1	4	29.77	7	21.22	8.55	28.73
1	5	22.05	6	15.59	6.46	29.30
1	6	15.45	5	10.83	4.62	29.92

1	7	10.09	4	6.93	3.16	31.34
1	8	5.85	3	3.90	1.96	33.44
1	9	2.74	2	1.73	1.01	36.80
1	10	0.75	1	0.43	0.31	42.06
rectangle (measurements are in mm)						
image number	**clast number**	**area**	**length (l) / width (w)**	**actual area (w*l)**	**error**	**% error**
1	4	24.79	7/ 3.5	24.5	0.29	4.13
1	7	8.22	4 /2	8	0.22	5.54
2	3	313.91	25 /12.5	312.5	1.41	5.64
1	9	2.12	2 / 1	2	0.12	5.88
1	3	32.89	8 / 4	32	0.89	11.07
3	2	1255.89	50 / 25	1250	5.89	11.78
1	8	4.98	3 / 1.5	4.5	0.48	16.09
1	2	41.98	9 / 4.5	40.5	1.48	16.44
2	5	109.87	15 / 7.5	112.5	2.63	17.54
3	1	2799.28	75 / 37.5	2812.5	13.22	17.63
1	5	19.06	6 / 3	18	1.06	17.65
2	2	455.29	30 / 15	450	5.29	17.65
1	6	13.70	5 / 2.5	12.5	1.20	24.05
1	10	0.75	1 / 0.5	0.5	0.25	24.74
2	1	622.84	35 / 17.5	612.5	10.34	29.54
2	4	205.91	20 / 10	200	5.91	29.55
1	1	53.94	10 / 5	50	3.94	39.38
square (measurements are in mm)						
image number	**clast number**	**area**	**length of sides (a)**	**actual area (a^2)**	**error**	**% error**
1	5	36.00	6	36	0.00	0.00
2	2	900.00	30	900	0.00	0.00
2	5	224.97	15	225	0.03	0.01
1	8	8.97	3	9	0.03	0.35
2	3	619.10	25	625	5.90	0.95
3	2	2529.47	50	2500	29.47	1.16
2	4	404.72	20	400	4.72	1.17
3	1	5704.19	75	5625	79.19	1.39

1	4	49.70	7	49	0.70	1.41
1	3	63.03	8	64	0.97	1.54
2	1	1245.18	35	1225	20.18	1.62
1	7	16.44	4	16	0.44	2.69
1	6	25.91	5	25	0.91	3.51
1	2	84.08	9	81	3.08	3.67
1	1	104.64	10	100	4.64	4.43
1	9	4.36	2	4	0.36	8.25
1	10	1.12	1	1	0.12	10.80

Chapter 3: Rhyolitic dykes at Húsafell central volcano

3.1. Introduction

This chapter presents the macro- to micro-scale detail of the textures and geochemistry of dissected rhyolitic dykes at Húsafell central volcano. Broad geological mapping and dating of the volcano had been completed prior to this study, with the presence of numerous well-exposed rhyolitic dykes highlighted (Saemundsson and Noll, 1974). However, no detailed study of the dykes had been completed prior to the study that is presented here. The dyke exposures are broadly similar, but some textures are unique to individual exposures. Thus, to test the hypotheses of this chapter it was considered necessary to study multiple exposures. The aim was to gain insight into the intrusive emplacement and deformation of magma, whilst also considering the influence of these processes and the nature of the country rock on magmatic outgassing. The hypotheses that were tested in this chapter include:

- Geochemically homogenous dykes can form via the incremental emplacement of magma.
- During magma emplacement shear is localised along emplacement boundary layers and shear zones migrate between different boundary layers.
- Dyke opening involves the intrusion particle-laden gas currents, with particle dispersal and dyke propagation being governed by the permeability and strength of the country rock.
- Magma fragmentation can involve shear failure of bubble-free magma, or shear or tensile failure of bubbly magma.
- Crystals and lithics increase the outgassing ability of external tuffisite veins by helping to sustain their permeability.

3.2. Geological setting

3.2.1. Húsafell volcanic complex

Húsafell central volcano is an eroded Tertiary volcano located in west Iceland (**Fig. 3.1.i**), with volcanic deposits covering ~120 km^2. The following description of the deposits and volcanic activity is summarised from Saemundsson and Noll (1974). The eruptive period spanned from ~3 to 2.5 Ma and the volcano had a shield-like shape during this time. The volcanic activity consisted of three silicic phases that were separated by and interleaved with mafic eruptions and glacial events. Evidence of glacial events (e.g., hyaloclastites, pillow lavas and tillites) during the first phase is lacking, whereas six glacial events may have occurred during the second phase, and one at the end of the third phase.

The first phase of activity consisted of effusive and explosive behaviour, commencing with emplacement of dacitic lavas, followed by deposition of dacitic ash-fall units and the Hraunfossar ignimbrite. The lavas are >100 m thick and exposed west of Húsafell, between the rivers Reykjadalsá and Hvítá (see the geological map in **A.3.1.**). In contrast, the pyroclastic deposits are only ~40 m thick, forming the backdrop to the Hraunfossar waterfalls. The first phase of activity culminated with the emplacement of 4-10 m thick andesitic lava.

The second phase was dominated by explosive behaviour, represented by numerous rhyolitic ash-fall units and ignimbrites. One of the ignimbrites (Deildargil ignimbrite) is well exposed and easily accessed in Deildargil valley; it is locally ~100 m thick, can be traced along strike for ~20 km, with a volume of ~20-30 km^3. This is significantly greater than the deposit volume of the 1991 Pinatubo eruption (max. ~10 km^3; Self 2004), corresponding to an eruption magnitude of ~6.5-7.3, where magnitude = $\log_{10}$ (erupted mass in kg) – 7 (Pyle, 2000), and a VEI of 6 (Newhall and

Self, 1982). For comparison, the 1362 Öræfajökull eruption, which is thought to be the largest magnitude historic explosive eruption in Iceland (Sharma et al., 2008) had an estimated magnitude of ~5.3 (Owen, 2013).

The third phase of activity consisted of effusive and explosive behaviour, commencing with the emplacement of two andesitic lavas (exposed in the upper branches of Hringsgil valley and Deildargil valley), followed by deposition of a rhyolitic ash-fall and partially-welded ignimbrite (Giljatungar ignimbrite). The third phase culminated with the emplacement of rhyolitic and andesitic lavas. After this the volcano was buried by flood basalts that were sourced east of Húsafell (Saemundsson and Noll, 1974). Throughout the third phase, rhyolitic and composite intrusions were emplaced (**Fig. 3.1.ii**), which generally strike SW-NE, similar to the western rift zone. This study focused on some of these intrusions, which are exposed in Hringsgil valley and Deildargil valley (**Fig. 3.1.ii and 3.1.iii**); they are referred to as dykes, but some locally turn into sills.

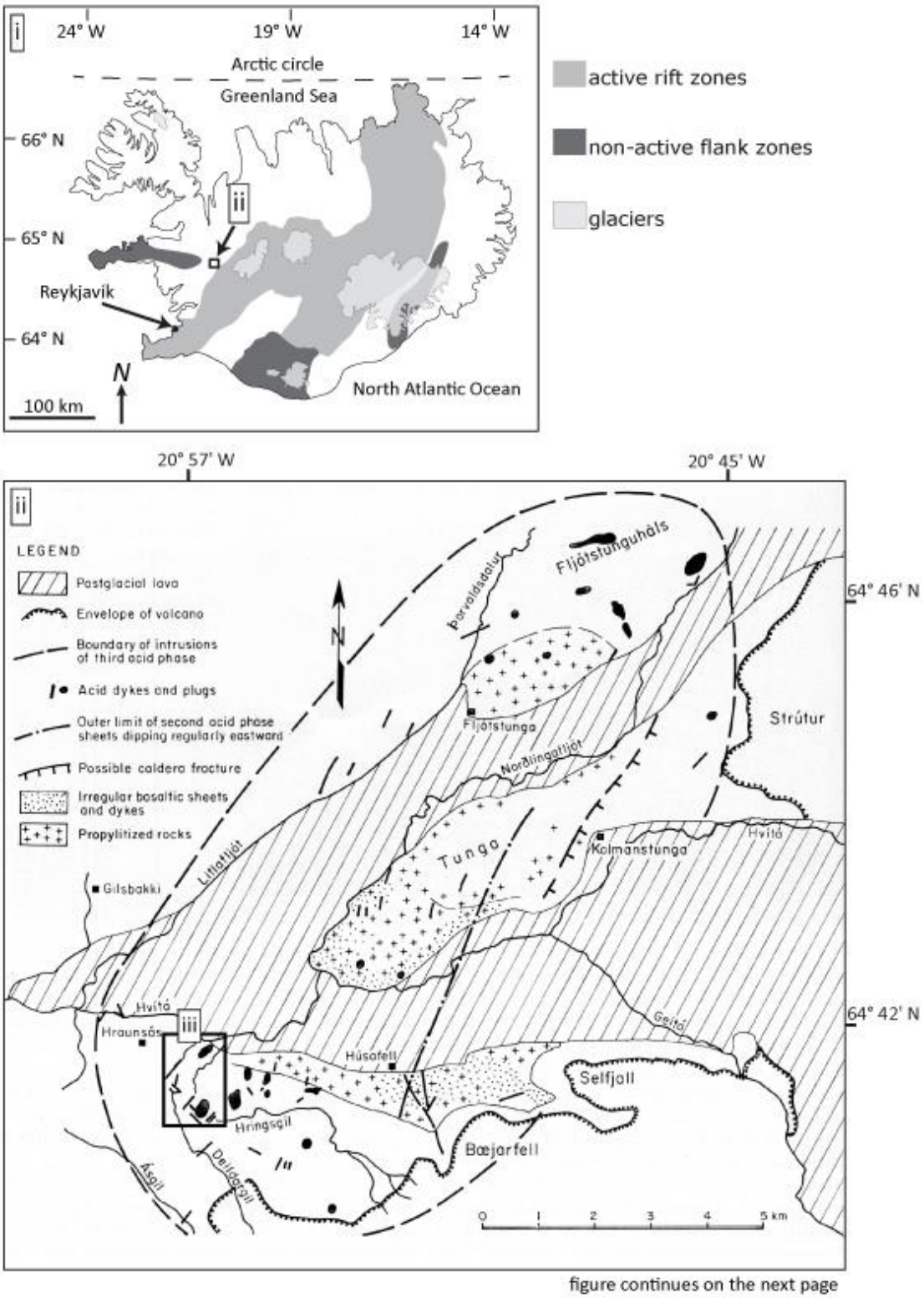

figure continues on the next page

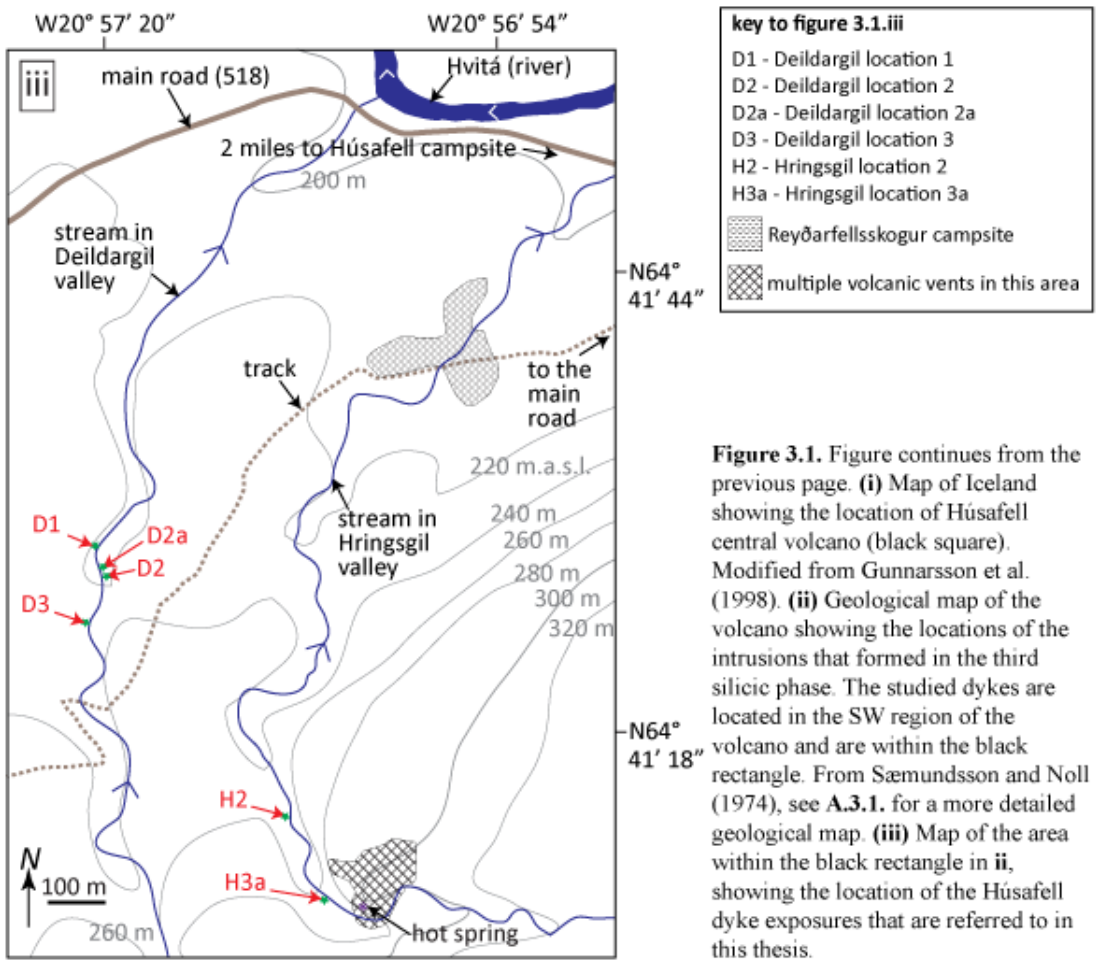

Figure 3.1. Figure continues from the previous page. **(i)** Map of Iceland showing the location of Húsafell central volcano (black square). Modified from Gunnarsson et al. (1998). **(ii)** Geological map of the volcano showing the locations of the intrusions that formed in the third silicic phase. The studied dykes are located in the SW region of the volcano and are within the black rectangle. From Sæmundsson and Noll (1974), see **A.3.1.** for a more detailed geological map. **(iii)** Map of the area within the black rectangle in **ii**, showing the location of the Húsafell dyke exposures that are referred to in this thesis.

3.2.2. Overview of the dykes and textural zones

Six dyke exposures have been studied in Húsafell, comprising four in Deildargil valley and two in Hringsgil valley (**Fig. 3.1.iii and 3.2.**). Multiple exposures may indeed belong to the same dyke. This is largely unconfirmed, but exposures at Deildargil locations 1, 2 and 2a probably belong to one dyke. The valley floors are ~200 m a.s.l. and ~50 m deep. The dyke exposures are ~2-50 m long and ~2-3 m wide, with different country rock bordering different exposures, including glacial conglomerate, brecciated basaltic lava, non-brecciated basaltic lava and a welded ignimbrite (**Table 3.1.**). Some dykes are near-horizontal, whereas others extend vertically 20-40 m up the valley walls. Five main textural zones have been identified,

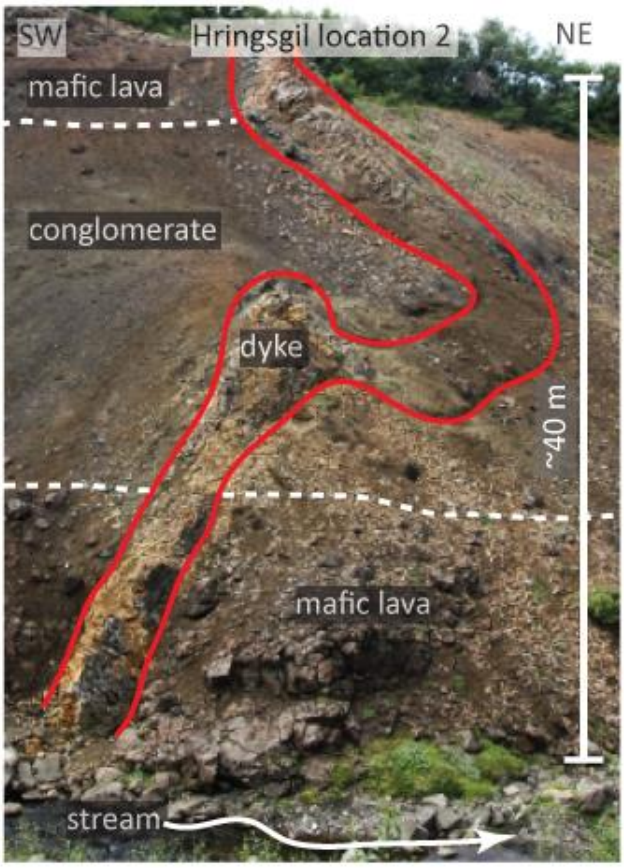

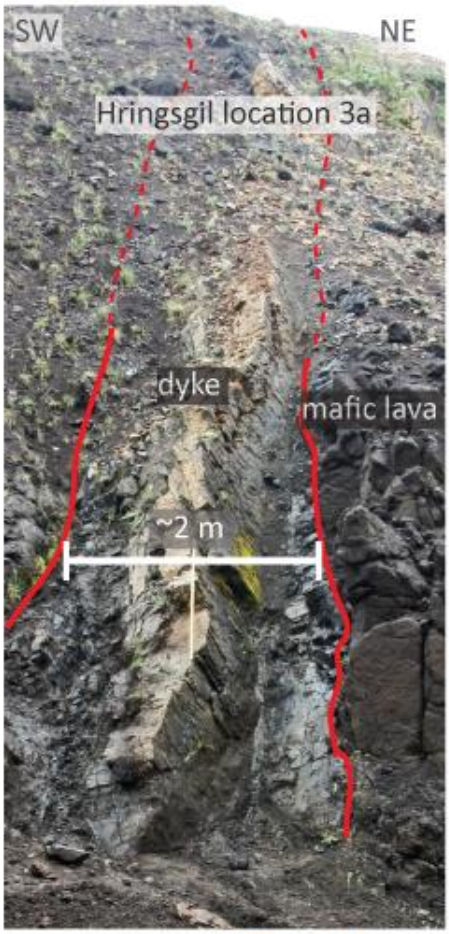

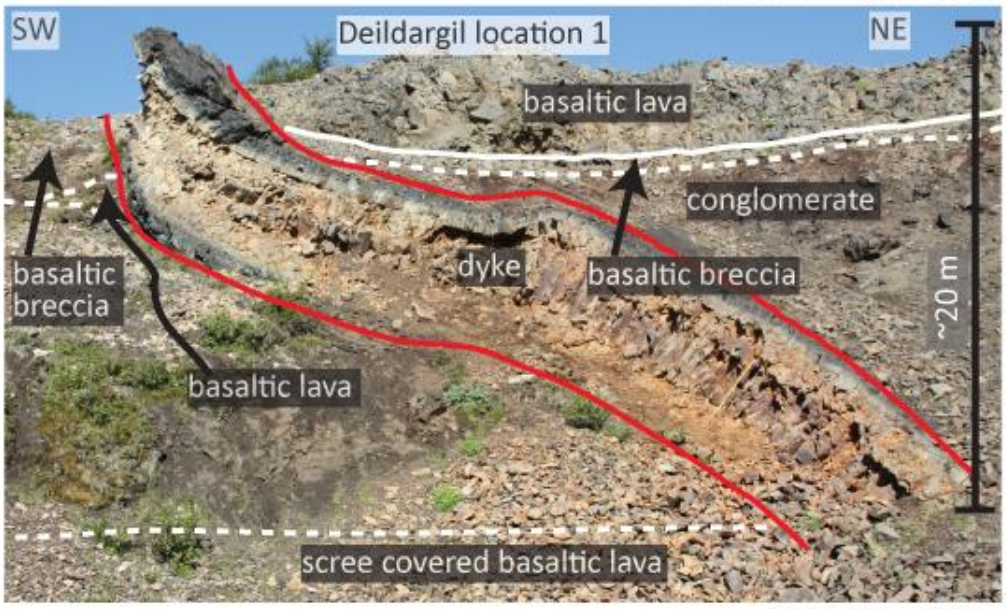

figure continues on the next page

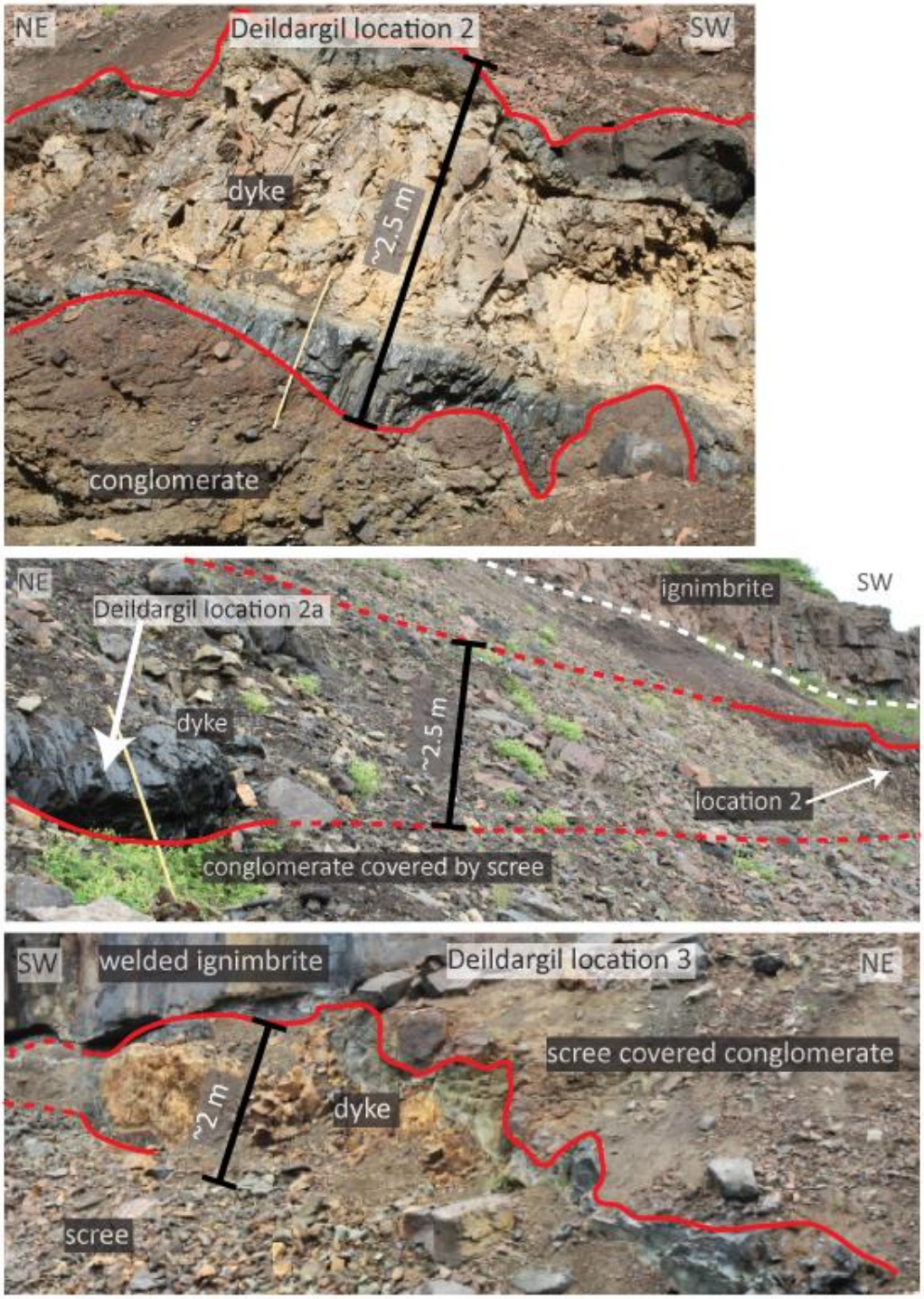

Figure 3.2. Figure continues from the previous page. The studied dyke exposures in Deildargil valley and Hringsgil valley.

Table 3.1. Measurements of dyke exposures and details of surrounding country rock.

dyke	latitude and longitude	country rock next to dyke	length / elevation change	maximum exposed width
Deildargil location 1	64°41'27.90"N 20°57'19.80"W	non-brecciated and brecciated basaltic lava (see section 3.4.1. for geochemistry) and conglomerate	~30 m / ~20 m	~2.5 m
Deildargil location 2	64°41'25.70"N 20°57'17.00"W (~65 m upstream from Deildargil location 1)	conglomerate (geochemistry not analysed)	~30 m / dyke is horizontal	~2.5 m
Deildargil location 2a	64°41'26.10"N 20°57'17.15"W (~10 m downstream from Deildargil location 2)	conglomerate (geochemistry not analysed)	~2 m / dyke is horizontal	~3 m
Deildargil location 3	64°41'23.20"N 20°57'20.60"W (~80 m upstream from Deildargil location 2)	conglomerate and welded base of an ignimbrite (geochemistry not analysed)	~10 m / ~5 m	~2 m
Hringsgil location 2	64°41'12.50"N 20°56'50.30"W	mafic lava and conglomerate (geochemistry not analysed)	~50 m / ~40 m	~2 m
Hringsgil location 3a	64°41'8.38"N 20°56'48.23"W (~120 m upstream from Hringsgil location 2)	mafic lava (geochemistry not analysed)	~35 m / ~30 m	~2 m

which are referred to as A, B, C, D and T, with categorisation based on textures and position within the dykes. The zones broadly consist of fragmented material (pumice, vesicle-free obsidian clasts, crystals and mafic lithic clasts), obsidian, microcrystalline rhyolite, clay with obsidian clasts and an obsidian-microcrystalline rhyolite mix, respectively. At Deildargil location 1, zone A is confined to veins that were pre-existing fractures in the country rock and also forms a vein-like layer at the dyke margins, whereas at Deildargil location 2a zone A is dispersed more randomly throughout intrusion-related fractures. Zones B and C are divided into seven sub-zones, referred to as B1, B2, B3, Bb, Bfb, Cc and Cm (**Fig. 3.3.**). The zone B sub-zones broadly consist of black obsidian (B1), grey obsidian (B2), green obsidian (B3), brecciated obsidian (Bb) and flow-banded obsidian (Bfb), whereas the zone C sub-

zones consist of microcrystalline rhyolite with relatively small, <1 mm wide, spherical vesicles (Cc) and microcrystalline rhyolite with relatively large, >1 mm long, elongate vesicles (Cm). It is not always possible to distinguish between the sub-zones of zone B due to weathering, and in such instances, the zone is referred to as B-. Sub-zones exist locally within different dyke exposures (**Fig. 3.3.**), but all exposures have obsidian margins (zone B) and microcrystalline centres (zone C). Zones and sub-zones are described further in the following sections, except zone D, as this appears to be a highly weathered and altered version of zone B.

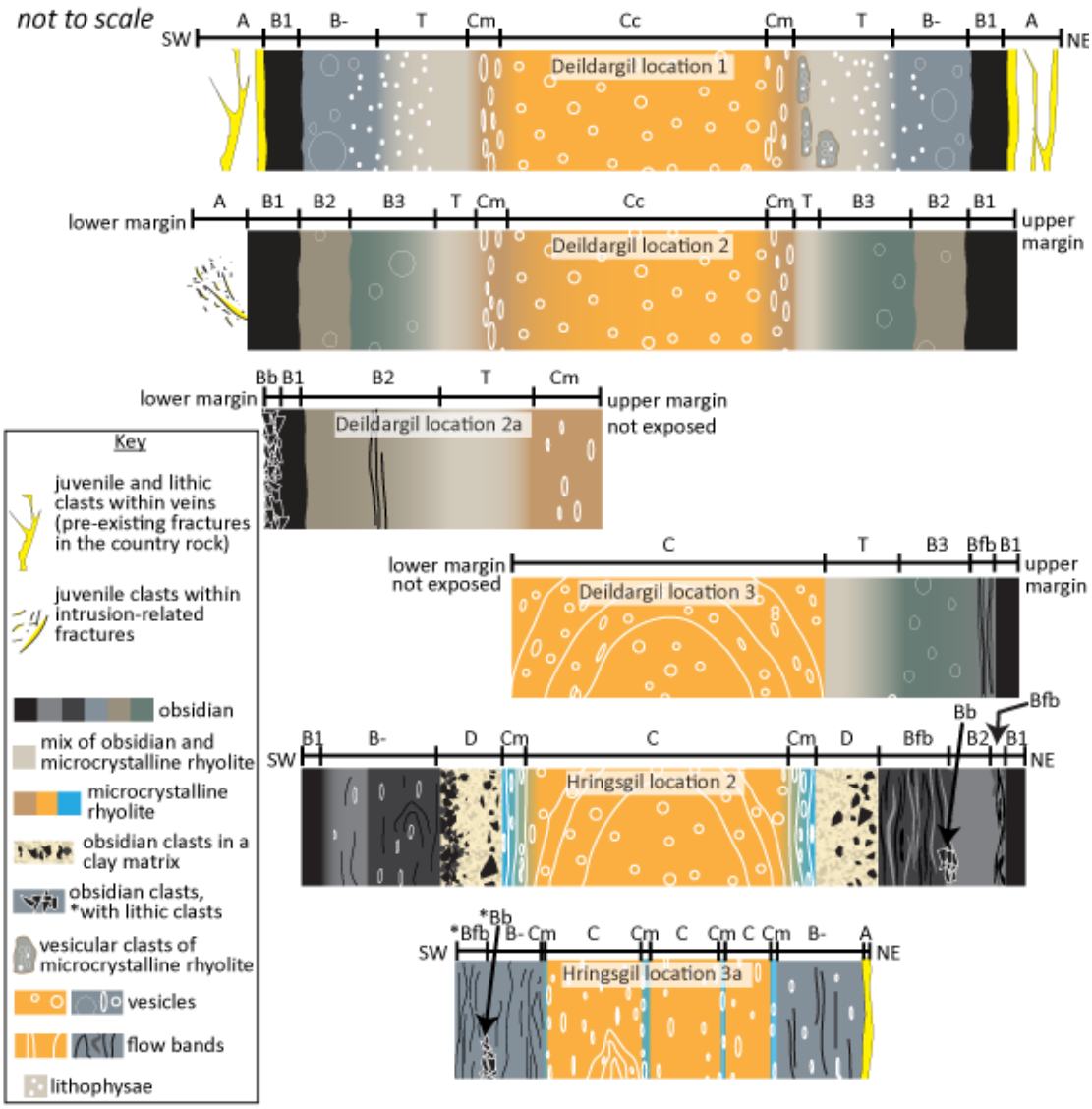

Brief description of the textural zones

Main zones

A: vesicular and vesicle-free obsidian clasts, and lithic clasts

B: obsidian

T: mix of obsidian and microcrystalline rhyolite

C: microcrystalline rhyolite

D: clay containing clasts of obsidian

Sub-zones

B1: black obsidian, next to the country rock or zone A

B2: grey obsidian, between B1 and B2

B3: green obsidian, between B2 and T

B-: unclear whether B1, B2, B3, Bb or Bfb

Bb: clasts of obsidian (zone B), *with lithic clasts

Bfb: discrete layer (>1 cm thick) of flow banded obsidian at the edge of B1, B2 or B3, *with lithic clasts

Cc: brown-orange, dyke centre, sometimes contains folded flow bands, the axial planes are parallel with dyke margins, vesicles are generally more circular than those in Cm

Cm: dark brown, blue or grey, borders Cc, sometimes contains flow bands that are relatively linear (in contrast to those in Cc) and parallel with dyke margins

Figure 3.3. Schematic illustration showing the location of the textural zones and sub-zones across the dyke exposures.

3.3. Description of the textural zones

3.3.1. Zone A

i) Macro-scale features: location and dimensions

Zone A is composed of ash (clasts <2 mm) and lapilli (clasts ~2-50 mm), which predominantly consist of juveniles, with ~15-30 % lithics. The zone occurs at Deildargil locations 1 and 2, and Hringsgil location 3a, but a detailed study was only conducted at the former locations; thus location 3a will not be discussed further in this section. At Deildargil location 1, zone A forms the upper dyke margins (**Fig. 3.4.**) and is outwardly bordered by the country rock (non-brecciated and brecciated basaltic lava, see **section 3.4.1.** for geochemistry). The contact between zones A and B is generally sub-planar, and varies between sharp and diffuse. The contact between zone A and the non-brecciated lava is sharp and sub-planar, whereas between zone A and the brecciated lava it is sharp and irregular, as zone A weaves between the breccia clasts. At the NE dyke margin the thickness of zone A is variable, always less than 100 mm, and it is exposed over a length of 1 m. Similarly at the SW margin, it is ~1-90 mm thick, ~5 m long and locally pinches out.

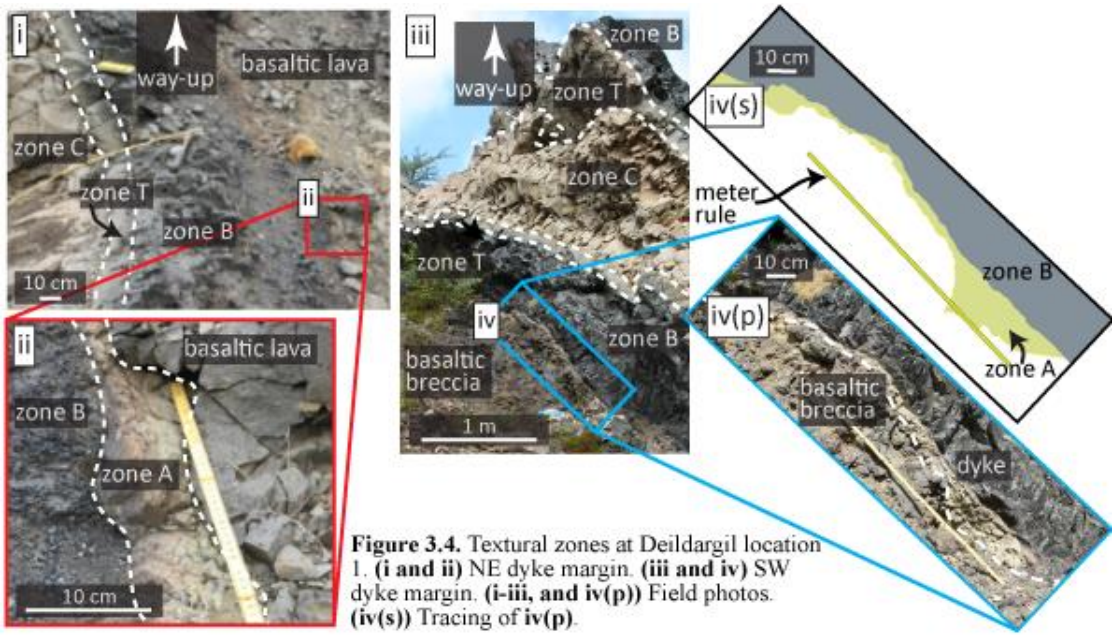

Figure 3.4. Textural zones at Deildargil location 1. **(i and ii)** NE dyke margin. **(iii and iv)** SW dyke margin. **(i-iii, and iv(p))** Field photos. **(iv(s))** Tracing of **iv(p)**.

Additionally at location 1, the fragmental material of zone A is confined to veins which are housed within the country rock next to the upper part of the dyke (**Fig. 3.5.**). The vein number density decreases with increased distance from the main part of the dyke, with visible veins lacking beyond 5 m. The veins form networks (**Fig. 3.5.**), consisting of main stems that extend outwards into shorter thinner veins (veinlets). The stems are >50 cm long, 1-50 mm wide, and generally thin upwards, whereas the veinlets are <30 cm long, 1-20 mm wide, and thin away from the stems.

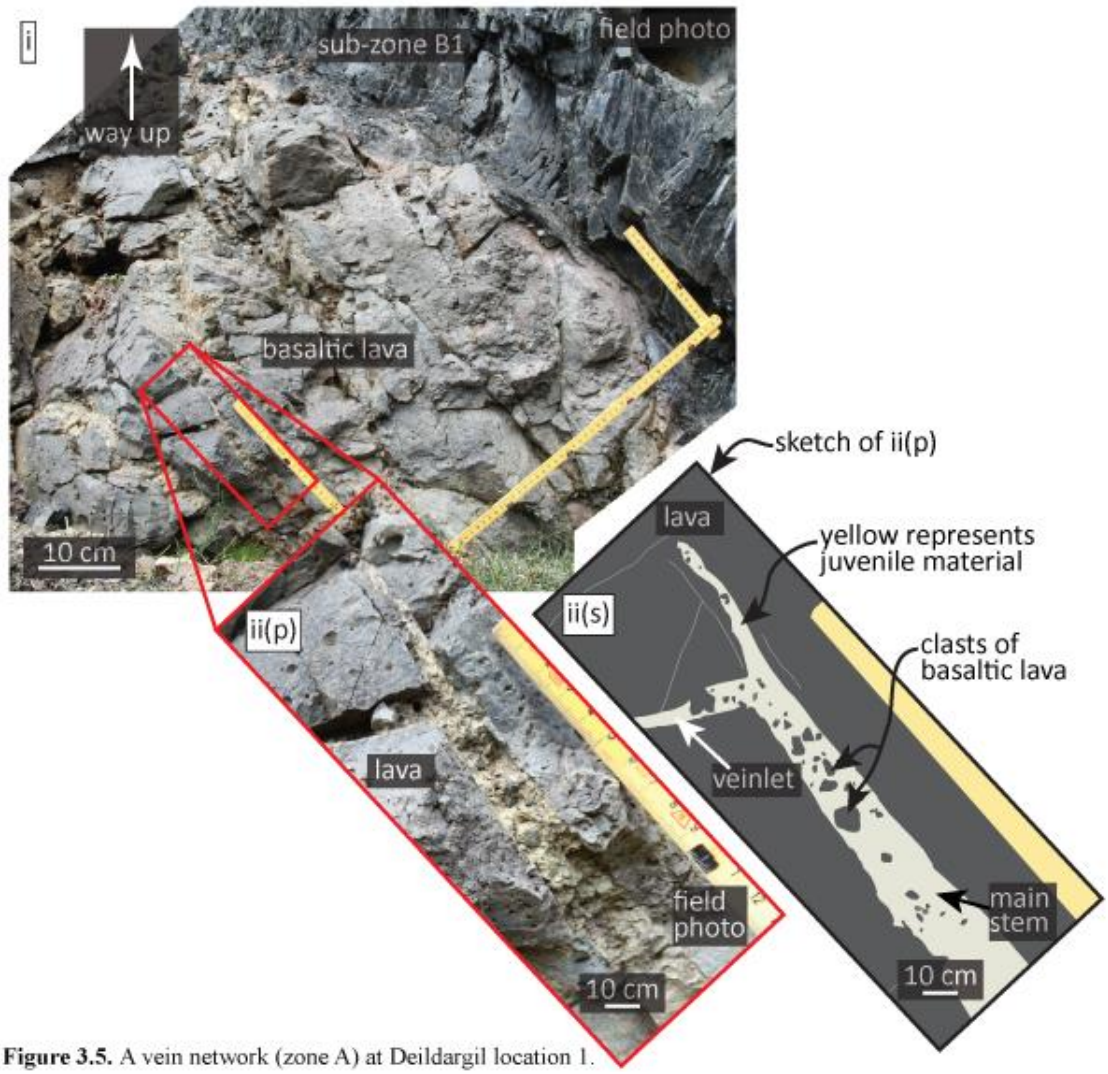

Figure 3.5. A vein network (zone A) at Deildargil location 1.

The non-brecciated lava is pervasively cut by >1 m long sub-vertical fractures and sub-horizontal <20 cm long fractures. The stems of zone A have similar orientations to the sub-vertical fractures (**Fig. 3.6.**), whereas the veinlets have similar

orientations to the sub-horizontal fractures. The non-brecciated lava surrounding the vein networks contains a high number density of short (<10 cm long) fractures, with random orientations, but such fractures are less common in the vein-free lava (**Fig. 3.6.**). Zone A is not confined to veins at Deildargil location 2, but is instead dispersed in the conglomerate throughout a ~30 x 70 cm domain, with a long axis orientated at ~45° to sub-zone B1, and which is truncated by B1 (**Fig. 3.7.**).

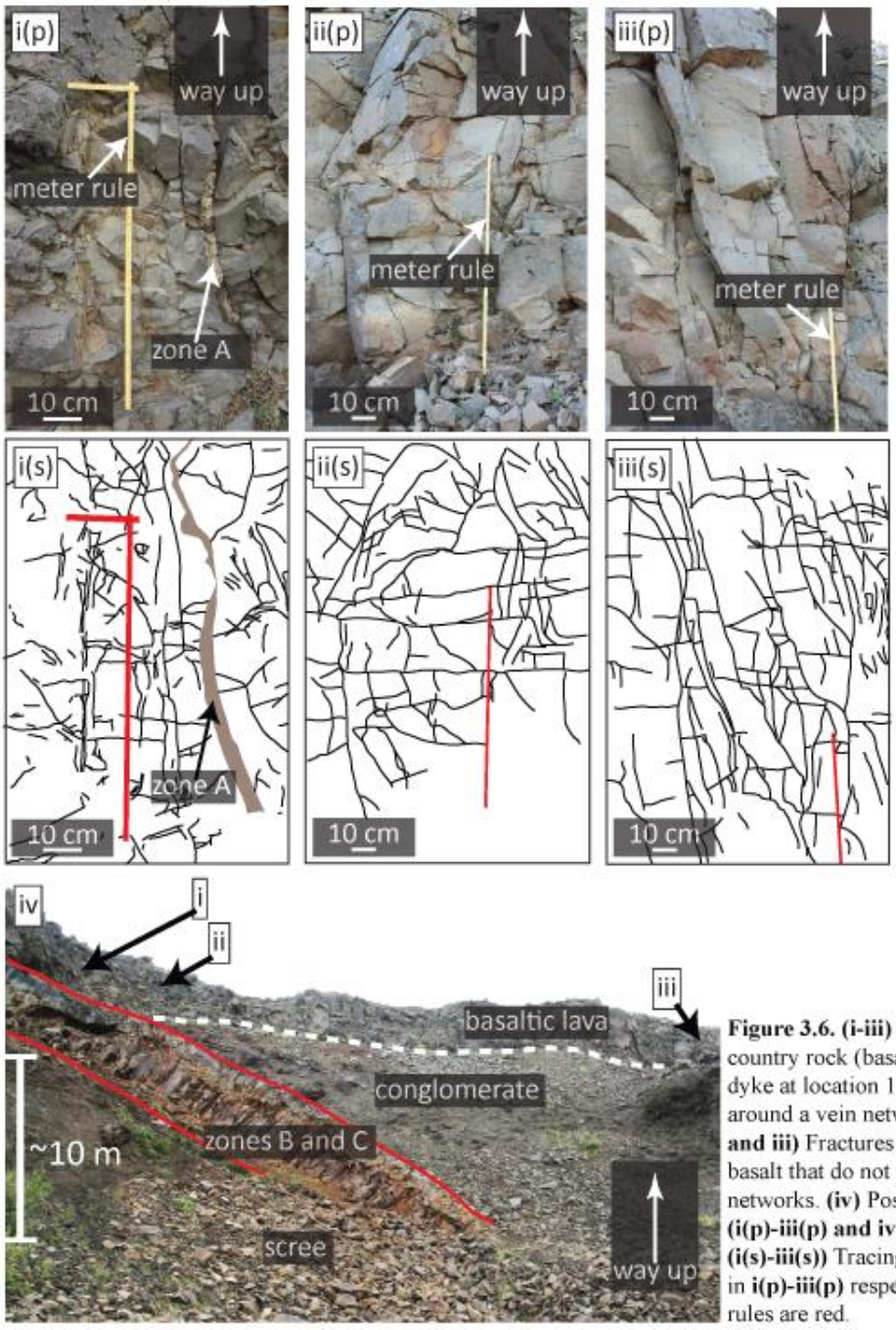

Figure 3.6. (i-iii) Fractures in the country rock (basaltic lava) near the dyke at location 1. **(i)** Fractures around a vein network (zone A). **(ii and iii)** Fractures in parts of the basalt that do not contain vein networks. **(iv)** Position of **i-iii**. **(i(p)-iii(p) and iv)** Field photos. **(i(s)-iii(s))** Tracings of the fractures in **i(p)-iii(p)** respectively, metre rules are red.

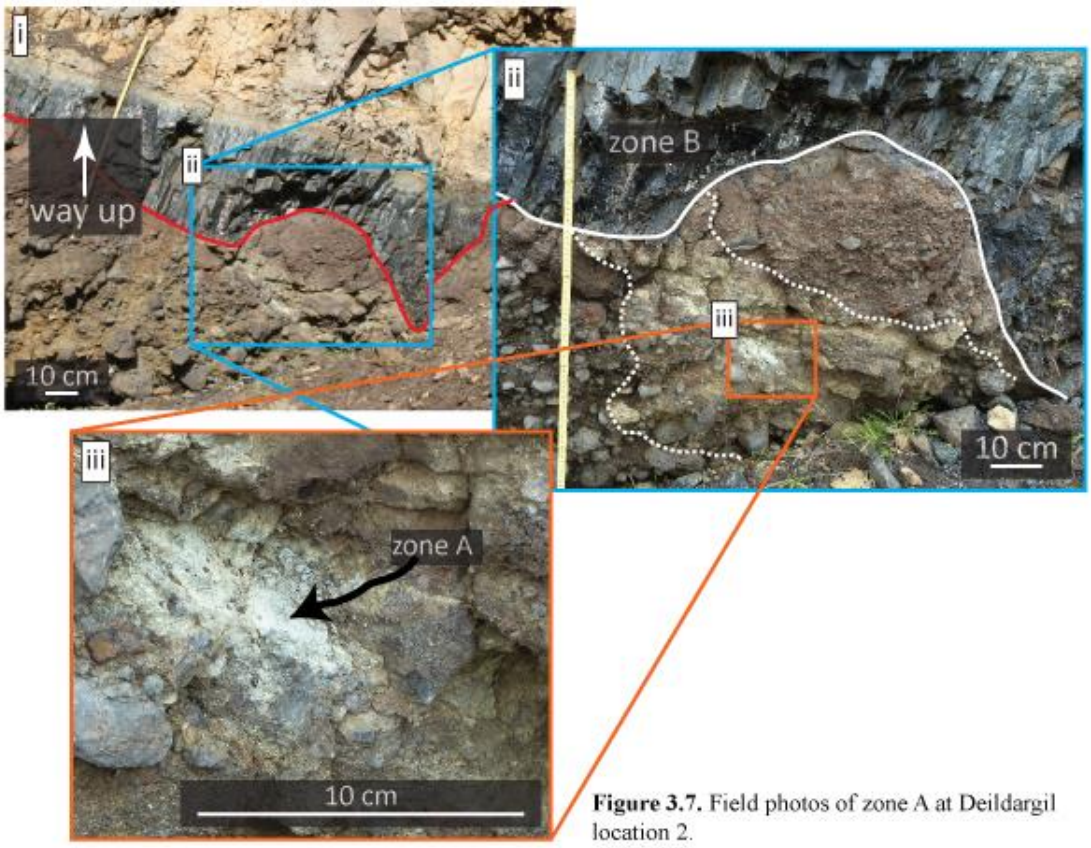

Figure 3.7. Field photos of zone A at Deildargil location 2.

ii) Meso-scale features: colour and sedimentary structures

The colour of the fragmental material at the SW margin of Deildargil location 1 is predominantly yellow next to the country rock and dark grey next to sub-zone B1 (**Fig. 3.8.i and ii**). The yellow and grey parts are ~5-90 mm and ~10-60 mm wide, respectively; both are thickest where the zone is thickest. The true clastic nature of the grey part is not apparent in the field, but it is in petrological thin sections. In contrast, the clastic nature of the yellow part is apparent in the field, with both pumice and lithic clasts visible. The yellow colour of the vein represents the pumice clasts, with lithics being grey or red. Lithic colours match the bordering country rock (brecciated and non-brecciated basaltic lava). In contrast to the dyke margins, the veins of fragmental material that are housed within the country rock are predominantly yellow

(i.e., the veins lack a dark grey part), with some grey lithic clasts that match the bordering country rock (non-brecciated basaltic lava; **Fig. 3.8.iii and iv**).

The yellow section of zone A at the SW dyke margin is locally grainsize-sorted, consisting of coarse-grained and fine-grained parts. The contact between the

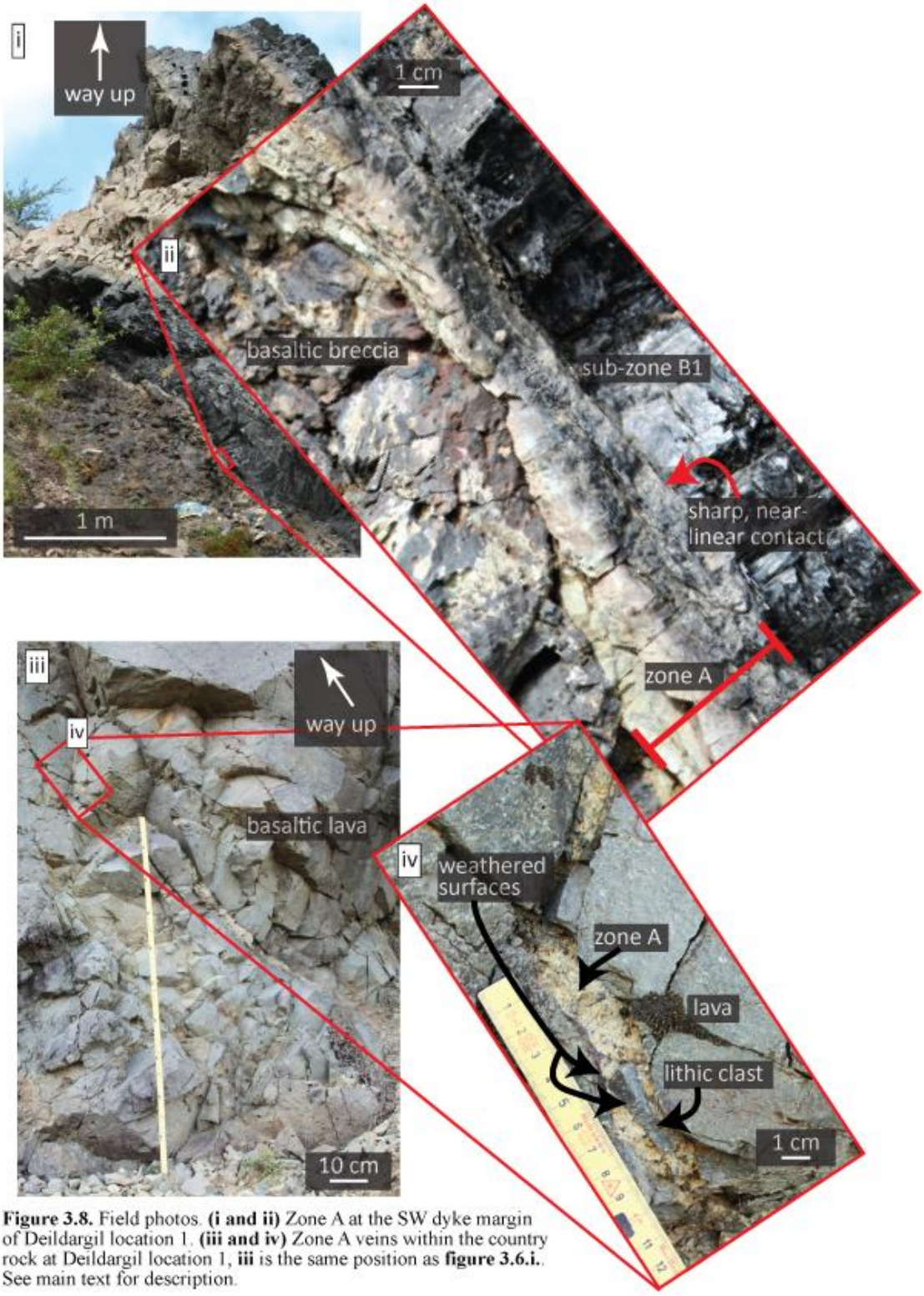

Figure 3.8. Field photos. **(i and ii)** Zone A at the SW dyke margin of Deildargil location 1. **(iii and iv)** Zone A veins within the country rock at Deildargil location 1, **iii** is the same position as **figure 3.6.i.**. See main text for description.

two parts is irregular and generally sharp, but is sometimes diffuse. The juvenile and lithic clasts within the coarse part consist of ash (clasts <2 mm) and lapilli (clasts ~2-10 mm), and this part is closest to the country rock, whereas in the fine part, which is furthest from the country rock, the clasts predominantly consist of ash (**Fig. 3.9.i**). The veins of fragmental material that are wholly housed within country rock are also locally grainsize sorted (**Fig. 3.9.ii**). None of the lithics or juveniles in zone A have a jigsaw fit when viewed with the naked eye.

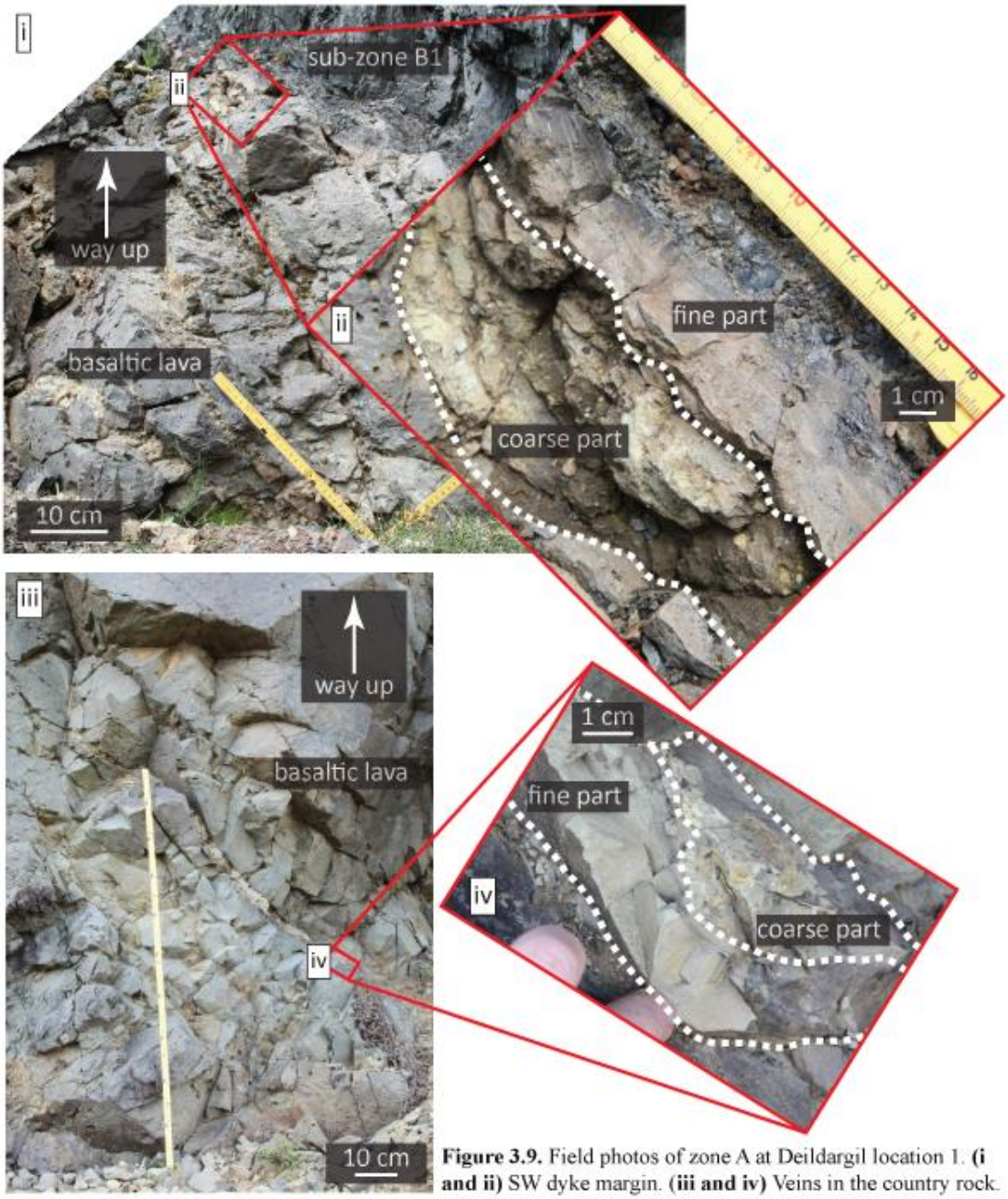

Figure 3.9. Field photos of zone A at Deildargil location 1. **(i and ii)** SW dyke margin. **(iii and iv)** Veins in the country rock.

The fine part of zone A contains laminations. In the veins housed within the country rock these are diffuse wispy lines, <50 mm long and ~1 mm wide; no coherent samples of these could be collected, thus, the sedimentary structures in these veins will not be discussed further. However, coherent samples were collected from the SW dyke margin. Here, the laminations can generally be traced over a length of ~50-100 mm, they then fade out, or become indistinct due to weathering. The laminations are commonly near-planar and parallel to the dyke margins, but cross laminations exist locally. The foresets of the cross laminations are truncated closest to sub-zone B1 (**Fig. 3.10. and 3.11.iv**), and orientated ~45-80° to the dyke margin. This

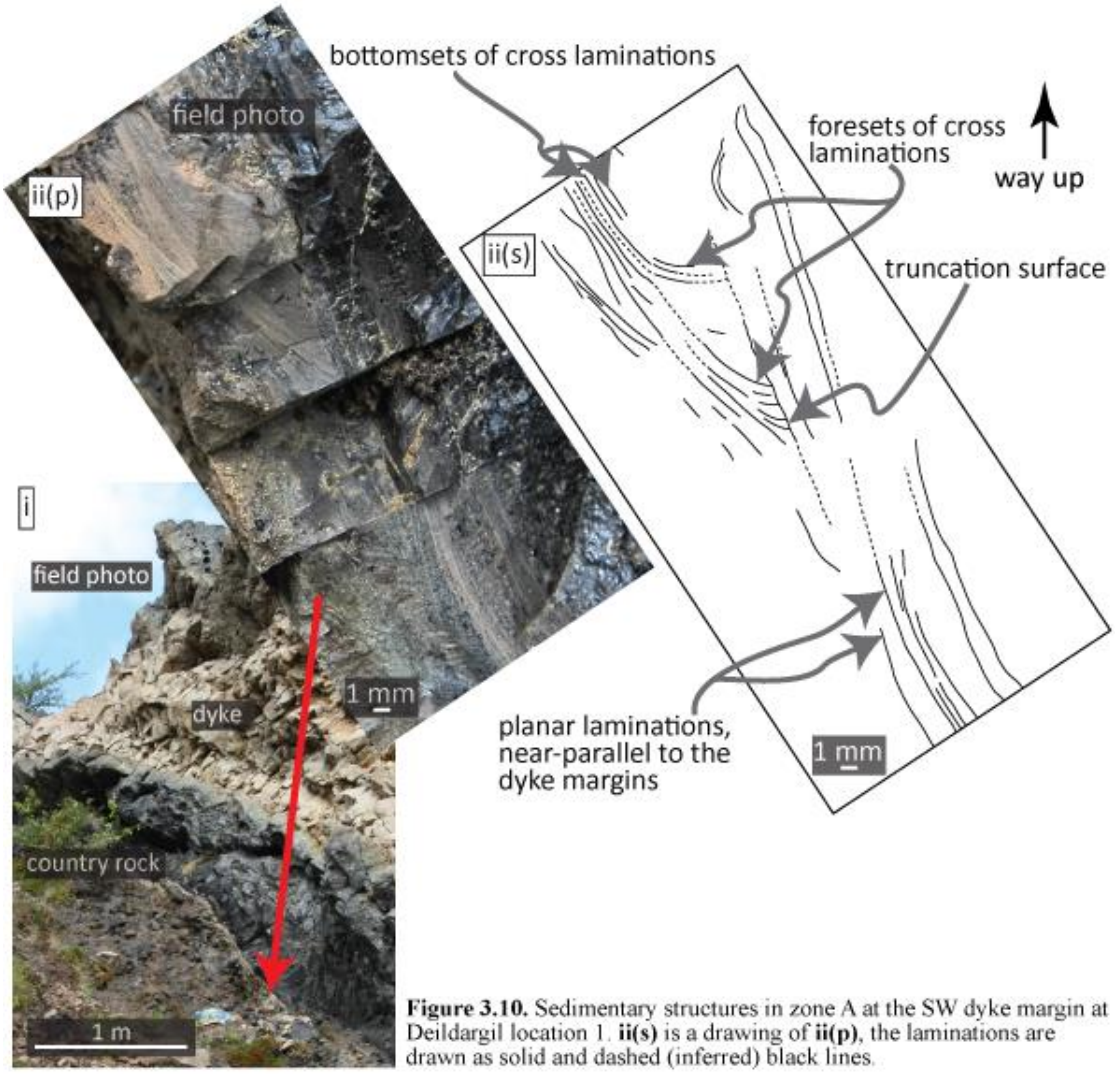

Figure 3.10. Sedimentary structures in zone A at the SW dyke margin at Deildargil location 1. **ii(s)** is a drawing of **ii(p)**, the laminations are drawn as solid and dashed (inferred) black lines.

angle decreases towards the country rock as the foresets pass into the bottomsets, with the bottomsets being near-parallel to the dyke margin. The laminations that consist of the finest ash (clasts <<0.1 mm) are generally ~100-200 μm wide, but their thickness varies next to relatively large clasts (clasts >2 mm; **Fig. 3.11.vi**). Convolute laminations also occur locally, extending from planar laminations, with some having fluidal ends that weave between surrounding clasts (**Fig. 3.12.**).

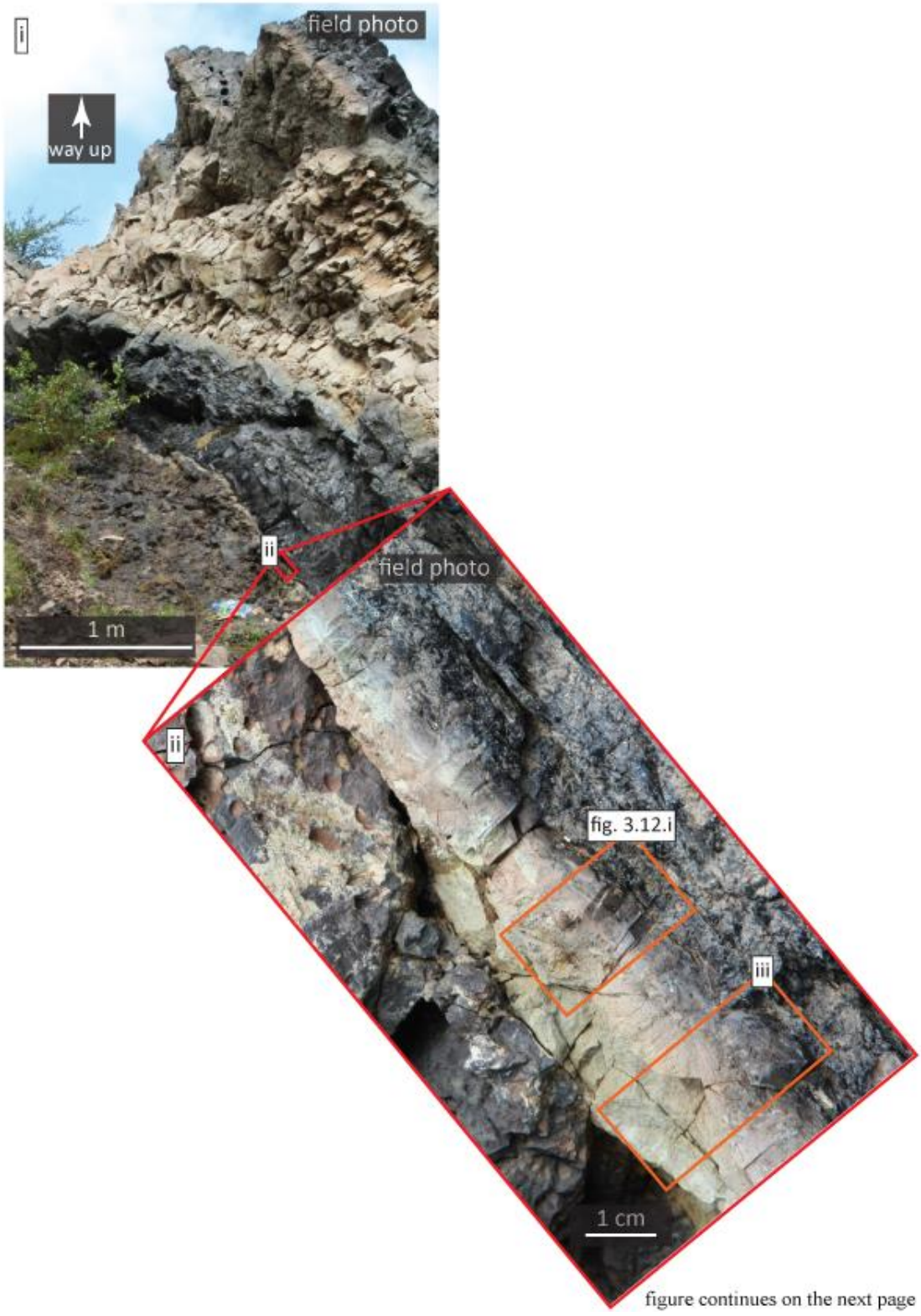

figure continues on the next page

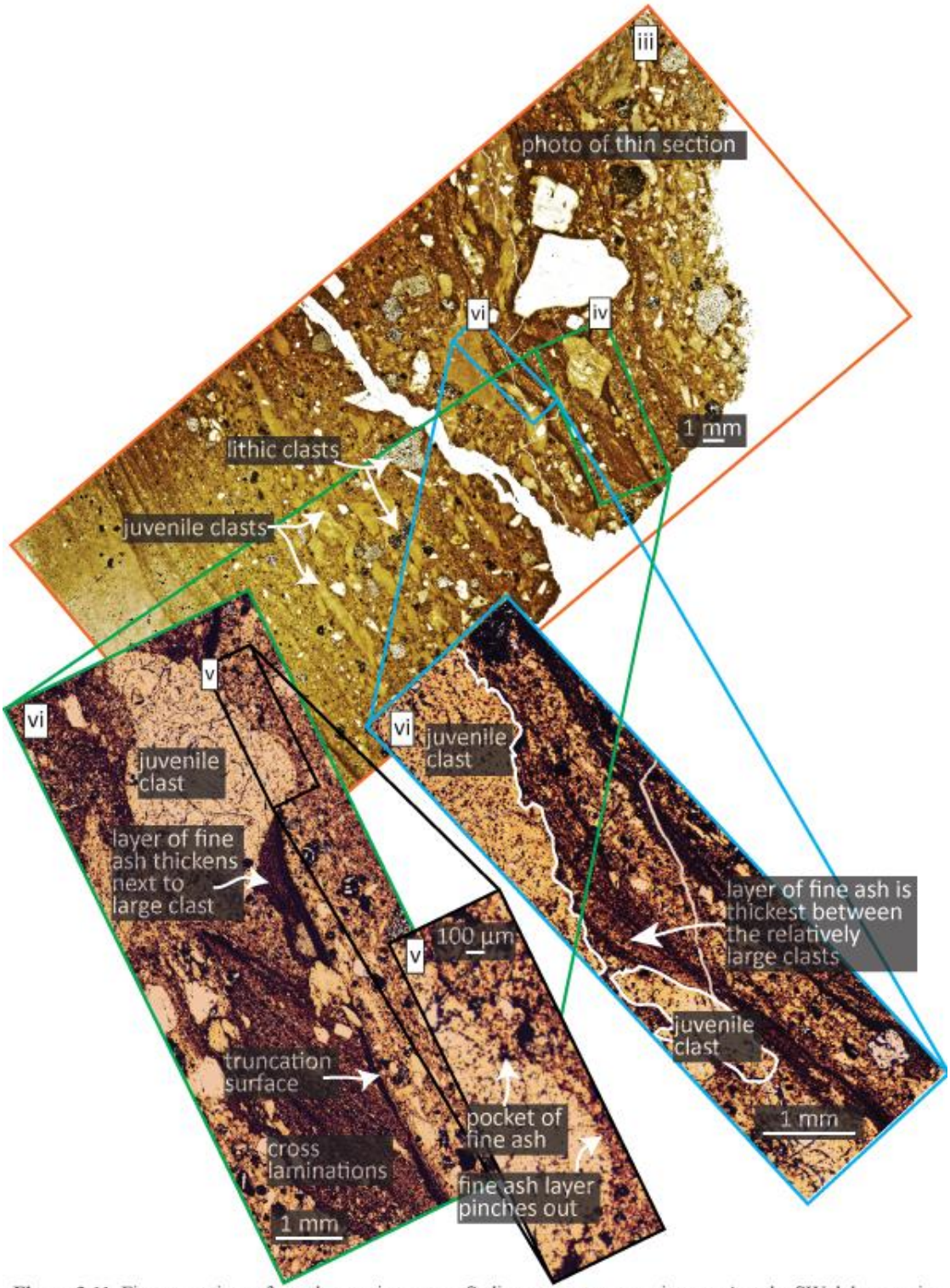

Figure 3.11. Figure continues from the previous page. Sedimentary structures in zone A at the SW dyke margin at Deildargil location 1 (sample D4). **(iv-vi)** Microphotographs taken in plane polarised light.

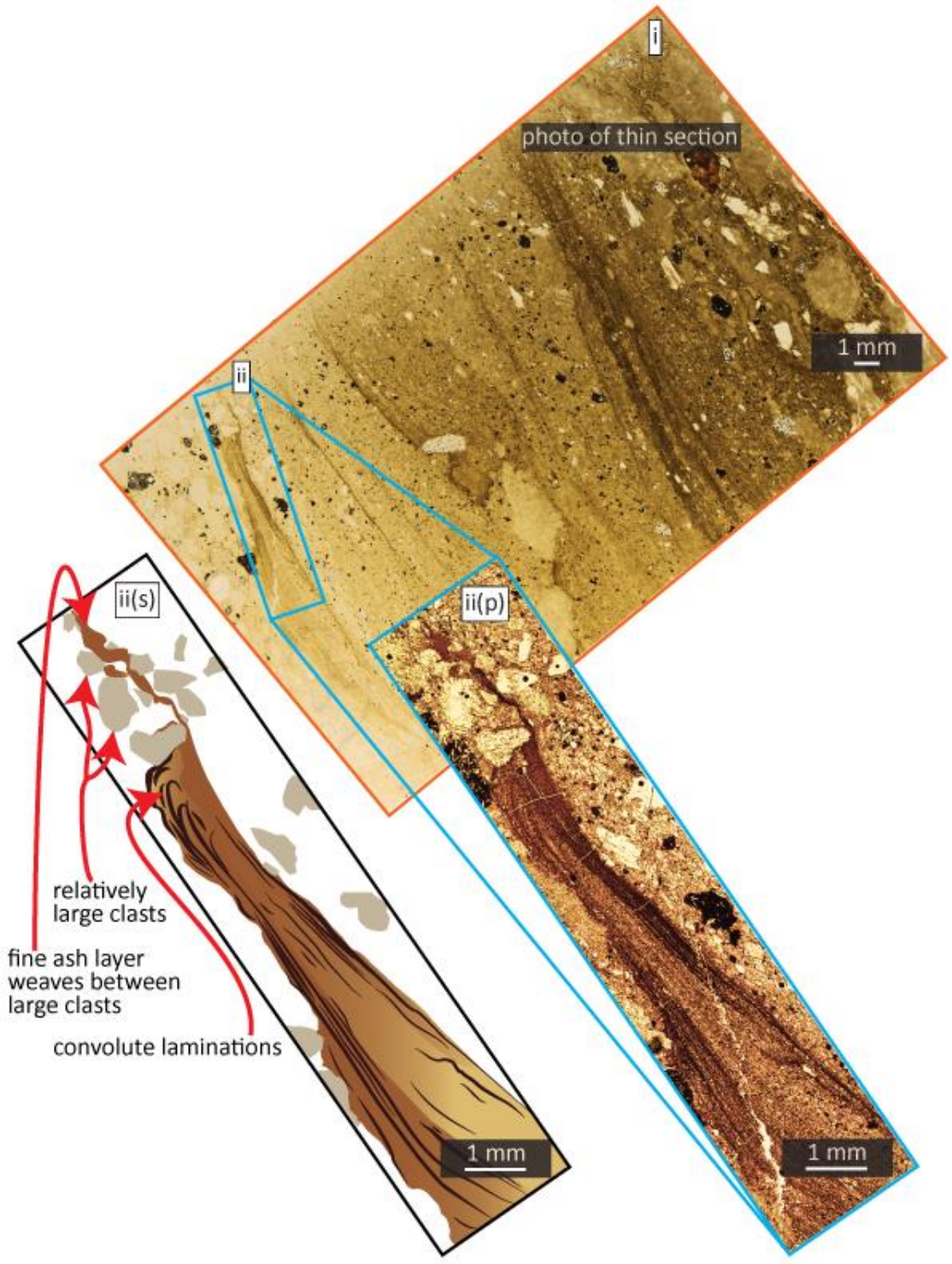

Figure 3.12. Sedimentary structures in zone A at the SW dyke margin at Deildargil location 1 (sample D4). **(iv(p))** Collage of microphotographs taken in plane polarised light. **(iv(s))** Sketch of **iv(p)**. The location of **i** is shown in **figure 3.11.ii**.

iii) Micro-scale features of the SW margin of Deildargil location 1: grainsize, clast textures and porosity

The juvenile and lithic clast sizes in zone A were determined by manually tracing the clasts using Adobe Illustrator in a photograph of a thin section and also in BSE images. ImageJ was then used to estimate individual clast areas. Diameters of circles with the same areas were then calculated, with sphere volumes then determined from the diameters (see **section 2.6.** for methodology and errors, and **A.3.2.** for clast tracings and data). This method was used because the forms of some juvenile clasts reflect viscous deformation, with clast lengths affected by deformation, but areas unaffected. The juvenile and lithic clasts have similar sizes, with diameters spanning ~1 μm - 10 mm (**Fig. 3.13.**), with the majority being <1 mm. Clasts with diameters >1 mm contribute >90 % of the total measured volume (**Fig. 3.13.**). The lithic lapilli are sub-circular with sub-rounded edges, whereas the pumice lapilli are generally more elongate, with feather-like edges (**Fig. 3.14.i**).

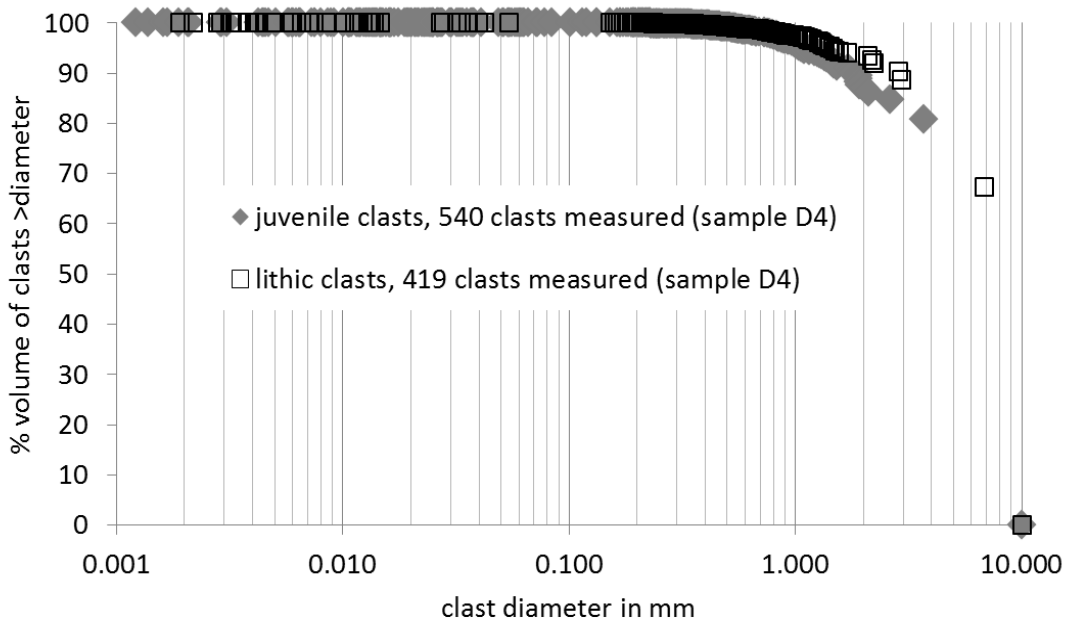

Figure 3.13. Clast sizes in zone A, at the SW dyke margin, Deildargil location 1.

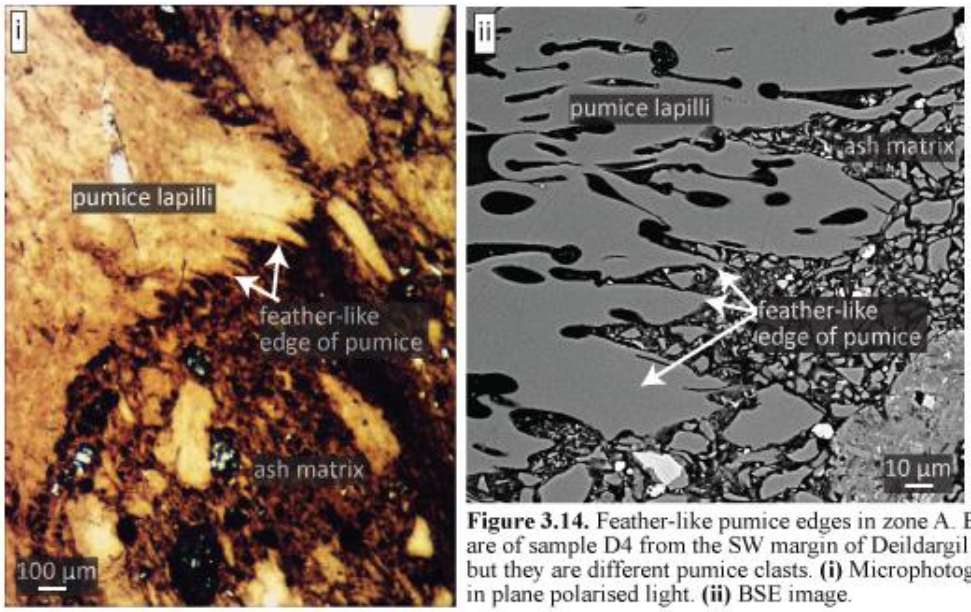

Figure 3.14. Feather-like pumice edges in zone A. Both images are of sample D4 from the SW margin of Deildargil location 1, but they are different pumice clasts. **(i)** Microphotograph taken in plane polarised light. **(ii)** BSE image.

The porosity of pumice clasts near the country rock is variable, spanning ~20-80 % by area (**Fig. 3.15.**). Some pumice clasts contain small circular to sub-circular vesicles, with diameters of ~10 µm, and also large, up to 400 µm long, irregular shaped vesicles. The vesicles occur throughout the pumice clasts, with vesicle walls commonly forming clast edges, resulting in the feather-like edges. A matrix of non-

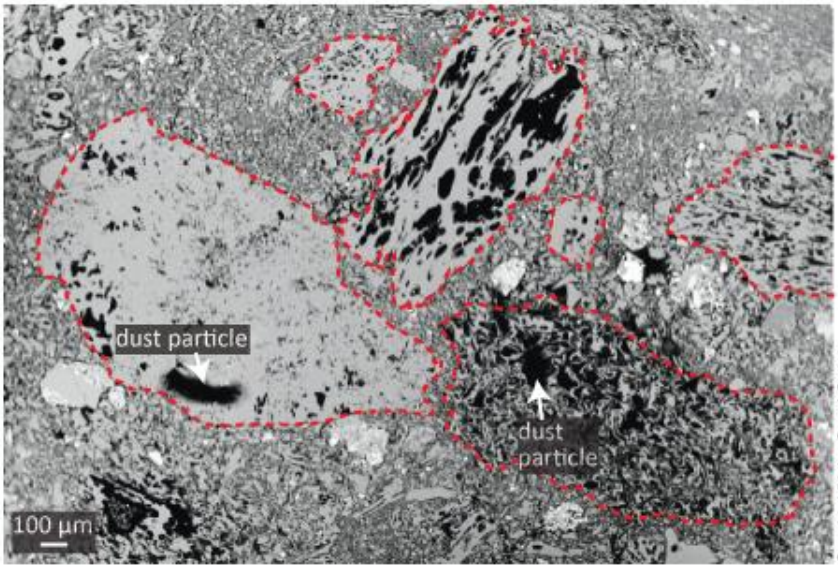

Figure 3.15. BSE image of pumice clasts (outlined by red dashed lines) with different porosities in zone A, sample D4 from the SW dyke margin at Deildargil location 1. Voids are black and obsidian is grey.

jigsaw fit ash, consisting of obsidian and country rock fragments commonly supports the pumice lapilli clasts. The obsidian ash has platy, bird-foot-like, cusp-like and equant shapes (**Fig. 3.16.i**), with sub-rounded to angular edges that are composed of

vesicle walls. The country rock clasts (**Fig. 3.16.ii**), which have the appearance of basalt (geochemistry not determined) are equant, with sub-rounded to angular edges that generally lack vesicle walls, but vesicles are often present in clast interiors.

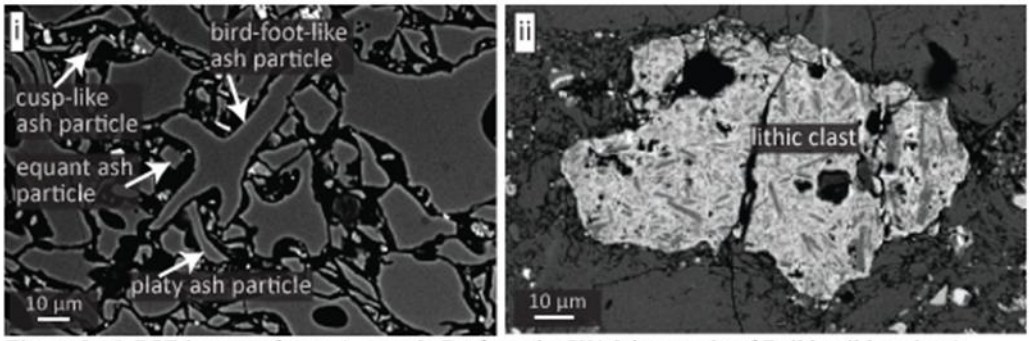

Figure 3.16. BSE images of zone A, sample D4 from the SW dyke margin of Deildargil location 1.

Crystals also constitute some of the ash; these appear (geochemistry not determined) to be plagioclase and pyroxene, and are thus similar to crystals in the basaltic clasts. The ash matrix locally has a jigsaw fit with pumice lapilli, but only at contacts between pumice lapilli with different porosities (**Fig. 3.17.i**). Vesicles are sometimes viscously deformed at these contacts (**Fig. 3.17.ii**), with jigsaw fit ash lacking.

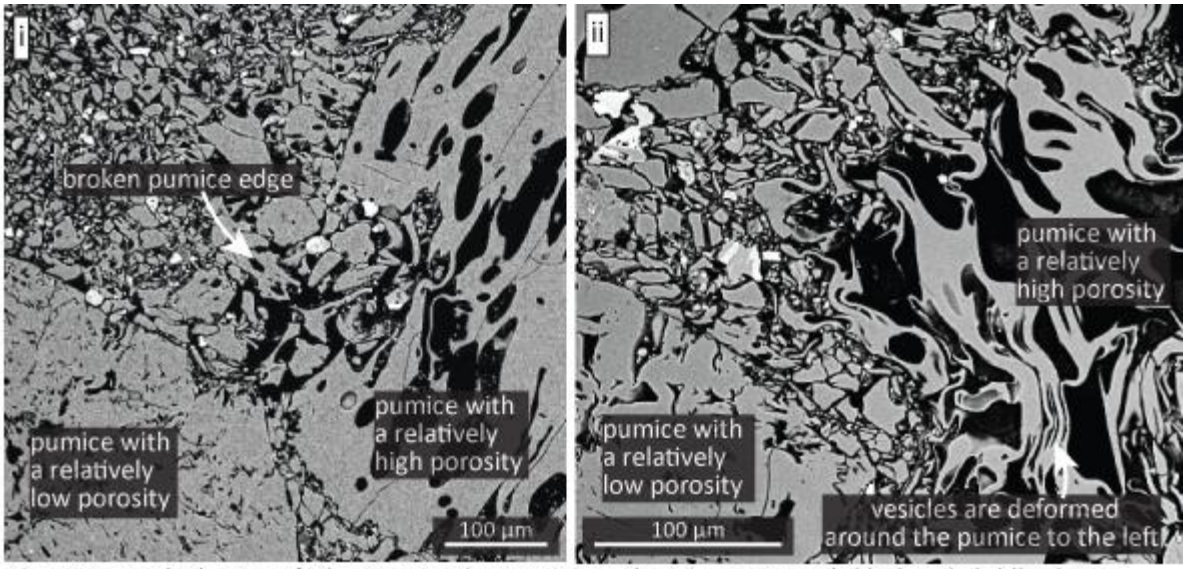

Figure 3.17. BSE images of micro-textures in zone A (sample D4). Pore space is black and obsidian is grey.

When obsidian walls separating small and large vesicles are ~10 µm wide, the smaller vesicles protrude into the larger vesicles (**Fig. 3.18.**). Similarly, when relatively large vesicles are close (i.e., when the porosity is particularly high), their

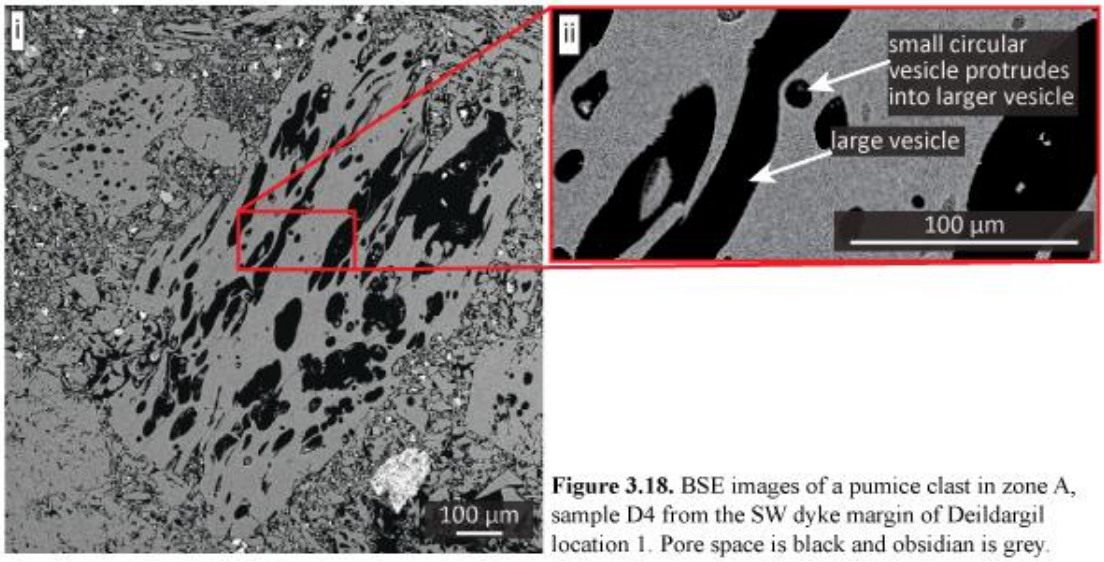

Figure 3.18. BSE images of a pumice clast in zone A, sample D4 from the SW dyke margin of Deildargil location 1. Pore space is black and obsidian is grey.

forms are irregular, their walls buckled, and they often protrude into one another (**Fig. 3.14. and 3.19.**).

Some of the larger vesicles have very thin walls, with some being <1 µm wide (**Fig. 3.19.**). Small and large vesicles are commonly connected by linear to curvilinear fractures (**Fig. 3.20.**), and some small vesicles are connected to one another by similar fractures (**Fig. 3.21.**). The fracture walls contrast with the smoother vesicle walls (**Fig. 3.20. and 3.21.**), and the apertures connecting the vesicles and fractures have angular to sub-rounded edges, sometimes displaying small (<5 µm) offset (**Fig. 3.21.i**). However, in a low porosity (<10 % by area) domain of a pumice clast, which displays a variable porosity, the apertures are smooth. Furthermore, in these domains fracture-vesicle connections consist of concave lobes (**Fig. 3.22.i and ii**), and some of the fractures and vesicles are partially closed, with their walls connected by obsidian bridges (**Fig. 3.22.iii and iv**).

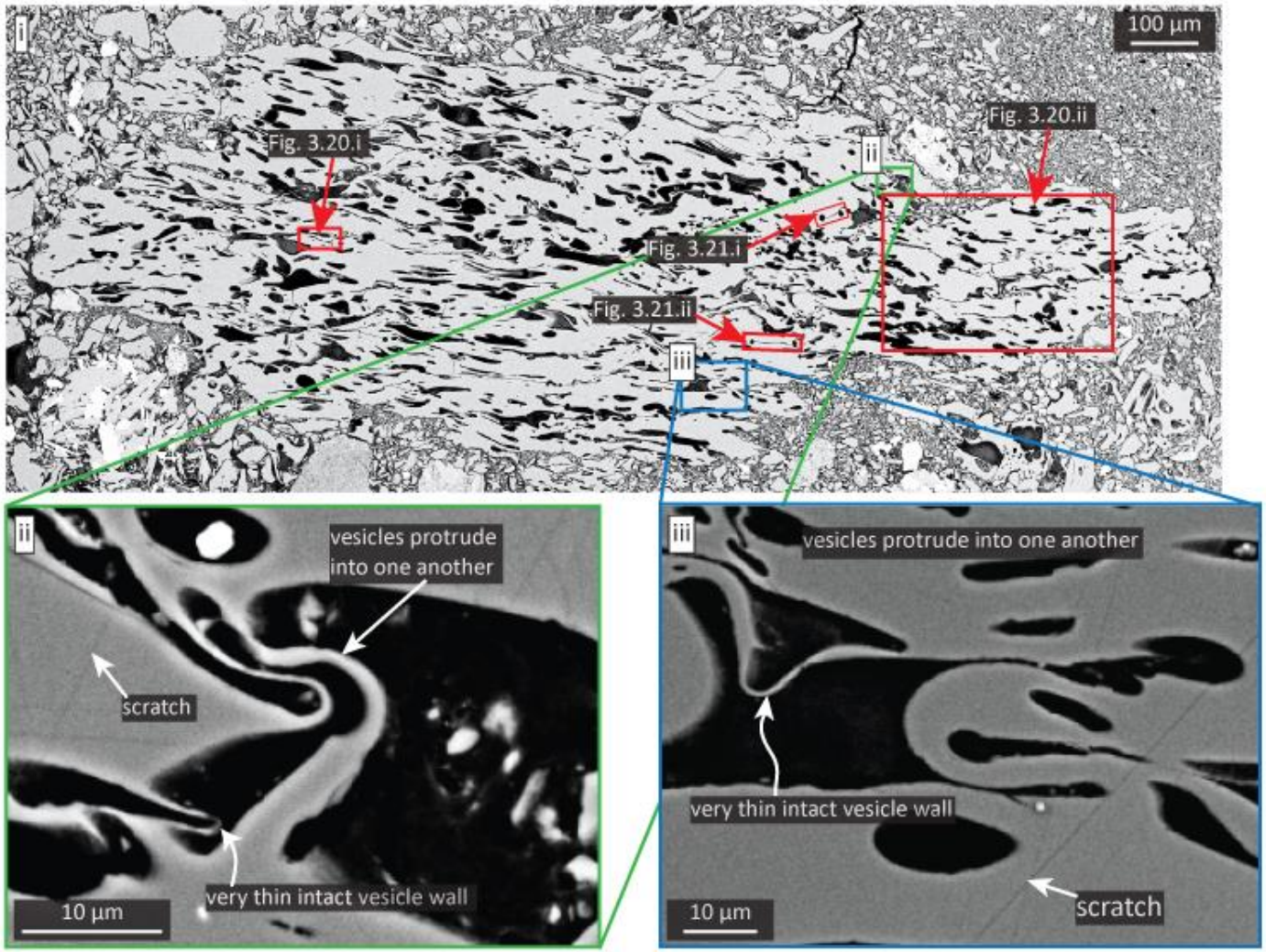

Figure 3.19. BSE images of a pumice clast in zone A, sample D4 from the SW dyke margin of Deildargil location 1. The voids are black and the obsidian is grey. See main text for further description.

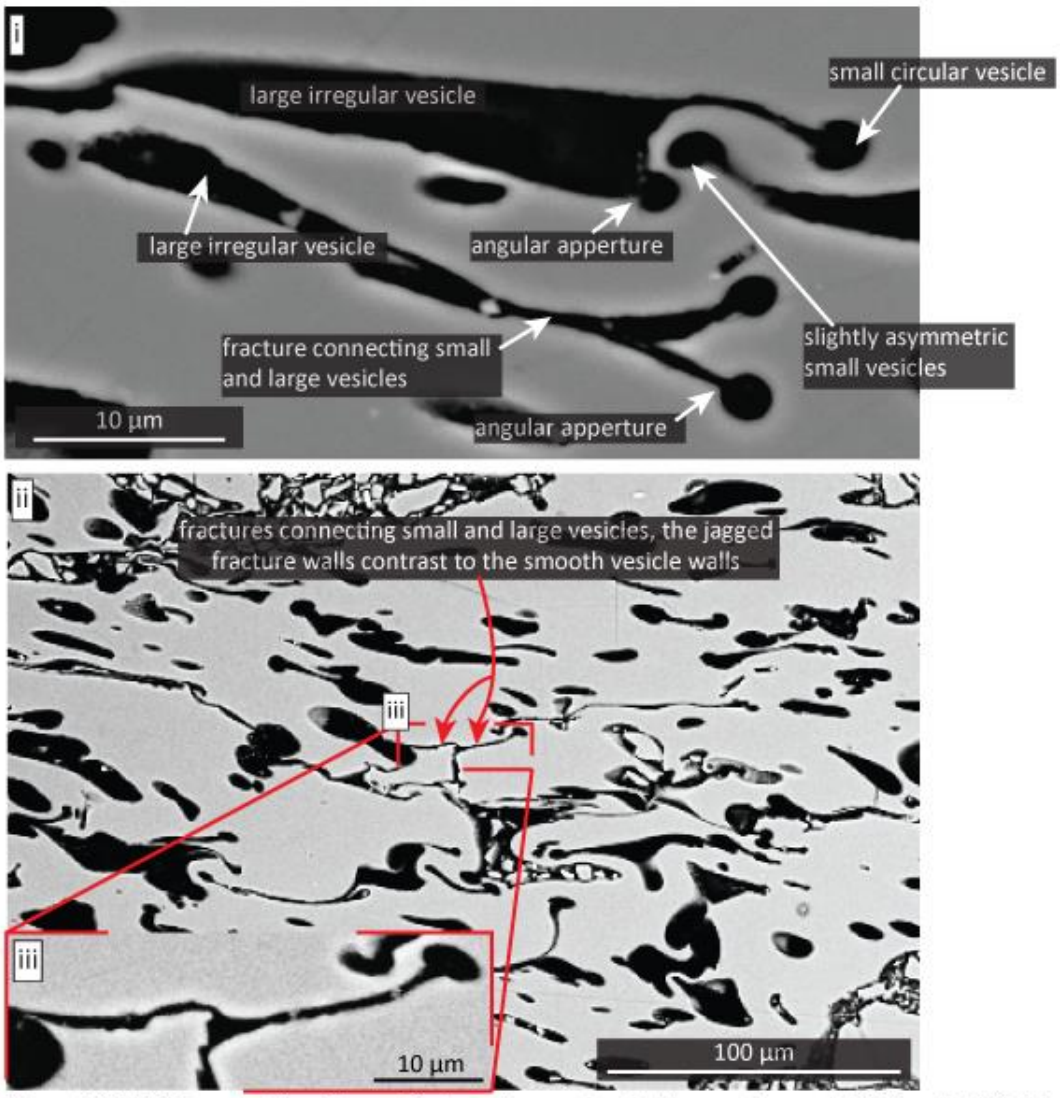

Figure 3.20. BSE images of vesicles and fractures in a pumice clast in zone A, sample D4 from the SW dyke margin at Deildargil location 1. Pore space is black and obsidian is grey. Position of the images is shown in **figure 3.19i**.

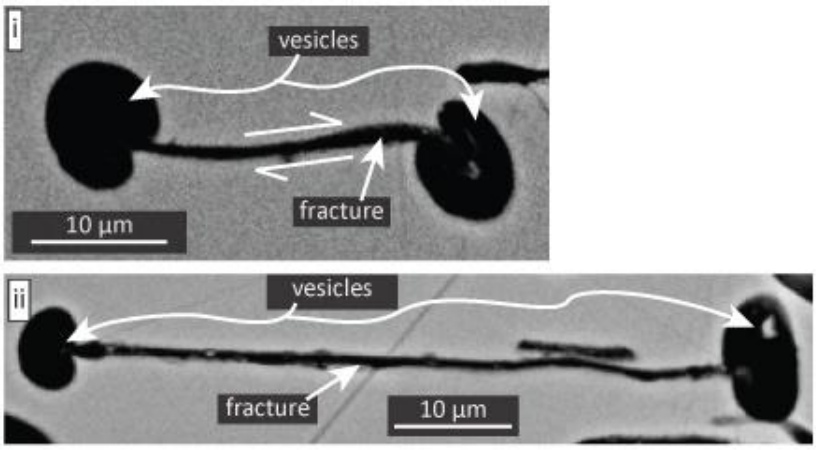

Figure 3.21. BSE images of vesicles and fractures in a pumice clast in zone A, sample D4 from the SW dyke margin at Deildargil location 1. Pore space is black and obsidian is grey. The position of the images is shown on **figure 3.19.i**.

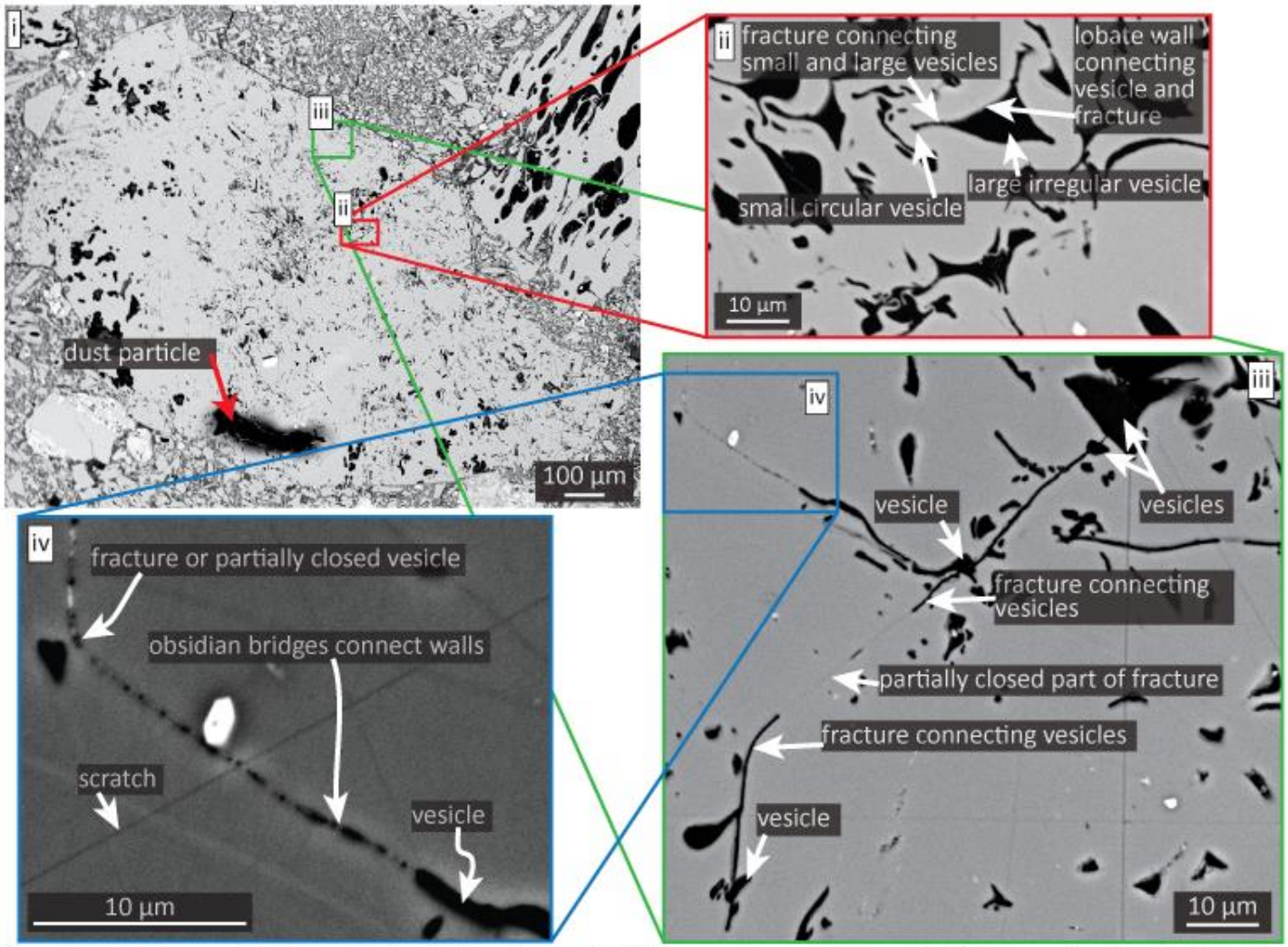

Figure 3.22. BSE images of vesicle and fracture textures in a pumice clast in zone A, sample D4 from the SW dyke margin of Deildargil location 1. Pore space is black and obsidian is grey. See main text and labels for description.

Towards sub-zone B1 the vesicles within all pumice clasts become thinner and many are partially closed, with adjacent walls locally joined by obsidian bridges; fully closed vesicle sections are defined by microlite trains (**Fig. 3.23.**). Near sub-zone B1, vesicles, partially closed vesicles and fractures connecting vesicles have pitted walls and are often filled with nanolites and microlites (**Fig. 3.24.**), with vesicle centres often containing aggregates of nanolites that have relatively weak backscatter intensities (**Fig. 3.24.i**). They have similar shapes to their host vesicle and are outlined by dashed lines, consisting of <1 μm wide microlites, with relatively strong backscatter intensities (**Fig. 3.24.i**). The dashed outlines are surrounded by lath-like microlites, with similar backscatter intensities to the central domains, but with weaker

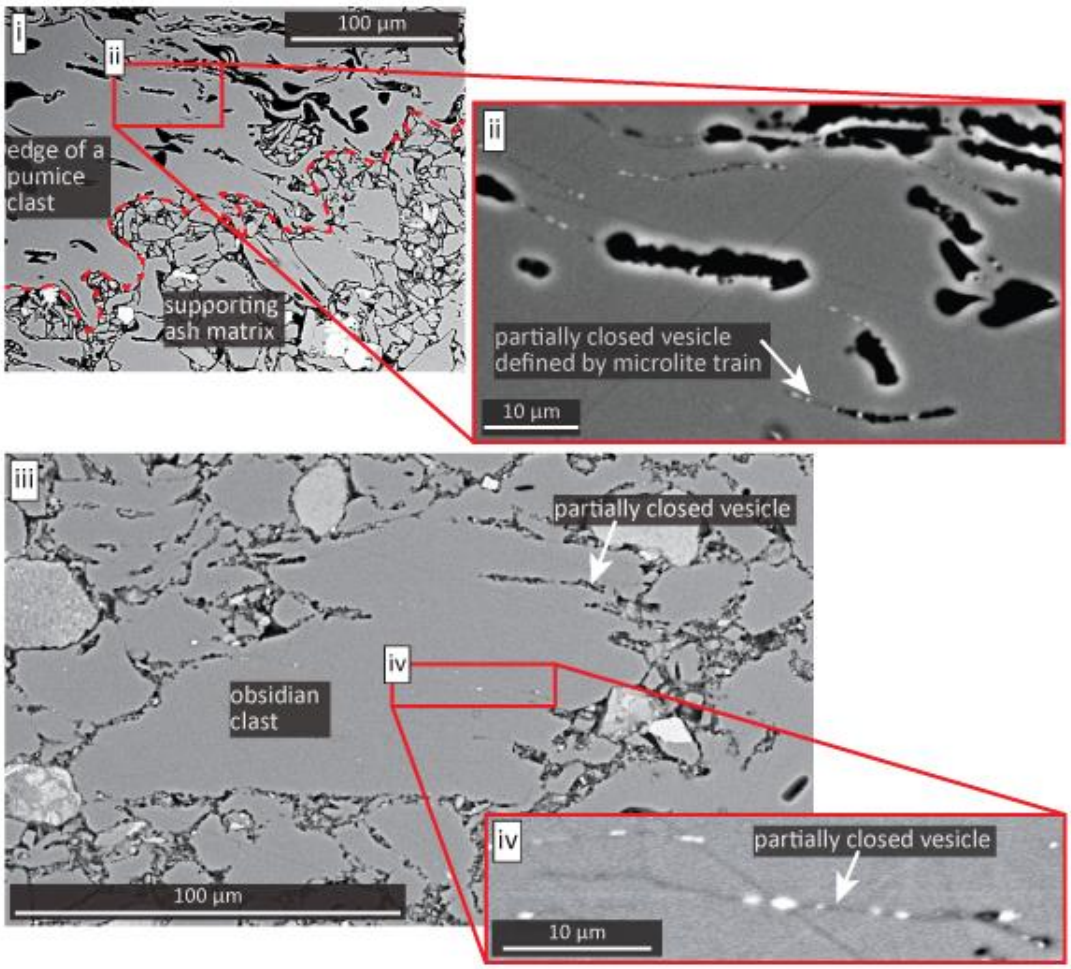

Figure 3.23. BSE images of clasts in zone A, near to sub-zone B1, sample D4 from the SW dyke margin of Deildargil location 1. See main text and labels for description.

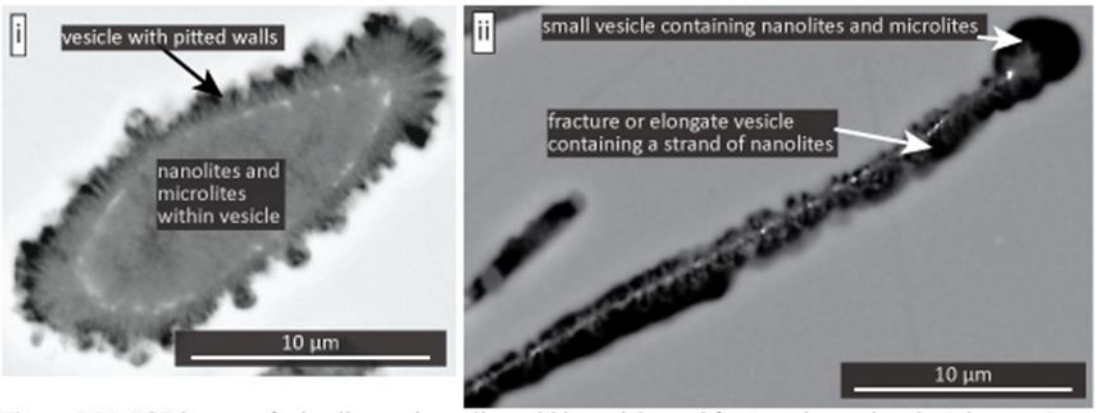

Figure 3.24. BSE images of microlites and nanolites within vesicles and fractures in pumice clasts in zone A, sample D4 from the SW dyke margin of Deildargil location 1.

intensities than the host obsidian. The laths are ~1 µm long, orientated perpendicular to the walls of their host vesicle, and they extend into the pits in the vesicle walls. Some vesicles lack microlites, nanolites and pitted walls, even though they occur proximal to microlite/nanolite-filled vesicles and fractures with pitted walls. The presence or absence of microlites and pitting is not correlatable with the size or connected nature of the vesicles and fractures, but such correlation may only be apparent with 3D analysis.

In addition to the reduction in clast porosity, the inter-clast porosity also decreases towards sub-zone B1 (**Fig. 3.25.i and ii**). Similarly to the vesicle walls, juvenile clast surfaces are also pitted near to sub-zone B1 (**Fig. 3.24. and 3.25.iii**), with adjacent clasts being joined by obsidian bridges (**Fig. 3.25.iv**). Pitting and obsidian bridges are absent near the country rock. The porosity of zone A is relatively low near B1 in comparison to nearer the country rock, but relatively high porosity domains do exist locally near B1 next to lithic clasts (**Fig. 3.25.v and vi**).

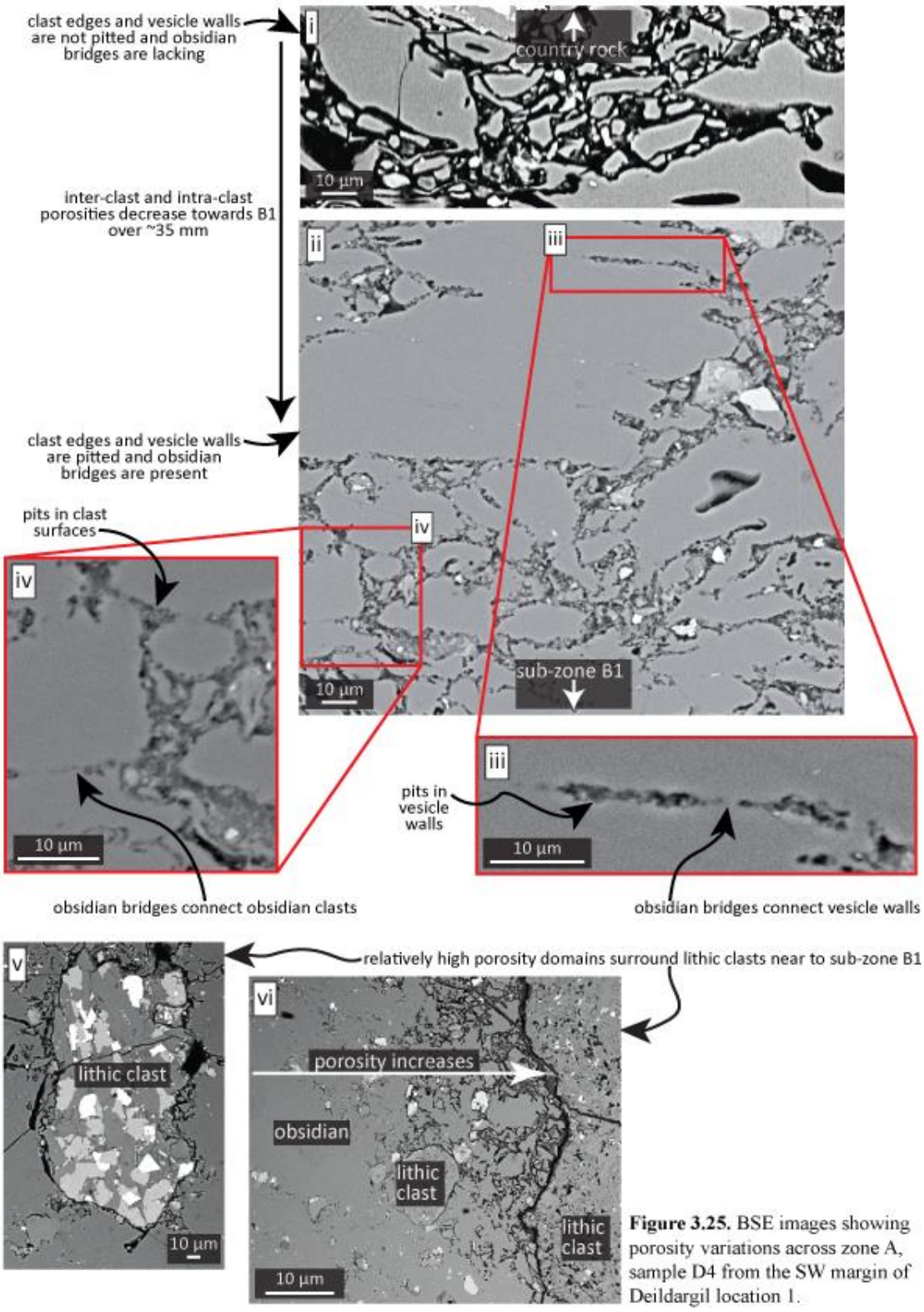

Figure 3.25. BSE images showing porosity variations across zone A, sample D4 from the SW margin of Deildargil location 1.

3.3.2. Zone B: sub-zones B1, B2 and B3

i) Macro-scale features: location and dimensions

The obsidian of zone B is situated between the country rock (or zone A when present) and the more central zones (T, D and C; **Fig. 3.3.**), and it is present at all locations. However, only at Deildargil location 2 are all of the sub-zones (B1-B3) of zone B distinguishable, which comprise an outer zone of black obsidian (B1), an inner zone of green obsidian (B3), with grey-brown-light green obsidian (B2) between B1 and B3. B2 is split into two parts (B2a and B2b); B2a consists of light brown obsidian and is next to B1, whereas B2b consists of dark brown-grey-light green obsidian and occurs between B2a and B3. Locally, the contact between B2a and B2b is clear, but sometimes it is more ambiguous. Sub-zones B1-B3 are present on opposite walls of the dyke (**Fig. 3.26.i**); their thicknesses span ~1 mm to 40 cm, with thickness variations being most dramatic next to a relatively large (~50 cm wide) boulder within the conglomeratic country rock. For instance, B1 is ~40 cm thick on the NE side of the boulder, thins to 1 mm up the side of the boulder, and pinches out over the top (**Fig. 3.26.ii**). Similarly, B2 pinches out and B3 is thinnest above the boulder. All of the sub-zones are present on the SW side of the boulder and they thicken away from it (**Fig. 3.26.ii**). Furthermore, on the SW side of the boulder, B3 contains a fluidal body of blue-grey obsidian and clasts of vesicular microcrystalline rhyolite (**Fig. 3.26. and 3.27.**).

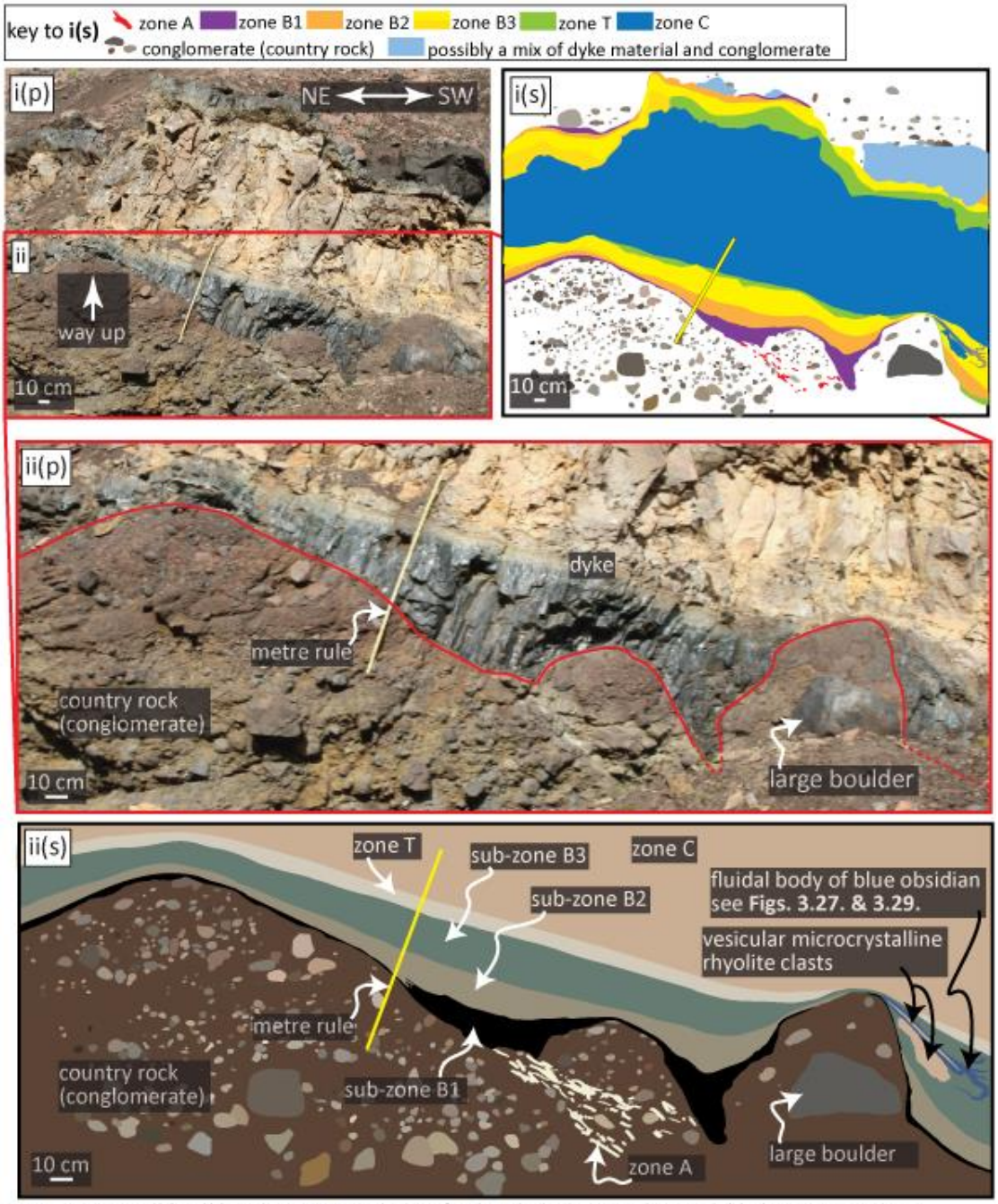

Figure 3.26. Deildargil location 2. See main text for description. **i(p)** and **ii(p)** Field photos. **i(s)** and **ii(s)** Sketchs of the photos.

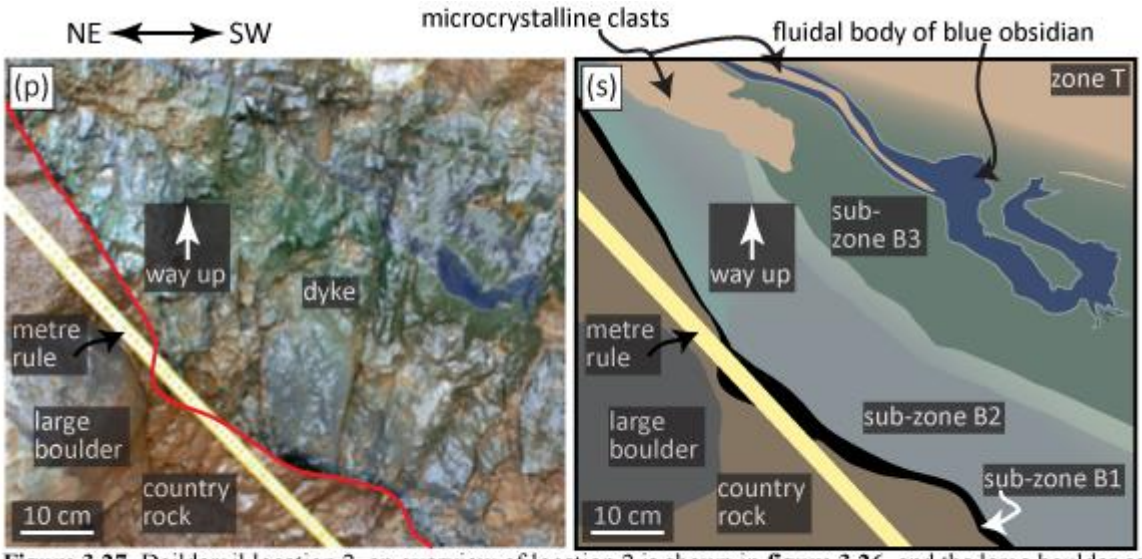

Figure 3.27. Deildargil location 2, an overview of location 2 is shown in **figure 3.26.** and the large boulder can be seen in that figure also. On the SW side of the boulder sub-zone B3 contains a fluidal body of blue obsidian and clasts of microcrystalline vesicular rhyolite. **(p)** Photograph of the dyke. **(s)** Tracing of **p**.

ii) Meso-scale features: contact relationships, optically coloured lenses, fluidal body, vesicles, and fractures

Contacts between the sub-zones of zone B are generally fluidal, with fluidal fingers of B3, B2b and B2a extending into B2b, B2a and B1, respectively (**Fig. 3.28.i-iii**). Optically coloured lenses occur in sub-zones B1-B3, these are ~1-4 mm wide and ~3-10 mm long; generally, they are linear or slightly wavy and bulbous, and parallel or sub-parallel to the sub-zone contacts and dyke margins. The lenses in each sub-zone decrease in size towards the country rock and they consist of multiple layers that have different colours (**Fig. 3.28.i, iv and v**). Coloured lenses also occur in the obsidian margins of the other dyke exposures (**A.3.3.**) and also within the fluidal body on the SW side of the boulder at Deildargil location 2. In the fluidal body (**Fig. 3.29.i**), the lenses are light blue, diffuse in the more central part of the body, and better defined at the margin, with their number density being highest at the margin (**Fig. 3.29.ii**). The margin of the fluidal body is variable, as it consists of either a single grey layer that is

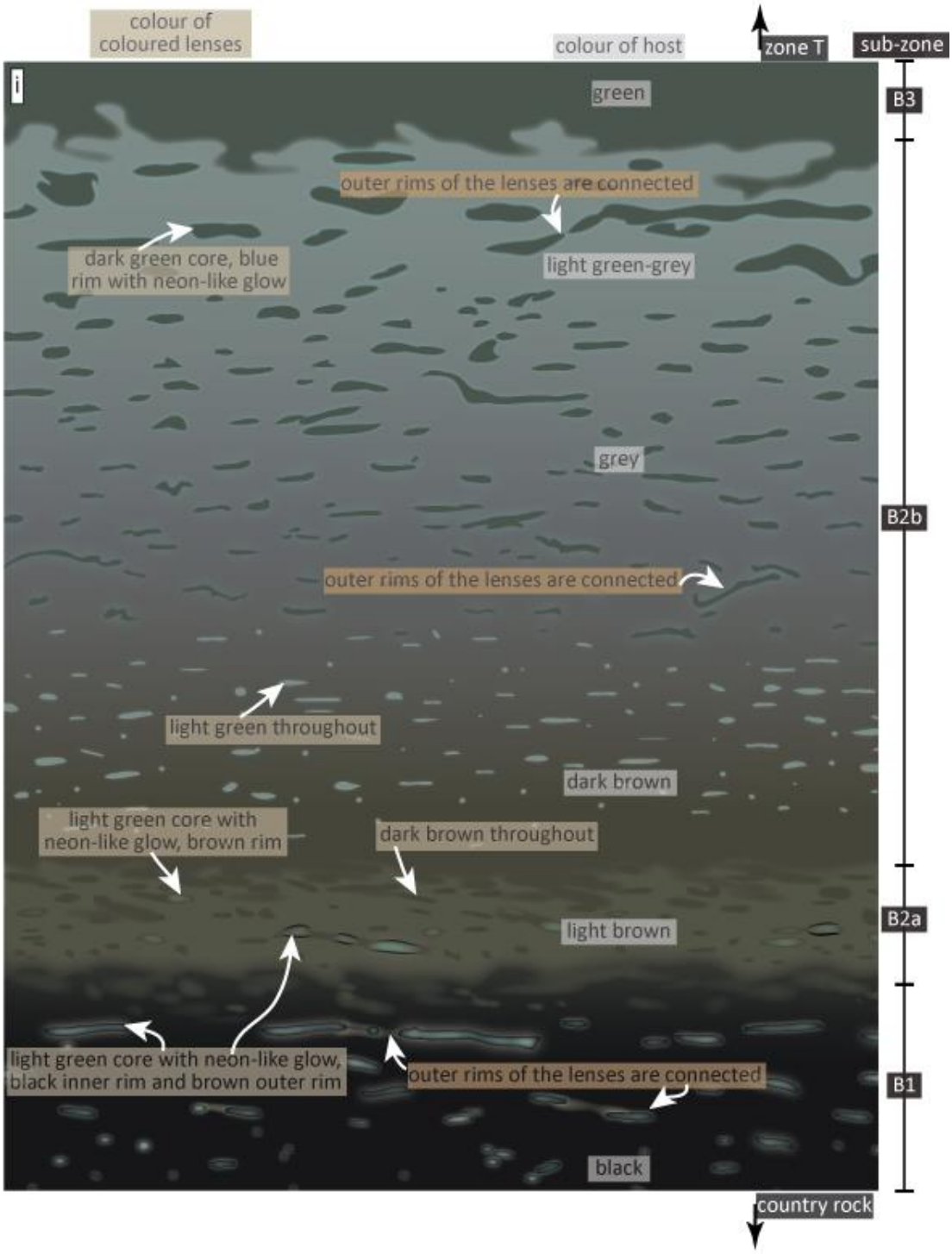

figure continues on the next page

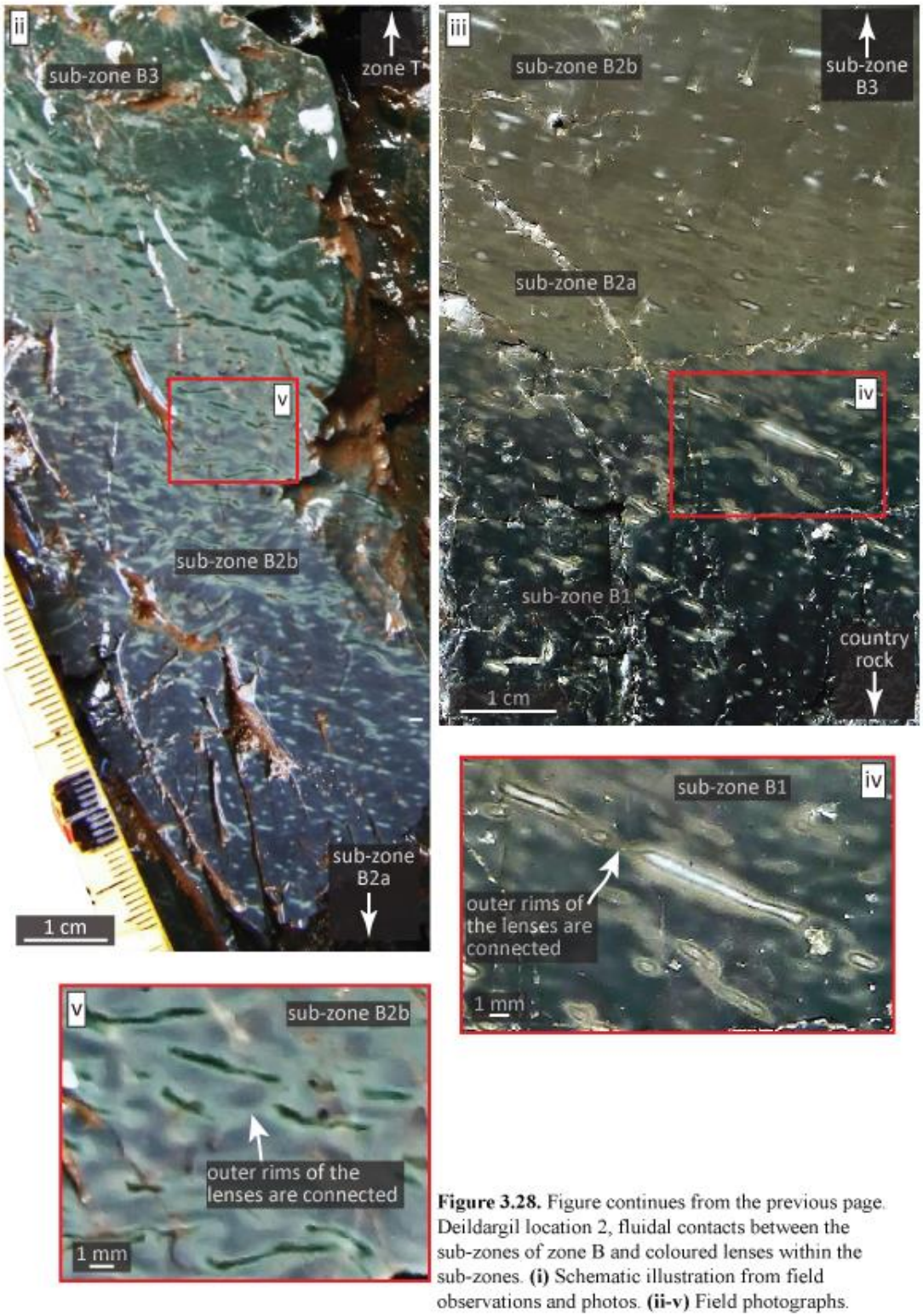

Figure 3.28. Figure continues from the previous page. Deildargil location 2, fluidal contacts between the sub-zones of zone B and coloured lenses within the sub-zones. **(i)** Schematic illustration from field observations and photos. **(ii-v)** Field photographs.

~3 mm wide (**Fig. 3.29.ii**), multi-coloured (red, brown and grey) layers, with a combined thickness of ~3 mm (**Fig. 3.29.iii**), or it is up to 15 mm wide and more irregular, having the appearance of merged red and blue watercolour paints (**Fig. 3.29.iv**). The host obsidian (sub-zone B3) around the fluidal body is locally relatively light green in colour, in contrast to the majority of the sub-zone which is dark green. The thickness of the lighter part ranges from ~3 to 10 mm (**Fig. 3.29.iii and iv**).

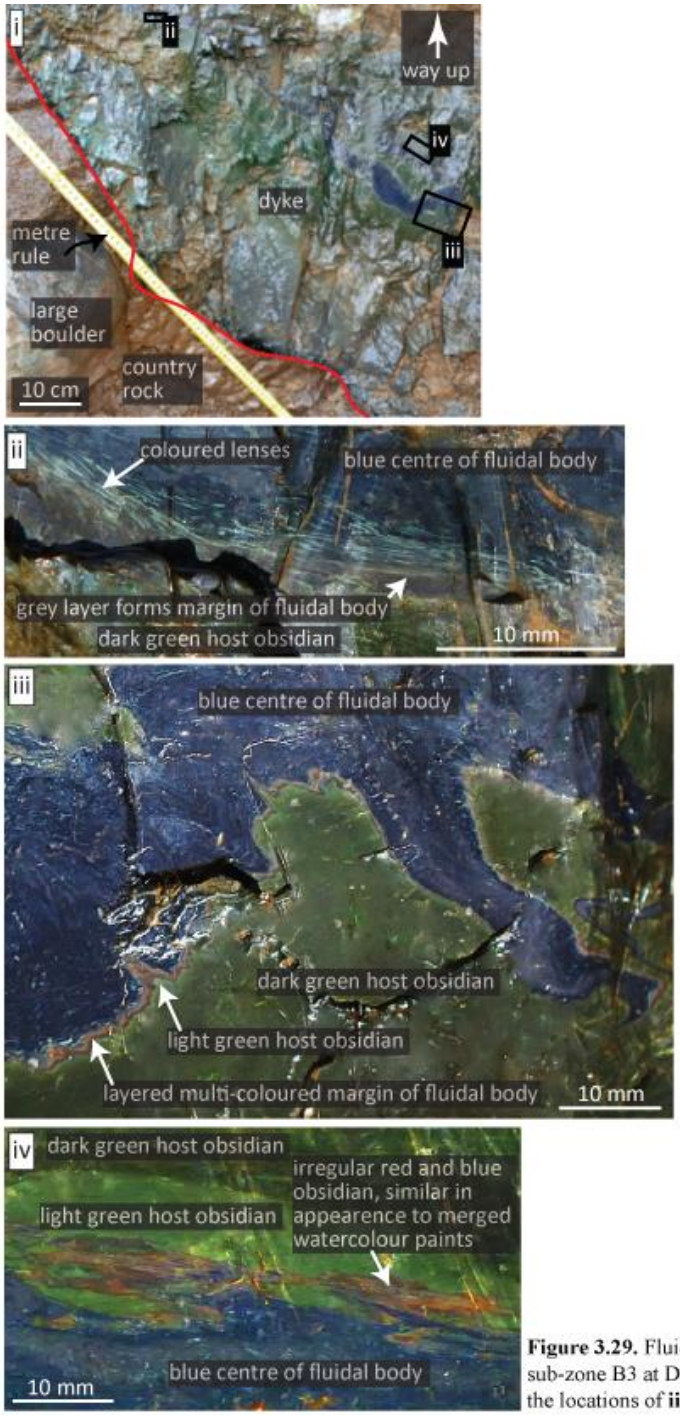

Figure 3.29. Fluidal body in sub-zone B3 at Deildargil location 2, the locations of **ii-iv** are shown in **i**.

Vesicles exist in zone B at all of the dyke exposures, and they are sub-spherical to elliptical, with diameters of ~5-170 mm. The largest vesicles (those with diameters >60 mm) were only found at Deildargil location 2 and the upper part of Deildargil location 1 (**Fig. 3.30.**). Many of the vesicles have linear furrows on their interior walls (**Fig. 3.30.i**). No correlation exists between vesicle size or shape and distance from the dyke margins. However, at Deildargil location 1 the largest vesicles occur near a bend in the upper part of the dyke.

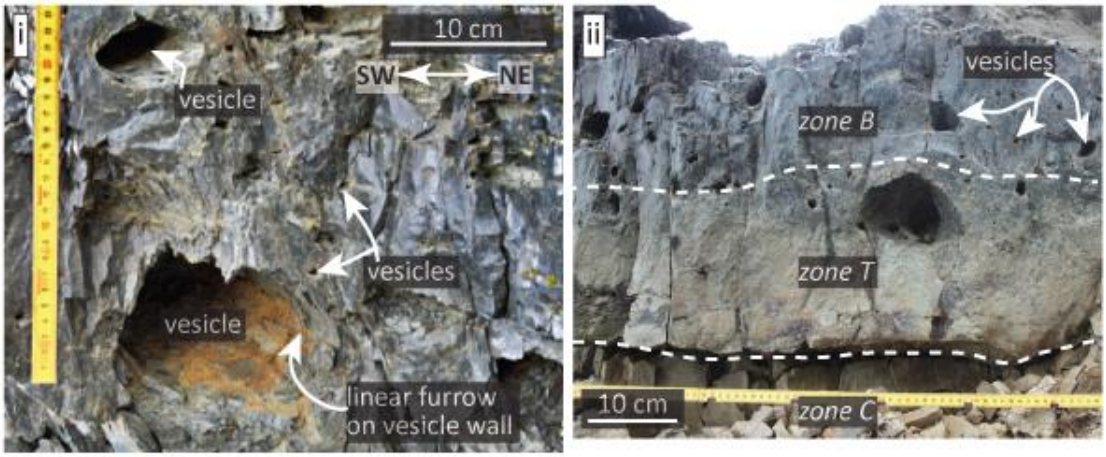

Figure 3.30. Vesicles in zone B at Deildargil location 1.

Two main types of fractures exist in zone B, which are best observed at Deildargil locations 1 and 2, and are referred to as type 1 and type 2 fractures, with no order of formation inferred. Type 1 fractures are planar, ~1 to 20 cm long, and perpendicular to the B-T contact, whereas type 2 are planar to arcuate, <10 cm long and sub-parallel with the B-T contact (**Fig. 3.31.i**). The planarity of type 1 changes next to vesicles, as they wrap around the vesicles (**Fig. 3.31.ii**). The type 1 fractures generally have a spacing of ~1-10 cm, with closer spacing nearer the country rock, whereas the type 2 fracture spacing is more random. Together, the two fracture types result in a blocky texture. Some of the type 1 fractures extend across zone B and into zone T, but not into zone C.

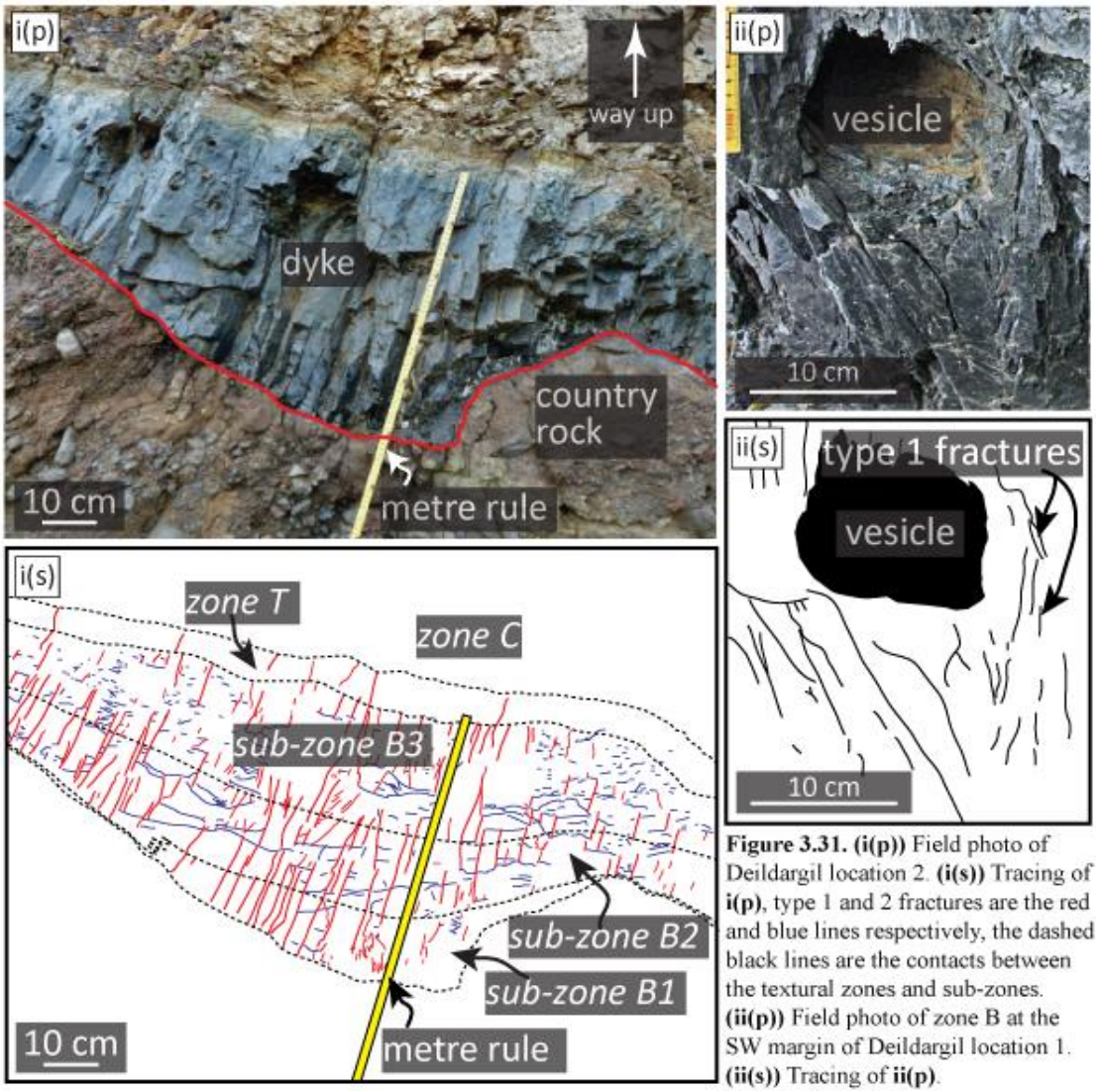

Figure 3.31. (i(p)) Field photo of Deildargil location 2. **(i(s))** Tracing of **i(p)**, type 1 and 2 fractures are the red and blue lines respectively, the dashed black lines are the contacts between the textural zones and sub-zones. **(ii(p))** Field photo of zone B at the SW margin of Deildargil location 1. **(ii(s))** Tracing of **ii(p)**.

iii) Micro-scale features: perlitic texture, optically coloured lenses and microlites

Sub-zones B1, B2 and B3 are riddled with micro-cracks that cut through all other textures. At Hringsgil dyke 2, much of the inner part of zone B consists of clay, which makes identification of the sub-zones impossible. Here, zone B loses all coherence and grades into zone D, which consists of clay and angular fissile obsidian clasts. The outer part of zone B at all locations generally loses coherence and gains a perlitic texture towards the country rock, but clay development is lacking. The perlitic nature is best appreciated in microphotographs of petrological thin sections (**A.3.4.**).

Zone B contains microlites and nanolites; the size and number density of these varies from sub-zone B1 to B2, with the size and number density within B3 unconfirmed. B1 contains a high number density (~90 %) of nanolites (**Fig. 3.32.i**), whereas crystals larger than 1 μm (i.e., microlites) are generally lacking. In contrast, sub-zone B2 contains ~5 % microlites that are ~1 μm wide, these microlites have nanolites-free haloes, but beyond the haloes there is a high number density (~80 %) of nanolites (**Fig. 3.32.ii**). Some of the microlites form discontinuous trains (**Fig. 3.32ii**).

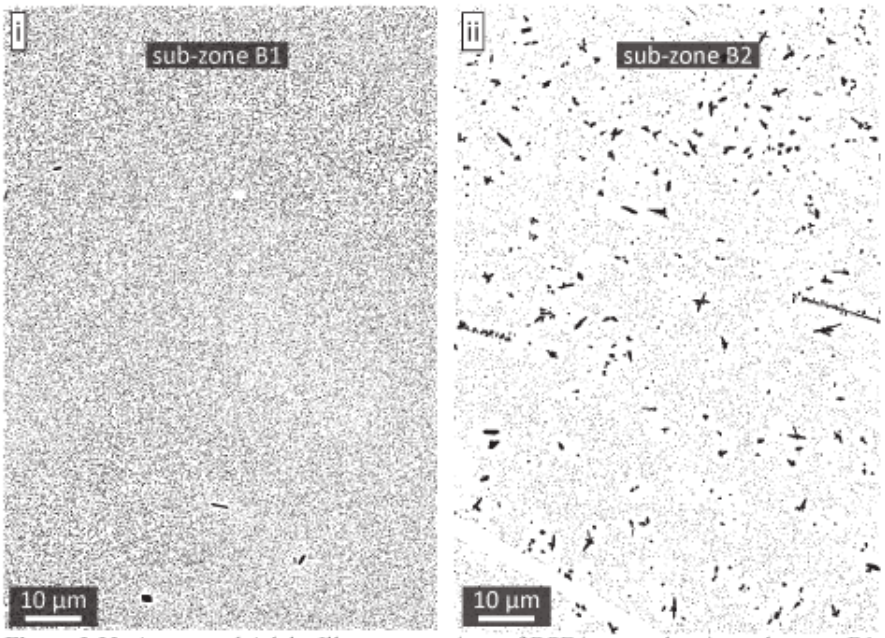

Figure 3.32. Automated Adobe Illustrator tracings of BSE images showing sub-zones B1 amd B2, microlites and nanolites are black. Sample Dmb-ts1 from Deildargil location 2a.

Micro-petrological examination of the coloured lenses reveals that some are deformed around phenocrysts (**Fig. 3.33.i**). The lenses have colourless central slits that are aligned with the major axis of the lenses (**Fig. 3.33.**). The lens cores are generally pale, whereas their rims are dark (**Fig. 3.33.**), but sometimes the pale cores are absent, with the dark rims coming together (**Fig. 3.34.**).

When viewed using high magnification BSE images, voids can be seen in the lens centres. Some of the voids are lens shaped, whereas others have more irregular forms. The voids are generally elongate and their major axes are aligned with the

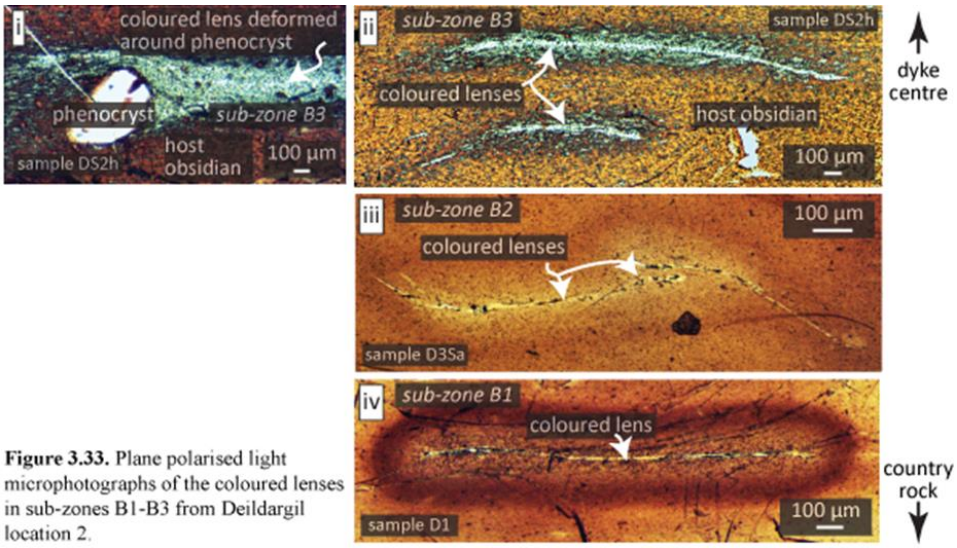

Figure 3.33. Plane polarised light microphotographs of the coloured lenses in sub-zones B1-B3 from Deildargil location 2.

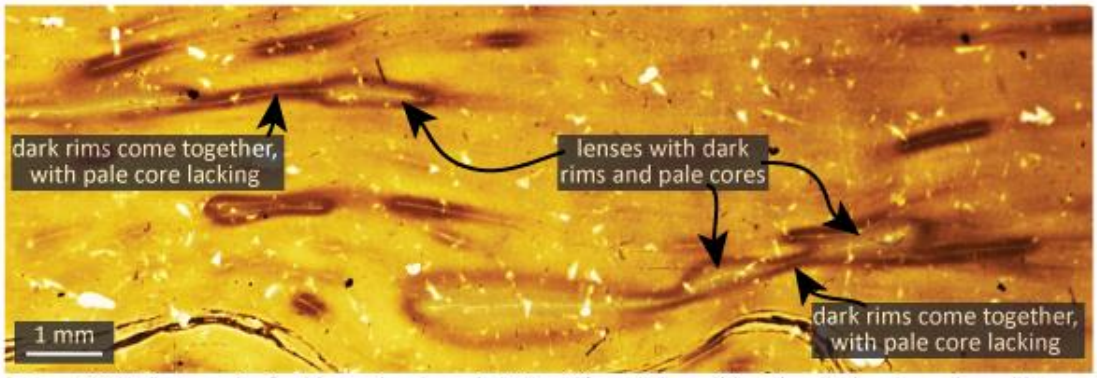

Figure 3.34. Photograph of a thin section (sample Hs3-ts2 from Hringsgil location 2) showing coloured lenses.

major axes of the coloured lenses. The margins of some voids consist of multiple lobes, from which stem discontinuous lines that have weak electron backscatter intensities, in contrast to the intensity of the surrounding obsidian. Similar lines form connections between multiple voids (**Fig. 3.35. and A.3.5.**). The lines are branch-like, with the main stem forming the connection and multiple discontinuous lines extending from the stems (**Fig. 3.35.**). Voids connected by lines occur in sub-zones B1, B2 and B3. The lines are distinguishable from the surrounding obsidian due to variations in the size and abundance of nanolites, which causes the lines to have relatively weak backscatter intensities.

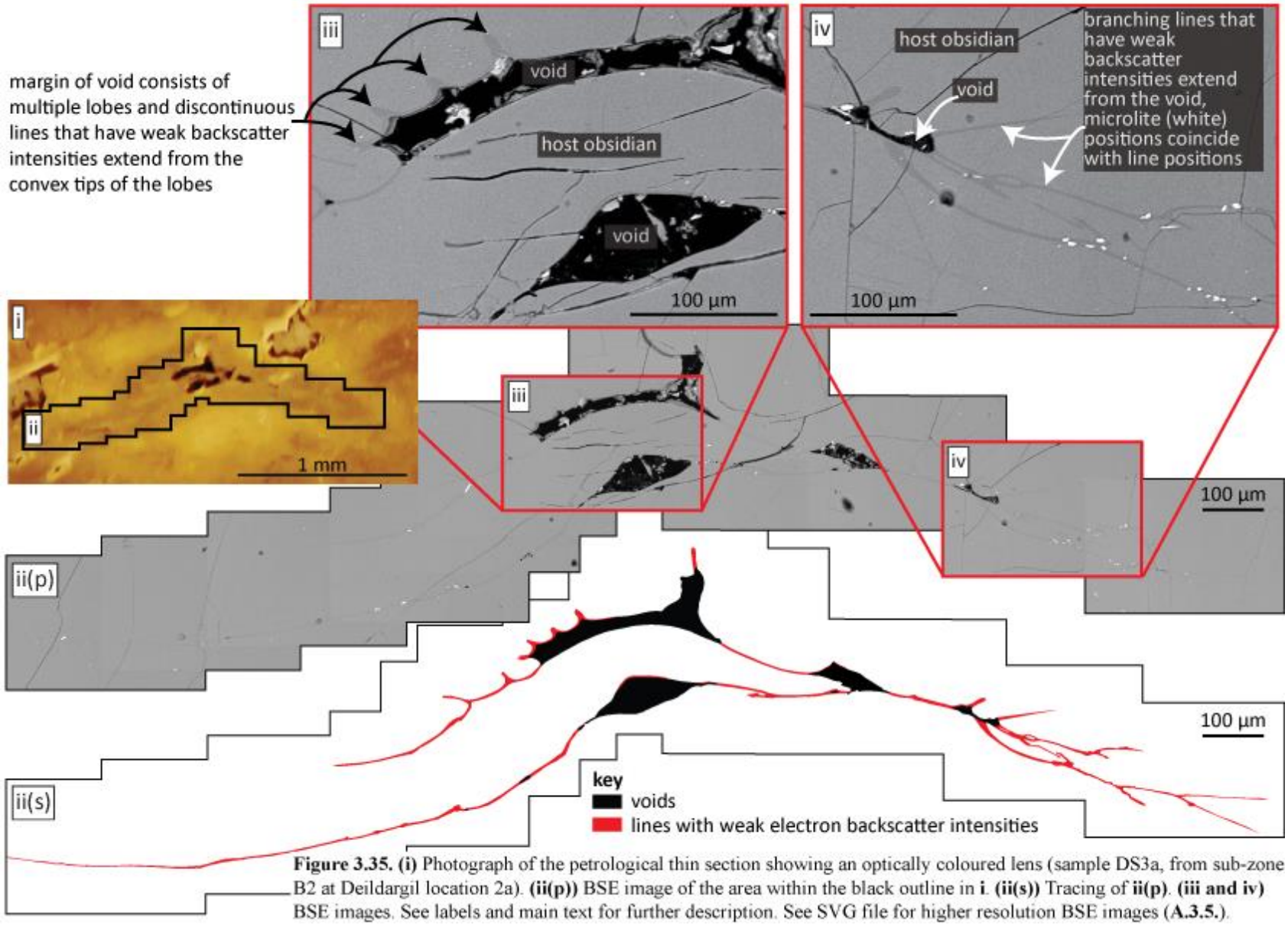

Figure 3.35. (i) Photograph of the petrological thin section showing an optically coloured lens (sample DS3a, from sub-zone B2 at Deildargil location 2a). **(ii(p))** BSE image of the area within the black outline in **i**. **(ii(s))** Tracing of **ii(p)**. **(iii and iv)** BSE images. See labels and main text for further description. See SVG file for higher resolution BSE images (**A.3.5.**).

3.3.3. Zone B: sub-zone Bb and localised variations within sub-zone B1

i) Macro- to micro-scale features, Deildargil location 2a

At Deildargil location 2a, sub-zone B1 is not brecciated next to sub-zone B2, whereas it consists of breccia next to the country rock; the brecciated part is referred to as sub-zone Bb (**Fig. 3.36.i and ii**). Sub-zone Bb is black, which is the typical colour of B1 in the field. However, at this location, B1 displays a gradational colour change with position. For instance, away from Bb and towards B2 its colour changes from black to blue to pink, with a green layer forming the B1-B2 contact (**Fig. 3.36.ii**).

In petrological thin sections B1 is light brown next to Bb and becomes progressively darker towards B2 and, as in the field, a green layer forms the B1-B2 contact (**Fig. 3.37.i**). The green layer contains coloured lenses, with dark brown cores and light green rims (**Fig. 3.37.i-ii**); some of the lenses have irregular shapes, but they will be referred to as lenses for convenience. The lenses are ~50 μm - 1 mm long and ~50-500 μm wide, their longest axes are generally parallel with the B1-B2 contact and also with the dyke margins. Similar lenses are found throughout B1, and some extend from the green layer into B1. The lenses vary with increased distance from the green layer. For instance, next to the green layer, they have yellow and green cores and dark brown rims (**Fig. 3.37.ii-iv**), whereas a few millimetres from the green layer they are lighter without green cores (**Fig. 3.37.v-vii**). The lenses are up to ~200 μm wide, and they are often connected to one another; one of the connected networks has a length of ~10 mm (**Fig. 3.37.v**). The lens cores contain colourless elongate slits, which are aligned with the major axes of the lenses. Voids are also common in the lens centres, and sometimes multiple voids are connected by the slits (**Fig. 3.37.iii-v**). At a distance of >2 mm from the green layer the majority of the lenses are much thinner (<50 μm)

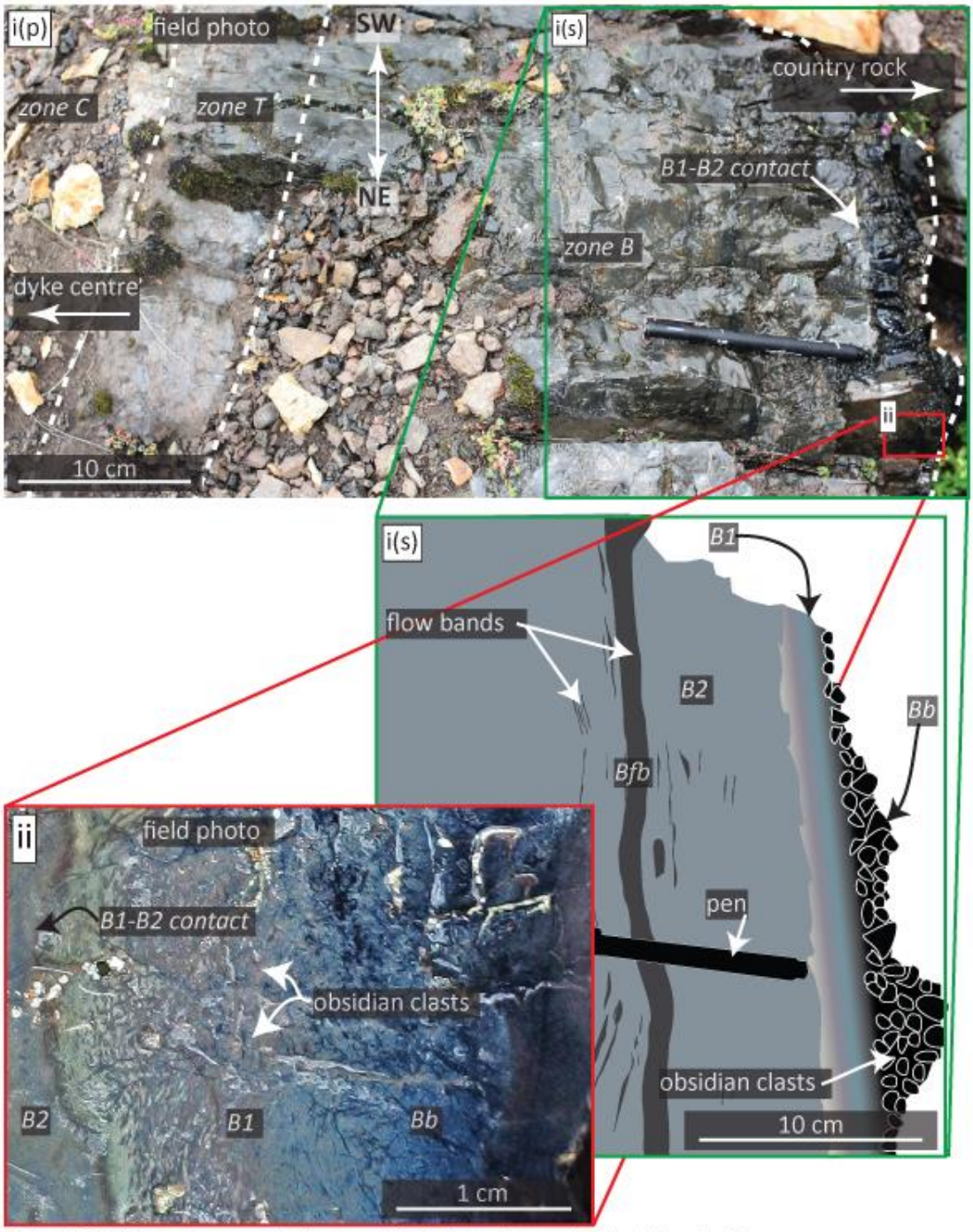

Figure 3.36. Textural zones and sub-zones (labelled in italics) at Deildargil location 2a.

and just consist of dark brown lenses, but they still harbour colourless central slits (**Fig. 3.37.vii**). A few wider lenses are found amongst the thin brown lenses; these are yellow with dark brown outer rims. Sometimes the rims encircle the whole lens, but more commonly the rims just extend along lens sides (**Fig. 3.37.vii**). The lenses appear to be less well connected further from the green layer. Those closest to the

green layer are subparallel with the B2-B1 contact, but their orientation changes progressively away from the green layer; next to the B1-Bb contact they are perpendicular to the B2-B1 contact (**Fig. 3.37.i**).

The part of B1 that is proximal to Bb is fractured, with this region representing the transition from the intact part of B1 to the brecciated obsidian that forms Bb. The fractures in this region are filled with dark brown material and they cut through the coloured lenses (**Fig. 3.38.i**). The dark brown material also forms the matrix between the brecciated obsidian clasts (**Fig. 3.38.i**). The clasts have angular to sub-rounded edges, and their sizes were measured using the already described method (see **section 2.6.** for methodology and errors). Clast diameters range from ~30 μm to ~2 mm (**Fig. 3.39.**), and of the measured clasts all but 5 have diameters <1 mm and clasts with diameters >0.5 mm contribute ~90 % to the total inferred volume. Smaller clasts than those measured probably constitute much of the brown matrix, but they cannot be seen with a petrological microscope, and the clastic nature of the rock is not apparent in BSE images, due to there being no variation in the electron backscatter intensity (**Fig. 3.38.ii and iii**). Indeed, no variation in the backscatter intensity exists between Bb, the fractured part of B1 or the intact part of B1.

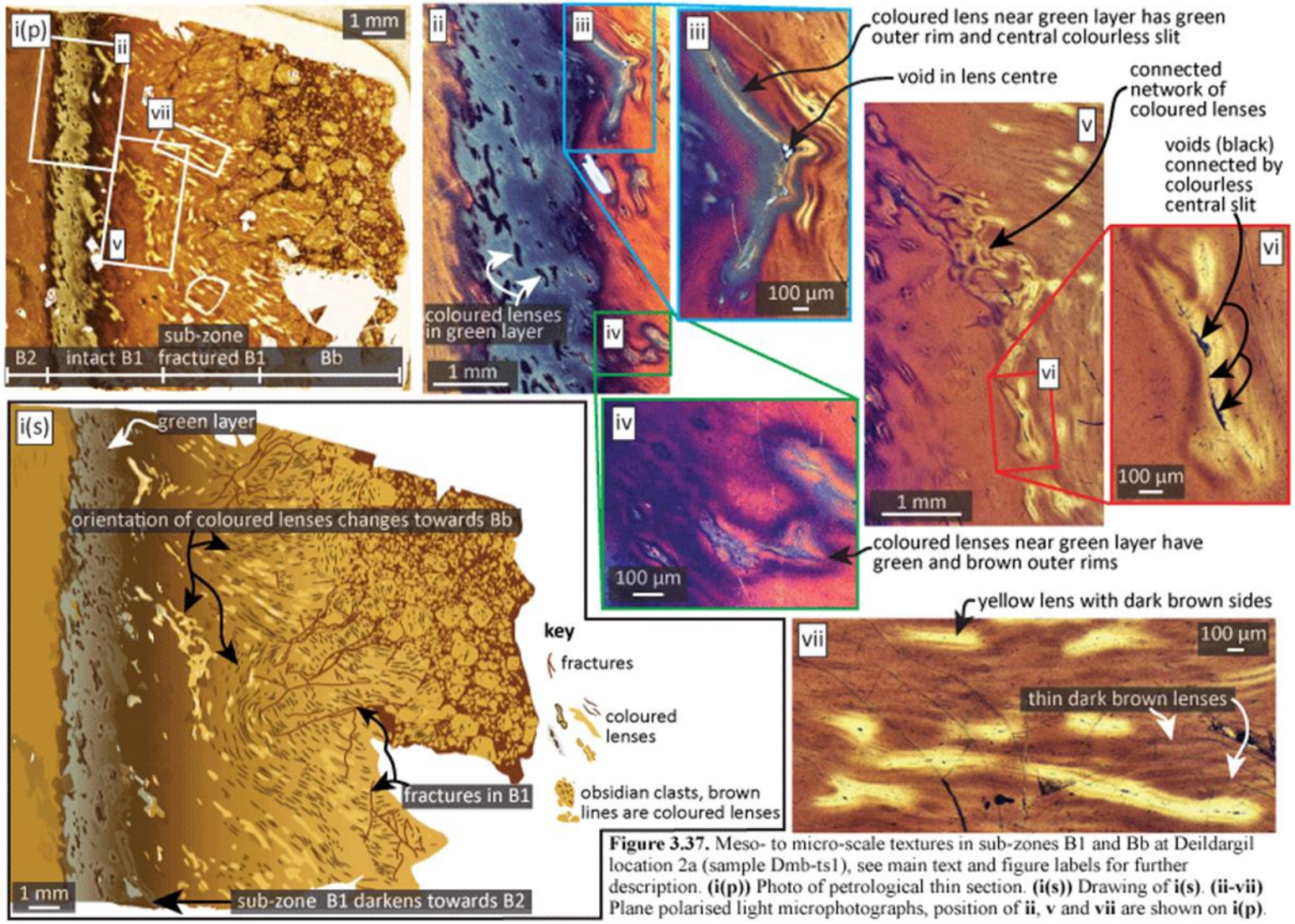

Figure 3.37. Meso- to micro-scale textures in sub-zones B1 and Bb at Deildargil location 2a (sample Dmb-ts1), see main text and figure labels for further description. **(i(p))** Photo of petrological thin section. **(i(s))** Drawing of **i(s)**. **(ii-vii)** Plane polarised light microphotographs, position of **ii**, **v** and **vii** are shown on **i(p)**.

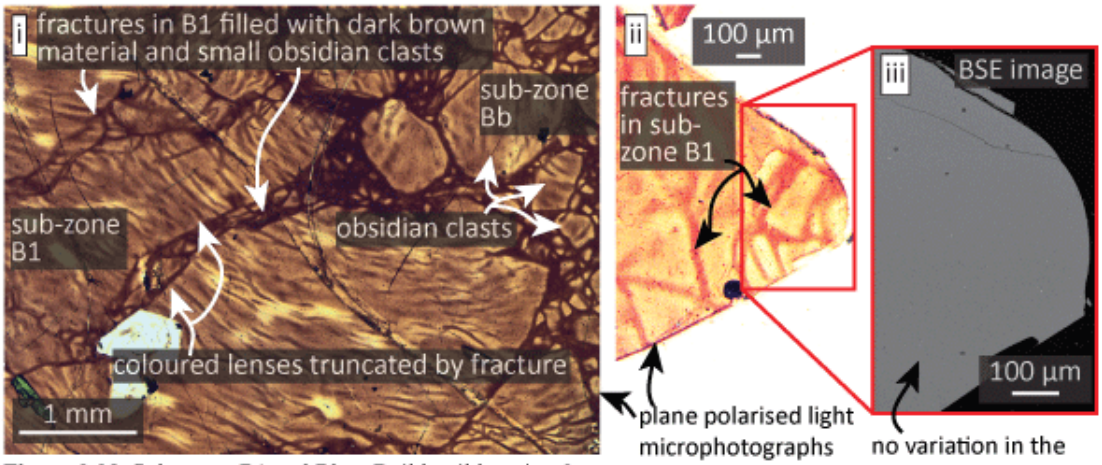

Figure 3.38. Sub-zones B1 and Bb at Deildargil location 2a (sample Dmb-ts1), see main text and figure labels for further description.

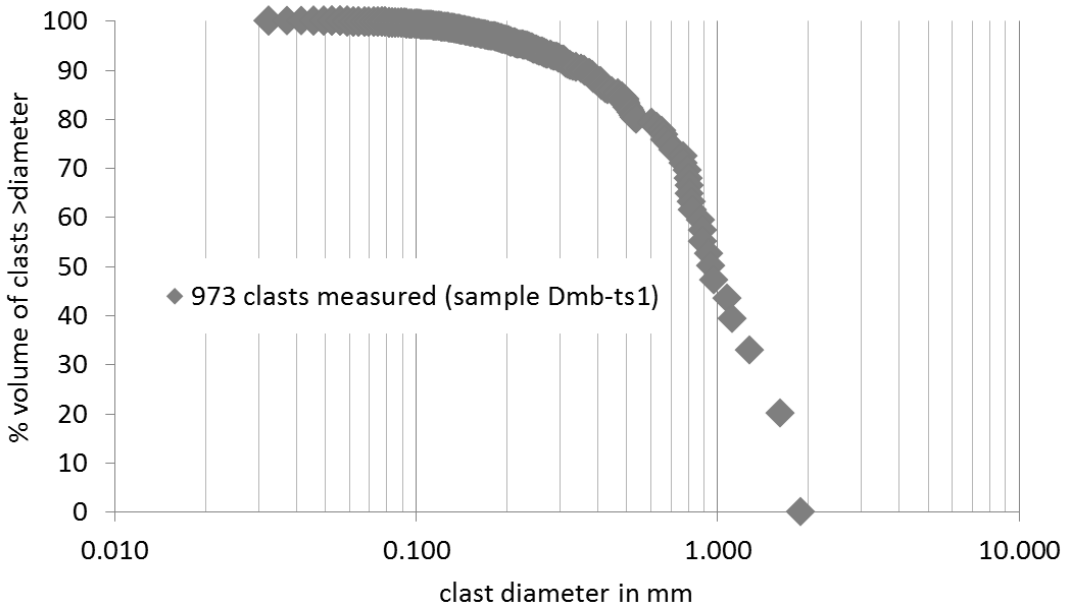

Figure 3.39. Size of obsidian clasts in sub-zone Bb at Deildargil location 2a.

At Deildargil location 2a, the microlite number density decreases across zone B towards the dyke centre; this is coupled with an increase in the microlite size (**Fig. 3.32; A.3.6.**). The size variations cause the microlites to change to nanolites, but as they are deemed to be the same population, they are just referred to as microlites for convenience. The number density and size changes are gradational, but the gradations are disrupted near to the coloured lenses. The microlite size and number density surrounding the lens cores progressively decreases and increases, respectively, with

increased distance from the cores (**Fig. 3.40.iii and vi**). These progressive changes occur over 10-30 μm; nearest the cores the microlites are ~3 μm wide, whereas furthest from the cores they are ~0.5 μm wide, which is close to the average microlite width in the surrounding obsidian, distal to the lenses. Progressive changes also occur in the microlite size and number density next to lenses in the green layer, but over a greater distance (~150 μm; **Fig. 3.40.vii and viii**). Lenses in the dark brown part of B1 (i.e., the part proximal to the green layer) have predominantly microlite-free cores, corresponding to the colourless slits in microphotographs (**Fig. 3.40.i-iii**). These regions contain a few sub-circular, ~3-5 μm wide microlites and sparse lath-like <50 μm long microlites (**Fig. 3.40.ii and iii**). Lens centres commonly contain voids, which mimic the form of their host lens (**Fig. 3.40.i and ii**). Similarly to the cores of the lenses in the brown part, those within the green layer contain a few microlites that are ~3-5 μm wide in their cores; however, in contrast to the former lenses, those in the green layer are also filled with very small microlites, which are ~0.3 μm wide. These small microlites are absent around the larger microlites (**Fig. 3.40.ix and x**). Microlite trains also occur near the lenses; these have widths of ~2 μm and are 10-100 μm long (**Fig. 3.40.ix and x**).

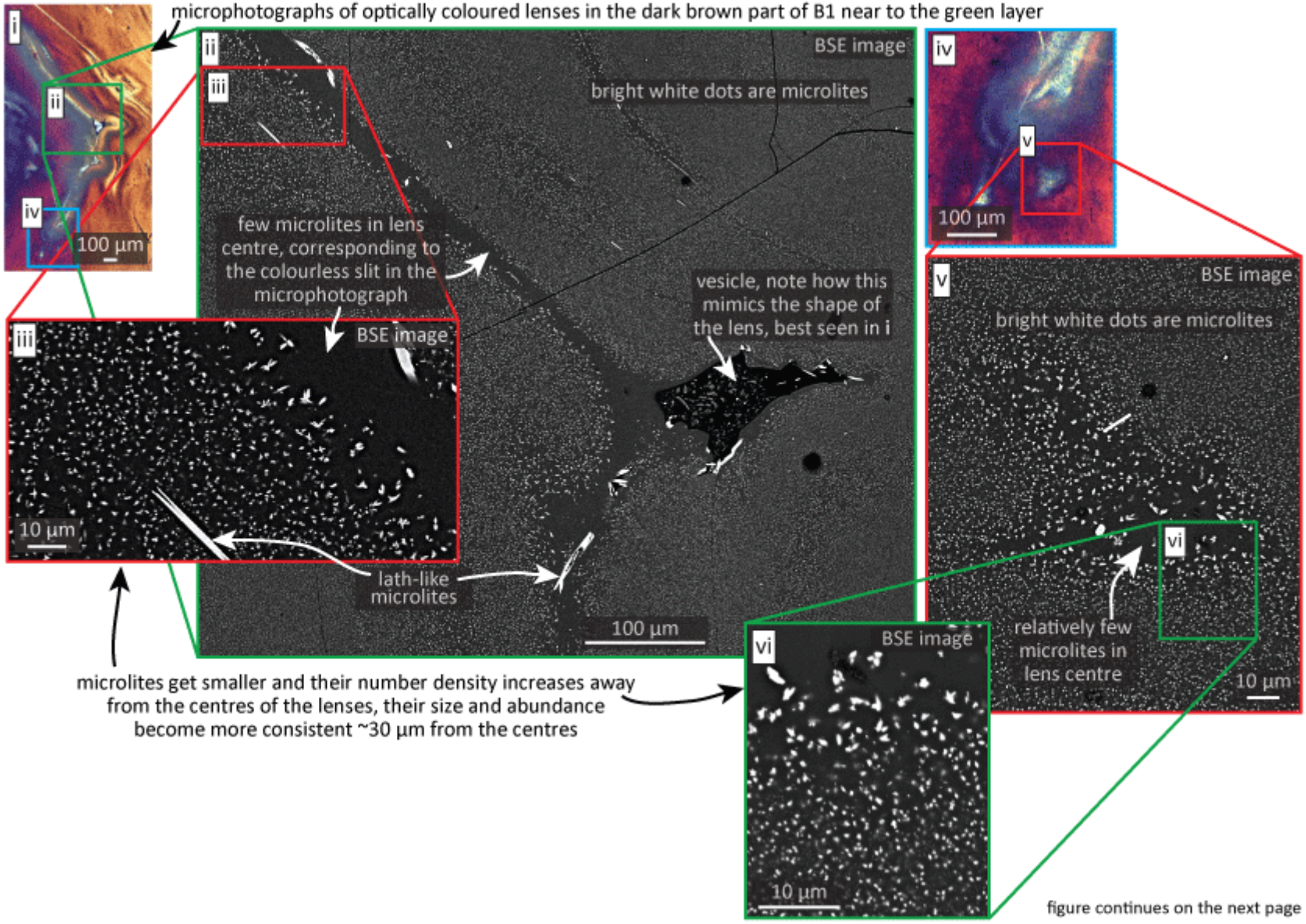

figure continues on the next page

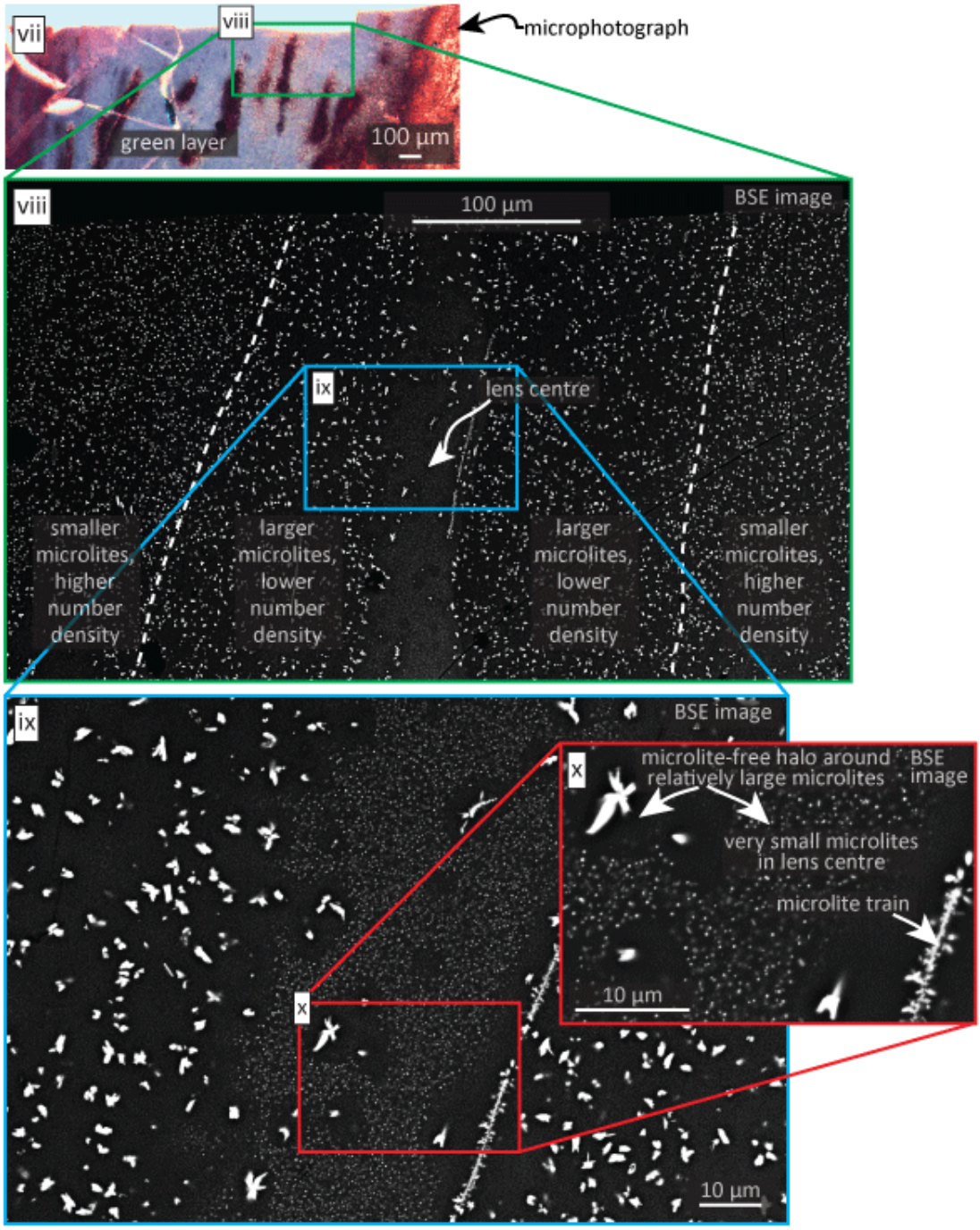

Figure 3.40. Figure continues from the previous page. Variations in the size and number density of microlites in the vicinity of optically coloured lenses (sample Dmb-ts1).

3.3.4. Zone B: sub-zones Bb and Bfb

i) Macro- to micro-scale features, Hringsgil location 2

At Hringsgil location 2, welded obsidian breccia (sub-zone Bb), with zero porosity, occurs locally in the lower part of the dyke (~2 m above the streambed), in a ~50 x 10

cm domain that is referred to as location 2.2. Here, Bb is located between the flow banded obsidian of sub-zone Bfb and sub-zone B2 (**Fig. 3.41.i-iii**), and it consists of obsidian clasts and phenocrysts (**Fig. 3.41.iv-vii**), with lithics lacking. The phenocrysts are within the obsidian clasts and are generally intact, with major axis lengths spanning 100 μm - 1 mm. Locally, obsidian clasts are deformed around phenocrysts. The clasts are yellow, brown, grey, blue or black in hand specimens and various shades of yellow and brown in petrological thin sections (**Fig. 3.41.iv and v**). Jigsaw fit clasts were not observed and clasts lack perlitic cracks. Many clasts contain different-coloured bands or lenses, which are often truncated at clast edges (**Fig. 3.41.vi**). In BSE images, it is apparent that the microlite size and number density varies between different clasts. The electron backscatter intensity of each clast is the same and individual clasts can only be distinguished from one another due to the differences in microlites (**Fig. 3.41.vii and viii**). Clasts are elongate with rounded edges, and their major axes are aligned with the sub-zone contacts and dyke margins. Clast sizes were determined by the already described method (see **section 2.6.** for methodology and errors). Their diameters span ~100 μm to ~4 mm (**Fig. 3.42.**).

Flow banded obsidian (sub-zone Bfb) was observed at multiple places along the dyke at Hringsgil location 2, but its characteristics at just two locations shall be described. The locations will be referred to as 2.4 and 2.12, and occur 4 m and 12 m along the dyke length respectively (measured from the streambed). At both locations sub-zone Bfb occurs either side of sub-zone B2, i.e., between B1 and B2, and between B2 and D. Location 2.4 (**Fig. 3.43.i**) is 2 m higher than location 2.2 on the same side (NE side) of the dyke. The breccia, which is present at location 2.2 is absent at location 2.4, being replaced by sub-zone Bfb. Similarly to sub-zone Bb, Bfb also contains phenocrysts that are ~100 μm to 2 mm long, with many being sub-euhedral

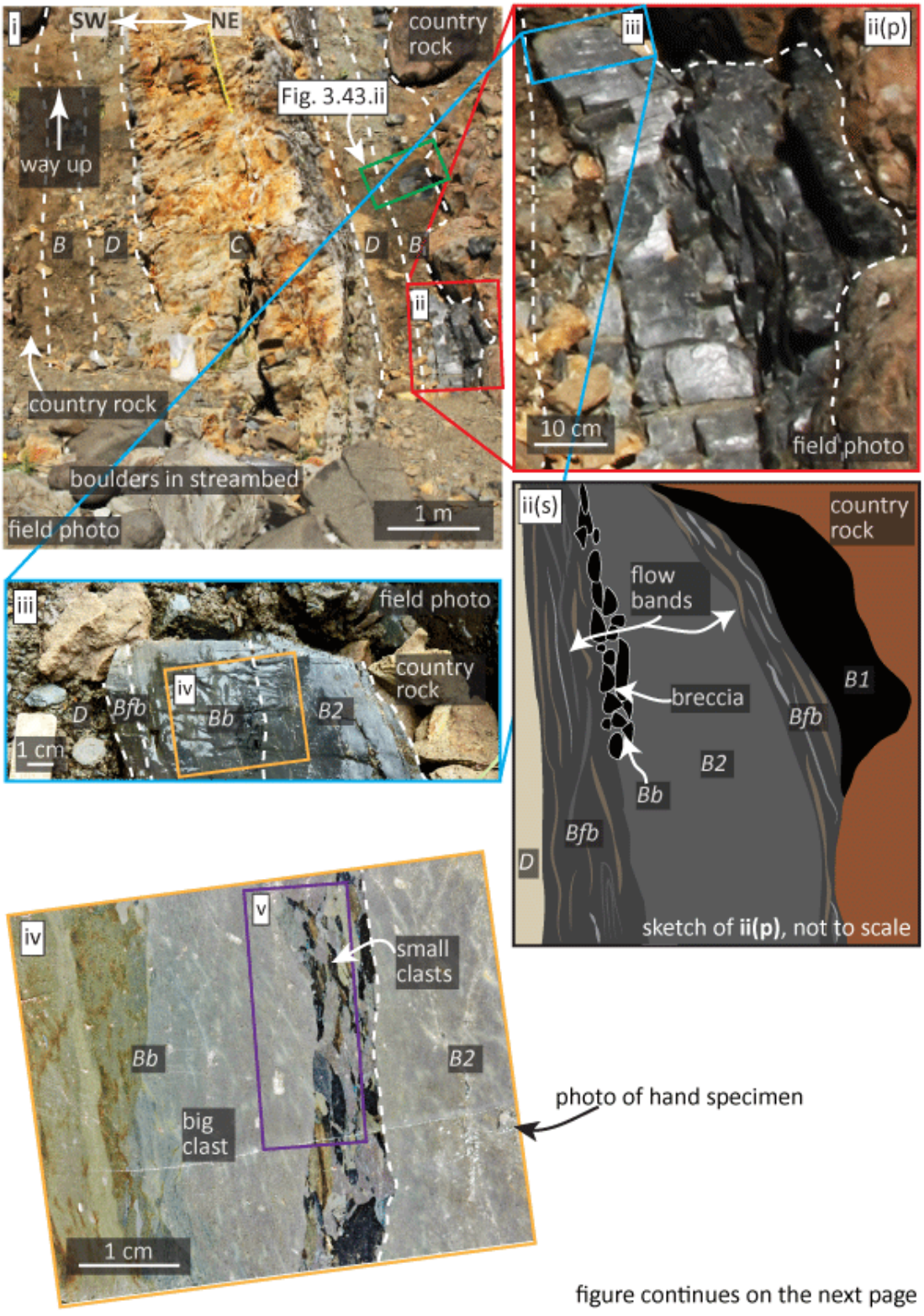

figure continues on the next page

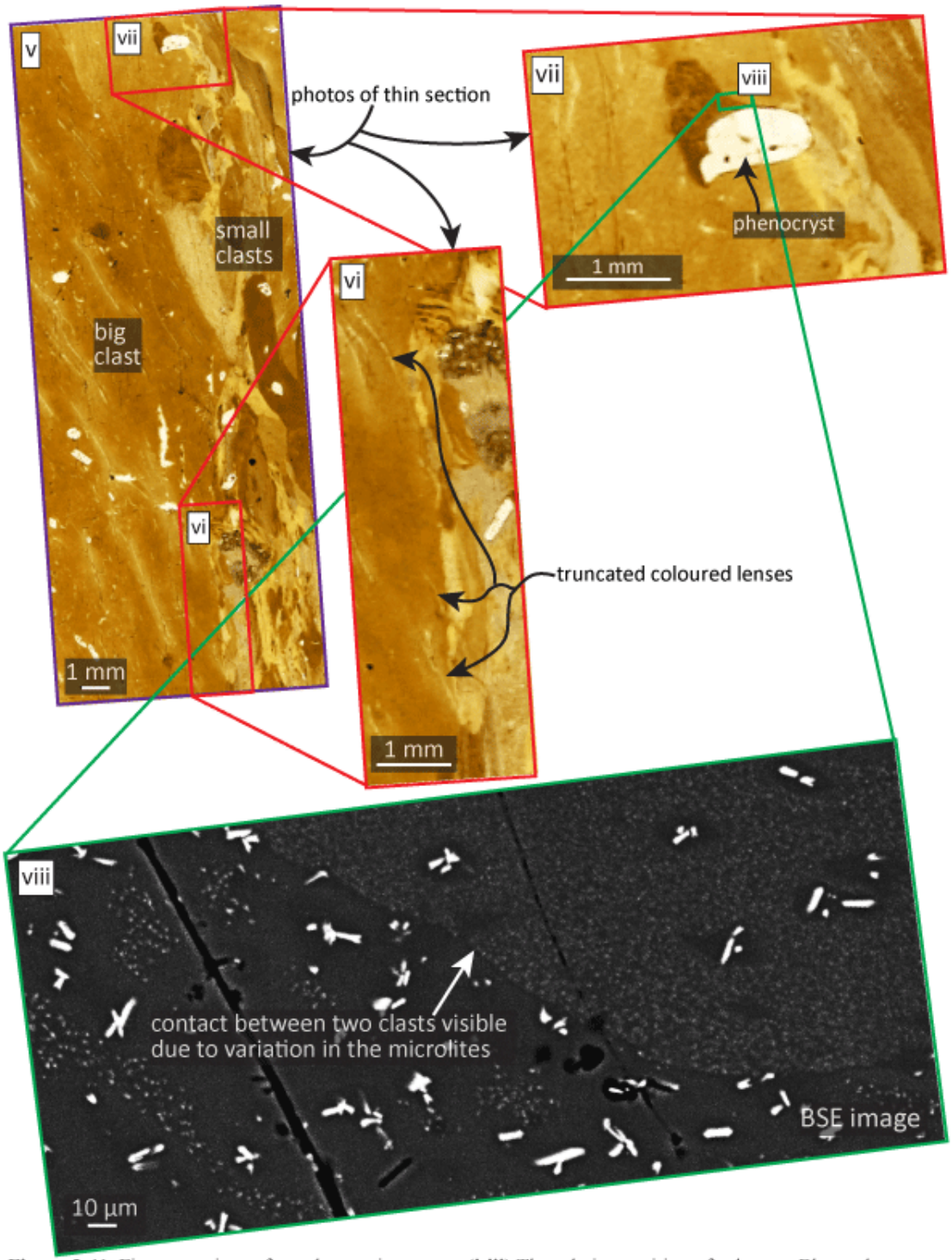

Figure 3.41. Figure continues from the previous page. **(i-iii)** The relative position of sub-zone Bb to other zones and sub-zones at Hringsgil location 2.2, the textural zones and sub-zones are labelled (italic letters). **(iii-viii)** Macro- to micro-scale textures of sub-zone Bb (sample HG-1), see main text and figure labels for further descriptions.

and intact. Also similarly to sub-zone Bb, no lithics occur in sub-zone Bfb at Hringsgil location 2. At location 2.4, the contacts between Bfb and the surrounding sub-zones are linear and vary from gradational to sharp. The width of Bfb is ~5-10 cm and it is exposed over a length of ~10-20 cm. Individual flow bands are discontinuous, ~1 mm to >10 cm long and their widths are commonly <1 mm (**Fig. 3.43. ii-iv**). The bands have different colours, being light grey, brown, blue or black; they are sub-planar and aligned with the sub-zone contacts and dyke margins, and many are slightly buckled giving them a wavy appearance in the field (**Fig. 3.43.iii and iv**). Micro-analysis of the bands reveals that many contain micro-folds and that they are often deformed around phenocrysts (**Fig. 3.43.v-vii**).

Similarly to location 2.4, sub-zone Bfb occurs at both margins of sub-zone B2 at location 2.12 (**Fig. 3.44.i -iii**). However, in contrast to location 2.4, the sub-zone has a maximum thickness of ~50 cm, which is five times larger than its maximum thickness at location 2.4. In addition, the meso-scale structure of the flow bands is more complex than at location 2.4. For instance, some bands have irregular shapes, with feather-like edges (**Fig. 3.44.iv**) and some are folded (**Fig. 3.44.v**), with folds

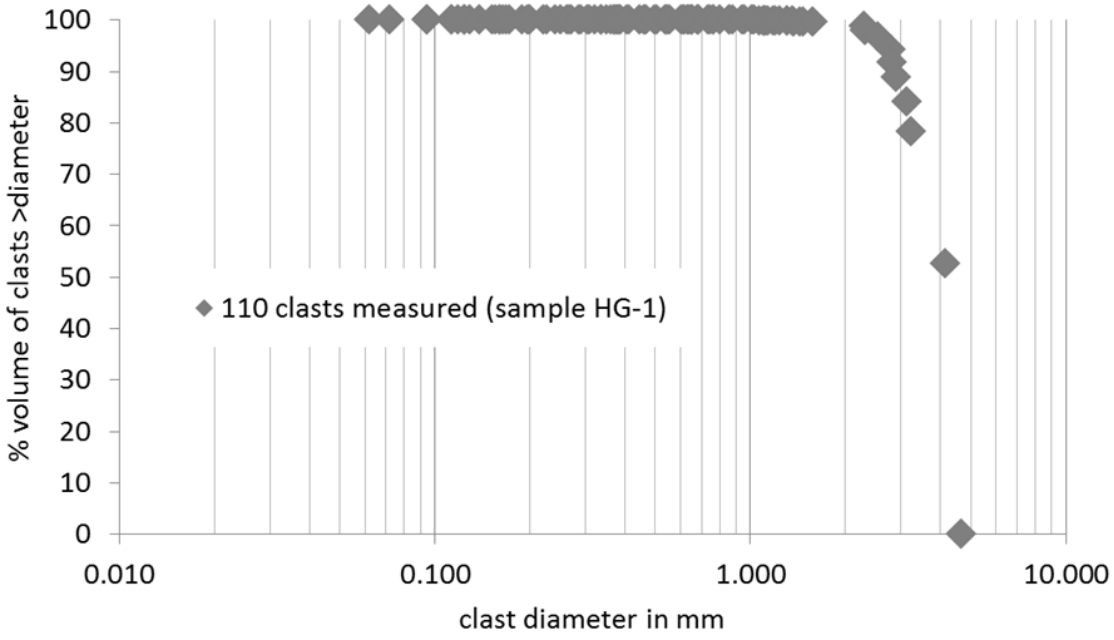

Figure 3.42. Size of the obsidian clasts in sub-zone Bb at Hringsgil location 2.

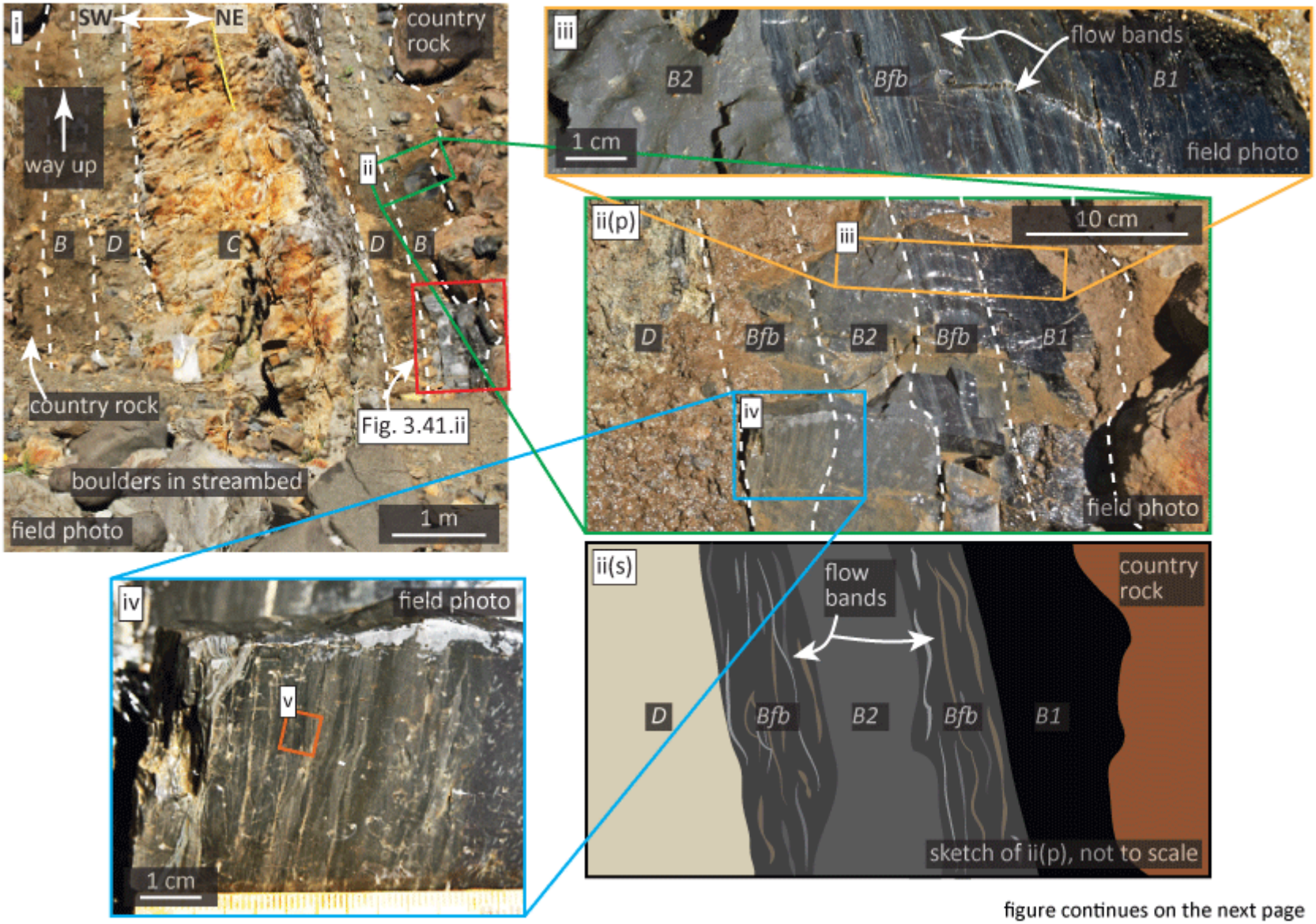

figure continues on the next page

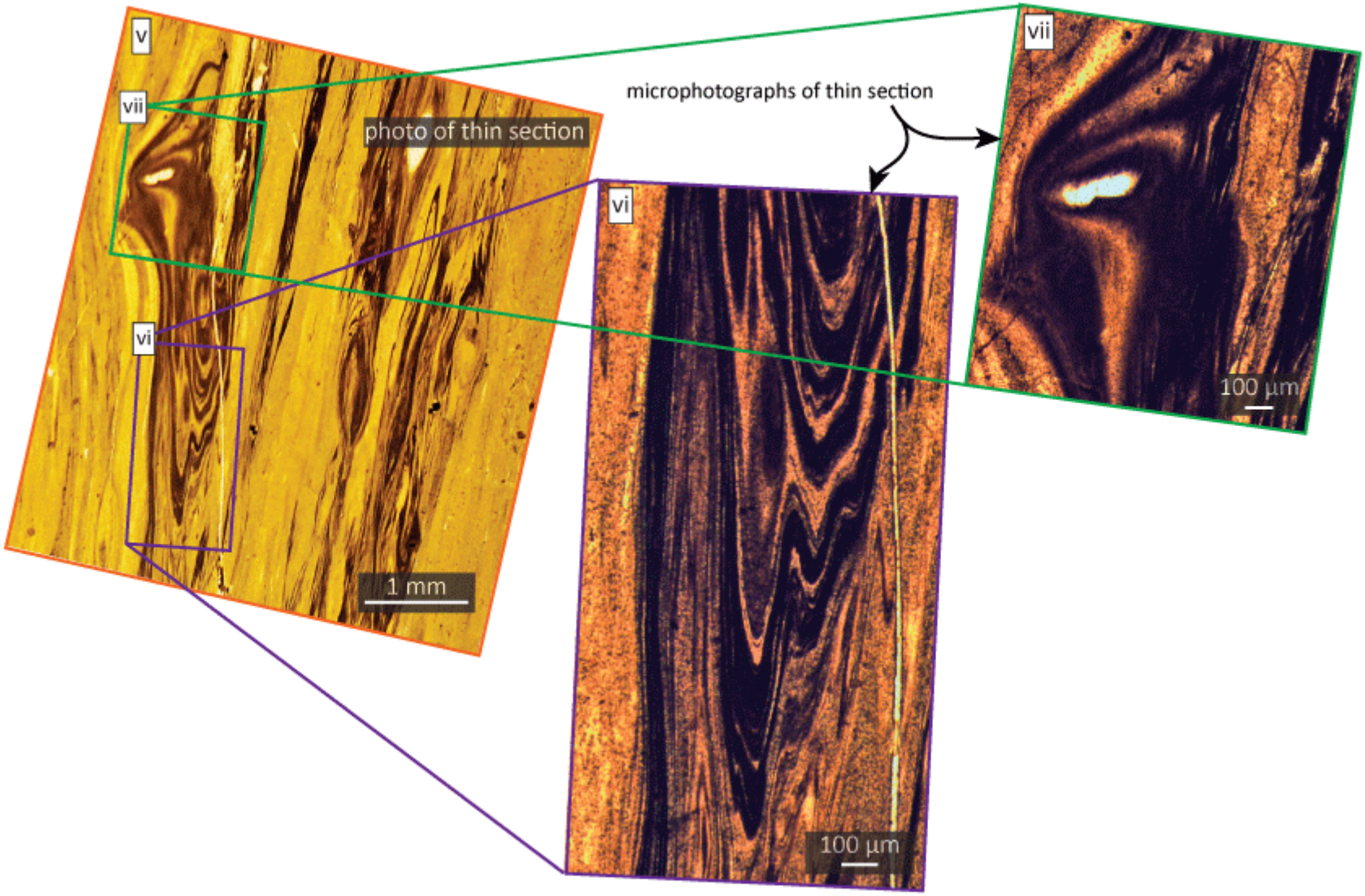

Figure 3.43. Figure continues from the previous page. Macro- to micro-scale texture of sub-zone Bfb at Hringsgil location 2.4. **(iv-vii)** Sample HS1e. See main text and labels for description. The microphotographs were taken in plane polarised light.

locally wrapping around vesicles (**Fig. 3.44.vi and vii**). Similarly to the flow bands at location 2.4, those at location 2.12 are also deformed at a micro-scale. For instance, some of the meso-scale folds have small ptygmatic folds along their limbs (**Fig. 3.44.viii and ix**), and sheath folds occur locally (**Fig. 3.44.x and xi**). The different-coloured flow bands in sub-zone Bfb are defined by variations in the size and abundance of microlites, similar to the different-coloured clasts in sub-zone Bb.

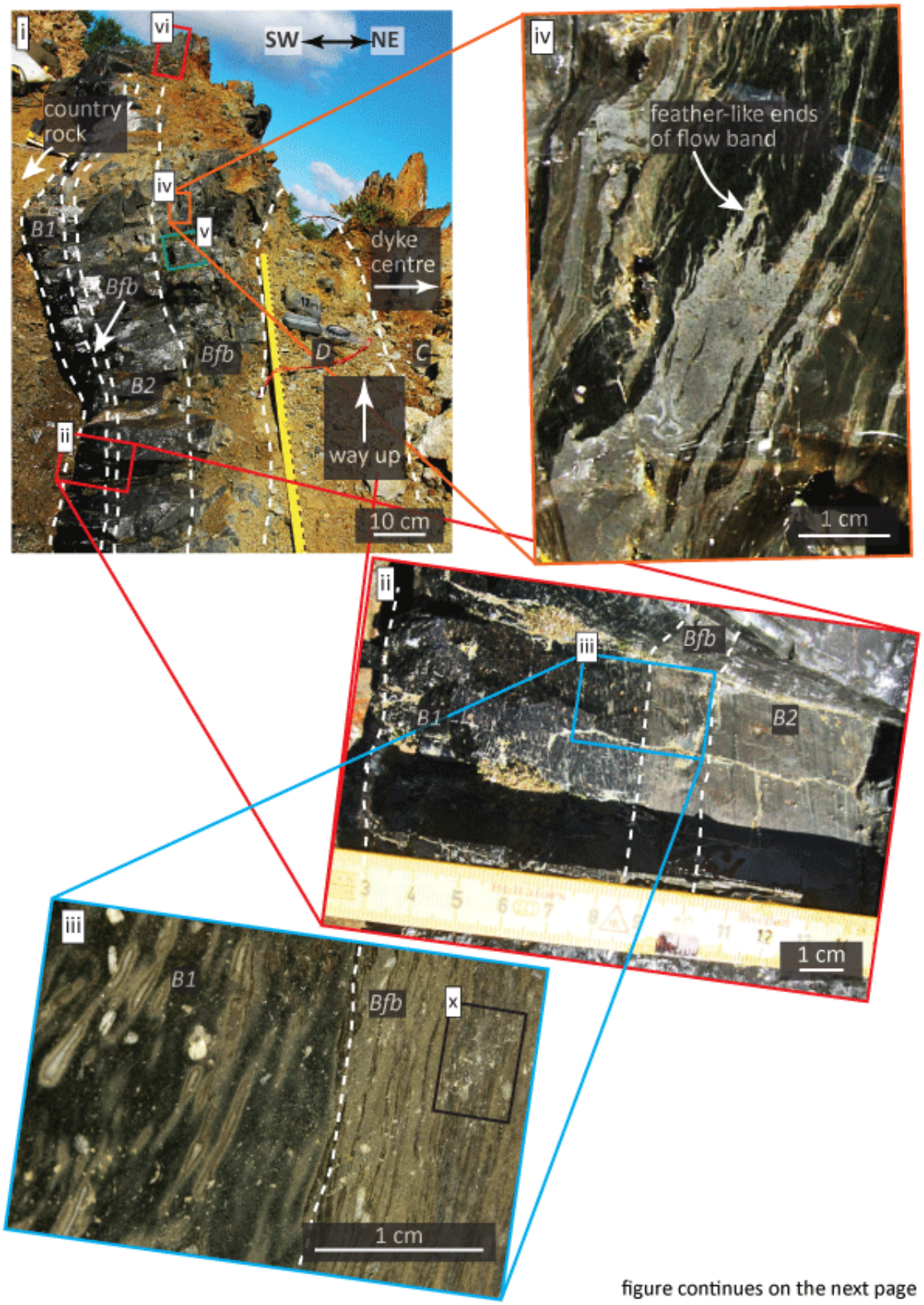

figure continues on the next page

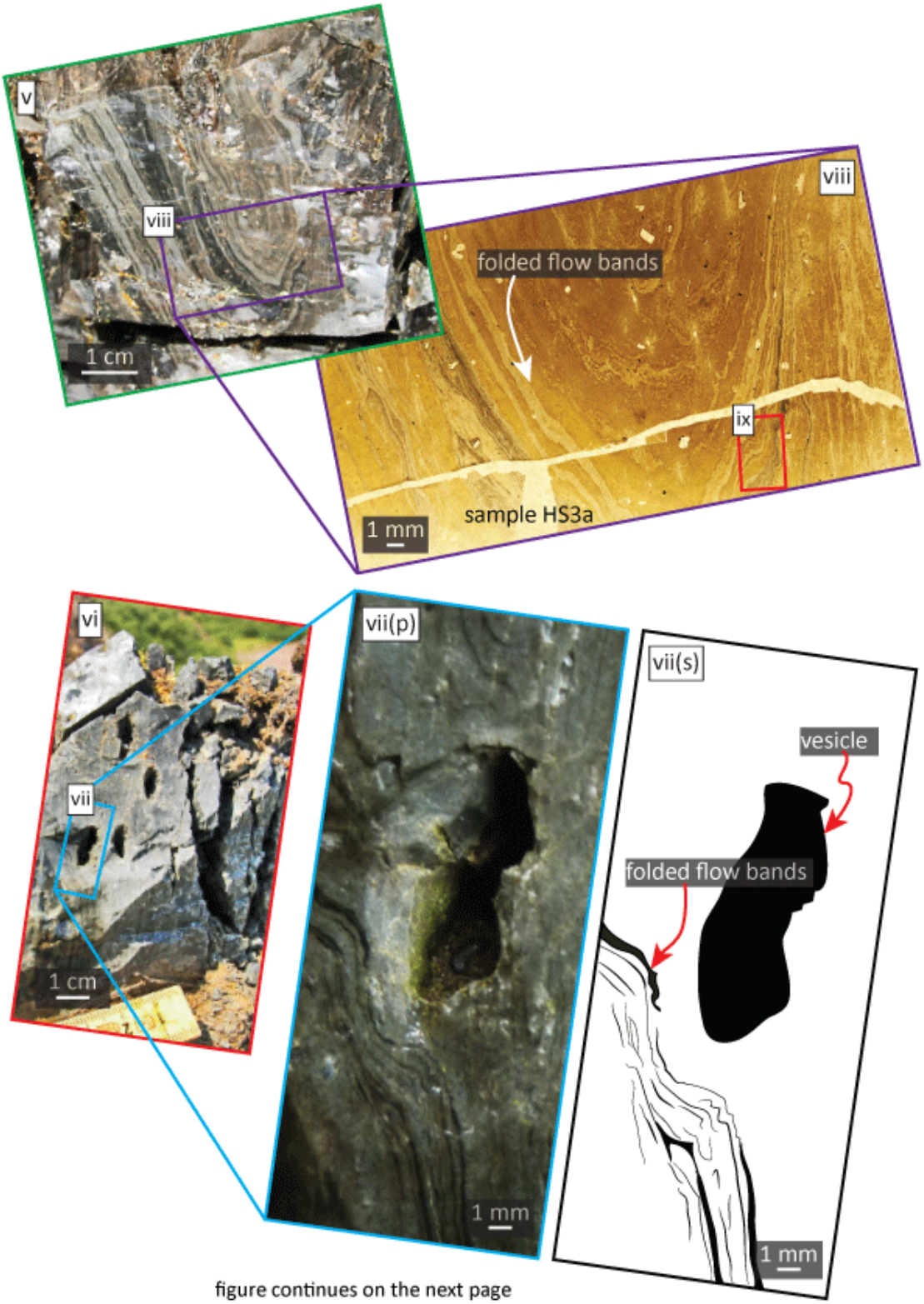

figure continues on the next page

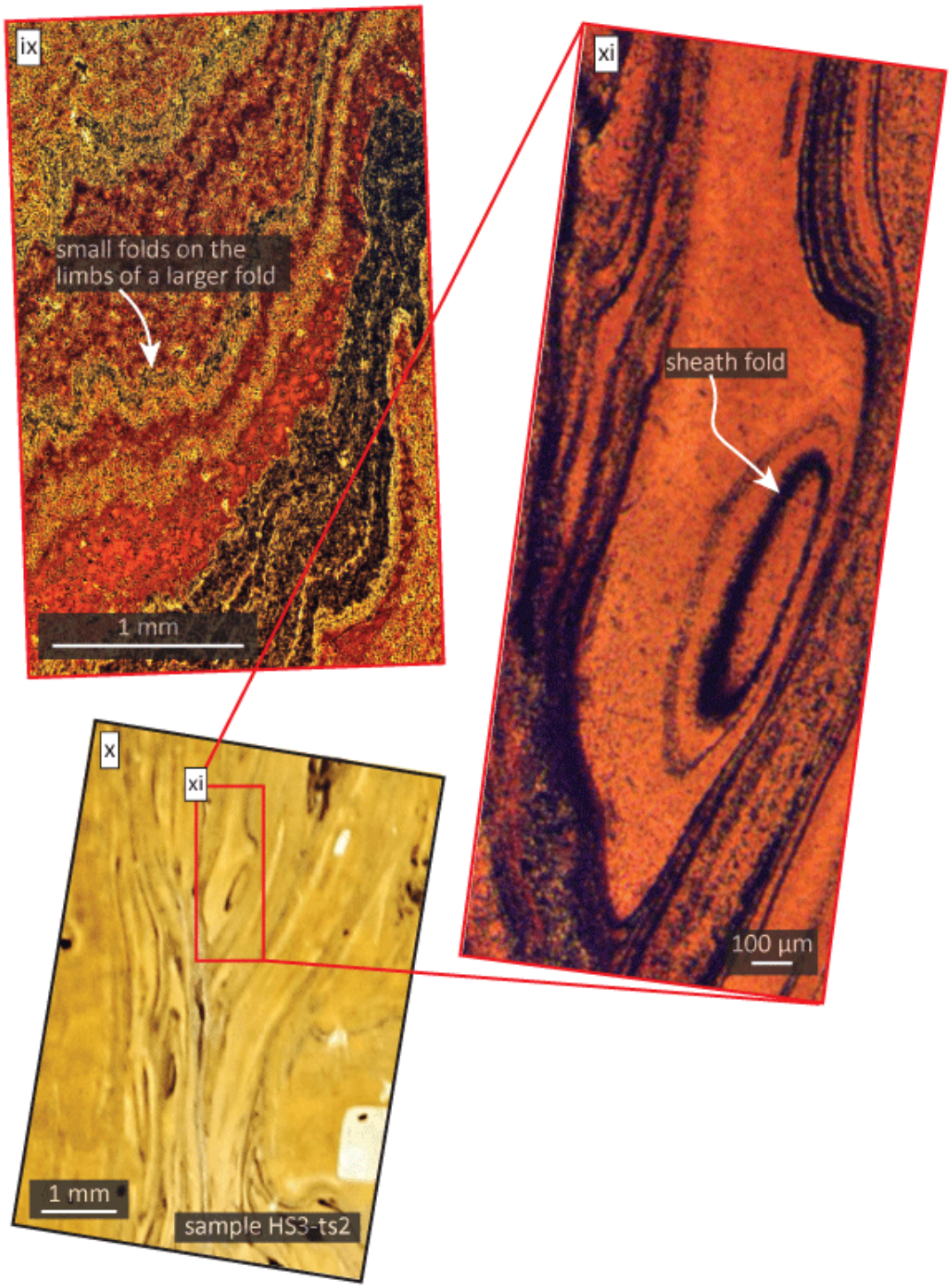

Figure 3.44. Figure continues on the next page. Macro- to micro-scale texture of sub-zone Bfb at Hringsgil location 2.12. **(i, ii and iv-vii)** Field photos. **(iii)** Photo of hand specimen. **(viii and x)** Photos of thin sections. **(ix and xi)** Microphotographs taken in plane polarised light. See main text and labels for description.

ii) Macro- to micro-scale features, Hringsgil location 3a

In contrast to Hringsgil location 2, at Hringsgil location 3a sub-zone Bb contains lithic clasts, which occur with juvenile, vesicle-free obsidian clasts. At location 3a, Bb is bordered to the SW by flow banded obsidian (sub-zone Bfb) and to the NE by a weathered version of zone B; it is exposed over ~1 m of the dyke length and is ~0.5 m wide (**Fig. 3.45.i and ii**). The obsidian clasts that form the breccia are green, grey or black in the field, and various shades of brown in petrological thin sections (**Fig. 3.45.iii-v**). The clasts often contain different coloured bands or lenses, which are commonly truncated at the clast edges and viscously deformed next to lithic clasts (**Fig. 3.45.iv**). Many of the obsidian clasts are elongate; their major axes are aligned with the contacts between the textural zones and dyke margins, and some have irregular forms because they are viscously deformed around lithic clasts or other obsidian clasts (**Fig. 3.45.iv and v**). Both the obsidian and lithic clasts have sub-rounded edges, and in contrast to the elongate forms of the obsidian clasts, many of the lithic clasts are sub-circular. However, this only applies to clasts >1 mm, as those smaller than this, which form laminations (**Fig. 3.45.vi**), have angular edges and are undeformed (**Fig. 3.45.vii**). The smaller clasts locally form a supporting matrix between larger clasts, but some larger clasts are in contact with one another. Some lithic clasts contain irregular shaped glassy domains, which are ~100 μm to 2 mm across (**Fig. 3.45.vi**). The relatively large (>1 mm) obsidian clasts contain intact phenocrysts and fragments of similar phenocrysts constitute part of the fine ash matrix.

It is not always possible to distinguish between the obsidian and lithic clasts in BSE images, and because these images were required for grainsize analysis of the smallest clasts, the clasts have been grouped together in the analysis. Clast sizes were

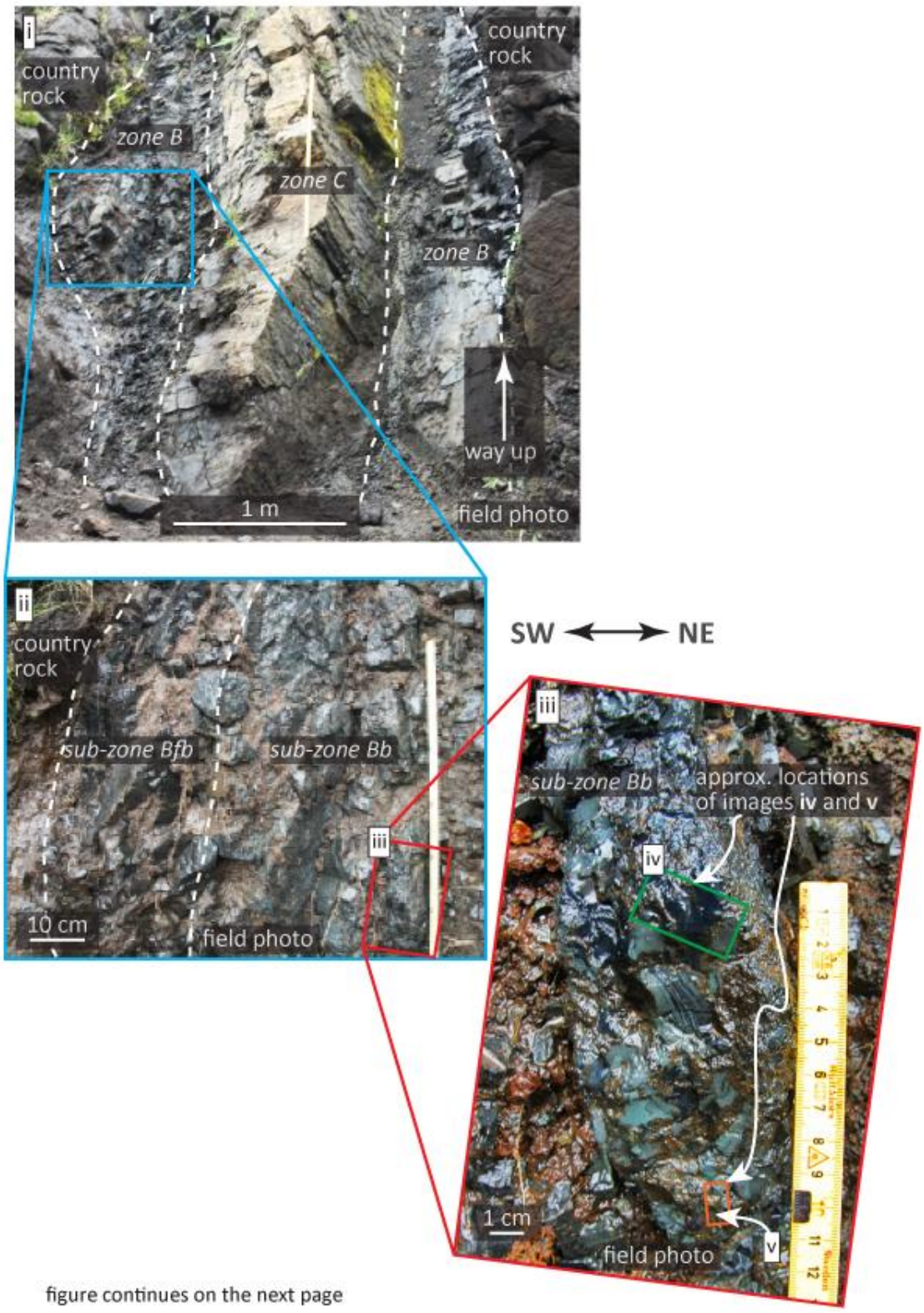

figure continues on the next page

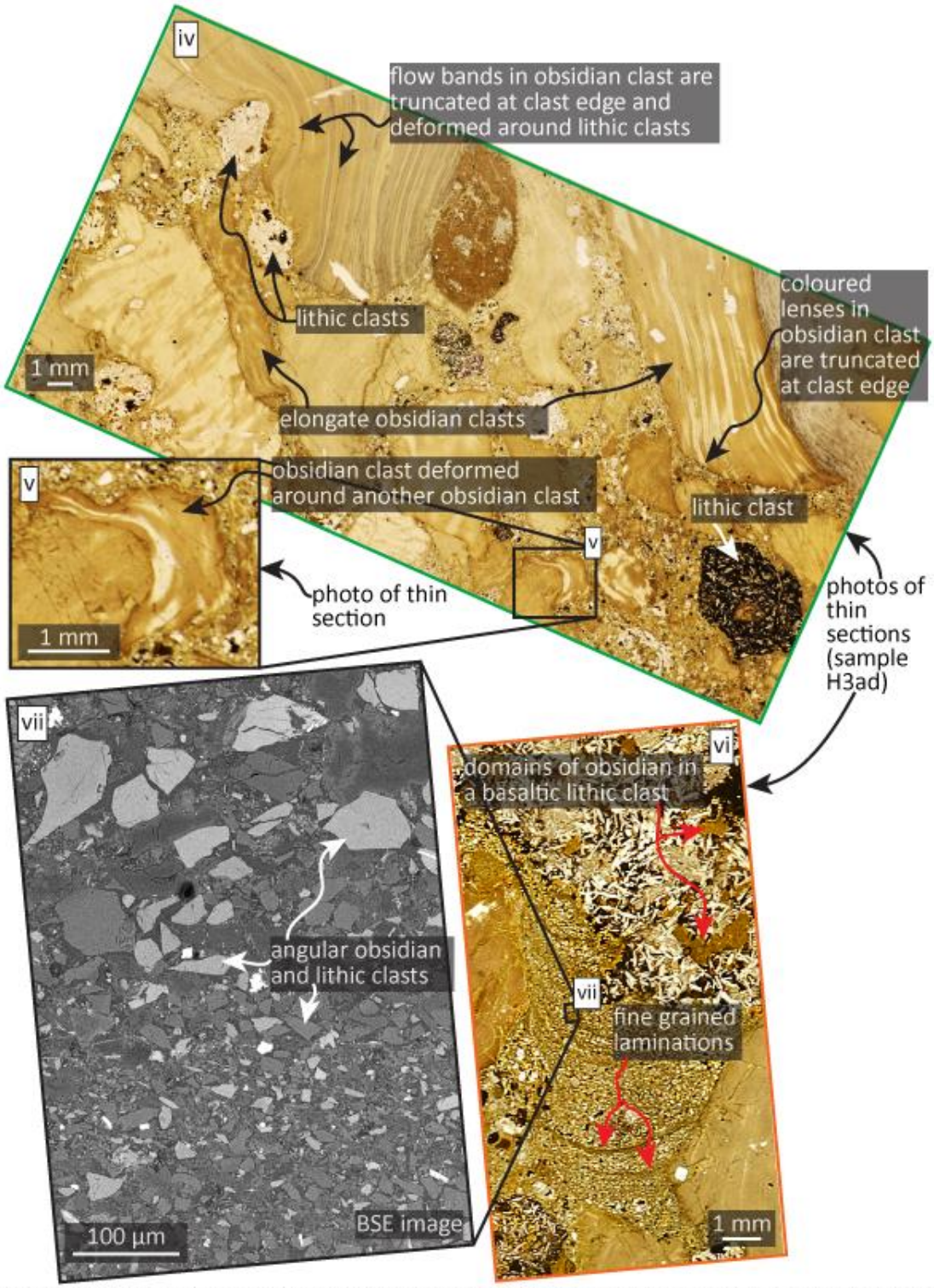

Figure 3.45. Figure continues from the previous page. Macro- to micro-scale texture of sub-zone Bb at Hringsgil location 3a. See main text and labels for description.

determined by the method already described (see **section 2.6.** for methodology and errors). Clast diameters range from ~1 μm to 13 mm, and clasts with diameters >1 mm make up more than 99 % of the total inferred volume (**Fig. 3.46.**).

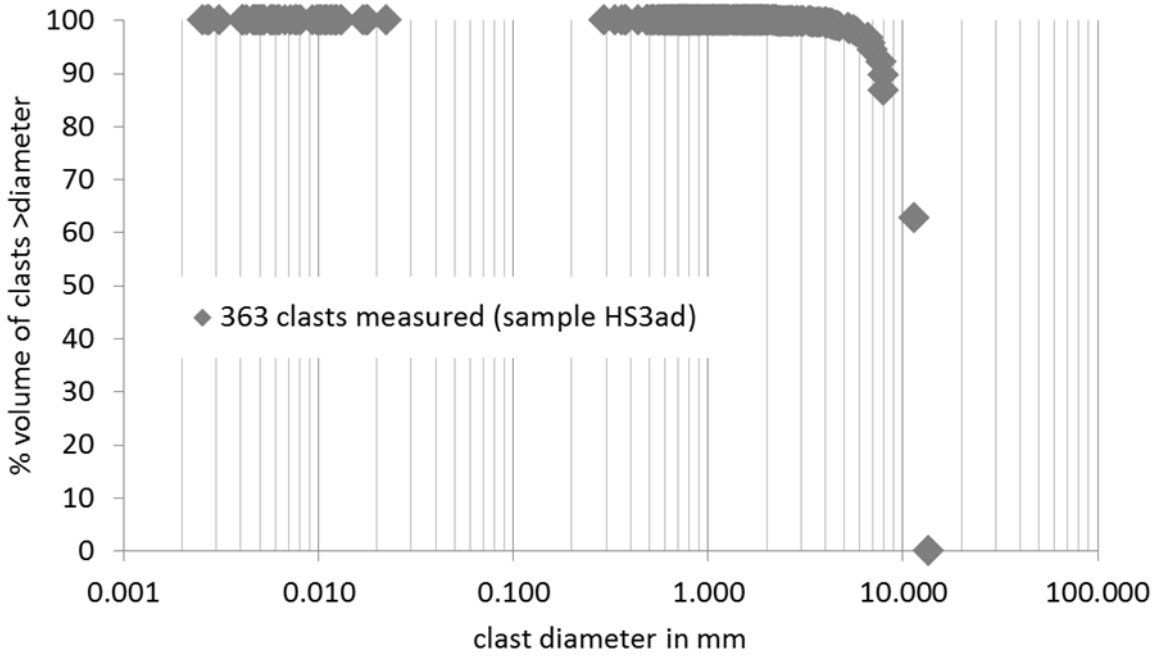

Figure 3.46. Size of the juvenile and lithic clasts in sub-zone Bb at Hringsgil location 3a. The gap in the data represents clasts that have diameters between 23 and 296 μm, such clasts do exist, but they are rare, as the clasts are dominated by coarser clasts which are supported in the finer matrix.

Sub-zone Bfb at Hringsgil location 3a lies between Bb and the country rock (**Fig. 3.47.i and ii**). Here, Bfb is exposed over ~3 m of the dyke length and is ~30 cm wide. The sub-zone consists of elongate black obsidian clasts, supported by a grey matrix (**Fig. 3.47.iii and iv**), with the elongate clast forms giving the rock its flow-banded appearance. In petrological thin sections, the obsidian clasts are yellow and the matrix is dark brown (**Fig. 3.47.v and vi**). The obsidian clasts are ~100 μm - 15 mm long and ~10 μm - 1 mm wide. The clasts contain a few phenocrysts that are relatively intact, whereas phenocrysts within the matrix ash are fragmented. Part of the matrix consists of lithic clasts that range in size from ~10 μm to 1 mm; these are sub-circular, and thus contrast with the elongate obsidian clasts. The obsidian clasts are commonly deformed around the lithic clasts.

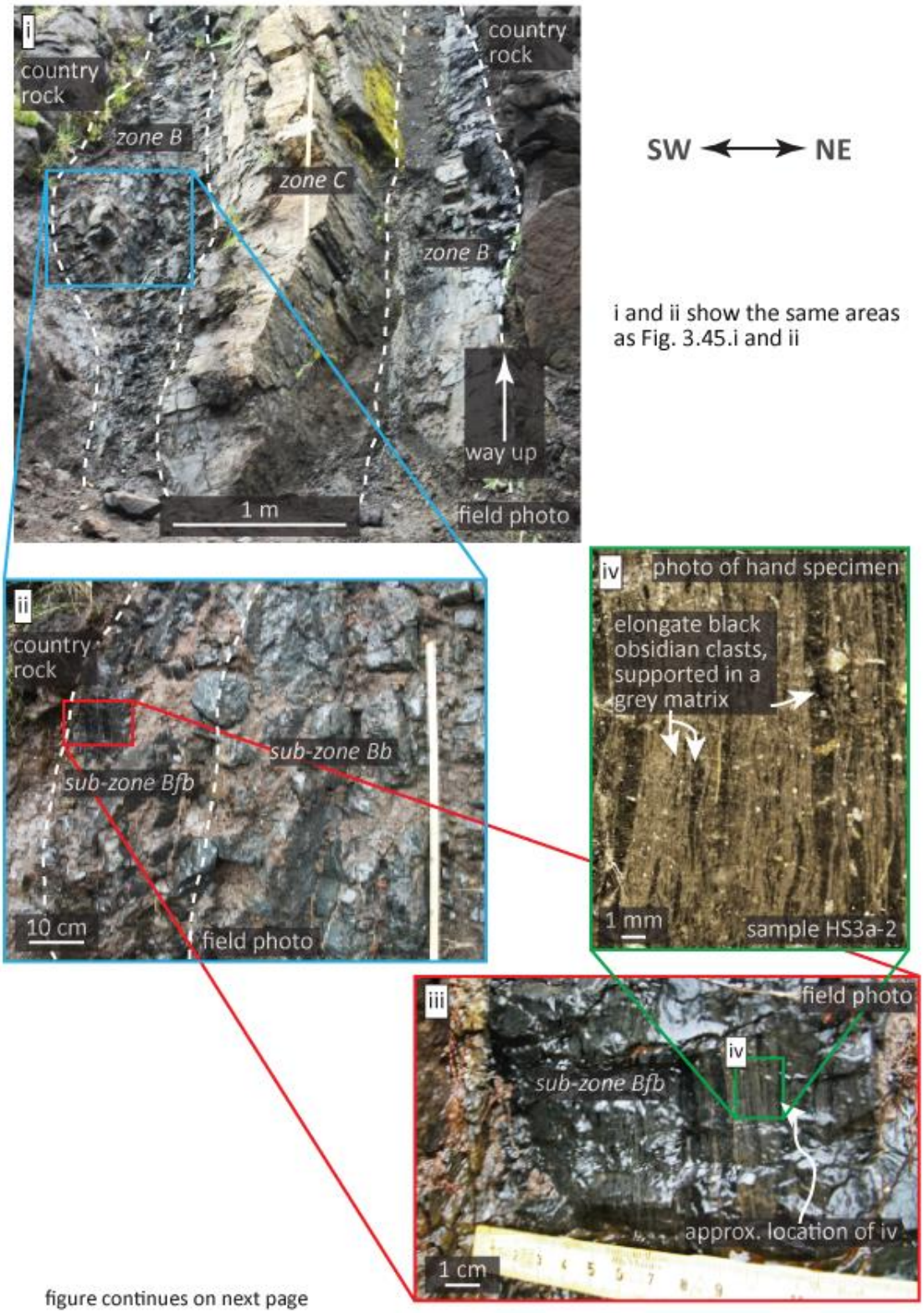

figure continues on next page

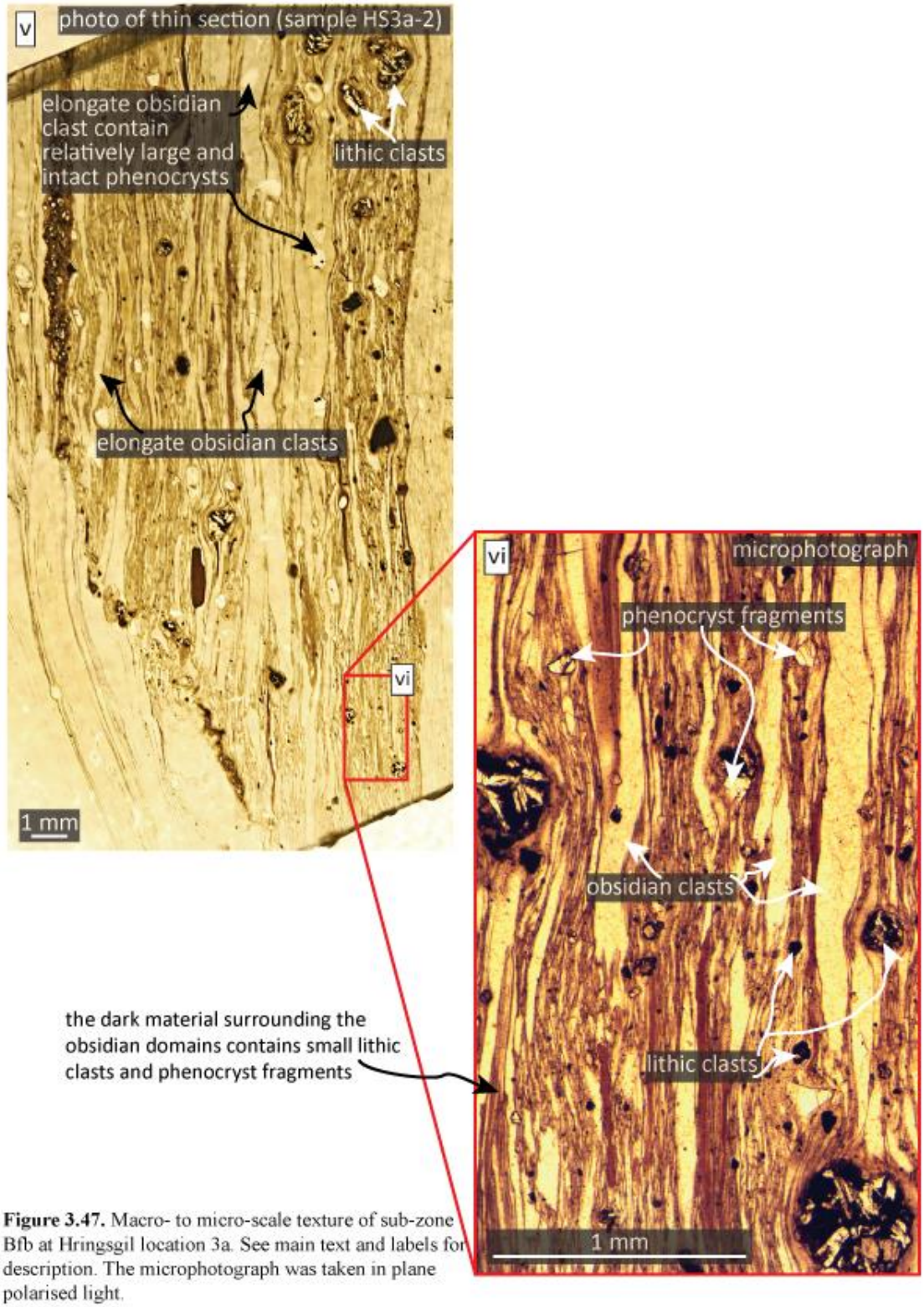

Figure 3.47. Macro- to micro-scale texture of sub-zone Bfb at Hringsgil location 3a. See main text and labels for description. The microphotograph was taken in plane polarised light.

3.3.5. Zone T

i) Macro to micro-scale features, Deildargil location 1

The best examples of zone T occur at Deildargil locations 1 and 2, where it forms the gradational contact between zones B and C. Zone T consists of obsidian and microcrystalline rhyolite. The obsidian contains beige domains (**Fig. 3.48.i**), which are lacking in zone B. In the field, the domains appear as elongate lenses proximal to zone B and become more spherical towards zone C. Their number density also increases towards zone C; eventually their number density is so high that they merge with one another and individual domains cannot be distinguished (**Fig. 3.48.ii**). Proximal to zone B, the major axes of some domains are up to ~3 cm long, whereas proximal to zone C they do not exceed 5 mm. In petrological thin sections, many of the domains appear to connect with one another and they have brown outer rims no wider than a few hundred microns. Their cores are predominantly yellow, with patches of brown, and they commonly contain holes (**Fig. 3.48.iii**). In BSE images, the domains are outlined by pitted obsidian, with the pits containing clasts and lath-like microlites. The clasts are similar to the yellow material in the cores, which can also be seen to consist of clasts in BSE images; the clasts have weak electron backscatter intensities relative to the host, and a fish-scale-like texture (**Fig. 3.48.iv-vii**). The lath-like microlites in the pits have relatively strong backscatter intensities in comparison to the host obsidian. The brown rims appear identical to the host in BSE images, as do the brown patches within the cores (**Fig. 3.48.iv-vii**).

Proximal to zone B, zone T contains sub-circular vesicles, with diameters of ~5-50 mm, which are similar to those in the adjacent part of zone B. Zone T also contains lens-shaped pumice clasts, the major axes of the clasts are ~1-20 cm long, and sub-parallel with the dyke margins and textural zone contacts (**Fig. 3.49.**). The

zone T-C transition is commonly defined by a sharp weathered surface (**Fig. 3.49.i**), but sometimes the contact is gradational.

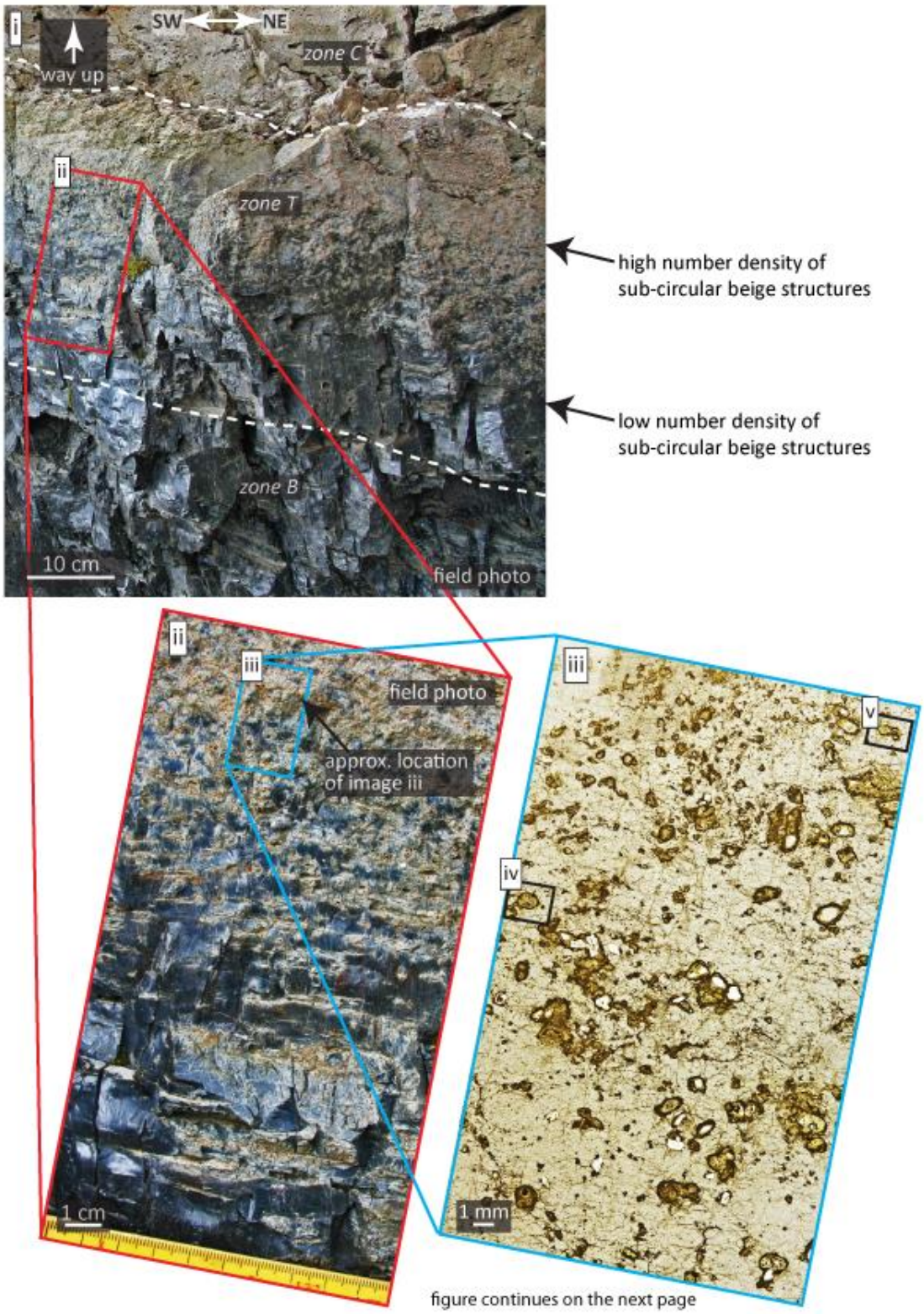

figure continues on the next page

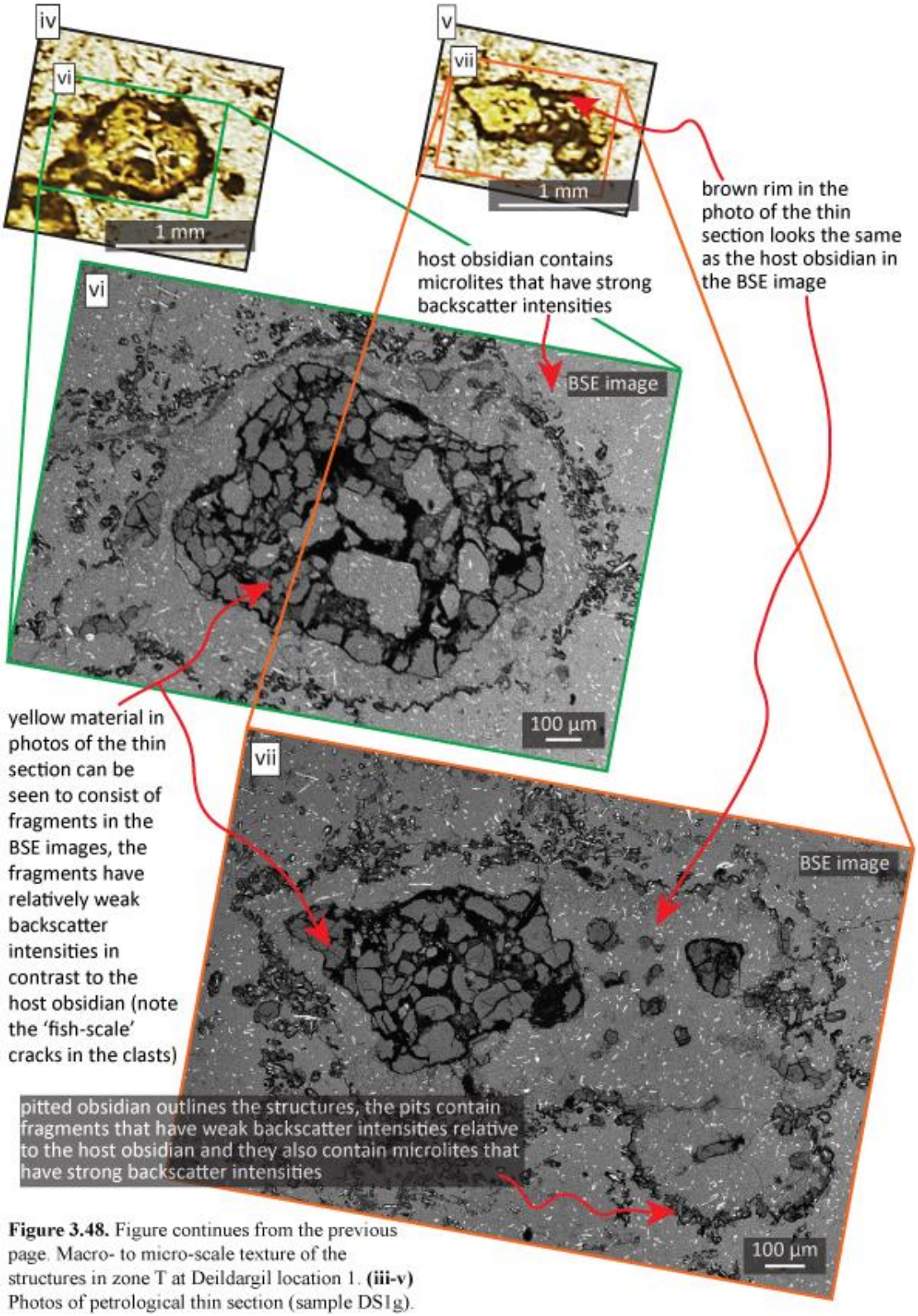

Figure 3.48. Figure continues from the previous page. Macro- to micro-scale texture of the structures in zone T at Deildargil location 1. **(iii-v)** Photos of petrological thin section (sample DS1g).

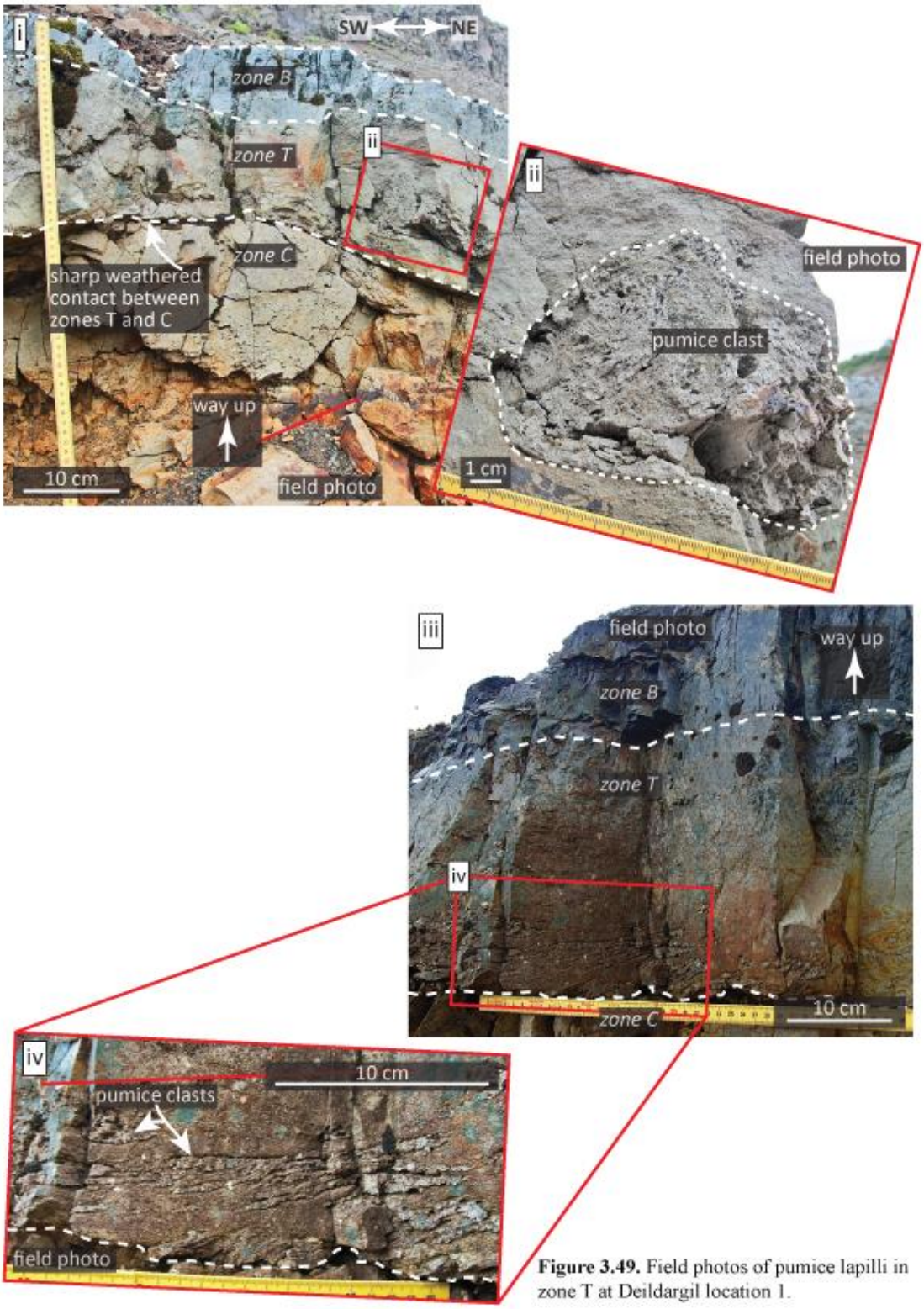

Figure 3.49. Field photos of pumice lapilli in zone T at Deildargil location 1.

3.3.6. Zone C

i) Macro- to micro-scale features, Deildargil locations 1 and 3, and Hringsgil locations 2 and 3a

Zone C consists of microcrystalline rhyolite, and forms the centre of all the dykes. At Deildargil location 3, zone C is orange-brown and contains grey 1-10 mm wide flow bands, which form open folds beneath the welded base of an overlying ignimbrite, with the fold limbs and axis being at the zone margins and centre respectively (**Fig. 3.50.i and ii**). Similar folded flow bands occur in zone C at Hringsgil dykes 2 and 3a. However, these flow bands do not extend to the zone margins. For instance, at location 3a the flow bands only extend across around half of the dyke width, with flow bands lacking from the other side of the dyke (**Fig. 3.50.iii and iv**). In petrological thin sections, it is apparent that the flow bands are deformed around intact phenocrysts and the bands are near-identical to the surrounding material, except that they are a different colour.

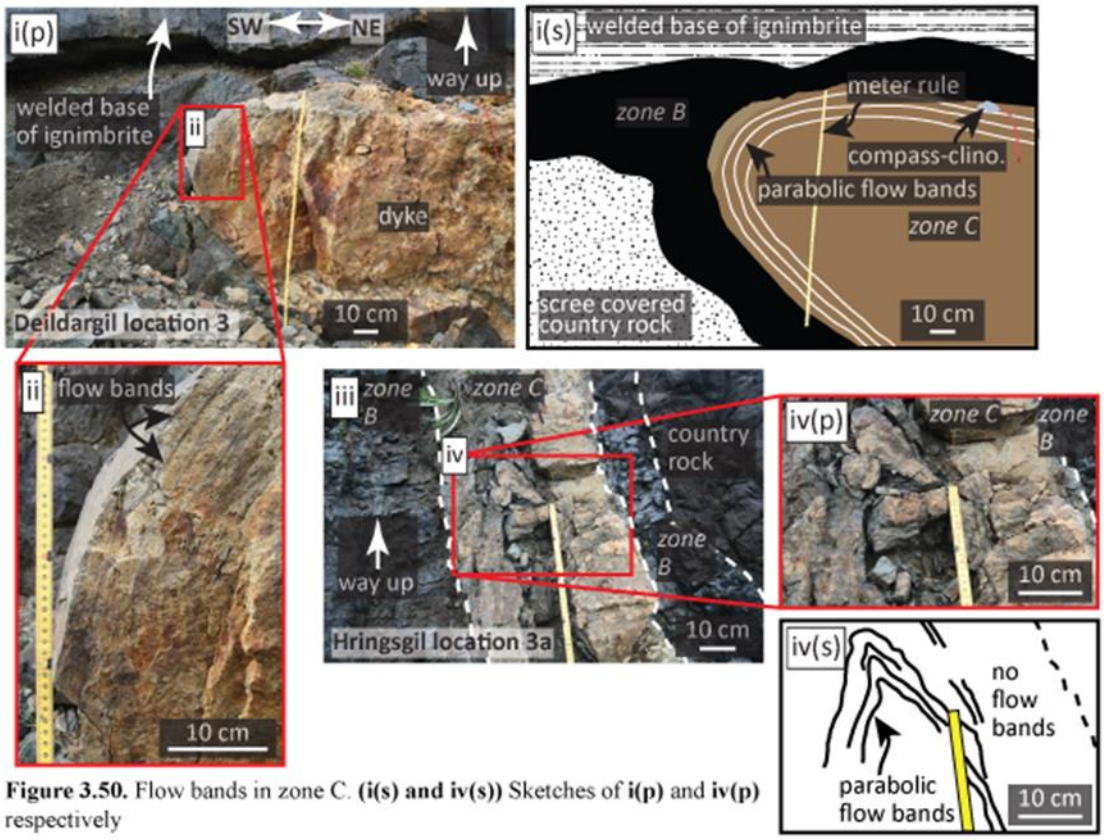

Figure 3.50. Flow bands in zone C. **(i(s) and iv(s))** Sketches of **i(p)** and **iv(p)** respectively

Vesicles occur throughout zone C; at the zone margins (sub-zone Cm) the vesicles are elongate, ~1-20 mm long and parallel with both the dyke margins and contacts between the textural zones and sub-zones (**Fig. 3.51.i-iv**). In contrast, the zone centre (sub-zone Cc) contains small, ~1 mm wide vesicles. At Deildargil location 2, vesicle-rich domains with clast-like forms occur locally within sub-zone Cc (**Fig. 3.51.v and vi**).

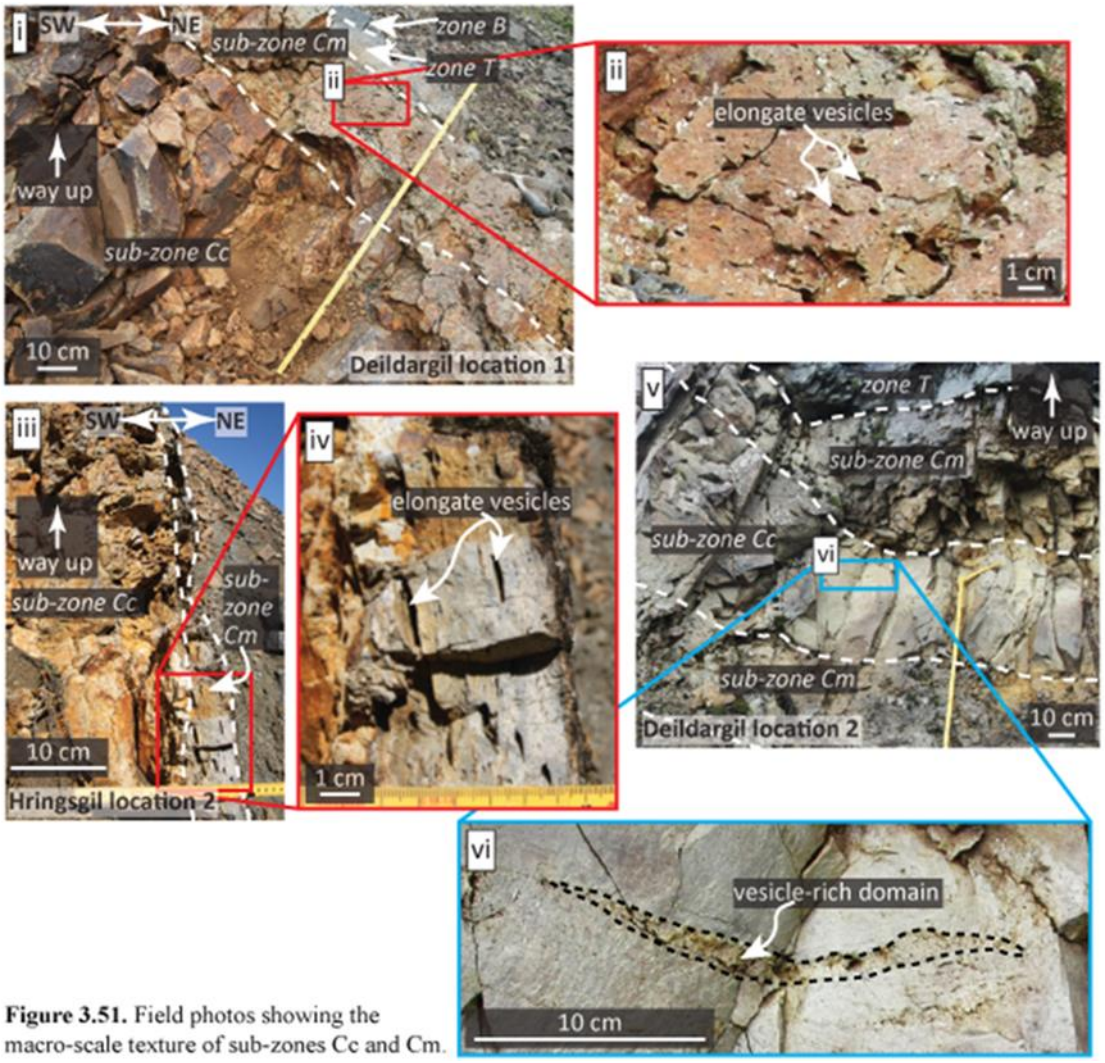

Figure 3.51. Field photos showing the macro-scale texture of sub-zones Cc and Cm.

Sub-zone Cc contains two types of fractures, which will be referred to as F1 and F2 fractures, with no order of formation implied. The F1 fractures are ~1 m long, and extend across the sub-zone, being perpendicular to the dyke margins and the contacts between the textural zones and sub-zones. These fractures are planar to curvi-

planar and generally ~10 cm apart (**Fig. 3.52.**). In contrast, the spacing, orientation and length of the F2 fractures are more random. The F2 fractures are at an angle to the F1 fractures; together the two fractures result in a blocky texture. Sub-zone Cm contrasts with Cc because it does not contain these fractures; instead Cc contains randomly spaced, hackly fractures.

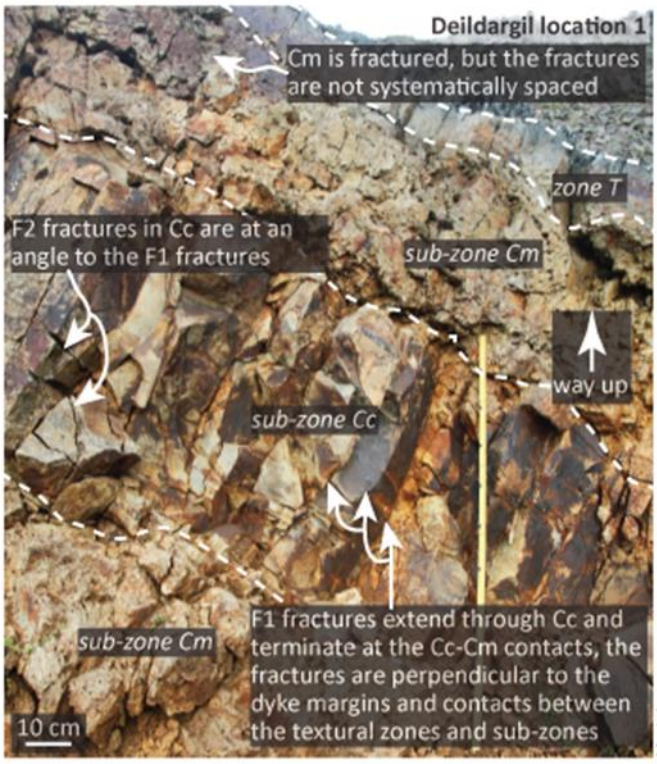

Figure 3.52. Field photo showing the fractures in zone C.

At Hringsgil locations 2 and 3a the contact planes between some of the textural zones have been exposed via weathering. At location 2, the planes between zones C and D are locally exposed, and at location 3a the planes between zones C and B are exposed (**Fig. 3.53.i**). In addition, planar surfaces exist in the middle of zone C at location 3a (**Fig. 3.53.i**). At both locations the surfaces of the planes have a ropy appearance and some of the 'ropes' locally form folds, whereas others form wavy lines (**Fig. 3.53.ii and iii**). Both the lines and the axial surfaces of the folds are perpendicular to the linear flow bands and also the axial surfaces of the flow bands in

zone C. The ropy texture protrudes from the surface, being convex towards the dyke margins.

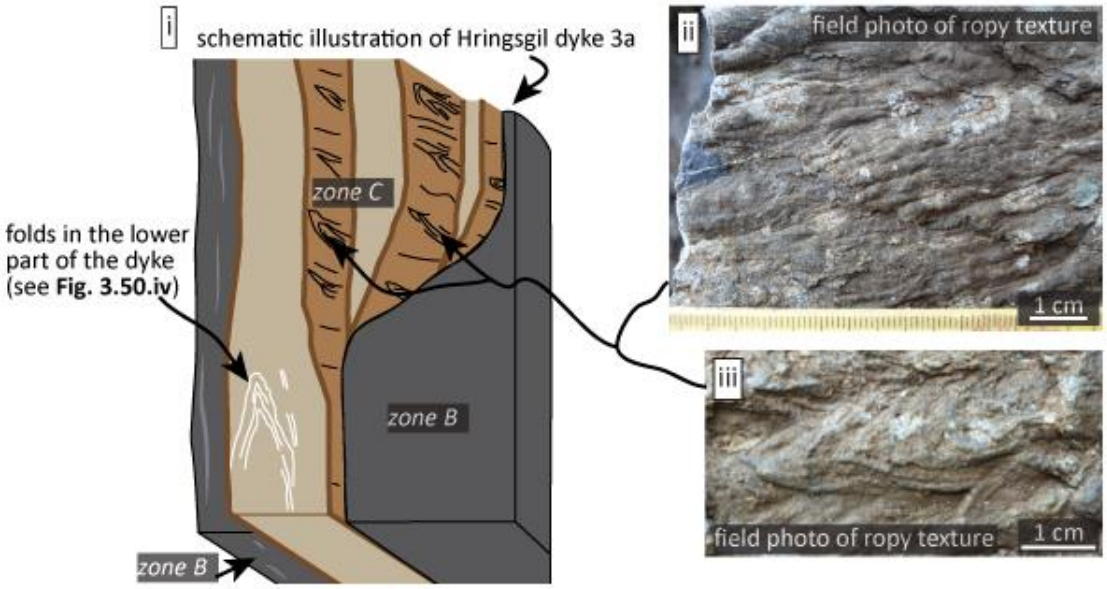

Figure 3.53. Ropy texture on planar surfaces within zone C and between zones B and C.

3.4. Geochemical analytical results

3.4.1. Bulk rock major element composition

Bulk rock major element X-ray Fluorescence (XRF) analysis was conducted with the purpose of determining whether geochemical variation exists between the different textural zones. The analysis was carried out on dyke samples from Deildargil locations 1 and 2, and Hringsgil location 2, plus country rock from Deildargil location 1 (see **section 2.4.** for methodology and errors, and **A.3.7.** for data). The results demonstrate that zones B and C of Deildargil location 2 and Hringsgil location 2 are rhyolitic (**Fig. 3.54.**), that zone A at Deildargil location 1 is dacitic, and that some of the country rock at location 1 is basaltic (**Fig. 3.54.**). Therefore, the major element composition of zone A at Deildargil location 1 is intermediate between the country rock and the textural zones that consist of juvenile lava. The major element compositions of the zone B sub-zones at Deildargil location 1 and Hringsgil location 2

are similar to one another (**Fig. 3.54. and 3.55.**). However, zone C contains ~1-5 wt. % more silica (**Fig. 3.54.**), and is depleted in Fe_2O_3, MnO, CaO and K_2O relative to zone B (**Fig. 3.55.**). Additionally, zone C of Hringsgil dyke 2 is also depleted in Al_2O_3 relative to zone B (**Fig. 3.55.**).

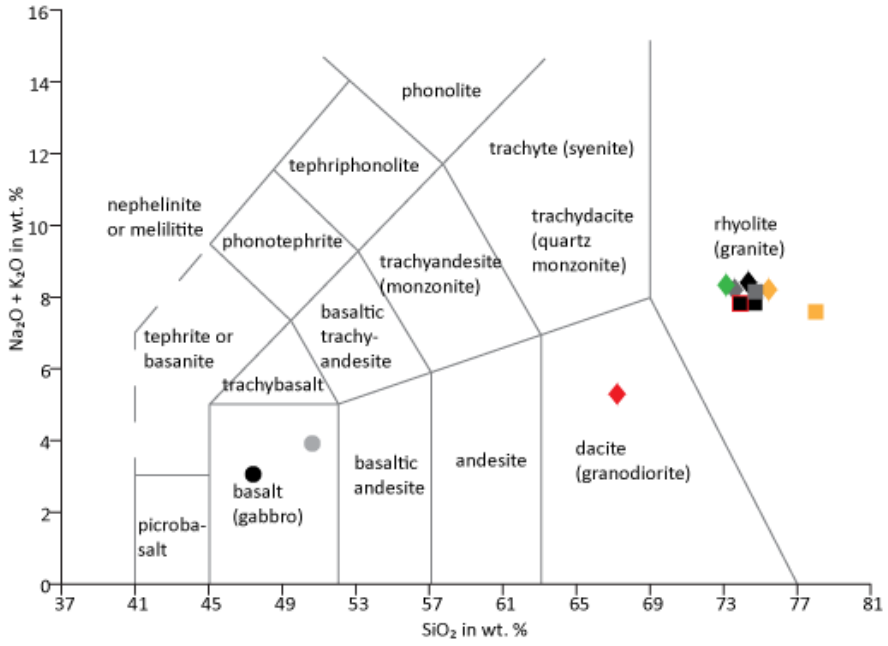

Key

- **country rock** from the upper part of Deildargil location 1 (sample D2)
- **country rock** from the lower part of Deildargil location 1 (sample D1)
- **zone A** from the upper SW margin of Deildargil location 1 (sample D5)
- **sub-zone B1** from Deildargil location 2 (sample Dg4)
- **sub-zone B2** from Deildargil location 2 (sample Da)
- **sub-zone B3** from Deildargil location 2 (sample Dh)
- **zone C** from Deildargil location 2 (sample DS2b)
- **sub-zone B1** from Hringsgil location 2 (sample HS1f)
- **sub-zone B1** from Hringsgil location 2 (sample HS3a)
- **sub-zone B2** from Hringsgil location 2 (sample HS3b)
- **zone C** from Hringsgil location 2 (sample HS1b)

Figure 3.54. Major element geochemistry of the dykes and some of the country rock. Loss on ignition is not included, see **section 2.4.** for methodology and errors. The error bars are smaller than the data points.

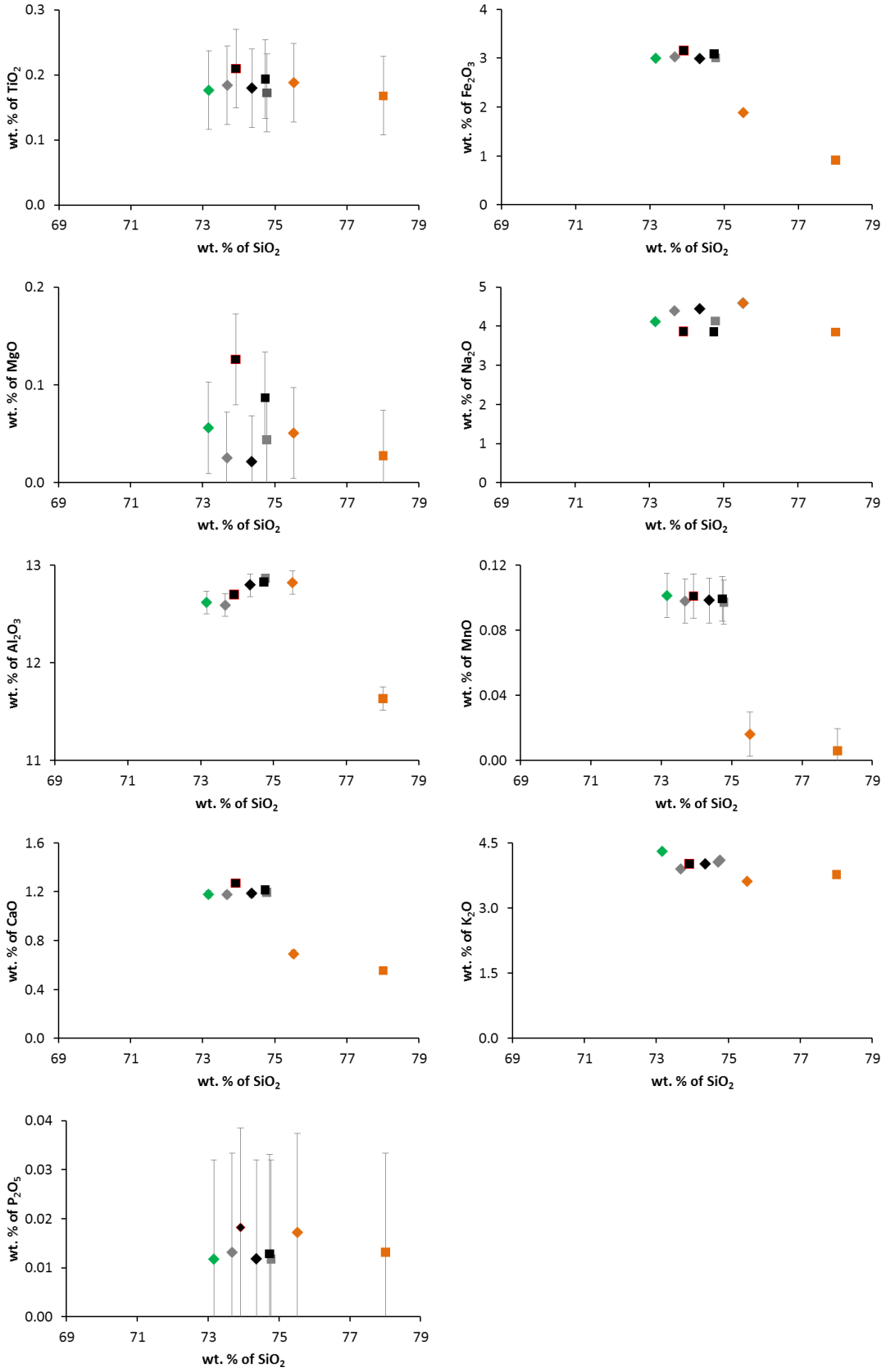

Figure 3.55. Major element geochemistry of the dykes. Loss on ignition is not included; see **section 2.4.** for methodology and errors. Some of the error bars are smaller than the data points. See **figure 3.54.** for key.

3.4.2. Localised composition around perlitic cracks and coloured lenses

Scanning electron microscopic X-ray spectroscopy was used to determine the relative amount of some major elements within zone B (see **section 2.2.** for methodology) at Deildargil location 2a. The first purpose of the element mapping was to differentiate between magmatic and post-magmatic geochemical signatures. Maps were therefore collected around perlitic cracks to look for compositional variations (e.g., Jezek and Noble, 1978). The second purpose of the element mapping was to establish whether variation exists in the concentration of major elements around the optically coloured lenses.

The element maps demonstrate that geochemical variation does indeed occur around cracks, with obsidian bordering cracks being Na-depleted and K-enriched, relative to the far-field obsidian (**Fig. 3.56.**). These depleted and enriched areas are ~50-100 µm wide and have strong electron backscatter intensities relative to the far-field obsidian (**Fig. 3.56.i**). In contrast, the coloured lenses do not display any variation in the electron backscatter intensity or in the concentration of some major elements (**Fig. 3.57.**). The small microlites that surround the lenses and the larger microlites in the lens cores are enriched in Fe and have strong backscatter intensities relative the host obsidian (**Fig. 3.57.i and ii**). Furthermore, the larger microlites are also enriched in Mn and Ti and depleted in Na, K and Al, relative to the host obsidian and smaller microlites (**Fig. 3.57.iii-vii**).

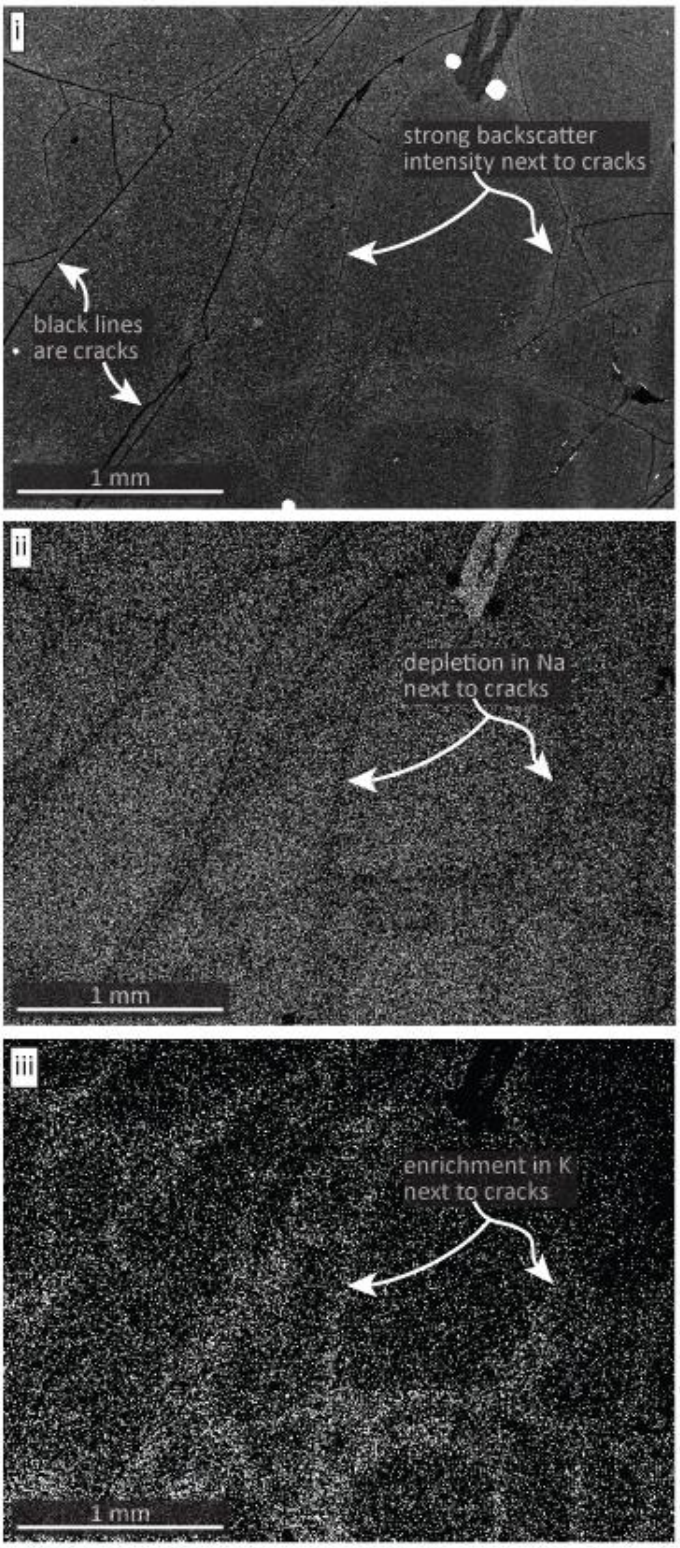

Figure 3.56. (i) BSE image, light grey and dark grey areas correspond to strong and weak backscatter intensities respectively. **(ii and iii)** SEM X-ray spectroscopic images, showing the relative concentration of Na and K respectively, dark and light areas correspond to low and high concentrations respectively. Sample Dmb-ts1 from Deildargil location 2a.

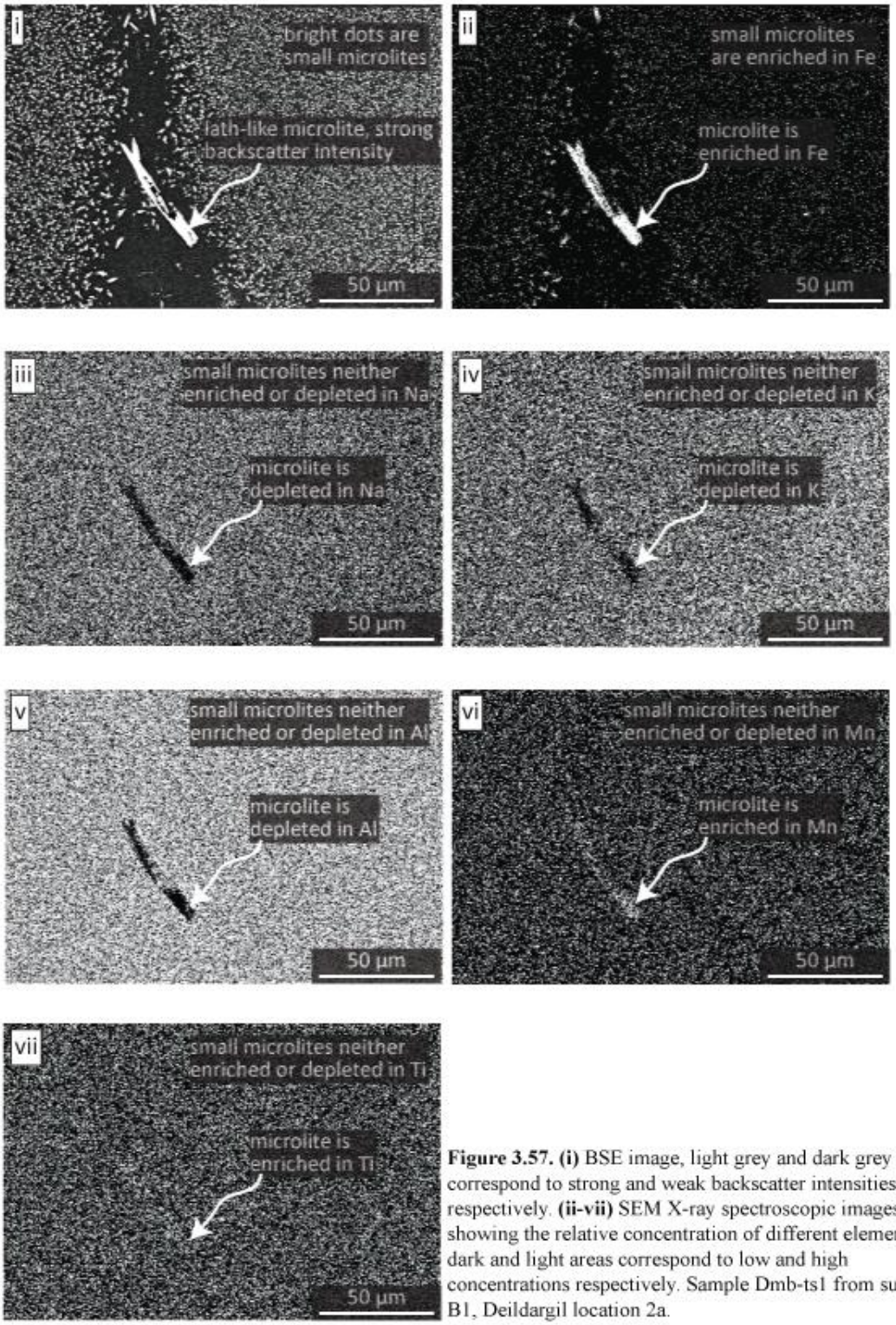

Figure 3.57. (i) BSE image, light grey and dark grey areas correspond to strong and weak backscatter intensities respectively. **(ii-vii)** SEM X-ray spectroscopic images showing the relative concentration of different elements, dark and light areas correspond to low and high concentrations respectively. Sample Dmb-ts1 from sub-zone B1, Deildargil location 2a.

3.5. Results from measurements of the dissolved water content

The water content of Húsafell dyke samples had not been measured prior to this study. Due to the age of the dykes and their perlitic texture, it was hypothesised that the dykes had been hydrated via the addition of meteoric water. However, it was deemed worthwhile to take water measurements because meteoric water is added as molecular water (H_2O_m), with water in the form of hydroxyl groups (OH^-) unaffected during post-magmatic hydration (Stolper, 1982b; McIntosh et al., 2014a), and the OH^- content may be used in conjunction with speciation models (Stolper, 1982a; Nowak and Behrens, 2001) to estimate the dissolved magmatic water content, and thus the emplacement depth of the dykes. Furthermore, the water measurements are a first step towards understanding whether magmatic water escaped from the magma, but clarification of this will also require determination of the pre-eruptive water content (e.g., Stasiuk et al., 1996).

The water content was measured using FTIR spectroscopy in one sample (D2S3) from sub-zone B3 of Deildargil dyke 2 and one sample (HGS3f) from sub-zone B1 of Hringsgil dyke 2. In the former sample, a total of twenty measurements were made across four transects, and in the latter sample a total of five measurements were made across one transect (see **section 2.3.** for details on methodology and errors, and **A.3.8.** for the data). The average H_2O_m content is 3.7 wt. % in both dykes, determined using the 5200 cm^{-1} absorption peak (Newman et al., 1986). The average OH^- content is much less, being 0.84 wt. % in the Deildargil dyke and 0.86 wt .% in the Hringsgil dyke, determined using the 4500 cm^{-1} absorption peak (Newman et al., 1986). The amount of OH^- spans 0.72 to 1.1 wt. % and 0.82 to 0.89 wt. % for Deildargil and Hringsgil, respectively (**Fig. 3.58.**); the average for both dykes, i.e., of all the measurements, is 0.84 wt. %. One FTIR transect (DA) passed across a coloured

lens (**Fig. 3.58.i and ii**), and there is no systematic variation in OH^- across this transect, with existing variation being within error.

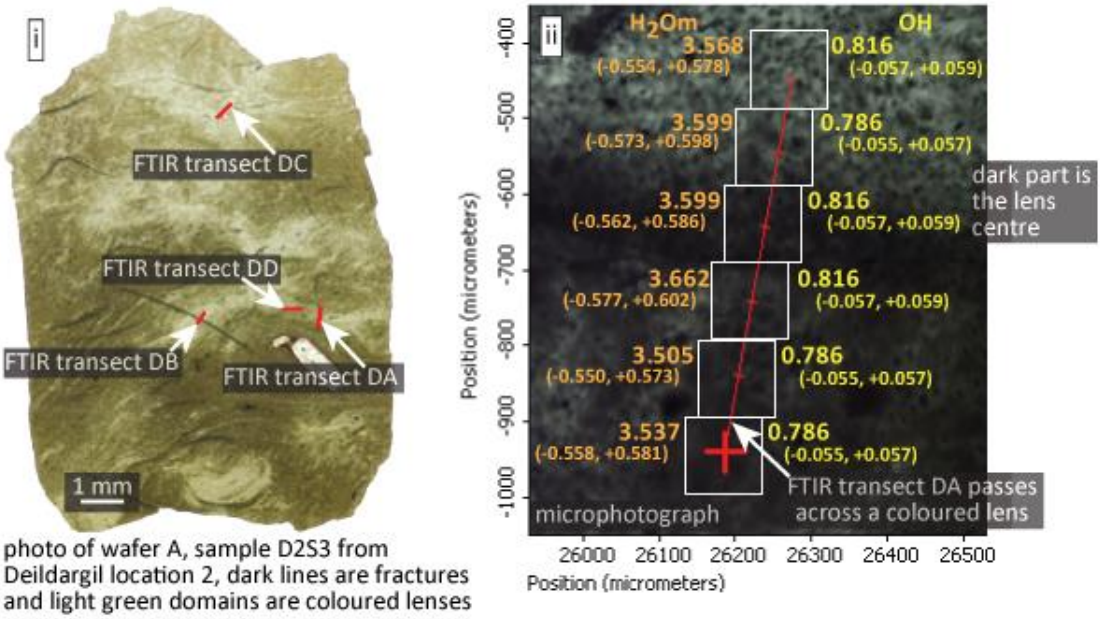

photo of wafer A, sample D2S3 from Deildargil location 2, dark lines are fractures and light green domains are coloured lenses

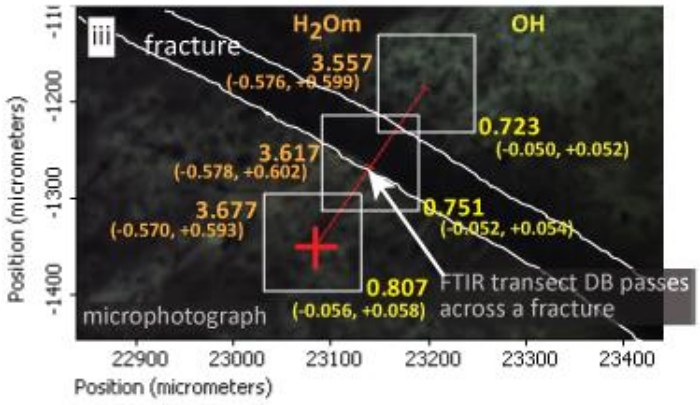

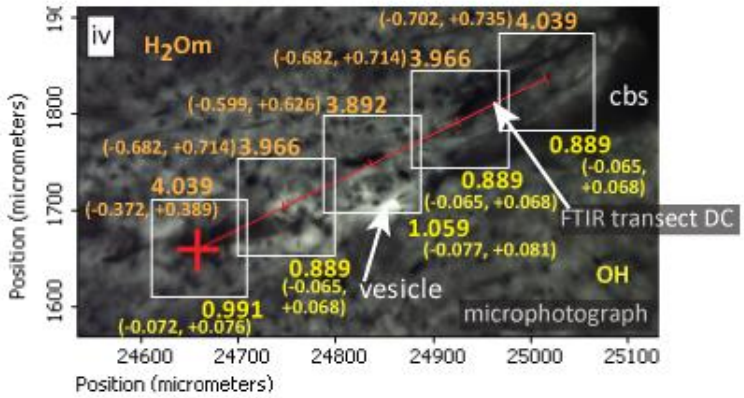

figure continues on the next page

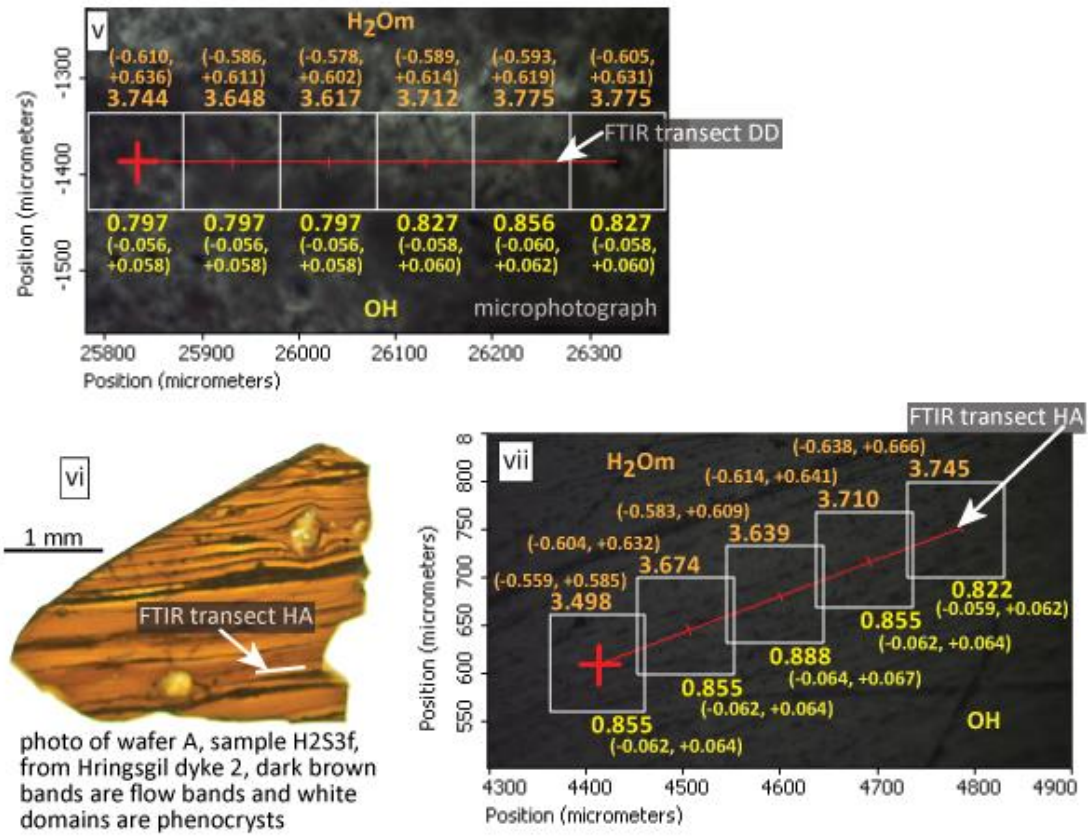

Figure 3.58. Figure continues from the previous page. FTIR transects and water concentration (error in brackets) in Húsafell samples.

3.6. Interpretation of textures

The diverse structure and texture of the dykes, along with the geochemical data will now be interpreted, leading to models for the emplacement and deformation history of the Húsafell dykes.

3.6.1. Zone A

i) Vesiculation and brittle-ductile transitions

In this section a model is presented inferring how some of the pumice clasts in zone A, at the SW margin of Deildargil location 1 formed, with particular reference to clasts displaying the following three textures, 1) large (lengths of a few hundred microns) irregular vesicles, often with buckled walls, 2) relatively small (diameters of

~10 μm) circular vesicles, and 3), fractures that connect the small and large vesicles (e.g., **Fig. 3.18. - 3.22.**).

Discounting the small vesicles and fractures (i.e., just considering the large vesicles), clast porosities span ~20-80 % by area. Taking this to be a good approximation for porosity by volume means that porosities generally exceed the percolation threshold (30 vol. %; Saar and Manga 1999; Blower 2001; Okumura et al. 2009). The buckled walls of the large vesicles are broken at clast edges (e.g., **Fig. 3.14.ii and 3.19.i**), with evidence of in-situ clast deformation commonly lacking. The bubbles therefore experienced viscous deformation prior to clast formation from magma that contained permeable, interconnected bubble networks. It is proposed that the networks formed during magma ascent via shear-induced bubble coalescence, at the margins of a deep unexposed part of the dyke (**Fig. 3.59. time 1**; Stasiuk et al., 1996; Bluth and Rose, 2004; Okumura et al., 2006; Okumura et al., 2008; Okumura et al., 2009; Okumura et al., 2013), and some network-assisted outgassing may have occurred. Buckled vesicle walls probably formed due to vapour pressure differentials between neighbouring bubbles (Castro et al., 2012a), shear stress and partial bubble collapse, with the latter being a consequence of gas loss (**Fig. 3.59. time 2**). The irregular vesicle forms are unlikely to have resulted from resorption and bubble shrinkage (McIntosh et al., 2014a), because evidence of resorption, such as small vesicles surrounding the large vesicles (Watkins et al., 2012) is lacking.

However, small vesicles do occur with the large irregular vesicles, with some being proximal to large vesicles. These small vesicles are sub-circular, and they often protrude into buckled walls of large vesicles (e.g., **Fig. 3.18.**). The small and large vesicles probably represent two discrete bubble nucleation and growth events because 1) they are a substantially different size to one another, 2) the small bubbles are

relatively undeformed, in comparison to the large vesicles, which means they probably grew after viscous deformation of large bubbles, and 3) the small vesicles protrude into the walls of the large vesicles. Similarly to the large vesicles, the small vesicles are also broken at clast edges (e.g., **Fig. 3.14.ii**); the small bubbles must therefore also have formed prior to clast formation. Conceptually, a rapid decompression event triggered nucleation and growth of small bubbles (**Fig. 3.59. time 3**). The cause of decompression is unclear, with possible mechanisms including unloading or plug slip. Rapid decompression is inferred to create sufficient supersaturation for bubble nucleation (Gardner et al., 1999).

The micro-fractures that connect vesicles (e.g., **Fig. 3.20.-3.22.**) arguably formed after the small bubbles, because the fracture-vesicle connecting apertures are angular (e.g., **Fig. 3.20.i and 3.21.**), and it is expected that such angularity would be lost during bubble growth. It is proposed that the fractures formed via another decompression event, which was either more rapid than the preceding event, or the melt viscosity had increased following degassing. Thus, rather than triggering bubble nucleation and growth, this decompression event resulted in tensile failure of bubble walls. Failure may have occurred below the fragmentation threshold, due to gas overpressure in small isolated bubbles (e.g., Heap et al. 2015), with gas overpressure in larger connected bubbles being insufficient to cause tensile failure of their walls, due to their connectivity permitting gas loss. This explains why many walls of large vesicles are intact, despite their thinness (e.g., **Fig. 3.19.ii and iii**) and thus fragility. Micro-fractures are therefore thought to have emanated from small bubbles and propagated through other small bubbles or/and larger bubbles (**Fig. 3.59. time 4**). Interlinking of fractures and bubbles arguably culminated in macroscopic fragmentation, forming the pumice clasts (e.g., **Fig. 3.15., 3.18.i and 3.19.i**) and the

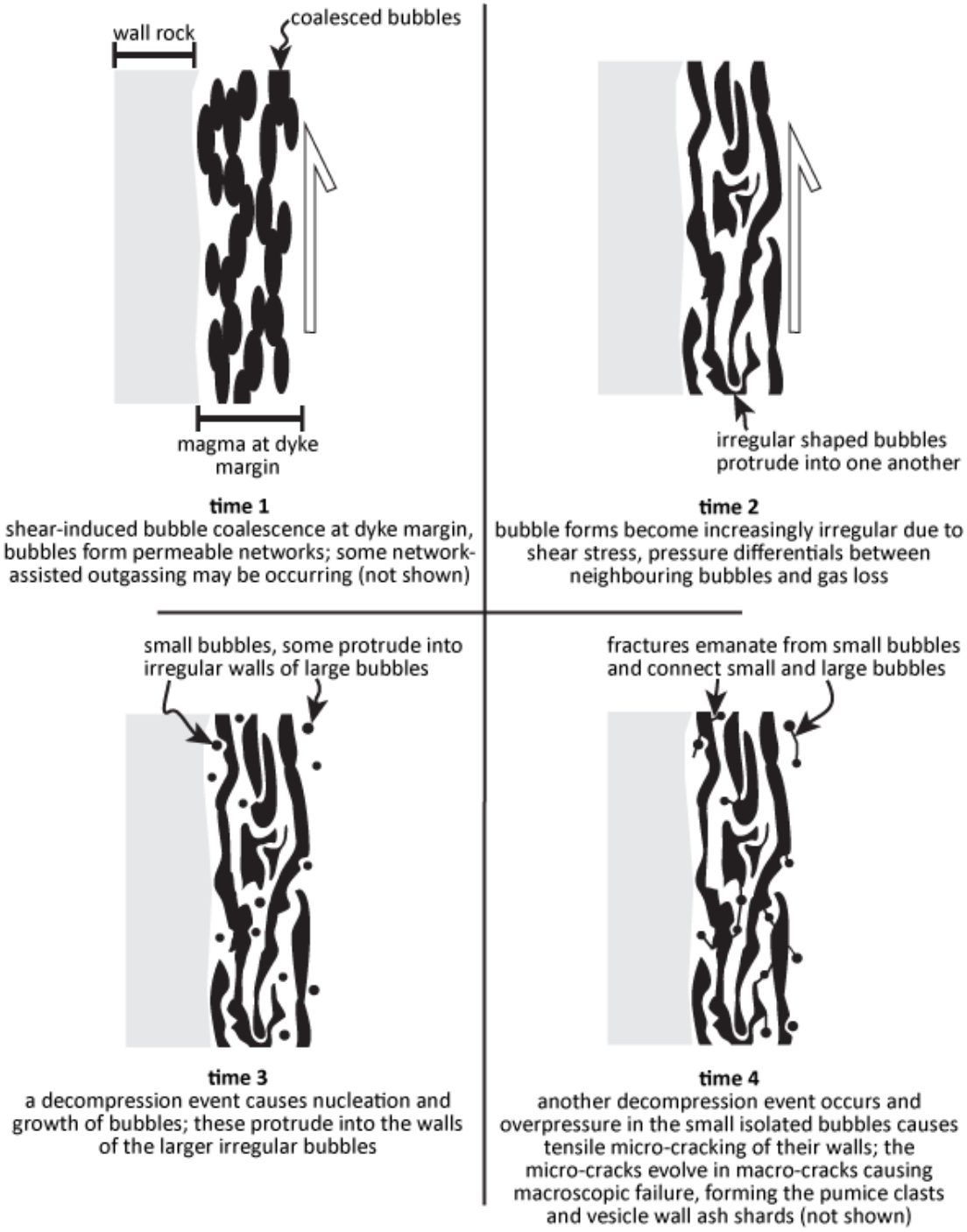

Figure 3.59. Schematic illustrations that depict bubble and fracture evolution. See main text for further details.

vesicle wall ash shards (e.g., **Fig. 3.16.i**). Implicating gas overpressure in small bubbles as the catalyst for macroscopic fragmentation is consistent with the textures, and also with a numerical model of magma fragmentation (e.g., Heap et al., 2015).

In relatively low porosity (<20 % by area) domains of a pumice clast, the fractures together with their adjoining vesicles form concave lobes (e.g., **Fig. 3.22.i and ii**), indicative of melt relaxation (**Fig. 3.60.i**). Furthermore, in this clast some fracture and vesicle walls are sintered, as represented by obsidian bridges (e.g., **Fig. 3.22.iii and iv**). In pumice clasts with higher porosities (>30 % vesicles by area), apertures between the fractures and vesicles have retained their angularity (e.g., **Fig. 3.20. and 3.21.**), and thus did not relax. In addition, obsidian bridges are lacking in these clasts, indicating that sintering did not occur. Perhaps less vesicular domains were also less viscous due to a relative lack of volatile exsolution; thus, relaxation and sintering timescales would have been shorter. The offset fracture-vesicle apertures and accompanying vesicle wall asymmetry support fracture formation in the glass transition interval (e.g., **Fig. 3.21.i**), as they indicate that viscous deformation followed fracture formation (**Fig. 3.60.ii**). In addition, some of the fractures have

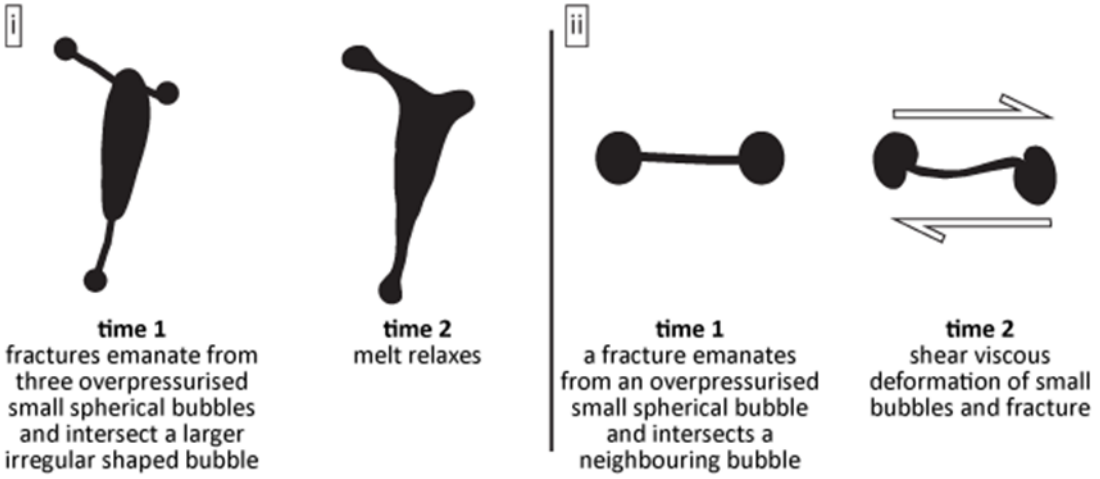

Figure 3.60. Schematic illustrations, which depict how melt relaxation and viscous deformation modified bubbles and fractures. See main text for further details.

arcuate forms (e.g., **Fig. 3.20.ii**) possibly resulting from viscous deformation. However, the relaxed lobes, sintered walls and vesicle wall asymmetry are the best evidence for post-fracturing viscous deformation, because fractures may propagate along curved paths.

ii) Clast source regions, fragmentation and deposition

The pumice clasts within zone A, at the SW margin of Deildargil location 1 are diverse. In this section the reasons for this diversity will be addressed, with only those clasts that are near to the country rock being considered, where post- or syn-depositional clast-modification is minimal.

The porosity of the different pumice clasts is variable, spanning ~20-80 % by area (e.g., **Fig. 3.15.**). Additionally, the porosity is sometimes variable within individual clasts (e.g., the large pumice clasts on the left hand side in **Fig. 3.15.**), which may imply annealing of clasts with varying porosities. Vesicles at clast edges are always broken, indicating that bubbles were present prior to clast formation. The bubble content of a geochemically homogenous magma will generally decrease with increased depth, due to the relationship between water solubility and depth (i.e., pressure). Varying vesicularities may therefore reflect differences in clast source depth, with least vesicular clasts being sourced from greater depths. Alternatively, the variations may reflect different upward clast-transport velocities, with greater velocities decreasing the time available for volatile loss via diffusion.

The shape of the large vesicles (major axis >>10 μm) varies between different pumice clasts. For instance, in some clasts the vesicles have lensoidal forms (e.g., large pumice clast top centre of **Fig. 3.15.**), whereas in other clasts the vesicles have highly irregular forms, often with buckled walls (e.g., **Fig. 3.19.i** and large pumice in

bottom right of **Fig. 3.15.**). Vesicle forms generally become more irregular with increased porosity, perhaps implying that pressure differentials between neighbouring bubbles (Castro et al., 2012a) had a greater influence on bubble forms in clasts with higher porosities. Irregular vesicle forms may also reflect partial bubble collapse, and variations in shear stress, i.e., lateral variations in clast-source regions.

The grainsize distribution of zone A is similar to that of subaerial deposits from violent Strombolian to Vulcanian eruptions (**Fig. 3.61.**; Rust and Cashman, 2011). The grainsize distribution does not therefore rule out a fragmentation process

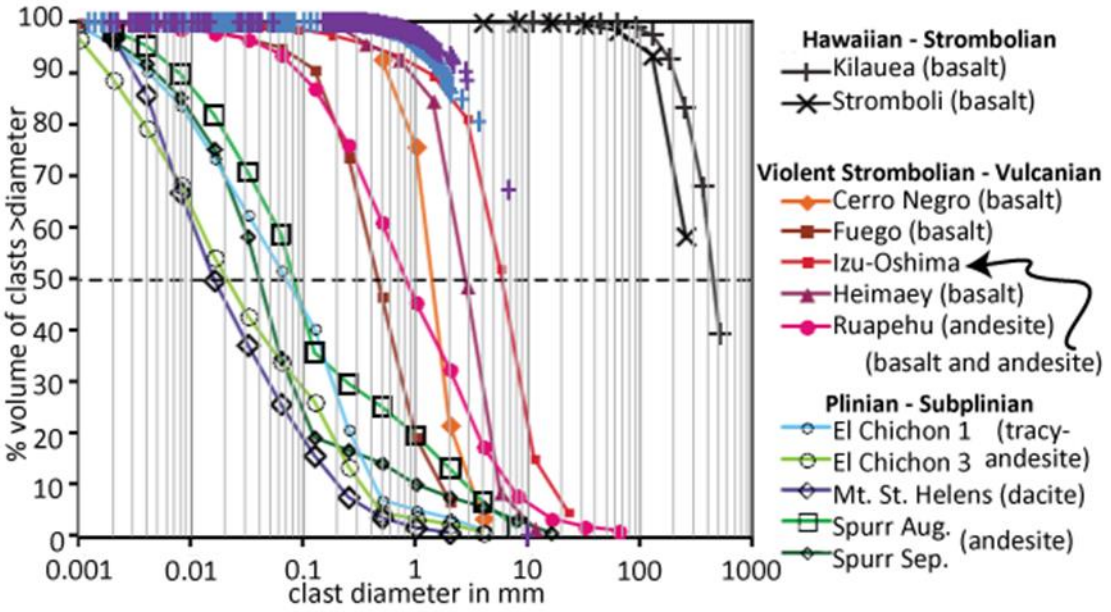

Figure 3.61. A compilation of grainsize distributions for different eruptions from Rust and Cashman (2011). Measurements of juvenile clasts (blue crosses) and lithic clasts (purple crosses) from the tuffisite vein at the SW margin of Deildargil location 1 (same data as shown in **figure 3.13.**) have been added for comparison. See Rust and Cashman (2011) for details of where they sourced the data. Compositional information was obtained from Parfitt (1998), Ripepe et al. (1993), Rose et al. (1973), Rose et al. (2008), Mannen 2006, Self et al. (1974), Bonadonna and Houghton (2005), Espindola et al. (2000), Rose and Durant (2009) and Nye et al. (1995) for Kilauea, Stromboli, Cerro Negro, Fuego, Izu-Oshima, Heimaey, Ruapehu, El Chichon, Mt. St. Helens and Spurr, respectively.

that was mechanistically similar to that active during Vulcanian eruptions, i.e., pressurisation-decompression cycles (Morrissey and Mastin, 2000; Clarke et al., 2009). The grainsize distribution is thought to represent the initial fragmentation event, rather than comminution or post-depositional grainsize modification, because 1) angular and fragile clast edges are preserved, 2) the pumice clasts that broke during

or after deposition (i.e., those with jigsaw fits) were not included in the measurements, and 3), evidence of grainsize reduction along shear zones, such as Riedel shear zones and cataclasite (Tuffen et al., 2003; Tuffen and Dingwell, 2005; Cashman et al., 2008; Kendrick et al., 2012; Lavallée et al., 2014) is lacking.

Zone A at Deildargil location 1 is interpreted as consisting of tuffisite veins, because of the vein-like geometry of the zone (e.g., **Fig. 3.4., 3.5., 3.6 and 3.8.**), and also because the sedimentary structures (e.g., grainsize sorting, and truncated, planar and cross laminations) indicate that particle-laden gas currents travelled through and deposited particles within the veins. Grainsize sorting can occur along shear zones, but this would merely cause migration of fine material, producing a fine grained zone and a fines-depleted zone (Schwarzkopf et al., 2002; Lavallée et al., 2014), and not the complexity of sedimentary structures found within the veins, such as multiple grainsize-sorted laminations which are indicative of intrusive deposition from particle-laden gas currents (Heiken et al., 1988; Stasiuk et al., 1996; Tuffen and Dingwell, 2005). The veins are classed as external tuffisite veins because they occur at the dyke margins and within the country rock. The numerous tuffisite veins at Deildargil location 1 are probably linked to one another; it is possible that the veins formed during a single event and that some fed gas jets or jets of particles and gas at the surface, akin to the jetting activity that occurred during the 2011-12 Cordón Caulle eruption (Schipper et al., 2013).

Some laminations within the tuffisite vein at the SW margin of Deildargil location 1 are truncated (e.g., **Fig. 3.10.** and **3.11.iv**), which arguably records erosive periods (Heiken et al., 1988). Erosion may also explain the discontinuity of some laminations, but this may equally record alternating periods of deposition and current by-passing (Branney and Kokelaar, 2002). The thickening of fine grained laminations

(clasts <<0.1 mm) proximal to relatively large clasts (clasts >1 mm; e.g., **Fig. 3.11.vi**) may reflect localised enhancements in deposition and/or preservation on the lee side of large clasts. Laminations within the veins are generally linear and parallel to the country rock contact (e.g., **Fig. 3.10.ii and 3.11.iii**), indicating that this was the dominant orientation of the depositional plane. However, cross laminations occur locally (e.g., **Fig. 3.10.ii and 3.11.iv**), with truncated surfaces being proximal to sub-zone B1, showing enhanced deposition and preservation on the lee slope of large clasts. If this interpretation is correct, then the particle-laden gas currents must have travelled upwards (**Fig. 3.62.**). However, deposition was arguably more complex at times, because some fine-grained layers locally weave between larger clasts (e.g., **Fig. 3.12.iv**), which is thought to reflect intrusion of finer material between larger clasts. In addition, it is likely that slumping of sediments and winnowing were both common processes within the veins, contributing to the diversity of the sedimentary structures.

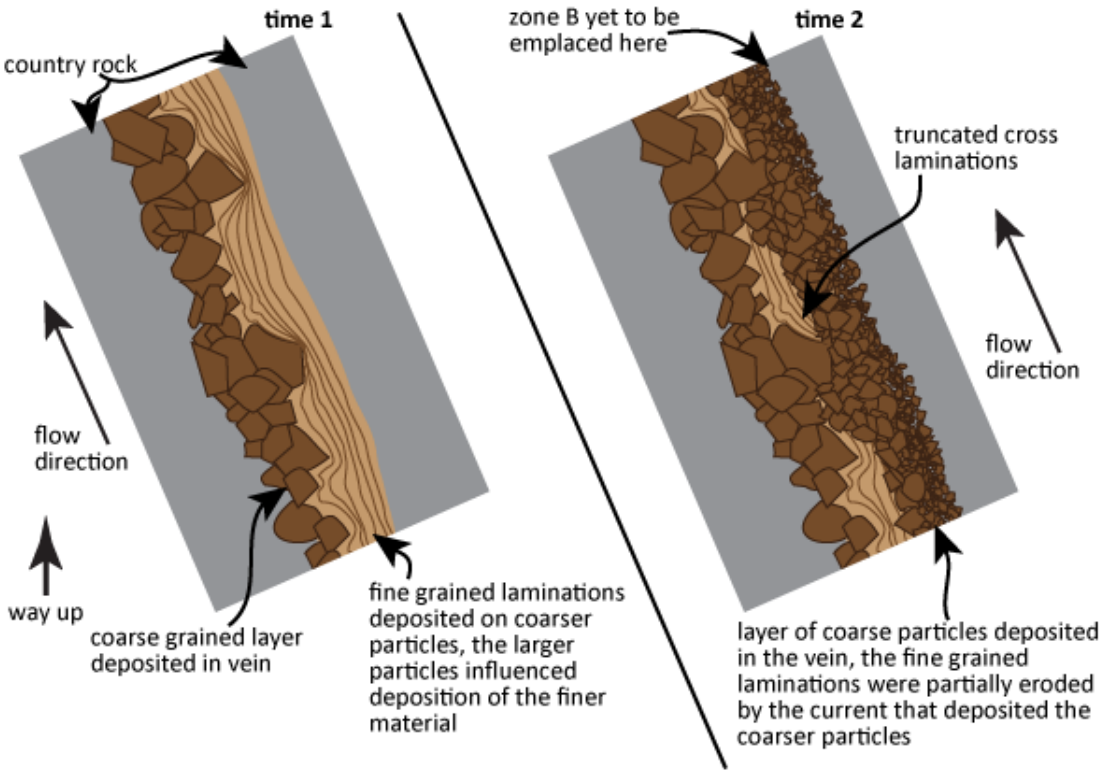

Figure 3.62. Schematic illustrations that depict the formation and evolution of sedimentary structures within the external tuffisite vein at the SW margin of Deildargil location 1. See main text for further details.

iii) Formation of external tuffisite veins and influence of the country rock

The distribution of the fragmented material that forms zone A differs between Deildargil locations 1 and 2; possible reasons for this variation will be discussed in this section. It shall also be discussed as to why external tuffisite veins are lacking in the welded ignimbrite at Deildargil location 3.

External tuffisite veins occur within the country rock (e.g., **Fig. 3.5. and 3.6.**) and form the upper 10 m of the dyke margin at Deildargil location 1 (e.g., **Fig. 3.4.**). Tuffisite veins probably also form lower parts of the dyke margins, but exposure is insufficient for clarification of this. The country rock at Deildargil location 1 consists of brecciated and non-brecciated basaltic lava, with both lava types hosting tuffisite veins. The non-brecciated lava contains fractures throughout, with the spacing and orientations of the fractures being fairly systematic (e.g., **Fig. 3.6.**), indicating that they probably formed via contraction during lava cooling. The tuffisite veins occur locally, with similar orientations to the cooling fractures (e.g., **Fig. 3.6.**). The cooling fractures represent mechanically weak zones in the lava; conceptually, particle-laden gas currents exploited and propped open these fractures, with the fractures governing the vein-like (sheet-like in 3D) distribution of the fragmented material (**Fig. 3.63.i**). Vein formation involved some damage and erosion of country rock because 1) preliminary observations indicate that small (<10 cm long) fractures are most common proximal to tuffisite veins (e.g., **Fig. 3.6.**), and 2), basaltic lithic clasts occur within veins (e.g., **Fig. 3.8.iv**).

In contrast to Deildargil location 1, the fragmented material that forms zone A at Deildargil location 2 is not confined to veins, but instead occupies a broad, dyke-marginal domain (e.g., **Fig. 3.7.**). The country rock at location 2 is a moderately consolidated conglomerate, consisting of a poorly-sorted mix of ash-sized to boulder-

sized clasts (e.g., **Fig. 3.26.**). The lack of pre-existing fractures in the conglomerate forced gas-charged particle-laden flows to form their own fractures, which caused them to follow more tortuous paths (**Fig. 3.63.ii**) than in the lava.

The dominant influences on the distribution of the fragmented material were arguably the permeability and mechanical strength of the country rock. This interpretation is supported by the absence of zone A in the welded ignimbrite at Deildargil location 3, and also by the change in dyke orientation at the ignimbrite's base (e.g., **Fig. 3.50.i**). The welded and intact nature of the ignimbrite provides it with a low permeability and high mechanical strength, relative to the lava and conglomerate. These attributes ultimately prevented the ignimbrite from being intruded and consequently the dyke was deflected at the base of the ignimbrite (**Fig. 3.63.iii**).

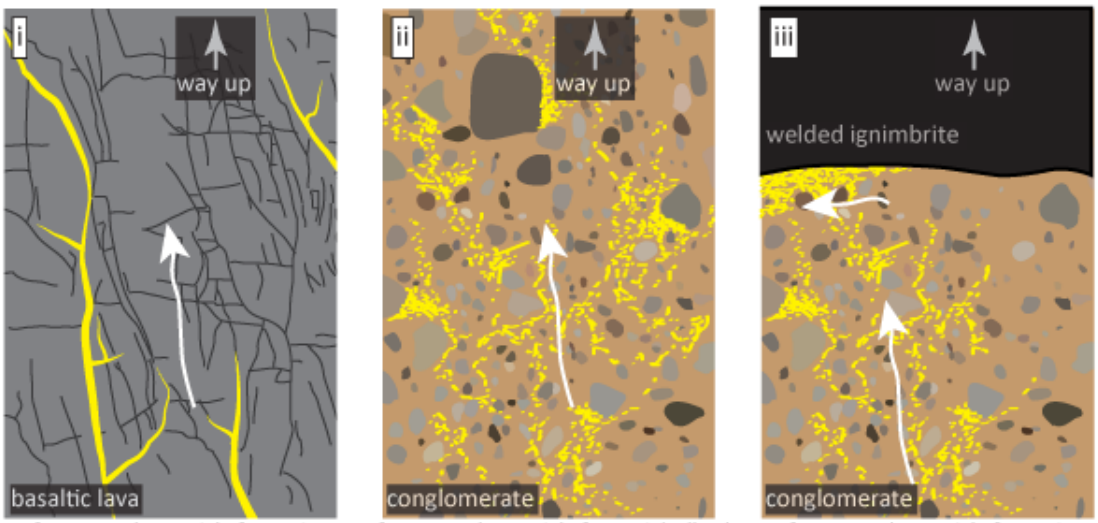

Figure 3.63. Schematic illustrations that depict how different types of country rock influenced dyke propagation and the distribution of the fragmental material, which forms zone A. White arrows indicate the dominant propagation direction. See main text for further details.

iv) Tuffisite veins: welding versus permeability retention

The external tuffisite vein that forms the SW margin of the dyke exposure at Deildargil location 1 exhibits textural variations across its width. Possible reasons for this variation are discussed in this section.

Both the inter- and intra-clast porosity of the tuffisite vein decrease towards zone B (e.g., **Fig. 3.25.i and ii**), i.e., the porosity decreases with increased distance from the country rock. Next to zone B, porous domains only exist proximal to lithic clasts (e.g., **Fig. 3.25.v and vi**) and many vesicles are fully or partially closed, with closed parts defined by discontinuous microlite trains (e.g., **Fig. 3.23.**). Such trains are bubble collapse structures, similar to collapsed bubbles previously observed in rhyolite (Iddings, 1888; Ross and Smith, 1961; Manley, 1995; Manley, 1996; Kano et al., 1997; Tuffen and Castro, 2008; Tuffen and Castro, 2009). Microlites grew on bubble wall interiors, as demonstrated by their presence on vesicle wall interiors today. The microlites have strong electron backscatter intensities and are interpreted as being Fe oxides.

Porosity reduction via viscous compaction is part of the welding process (Smith, 1960). Porosity reduction towards zone B arguably resulted from compaction caused by shear stress, associated with emplacement of zone B, with localised porosity retention only possible in pressure shadows next to lithic clasts and crystals, as these did not melt at the rhyolitic eruptive temperature. Welding also involves sintering at contact points (Smith, 1960), being characterised by melt bridges (Keulen et al., 2008; Vasseur et al., 2013). The vesicle and juvenile clasts proximal to zone B show evidence of sintering in the form of obsidian bridges (e.g., **Fig. 3.22.iv** and **3.25.iii**), but such bridges are absent near the country rock (e.g., **Fig. 3.25.i**), and are also lacking from lithic clast surfaces (e.g., **Fig. 3.25.v and vi**). Sintering probably

occurred simultaneously with viscous compaction, aided by viscous heating (Hess et al., 2008; Cordonnier et al., 2012b) and conductive heating of zone A by zone B (**Fig. 3.64.**); a temperature increase would decrease melt viscosity, assisting compaction, whilst also decreasing the sintering timescale. This is consistent with experimental results, which have demonstrated that porosity will decrease more rapidly at higher temperatures (Friedman et al., 1963) and that increases in temperature will reduce permeability (Chadderton et al., 2015). The more mafic composition and crystalline nature of the lithics explains why they did not sinter.

Vesicles and juvenile clasts near zone B have pitted walls (e.g., **Fig. 3.24. and 3.25.iii**) and surfaces (e.g., **Fig. 3.25.iv**), respectively, and the vesicles are crystal-filled (e.g., **Fig. 3.24.**). Pitting of vesicle walls must have preceded crystal growth, because lath-like crystals extend into the pitted walls (e.g., **Fig. 3.24.**). Both crystal growth and pitting must have followed viscous deformation of the vesicles, as crystal aggregates within vesicle cores mimic the form of the deformed vesicles (e.g., **Fig. 3.24.**). Following the deposition of particles, magmatic gas arguably continued to flow through the tuffisite vein corroding vesicle walls and juvenile clast surfaces, forming the pits. Such corrosion may occur if F or Cl are present in the gas phase (Horwell et al., 2013). Crystal compositions are undetermined, but they are thought to be vapour phase precipitates, predominantly cristobalite, which can be precipitated following the corrosion of silica-rich glass (Horwell et al., 2013; Schipper et al., 2015). Corrosion features (pits) and precipitates (cristobalite) are lacking near the country rock, and some vesicles within this part of the tuffisite vein are very thin (e.g., **Fig. 3.17.ii**), but none are collapsed. Collapse was probably prevented here due to magmatic gas flowing through the vein, with the gas sourced from a deeper part of the magmatic system (e.g., Rust et al., 2004), with more rapid quenching possibly being important

also. The less-welded part of the tuffisite vein next to the country rock will be more permeable than nearer zone B, where welded is more advanced. Gas would therefore have been able to pass through the more permeable part of the tuffisite vein, rather than linger, which may explain why corrosion features are lacking near the country rock considering that a low permeability favours corrosion and vapour phase precipitation (Schipper et al., 2015). Higher temperatures and pressures will also favour corrosion (Horwell et al., 2013), which may also explain why corrosion only occurred near to zone B, where the thermal and shear effects imparted by zone B were greatest (**Fig. 3.64.**).

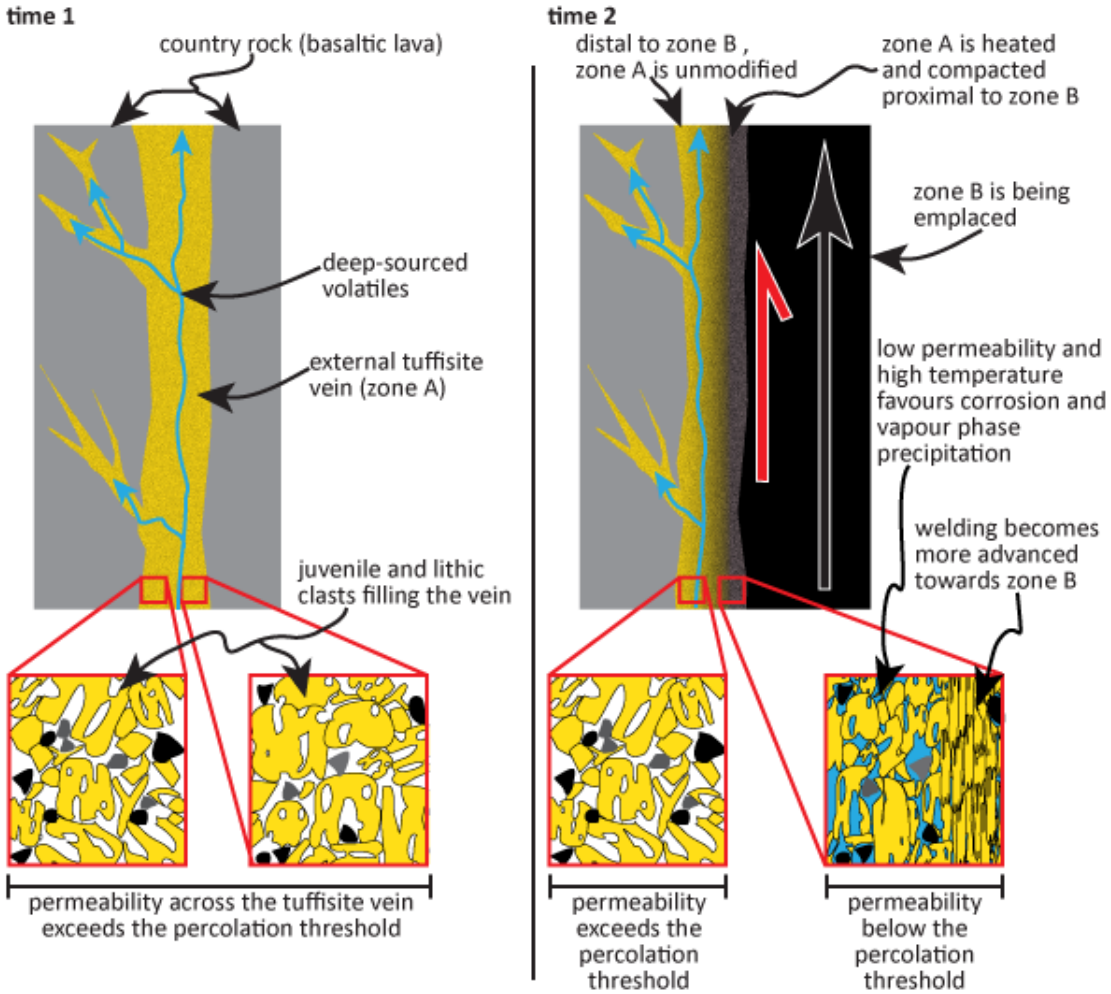

Figure 3.64. Schematic illustrations that depict the evolution of the external tuffisite vein at the SW margin of Deildargil location 1. See main text for further details.

3.6.2. Zone B

Zone B was emplaced after zone A, because 1) the inner margin of zone A at Deildargil location 1 became welded during emplacement of zone B, and 2) zone B truncates zone A at Deildargil location 2 (e.g., **Fig. 3.7.**). The emplacement and deformation history of zone B is discussed in this section.

i) Incremental emplacement from discrete magma pulses

The textures within sub-zones B1-B3 at Deildargil location 2 provide insight into magma emplacement and deformation. Models are presented in this section regarding the emplacement and deformation history of these sub-zones.

It is postulated that sub-zones B1, B2 and B3 were accreted from discrete pulses of magma, with each sub-zone representing a single pulse. This interpretation is made because the sub-zones comprise different coloured obsidian with sharp contacts between the different sub-zones (e.g., **Fig. 3.26. and 3.28.i-iii**). There was arguably little time for cooling between each emplacement pulse, because the contacts between the sub-zones are fluidal, yet sharp (e.g., **Fig. 3.28.i-iii**), and because the F1 and F2 fractures, interpreted as cooling fractures, dissect all sub-zones (e.g., **Fig. 3.31.i**). The presence of the sub-zones on opposite dyke walls, coupled with the smoothing of contacts towards the dyke centre (e.g., **Fig. 3.26.**), indicates that each pulse propagated down the centre of the previously-accreted pulse, with the order of emplacement being B1-B2-B3 (**Fig. 3.65.**). The Húsafell dykes therefore grew progressively, via pulsatory emplacement, in a similar manner to the growth of composite dykes (Guppy and Hawkes, 1925; Gibson and Walker, 1963; Walker and Skelhorn, 1966).

The F1 cooling fractures are not perpendicular to the dyke-country rock contact. Their orientation may indicate that the country rock acted as a heat sink during emplacement, with cooling isotherms not simply perpendicular to the dyke-country rock contact. The irregular contact between B1 and the country rock (conglomerate) at Deildargil location 2 would have been governed by the morphology of fractures that formed during intrusion of zone A, but probably also reflects the erosive nature of the magma. Indeed, the thickening of B1 at the sides of the boulder indicates that it cut relatively deep into the conglomerate here, with the boulder being resistant to erosion (**Fig. 3.65. time 1**). Each magma pulse was arguably mechanically erosive, with B2 eroding B1, and B3 eroding B2 and possibly B1, which may explain the absence of B1 and B2 above the large bolder (**Fig. 3.65. time 2 and 3**). The fluidal body next to the large boulder (e.g., **Fig. 3.27. and 3.29.**) may be an inclusion of an early-accreted pulse, which became entrained within a latter pulse, thus providing more evidence of erosion.

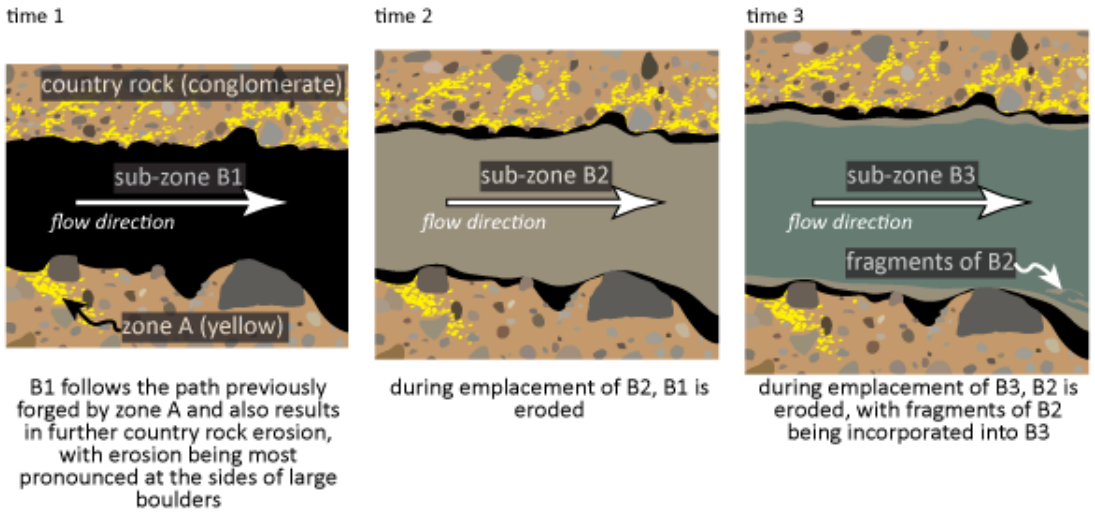

Figure 3.65. Schematic illustrations showing the emplacement of sub-zones B1-B3. Modelled on the textural characteristics of Deildargil location 2. Note how the emplacement boundary layer becomes less irregular (i.e., more linear) with time. Emplacement of zone C (not shown) followed zone B emplacement.

Sub-zones B1, B2 and B3, are black, brown-grey-light green and dark green, respectively (e.g., **Fig. 3.28.i-iii**). The different colours are not thought to represent different cooling rates because it is expected that cooling would produce a gradational

colour change, and the changes are abrupt. Instead, the colour differences could reflect microlite or nanolite size and number density variations, or redox state variations. The nanolite and microlite number density is greater in B2 than in B1 (e.g., **Fig. 3.32. and A.3.6.**). Microlites always have nanolite-free haloes (e.g., **Fig. 3.32.ii**), illustrating that microlite growth preceded nanolite growth. The shape, number density and size of microlites and nanolites can be influenced by decompression (Hammer and Rutherford, 2002; Castro and Gardner, 2008). For instance, decompression experiments on rhyolitic (Martel and Schmidt, 2003; Martel, 2012) and rhyodacitic (Brugger and Hammer, 2010) melts demonstrated a positive correlation between microlite number density and decompression rate. Therefore, the higher number density of nanolites in B1 arguably indicates that the decompression rate of B1 was greater than that of B2. The aforementioned decompression experiments further demonstrated that a time lag exists between decompression and microlite nucleation, as also found for andesitic melts (Couch et al., 2003). The nanolites probably nucleated after magma accretion, explaining the nanolite-free haloes around microlites, as viscous strain during accretion would disperse nanolites and remove haloes. Microlite growth clearly preceded nanolite growth, but the relative timing of microlite growth and accretion is unclear.

Microlite and nanolite variations could plausibly cause the colour variation of sub-zones B1-B3. However, variations in the redox state of Fe are the more likely cause, with black obsidian (B1) being the most oxidised, green obsidian (B3) being the most reduced, and grey-brown-light green obsidian (B2) having a redox state intermediate of B1 and B3 (Fuller, 1927; Gaillard et al., 2002; Donald et al., 2006; Moriizumi et al., 2009). Decreases in H_2 fugacity can increase O_2 fugacity (Sato and Wright, 1966; Gaillard et al., 2002; Castro et al., 2009). This considered, the inferred

variation in the redox state between B1-B3 may reflect differing degrees of H_2 loss, with more H_2 having been lost from B1 relative to B2 and B3.

ii) Bubbly magma to vesicle-free obsidian

Some textures within zone B provide insight into vesiculation and bubble collapse during magma emplacement, which is discussed in this section.

The discontinuous microlite trains within sub-zones B1-B3 (e.g., **Fig. 3.32. and 3.40.**) are interpreted as being bubble collapse structures, consistent with previous interpretations regarding similar trains in rhyolite (Iddings, 1888; Ross and Smith, 1961; Kano et al., 1997; Tuffen and Castro, 2008; Tuffen and Castro, 2009). Bubble nucleation and growth may have occurred on microlites (Hurwitz and Navon, 1994; D'Oriano et al., 2013), but microlite nucleation and growth may equally have occurred on bubble wall exteriors, or microlites may have been deposited within bubbles as vapour phase precipitates (Müller et al., 2001; Horwell et al., 2013; Schipper et al., 2015).

The coloured lenses in zone B (e.g., **Fig. 3.28., 3.34., 3.35., 3.37. and 3.40. A.3.3.**) are also interpreted as being bubble collapse structures because many of the lenses have voids in their centres (**Fig. 3.35. and 3.40.ii and A.3.5.**), interpreted as being vesicles, i.e., non-collapsed parts of bubbles, consistent with previous interpretations of similar textures (e.g. **Fig. 1.2ii**; Owen et al. 2012). However, even stronger evidence for them being collapsed bubbles is thought to be recorded by the variations in the number density of nanolites and microlites around the lenses, with these variations arguably having resulted from heterogeneities in the water content that formed during bubble growth and collapse (discussed below). In addition, the colour variations are thought to be further evidence that the lenses are indeed

collapsed bubbles; the lens rims are darker than the host obsidian, whereas the cores are paler than the host, with some cores being green (e.g., **Fig. 3.34.**), indicating that the rims and cores are relatively oxidised and reduced, respectively, in comparison to the host (Moriizumi et al., 2009; Castro et al., 2009). Decreases in H_2 fugacity can raise O_2 fugacity (Sato and Wright, 1966; Gaillard et al., 2002; Castro et al., 2009); the oxidised rims may therefore reflect H_2 diffusion into bubbles, with the reduced cores reflecting H_2 resorption during bubble collapse. Some parts of connected lenses lack reduced cores, reflecting asymmetric bubble collapse (**Fig. 3.66.**). Microlites and nanolites decrease in size away from the lenses and this is coupled with an increase in

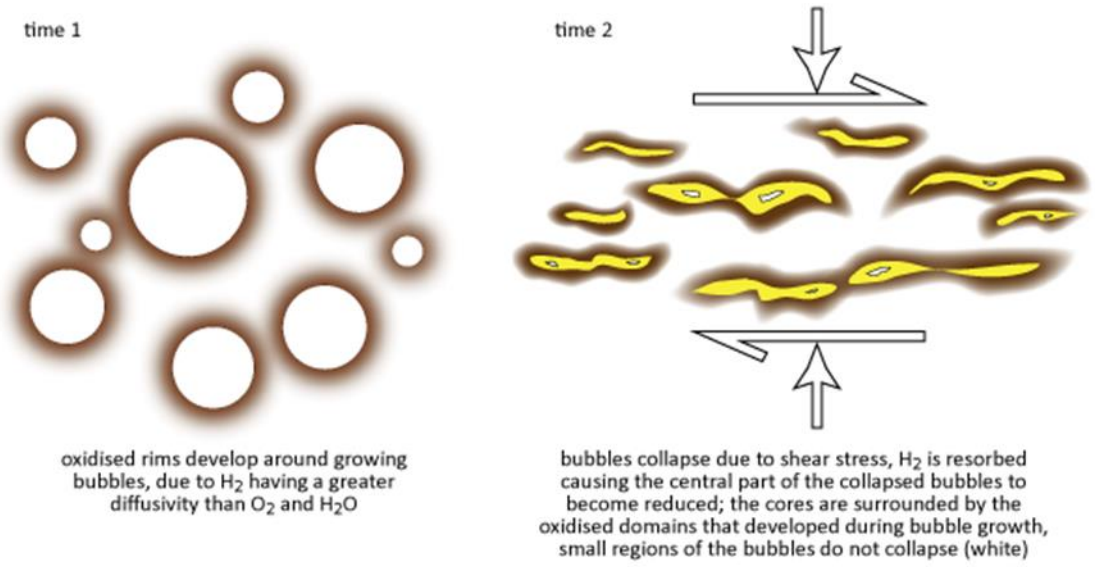

Figure 3.66. Schematic illustrations depicting the formation of the coloured lenses (see main text for further details).

their number density. The length scale over which these variations occur spans 10-150 μm (e.g., **Fig. 3.40.**) and increases away from the country rock. These lengths are not dissimilar to the scale of water concentration gradients (300-1000 μm) next to vesicles (Castro et al., 2005; Watkins et al., 2012). The crystal gradients may have formed due to variations in the water content around bubbles, with increased gradient lengths reflecting slower cooling towards the dyke centre and partial re-equilibration of the water content. If these two interpretations are correct, the colour variations cannot be a

function of post-magmatic alteration, giving credence to the notion that the colour variations reflect H_2 diffusion and resorption. There is a high number density of coloured lenses in the margin of the fluidal body at Deildargil location 2 (e.g., **Fig. 3.29.**). This body is interpreted as being an erosional feature and the high number density of lenses arguably indicates that bubble nucleation and growth were enhanced at its margin, possibly linked to viscous heating (Nelson, 1981; Hess et al., 2008; Cordonnier et al., 2012b).

Voids within cores of coloured lenses sometimes have lobate margins (e.g., **Fig. 3.35.**), these are thought to record micro-cracking of bubble walls and subsequent melt relaxation. A similar interpretation may explain lobate tuffisite vein margins, observed in pyroclastic bombs (Hugh Tuffen, personnel communication, 2015, see figure 1d in Castro et al., 2012b). The cracks may have formed due to a strain rate increase (Dingwell, 1996), with cracks nucleating at bubble walls and propagating through relatively water-depleted viscous haloes which would have been present following bubble growth (**Fig. 3.67.i**). The cracks may have terminated at halo edges, where the melt would have been relatively water-enriched, and thus less viscous. Indeed, melt viscosity variations around bubbles, caused by heterogeneities in the water content have been experimentally shown to influence the propagation distance of fractures (McIntosh et al., 2014a). Alternatively, the cracks may have formed via tensile failure, due to overpressure within bubbles (**Fig. 3.67.ii**), with such micro-cracking of bubble walls being possible below the fragmentation threshold (Heap et al., 2015). Following brittle deformation it is envisaged that the melt relaxed, forming the lobes.

The microlite trains and coloured lenses which are interpreted as being bubble collapse structures may record two different episodes of bubble nucleation and

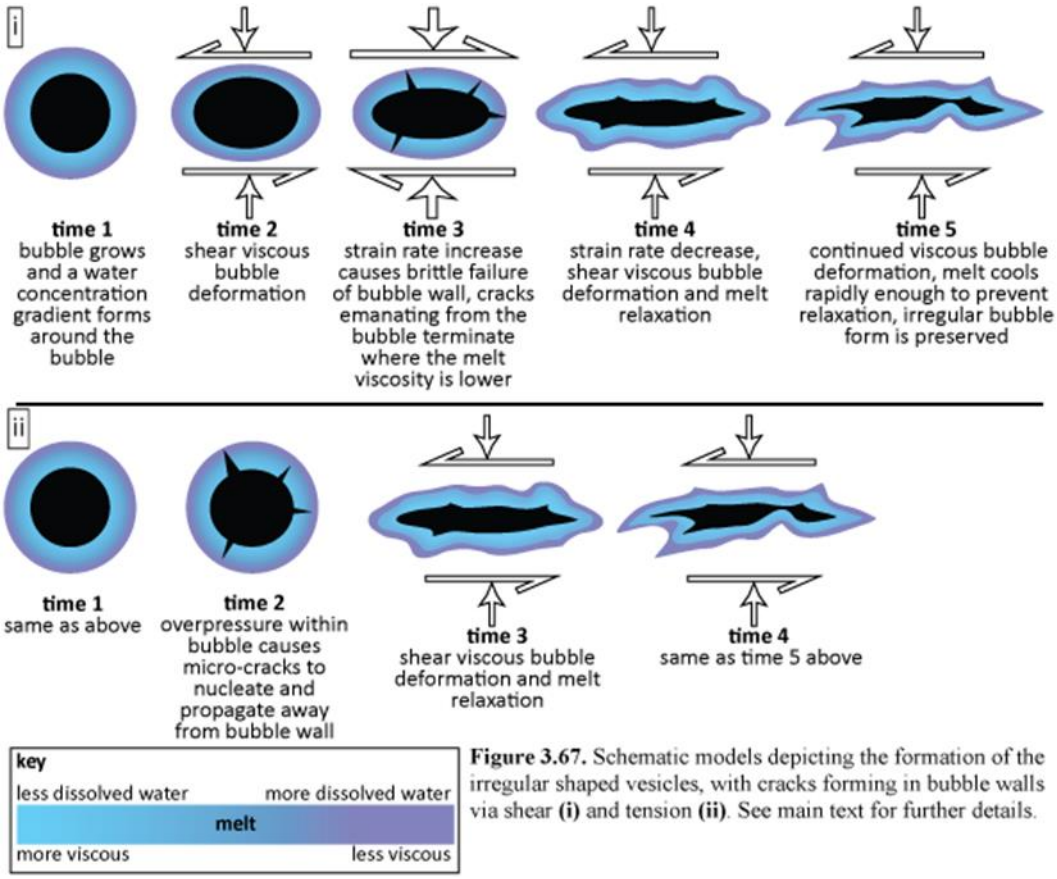

Figure 3.67. Schematic models depicting the formation of the irregular shaped vesicles, with cracks forming in bubble walls via shear **(i)** and tension **(ii)**. See main text for further details.

growth. The fact that the magma contained bubbles indicates that it is was volatile-saturated, and the collapsed bubbles indicate that the bubbles collapsed within the dykes. Bubble collapse occurred via resorption, driven by a pressure increase associated with shear stress during emplacement (Westrich and Eichelberger, 1994; Watkins et al., 2012). Indeed, the major axes of the lenses and discontinuous microlite trains are generally parallel with the sub-zone contacts and dyke-country rock contacts, indicating that the principal stress was perpendicular to the contacts, consistent with syn-emplacement collapse. A third episode of bubble growth is recorded by the large relatively spherical vesicles in zone B (e.g., **Fig. 3.32.ii**), which arguably grew after accretion, because flow bands (i.e., viscously deformed clasts) are deflected around the vesicles (e.g., **Fig. 3.44.vii**), indicating that the bubbles grew after viscous deformation of the clasts (e.g., Manga, 2005). Furthermore, the vesicles are relatively undeformed and clearly shear stress was previously sufficient

throughout emplacement to viscously deform bubbles and clasts in zone B (see **section 3.6.2.**), but relaxation may have contributed to the relatively spherical vesicle forms.

iii) Boundary layer evolution at Deildargil location 2a

During magma emplacement shear stress would have been greatest along emplacement boundary layers, where deformation would have been localised. Evidence for such deformation is recorded by textures at Deildargil location 2a. The deformation and evolution of the boundary layers at this location are discussed in this section.

At this location brecciated obsidian (sub-zone Bb) forms the contact with the country rock, and this passes inward into a fractured version of sub-zone B1, with B1 becoming intact towards sub-zone B2 (i.e., towards the dyke centre, e.g., **Fig. 3.36. and 3.37.**). In petrological thin sections the brecciated obsidian consists of relatively large pale brown clasts, supported by a dark brown matrix (e.g., **Fig. 3.37.i and 3.38.i**). B1 is also brown and becomes gradationally darker towards the B1-B2 contact, with this contact consisting of a green obsidian layer (e.g., **Fig. 3.37.i and ii**). In contrast to B1, B2 does not display any colour variation proximal to the B2-B1 contact. Both B1 and B2 contain bubble collapse structures (i.e., coloured lenses and microlite trains), with the number density of these being particularly high in the green layer (e.g., **Fig. 3.37.**). The collapsed bubbles in the green layer are thought to be the same generation as those in B1 proximal to the green layer, because some extend from the green layer into B1, but other collapsed bubbles in B1 that are nearer to the country rock probably represent an earlier generation of bubble growth and collapse. It is important to note that unlike in B1, none of the collapsed bubbles in the green

layer extend into B2. The major axes of the collapsed bubbles within the green layer and within B1 proximal to the green layer are generally parallel or sub-parallel to the B1-B2 contact, but their orientation changes towards Bb, becoming perpendicular to the B1-B2 contact (e.g., **Fig. 3.37.i**), and fractures within B1 commonly truncate collapsed bubbles (e.g., **Fig. 3.38.**), illustrating that the fractures post-date bubble collapse.

It is proposed that B1 was relatively static during B2 emplacement, and that during emplacement of B2, shear stress was localised in a boundary layer at the B2-B1 contact, resulting in localised viscous heating (Nelson, 1981; Hess et al., 2008; Cordonnier et al., 2012b). This would have caused a localised reduction in the melt viscosity, which would have enabled bubbles to grow more easily, whilst also decreasing the solubility and diffusivity of volatiles (Sparks, 1978; Newman and Lowenstern, 2002). Consequently, a bubble-rich layer formed at the contact, as recorded by the green layer, where collapsed bubbles are abundant. The darkening of B1 towards the green layer may reflect a gradational increase in the oxidation state (Moriizumi et al., 2009; Castro et al., 2009), caused by the higher diffusivity of H_2 relative to H_2O and O_2, which ultimately raised O_2 fugacity towards the bubbly contact layer (**Fig. 3.68. time 1-3**; Castro et al., 2009; Gaillard et al., 2002; Nelson, 1981; Sato and Wright, 1966). Bubbles at the B1-B2 contact became elongate via shear, reducing the apparent magma viscosity (Manga and Loewenberg, 2001; Stein and Spera, 2002) and promoting magma ascent (**Fig. 3.68. time 4**; Okumura et al., 2013). The sharpness of the contact between the green layer and B2 is thought to reflect the relatively static nature of B1, in contrast to the mobile nature of B2. Bubble collapse at the B1-B2 contact was probably driven by shear stress, and it is thought that the green colour of the contact layer reflects H_2 resorption, which would have

caused a localised increase in H_2 fugacity and decrease in O_2 fugacity (**Fig. 3.68. time 5**). Following bubble collapse, magma ascent may have become inhibited, driving a slip-stick transition at the B1-B2 contact, and B1 became mobile once more, with the collapsed bubbles within B1 being rotated (**Fig. 3.68. time 5**). However, stresses increased sufficiently to cause slip at the B1-country rock contact, with the resultant strain rate driving brittle failure of the magma (**Fig. 3.68. time 6**), forming the obsidian breccia (sub-zone Bb). Brecciation becomes less intense with increased distance from the B1-country rock contact, which is probably because failure initiated at the contact. The clasts within Bb have a similar appearance to the intact part of B1, and are thus a fragmented version of B1.

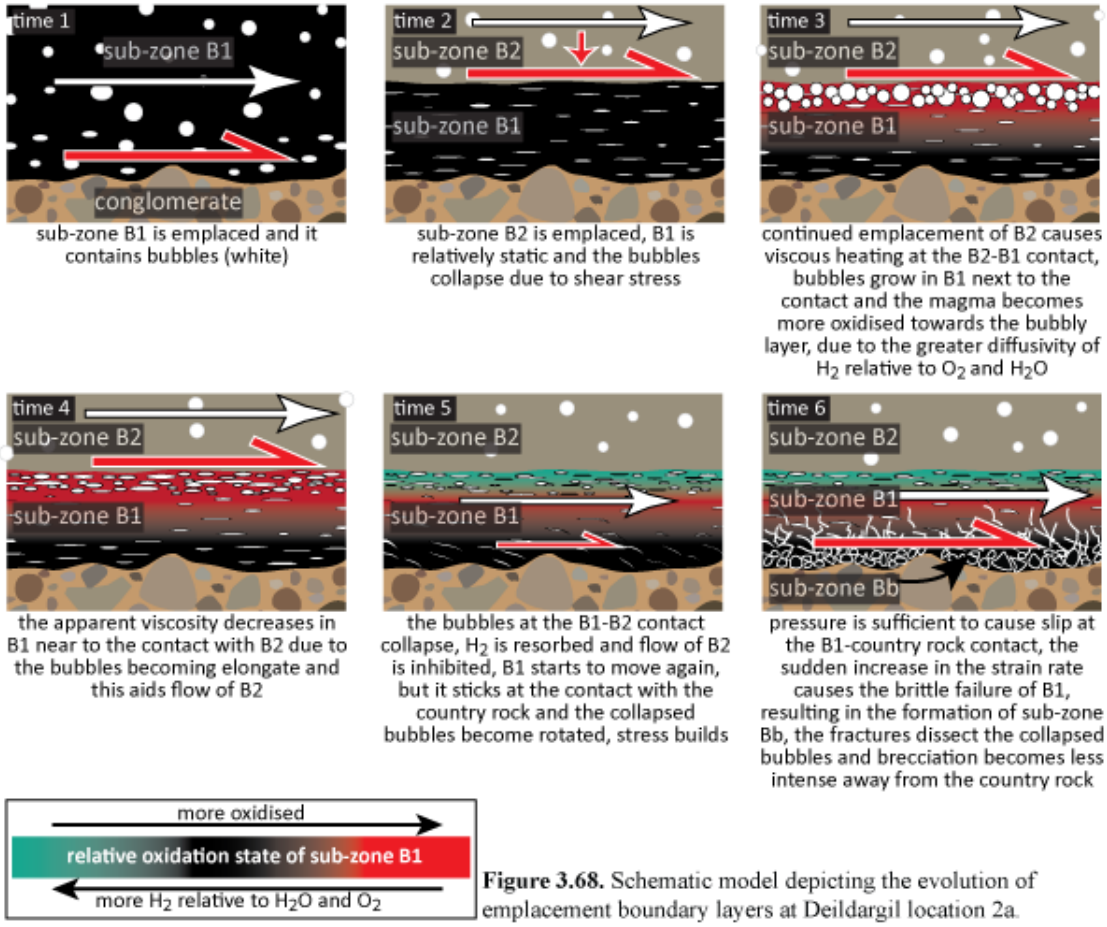

Figure 3.68. Schematic model depicting the evolution of emplacement boundary layers at Deildargil location 2a.

The dark brown matrix supporting paler Bb clasts, and present between fractures in B1, may be composed of fine grains (clast diameters <10 μm) of similar

glass to the larger paler clasts, based on the similar backscatter intensity (e.g., **Fig. 3.38.ii and iii**) that indicates a similar mean atomic number (Ginibre et al., 2002; Reed, 2005; Humphreys et al., 2008). The darker colour of the matrix ash may imply H_2 loss via diffusion, causing them to be relatively oxidised in comparison to the paler larger clasts. However, this is unlikely, because the rims of the large clasts would have been oxidised in a similar manner, and oxidised rims are lacking. One possible explanation is that the fine grains experienced frictional heating, with the increased temperature promoting the diffusive loss of H_2.

iv) Boundary layer evolution at Hringsgil location 2

Similarly to Deildargil location 2a which was discussed in the previous section, evidence of localised deformation along emplacement boundary layers is also preserved at Hringsgil location 2, and is discussed in this section.

In contrast to Deildargil location 2a, sub-zone Bb at Hringsgil location 2 is composed of a wide range of clast types, with various clasts having a similar appearance to those in sub-zones B1, B2 and Bfb (e.g., **Fig. 3.41.iv-vi**). In addition, unlike Deildargil location 2a, Bb at Hringsgil location 2 lacks fine grained material, with all clasts >60 μm in diameter. At Hringsgil location 2, Bb forms the contact between sub-zones B2 and Bfb (e.g., **Fig. 3.41.ii**), with Bfb being located on the side of Bb closer to the dyke centre. Given that Bb contains clasts of B1, B2 and Bfb, Bb formed after accretion of B1 and B2, and after the formation of Bfb. Indeed, it is thought that Bb formed during emplacement of a later magma pulse, possibly sub-zone B3 (although outcrop alteration obscures clear evidence for B3 here). During emplacement of a later pulse, the strain rate was sufficiently high at the contact with B2 to cause localised brittle failure of magma. Many Bb clasts contain coloured lenses

that are truncated at clast edges (e.g., **Fig. 3.41.v**); these lenses are interpreted as bubble collapse structures and they illustrate that brittle deformation must have followed bubble collapse. The diversity of clasts within Bb probably indicates sourcing from different depths and lateral positions, and transport by a gas phase (**Fig. 3.69. time 1**). This considered, Bb at Hringsgil location 2 is interpreted as an internal tuffisite vein. The inner margin of Bb grades into sub-zone Bfb and Bb is replaced by Bfb upwards (e.g., **Fig. 3.41. and 3.43.**). Bfb arguably records a localised brittle-ductile transition along the emplacement boundary layer, due to decreased strain rate and viscous deformation of Bb clasts (**Fig. 3.69. time 2**). This interpretation is made because the flow bands of Bfb have a similar colour range to the clasts that form Bb. Flow banding similarly indicates that a brittle-ductile transition occurred at the B1-B2 contact during B2 emplacement (e.g., **Fig. 3.41.ii**). At Hringsgil location 2, Bfb flow bands have complex micro-scale forms, including sheath and ptygmatic folds (e.g., **Fig. 3.43.v-vii**), reflecting lateral variations in strain.

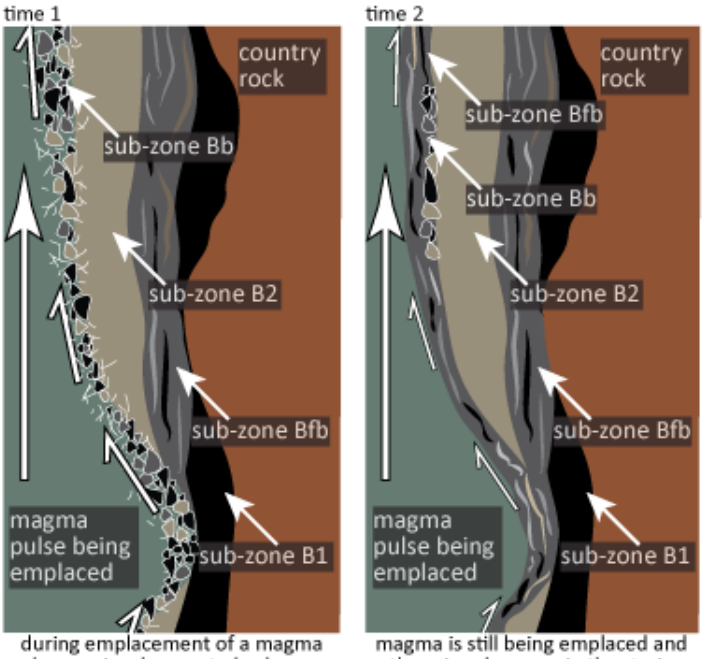

Figure 3.69. Schematic model depicting the formation of sub-zone Bb at the NE margin of Hringsgil location 2, and its subsequent evolution into sub-zone Bfb. See main text for a further description, bubbles and collapsed bubbles are not shown.

v) Boundary layer evolution at Hringsgil location 3a

Similarly to Deildargil location 2a, and Hringsgil location 2, brecciated (sub-zone Bb) and flow banded (sub-zone Bfb) obsidian are also present at Hringsgil location 3a, also reflecting localised deformation along emplacement boundary layers, which is discussed in this section.

Similarly to the other localities, sub-zone Bb and Bfb at Hringsgil location 3a also contain obsidian clasts, but unlike the other localities the sub-zones at Hringsgil location 3a also contain basaltic lithic clasts (e.g., **Fig. 3.45. iv-vi and 3.47.v-vi**), which are fragments of the local country rock. Identification of sub-zones B1-B3 is not possible, as the dyke margins consist of Bb and Bfb only (e.g., **Fig. 3.45.i-ii**). Bb contains clasts of Bfb (e.g., **Fig. 3.45.iii-iv**), and because of this, it is thought that Bfb formed first, in a similar manner to Bfb at Hringsgil location 2, i.e., by viscous deformation of brecciated obsidian (**Fig. 3.70. times 1 and 2**). Lithic clasts within Bfb indicate that country rock clasts were incorporated into the magma during shear deformation. Following the formation of Bfb, Bb is inferred to have formed via autobrecciation, during the emplacement of a later magma pulse (**Fig. 3.70. time 3**). Clasts of Bfb exist within Bb and so Bfb must have been eroded during the formation of Bb; the lithic clasts within Bb may have been sourced from Bfb or the shear zone may have propagated through Bfb causing further erosion of the country rock (**Fig. 3.70. time 3**). Clast diversity within Bb probably reflects lateral and vertical variations in the clast source regions. A gas phase must have been present to account for the distances travelled by the clasts. Bb at Hringsgil location 3a is therefore interpreted as being a tuffisite vein, and considering that the country rock was probably eroded during tuffisite vein formation, it is considered as being an external tuffisite vein.

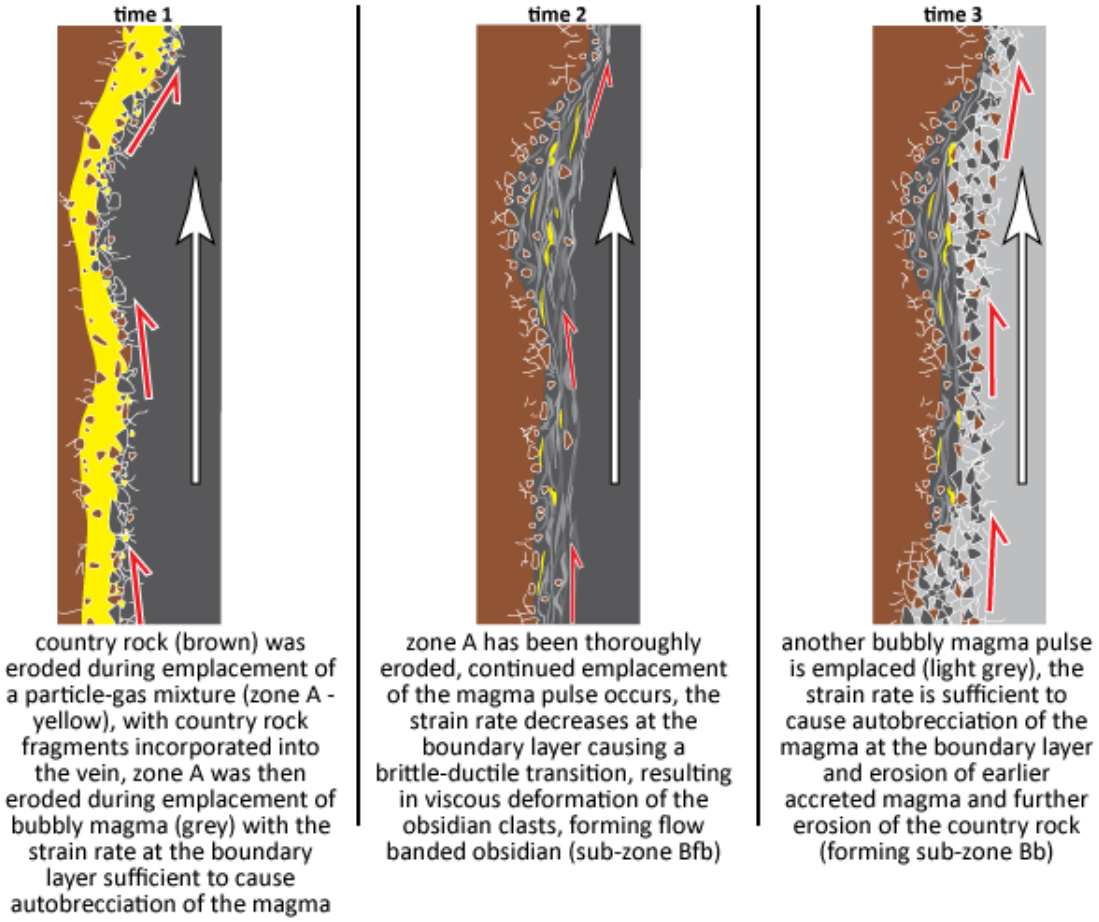

Figure 3.70. Schematic model depicting the formation and evolution of sub-zones Bb and Bfb at the SW margin of Hringsgil location 3a. See main text for further description.

The external tuffisite vein at Hringsgil location 3a contains finer grains (smallest grains ~2 μm) than the internal tuffisite veins at Hringsgil location 2 (smallest grains ~60 μm). In addition, the fine grains have angular edges and contrast with the surrounding larger clasts, which are elongate, with rounded edges (e.g., **Fig. 3.45.**). The elongate forms of the larger clasts were inherited during viscous deformation, and the angularity of the finer grains indicates that these must have been deposited after viscous deformation of the large clasts. In addition, some fine grained laminations wrap around larger clasts (e.g., **Fig. 3.45.vi**), indicating that the deposition of fines was influenced by large clasts. Furthermore, some fine grains have a jigsaw fit with larger clasts, illustrating that the fine grained currents were erosive, further supporting the notion that the fines were deposited after viscous deformation of the

large clasts. The absence of fines in the internal tuffisite veins, and their contrasting presence in the external tuffisite vein, may show that permeability was sustained within the external tuffisite vein throughout viscous deformation, whereas viscous deformation destroyed any permeability in the internal tuffisite veins. Permeability retention in the external tuffisite vein was possible due to the presence of basaltic lithic clasts, which resisted compaction and sintering, ultimately enabling the late influx of fine ash (**Fig. 3.71.**).

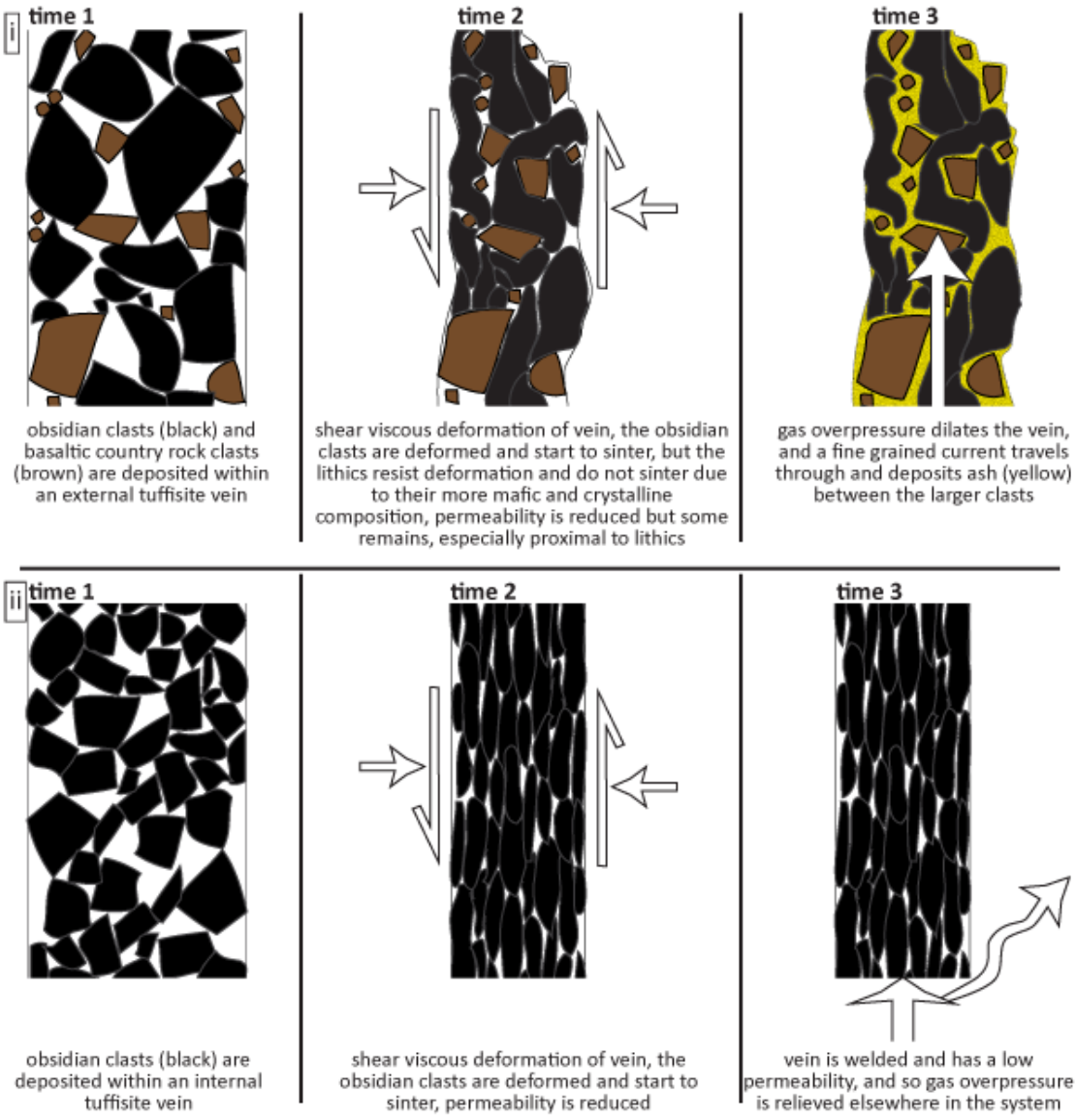

Figure 3.71. Schematic illustration depicting the permeability evolution of external **(i)** and internal **(ii)** tuffisite veins. The presence of lithic clasts within the external vein and contrasting lack of lithics within the internal vein causes the permeability of the external vein to be more sustainable than within the internal vein. Crystal fragments within internal veins would help sustain their permeability, but low concentrations (~5 %) of these exist within the internal veins at Húsafell, and thus, they probably had a negligible effect on permeability.

The grainsize distributions of sub-zone Bb at Deildargil location 2, and Hringsgil locations 2 and 3a, are similar to those of subaerial deposits from violent Strombolian to Vulcanian eruptions (**Fig. 3.72.**; Rust and Cashman 2011), which may indicate that the clast manufacture process was mechanistically similar to that active during Vulcanian eruptions, i.e., fragmentation via pressurisation-decompression cycles (Morrissey and Mastin, 2000; Clarke et al., 2009).

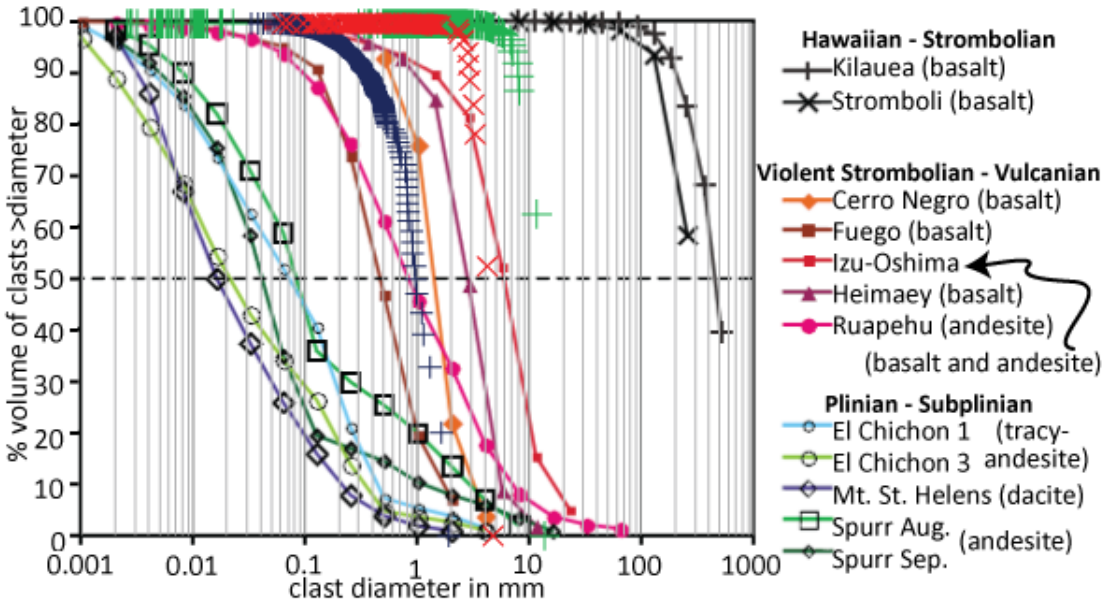

Figure 3.72. A compilation of grainsize distributions for different eruptions from Rust and Cashman (2011). Measured clasts in sub-zone Bb from Hringsgil location 2a (blue crosses, same data as in **figure 3.39.**), Hringsgil location 2 (red crosses, same data as in **figure 3.42.**) and Hringsgil location 3a (green crosses, same data as in **figure 3.46.**) have been added for comparison. See Rust and Cashman (2011) for details of where they sourced the data. See **figure 3.61.** for sources of compositional data.

3.6.3. Zones T and C

In this section, the textural characteristics of zones T and C will be discussed and used to infer the emplacement history of these zones.

Zone T forms the gradational contact between zone B and C at all Deildargil locations, and the gradational nature of the contact (e.g., **Fig. 3.48.i**) is thought to indicate that zone B had not fully cooled prior to zone C emplacement. Pumice clasts occur locally in zone T (e.g., **Fig. 3.49.**), and the sub-zone may consist entirely of

pumice clasts, with clast outlines destroyed via welding and devitrification. Therefore, zone T is considered to have formed via the fragmentation of bubbly magma, and is thus more akin to zone A than zone B. Fragmentation probably occurred because of bubble collapse and welding within zone B, which reduced permeability in the upper parts of the dykes enough to restrict gas loss, thus promoting pressurisation in a deeper part of the magmatic system (**Fig. 3.73. time 1**). Zone T lies between zones B and C on opposite dyke margins (e.g., **Fig. 3.26.i**); zone T must therefore have propagated down the centre of zone B, which indicates that the centre of zone B was the weakest part of the dykes during the formation of zone T. This considered, it is proposed that the centre of zone B contained bubbles prior to emplacement of zone T, with bubble collapse at the margins of zone B having preceded the emplacement of zone T (**Fig. 3.73. time 2**).

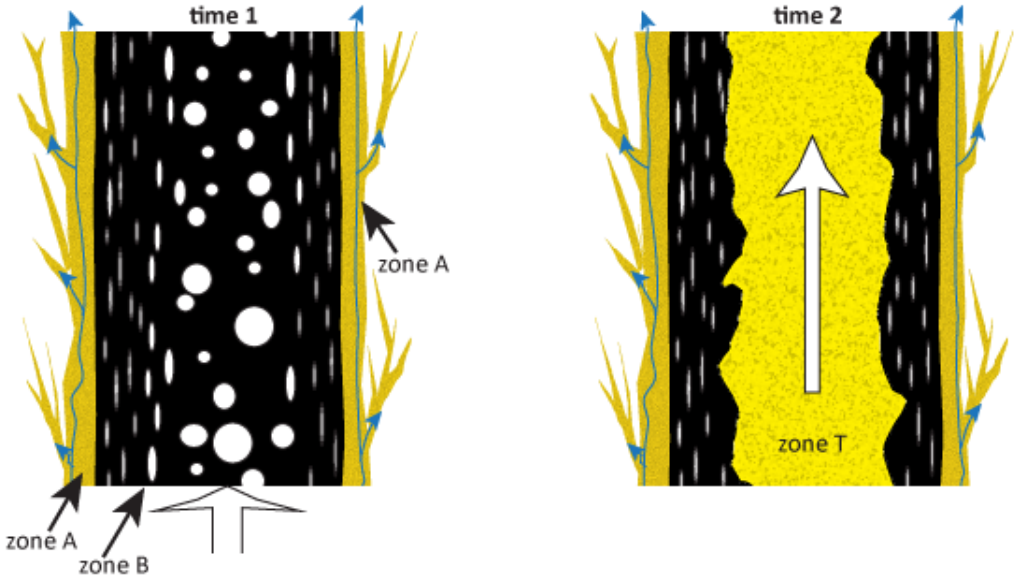

zones A and B have been emplaced, the permeability of zone B is low due to bubble collapse and welding, some gas loss occurs through zone A, but this is too little to prevent pressurisation, especially because the permeability of zone A has been reduced proximal to zone B (see **figure 3.64.**)

fragmentation has taken place in a deeper part of the magmatic system, the fragmented material is intruded into the weak bubbly centre of zone B, forming zone T

Figure 3.73. Schematic illustrations depicting the formation of zone T at Deildargil location 1. See main text for a further description.

Once the overpressure was relieved during the formation of zone T, the growth of the dykes entered a more effusive phase, recorded by zone C, which generally lacks

fragmented material. The vesicle-rich domains that have clast-like shapes and which occur within zone C (e.g., **Fig. 3.51.vi**) may record the incorporation of relatively water-rich clasts from greater depths, or localised zones of shear and viscous heating (Nelson, 1981). Zone C contains vesicles which are large and elongate at the zone margins (sub-zone Cm), but smaller and sub-spherical in the centre (sub-zone Cc). This may reflect greater shear stress at the margins, which promoted shear-induced bubble coalescence (Stasiuk et al., 1996). In some instances, zone C appears to have been emplaced as one pulse (**Fig. 3.74.i**), as recorded by the parabolic flow bands at Deildargil location 3, which extend across the zone (e.g., **Fig. 3.50.i**). In contrast, zone C appears to have been emplaced in multiple pulses in other dykes (**Fig. 3.74.ii**). For instance, at Hringsgil location 3a, parabolic flow bands only extend across part of the dyke, with flow bands generally lacking in other parts of the dyke (e.g., **Fig. 3.50.iii-iv**). Furthermore, in this dyke, sharp planar contacts with folded surfaces occur within the internal part of zone C (e.g., **Fig. 3.53.**), with some of these surfaces bordering the part of the dyke containing folded flow bands. These contacts are thought to separate discrete pulses, with the folds on contact surfaces reflecting shear along emplacement boundary layers.

The microcrystalline texture of zone C contrasts with the glassy nature of zone B, indicating slower cooling of zone C, consistent with greater distance from the country rock. The beige domains in zone T are thought to be lithophysae, and the number density of these increases towards zone C (e.g., **Fig. 3.48.i and ii**). Zone T possibly vesiculated via second boiling, due to crystallisation of zone C, with bubbles being transformed into lithophysae due to glass corrosion by magmatic gases and subsequent vapour phase precipitation. Indeed, the lithophysae are surrounded by pitted glass (e.g., **Fig. 3.48.vi and vii**), which is a hallmark of corrosion, and the

lithophysae contain minerals that have 'fish-scale' cracks (e.g., **Fig. 3.48.vi and vii**), which are characteristic of cristobalite, a common vapour phase precipitate in silicic glass (Horwell et al., 2013; Schipper et al., 2015). However, if the lithophysae originated as bubbles that formed during emplacement of zone C, it is unclear as to why they become more elongate further from zone C (e.g., **Fig. 3.48.ii**). The elongate forms and accompanying preservation of corrosion pits implies that the vesicles were deformed prior to their transformation into lithophysae, and that shear was greatest further from zone C. The formation and evolution of the lithophysae remains unresolved.

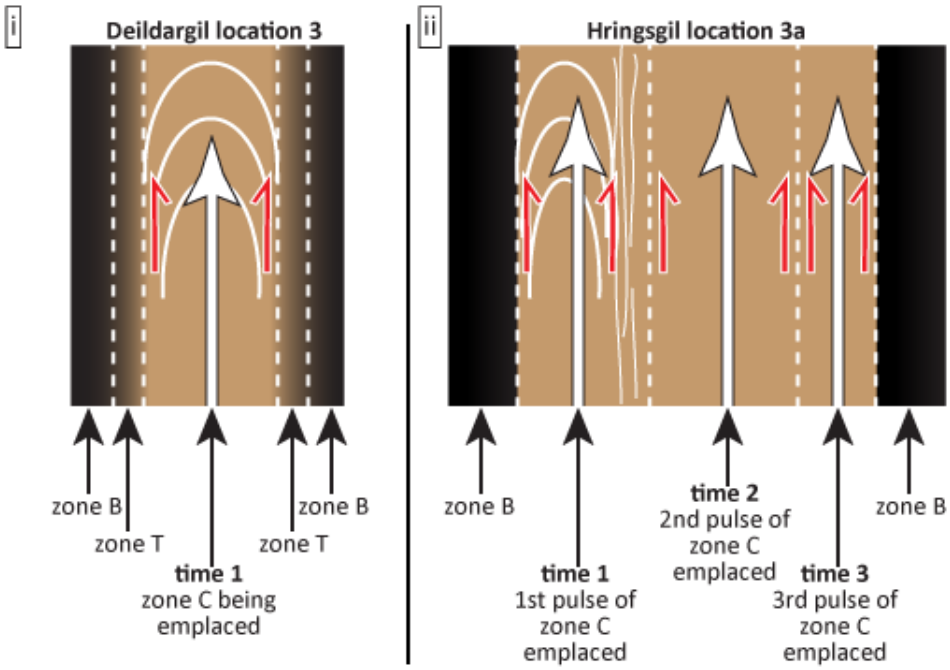

Figure 3.74. Schematic illustrations depicting the formation of zone C at Deildargil location 3 and Hringsgil location 3a. See main text for a further description.

3.7. Interpretation of the major element geochemistry

The major element compositions of zones B and C at Hringsgil location 2 and Deildargil location 2, along with zone A and the country rock at Deildargil location 1, were determined via bulk rock X-ray fluorescence analysis. In addition, the relative amounts of Na and K around perlitic cracks in zone B at Deildargil location 2a were

determined via scanning electron microscopic X-ray spectroscopic analysis. The results of the geochemical analysis are discussed in this section.

The major element compositions of sub-zones B1, B2 and B3 are similar (e.g., **Fig. 3.54. and 3.55.**), which is significant, because the sub-zones are thought to have been emplaced as discrete magma pulses, in a similar manner to the emplacement of composite dykes (Guppy and Hawkes, 1925; Gibson and Walker, 1963; Walker and Skelhorn, 1966). Considering the similar geochemistry of the sub-zones, it is proposed that magma was incrementally fed from a deep geochemically homogenous magma body into the shallow now-exposed parts of the dykes. Zone C is enriched in silica (by ~1-5 wt. %) relative to the sub-zones of zone B (e.g., **Fig. 3.54.**), which may merely reflect vapour phase precipitation of cristobalite within zone C (Horwell et al., 2013; Schipper et al., 2015), with such precipitation lacking in zone B. Other major element geochemical variations exist between zones B and C. For instance, in both dyke exposures, Fe, Ca, Mn and K are depleted in zone C relative to zone B, and zone C in the Hringsgil exposure is also depleted in Al relative to zone B (e.g., **Fig. 3.55.**). These variations probably reflect post-magmatic alteration, whereby fluids either removed elements from zone C or precipitated them within zone B. The scanning electron microscopic X-ray spectroscopic analysis also indicates that the dykes have experienced and probably still are experiencing post-magmatic alteration. For instance, the obsidian bordering perlitic cracks in zone B is relatively K-enriched and Na-depleted (e.g., **Fig. 3.56.**), with such variations being characteristic of post-magmatic alteration of volcanic glasses (Jezek and Noble, 1978).

The bulk rock major element analysis also revealed that zone A is compositionally intermediate between zones B and C, and the country rock, in terms of total alkali and silica concentrations (e.g., **Fig. 3.54.**). The silica content of zone C

is inferred to have increased via cristobalite precipitation; it is therefore deemed more appropriate to compare the silica content of zone A with zone B, rather than with zone C. The average silica content of all analysed zone B samples is 74 wt. %, for country rock samples 49 wt. % and for zone A 67 wt. %. Therefore, if the initial silica content of zones A and B were the same, zone A needs to consist of ~25 % lithic clasts, with the remainder being juvenile clasts, to explain its intermediate composition. This is consistent with the qualitative interpretation that zone A contains ~15-30 % lithic clasts.

Given that the geochemical variations between and within the textural zones and sub-zones are explainable by vapour phase precipitation, post-magmatic alteration or country rock assimilation, it is thought that all of the zones and sub-zones were sourced from a geochemically homogenous magma body which incrementally fed the dykes.

3.8. Interpretation of the dissolved water content

In this section, the results of the water measurements are considered, with specific consideration of whether or not the obsidian has experienced post-magmatic hydration. The water content is also used in conjunction with a speciation model to estimate the emplacement depth.

The total dissolved water content in the dyke exposures at Deildargil location 2 and Hringsgil location 2 is ~5 wt. %, with ~4 wt. % of this being molecular water (H_2O_m) and the remainder being in the form of hydroxyl groups (OH^-). If the total dissolved water content is wholly magmatic the emplacement depth of the exposed parts of the dykes would have been ~5 km (assuming an overburden density of 2700 kg m^{-3}, a magmatic temperature of 800 °C and CO_2-free magma; Newman and

Lowenstern, 2002), which is highly unrealistic. Considering this, the perlitic and weathered nature of the dykes, and the discussion regarding post-magmatic alteration in the preceding section, it is reasonable to suggest that a significant proportion of the total water content represents meteoric water. During low temperature alteration of volcanic glass, meteoric water is added in the form of molecular water (e.g., Stolper, 1982b; Roulia et al., 2006; Denton et al., 2009; Denton et al., 2012; McIntosh et al., 2014a). The minimum temperature at which species interconversion (i.e., conversion of H_2O_m to OH^-) takes place is currently unresolved, but assuming that alteration of the Húsafell dykes took place at a temperature low enough to prevent species interconversion, the OH^- content can be used in conjunction with speciation models to estimate the total concentration of dissolved magmatic water. Nowak and Behrens (2001) presented a speciation model that represents speciation values at magmatic temperatures, but this should only be used for samples that quenched in less than a few seconds, with such quenching rates being required to prevent species interconversion (e.g., Zhang et al., 1995). In contrast, Stopler (1982a) presented a speciation model that provides species equilibrium values at ~Tg (i.e., the approximate temperature at which species interconversion stops), and is thus more applicable to the Húsafell dykes, where cooling of the magma below Tg is likely to have taken far in excess of a few seconds.

The OH^- concentration in both dyke exposures is ~0.8 wt. %. By using this value, and Stolper's speciation model, the total amount of dissolved magmatic water is ~1.3 wt. % (**Fig. 3.75.**), which equates to an emplacement depth of ~500 m and pressure of ~13 MPa (Newman and Lowenstern, 2002), assuming an overburden density of 2700 kg m^{-3}, a magmatic temperature of 800 °C and CO_2-free magma. The density estimate is thought adequate for Icelandic basalt, but other types of country

rock are present in Húsafell, and given the variety of country rock the overburden density cannot be accurately determined. Similarly, the other two assumptions may be incorrect, as the magmatic temperature of the Húsafell dykes remains unconstrained, and the CO_2 content of the lava has not been measured. However, the temperature is encompassed by estimates for rhyolite, which include ~750-800 °C (Torfajökull volcano, Iceland; Gunnarsson et al. 1998), 800 °C (Chaitén volcano, Chile; Castro and Dingwell 2009) and 900 °C (Krafla volcano, Iceland; Elders et al., 2011, Cordón Caulle volcano, Chile; Farquharson et al., 2015). The emplacement depth estimate is considered a good first-order approximation.

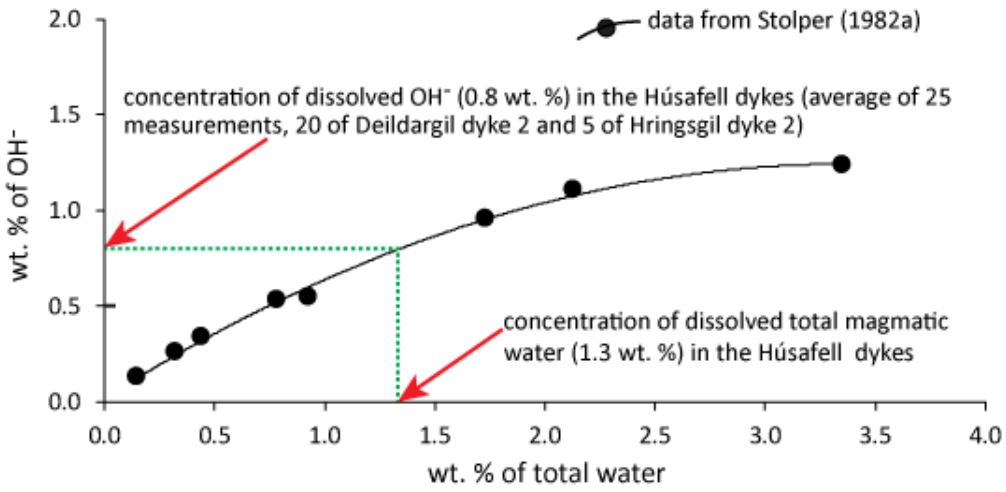

Figure 3.75. Estimation of the concentration of total dissolved magmatic water in the Húsafell dykes by using the measured amount of OH^- and Stolper's (1982a) speciation model. The amount of OH^- ranges from 0.72 to 1.1 wt. % and 0.82 to 0.89 wt. % for the Deildargil and Hringsgil dykes respectively. See **A.3.8.** for the data.

3.9. Summary of magma emplacement and deformation

Some of the dyke exposures at Húsafell clearly belong to the same dyke (i.e., exposures at Deildargil locations 1, 2 and 2a), with the relationship between other exposures less clear, but all dykes probably stem from one deeper dyke, and were most certainly fed from a common magma chamber.

All dykes are thought to have initially propagated via intrusion of gas-charged ash-laden currents, and the fractured nature of the country rock evidently dictated the intrusive dispersal and deposition of particles during initial dyke opening. In addition, the country rock's strength governed how easily it was intruded and eroded. Clasts within the early-formed external tuffisite veins (zone A at Deildargil location 1) formed via tensile failure of small isolated bubbles, with interlinking of the resultant micro-cracks causing macroscopic magma failure. In contrast, the late-formed external tuffisite veins (sub-zone Bb at Hringsgil location 2a and Deildargil location 3a) formed via localised shear failure of bubble-free magma, due to stress along emplacement boundary layers. The late-formed external tuffisite veins and internal tuffisite veins only formed within some dykes. This is unsurprising, as the strain rate was evidently temporally and spatially variable within individual dykes and would therefore also have been different between the different dykes.

Following emplacement of particle-gas currents (zone A), zone B was emplaced, generally as three distinct pulses of bubbly magma (sub-zones B1-B3). The internal tuffisite veins (zone T) that are thought to have propagated through the bubbly magma of zone B only occur in some dykes, which may reflect differing degrees of bubble collapse in zone B, as greater collapse would restrict gas loss to a greater extent making fragmentation at depth more likely. Alternatively, the presence of zone T in some dykes may reflect influxes of volatile enriched magma at depth, which did not occur during growth of the dykes that lack zone T. Following emplacement of zone T or B, more pulses of bubbly magma were emplaced in the dykes (zone C). The reason as to why zones B and C were emplaced as either one or up to three pulses remains unclear, but may reflect divergence of magma at depth, or differences in the amount of magma leaving the source.

Uncertainty remains as to why the lithophysae in zone T formed, but it is tentatively suggested that they may have formed via second boiling, as zone C crystallised. If this is correct, their absence at some dykes and presence at others may reflect differences in the length of time between emplacement of zones T and C, with longer durations allowing for greater cooling of accreted magma (i.e., zone T), prior to zone C emplacement. Allowing more time for cooling would have made the accreted magma more viscous, inhibiting volatile diffusion and bubble growth. The post-emplacement vesiculation events in zone B that are thought to record earlier localised resorbtion of magmatic water and volatile-enrichment only took place in some dykes, which may reflect differences in shear stress between the dykes, with greater shear making resorption more likely, and thus increasing the likelihood of post-emplacement vesiculation.

The textures show that the dyke exposures share broad similarities in terms of their emplacement and deformation histories. For instance, multiple exposures demonstrate that bubbly magma (zone B) was emplaced after the intrusion of particle-laden gas currents (zone A), and that the bubbly magma was commonly emplaced in up to three discrete pulses (sub-zones B1-B3). Furthermore, during incremental emplacement, shear stress was sufficient to cause bubble-collapse in earlier accreted magma. This reduced permeability of the magmatic plug, restricting gas loss, and in some instances this enabled pressurisation and fragmentation at depth (forming zone T), with dyke growth then returning to a more effusive phase, with up to three pulses of bubbly magma emplaced (zone C). Although aspects of magma emplacement and deformation are shared between the dyke exposures, the history of each exposure is unique (e.g., **Fig. 3.76.-3.81.**).

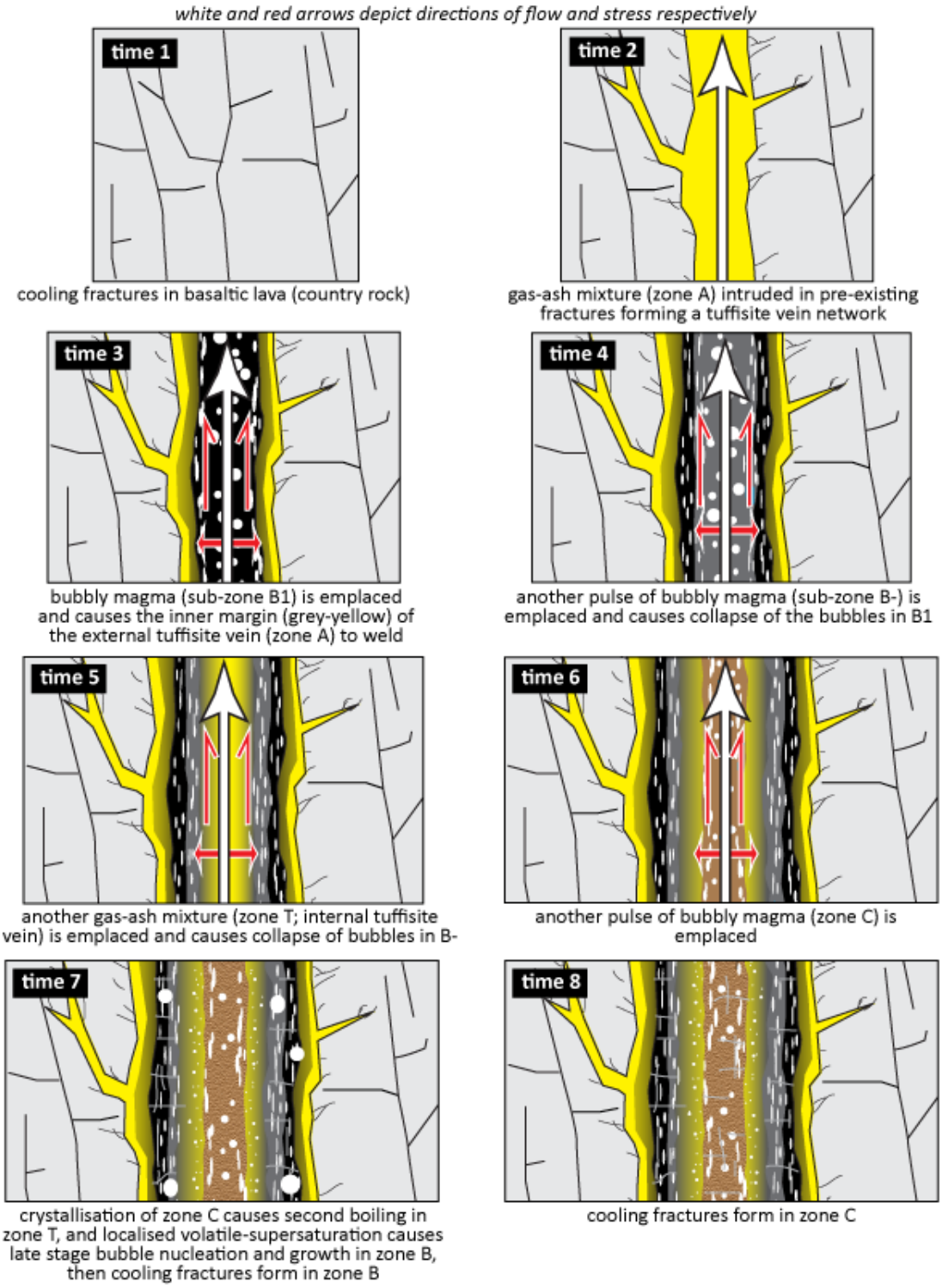

Figure 3.76. Schematic summary model depicting the main emplacement phases of the dyke exposure at Deildargil location 1. See main text and preceding figures for more details.

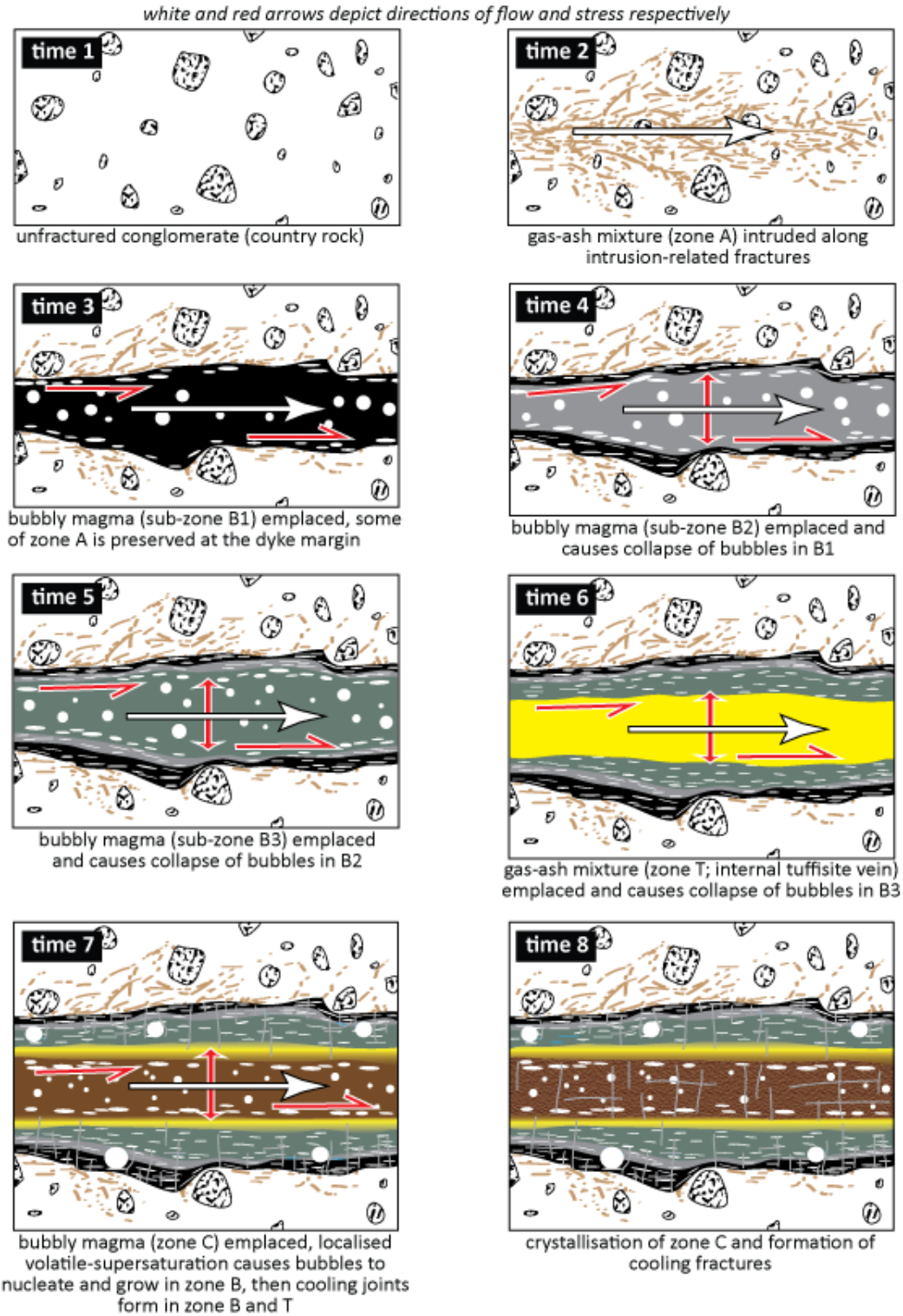

Figure 3.77. Schematic summary model depicting the main emplacement phases of the dyke exposure at Deildargil location 2. See main text and preceding figures for more details.

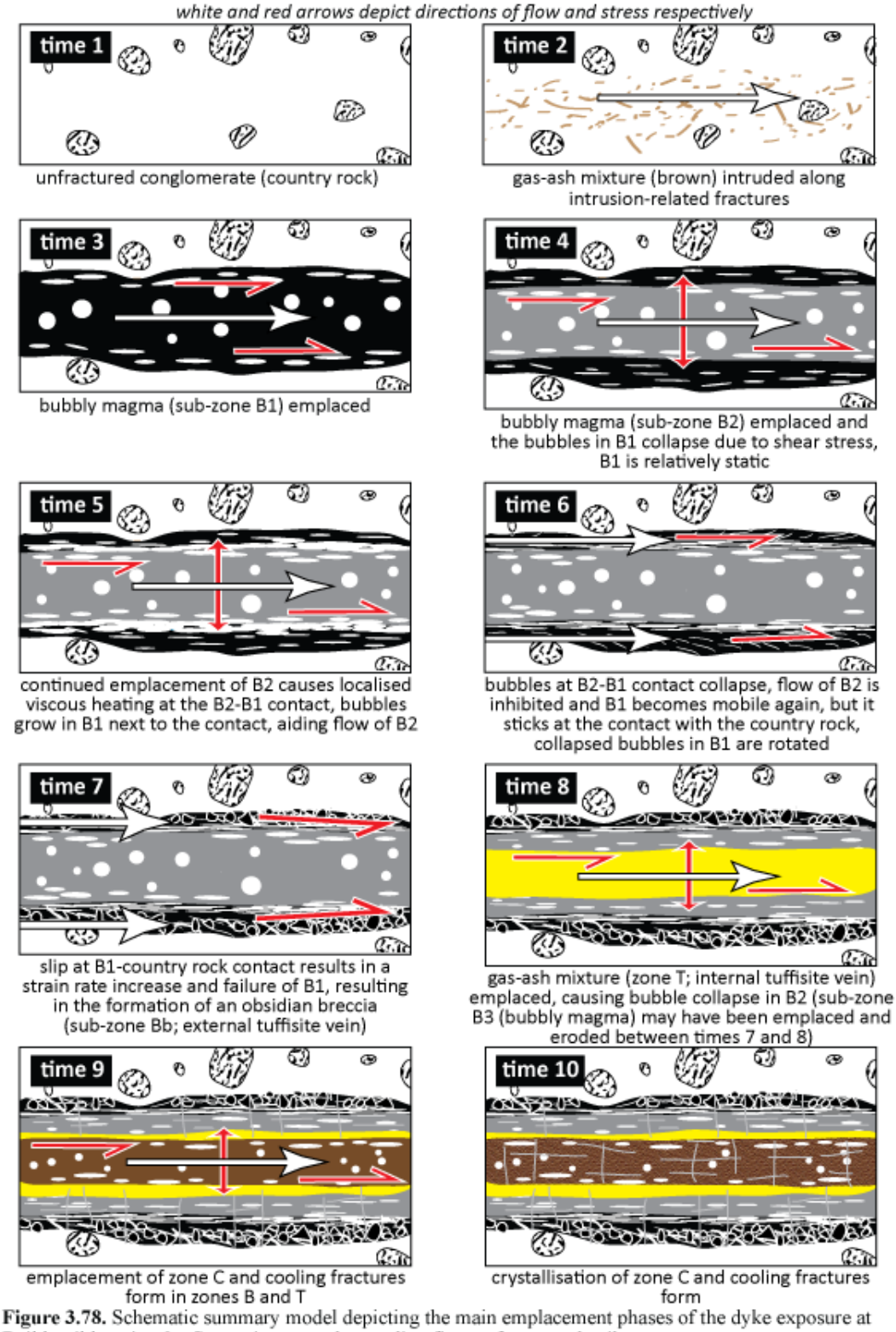

Figure 3.78. Schematic summary model depicting the main emplacement phases of the dyke exposure at Deildargil location 2a. See main text and preceding figures for more details.

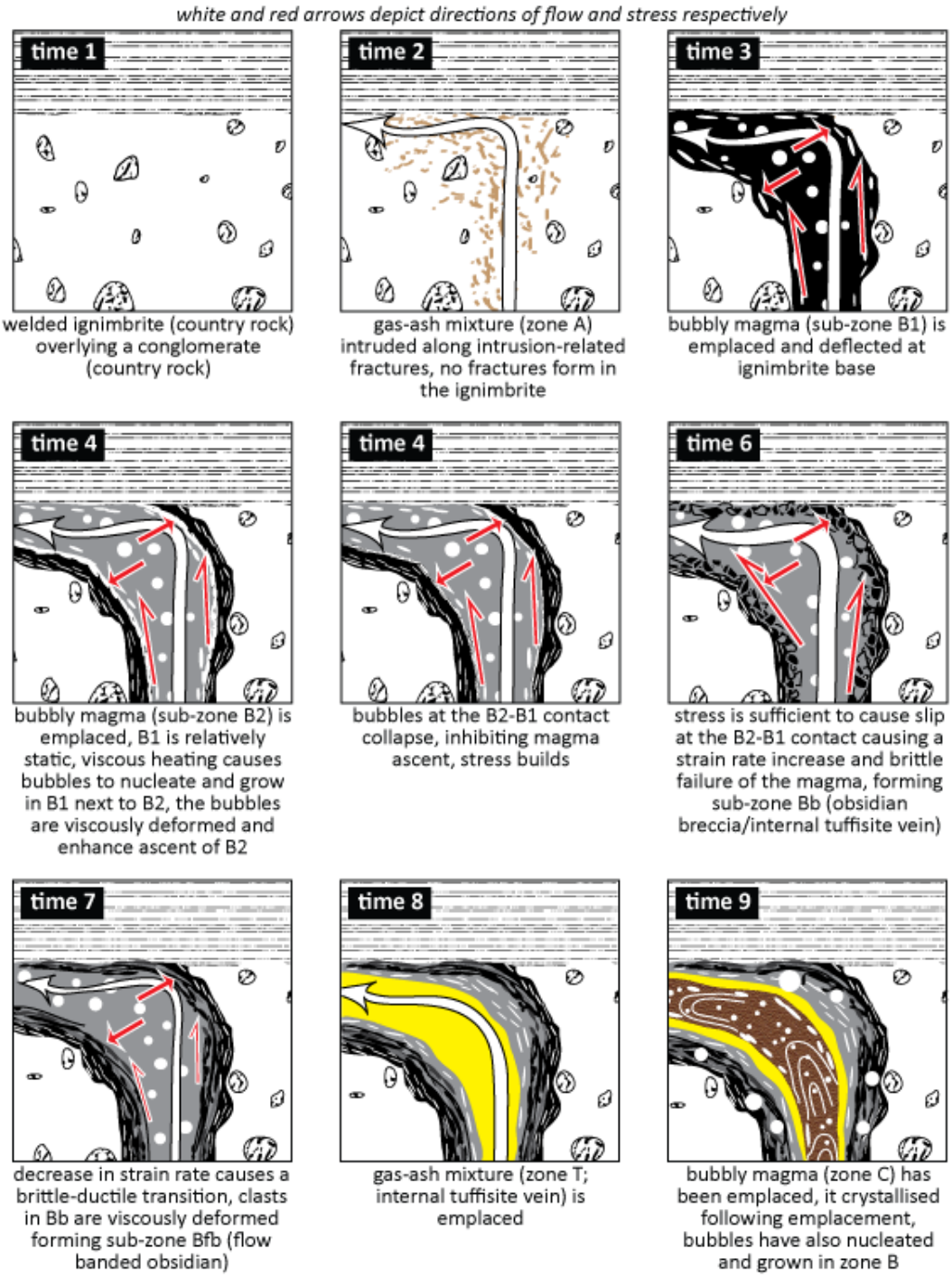

Figure 3.79. Schematic summary model depicting the main emplacement phases of the dyke exposure at Deildargil location 3. See main text and preceding figures for more details.

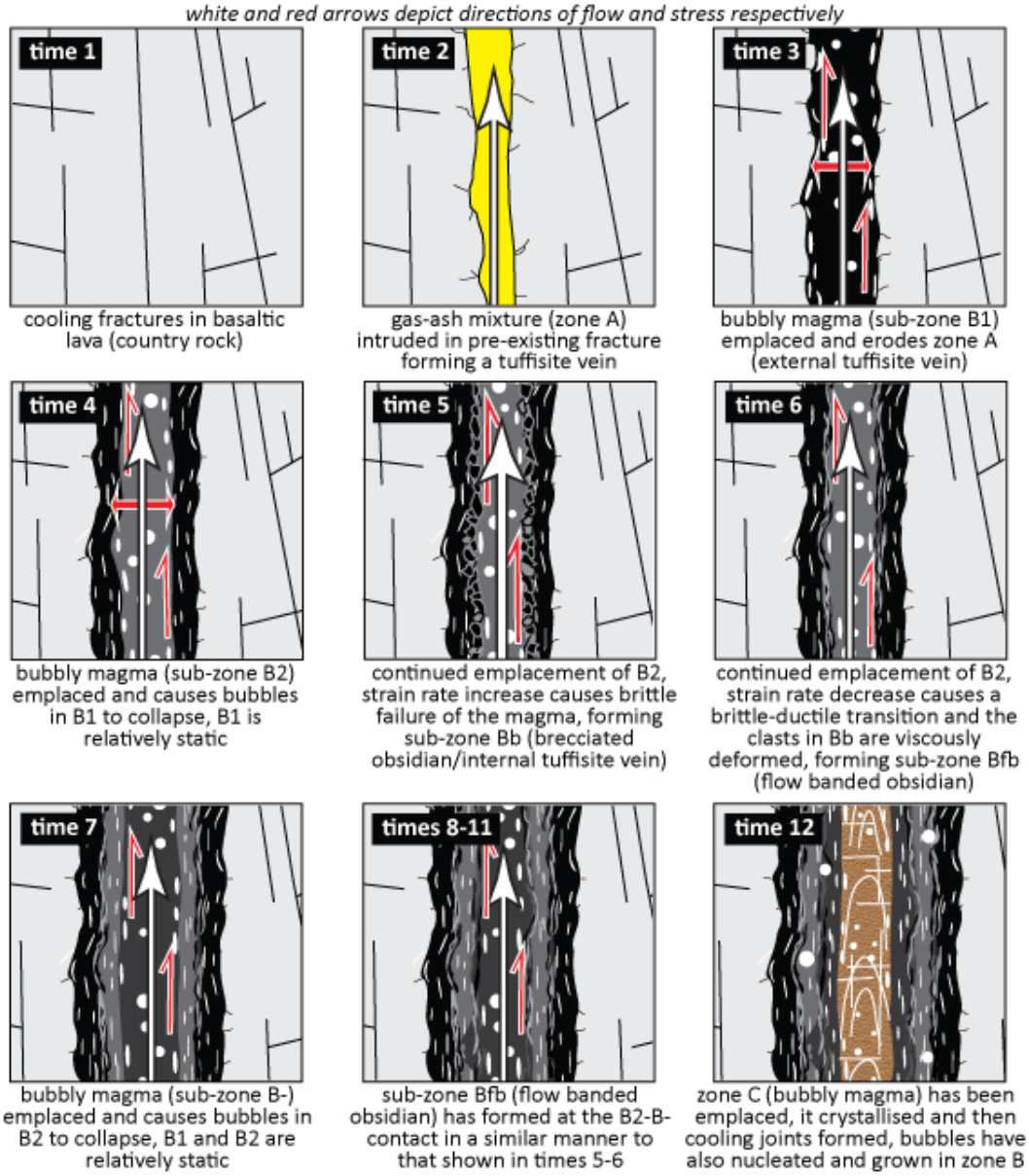

Figure 3.80. Schematic summary model depicting the main emplacement phases of the dyke exposure at Hringsgil location 2. See main text and preceding figures for more details.

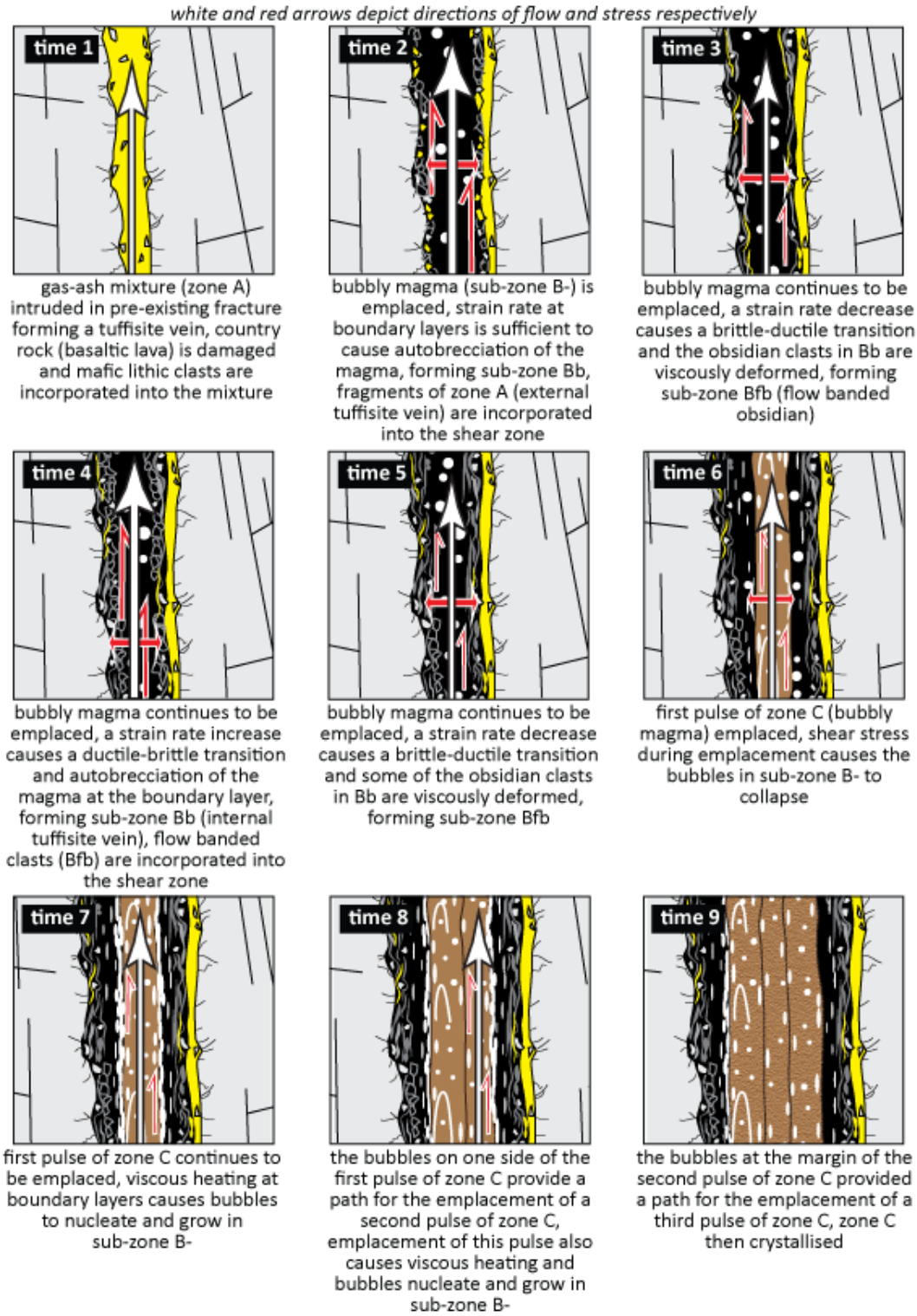

Figure 3.81. Schematic summary model depicting the main emplacement phases of the dyke exposure at Hringsgil location 3a. See main text and preceding figures for more details.

3.10. Summary of key findings

- The emplacement depth of the Húsafell dykes was ~500 m.
- Dyke opening involved the intrusion of gas-charged particle-laden currents, with particle dispersal and dyke propagation being governed by the permeability and strength of the country rock.
- The geochemically homogenous dykes formed via the incremental emplacement of magma.
- Shear deformation involved brittle-ductile and ductile-brittle transitions, and was localised along emplacement boundary layers.
- Shear zones migrated between different emplacement boundary layers.
- Magma flow was promoted in the presence of viscously deformed bubbles, with bubble collapse triggering ductile-brittle transitions.
- Bubble-free magma fragmented via shear, whereas bubbly magma failed via tension below the fragmentation threshold due to overpressure in small isolated bubbles.
- Bubbly magma collapsed during intrusive emplacement to form vesicle-free obsidian.
- Crystals and lithics helped to sustain the permeability of external tuffisite veins, which potentially increased the outgassing ability of these veins.

Chapter 4: Rhyolitic dykes at Torfajökull central volcano

4.1. Introduction

This chapter details the macro- to micro-scale textures and dissolved water content in two rhyolitic dykes at SE Rauðfossafjöll, part of Torfajökull volcano. Previous studies of these dykes provided a textural overview and a detailed account of the tuffisite vein textures (Tuffen, 2001; Tuffen et al., 2003; Tuffen and Dingwell, 2005). The dissolved (Tuffen, 2001; Tuffen et al., 2010; Berlo et al., 2013) and pre-eruptive (Owen et al., 2013a) water content of the dykes has also been determined in a couple of samples. These previous contributions provided insight into magma deformation, internal tuffisite vein evolution (Tuffen et al., 2003; Tuffen and Dingwell, 2005) and outgassing (Tuffen et al., 2010; Berlo et al., 2013; Owen et al., 2013a).

This study has built on these previous studies by analysing the textural relationship between the host obsidian and tuffisite veins, and also by analysing the grainsize and sedimentary structures within the tuffisite veins. In addition, the dissolved water content has been analysed at a higher spatial resolution than carried out previously, and determined at a range of elevations in one dyke, which had previously not been completed at SE Rauðfossafjöll. The work presented in this chapter further broadens our understanding of magma emplacement, deformation and outgassing during shallow (<50 m deep) ascent. The hypotheses to be tested include:

- The outgassing ability of bubble networks is enhanced if they are intersected by tuffisite veins.
- Bubbly magma collapses during intrusion to form vesicle-free obsidian.
- Fragmentation can involve shear and tensile failure of bubbly and bubble-free magma.

- Atmospheric gases may enter tuffisite veins prolonging their permeability lifespan and increasing their outgassing ability.
- Phenocryst fragments increase the outgassing ability of tuffisite veins by prolonging their permeability lifespan.
- Water concentration gradients next to tuffisite veins are modified during magma cooling.

4.2. Geological setting

4.2.1. Torfajökull volcanic complex

Torfajökull central volcano is in south-central Iceland, on the northern part of the non-rifting Southern Flank Zone, at the terminus of the active Eastern Rift Zone (**Fig. 4.1.i and ii**). The volcano is intersected by the NE-SW orientated and SW propagating Veidivötn fissure system (**Fig. 4.1.ii**). These fissures transport mafic magma into the silicic magma bodies at Torfajökull (**Fig. 4.2.**), and this process was probably the catalyst for much of the postglacial volcanic activity (Sparks et al., 1977; McGarvie, 1984; Blake, 1984; Mørk, 1984; McGarvie, 1985). Torfajökull volcanic complex (**Fig. 4.1.ii**) contains Iceland's largest area of exposed, silicic, extrusive deposits (Walker and Skelhorn, 1966; Gunnarsson et al., 1998), covering an elliptical area of 450 km^2, with an estimated volume of 250 km^3 (McGarvie et al., 2006). Deposits on land have an age of 67 ± 9 to 384 ± 20 ka (McGarvie et al., 2006), whereas tephra just off the Norwegian coast has an age of ~70 ka (Brendryen et al., 2010). The most recent eruptions took place around 1480, 900 and 150 years A.D. (Larsen, 1984). Today, the volcano is geothermally and seismically active (Soosalu et al., 2006), with high-frequency and low-frequency earthquakes occurring under the northwest and southern part of the volcano, respectively. The high-frequency earthquakes are thought to result from rock fracturing, caused by thermal-contraction around a roughly spherical, ~4

km wide magma body at a depth of ~4-10 km (Soosalu and Einarsson, 1997). In contrast, the low-frequency earthquakes and nearby geothermal activity may be due to the presence of an ascending cryptodome (Soosalu and Einarsson, 1997, 2004; Soosalu et al., 2006). If the seismic data were taken in isolation it may be expected that the next eruption will be located in the southern part of the volcano. However, the location is difficult to predict, because it will also depend on the southward propagating Veidivötn fissure swarm (Oskarsson et al., 1982). The next eruption from the southwest part of the fissure swarm may occur in the next ~100-300 years, based on the interval (600-800 years) between previous eruptions and the date (1480 years A.D.) of the most recent eruption (Larsen, 1984).

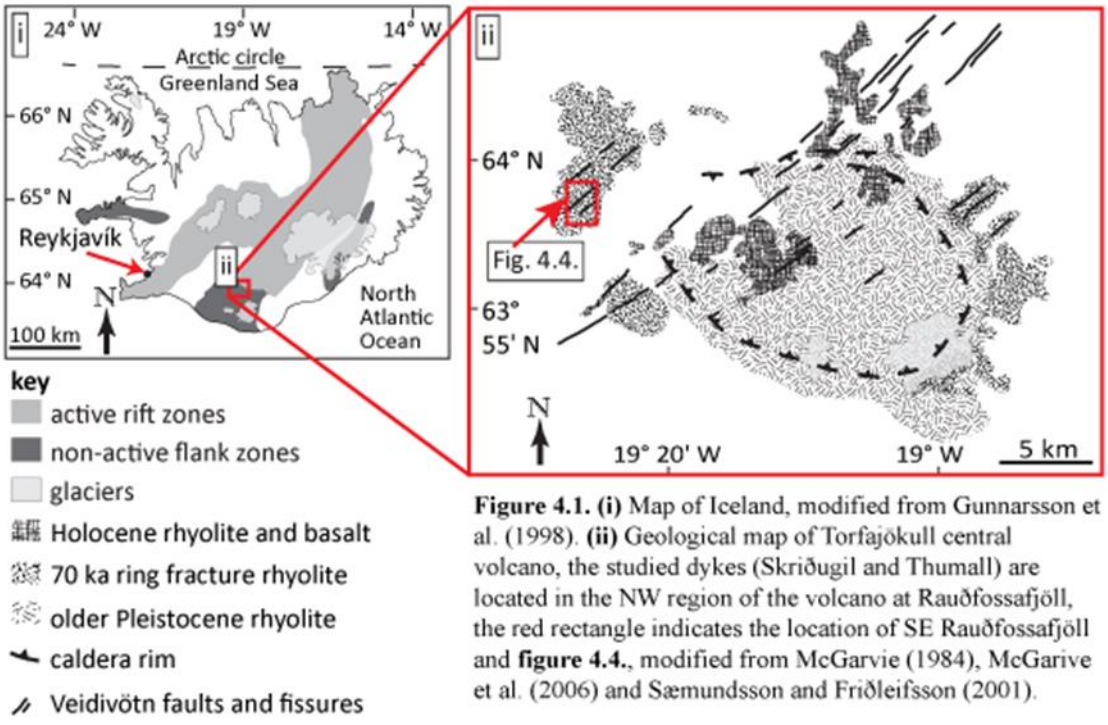

Figure 4.1. (i) Map of Iceland, modified from Gunnarsson et al. (1998). **(ii)** Geological map of Torfajökull central volcano, the studied dykes (Skriðugil and Thumall) are located in the NW region of the volcano at Rauðfossafjöll, the red rectangle indicates the location of SE Rauðfossafjöll and **figure 4.4.**, modified from McGarvie (1984), McGarive et al. (2006) and Sæmundsson and Friðleifsson (2001).

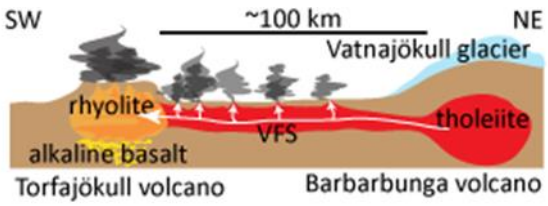

Figure 4.2. Schematic illustration showing the Veidivötn fissure system (VFS) directing mafic magma into the silicic magma body(s) beneath Torfajökull. Redrawn from McGarvie (1985).

4.2.2. SE Rauðfossafjöll

A subglacial eruption of Torfajökull volcano at 70 ka produced the Ring Fracture Rhyolites (McGarvie et al., 2006). These deposits contain mafic inclusions, indicating involvement of the Veidivötn fissure system (McGarvie, 1985). The Ring Fracture deposits have an estimated minimum volume of 18 km^3 (McGarvie, 1984, 1985; McGarvie et al., 2006). This is ~1.5 times the volume of the deposits from the 1991 Pinatubo eruption (Self et al., 2004), and ~1 order of magnitude greater than the volume of deposits from the largest historic explosive eruption in Iceland, the 1362 AD eruption of Öræfajökull (Selbekk and Trønnes, 2007). The Ring Fracture Rhyolite eruption had an estimated VEI of 6 (Newhall and Self, 1982) and a magnitude of 6.3 (Owen, 2013). The 1883 eruption of Krakatoa also had a VEI of 6, and this was the most deadly (36,140 deaths) eruption to have occurred in modern history (Mastin and Witter, 2000). However, these estimates are conservative because they are based on preserved deposits on land, and tephra will have been transported away in melt-water, in the wind, and some is thought to have been deposited in the sea.

Part of the Ring Fracture eruption involved the formation of Rauðfossafjöll (McGarvie, 1984). Rauðfossafjöll is situated in the NW region of Torfajökull volcano (**Fig. 4.1.ii**), and mainly consists of four NE-SW orientated tuyas (**Fig. 4.1.ii**), with an estimated combined volume of 5.5 km^3 (McGarvie et al., 2006). The south-eastern tuya (SE Rauðfossafjöll, **Fig. 4.3. and 4.4.**) has an area and volume of ~4 km^2 and ~1 km^3, respectively. The lower part of SE Rauðfossafjöll consists of a steep sided pile of unbedded and poorly consolidated rhyolitic ash, which is mostly covered by scree (Tuffen, 2001; Tuffen et al., 2002). This represents the early subglacial phase of the eruption that took place within a well-drained ice vault (Tuffen, 2001; Tuffen et al., 2002), with perlitic textures, peperites and blocky ash shards providing evidence for

Figure 4.3. SE Rauðfossafjöll tuya as seen from the north and the location of the two studied dykes (Thumall and Skriðugil). Photo taken by Dave McGarvie.

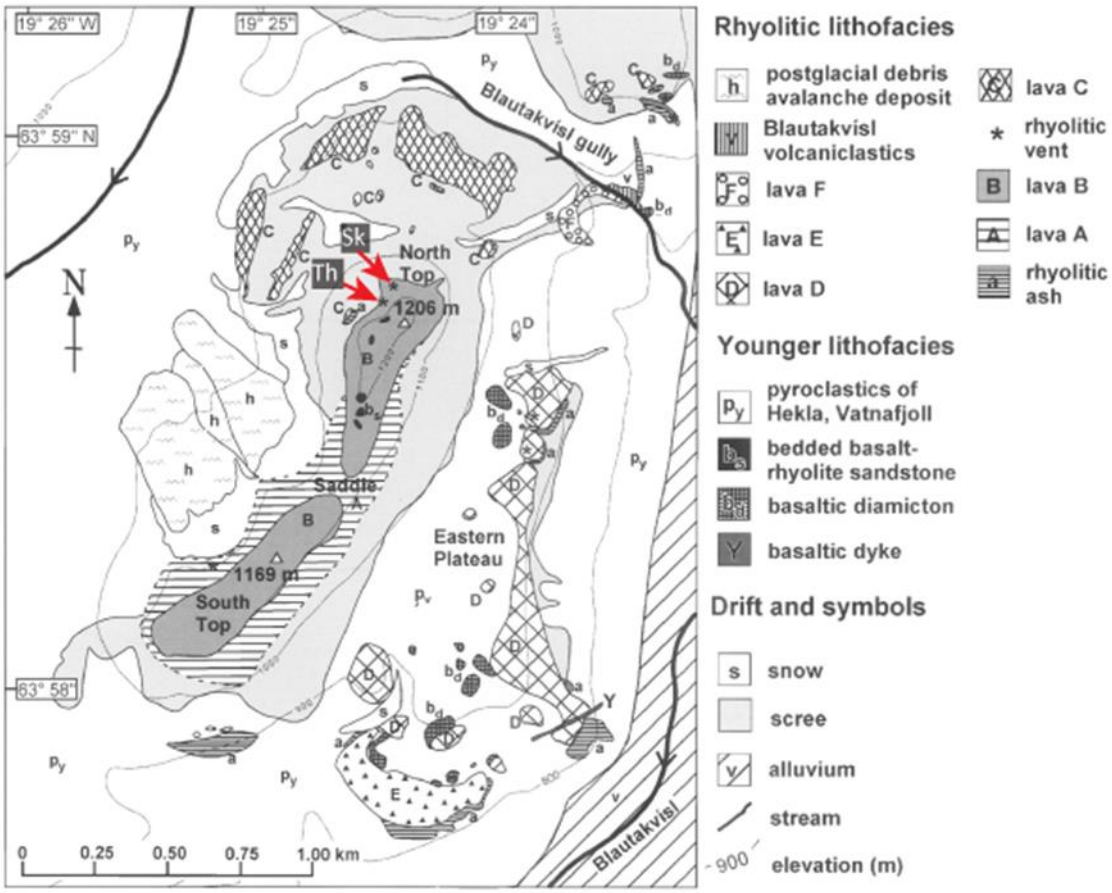

Figure 4.4. Geological map of SE Rauðfossafjöll showing the location of Skriðugil (Sk) and Thumall (Th) on the NW part of the tuya. From Tuffen et al. (2002).

magma-water interaction (Tuffen, 2001; Tuffen et al., 2002). During the eruption, the ice surface was ~100-200 m above the tuya (McGarvie et al., 2006). This estimate is based on the lithofacies and overall architecture of tuyas (Tuffen, 2001; Stevenson, 2005). During the latter part of the eruption, subaerial lava flows were produced from multiple vents (Tuffen, 2001; Tuffen et al., 2002). The eruption therefore underwent an explosive to effusive transition. The lavas form a flat-topped cap, ~1.5 km long and 250-500 m wide, which overlies the rhyolitic ash pedestal. The lavas were emplaced

in an ice cauldron, consistent with the occurrence and orientation of cooling joints (Tuffen, 2001; Tuffen et al., 2002; McGarvie et al., 2006).

4.3. Textures within the dykes (Thumall and Skriðugil)

4.3.1. Overview of dyke structure and tuffisite veins

Partial collapse of SE Rauðfossafjöll's western flank has exposed two NNE-SSW orientated fissure-like dykes, named Thumall and Skriðugil (Tuffen and Dingwell, 2005). Skriðugil's western wall grades into the lower lava body, indicating that the dykes fed part or all of the tuya-capping lava (Tuffen, 2001; Tuffen et al., 2002; Tuffen et al., 2003; Tuffen and Dingwell, 2005). The dyke orientation is similar to that of the tuyas of Rauðfossafjöll and the Veidivötn fissure swarm (**Fig. 4.1.ii**), which when coupled with the lack of evidence for contact with ice walls and the vertical fabric (described below) supports them being dykes and not lava flows (Tuffen, 2001).

The dykes are exposed on the north-west tip of the tuya (**Fig. 4.3. and 4.4.**), at ~1180 m a.s.l. and they are dissected to a depth of ~40 m. They are 10-20 m wide and their contacts with the country rock are not exposed. Thumall may be accessed over the vertical extent of its dissection, whereas precipitous slopes limit access to Skriðugil to a vertical section of ~10 m. Based on the position of the flow-top carapace it is inferred that lava with a thickness of ~10 m has been eroded from above the dykes (Tuffen, 2001; Tuffen et al., 2002; Tuffen et al., 2003; Tuffen and Dingwell, 2005). Considering this, and the depth of dissection, the exposed parts of the dykes were emplaced at a depth of 10-50 m.

Tuffen and Dingwell (2005) divided the dykes into four main textural zones; Skriðugil has a vesicular interior (zone A), surrounded by vesicle-free obsidian (zone B), with devitrified breccia (zone C) and devitrified intact lava (zone D) outwardly

bordering zone B (**Fig. 4.5.i**). In contrast, Thumall's core consists of devitrified intact lava (zone D), which is bordered by vesicle-free obsidian (zone B), with the western wall consisting of devitrified intact lava (zone D) and an outermost zone of devitrified breccia (zone C; **Fig. 4.5.ii**). Both dykes contain tuffisite veins, with those in Thumall defining a vertical fabric together with microlites (Tuffen and Dingwell, 2005). Many

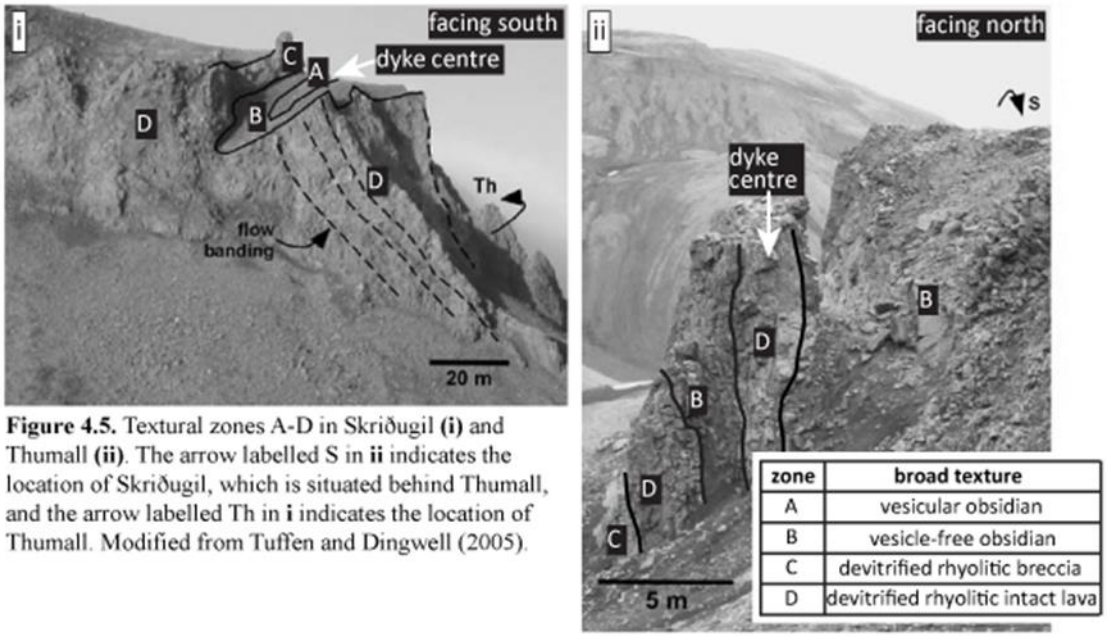

Figure 4.5. Textural zones A-D in Skriðugil **(i)** and Thumall **(ii)**. The arrow labelled S in **ii** indicates the location of Skriðugil, which is situated behind Thumall, and the arrow labelled Th in **i** indicates the location of Thumall. Modified from Tuffen and Dingwell (2005).

of the tuffisite veins are viscously deformed and truncated by later generations of tuffisite veins, indicative of repeated fracturing and healing of magma during shallow ascent, with this process being a potential trigger mechanism for hybrid earthquakes (Tuffen et al., 2003). Tuffen and Dingwell (2005) presented a model depicting the formation and evolution of internal tuffisite veins, identifying three types (fault veins, reservoir zones and injection veins; **Fig. 4.6. and Table 4.1.**) and four generations of tuffisite veins. In their model, phase 1 of tuffisite vein evolution involves shear failure of magma in the glass transition interval, with failure driven by a strain rate increase or cooling. During this phase, fault veins are formed, with injection veins and reservoir zones forming via extensional failure of fault vein walls, perhaps driven by high gas pressure. During phase 1, particles were produced via abrasion of fracture

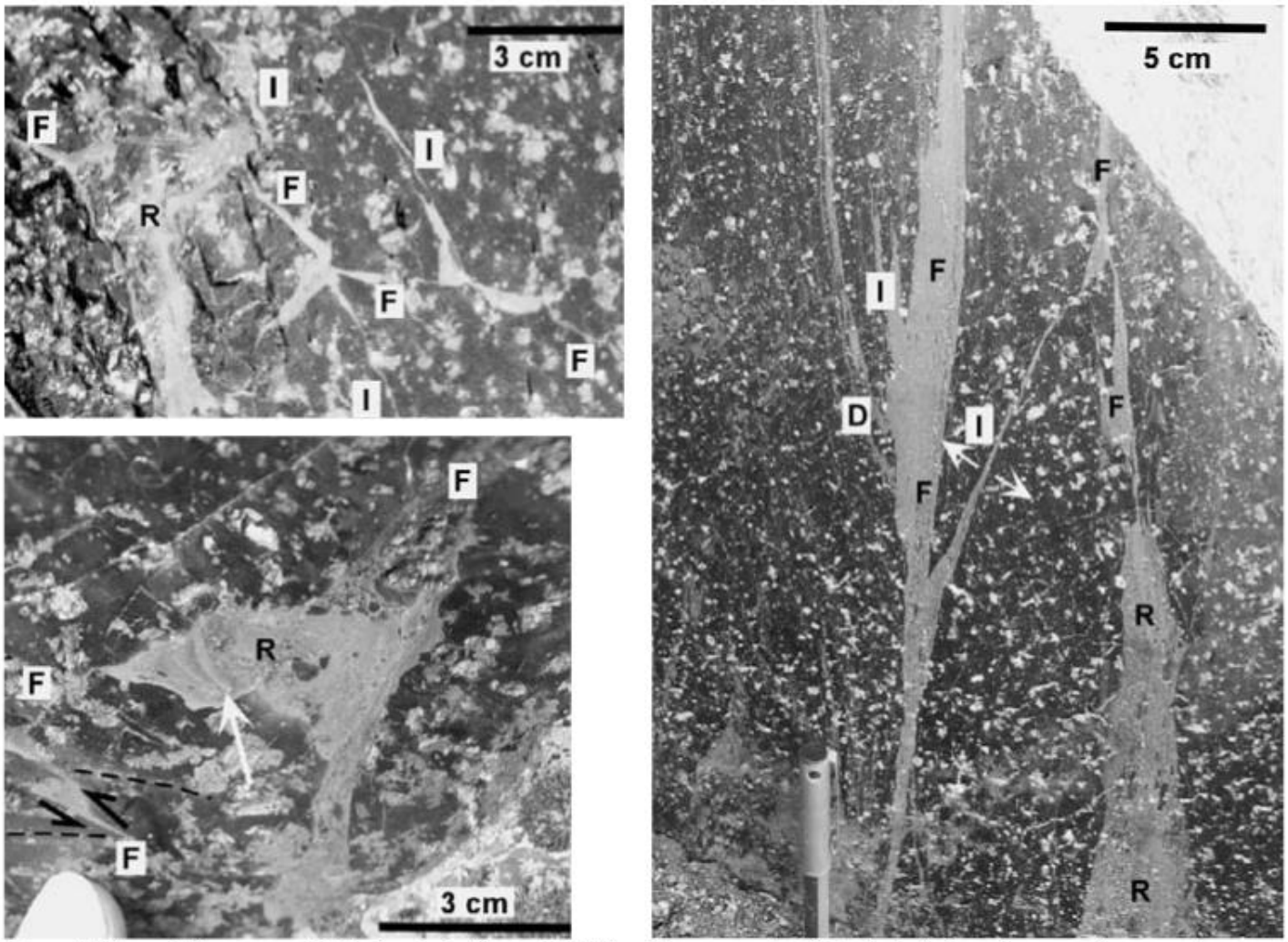

Figure 4.6. Three different types of tuffisite veins in Thumall. F, I, R and D correspond to fault vein, injection vein, reservoir zone and a truncated displacement marker respectively. From Tuffen and Dingwell (2005).

Table 4.1. The different types and phases of tuffisite veins within the dykes. Summarised from Tuffen and Dingwell (2005).

type	morphology	interpreted mode of formation
fault vein	near-planar, 1–20 mm wide, linked to reservoir zones and injection veins	shear failure
injection vein	narrow and tapering, 1–10 mm wide, linked to fault veins and reservoir zones	tensile failure of fault vein walls
reservoir zone	irregular forms, up to 80 mm wide, linked to fault veins and injection veins	tensile failure of fault vein walls
generation	**main characteristics**	**process**
phase 1 (the least common textural type)	branching with random orientations, not folded, truncate and are discordant with phase 2-4 veins.	initial fracture formation
phase 2	branching with random orientations, not folded, contain cataclasite and Riedel shear zones	in-situ grainsize reduction along shear zones
phase 3 (the most abundant textural type)	commonly folded, orientated normal to dyke margins	ductile deformation and rotation of phase 1-2 tuffisite veins and a cessation of brittle deformation
phase 4	microlite-rich bands, formed of deformed microlite-coated obsidian clasts	ductile deformation of phase 3 tuffisite veins

walls or/and via spalling of fragments from extension fractures. The tuffisite veins contain sedimentary structures (e.g., truncation surfaces, graded, poorly sorted, cross and planar laminations) that are indicative of deposition from ash-laden gas currents. The tuffisite veins also contain mosaic micro-structures, micro-fractures within clasts, and trails of angular particles, which record the development of localised cataclastic shear zones, representing phase 2. Following this, brittle-ductile transitions occurred via frictional heating, or decreases in the strain rate, with viscous deformation and welding characterising phase 3. During phase 4 clast outlines were destroyed, with the previous clastic nature of the lava only being apparent due to the presence of microlites, which coat clast surfaces. Following phase 4 the magma fractured again (phase 1), due to a strain rate increase or cooling, thus initiating the commencement of another deformation cycle. It is possible that hybrid earthquakes formed during phases 1 and 2, with phases 3 and 4 being aseismic (Tuffen and Dingwell 2005; **Fig. 4.7.**).

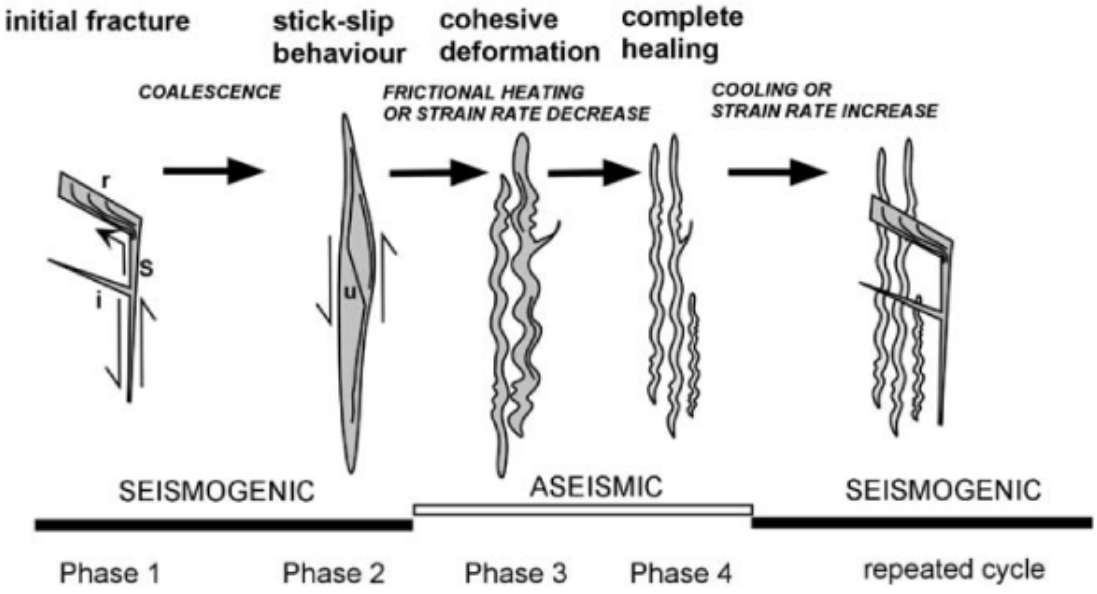

Figure 4.7. Phases of tuffisite vein evolution, S, I, R and U correspond to fault vein, injection vein, reservoir zone and ultracataclasite zone respectively. Image from Tuffen and Dingwell (2005).

4.3.2. Macro- to micro-scale

i) Sampling

The objective of sampling was threefold; 1) to sample different phases of tuffisite veins, 2) to sample from different elevations of Thumall, and 3), to sample tuffisite veins hosted in vesicular and vesicle-free obsidian. Sample locations in Thumall (**Fig. 4.8.i and ii,** also see **A.4.1.** for sample elevations) were recorded in photos and a 3D reconstruction (**Fig. 4.8.iii**) was made using the method of James and Robson (2012) and the photos. Sample elevations were determined by measuring the distance between the reference point (1179 m) and sample locations, and then by subtracting or adding these distances from or to 1179 m (**section 2.1.** - methodology and errors). Samples were also collected from zones A and B of Skriðugil (**Fig. 4.8.iv**).

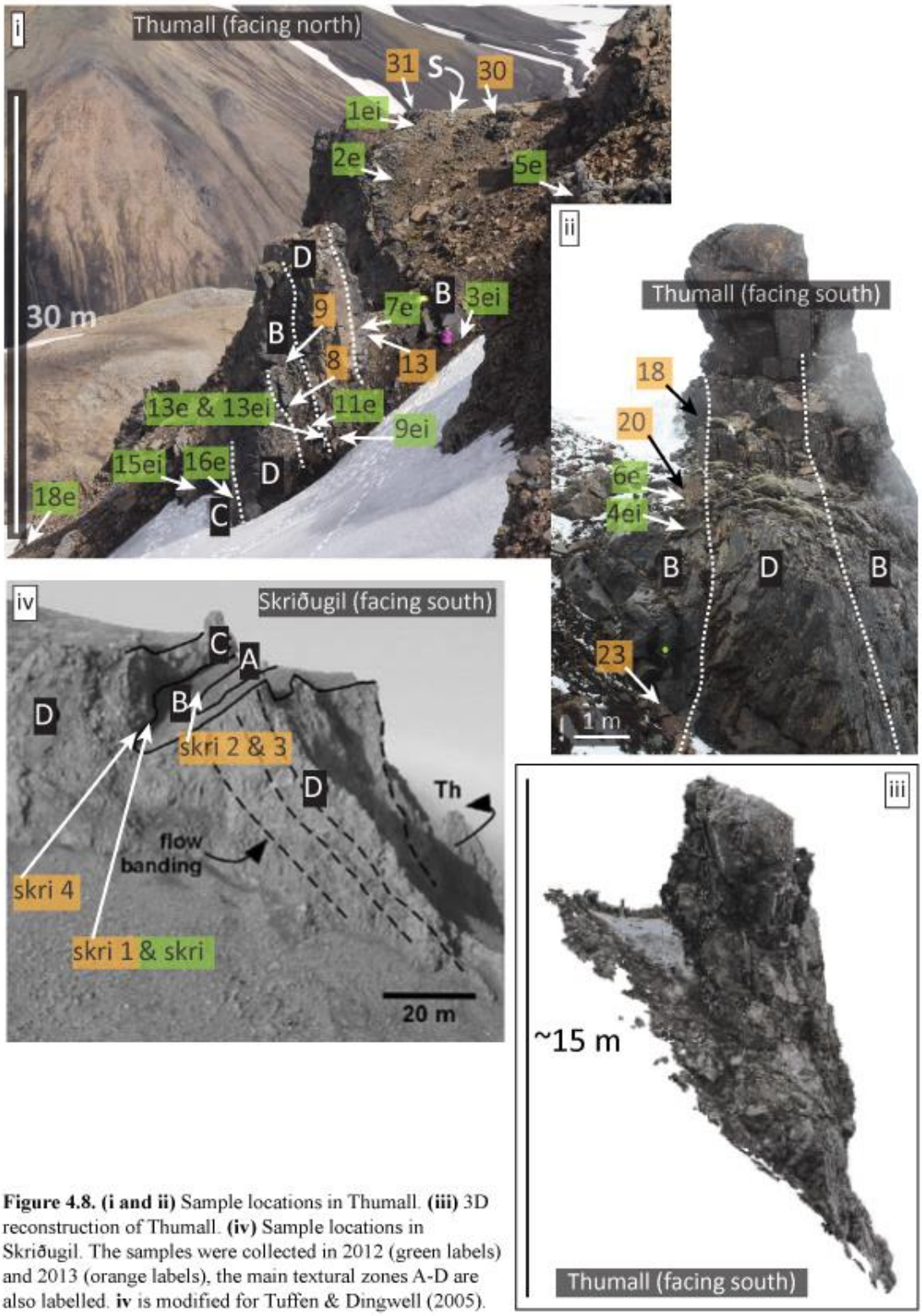

Figure 4.8. (i and ii) Sample locations in Thumall. **(iii)** 3D reconstruction of Thumall. **(iv)** Sample locations in Skriðugil. The samples were collected in 2012 (green labels) and 2013 (orange labels), the main textural zones A-D are also labelled. **iv** is modified for Tuffen & Dingwell (2005).

ii) Distribution and orientation of tuffisite veins, vesicles and phenocrysts

The phase 3-4 tuffisite veins within the vesicle-free lava of Thumall define planes that are normal to the dyke margins (**Fig. 4.9.**), whereas the phase 1-2 reservoir zones and injection veins in Skriðugil's centre are branching and discordant with the dyke margins (**Fig. 4.9.**). The longest measured tuffisite vein network is ~5 m long and located in Thumall (Tuffen and Dingwell, 2005), but more extensive networks probably exist, considering their hidden 3D geometry. The distribution of the tuffisite veins is variable, with the number of veins per horizontal metre spanning ~10-150 (**A.4.2**.). No systematic distribution of the different types and phases of tuffisite veins exists, except that phase 1-2 fault veins were only found in the upper part of Thumall.

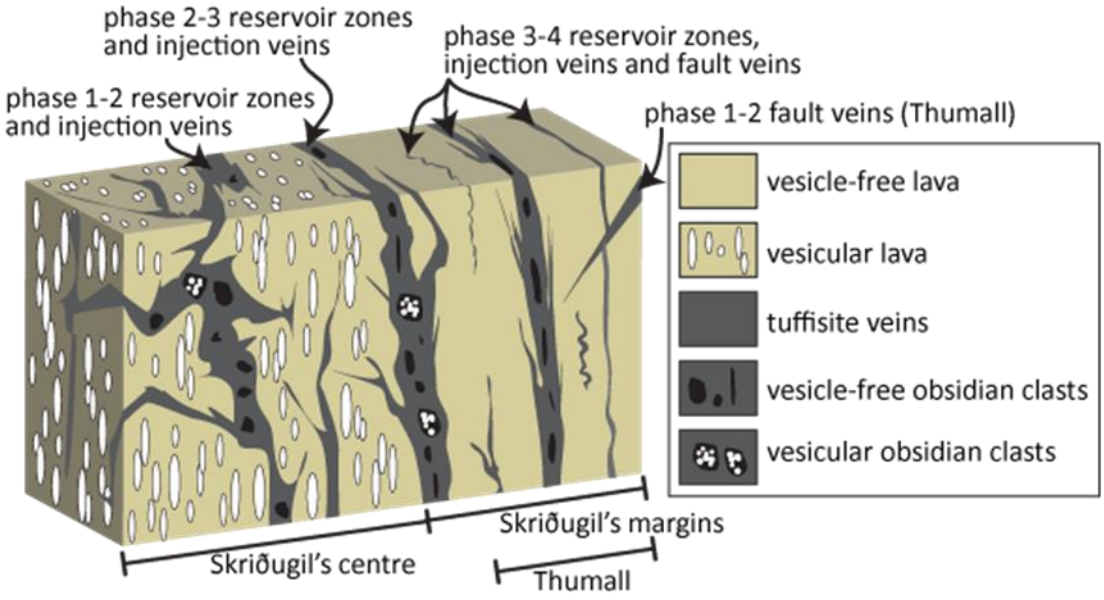

Figure 4.9. Schematic illustration showing the distribution and orientation of the different types and phases of tuffisite veins in the dykes, the distribution of vesicular and vesicle-free lava is also shown.

The vesicular host obsidian of Skriðugil's centre contains ~35 % vesicles, determined from an X-ray computerised tomographic image (**A.4.3.** - measurements, **sections 2.5.** - methodology). The vesicles are 5 mm long and generally <1 mm wide, elongate and interconnected, with many having irregular forms due to them wrapping around phenocrysts (**Fig. 4.10.**).

Figure 4.10. Photograph of the vesicular host obsidian, which forms Skriðugil's centre (zone A).

Contacts between the vesicular host obsidian and the tuffisite veins are sharp, and it is ambiguous as to whether the veins dissect vesicles. The veins follow the major-axis of the elongate vesicles (**Fig. 4.11.**), and the distance between vein margins and vesicles spans ~0.1-2 mm. There is no difference between the host obsidian that is proximal and distal to the veins. Furthermore, vesicles proximal and distal to the veins have similar forms and are a similar size.

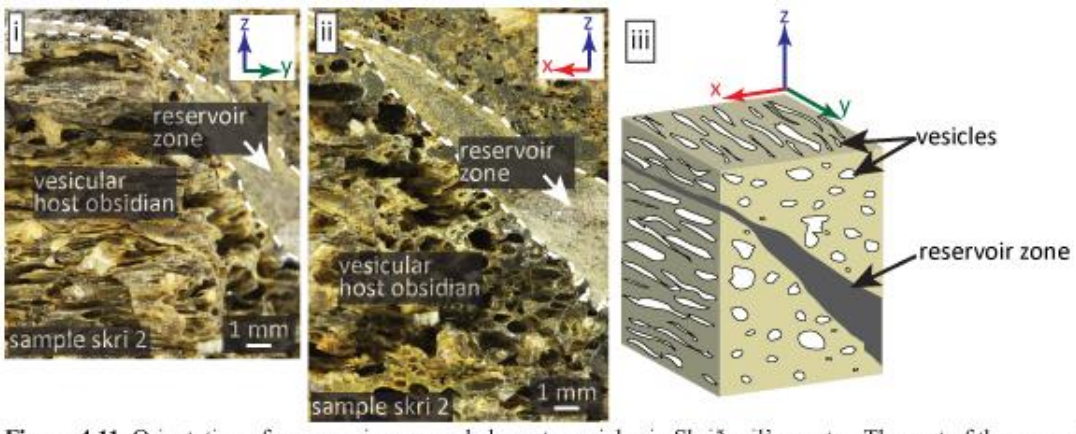

Figure 4.11. Orientation of a reservoir zone and elongate vesicles in Skriðugil's centre. The part of the reservoir zone on the z-y plane follows the orientaion of the elongate vesicles. **(i and ii)** Photographs of hand specimen. **(iii)** Schematic illustration.

Obsidian clasts occur within the tuffisite veins throughout both dykes, and they are generally vesicle-free. However, veins towards and within Skriðugil's centre also

contain vesicular clasts, with the vesicles having intact walls and sub-spherical forms (**Fig. 4.12.**); thus contrasting with the elongate vesicles in the host obsidian of Skriðugil's centre. The vesicular clasts abut vesicle-free clasts with irregular forms (**Fig. 4.12.**), and the vein margins are irregular next to the vesicular and vesicle-free clasts (**Fig. 4.12.**).

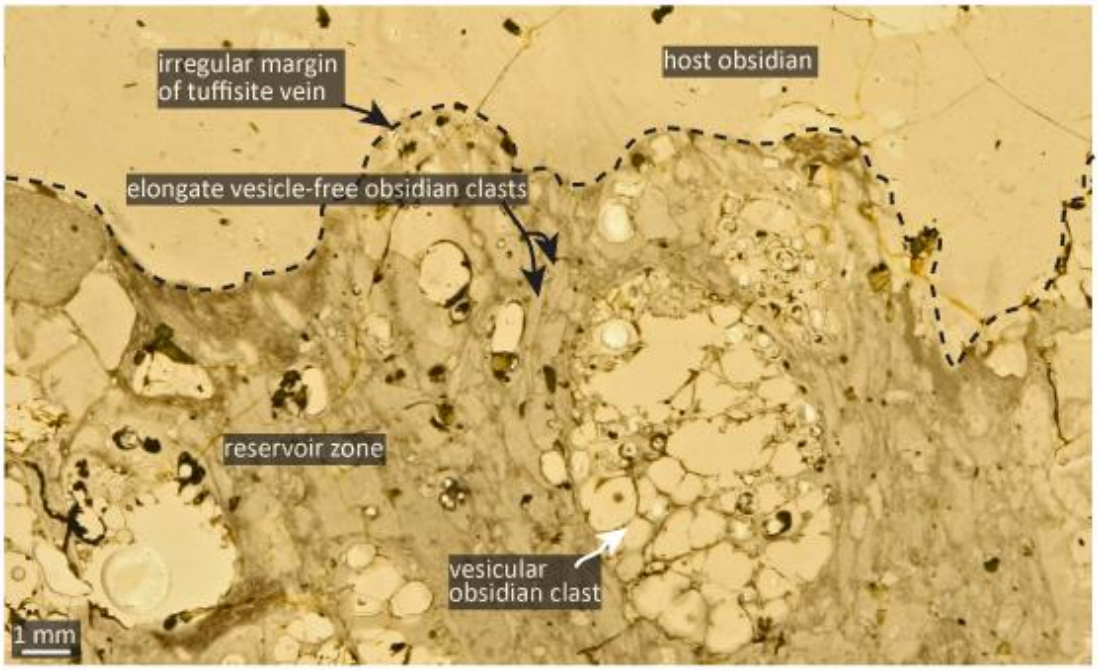

Figure 4.12. Photograph of a petrological thin section (sample skri 1). Vesicular and vesicle-free obsidian clasts in a phase 2-3 reservoir from Skriðugil.

The host obsidian of textural zones A-D contains ~10-25 % intact phenocrysts (**Fig. 4.13.**), which are generally euhedral. The phenocrysts consist of clinopyroxene, fayalite and predominantly alkali feldspar, and are <5 mm long (Tuffen and Dingwell, 2005). Tuffisite veins are commonly found next to the phenocrysts, with the veins going around the phenocrysts, rather than cutting through them, and some veins are thinnest between phenocryst clusters (**Fig. 4.14.**).

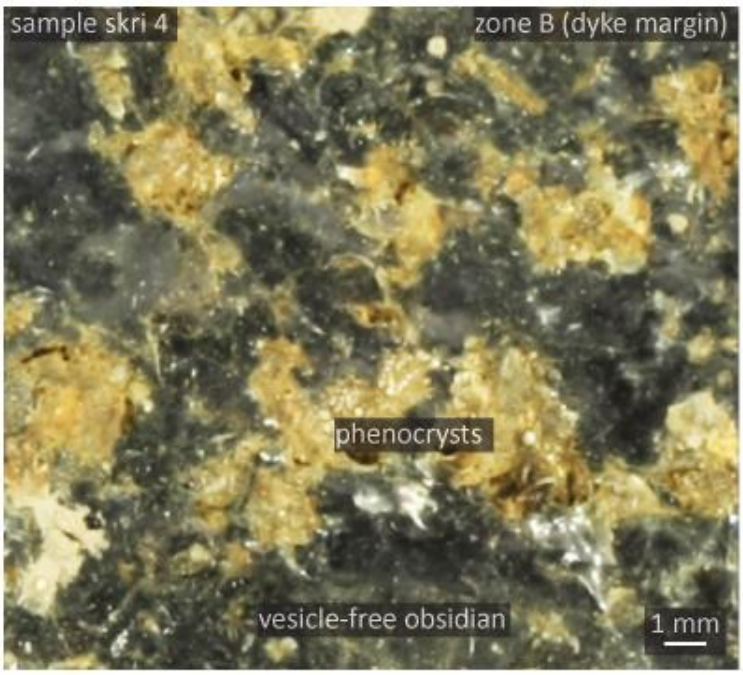

Figure 4.13. Photograph of the vesicle-free host obsidian, which forms Skriðugil's centre (zone B).

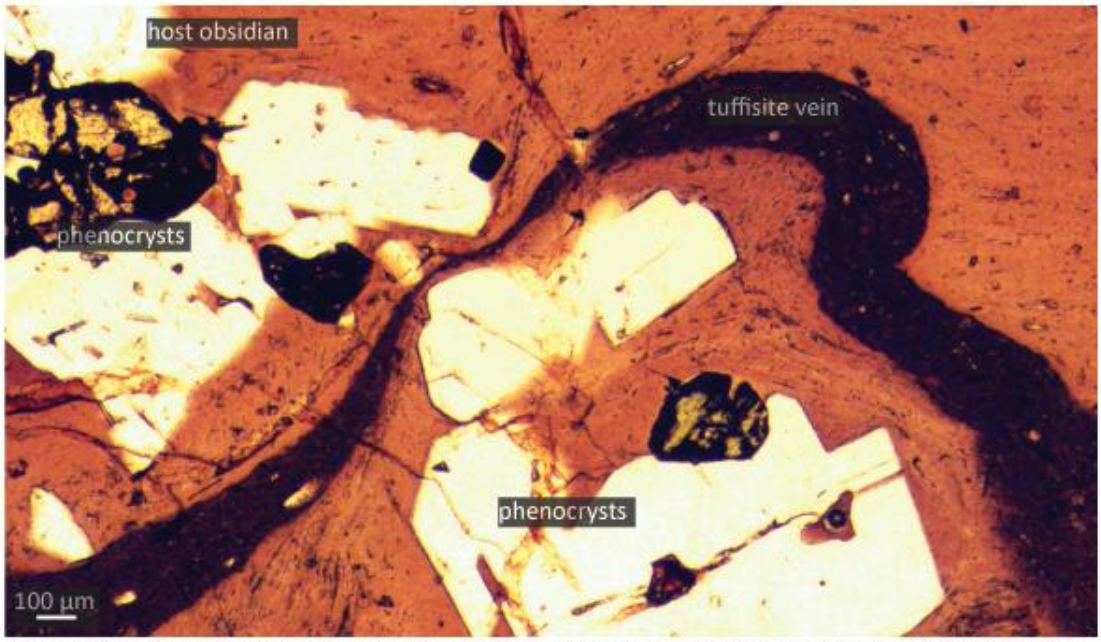

Figure 4.14. Microphotograph taken in plane polarised light (sample 2e). The tuffisite vein is thinnest between the phenocryst clusters.

4.3.3. Meso- to micro-scale

i) Tuffisite veins

Obsidian clast and phenocryst fragment sizes were determined by tracing the clasts and fragments in photographs of petrological thin sections and also in BSE images,

using Adobe Illustrator. ImageJ was then used to estimate clast areas; the diameter of a circle with the same area was then calculated and inferred sphere volumes were calculated from the diameters (**A.4.4.** - clast tracings, **A.4.5.** - measurements, **section 2.6.** - methodology and errors). This method was used because viscous deformation modified clast forms (**Fig. 4.15.**; Tuffen and Dingwell 2005). Clast diameters span ~2 μm - 5 mm, with 87 % of the inferred total volume having diameters >1 mm, and 88 % having diameters <500 μm (**Fig. 4.16.i**). Clasts in the phase 1-2 tuffisite veins are relatively circular (**Fig. 4.16.ii**), with angular to sub-rounded edges, whereas those in the phase 2-3 tuffisite veins have rounded edges and are more elongate (**Fig. 4.16.ii**).

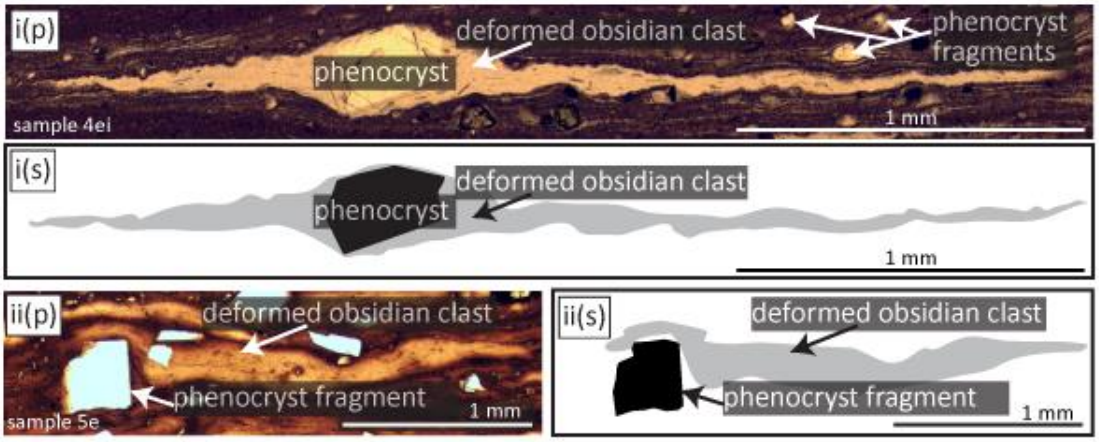

Figure 4.15. Deformed obsidian clasts inside phase 3 fault veins or reservoir zones from Thumall. **(i(p) and ii(p))** Plane polarised light microphotographs. **(i(s) and ii(s))** Tracings of **i(p) and ii(p)**.

The phenocryst fragment major axes span ~2 μm - ~1 mm, with the fragments contributing ~8-15 % (**A.4.6.**) to the vein-filling material, which is close to the estimated amount of intact phenocrysts in the host (~10-25 %). The fragments appear to have a similar composition to those in the host, but confirmation of this requires geochemical analysis. Angular obsidian clasts and phenocryst fragments also occur within some vesicles in Skriðugil's centre, and these are thought to derive from the thin section-making process (**A.4.7.**), and will not be discussed further.

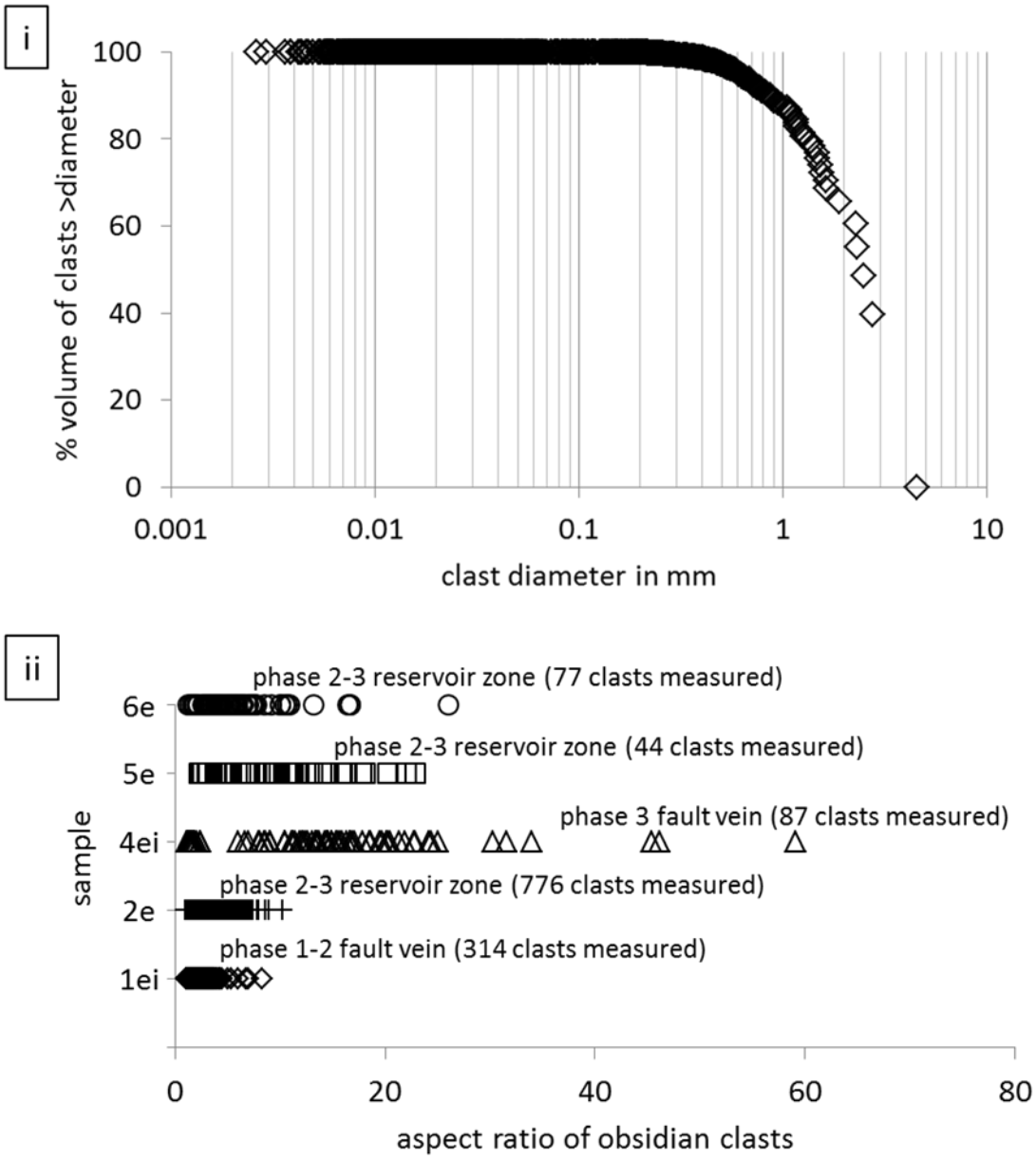

Figure 4.16. (i) Size of obsidian clasts in tuffisite veins, 1295 clasts were measured in five tuffisite veins from Thumall (samples 1ei, 2e, 4ei, 5e and 6e). **(ii)** Aspect ratios of the same clasts.

Some authors have reported the finest material within tuffisite veins as commonly occurring at the vein margins (Heiken et al., 1988; Tuffen et al., 2003; Tuffen and Dingwell, 2005; Goto et al., 2008). However, the margins of the reservoir zones were found to consist of fine (grains <10 μm), or fine to coarse ash (grains <10 μm to 1 mm), whereas injection veins are only filled with fine grained material. Fine grained tuffisite vein margins commonly have irregular feather-like edges (**Fig. 4.17.**). Fine material, which commonly occurs along reservoir zone margins is often

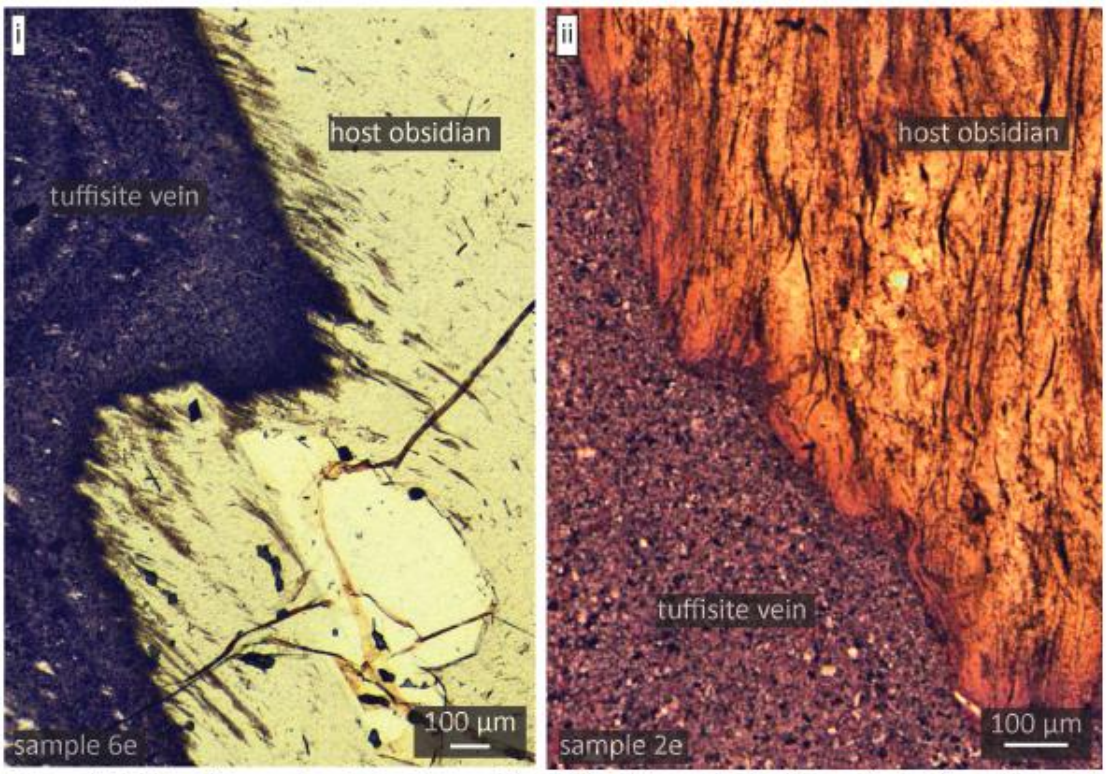

Figure 4.17. Microphotographs taken in plane polarised light of fine grained tuffisite vein margins, with feather-like edges.

laminated, with individual laminations being ~100-500 µm wide; some laminations are continuous throughout petrological thin sections, whereas others are discontinuous, being no longer than a couple of millimetres. The grains within the laminations are generally smaller than 10 µm. Grains often coarsen across the width of laminations, but sometimes the grains are a similar size throughout (**Fig. 4.18.i**). Some laminations are truncated (**Fig. 4.18.i**), it is common for there to be a few relatively large (~100-500 µm) obsidian clasts within the fine grained marginal laminations (**Fig. 4.18.ii**). The fine grained laminations at the reservoir zone margins sometimes continue gradationally into the injection veins (**Fig. 4.18.ii**). However, sometimes the contact between the injection veins and reservoir zones is defined by a sharp surface and abrupt change in grainsize, with the injection vein consisting of fine material and the reservoir zone being coarser grained (**Fig. 4.18.iii**). In such instances the fine material in the injection vein usually continues in one direction for a few millimetres

along the reservoir zone wall (**Fig. 4.18.iii**). Not all of the tuffisite veins contain laminations and not all display grainsize sorting. For instance, some phase 1-2 fault veins just contain a poorly sorted mix of fine to coarse grains (**Fig. 4.19.**).

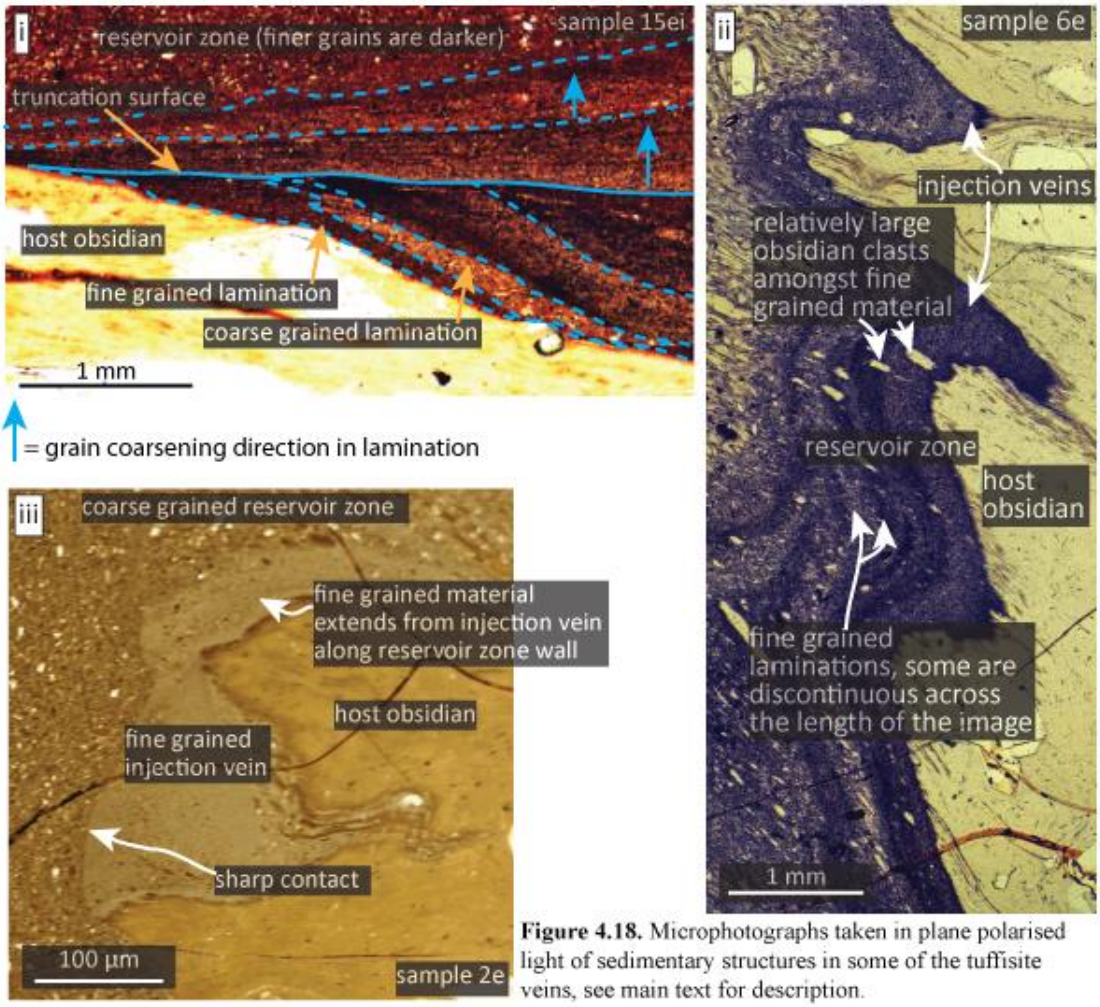

Figure 4.18. Microphotographs taken in plane polarised light of sedimentary structures in some of the tuffisite veins, see main text for description.

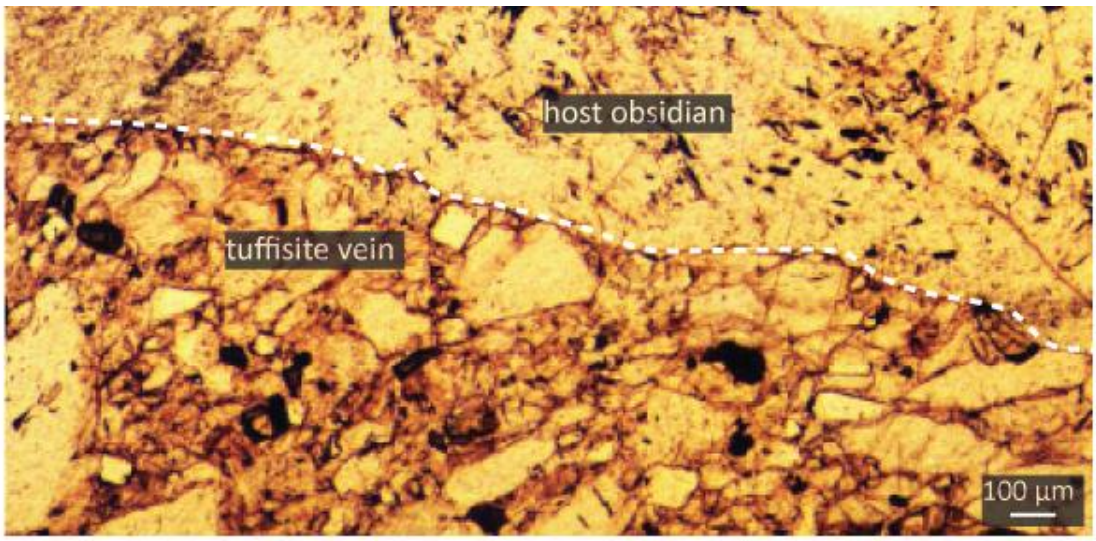

Figure 4.19. Poorly sorted grains in a phase 1-2 fault vein (sample 1ei).

Similarly, the reservoir zone centres generally just consist of a poorly sorted mix of grains. However, some discrete, well sorted, fine grained layers occur locally in the reservoir zone centres. In such instances, the fine grained layers weave between coarser grained layers (**Fig. 4.20.i**); the contrasting layers have different orientations, with the coarser grained layers being parallel or sub-parallel to the vein margins and the fine grained layers having more random orientations. Some of these fine grained layers are truncated (**Fig. 4.20.ii**). The fine grained material within the reservoir zones is not only found in layers, as fine grained ash aggregates occur within coarser grained parts of reservoir zones. The aggregates have sub-circular forms, and thus contrast with surrounding obsidian clasts, which have irregular forms, being deformed next to the aggregates (**Fig. 4.21.**).

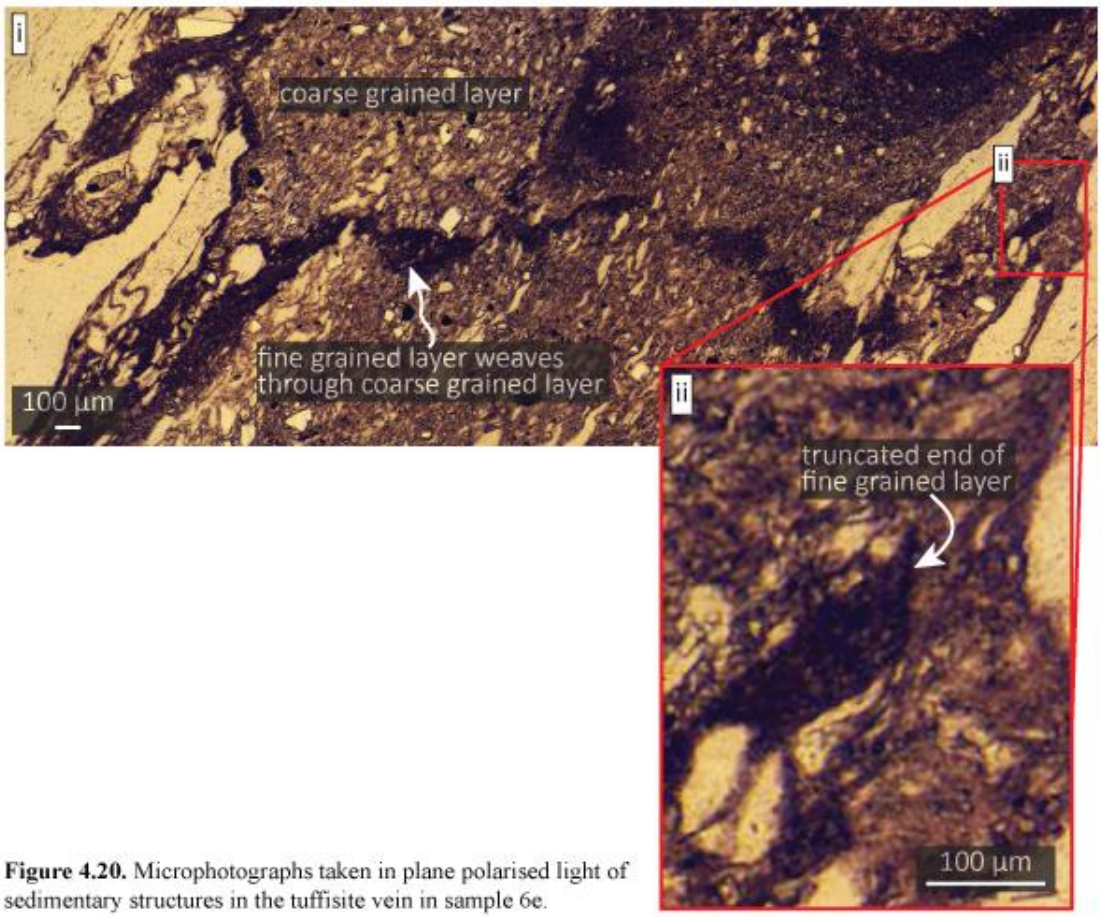

Figure 4.20. Microphotographs taken in plane polarised light of sedimentary structures in the tuffisite vein in sample 6e.

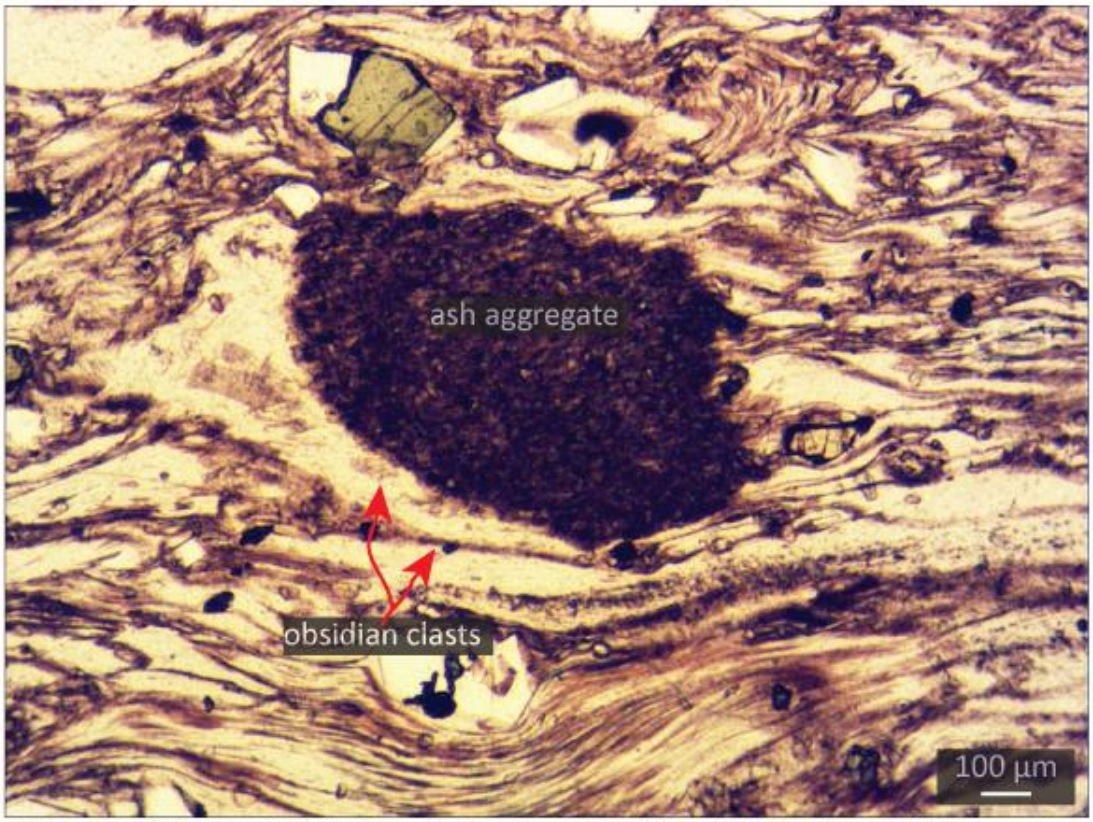

Figure 4.21. Microphotograph of a fine grained ash aggregate within the tuffisite vein in sample 6e.

ii) Bubbles and microlites

The host obsidian and obsidian clasts in the phase 1-2 tuffisite veins in the upper part of Thumall contain bubbles that are 100 µm - 1.5 mm long. The bubbles are elongate, with some having regular lenticular forms. However, many have irregular pinch-and-swell forms, with rounded and angular edges (**Fig. 4.22.i**). The bubbles are often proximal to other bubbles, phenocrysts, microlite trains or microlite laths. Some bubbles have microlites on their surfaces (**Fig. 4.22.ii**) and a few are intersected by unhealed arcuate to linear cracks.

Discontinuous microlite trains and clusters occur throughout Thumall in the vesicle-free host obsidian and also within vesicle-free obsidian clasts in the tuffisite veins. Two types of microlites form the trains and clusters; some are sub-circular and <5 µm wide, whereas other are 1-20 µm long and lth-like. These microlites also occur

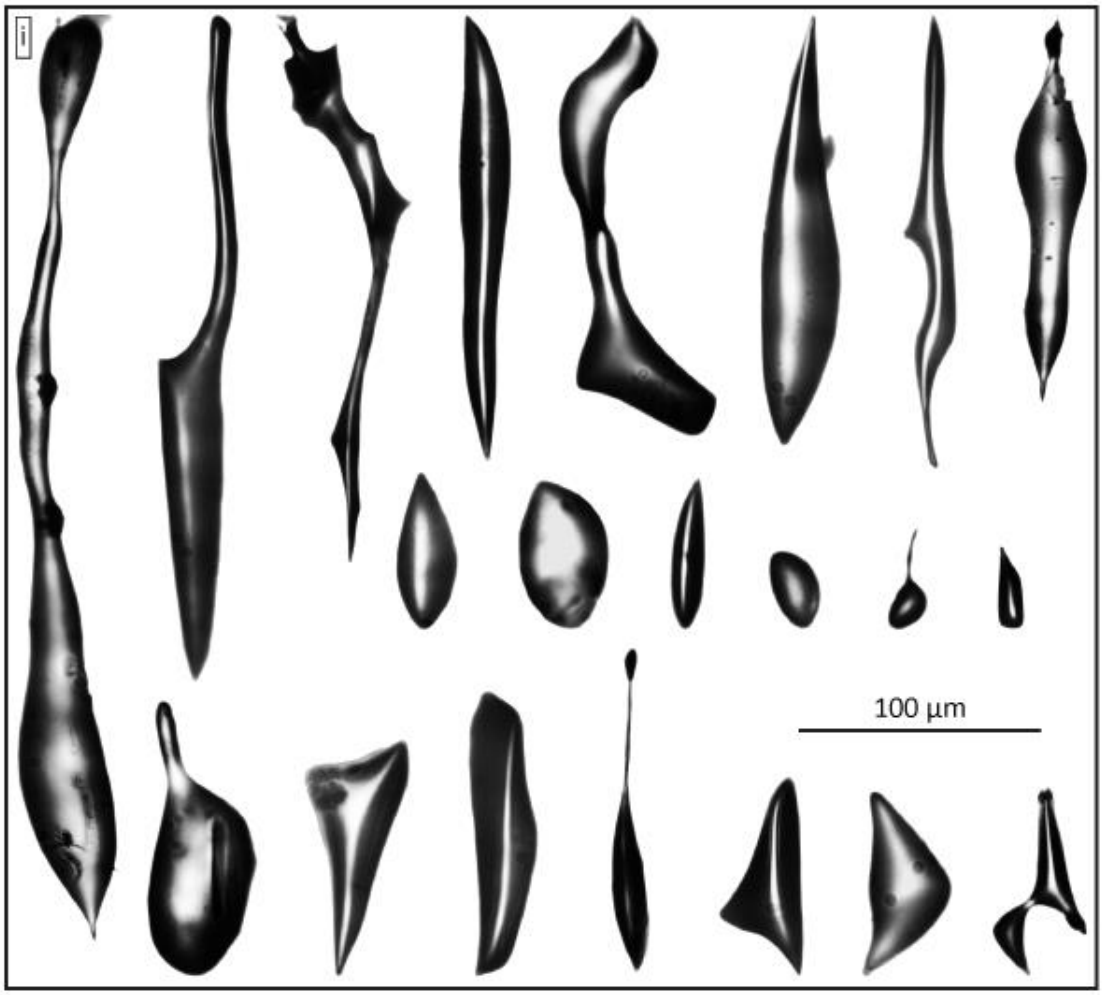

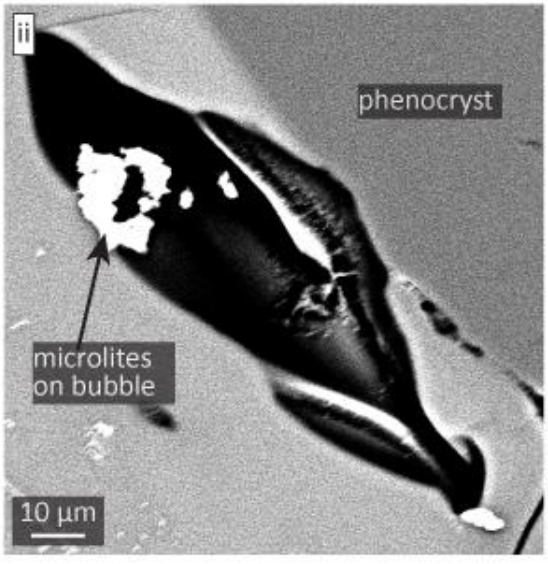

Figure 4.22. (i) Irregular shaped bubbles in the host obsidian in sample 1ei. Each bubble is an individual microphotograph taken in plane polarised light, backgrounds were converted to white in Photoshop. **(ii)** BSE image of a bubble in the host obsidian in sample 1ei, the bubble has microlites on its surface.

on some bubble surfaces and extend from bubbles into the trains (**Fig. 4.23.i-v**), and it is common for two trains to surround a central cluster of microlites (**Fig. 4.23.vi**), with bubbles lacking.

Individual microlite trains are ~10-200 µm long. Train and cluster number

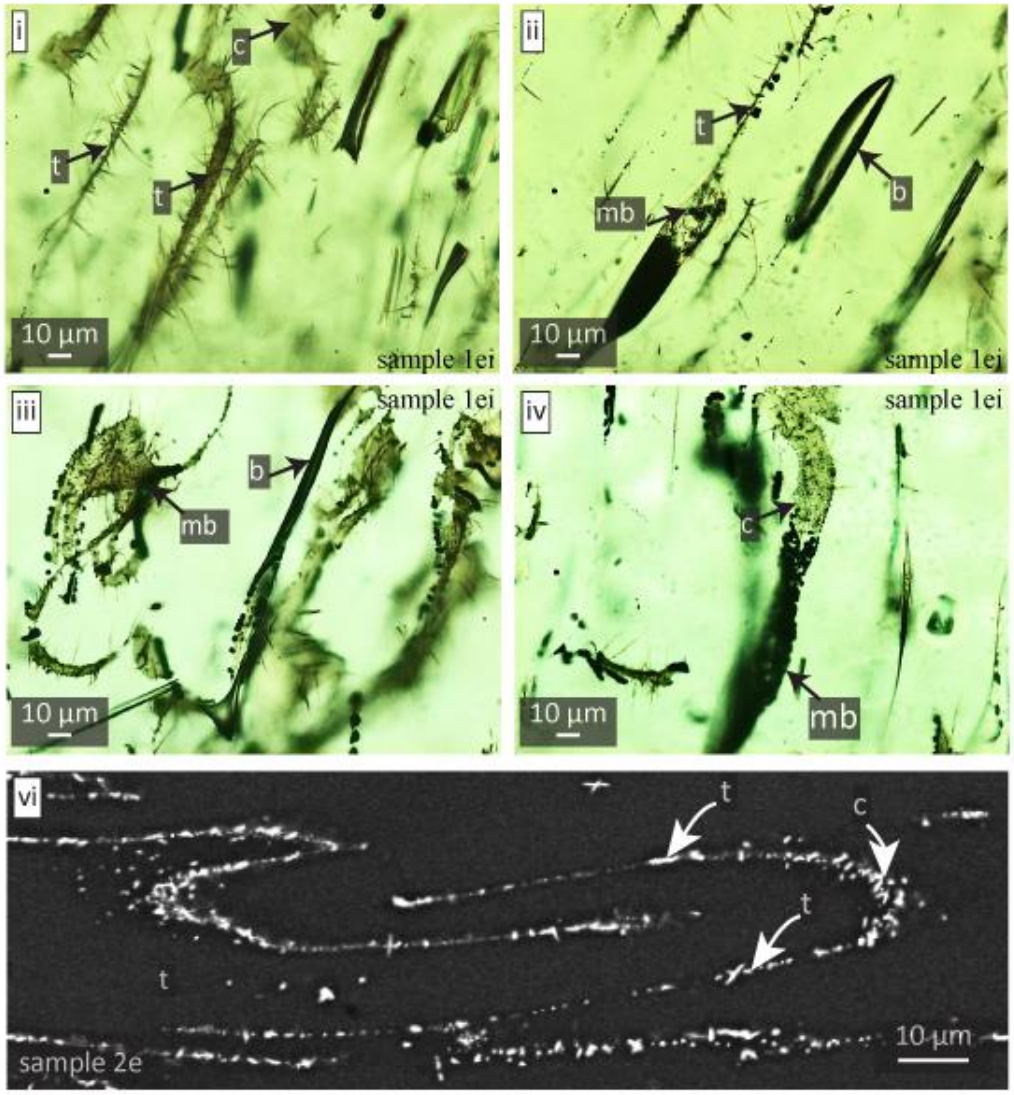

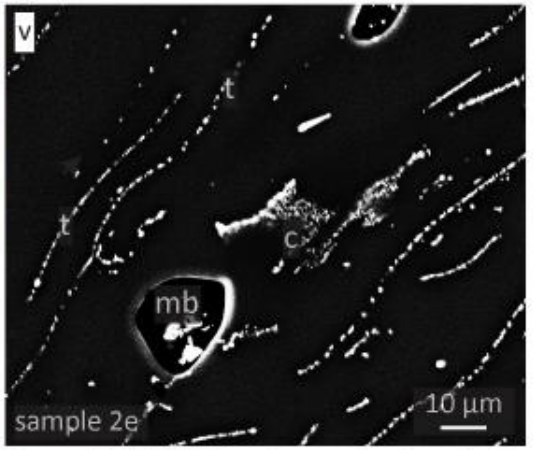

Figure 4.23. (i-vii) Discontinuous microlite trains (t), clusters of microlites (c) and microlites on bubble (b) surfaces (mb) in the host obsidian. **(i-iv)** Plane polarised light microphotographs. **(v and vi)** BSE images.

density is variable in the host, and particularly high in the host bordering the feather-like tuffisite vein margins (**Fig. 4.24.i and ii**), but lower next to the relatively linear vein margins (**Fig. 4.24.iii and iv**). The microlite trains form a fabric in the host, which is generally concordant with the phase 3 veins, and discordant with, and truncated by phase 1-2 veins (Tuffen and Dingwell 2005).

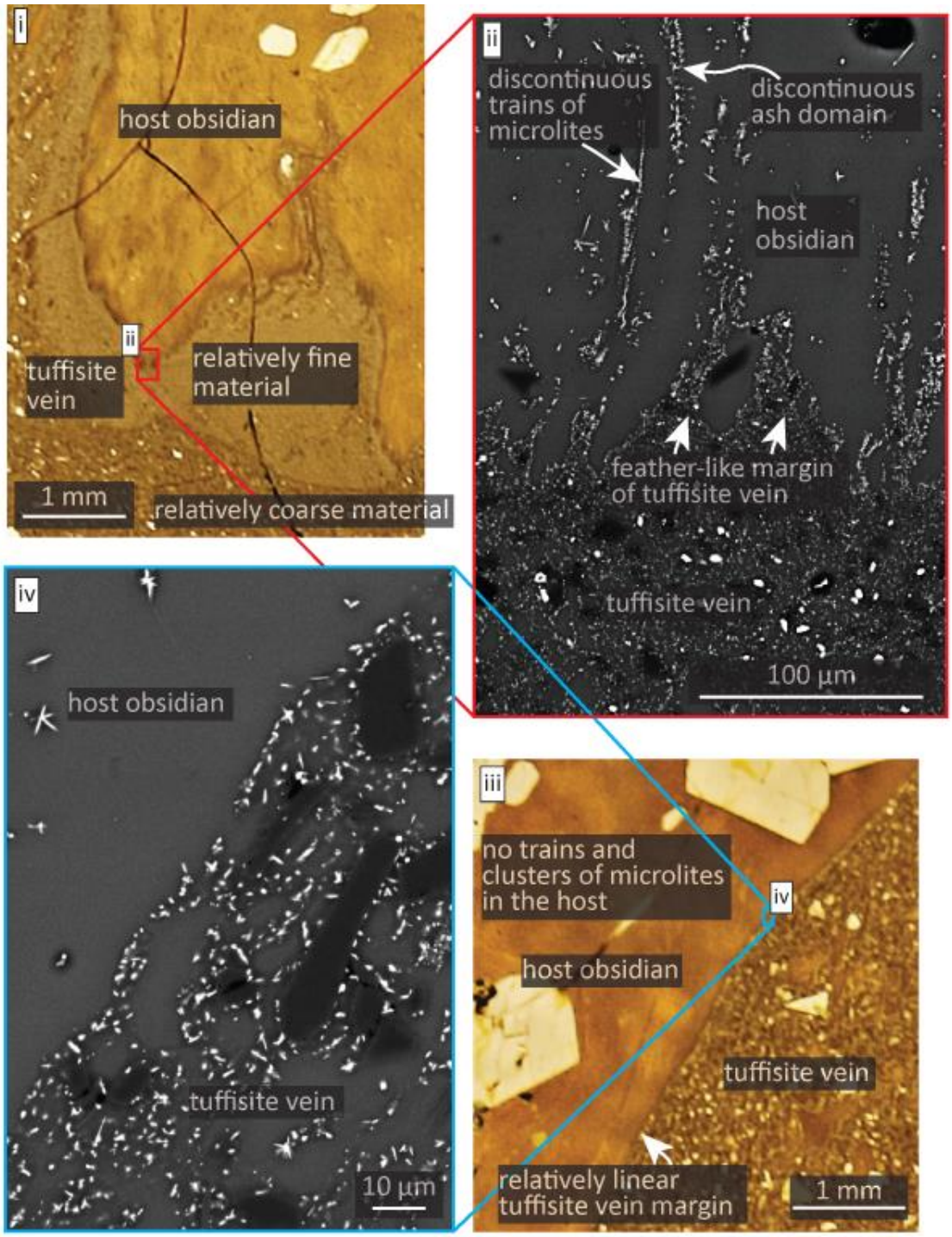

Figure 4.24. The host-tuffisite vein contact in sample 2e, see main text and labels for description. **(i and iii)** Photographs of the petrological thin section. **(ii and iv)** BSE images.

Microlite trains and clusters also occur within some obsidian clasts in the tuffisite veins (**Fig. 4.25.i**), but no correlation was found between clast size and the presence or absence of trains. In phase 2-3 veins, the trains are deformed around phenocryst fragments (**Fig.4.25.ii-v**). The trains and clusters are absent in Skriðugil's vesicular centre and in the vesicular clasts; it remains unconfirmed as to whether they occur in Skriðugil's margins. Similar microlites to those that form the trains and clusters occur on obsidian clast surfaces (Tuffen and Dingwell, 2005; **Fig. 4.26.**).

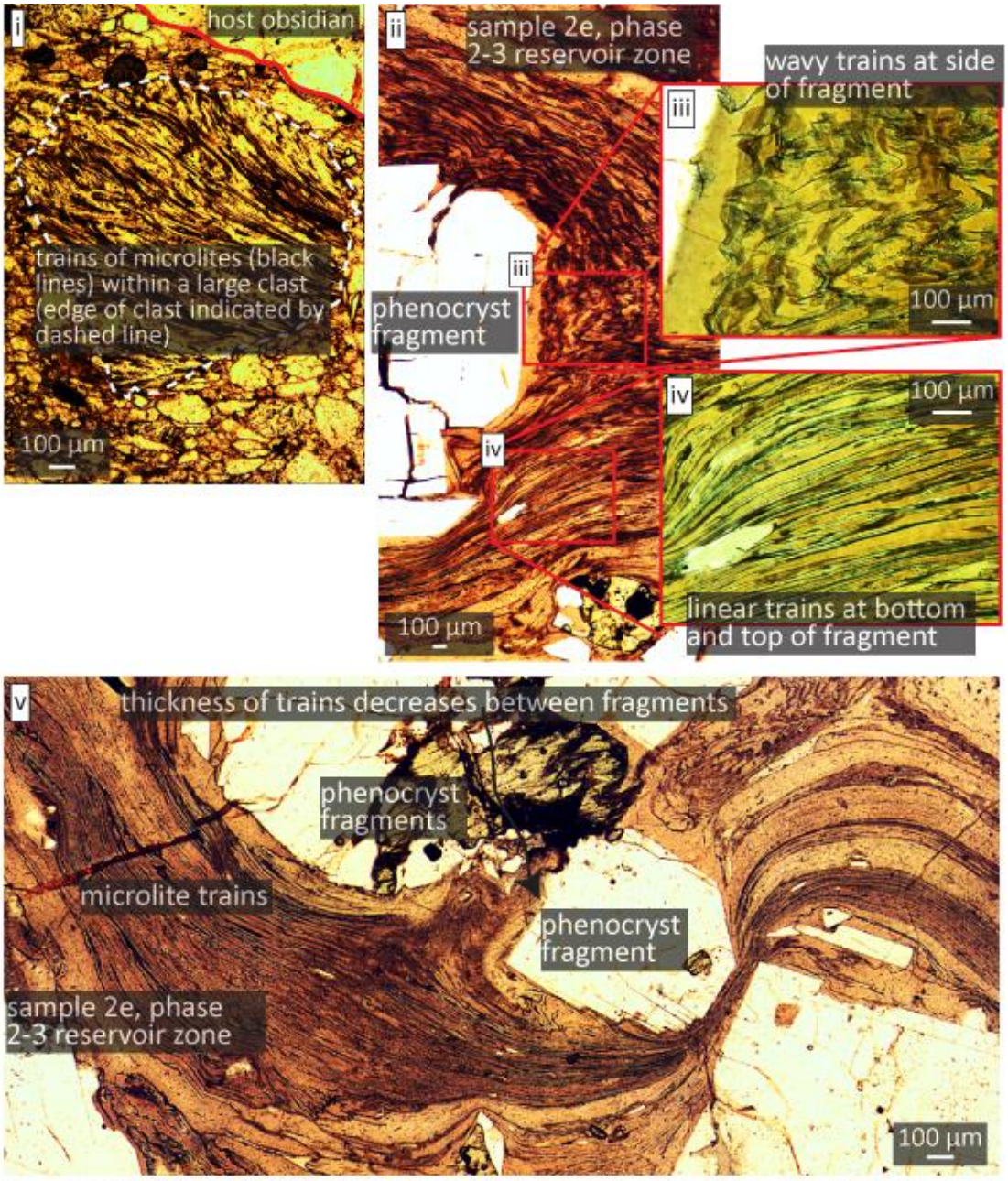

Figure 4.25. Plane polarised light microphotographs of microlite trains within tuffisite veins. The trains are deformed next to phenocryst fragments.

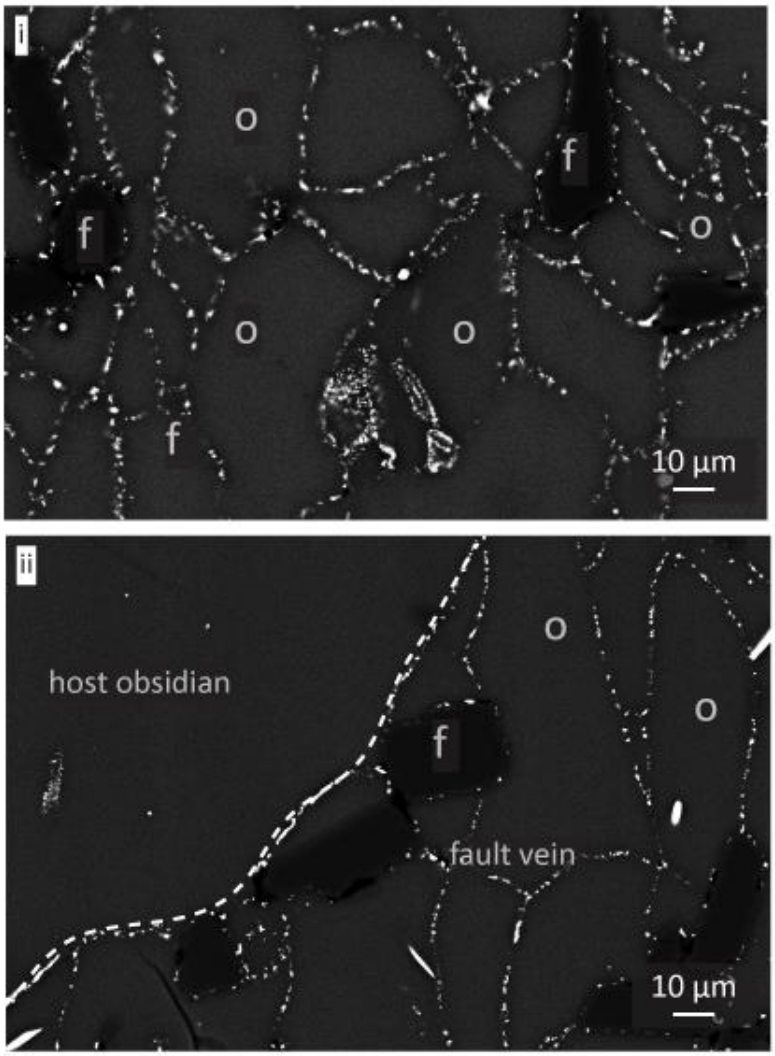

Figure 4.26. (i) BSE image of a phase 1-2 fault vein in sample 1ei from Thumall. **(ii)** BSE image of the same fault vein as in **i** and the bordering host obsidian. Obsidian clast (o) edges are defined by microlites (white) that coat the clast surfaces. Phenocryst fragments (f) do not have microlites on their surfaces.

Isolated lath-like microlites that are ~10 µm wide and ~100 µm long also occur in the host obsidian and within obsidian clasts in the tuffisite veins. These generally have a similar orientation to one another and constitute 2-10 % of the host obsidian. Proximal to a tuffisite vein in Skriðugil, the lath-like microlites are perpendicular to the vein margin, but their orientation changes progressively away from the margin (**Fig. 4.27.**).

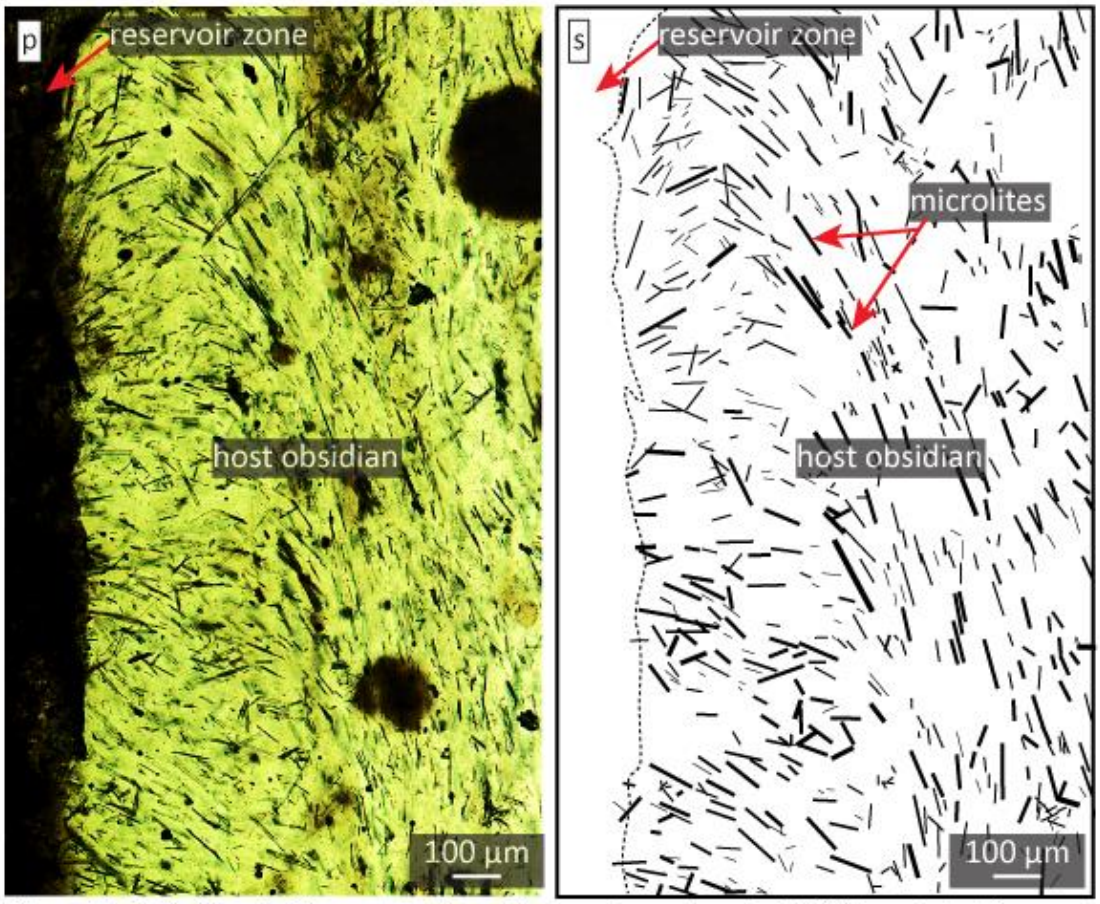

Figure 4.27. Lath-like microlites next to a phase 1-2 reservoir zone (sample skri 2). See main text for description. **(p)** Plane polarised light microphotograph. **(s)** Tracing of **p**.

4.4. Obsidian colour in microphotographs and electron backscatter intensity in BSE images

The obsidian colour in any two samples is often different, ranging from yellow to dark brown in petrological thin section. The colour also varies within individual samples; for instance, in sample 3ei the host is predominantly dark brown, but yellow bands occur next to phase 3 tuffisite veins (**Fig. 4.28.i and ii)**. The bands are ~100 µm to 1 mm wide and are deflected around a phenocryst (**Fig. 4.28.i**). The colour variation does not correspond to variation in the electron backscatter intensity (**Fig. 4.28.iii**) or the amount of microlites or nanolites.

Some of the obsidian clasts within the phase 2-3 tuffisite veins also display colour variations, as large clasts have light coloured centres and dark rims, whereas

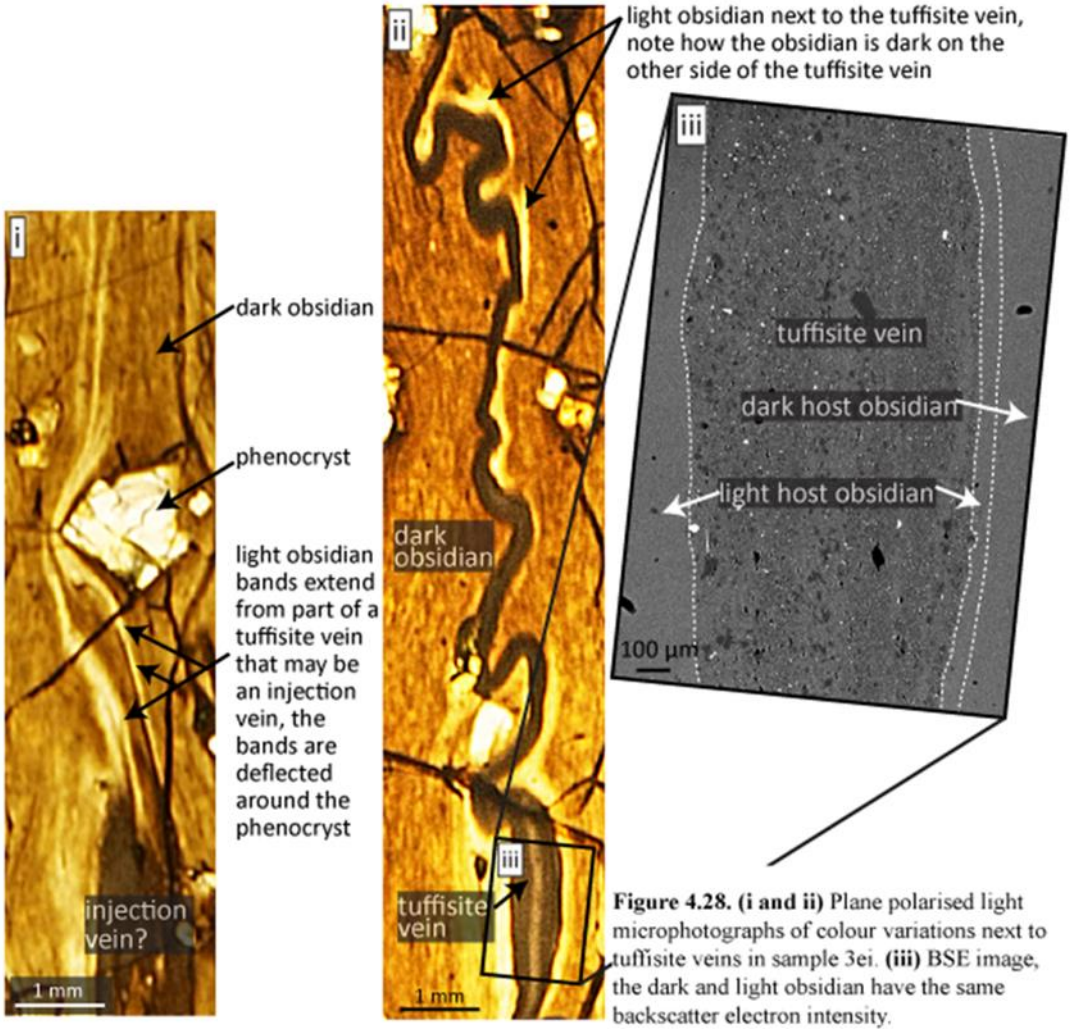

Figure 4.28. (i and ii) Plane polarised light microphotographs of colour variations next to tuffisite veins in sample 3ei. **(iii)** BSE image, the dark and light obsidian have the same backscatter electron intensity.

smaller clasts are dark throughout (**Fig. 4.29.i and ii**). However, these may be the edges of large clasts, i.e., cross sections positioned near clast edges and not through clast centres. The colour variation conforms to the irregular shape of the clasts (**Fig. 4.29.ii**). Similar colour variations occur in welded pyroclastic deposits (Ross and Smith 1961; **Fig. 4.29.iv**). None of the aforementioned colour variations correspond to variation in the electron backscatter intensity (**Fig. 4.29.iii**).

However, variations in the backscatter intensity do occur, coming in three forms. Firstly, the host obsidian locally contains polygonal shapes, the edges of which are defined due to them having weak backscatter intensities relative to the bulk of the host, and microlite positions commonly coincide with the shape edges (**Fig. 4.30.i**).

Secondly, areas with weak backscatter intensities also occur in ~15 μm wide bands of the host obsidian next to some fractures (**Fig. 4.30.ii**). Some of these bands are continuous along fracture lengths, whereas others are not. These fractures are linear to arcuate, ~1->10 cm long, unhealed, and they cut through all other textures.

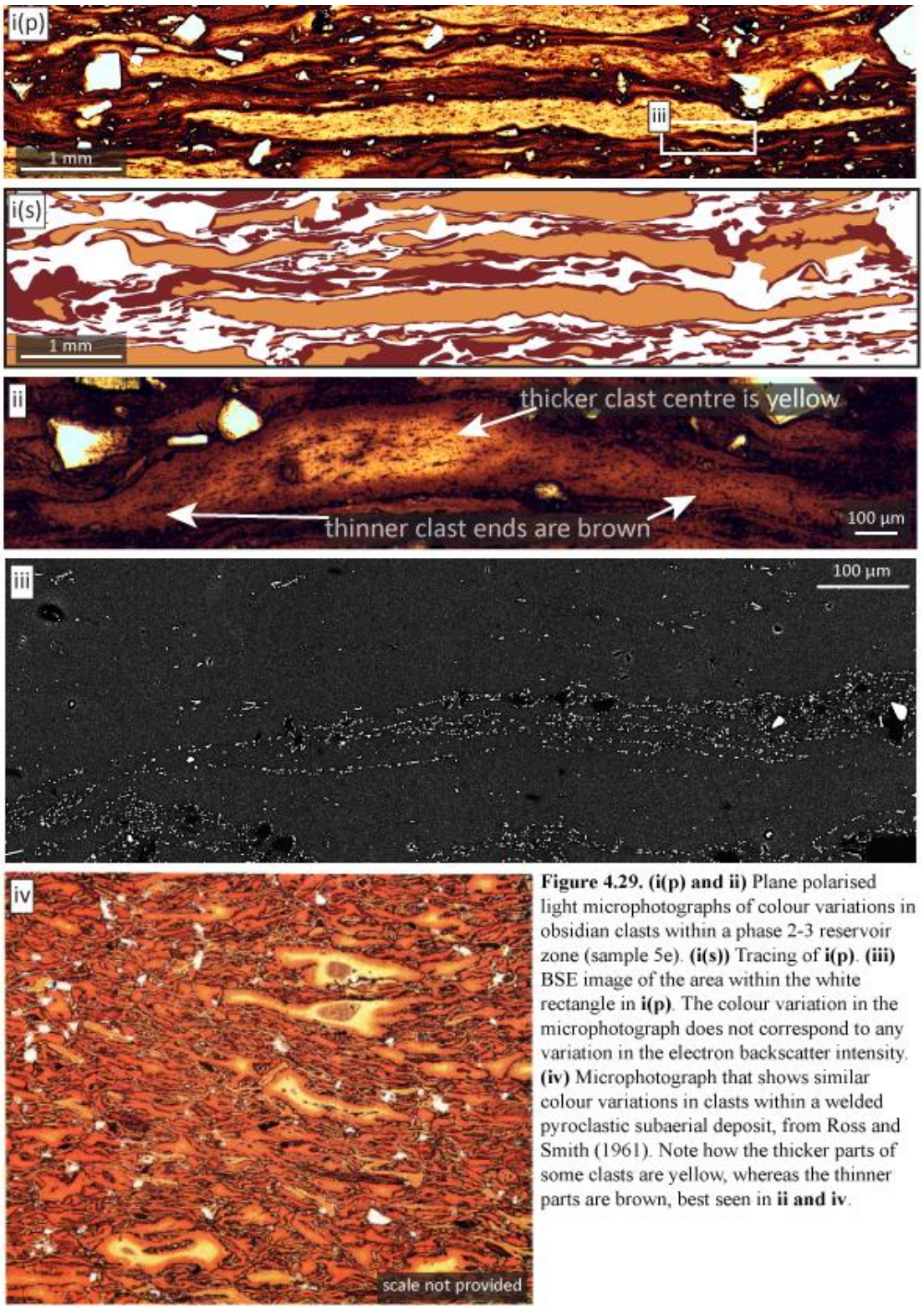

Figure 4.29. (i(p) and ii) Plane polarised light microphotographs of colour variations in obsidian clasts within a phase 2-3 reservoir zone (sample 5e). **(i(s))** Tracing of **i(p)**. **(iii)** BSE image of the area within the white rectangle in **i(p)**. The colour variation in the microphotograph does not correspond to any variation in the electron backscatter intensity. **(iv)** Microphotograph that shows similar colour variations in clasts within a welded pyroclastic subaerial deposit, from Ross and Smith (1961). Note how the thicker parts of some clasts are yellow, whereas the thinner parts are brown, best seen in **ii and iv**.

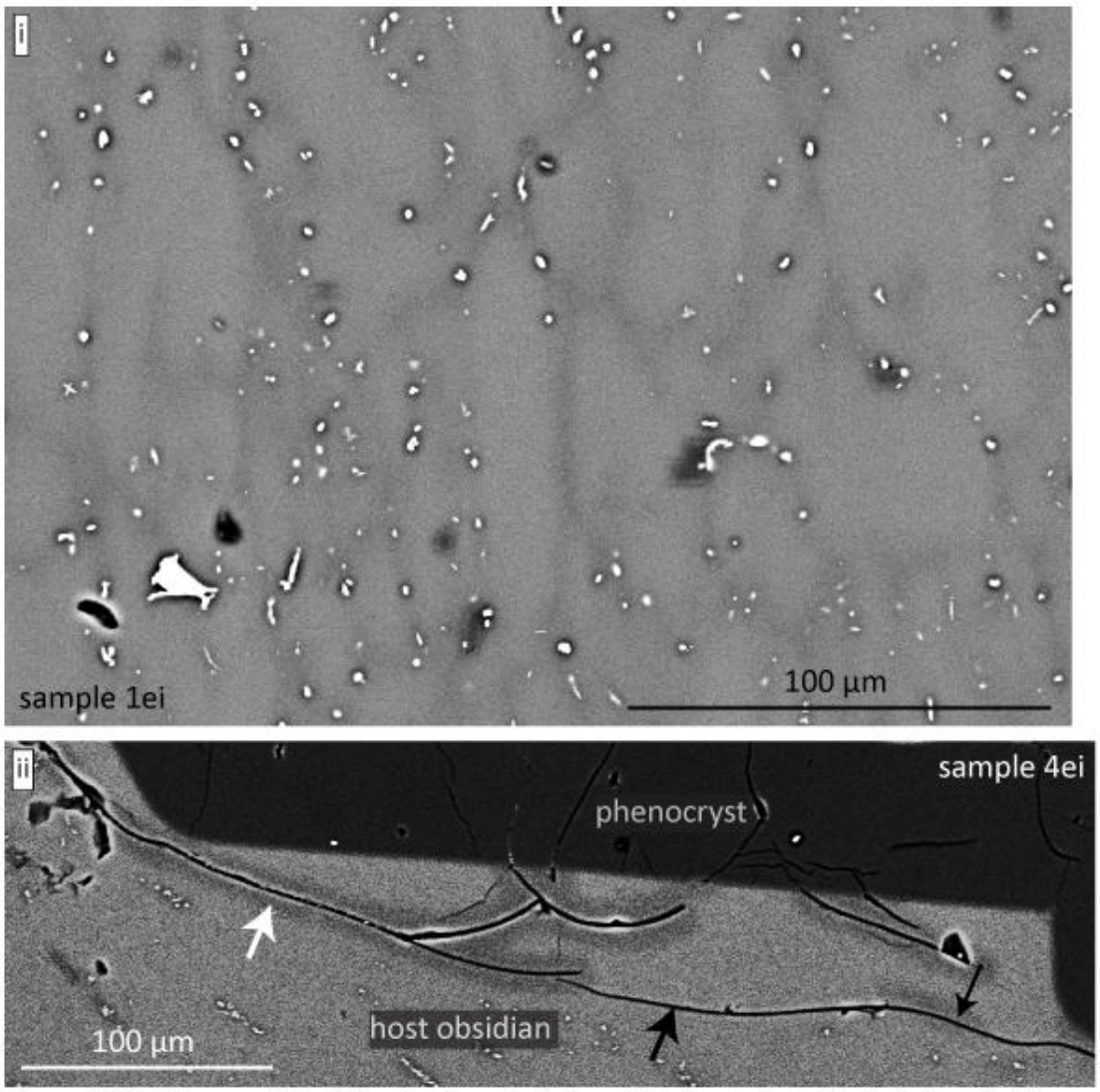

Figure 4.30. BSE images. **(i)** Dark lines that have relatively weak backscatter intensities in the host obsidian define polygonal shapes, microlites (white) occur on the lines. **(ii)** Dark areas that have relatively weak backscatter intensities occur in the host obsidian next to fractures (black lines). The white arrow points to a dark band that is continuous along a fracture length, the lower black arrow points to part of a fracture where there is no dark band and the upper black arrow points to a discontinuous dark band next to the same fracture. The dark areas have weak electron backscatter intensities relative to the bulk of the host obsidian.

4.5. Water concentration

4.5.1. Macro-scale

Water measurements were made using benchtop and synchrotron-source Fourier transform infrared spectroscopy (BFTIR and SFTIR, respectively). Please see **section 2.3.** for methodology and errors, and **A.4.1.** for sample thicknesses, elevations, errors and details of water measurements. The 3570 cm^{-1} absorption peak represents the

combined concentration of dissolved molecular water (H_2O_m) and water dissolved as hydroxyl groups (OH^-), i.e., the total dissolved water content (H_2O_t; Newman et al., 1986). This peak was used to determine H_2O_t in the obsidian; other absorption peaks are unique to H_2O_m and OH^-, but the water content in the dykes is too low for any detectable absorption at these peaks (**section 2.3.**). H_2O_t was measured in the host obsidian at various elevations of Thumall, and in fine grained (grains <10 μm) zones and relatively large (100 μm to 1 mm) obsidian clasts within tuffisite veins from Thumall by using BFTIR and SFTIR. The water content was also measured along transects in the host obsidian next to tuffisite veins from Thumall and Skriðugil using SFTIR. The measured values from the SFTIR and BFTIR are similar, with maximum variation for individual samples being 0.01 wt. % (**A.4.1.**).

The host obsidian water content within Thumall is variable at each elevation, and decreases with increased elevation (**Fig. 4.31.**). The maximum horizontal and vertical variations are ~0.02 wt. % and ~0.08 wt. %, respectively. There is no systematic difference in the water content between large clasts and host obsidian, whereas fine grained zones have water concentrations lower than or similar to those of the host and large clasts (**Fig. 4.31.**). A large contribution of the total error (**Fig. 4.31.i**) associated with the water measurements will cause the data points to move by the same amount, i.e., the broad trend of decreasing water with increased elevation will be preserved. In contrast, errors associated with wafer thickness measurements are unique to each measurement, but these errors are relatively small (**Fig. 4.31.ii**) and will not cause the broad trend in the data to be lost. See **section 2.3.6.** for more details on errors.

Solubility pressure curves were made using VolatileCalc (Newman and Lowenstern, 2002), employing a similar method to that previously used to reconstruct

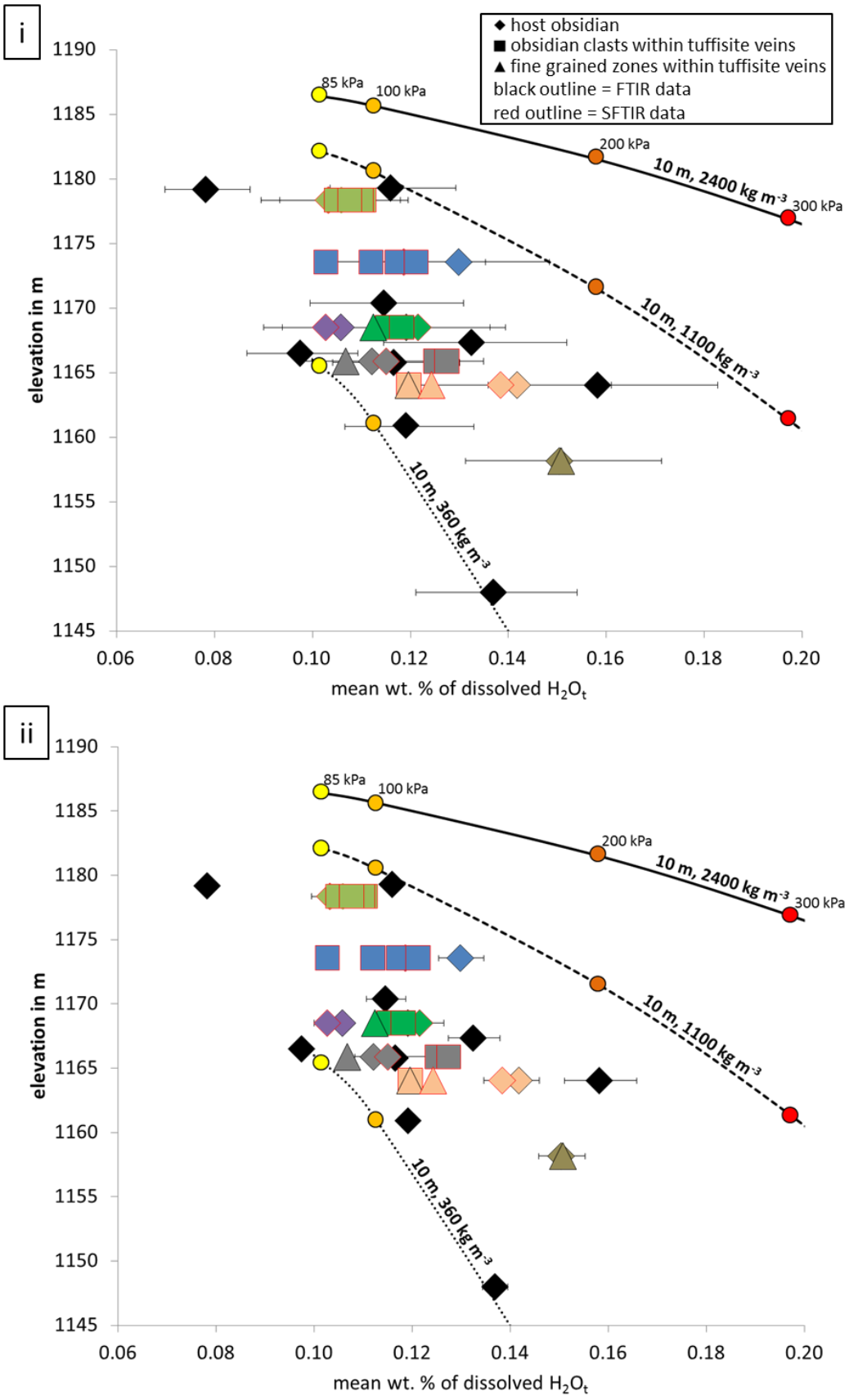

Figure 4.31. Water content in Thumall, the different colours represent different samples, except for black, which represents multiple samples. **(i)** Total error. **(ii)** Just error associated with thickness measurements, some error bars are smaller than the data points. See main text for further information. The elevation error bars are smaller than the data points. Lines are solubility pressure curves that represent different densities (labelled) of overburden and an overlying lava thickness of 10 m.

palaeo-ice thicknesses (Tuffen et al., 2010; Owen et al., 2012; Owen et al., 2013b; Owen, 2013). Please see **section 2.3.5.** for methodology and **A.4.8.** for solubility pressure curves representing a range of conditions. The curves assume that the obsidian is CO_2-free; it is expected that CO_2 would have escaped early in the eruption, especially given the low water concentration today, and the lower solubility of CO_2 relative to H_2O (Tuffen et al., 2010). Furthermore, if any CO_2 remains it is below the detection limit (30 ppm; Tuffen et al., 2010) of the BFTIR and the SFTIR. An additional assumption is that the magmatic temperature was 800 °C, which is consistent with the estimated magmatic temperature for rhyolite at SW Torfajökull (750-800 °C; Gunnarsson et al., 1998).

Two solubility pressure curves bracket the data (**Fig. 4.31.**). These represent overburden (lava overlying and infilling the dyke) densities of 360 kg m^{-3} and 1100 kg m^{-3} and an overlying lava thickness of 10 m (**Fig. 4.32.**). An overlying lava thickness of 10 m is reasonable given the position of the lava carapace today (Tuffen, 2001; Tuffen and Dingwell, 2005). A solubility pressure curve representing a magmatic temperature of 800 °C, an overburden density of 2400 kg m^{-3} and an overlying lava thickness of 10 m is not consistent with the measured water content (**Fig. 4.31.**). A density of 2400 kg m^{-3} is considered an adequate estimate for vesicle-free rhyolite for three reasons. Firstly, it is similar to the density estimate of the vesicle-free lava in Thumall (2410 kg m^{-3}), determined using the water displacement methods (**A.4.3.** - measurements, **section 2.3.** - methodology and errors). Secondly, it is similar to the density estimate (2470 kg m^{-3}) for other samples from Torfajökull (Owen et al., 2012; Owen, 2013). Lastly, it is similar to the density (2348 kg m^{-3}; **A.4.3.**) estimated using the KWare Magma Software (Wohletz, 2002) and sample composition (Tuffen, 2001).

The water content within the host obsidian in two samples is less than expected, considering atmospheric pressure (~85 kPa) at 1180 m (**Fig. 4.31.**).

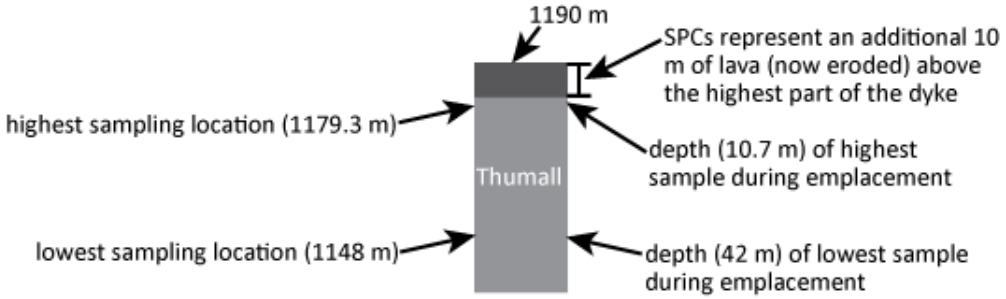

Figure 4.32. Schematic illustration explaining the conditions represented by the SPCs. Different densities of overburden are represented by different SPCs, which is not represented in the illustration.

4.5.2. Micro-scale

The water content was measured along ~300-500 μm long transects in the host obsidian, perpendicular to one phase 1-2 fault vein, four phase 2-3 reservoir zones and two phase 3 tuffisite veins (reservoir zones or fault veins) from Thumall, and one phase 2-3 reservoir zone from Skriðugil. The measurements were taken at a spacing of 8 or 12 μm, using an analytical area of 8×8 μm. Generally, there is little variation in the water content (**Fig. 4.33.**), and the water content is similar in the light and dark obsidian in sample 3ei (**Fig. 4.34.**). However, the water content is depleted (relative to the far-field host) over ~50 μm next to a tuffisite vein in this sample and next to a phase 2-3 reservoir zone from Skriðugil (**Fig. 4.34. and 4.35.**).

In contrast to the host obsidian, the water content in the tuffisite veins is more variable (**Fig. 4.36.**), and generally lower than in the surrounding host. In addition, relatively large depletions (~0.04-0.08 wt. % less than the host obsidian) coincide with phenocryst fragments and obsidian clasts that are ~100 μm wide (**Fig. 4.36.**). The water content in larger (>100 μm) clasts is less variable (**Fig. 4.37. and 4.38.**) than within fine grained zones.

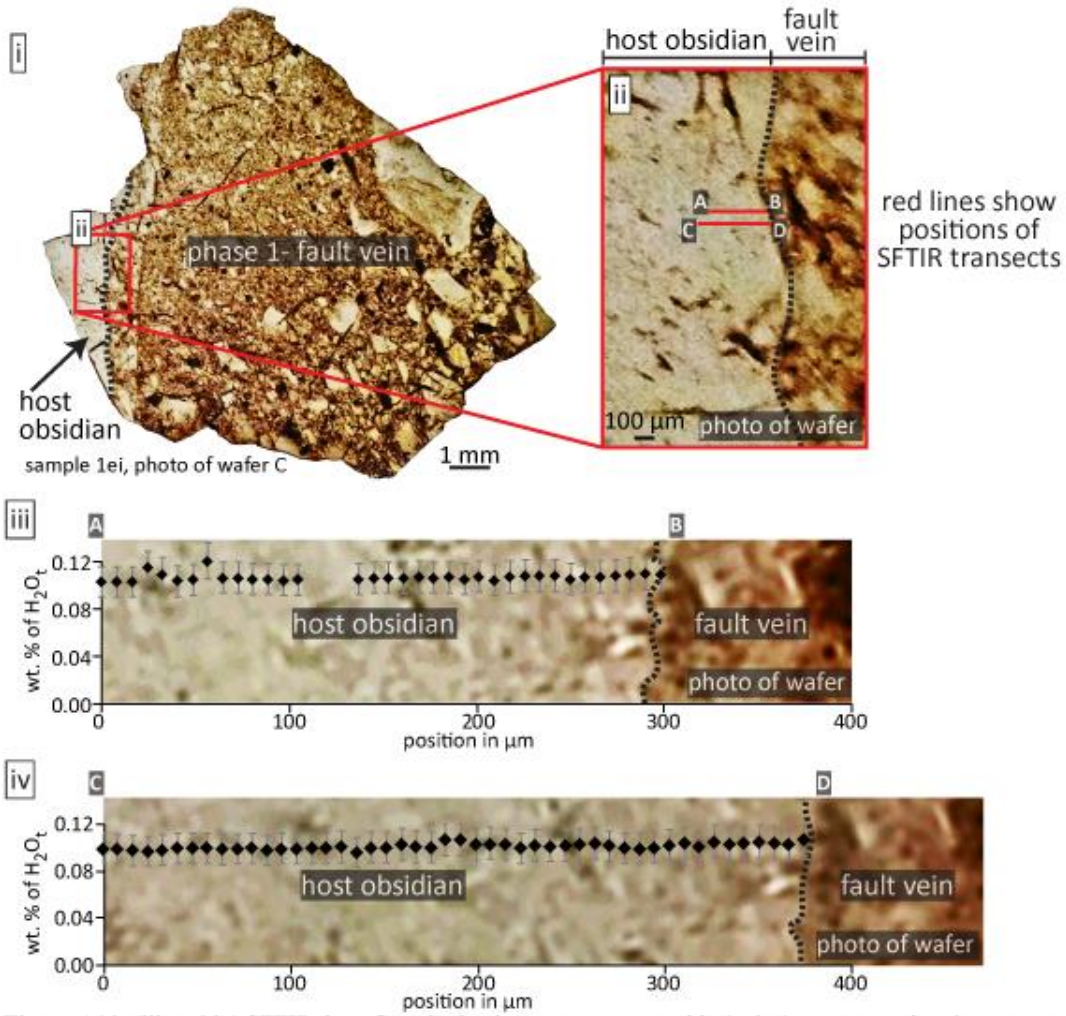

Figure 4.33. (iii and iv) SFTIR data. Gaps in the data represent unusable (noisy) spectra, each point represents an analytical spot size of 8×8 µm and the spacing between points is 8 µm.

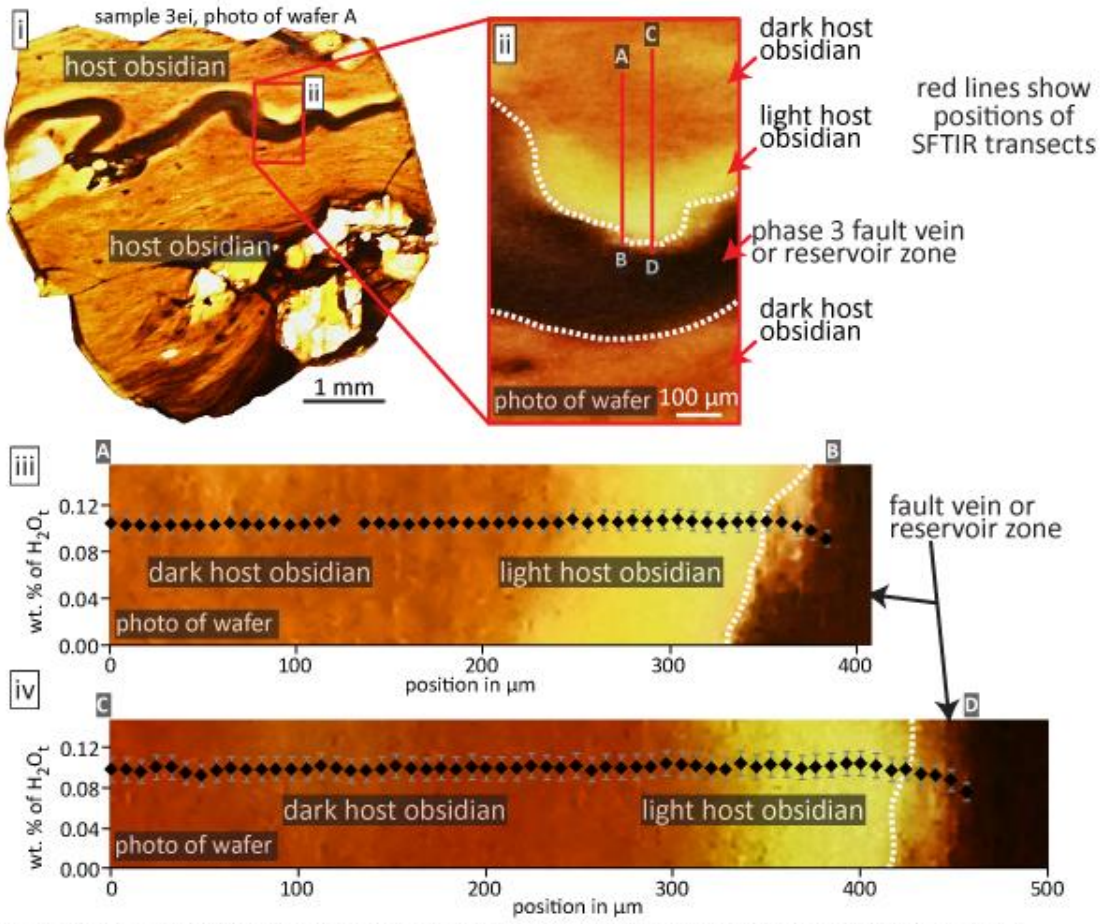

Figure 4.34. (iii and iv) SFTIR data. Gaps in the data represent unusable (noisy) spectra, each data point represents an analytical spot size of 8×8 µm and the spacing between the points is 8 µm.

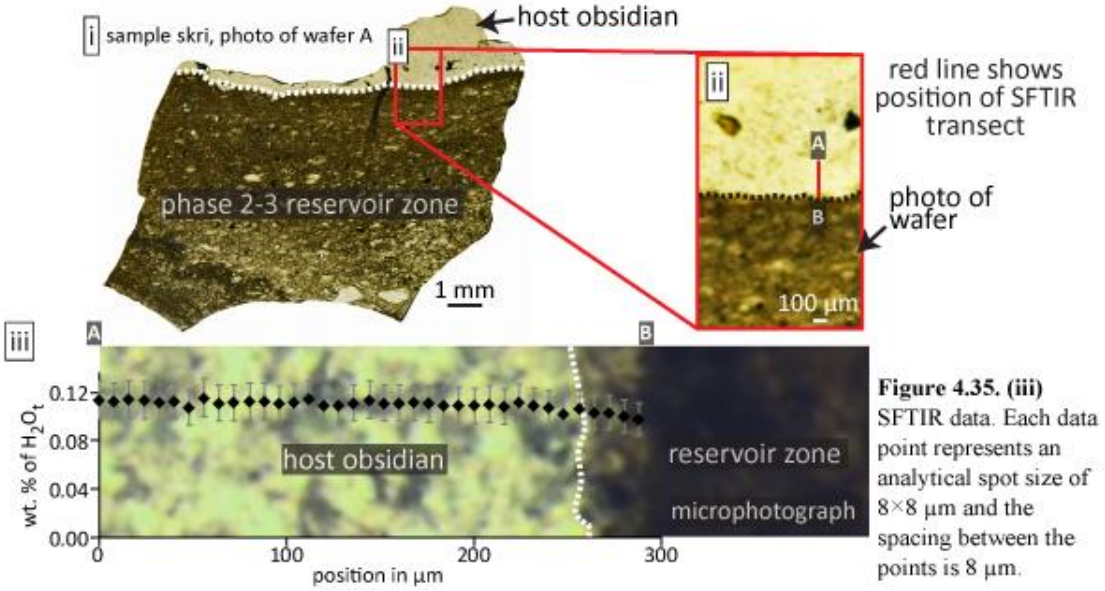

Figure 4.35. (iii) SFTIR data. Each data point represents an analytical spot size of 8×8 µm and the spacing between the points is 8 µm.

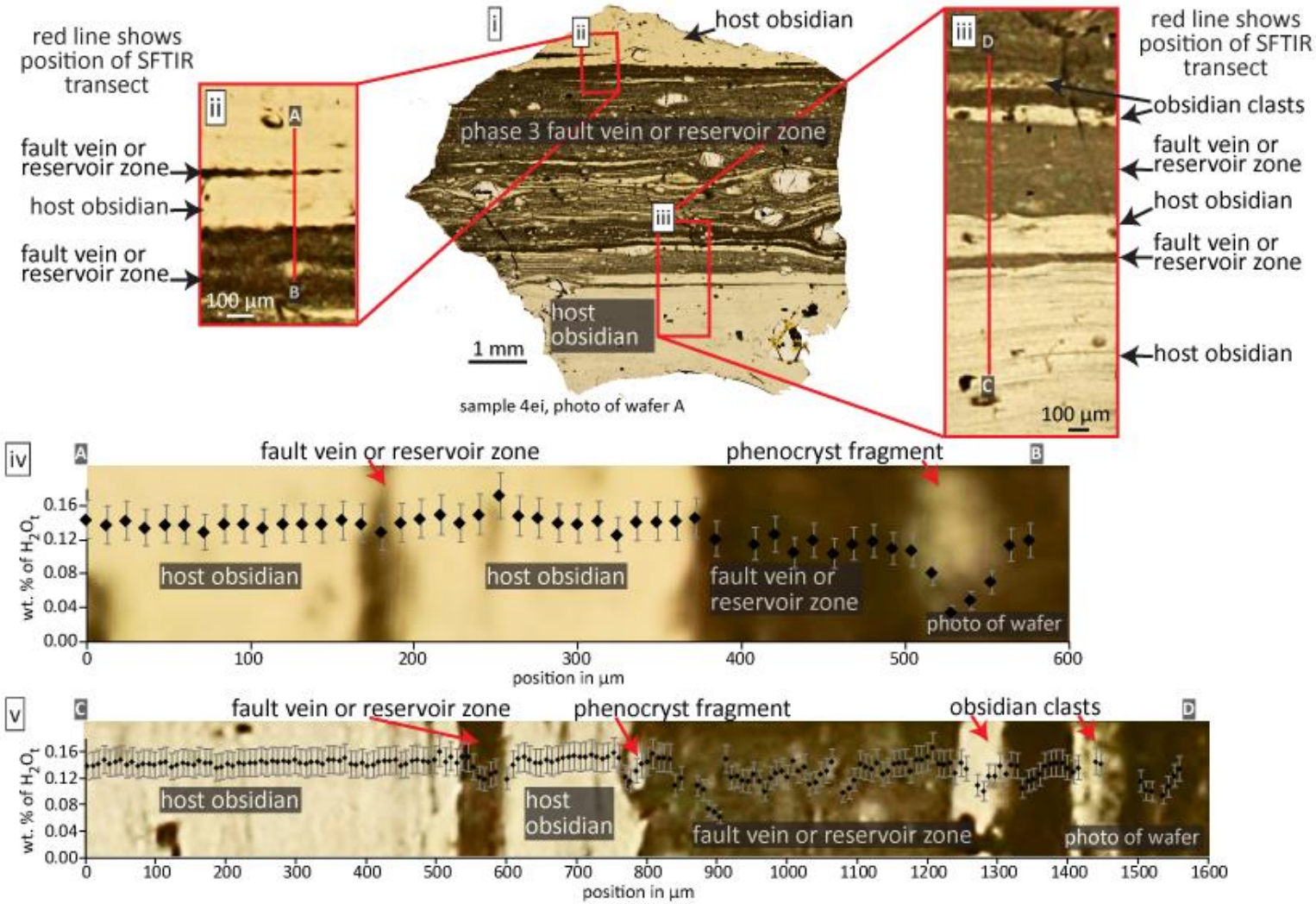

Figure 4.36. (iv and v) SFTIR data. Gaps in the data represent unusable (noisy) spectra, each data point represents an analytical spot size of 8×8 µm and the spacing between the points is 12 µm in transect A-B and 8 µm in transect C-D.

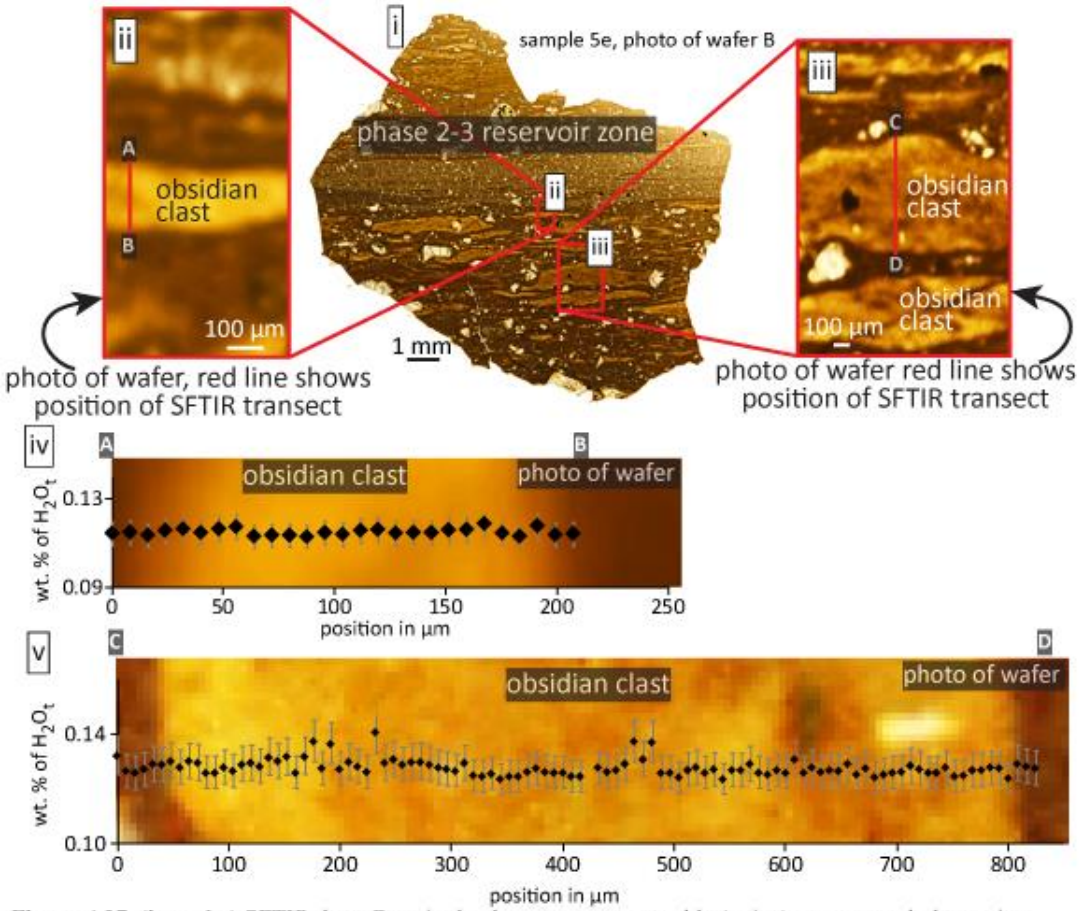

Figure 4.37. (iv and v) SFTIR data. Gaps in the data represent unusable (noisy) spectra, each data point represents an analytical spot size of 8×8 µm and the spacing between the points is 8 µm.

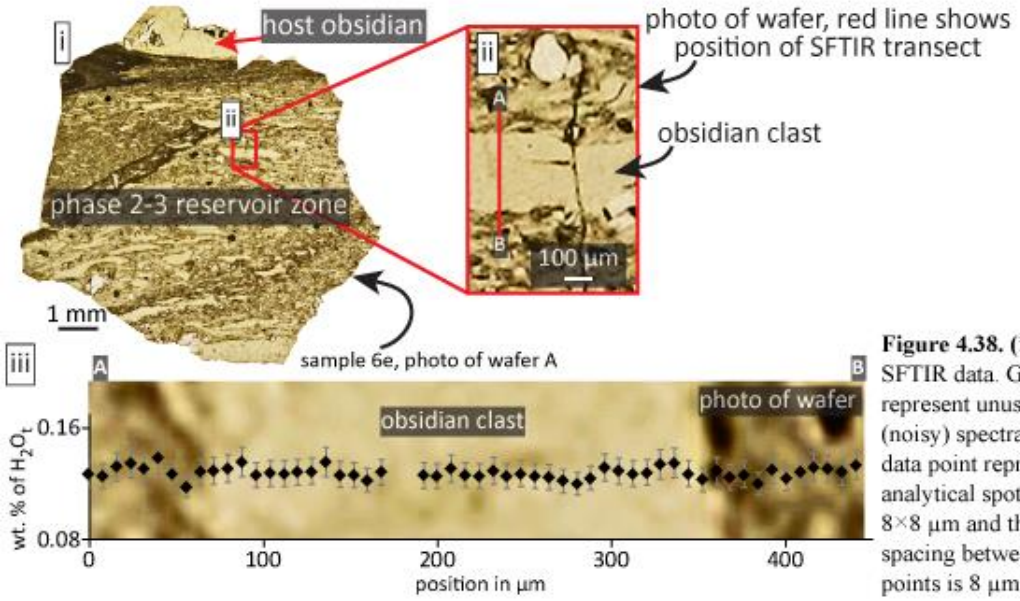

Figure 4.38. (iii) SFTIR data. Gaps represent unusable (noisy) spectra, each data point represents an analytical spot size of 8×8 µm and the spacing between the points is 8 µm.

4.6. Interpretation of textures

In this section the significance of the textures is discussed, and new models are presented regarding the formation and evolution of bubble networks and tuffisite veins during shallow (<50 m deep) magma ascent and emplacement.

4.6.1. Bubbles and tuffisite veins

In agreement with Eichelberger et al. (1986) here it is also argued that magma may ascend as permeable foam, which later collapses. However, in contrast to Eichelberger et al. and more in line Fink et al. (1992) here it is argued that bubble collapse occurred within the dykes, because the microlite trains and clusters are interpreted as being bubble collapse structures, as they sometimes extend from bubbles (e.g., **Fig. 4.23.i-iv**), and also because they are similar to bubble collapse structures previously observed in rhyolite (Iddings, 1888; Ross and Smith, 1961; Manley, 1995; Manley, 1996; Kano et al., 1997; Tuffen and Castro, 2008; Tuffen and Castro, 2009). The bubble collapse structures have a similar appearance to the deformed, microlite-coated obsidian clasts which characterise phase 4 tuffisite veins (Tuffen and Dingwell, 2005), but distinguishing between bubble collapse structures and phase 4 veins is possible by using five criteria. Firstly, the trains and clusters that are bubble collapse structures sometimes extend from bubbles (e.g., **Fig. 4.23.i-iv**). Secondly, some trains and clusters occur within obsidian clasts (e.g., **Fig. 4.25.**) and they cannot therefore be deformed obsidian clasts. Thirdly, the trains and clusters in the host obsidian are not intermixed with phenocryst fragments, and this would be expected if they were deformed obsidian clasts, because the obsidian clasts within the tuffisite veins are always intermixed with phenocryst fragments. Fourthly, two microlite trains commonly surround a central cluster (e.g., **Fig. 4.23.vi**), and this shape is thought to

reflect the lensoidal form of a deformed bubble. Finally, the trains and clusters were only observed in the vesicle-free obsidian, and not in the vesicular obsidian.

The microlites that define the bubble collapse structures are probably Fe-Ti oxides. Indeed, their strong electron backscatter intensities suggest that they have a high mean atomic number (Ginibre et al., 2002; Reed, 2005; Humphreys et al., 2008; Berlo et al., 2013) consistent with them being Fe-Ti oxides, but geochemical analysis of these phases has not been completed. Manley (1996) suggested that oxidised haloes may form around growing bubbles due to the greater diffusivity of H_2 relative to H_2O and O_2, and that this could promote microlite nucleation and growth. However, similar microlites to those found on the bubbles also occur on clast surfaces, some of which are not oxidised. Therefore, oxidation is not a prerequisite for the nucleation and growth of oxides; oxides will nucleate on a surface regardless of its redox state. This considered, it is thought that the microlites grew on bubble wall exteriors, especially as microlites occur on non-collapsed bubbles today (e.g., **Fig. 4.22.ii**). However, it cannot be dismissed that some microlites nucleated and grew on bubble wall interiors via vapour phase precipitation (Müller et al., 2001; Horwell et al., 2013; Schipper et al., 2015). It is also conceivable that some bubbles nucleated and grew on microlites, which has been observed during experimental heating of basalt (D'Oriano et al., 2013) and rhyolite (Hurwitz and Navon, 1994). However, if this did occur, it is expected that bubbles would have also nucleated on phenocrysts, and evidence of this is lacking.

Arguably, the microlites had nucleated and had at least started to grow prior to the bubbles collapsing, with bubble collapse following gas loss. Shear is known to promote bubble coalescence (Stasiuk et al., 1996; Burgisser and Gardner, 2004; Okumura et al., 2008), and once the vesicularity is >30 vol. % the percolation threshold is exceeded (Saar and Manga, 1999; Blower, 2001; Okumura et al., 2009).

Shear-induced bubble coalescence probably initially formed bubble networks at the dyke margins (Stasiuk et al., 1996), permitting vertical and perhaps lateral outgassing (Eichelberger et al., 1986), with outgassing bolstered by the tuffisite veins, which are thought to have intersected bubbles (Castro et al., 2012b; Castro et al., 2014). Evidence of tuffisite veins propagating through bubbly magma is recorded by the feather-like tuffisite vein margins (e.g., **Fig. 4.17.**); such feather-like margins are common on welded pumice clasts, where they reflect broken vesicles at clast edges. The number density of bubble collapse structures is particularly high around the feather-like margins, which records the previous bubbly nature of the magma. Some tuffisite vein margins change from feather-like to linear along their length, and bubble collapse structures are less common next to the linear margins (e.g., **Fig. 4.24.**), reflecting the less vesicular nature of the magma. This considered, it is thought that some tuffisite veins traversed from bubbly to bubble-free magma.

The tuffisite veins housed within the vesicular obsidian of Skriðugil's centre arguably formed after magma vesiculation, i.e., these veins propagated through bubbly magma. There are three reasons for this suggestion; 1) the tuffisite veins follow the vesicle elongation direction, indicating that bubble deformation occurred prior to vein formation (e.g., **Fig. 4.11.**), which is supported by the contrasting viscously deformed vesicle forms and undeformed veins. 2) If bubbles grew after vein formation it is expected that there would be a continuous vesicle-free layer surrounding the veins, assuming firstly that volatiles diffused into the veins, and secondly that such diffusion left the magma volatile-undersaturated, and no vesicle-free layers exist. 3) None of the vesicles deform the vein margins, and it is expected that bubbles growing next to a tuffisite vein would deform the margin, because such textures exist in pyroclastic bombs (Hugh Tuffen, pers. comm. 2015). Assuming that the tuffisite veins formed last

it may be questioned as to why they do not intersect vesicles today. In answer to this question, intersected bubbles would have collapsed or been filled with ash, making them difficult to identify. Indeed, collapsed bubbles may not always be preserved (Westrich and Eichelberger, 1994) and ash-filled vesicles may be indistinguishable from tuffisite veins.

So, how did the tuffisite veins form? Brittle failure of magma is commonly envisaged to occur when the magma's shear strength is exceeded (Denlinger and Hoblitt, 1999; Goto, 1999; Gonnermann and Manga, 2003; Tuffen et al., 2003; Rust et al., 2004; Tuffen and Dingwell, 2005; Green and Neuberg, 2006; Neuberg et al., 2006; Collier and Neuberg, 2006; Lensky et al., 2008; Wright and Weinberg, 2009; Holland et al., 2011; Okumura et al., 2013; Schipper et al., 2013), with failure often depicted as being confined to conduit margins (Denlinger and Hoblitt, 1999; Gonnermann and Manga, 2003; Rust et al., 2004; Lensky et al., 2008; Holland et al., 2011; Okumura et al., 2013). However, tuffisite veins are pervasive throughout the dykes, demonstrating that brittle failure did not just occur at the margins. This is in accordance with observations of the 2011-12 Cordón Caulle eruption, where the possible surface expression (jets of gas and particles) of tuffisite veins consisted of multiple vents, which were mostly located within the interior of the proto-lava dome (Schipper et al., 2013). It has previously been demonstrated that deformation within the dykes was characterised by the repeated failure and healing of magma (Tuffen et al., 2003; Tuffen and Dingwell, 2005). Brittle failure was thus spatially and temporally variable. It is envisaged that initially shear localisation formed permeable networks of coalesced bubbles at the dyke margins (**Fig. 4.39. time 1**), with some network-assisted outgassing occurring at this time. Then the bubble networks failed under protracted strain, with gas and bubble wall fragments being incorporated into the fractures,

giving birth to tuffisite veins. It is further proposed that during shear failure the magmatic plug slipped, resulting in sudden decompression and tensile failure of bubble walls in the dyke interior (**Fig. 4.39. time 2**). A pressure drop of ~3 MPa would have been sufficient to cause macroscopic failure of magma with a vesicularity of 35 vol. % (the estimated vesicularity of Skriðugil today), but this pressure drop is merely an estimate, made using the calculation of Spieler et al. (2004), and it does not take permeability into consideration (e.g., Mueller et al., 2008). Inferring that bubble

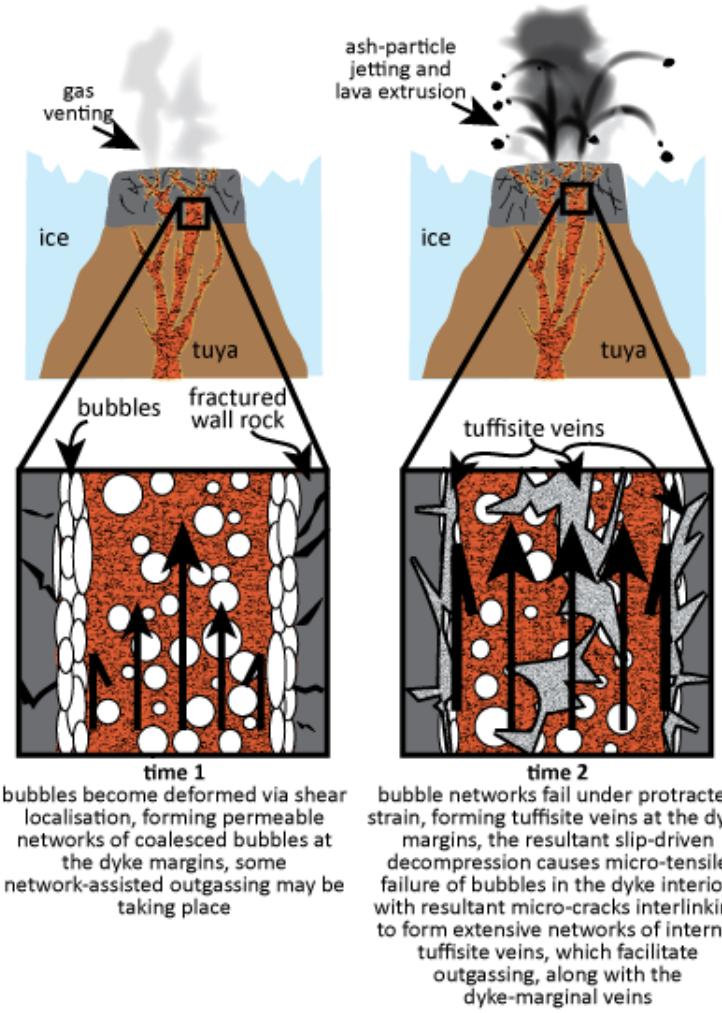

Figure 4.39. Schematic model depicting the formation of internal tuffisite veins within the dykes.

overpressures of 3 MPa occurred within the dykes is reasonable when it is considered that bubble overpressures of ~4-12 MPa may have existed in the Cordón Caulle vent (Schipper et al., 2013). However, given that fragmentation was localised it is perhaps more likely that failure occurred below the fragmentation threshold via tensile micro-

cracking of bubble walls, with cracks merging to form tuffisite veins (e.g., Heap et al., 2015). Because the internal tuffisite veins propagated through bubbly magma they would have been highly efficient outgassing pathways, given their access to significant quantities of exsolved volatiles.

Tensile micro-cracking of bubble walls (**Fig. 4.40.**) may be recorded by the irregular shaped bubbles with angular edges (e.g., **Fig. 4.22.**), but these cracks did not evolve into larger fractures. It is also possible that the irregular-shaped bubbles represent shear failure of dehydrated bubble haloes (**Fig. 4.41.**) or gas-filled domains between sintered clasts. The latter interpretation is supported by the polygonal shapes that occur in the same sample as the irregular bubbles. The shape edges are visible due to them having weak electron backscatter intensities relative to the shape centres

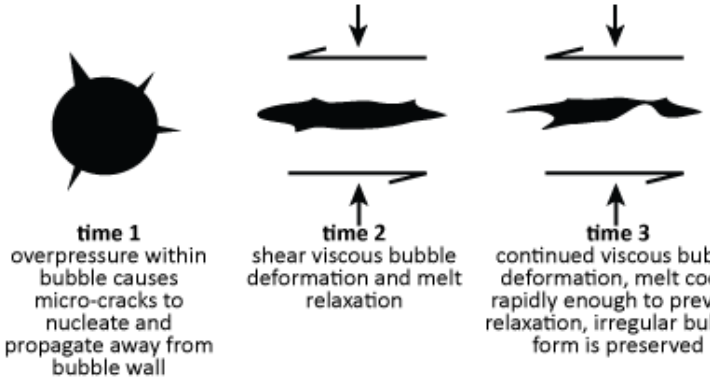

Figure 4.40. Schematic model depicting bubble shape evolution due to tensile failure and subsequent shear deformation and melt relaxation. Crystals proximal to the deforming bubble are also likely to have influenced the bubble shape.

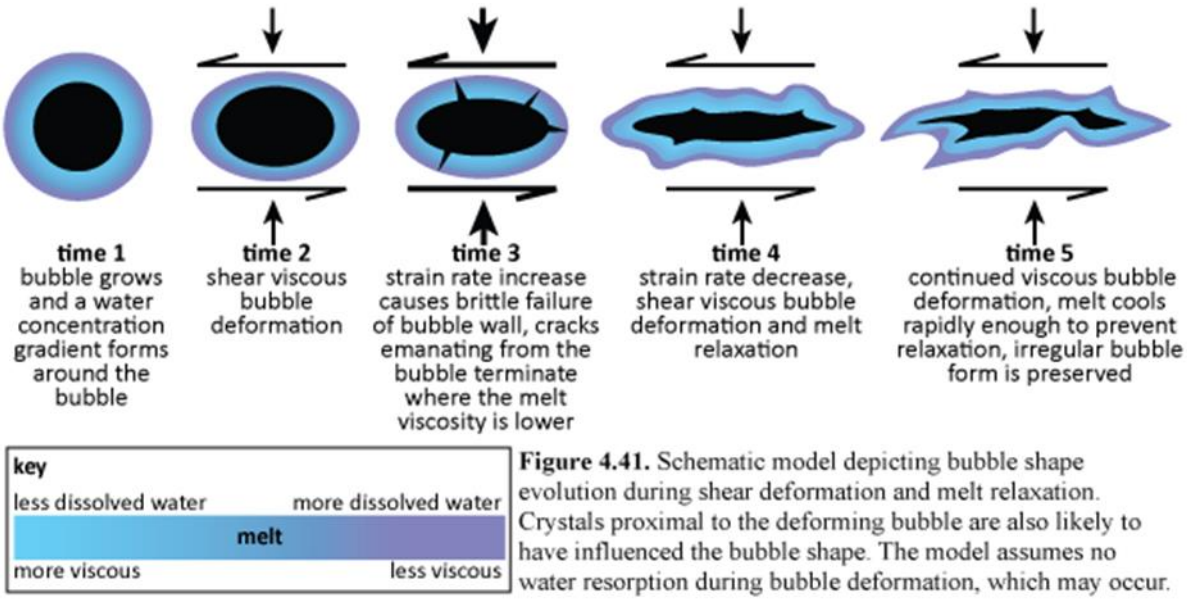

Figure 4.41. Schematic model depicting bubble shape evolution during shear deformation and melt relaxation. Crystals proximal to the deforming bubble are also likely to have influenced the bubble shape. The model assumes no water resorption during bubble deformation, which may occur.

(e.g., **Fig. 4.30.**). The shapes are clast-like, and interpreted as being sintered clasts (**section 4.7.1.**). Gas-filled domains with similar shapes to the bubbles form between sintering clasts during hotstage experiments (Hugh Tuffen, pers. comm. 2015; **Fig. 4.42.**), and occur between sintered clasts in obsidian pyroclasts (Rust et al., 2004), frictional melts (Plail et al., 2014) and welded kimberlite pipes (Brown et al., 2008). The origin of the irregular-shaped bubbles remains unresolved.

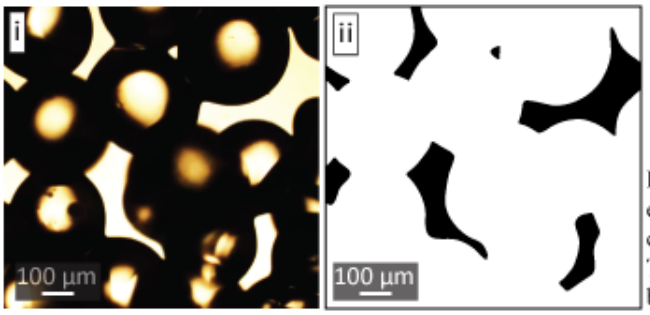

Figure 4.42. (i) Microphotograph of hot stage experiment (taken at 870 °C). Borosilicate clasts are sintering (image courtesy of Hugh Tuffen). **(ii)** Tracing of gas-filled domains between the sintering clasts.

4.6.2. Source, transport and deposition of particles within tuffisite veins

Deposition and erosion within tuffisite veins will be influenced by the particle to gas ratio, particle size, current velocity, fracture geometry and wall roughness, and clast to clast interactions. Arguably, all of these parameters will be spatially and temporally unsteady, which presents challenges when modelling particle transport and deposition within tuffisite veins. Sedimentary structures may be used to gain insight into particle transport and deposition, but the tuffisite veins within the dykes experienced deformation, which modified some sedimentary structures, whilst also causing localised reductions in grainsize (Tuffen and Dingwell, 2005). However, it is still thought that some sedimentary structures and obsidian clast textures shed light on particle transport and deposition.

For instance, some tuffisite veins contain a poorly sorted mix of particles (e.g., **Fig. 4.19.**), which may reflect rapid deposition, or a high particle to gas ratio, i.e.,

there was insufficient time for sorting or sorting was prevented due to tight particle packing respectively. Such poorly sorted tuffisite veins are uncommon, with the majority of veins containing laminations of sorted particles. Often, particles coarsen towards vein centres (e.g., **Fig. 4.18.i**), which arguably records deposition from waning currents within inclined or horizontal tuffisite veins (**Fig. 4.43.**), during the latter stages of venting. Indeed, it is difficult to envisage how such sorting would occur within vertical veins, and multiple laminations of sorted particles are unlikely to form during comminution (Lavallée et al., 2014). However, it cannot be dismissed that some grainsize segregation occurred along shear zones within the tuffisite veins, as

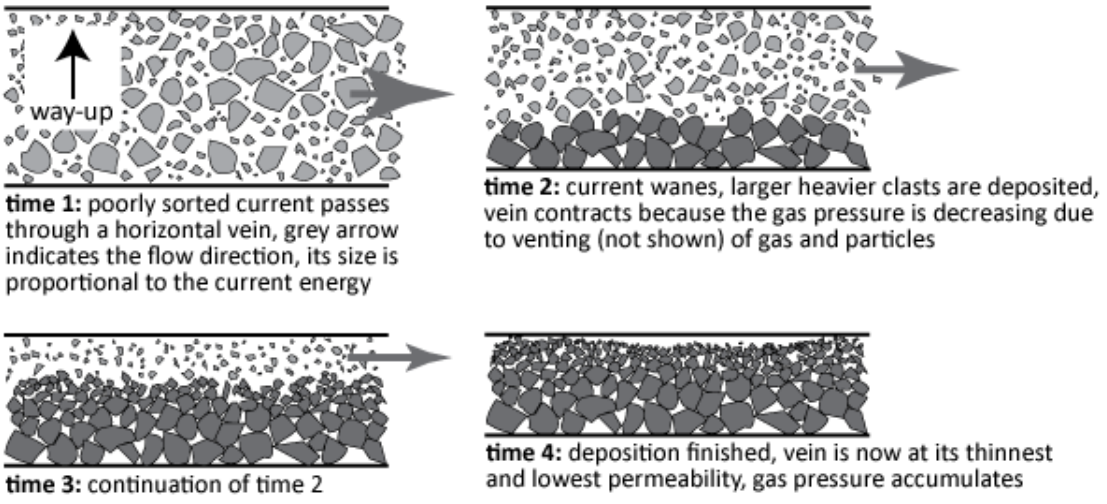

Figure 4.43. Schematic illustration depicting how graded laminations may form within tuffisite veins. Vein welding will affect the path taken by currents (discussed in the following section).

shear zones were active in the veins (Tuffen and Dingwell, 2005), and grainsize segregation can occur along shear planes (Lavallée et al., 2014). If the coarsening of particles towards vein centres does reflect initial deposition within horizontal veins then it may be suggested that the initial orientations of the veins was highly variable, even though many of the veins are vertical today. This interpretation is in agreement with Tuffen and Dingwell (2005) who suggested that the present orientation of the veins reflects rotation during viscous deformation, with only phase 1-2 tuffisite veins retaining their original orientation.

Grainsize variations within the tuffisite veins are not just thought to have resulted from depositional processes, as some sorting is thought to have occurred during transport within vertical or near-vertical tuffisite veins. This is arguably recorded by the injection veins, which are always well sorted and fine grained, in contrast to their adjoining fault vein or reservoir zone, which are relatively poorly sorted. In some instances, contacts between injection vein ash and reservoir zone ash is sharp, with ash often extending from injection veins for a short distance in one direction along reservoir zone walls (e.g., **Fig. 4.18.ii**). To explain the aforementioned characteristics it is proposed that particle-laden currents travelled through vertical fracture networks, with particles becoming sorted via the elutriation of the finest grains into the current nose (**Fig. 4.44. time 1**). Some of these particles were vented, whilst others became trapped (i.e., deposited) within injection veins (**Fig. 4.44. time 2**). During the latter stages of venting, as the current energy decreased, the poorly sorted current tails were deposited in the fault vein or reservoir zone (**Fig. 4.44. time 3**).

The truncated laminations that occur in some veins (e.g., **Fig. 4.18.ii**) are thought to indicate that some currents were periodically erosive (e.g., Heiken et al., 1988). Erosion may also be recorded by the discontinuous laminations (e.g., **Fig. 4.18.ii**), but these may equally record localised deposition. In addition, it is thought that the relatively large obsidian clasts within finer grained laminations (e.g., **Fig. 4.18.ii**) record erosion of the host obsidian, or erosion of previously deposited relatively coarse grained material. In many tuffisite veins deposition is thought to have taken place from multiple currents, as represented by the laminations within the veins. Because pulsatory deposition is inferred, it may also be argued that venting from individual veins was pulsatory. Pulsating jets of particles and gas originated from

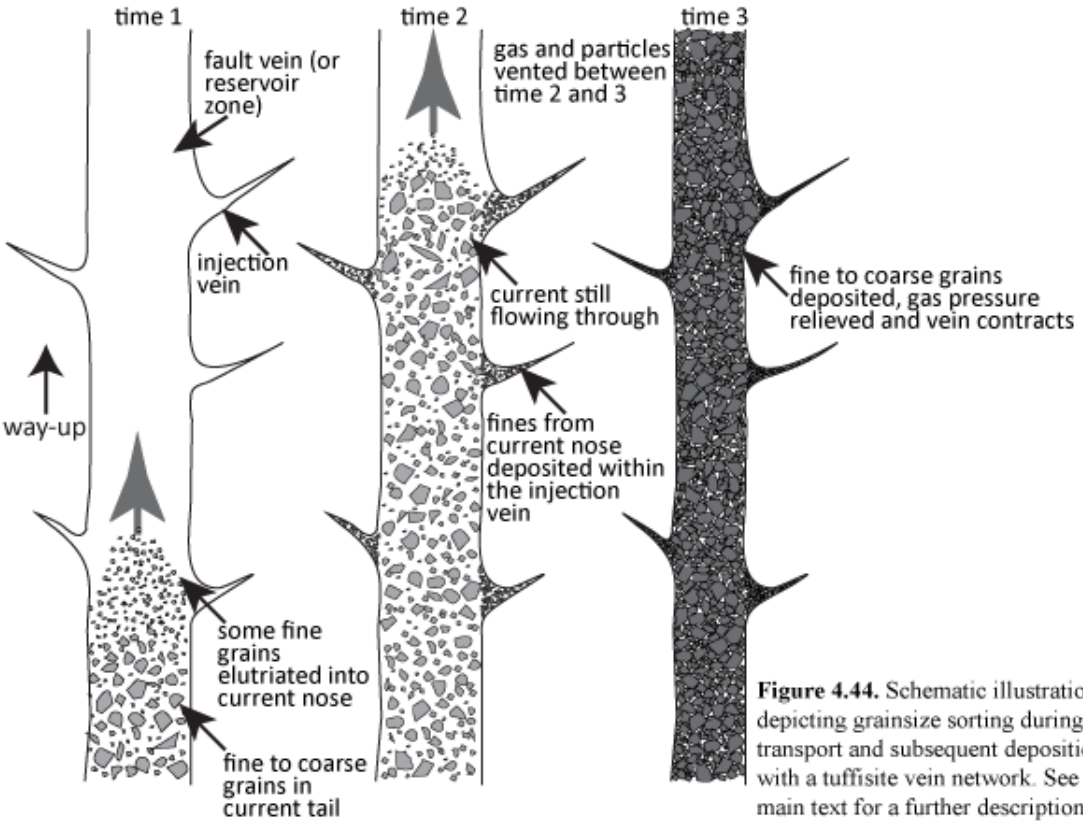

Figure 4.44. Schematic illustration depicting grainsize sorting during transport and subsequent deposition with a tuffisite vein network. See main text for a further description.

multiple locations during the semi-continuous jetting activity at Cordón Caulle (Schipper et al., 2013). The shallow conduit architecture of the Cordón Caulle vent is hidden, but it is quite likely that the jets observed during this eruption were fed by similar tuffisite veins to those in Thumall and Skriðugil.

Another similarity between the recent rhyolitic eruptions in Chile and the dykes is represented by the obsidian clasts textures. Some obsidian clasts within the tuffisite veins lack bubble collapse structures, which may reflect either a lack of bubble growth, or that bubbles collapsed and left no trace (e.g., Westrich and Eichelberger, 1994). The former interpretation is preferred because the clast surfaces are microlite coated, and it is expected that microlites would have similarly grown on bubbles, with such growth leaving a record of bubble collapse. However, some clasts contain bubble collapse structures or vesicles, indicating that bubble growth took place in these clasts. There are three possible reasons explaining why some clasts vesiculated and others did not; 1) the clasts had different upward velocities (**Fig.**

4.45.i-iv), 2) the clasts were different sizes (**Fig. 4.45.v-vii**), or 3), the clasts were sourced from different depths (**Fig. 4.45.viii-ix**). Arguably, all of these processes influenced clast degassing histories to varying degrees, with the latter process being in line with water measurements of obsidian clasts in tuffisite veins from Chaitén, which are thought to indicate vertical clast transport distances of ~500 m (Castro et al., 2014).

Some clasts clearly vesiculated within tuffisite veins, as recorded by the vesicular clasts in Skriðugil's centre (e.g., **Fig. 4.13.**); the vesicle walls within these clasts are generally intact, and it is expected that the walls would be broken if the clasts were bubbly prior to being incorporated into the tuffisite veins. In addition, the vesicles are undeformed (i.e., they are circular), which contrasts with the deformed vesicles in the host and the deformed vesicle-free clasts in the veins. Clast vesiculation must therefore have occurred after viscous deformation. It is unlikely that the circular vesicle forms resulted from relaxation, because it is expected that the similar-sized bubbles in the host would also have relaxed. In situ clast vesiculation arguably resulted in viscous deformation of nearby vesicle-free clasts and perhaps also the tuffisite vein margin (discussed further in the following section), whilst also decreasing inter-clast porosity.

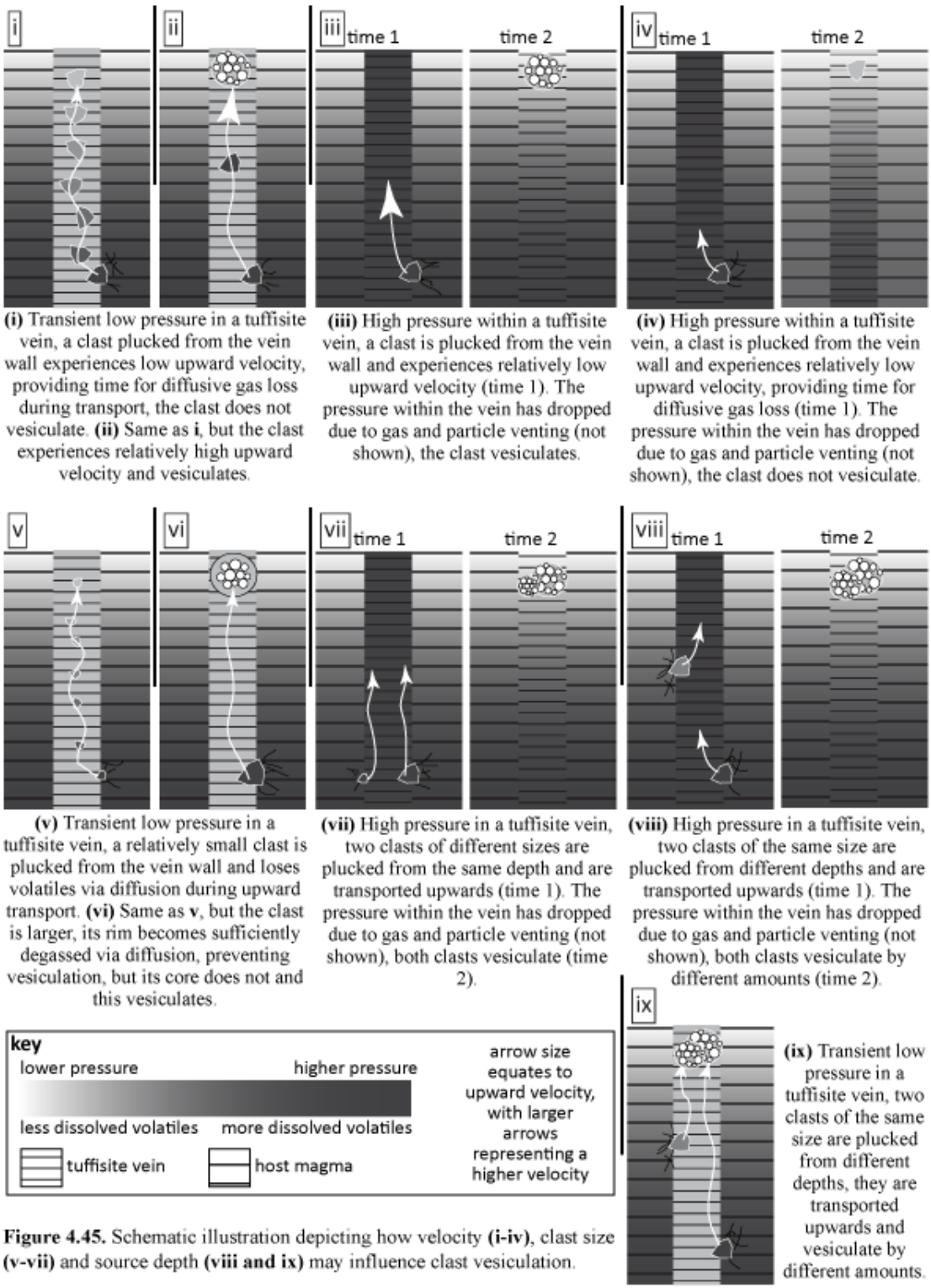

(i) Transient low pressure in a tuffisite vein, a clast plucked from the vein wall experiences low upward velocity, providing time for diffusive gas loss during transport, the clast does not vesiculate. **(ii)** Same as **i**, but the clast experiences relatively high upward velocity and vesiculates.

(iii) High pressure within a tuffisite vein, a clast is plucked from the vein wall and experiences relatively low upward velocity (time 1). The pressure within the vein has dropped due to gas and particle venting (not shown), the clast vesiculates.

(iv) High pressure within a tuffisite vein, a clast is plucked from the vein wall and experiences relatively low upward velocity, providing time for diffusive gas loss (time 1). The pressure within the vein has dropped due to gas and particle venting (not shown), the clast does not vesiculate.

(v) Transient low pressure in a tuffisite vein, a relatively small clast is plucked from the vein wall and loses volatiles via diffusion during upward transport. **(vi)** Same as **v**, but the clast is larger, its rim becomes sufficiently degassed via diffusion, preventing vesiculation, but its core does not and this vesiculates.

(vii) High pressure in a tuffisite vein, two clasts of different sizes are plucked from the same depth and are transported upwards (time 1). The pressure within the vein has dropped due to gas and particle venting (not shown), both clasts vesiculate (time 2).

(viii) High pressure in a tuffisite vein, two clasts of the same size are plucked from different depths and are transported upwards (time 1). The pressure within the vein has dropped due to gas and particle venting (not shown), both clasts vesiculate by different amounts (time 2).

(ix) Transient low pressure in a tuffisite vein, two clasts of the same size are plucked from different depths, they are transported upwards and vesiculate by different amounts.

Figure 4.45. Schematic illustration depicting how velocity **(i-iv)**, clast size **(v-vii)** and source depth **(viii and ix)** may influence clast vesiculation.

The obsidian clasts within the tuffisite veins are of a similar size to the grainsize distribution of subaerial deposits, produced during violent Strombolian to Vulcanian basaltic-andesitic eruptions (Rust and Cashman, 2011; **Fig. 4.46.**). This may imply that the clast manufacture process was mechanistically similar to the cyclical accumulation and release of pressure, which characterises Vulcanian eruptions (Morrissey and Mastin, 2000), giving further credence to the notion that vein activity from the dykes may have been akin to the semi-continuous jetting activity that

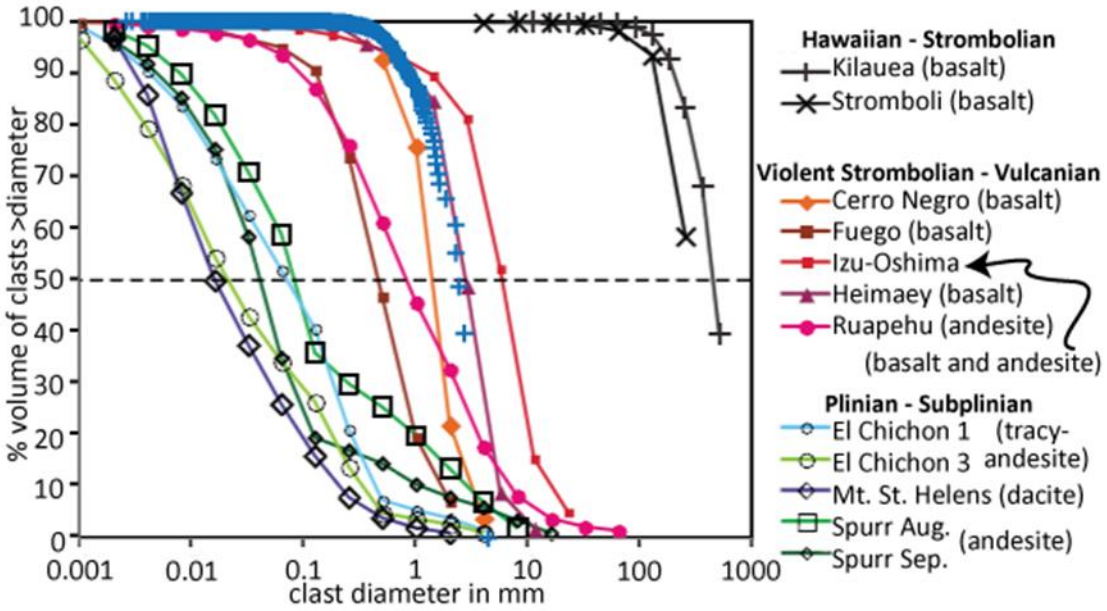

Figure 4.46. A compilation of grainsize distributions for different eruptions from Rust and Cashman (2011). Measurements of obsidian clasts (blue crosses) from tuffisite veins in the dykes (same data as shown in **figure 4.16.i**) have been added for comparison. See Rust and Cashman (2011) for details of where they sourced the data. Compositional information was obtained from Parfitt (1998), Ripepe et al. (1993), Rose et al. (1973), Rose et al. (2008), Mannen 2006, Self et al. (1974), Bonadonna and Houghton (2005), Espindola et al. (2000), Rose and Durant (2009) and Nye et al. (1995) for Kilauea, Stromboli, Cerro Negro, Fuego, Izu-Oshima, Heimaey, Ruapehu, El Chichon, Mt. St. Helens and Spurr, respectively.

occurred during the Vulcanian phase of activity from Cordón Caulle (Schipper et al., 2013). However, grain sizes were modified along shear zones during phase 2 of tuffisite vein evolution (Tuffen and Dingwell, 2005). The grainsize may therefore not be representative of the initial fragmentation mechanism, but may instead reflect comminution. Only grains finer than 10 microns are thought to avoid comminution (Kennedy and Russell, 2012), and because ~85 % of the measured grains are larger

than this (**A.4.5.**), comminution was probably particularly important in reducing the size of particles.

4.6.3. Welding and reactivation of tuffisite veins

Similarly to the formation of welded ignimbrites (Smith, 1960), welding of tuffisite veins will involve sintering at contact points between clasts and porosity reduction through compaction, of additional importance in veins will be sintering between clasts and vein walls. Welding will decrease vein permeability, and is thus an important process to consider when evaluating the outgassing ability of tuffisite veins.

In the previous section it was not discussed as to whether or not deposition took place via agglutination, i.e., via particles sintering upon their initial impact with vein walls. To evaluate the likelihood of agglutination, the sintering timescale (τ_s) of the smallest obsidian clasts (diameter of 1 μm) is estimated using the following equation; $\tau_S = \frac{r \times \eta_s}{\Gamma}$ where r is the clast radius, η_s is the melt viscosity, and Γ is surface tension (Uhlmann et al., 1975; Vasseur et al., 2013). Clasts with viscosities of 10^8 Pa s and 10^{11} Pa s would have taken ~3 minutes to ~2 days to sinter respectively; viscosities were determined using the model of Giordano et al. (2008a), the dyke lava composition (Tuffen, 2001) and water contents of 1 wt. % and 0.1 wt. % respectively. A value of 0.3 N m^{-1} was used for surface tension (Bagdassarov et al., 2000). Considering these sintering timescale estimates it is not thought that agglutination took place within the tuffisite veins. Some particles would indeed have collided with one another and also with the vein walls during transport, but contact times would have been too short for agglutination to occur.

Viscous deformation and welding took place after the deposition of particles, during phases 3 and 4 of tuffisite vein evolution (Tuffen and Dingwell, 2005). Some

phase 1 tuffisite veins cut through phase 3 and 4 tuffisite veins, demonstrating that the magma experienced repeated brittle-ductile-brittle transitions (Tuffen et al., 2003; Tuffen and Dingwell, 2005). Arguably, some tuffisite veins may have been thoroughly welded before being intersected by new fractures. However, in some instances it is thought that gas pressure was relieved by reactivation of partially welded veins, with this recorded by fine grained laminations that weave between coarser grained laminations (e.g., **Fig. 4.20.**); it is advocated that following deposition of coarse grains, pressurisation resulted in pore space dilation and influx of fine grained currents (**Fig. 4.47.**).

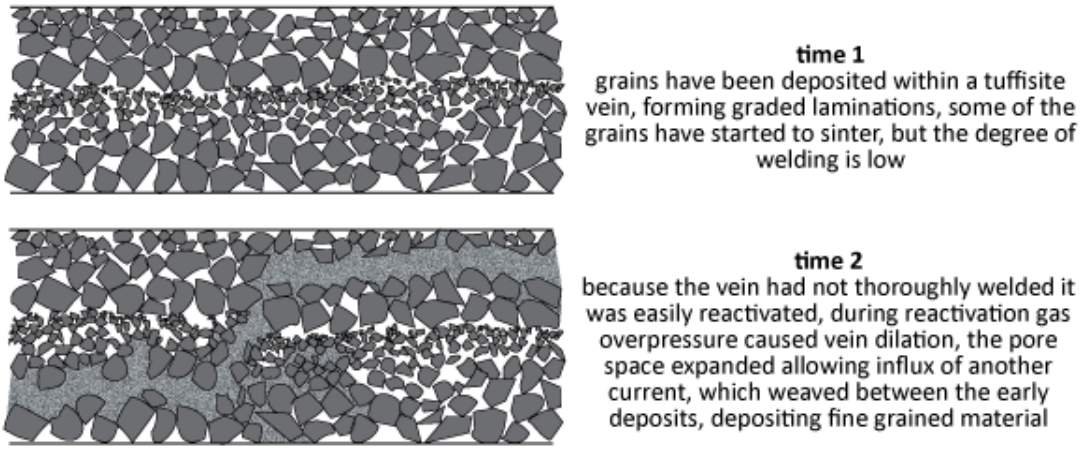

Figure 4.47. Schematic illustration depicting reactivation of a poorly welded tuffisite vein.

Some tuffisite veins are thought to have remained active during welding. This is arguably recorded by tuffisite veins that contain fine grained ash aggregates which are surrounded by relatively large obsidian clasts (e.g., **Fig. 4.21.**). It is envisaged that following deposition of fine ash the grains started to sinter; a new current then passed through the vein and eroded some of the partially welded material. The sub-circular forms of the aggregates contrast with the deformed shapes of the surrounding relatively large obsidian clasts (e.g., **Fig. 4.21.**), implying that the aggregates acted as rigid objects around which the clasts deformed. The rigidity of the aggregates and contrasting plasticity of the large clasts may imply that the aggregates contain a high

proportion of phenocryst fragments, or that the aggregates had lost more water and were thus more viscous than the larger clasts, or that the larger clasts were bubbly, and thus more easily compressed than the aggregates. Any of these interpretations may be valid, but the presence of bubble collapse structures in the larger clasts supports the latter interpretation.

Today, all tuffisite veins within Thumall and those within Skriðugil's margins are thoroughly welded, i.e., the clasts are sintered and vesicle-free, and inter-clast porosity is lacking. Clasts in Skriðugil's centre are also sintered and inter-clast porosity is lacking, but the degree of welding is lower here because vesicular clasts exist. These vesicular clasts are surrounded by viscously deformed vesicle-free clasts, and the tuffisite vein walls are bulbous (e.g., **Fig. 4.13.**). Arguably, in situ clast-vesiculation caused compaction and viscous deformation of surrounding bubble-free clasts and the vein wall, whilst also reducing the inter-clast porosity (**Fig. 4.48.**) and potentially decreasing the outgassing ability of the veins.

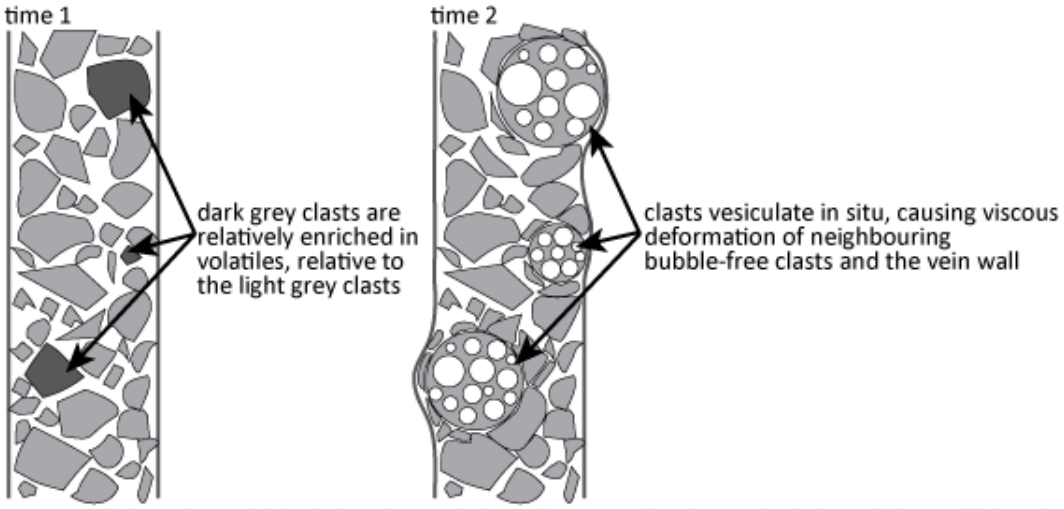

Figure 4.48. Schematic model depicting viscous deformation caused by clast vesiculation within a tuffisite vein.

Viscous deformation caused clast elongation (Tuffen and Dingwell, 2005). This is represented by the increase in clast aspect ratios from the phase 1 to phase 3 veins (e.g., **Fig. 4.16.ii**). In some instances the relative timing of clast compaction and sintering can be determined. For instance, some deformed clasts have oxidised rims,

and as rim thicknesses conform to the shapes of the deformed clasts (e.g., **Fig. 4.29.ii**) deformation must have preceded sintering (**section 4.7.2.**). The form of collapsed bubble structures within deformed clasts (e.g., **Fig. 4.25.**) and the host obsidian, demonstrate that pressure shadows existed next to phenocryst fragments and intact phenocrysts, respectively (**Fig. 4.49.i and ii**). In addition, some tuffisite veins are thinnest between phenocryst clusters (e.g., **Fig. 4.14.**), indicating that veins were compressed between phenocrysts (**Fig. 4.49.iii**).

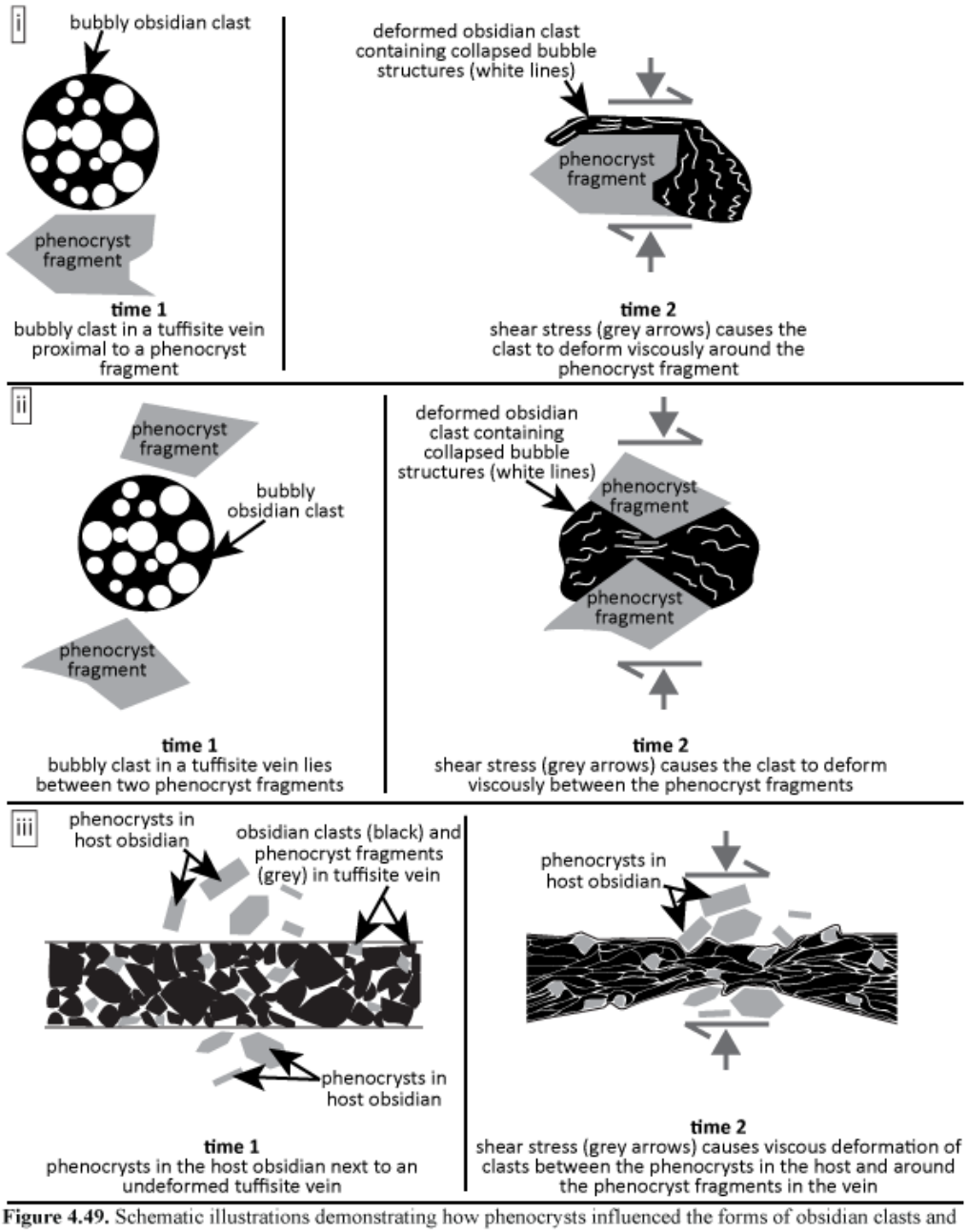

Figure 4.49. Schematic illustrations demonstrating how phenocrysts influenced the forms of obsidian clasts and tuffisite veins during ductile deformation.

4.7. Interpretation of backscatter electron intensity and obsidian colour

In this section models will be proposed that explain the variations in electron backscatter intensity and obsidian colour.

4.7.1. Geochemical variation

The unfilled arcuate to linear unhealed cracks, which occur in both dykes and that cross-cut all other textures arguably formed due to thermal contraction during magma cooling. Indeed, their unhealed nature indicates formation below Tg, and as they cut through all other textures they must have formed at a late stage of dyke evolution. The regions of the host obsidian bordering the cracks with weak electron backscatter intensities (e.g., **Fig. 4.30.ii**) are either depleted or enriched in heavy or light elements respectively. This is because backscatter intensity is a function of the mean atomic number, with weaker intensities reflecting a lower mean (Ginibre et al., 2002; Reed, 2005; Humphreys et al., 2008; Berlo et al., 2013). The weak intensities may record local hydration by meteoric water (Denton et al., 2012; von Aulock et al., 2013), with enrichments of relatively light elements (e.g., H and O). Alternatively, the domains may be depleted in K and enriched in Na, which may occur in the presence of meteoric water (Cerling et al., 1985). Such variations in K and Na would result in weak backscatter intensities because K has a higher atomic number than Na.

The polygonal shape edges that are defined by weak backscatter intensities (e.g., **Fig. 4.30.i**) are thought to be sintered clast edges, because they have clast-like shapes, and because they occur with microlites which are thought to have nucleated on the clast surfaces. In addition, they are proximal to irregular shaped bubbles, which may be inter-clast voids (**section 4.6.3.**). It remains unclear as to why the edges of the polygonal shapes have weak backscatter intensities, but they must be enriched or

depleted in atomically light or heavy elements respectively (Ginibre et al., 2002; Reed, 2005; Humphreys et al., 2008; Berlo et al., 2013), in comparison to the surrounding obsidian.

4.7.2. Variations in Fe redox state

The obsidian colour variations in microphotographs do not correspond with variations in the electron backscatter intensity (e.g., **Fig. 4.28.ii, iii, 4.29.ii and iii**), indicating they do not reflect major element variations (Ginibre et al., 2002; Reed, 2005; Humphreys et al., 2008; Berlo et al., 2013). The pale bands are viscously deformed around phenocrysts. The colour variation could therefore not have resulted from post-magmatic alteration. Obsidian colour can reflect Fe redox state (**chapter 1 section 1.7.** and references therein), with pale obsidian being more reduced than dark obsidian (Castro et al., 2009). This considered, it is hypothesised that the pale obsidian next to some phase 3 tuffisite veins (e.g., **Fig. 4.28.**) is relatively reduced. An increase in hydrogen fugacity has been shown to increase oxygen fugacity (Sato and Wright, 1966; Gaillard et al., 2002; Castro et al., 2009). The cause of the pale bands is unclear, but they may have resulted from vein pressurisation and volatile diffusion into the host (McGowan et al., 2015), with the host becoming relatively enriched in H_2 due to H_2 having a greater diffusivity than O_2 and H_2O (Sato and Wright, 1966).

The dark clast rims in sample 5e (e.g., **Fig. 4.29.**) must have formed before sintering, in order to preserve individual clast shapes. These colour variations therefore did not result from post-magmatic alteration. Dark obsidian is generally oxidised relative to light obsidian (Castro et al., 2009); it is therefore hypothesised that the dark rims are oxidised relative to the clast centres. Oxidation of the rims may have occurred due the diffusive loss of volatiles from the clasts, with more H_2 escaping

relative to O_2 and H_2O. Alternatively, oxidation of the rims may have resulted from the ingress of atmospheric gases into the veins (**Fig. 4.50.**), in a similar manner to oxidation of subaerial pyroclastic deposits (e.g., **Fig. 4.29.iv**; Ross and Smith, 1961; Manley, 1995). Inferring atmospheric gases as the oxidising agent requires that some tuffisite veins connected with the surface.

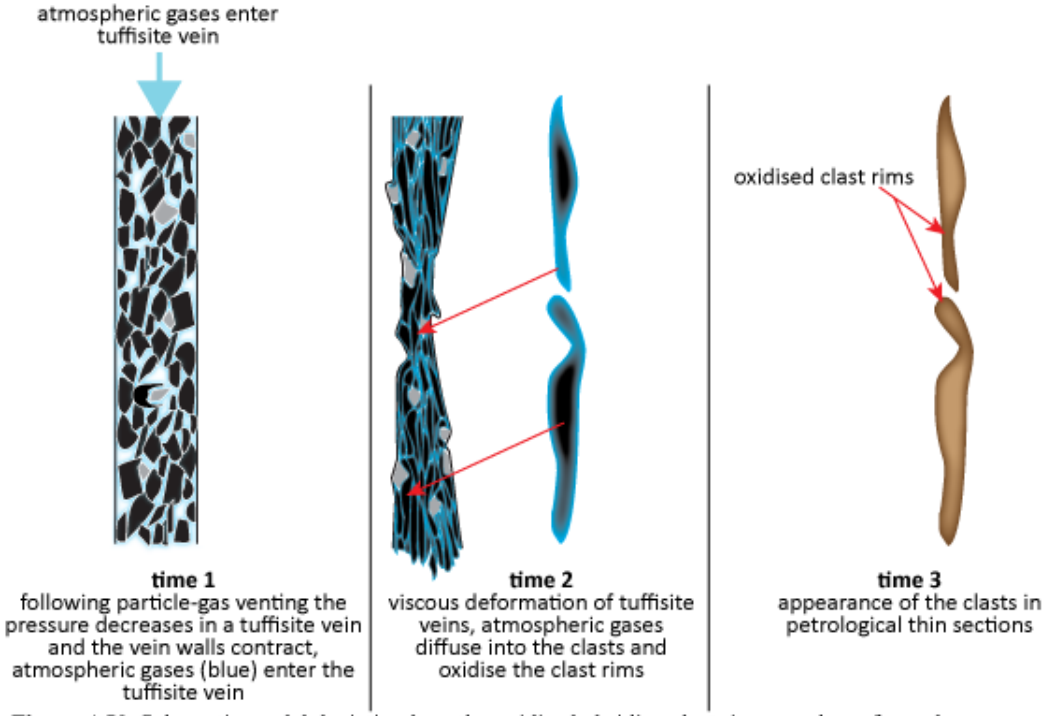

Figure 4.50. Schematic model depicting how the oxidised obsidian clast rims may have formed.

4.8. Interpretation of water measurements

The results of the water measurements support the interpretations that have been built from the textures, whilst also providing further insight into emplacement and magmatic outgassing. In this section the significance of the macro- to micro-scale water concentrations will be discussed.

4.8.1. Macro-scale: loss of magmatic water

The similar water values from the BFTIR and SFTIR indicates the robustness of these analytical techniques. The water content in the dykes is thought to be wholly

magmatic because post-magmatic alteration has only affected local areas next to cooling cracks (**section 4.7.1.**). These areas are no wider than 10 µm, and were therefore easily avoided when taking the water measurements. Furthermore, the measured water content decreases with increased elevation and such a trend is unlikely to form via post-magmatic hydration. In addition, it is expected that the water content of the samples would be higher if they did experience post-magmatic hydration. Ideally, water speciation (Stolper, 1982b; McIntosh et al., 2014b), thermogravimetric analysis (Roulia et al., 2006; Denton et al., 2009; Denton, 2010; Denton et al., 2012) or isotopic analysis (Friedman and Smith, 1958) would be used to confirm that the water is indeed wholly magmatic. However, because the water content is very low, various water speciation peaks are not discernible using FTIR analysis and achieving total sample dehydration via thermogravimetric analysis is work in progress.

The pre-eruptive magmatic water content in Thumall is ~4 wt. % (Owen et al., 2013a), which would have resulted in the magma being water saturated at a depth of ~4 km (Newman and Lowenstern, 2002), assuming a magmatic temperature of 800 °C, an overburden density of 2400 kg m^{-3} and a CO_2-free melt (assumptions justified below). Water saturation would have resulted in exsolution and bubble growth, with the bubble collapse structures and vesicles indicating that the magma was indeed water-saturated. Today, the dissolved water content is >1 order of magnitude less than the pre-eruptive water content; magmatic water must therefore have escaped from the magma.

The decreasing water content with increased elevation reflects decreasing pressure with increased elevation (Tuffen and Castro, 2009; Tuffen et al., 2010; Owen et al., 2012; Owen, 2013; Owen et al., 2013b). Today, the vesicle-free lava from

Thumall has a density of 2400 kg m^{-3}, but solubility pressure curves bracketing the water data represent densities of 360 kg m^{-3} and 1100 kg m^{-3}. The pressures represented by the curves probably partly reflect the bubbly and thus less dense nature of the magma. Densities of 360 kg m^{-3} and 1100 kg m^{-3} equate to porosities of 85 vol. % and 44 vol. %, respectively. Skriðugil's centre contains 35 % vesicles today. The bubble content of the magma would have been highly heterogeneous, so determining the bubble content at the time of emplacement is difficult. Previous studies have used the ideal gas law and pre-eruptive water content to determine vesicularities (e.g., Eichelberger et al., 1986; Jaupart and Tait, 1990; Owen et al., 2013b; Schipper et al., 2013), but there are many assumptions built into such models. All that will be said with certainty is that the magma was bubbly. If the bubble content exceeded 35 vol. %, which may have been so, the volumetric loss that would have occurred following bubble collapse may have been counteracted by the ascent of more buoyant volatile-rich magma in the dyke centre and perhaps also by country rock relaxation (Walker, 1969; Almond, 1971). Cooling fractures in the lava cap and upper dyke would also have lowered the overburden density, because non-fractured lava has a higher bulk density than fractured lava, but the effect of such fractures on the overburden pressure is thought to be negligible, relative to the effect of the bubbles.

The solubility pressure curves may give a misleading estimate of the overburden pressure because the water content may also record localised transient excursions to sub- or supra-magmatic pressure during tuffisite vein evolution. Indeed, analysis of tuffisite veins in obsidian pyroclastic bombs indicates that the pressure within tuffisite veins can be lower than in the surrounding magma, as recorded by depletions in water (Castro et al., 2012b; McGowan et al., 2015; Cabrera et al., 2015) and lithium (Berlo et al., 2013) adjacent to the tuffisite veins. Furthermore, the

pressure within tuffisite veins may be higher than that of the surrounding magma, as recorded by water enrichments adjacent to tuffisite veins in obsidian pyroclastic bombs (McGowan et al., 2015). The dissolved water concentration within Thumall arguably represents the bubbly nature of the magma and the diffusive exchange of water between tuffisite veins and host magma.

Some samples in the dykes have water concentrations that are lower than expected, considering atmospheric pressure (~85 kPa) at 1180 m a.s.l.. Localised low pressure domains in fold hinges (Castro et al., 2002a; Cabrera, 2013) or next to phenocrysts may have caused local decreases in water solubility. Similar decreases in solubility may also have resulted from localised high temperatures, caused by viscous heating (Nelson, 1981; Hess et al., 2008; Cordonnier et al., 2012b) or frictional heating (Tuffen and Dingwell, 2005; Kendrick et al., 2012; Kendrick et al., 2014). Alternatively, the lower water concentration may be explained by the accidental incorporation of anhydrous crystals into the analysis, but this is unlikely, as devitrified domains and phenocrysts were carefully avoided.

Discovering that the water content within the dykes is lower than that expected if the magma were free of bubbles, tuffisite veins and fractures is not unique. For instance, the magmatic water content in rhyolitic melt that lies ~2 km beneath Krafla volcano indicates a pressure between lithostatic and hydrostatic (Elders et al., 2011; Zierenberg et al., 2012). Disruption to the circulation of drill-water during sampling indicated that the country rock overlying this melt is highly permeable (Zierenberg et al., 2012). The presence of fractures or tuffisite veins in the country rock may explain its high permeability and the lower than expected pressure.

Berlo et al. (2013) found the water content in the host obsidian and an obsidian clast from Skriðugil to span ~0.6-1 wt. %, which is significantly higher than the

values reported in this study (0.08-0.16 wt. %). These authors also found a water concentration gradient in a vesicular clast in a tuffisite vein from Skriðugil, with the water content decreasing towards the clast edge. Recalculating the water content of their sample, using the same absorption coefficient and density as used in this thesis, with the peak heights and wafer thickness (50 μm) provided in the supplementary material of Berlo et al. (2013), gives a water content that still differs by 1 order of magnitude, in comparison to the values reported in this thesis. The actual rock wafer that was analysed by Berlo et al. (2013) cannot be located, and thus cannot be reanalysed (K. Berlo pers. comm. 2014). The water values reported in this thesis are thought to be accurate because similar values were obtained from multiple measurements of individual samples by using the FTIR and SFTIR. Interestingly, if the thickness of the Berlo et al. sample was in fact 500 μm, instead of the reported value of 50 μm, the water content in their sample would match the values reported in this thesis. An alternative explanation may be that their sample experienced post-magmatic hydration, but this does not explain the concentration gradient in the vesicular clast. The reason for the discrepancy in the water content between this study and that of Berlo et al. remains unclear.

Tuffen (2001) analysed a sample from Thumall and found the water content to span 0.14-0.24 wt. % in the host obsidian and 0.14-0.27 wt. % in a tuffisite vein. Some of the values reported by Tuffen (2001) are therefore higher than those reported in this study. The reason for this discrepancy also remains unclear, but the higher values could represent localised post-magmatic hydration.

4.8.2. Micro-scale: prolonged cooling

Water concentration gradients occur in obsidian bordering fractures and tuffisite veins in pyroclastic bombs from Monte Pilato in Lipari (Cabrera et al., 2011; Cabrera et al., 2015) and bordering tuffisite veins in bombs from Chaitén in Chile (Castro et al., 2012; McGowan et al., 2015). Lithium concentration gradients have also been found in bombs from Chaitén (Berlo et al., 2013). In contrast, there is little variation in the host water content next to the tuffisite veins in Skriðugil and Thumall. Berlo et al. (2013) also found there to be little variation next to a tuffisite vein from Skriðugil. Similarly, little variation exists in the large obsidian clasts within the tuffisite veins. This contrasts with previous analysis of obsidian clasts in pyroclastic bombs from Chile, in which concentration gradients in water (Castro et al., 2012b) and lithium (Berlo et al., 2013) exist. Furthermore, Berlo et al. (2013) found variation in the water content in a vesicular clast from Skriðugil. The obsidian clasts measured in this study were only from Thumall, so there may indeed be variation in the water content in clasts from Skriðugil, as found by Berlo et al. (2013), but gradients could also reflect tapering clasts and thus incorporation of fine grained anhydrous phenocryst fragments in the matrix ash (discussed below).

There is no variation in the electron backscatter intensity of the host obsidian bordering the tuffisite veins or in the obsidian clasts, supporting there being negligible variation in the water content, as backscatter intensity is a function of the mean atomic number (Ginibre et al., 2002; Reed, 2005; Humphreys et al., 2008; Berlo et al., 2013).

Concentration gradients in the host bordering tuffisite veins demonstrate that diffusive volatile exchange takes place between tuffisite veins and the surrounding magma (Castro et al., 2012b; Berlo et al., 2013; McGowan et al., 2015; Cabrera et al., 2015). This considered, it is quite reasonable to assume that diffusive water exchange

took place between the tuffisite veins and host magma in both dykes. Therefore, the absence of water concentration gradients implies that cooling of the melt across Tg took longer than water re-equilibration via diffusion. It is thought that re-equilibration occurred throughout the dykes.

The fine grained domains within the tuffisite veins have consistently lower water concentrations than those of the host obsidian and the large obsidian clasts, which is probably because anhydrous phenocryst fragments constitute some of the fine grained material. This being correct, a quantitative comparison should find a correlation between the percentage of phenocryst fragments and the percentage of water depletion. However, the estimated percent of phenocryst fragments does not always match the percent of water depletion (**Table 4.2.**). This may be due to the volumetric difference in the quantitative analysis. For instance, the percentages of phenocryst fragments were measured in the upper part of petrological thin sections, whereas the water content represents the whole wafer depth, and there may be more or less fragments in the 3D volume than represented on the surface. Furthermore, phenocryst fragments were counted in a different part of the tuffisite veins from where the water was measured, because the phenocryst estimates were made using BSE images of petrological thin sections and the water measurements were made in wafers. This considered, it is still deemed most likely that the relatively low water content of the fine grained zones results from the incorporation of anhydrous phenocryst fragments in the analysis. An alternative explanation would be that the smaller obsidian clasts lost all their water via diffusion, whereas the larger clasts did not, and that this is preserved by the water content today. However, this is unlikely, because as previously stated it is thought that the water content re-equilibrated during prolonged cooling. The depletions in the water content over the few 10s of microns next to some

tuffisite veins (e.g., **Fig. 4.34. and 4.35.**) are likely to result from the edge of the tuffisite vein being wedge-like, i.e., the depletions reflect incorporation of anhydrous phenocryst fragments into the measurements (**Fig. 4.51.**).

Table 4.2. Comparison of the water content and the percentage of phenocryst fragments in the tuffisite veins.

sample	estimated % of phenocryst fragments in tuffisite vein	wt. % H_2O in host	wt. % H_2O in fine grained zone of tuffisite vein	water content in tuffisite vein relative to the host	are the depletions in water explainable by the presence of anhydrous phenocryst fragments in the tuffisite veins?
1ei	14%		not measured	N/A	N/A
2e	9%		not measured	N/A	N/A
4ei	12%	0.147	0.121	-18%	the amount of phenocryst fragments is insufficient to explain the difference in the water content
5e	15%	0.124	0.114	-8%	the amount of phenocryst fragments is greater than the difference in the water content
6e	13%	0.114	0.108	-5%	the amount of phenocryst fragments is greater than the difference in the water content
15ei	9%	0.152	0.153	+1%	there is negligible variation in the water content but phenocryst fragments are present

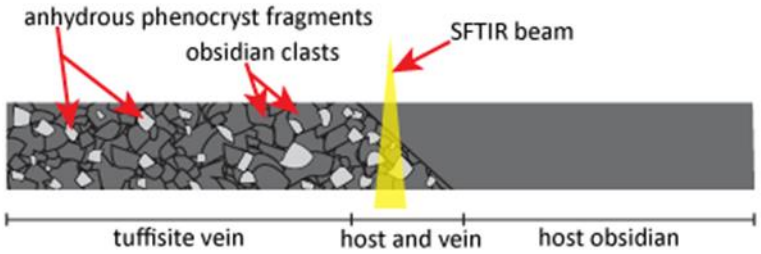

Figure 4.51. Schematic illustration demonstrating how the water measurements proximal to the contact between a tuffisite vein and the host obsidian may reflect both the contents of the tuffisite vein and also the host obsidian.

4.9. Summary of key findings

- During intrusion bubbly magma collapsed and formed vesicle-free lava.
- Internal tuffisite veins propagated through bubbly magma, which promoted outgassing.
- Shear failure of magma triggered tensile failure of bubbly magma.

- Internal tuffisite veins tapped into deep volatile-rich magma, promoting outgassing.

- Internal tuffisite veins were reactivated, which may have been possible due to the presence of atmospheric gases, phenocryst fragments and relatively large obsidian clasts, as these could have increased the welding timescale of the veins.

- The geometry and orientation of the internal tuffisite veins influenced the intrusive deposition of particles.

- Grainsize distributions within tuffisite veins are not characteristic of the initial fragmentation mechanism.

- Water escaped from the magma.

- The cooling time was sufficient to cause near-re-equilibration of the water content.

- Water measurements highlight the importance of constraining the angle of the contact plane between tuffisite veins and the host, prior to interpreting water measurements at these contacts.

Chapter 5: Discussion

This research was geared towards answering four questions (**section 1.9.**). The ultimate goal was to broaden understanding into magma emplacement and deformation within rhyolitic dykes, with the purpose of gaining insight into how these processes influence magmatic outgassing during rhyolitic eruptions. The significance of the findings with regards to conduit processes during rhyolitic eruptions, and also with regards to the textural evolution of extrusive lava, is discussed in this chapter.

5.1. Rhyolitic dyke propagation: squeezing toffee through a crack

The propagation path of the Húsafell dykes was forged by gas-charged particle-laden currents. In country rock that contained pre-existing fractures the currents and particle deposition were localised in these fractures (e.g., Deildargil location 1), resulting in the formation of vein-like deposits. In contrast, the currents and therefore particle deposition were focused along intrusion-related fractures in the country rock that lacked pre-existing fractures (e.g., Deildargil location 2), and the geometry of these fractures is not vein-like, but more irregular. If pre-existing fractures are present in country rock their orientation and extensiveness will govern the orientation and extensiveness of external tuffisite veins. This was evidently so at Deildargil location 1, where the country rock contained lots of pre-existing fractures, and where extensive networks of external tuffisite veins formed.

External tuffisite veins can form as overpressurised meteoric (e.g., Heiken et al., 1988) or magmatic fluids fracture the country rock, and this requires greater overpressure than to prop open pre-existing fractures (Heiken et al., 1988). Dyke or conduit opening arguably always commences with the intrusion of gas-charged

currents that are laden with particles, and the formation of external tuffisite veins. Indeed, clastic layers which form the margins of the rhyolitic Mule Creek vent in New Mexico (Stasiuk et al., 1996) and the rhyodacitic conduit of Obsidian Dome in California are probably external tuffisite veins, even though the significance of the material at Mule Creek with regards to magmatic outgassing was not commented upon by the authors, and the material at Obsidian Dome has been interpreted as fall-back tephra (Eichelberger et al., 1986).

5.2. The influence of shallow dyke permeability runs deep

Following the formation of the external tuffisite veins (zone A), intact magma was sequentially emplaced within the Húsafell dykes, as represented by sub-zones B1, B2 and B3, and significantly, the size and number density of microlites and nanolites varies between these subzones, implying that the decompression rate decreased throughout zone B emplacement (e.g., Martel and Schmidt, 2003; Brugger and Hammer, 2010; Martel, 2012). The intrusion of gas-charged currents that were laden with particles preceded and followed zone B emplacement, as represented by zones A and T. These gas-charged currents probably ascended more rapidly than the zone B magma. This considered, it is proposed that the decompression rate substantially decreased between the formation of zones A and B, progressively decreased throughout zone B emplacement, and then rapidly increased during ascent of zone T. These fluctuations in the ascent rate were arguably governed by the shallow (<500 m) dyke permeability, with low permeability favouring greater pressurisation at depths >>500 m. For instance, particles that were intruded during dyke opening probably had a greater inter-particle permeability relative to the pre-existing country rock permeability, thus decreasing the likelihood of pressurisation and deep fragmentation

of zone B magma. However, as bubbles collapsed in zone B and as zone A started to weld, the shallow dyke permeability would have decreased, causing pressurisation and fragmentation at depth, forming zone T. It is therefore argued that throughout dyke emplacement the pressure within the source region did not remain steady, but was instead unsteady due to changes in permeability at shallow depths.

5.3. Volatile resorption and implications for the texture of extrusive lava

The collapsed bubble structures in the SE Rauðfossafjöll and Húsafell dykes clearly demonstrate that bubbles may collapse during magma intrusion. Collapse may occur via gas loss through permeable bubble networks (Taylor et al., 1983; Eichelberger et al., 1986), with networks forming via shear-induced bubble coalescence (Stasiuk et al., 1996; Burgisser and Gardner, 2004; Okumura et al., 2008; Okumura et al., 2009; Okumura et al., 2010; Okumura et al., 2013). However, pressure increases associated with shear deformation and resultant volatile resorption (Sparks et al., 1999; Watkins et al., 2012) were arguably the dominant mode of bubble collapse, as this evidently occurred at Deildargil location 2a, where relatively reduced domains coincide with collapsed bubble structures, with reduced domains representing enrichments in H_2 and decreased fO_2 (e.g., Castro et al., 2009).

Shear deformation and bubble collapse through resorption were localised along emplacement boundary layers in the Húsafell dykes and the water content would therefore have been heterogeneous throughout the dykes, with localised enrichments along boundary layers. Decompression of volatile enriched domains may trigger late-stage vesiculation (Watkins et al., 2012), which may explain the localised post-emplacement vesiculation that took place in the Húsafell dykes, represented by the relatively large circular vesicles, around which flow bands are deformed.

Alternatively, volatile-enriched domains may not experience sufficient decompression until lava extrusion, which would require continuous shear deformation up until extrusion. This considered, vesicle heterogeneities in lava domes/flows and endogenic dome/flow explosions may not just be artefacts of surface processes (Manley and Fink, 1987; Fink et al., 1992; Castro et al., 2002a), but may also result from bubble collapse through volatile resorption that took place prior to lava extrusion (i.e., bubble collapse within the dyke or conduit). Lava is therefore likely to be extruded with pre-existing heterogeneities in the water content (Fink et al., 1992), rather than being fully degassed to near-atmospheric pressure (Eichelberger et al., 1986), with further heterogeneities in the water content likely to form during extrusive processes (Manley and Fink, 1987; Castro et al., 2002a; Shields et al., 2016).

5.4. Mobility of rhyolitic magma: a sticky situation

Rhyolitic melts have high viscosities compared with more mafic melts, and become increasing viscous during ascent as volatiles exsolve. The melt in the SE Rauðfossafjöll and Húsafell dykes was largely degassed during later stages of emplacement and would thus have been highly viscous. For example, considering the dissolved concentration of magmatic water (~0.1 wt. % and ~0.8 wt. % in the SE Rauðfossafjöll and Húsafell dykes, respectively) and major element geochemistry (SE Rauðfossafjöll; Tuffen, 2001, Húsafell; this study), melt viscosities of 10^{11} Pa s and 10^{8} Pa s are obtained for SE Rauðfossafjöll and Húsafell respectively, assuming a magmatic temperature of 800 °C (rhyolitic melt temperatures fall between 750 and 900 °C; Gunnarsson et al., 1998; Castro and Dingwell, 2009; Elders et al., 2011; Farquharson et al., 2015) and using the viscosity model of Giordano et al. (2008b). Such high viscosities would inhibit magma mobility, but deformed bubbles may

reduce the apparent viscosity of rhyolitic magma by a factor of five (Stein and Spera 2002; **section 1.5.2.i**), aiding magma mobility (Okumura et al., 2013). This occurred at Deildargil location 2a, recorded by the emplacement boundary layer with a high number density of collapsed bubbles. Of further significance, the bubbles at this locality collapsed, causing migration of the shear zone to a previously active external boundary layer that lay dormant prior to bubble collapse at the inner boundary layer. However, the outer boundary layer, which formed the country rock-magma contact did not contain bubbles, and so the magmatic plug stuck, enabling stress accumulation and culminating in localised brittle failure of bubble-free magma, as the shear stress exceeded the magma's shear strength (e.g., Tuffen et al., 2003; Gonnermann and Manga, 2003). This demonstrates that although the Húsafell dykes grew via emplacement of discrete magma pulses, accreted and relatively static magma had the potential to regain its mobility. Thus, at times, different pulses flowed as a single plug. Bubble collapse and shear zone migration probably plays a pivotal role in generating some of the tuffisite veins in the conduits of erupting volcanoes, and also brittle shear zones in extrusive lava flows.

During magma ascent, shear stress is expected to be greatest at dyke or conduit margins (Gonnermann and Manga, 2003; Bluth and Rose, 2004; Neuberg et al., 2006; Holland et al., 2011; Okumura et al., 2013), and close to the base of lava during extrusive flow. However, it has been recognised that shear zones migrate towards the centre of extrusive lava flows with time (Smith, 1996), and that multiple shear zones may develop within rhyolitic dykes/conduits (Tuffen et al., 2003; Tuffen and Dingwell, 2005; Schipper et al., 2013) and extrusive lava flows (Manley and Fink, 1987; Shields et al., 2016). Shear zones that are similar to those that formed along emplacement boundary layers within the Húsafell dykes and those within the SE

Rauðfossafjöll dykes (Tuffen et al., 2003; Tuffen and Dingwell, 2005) will undoubtedly develop within extrusive rhyolitic lava flows (e.g., Shields et al., 2016), and it is highly probable that shear zones migrate during extrusive lava emplacement. This considered, during lava extrusion, processes such as bubble collapse (Eichelberger et al., 1986), volatile resorption (Watkins et al., 2012; McIntosh et al., 2014a), thermal-induced vesiculation (Nelson, 1981; Lavallée et al., 2015) and the formation of brittle-ductile shear zones (Smith, 1996), will undoubtedly contribute to the extreme textural heterogeneity of extrusive rhyolitic flows (e.g., Manley and Fink, 1987; Shields et al., 2016).

5.5. Magma fragmentation and permeability evolution of external and internal tuffisite veins

5.5.1. Micro-cracks to pyroclasts

Internal tuffisite veins are generally inferred to form via shear failure of magma (Goto, 1999; Marti et al., 1999; Tuffen et al., 2003; Gonnermann and Manga, 2003; Bluth and Rose, 2004; Tuffen and Dingwell, 2005; Wright and Weinberg, 2009; Holland et al., 2011; Schipper et al., 2013), and less commonly inferred to form via tensile failure (Tuffen and Dingwell, 2005; Heap et al., 2015). Textural evidence for the shear failure of bubbly magma is preserved in pyroclasts (Marti et al., 1999; Wright and Weinberg, 2009; Schipper et al., 2013), and injection veins in the SE Rauðfossafjöll dykes may have formed via tensile failure of fracture walls, due to high gas pressures within tuffisite veins (Tuffen and Dingwell, 2005). Shear failure within the SE Rauðfossafjöll dykes may also have triggered slip events, which culminated in decompression and tensile failure of bubble walls below the fragmentation threshold, with resultant micro-cracks interlinking and evolving into extensive networks of internal tuffisite

veins (e.g., Heap et al., 2015). Tensile micro-cracking of bubble walls was also instrumental in forming the clasts within the external tuffisite vein at the SW margin of Deildargil location 1. The irregular-shaped bubbles and vesicles in the SE Rauðfossafjöll and Húsafell dykes, respectively, may also record tensile micro-cracking of bubble walls. Therefore, localised magma fragmentation should not always be considered as resulting from either shear or tension in isolation, as both can be important.

The grainsize within internal tuffisite veins at SE Rauðfossafjöll, and also within the internal and external tuffisite veins at Húsafell falls within the grainsize distribution of Vulcanian subaerial deposits (Rust and Cashman, 2011). This may be used to infer that fragmentation was mechanistically similar to that which operates during Vulcanian eruptions, broadly implying fragmentation via pressurisation-decompression cycles (Morrissey and Mastin, 2000). Such cyclicity was undoubtedly pivotal in deforming the magma within the dykes, but grain morphologies, together with the broader dyke textures, demonstrate that fragmentation involved a complex interplay of shear, tension and micro- to macro-scale deformation of bubbly and bubble-free magma. In addition, grains within the SE Rauðfossafjöll internal tuffisite veins clearly experienced secondary fragmentation via comminution (Tuffen and Dingwell, 2005), yet they still fall within the grainsize distribution of Vulcanian eruptions (Rust and Cashman, 2011). It is therefore inappropriate to solely use the grainsize of subaerial deposits or indeed particle morphology to infer fragmentation mechanisms; when possible, a combination of studies should be used, including observations of eruptions (Schipper et al., 2013), the size distribution (Rust and Cashman, 2011) and morphology (Heiken, 1974) of subaerially deposited particles, and the size and morphology of particles within tuffisite veins (Heiken et al. 1988;

Tuffen et al., 2003; Tuffen and Dingwell 2005; Schipper et al., 2013; Castro et al., 2014; this study).

5.5.2. To weld or not to weld?

Two characteristics of external and internal tuffisite veins will govern their outgassing ability; their access to pre-exsolved volatiles (Castro et al., 2012b; Castro et al., 2014), and the sustainability of their permeability. Assessing the outgassing ability of tuffisite veins therefore requires constraint of the factors that influence their permeability.

One external tuffisite vein that formed during dyke opening at Deildargil location 1 became the focus of later magma emplacement, with some of the vein being preserved at the dyke margin as magma was emplaced. Preservation was possible because the vein experienced viscous shear stress during later magma emplacement, with associated pressure and heating causing its inner margin to weld, creating a low-permeability, high-strength barrier between magma flowing in the dyke interior and the outer margin of the vein. This barrier protected the outer margin of the vein from erosion and shear deformation, allowing it to retain permeability throughout dyke growth.

External tuffisite veins are bordered by relatively cold, static country rock, whereas internal tuffisite veins exist within the hot, mobile interiors of dykes and conduits. Higher temperatures and greater shear stress will favour welding (e.g., Smith, 1960; Tuffen et al., 2003; Chadderton et al., 2015), and so the permeability of internal veins will generally be more transient than that of external veins, but this is not necessarily always the case. For instance, atmospheric gases appear to have entered the internal veins at SE Rauðfossafjöll, which arguably increased the welding timescale via cooling or the presence of insoluble nitrogen (e.g., Spark et al., 1999),

thus prolonging their permeability. Furthermore, welding of tuffisite veins is not just governed by temperature and shear stress, but also by comparing particle sizes within veins (e.g., Vasseur et al., 2013). The Húsafell external tuffisite veins and SE Rauðfossafjöll internal tuffisite veins experienced incremental deposition of particles, perhaps consisting of unsteady deposition from one current, but with most veins probably experiencing deposition from multiple currents. Indeed, veins at Húsafell and SE Rauðfossafjöll display evidence of reactivation, which at Rauðfossafjöll followed partial vein welding. Vein reactivation requires permeability retention, for if permeability has been lost via thorough welding, with strength re-gained (e.g., Kolzenberg et al., 2012), high shear stress or gas pressure will be relieved via fresh fracturing (e.g., Tuffen et al., 2003; Tuffen and Dingwell, 2005) rather than reactivation. The multiple generations of cross-cutting veins within the SE Rauðfossafjöll dykes demonstrate that magma failure was temporally and spatially variable, with brittle-ductile and ductile-brittle transitions being driven by fluctuations in the strain rate and/or temperature (Tuffen et al., 2003; Tuffen and Dingwell, 2005). Similarly, flow-banded domains at Húsafell, which formed via viscous deformation of brecciated obsidian, and the flow-banded clasts, which formed via auto-brecciation of flow-banded domains, demonstrate that the magma experienced brittle-ductile-brittle deformation cycles. It is quite possible that further ductile and brittle events occurred, but these would be texturally unidentifiable. Considering that magma in the Húsafell and SE Rauðfossafjöll dykes experienced repeated failure and welding, pressurisation was not always relieved via vein reactivation, but in some instances it was.

Internal veins at Húsafell lack evidence of reactivation and contain <10 % phenocrysts and phenocryst fragments, whereas the external veins at Húsafell and the internal veins at SE Rauðfossafjöll that display evidence of reactivation contain ~15-

30 % mafic lithic clasts and crystals, and ~15 % phenocryst fragments, respectively. It is therefore inferred that vein reactivation is more likely when the vein-filling material contains >15 % mafic lithics or crystal fragments, as these constituents will resist welding at rhyolitic eruptive temperatures, unlike rhyolitic melt. Small amounts of crystals and mafic lithics may therefore make a huge difference in terms of the permeability lifespan, and thus the outgassing ability of tuffisite veins. Prior to sintering, microlites had nucleated and grown on rhyolitic melt clasts within the internal SE Rauðfossafjöll veins, which may have slightly increased the sintering timescale (e.g., Vassaur et al., 2013), thus prolonging permeability. However, the microlites do not form a complete shell around the clasts, and may thus have been negligible in terms of prolonging permeability, as microlite-free edges would have sintered. In contrast, the size of particles within reactivated veins appears to have influenced the welding timescale, as fine ash layers deposited during reactivation always weave between coarse grains. This suggests that either the large clasts had not commenced sintering prior to reactivation or that inter-clast bonds were broken more easily when the clasts were large. The largest obsidian clasts are ~1 mm in diameter. Neglecting compaction, the sintering timescale (τ_s) can be estimated using the following equation (Uhlmann et al., 1975; Vasseur et al., 2013): $\tau_S = \frac{r \times \eta_s}{\Gamma}$ where r is the clast radius, η_s is the melt viscosity, and Γ is surface tension, taken to be 0.3 N m^{-1} (Bagdassarov et al., 2000). Clasts 1 mm across with melt viscosities of 10^8 Pa s and 10^{11} Pa s would have taken ~2 days and ~5 years to sinter respectively (viscosities determined using the model of Giordano et al. (2008a), and the glass composition of Thumall lava (Tuffen, 2001), and water contents of 1 wt. % and 0.1 wt. %, respectively). Considering these sintering timescale estimates, it is unsurprising that the coarser-grained parts of the veins were reactivated, especially since measured

water concentrations in the exposed upper parts of the SE Rauðfossafjöll dykes are closer to 0.1 wt. % than 1 wt. %, and since tuffisite vein-sourced jets of particles and gas occurred at intervals of seconds to minutes from individual sub-vents during the Cordón Caulle eruption (Schipper et al., 2013).

Vapour phase precipitates, such as cristobalite, could inhibit magmatic outgassing through the upper 500 m of conduits by blocking permeable pathways (Boudon et al., 1998). However, glass corrosion and subsequent precipitation requires a permeability that is already sufficiently low to trap gas (Schipper et al., 2015). Corrosion pits and precipitates are restricted to the least permeable zones of the external tuffisite vein at the SW margin of Deildargil location 1. Therefore, vapour phase precipitates arguably exert a minor influence over outgassing, as corrosion and precipitation only occur in magma that is already below the percolation threshold.

5.6. Modification and preservation of water gradients

It is reasonable to assume that diffusive volatile exchange between the host magma and internal tuffisite veins occurred at SE Rauðfossafjöll, and that the water content subsequently re-equilibrated during magma cooling. A relatively straightforward method of calculating the time (t) taken for a water concentration gradient to form over a particular length (d) is given by $t = d^2 / D_{H_2O_t}$ (Watkins et al., 2012; McIntosh et al., 2014a), and is based on Fick's first law of diffusion. For a rhyolitic melt containing ≤2 wt. % total water (H_2O_t), water diffusivity ($D_{H_2O_t}$) in $m^2\ s^{-1}$ may be estimated by using the following equation;

$$D_{H_2O_t} = \frac{C}{C_0} \exp\left(-16.83 - \frac{10992}{T}\right)$$

where C is the H_2O_t content in wt. %, C_0 is 1 wt. %, and T is the temperature in Kelvin (Zhang et al., 1991; Zhang, 1999). The largest clasts in the SE Rauðfossafjöll veins

have diameters of ~500 μm, and water concentration gradients next to internal tuffisite veins in rhyolitic pyroclasts are similarly ~500 μm long (Castro et al., 2012b). It would take ~2 days or ~16 days to re-equilibrate the water content over 500 μm, assuming a magmatic temperature of 1073 K (Gunnarsson et al., 1998) and H_2O_t content of 1 wt. % and 0.1 wt. %, respectively. Based on thermal diffusivity within rhyolitic melts (5.5×10^{-7} m^2 s^{-1}; Romine et al., 2012) and Fick's first law of diffusion, it would take ~85 days for a 2 m wide dyke to cool. Given that all the studied dykes are wider than 2 m it is not surprising that the water content re-equilibrated over 500 μm-long transects. However, as demonstrated in the Húsafell dykes, variations in the size and number density of micro-crystal populations and also in the redox state of Fe may reflect water concentration gradients in melt that were then lost or modified during cooling. It may therefore still be possible to determine whether or not volatile diffusion occurred, even if primary evidence is lost or modified.

5.7. Nature of the country rock and role of external water

As discussed in **section 5.1.** the path taken by particle-gas currents and the geometry of the early-formed tuffisite veins was clearly influenced by whether or not the country rock contained pre-existing fractures prior to dyke propagation. The consolidated nature of the country rock was also an important influence on dyke propagation. Some of the Húsafell dykes propagated through conglomerates, which are moderately to well cemented today; it is difficult to determine how well consolidated they were at the time of dyke emplacement, but clearly the sediments were eroded with relative ease, given the irregular dyke margins and the local regions within the dyke exposure at Deildargil location 2a that appear to be a mix of lava and conglomerate. Húsafell dyke widths show no correlation with the type of country

rock, so although the conglomerate would have been more easily eroded than the lava this did not greatly influence dyke widths. This was arguably because erosion generally took place during the early stages of dyke propagation i.e., during emplacement of zone A and sub-zone B1. Following this, welded particles (inner margin of zone A) or dense lava lined the dyke walls, which protected the original country rock from erosion. However, in some instances minor erosion did occur during later emplacement, during formation of external tuffisite veins.

The SE Rauðfossafjöll dykes formed when much of the tuya was ice covered, and although the Húsafell dykes formed during an interglacial period there was probably significant quantities of meteoric water around, especially as some of these dykes propagated through glacial conglomerates and given that the volcanic activity at Húsafell volcano was punctuated by periods of glaciation. It is quite possible that the SE Rauðfossafjöll dykes are surrounded by external tuffisite veins that formed via hydrofracturing as magma interacted with meteoric water, in a similar manner to the formation of external tuffisite veins next to the Obsidian Dome feeder dyke and conduit (Heiken et al., 1988). Unfortunately, the country rock surrounding the SE Rauðfossafjöll dykes is not exposed, although breccia does occur locally on the west side of Thumall; this may be worth examining for evidence of magma-water interactions. It is possible that some meteoric water entered the internal tuffisite veins at SE Rauðfossafjöll, especially given that atmospheric gases appear to have entered the veins. Blocky particles, clay-coated clasts and solution pits are characteristic of magma-water interaction (Heiken et al., 1988), but a lack of such textures does not mean that no magma-water interactions took place (White and Valentine, 2016). It is therefore difficult to say for certain whether magma-water interactions played some role in forming the Rauðfossafjöll vein textures.

Clay-coated clasts are also lacking at Húsafell, some solution pits exist in the external tuffisite vein at Deildargil location 1, but these occur distal to the country rock and are more likely to record the presence of corrosive magmatic gases (see **section 3.6.1.iv**) rather than prolonged contact with meteoric water, especially given that the pits are lacking near the country rock, where it is expected that access to meteoric water would have been greatest. The external tuffisite veins at Deildargil location 1 clearly record the propagation of gas-particle currents through pre-existing fractures, rather than through a new generation of fractures formed during dyke emplacement. However, it cannot be dismissed that the external tuffisite vein at Deildargil location 2 formed via hydrofracturing (the micro-texture of the vein-fill at this locality has not been examined). The external tuffisite vein at Deildargil location 2a clearly formed via shear failure of magma (see **section 3.6.2.iii**) and thus hydrofracturing is not thought to have been important here.

5.8. Magmatic outgassing

The main motivation for this study was to gain insight into the processes that facilitate and assist outgassing of rhyolitic magma, as this governs the eruption behaviour of rhyolitic volcanoes. Previous conceptions of magmatic outgassing processes are discussed in this section, along with the new insight provided by the SE Rauðfossafjöll and Húsafell dyke textures.

Prior to this study rhyolitic dykes had certainly not been overlooked during geological mapping of volcanoes, but they had in terms of their potential contribution to understanding magmatic outgassing. Eichelberger (1995) highlighted a need for their examination, with a few authors providing insight into magmatic outgassing by studying dykes (Tuffen, 2001; Tuffen et al., 2003; Tuffen and Dingwell, 2005) and

conduits (Eichelberger et al., 1986; Heiken et al., 1988; Stasiuk et al., 1996). One reason for perhaps overlooking rhyolitic dykes in terms of magmatic outgassing is that they may be viewed as representing the last gasps of eruptions or even post-eruptive processes, and thus cannot really inform us about eruptive processes. This was certainly the view of some early studies, which envisaged dyke or conduit welding as being temporally connected to explosive-effusive eruption transitions (Walker, 1969; Almond, 1971; Wolff, 1986; Reedman et al., 1987).

Early studies that perceived rhyolitic eruptions as being characterised by a simple explosive to effusive transition built their interpretations on subaerial deposits and borehole cores (Taylor et al., 1983; Eichelberger et al., 1986; Newman et al., 1988; Dobson et al., 1989; Taylor et al., 1991; Rust et al., 2004). However, it may be questioned as to how representative borehole cores are of a whole conduit, as they may easily fail to intersect key textures such as internal tuffisite veins. Additionally, pyroclastic subaerial deposits produced during particle-gas jetting, like that which occurred during the hybrid explosive-effusive phase of the recent Cordón Caulle eruption (Schipper et al., 2013) may not be preserved or may be difficult to identify, as they will only represent a small fraction of the erupted magma, even though they facilitate the loss of significant amounts of magmatic gas. The recent rhyolitic eruptions of Chaitén and Cordón Caulle in Chile heralded opportunities to gain unique insight in the eruptive dynamics of rhyolitic volcanoes, dispelling the myth that a simple explosive-effusion transition characterises rhyolitic eruptions, with prolonged hybrid explosive-effusive behaviour observed (Castro et al., 2012b; Schipper et al., 2013; Castro et al., 2014). With this new perspective of rhyolitic eruption behaviour in mind, and considering the previously identified tuffisite veins in dissected dykes and conduits (Heiken et al., 1988; Stasiuk et al., 1996; Tuffen, 2001; Tuffen et al., 2003;

Tuffen and Dingwell, 2005), dissected volcanic realms can arguably tell us a great deal about processes that govern magmatic outgassing. This is because similar tuffisite veins to the dissected ones probably fed the jets of particles and gas observed during the Cordón Caulle eruption (Schipper et al., 2013), and evidently also existed within the Chaitén conduit (Castro et al., 2012b; Castro et al., 2014).

It has long been recognised that during a single eruption, rhyolitic magma with a given pre-existing water content may produce degassed lava and comparatively undegassed pyroclasts (e.g., Taylor et al., 1983; Eichelberger et al., 1986; Newman et al., 1988; Rust et al., 2004). So, how have textures in the Húsafell and SE Rauðfossafjöll dykes re-shaped previous conceptions of magmatic outgassing processes, and what new insight has been obtained?

Permeable networks of coalesced bubbles have been inferred as being important facilitators of outgassing, with gas escaping laterally from the networks into permeable wall rock at conduit margins (Taylor et al., 1983; Eichelberger et al., 1986; Jaupart and Allègre, 1991). In this framework, significant long-lived permeability is required in the upper 500 m of both magma within conduits and the rock lining the conduit walls. However, the permeable foam model is deemed an improbable mechanism of outgassing for three reasons; 1) vertically extensive bubble networks will be unsustainable due to vertical pressure differentials; 2) high temperature and shear stress would cause marginal tephra to weld, reducing its permeability, and 3), bubbles would collapse following gas loss, or through resorption due to pressure increases associated with shear deformation. It has also been proposed that bubble networks extending from surface vents to depths of over one kilometre may facilitate effusive gas venting during rhyolitic eruptions (Schipper et al., 2013; Okumura et al., 2013), but this is also improbable, as permeable bubble networks are unlikely to have

vertical extensions of more than a few metres or tens of metres, because 1) vertical pressure differentials would make them unstable, and 2), shear localisation probably occurs in multiple patches, due to the heterogeneous distribution of bubbles and shear strain. Indeed, domains of collapsed bubbles in the Húsafell dykes can only be traced over a few metres at most, and those within the SE Rauðfossafjöll dykes vary at a cm-scale in terms of their number density.

Domains of coalesced bubbles may fail under protracted strain (Marti et al., 1999; Wright and Weinberg, 2009; Schipper et al., 2013), with resultant internal tuffisite veins enabling gas to escape at the vent. Such interactions are considered fundamental in outgassing of rhyolitic magma (Castro et al., 2012b; Castro et al., 2014), as they connect permeable escape paths (i.e., tuffisite veins) with significant accumulations of exsolved magmatic gas (i.e., bubbles). The internal tuffisite veins in the SE Rauðfossafjöll dykes probably made a significant contribution to outgassing, by linking multiple bubbles and creating extensive outgassing pathways.

Beyond their role of removing pre-exsolved magmatic water, internal tuffisite veins are thought to create transient permeability, allowing diffusive gas loss from host magma bordering the veins. This gas loss through internal tuffisite veins may be negligible over eruptive timescales (Castro et al., 2012b), due to sluggish water diffusion in rhyolitic melts (Yoshimura and Nakamura, 2008) and rapid welding of veins over minutes to hours (Tuffen et al., 2003), but this gas loss mechanism may become more important if veins are closely spaced (<1 mm spacing; Castro et al. 2012). Repeated fracturing and healing of magma during shallow ascent resulted in a high number density of internal tuffisite veins in the SE Rauðfossafjöll dykes (Tuffen et al., 2003; Tuffen and Dingwell, 2005), but the average vein spacing in Thumall is ~2 cm, and thus far larger than the 1 mm spacing requirement. However, due to the

higher phenocryst content in Torfajökull rhyolite (~15 vol. %; Tuffen and Dingwell, 2005; this study) as opposed to <5 vol. % at Chaitén (Castro and Dingwell, 2009), permeability reduction via welding would perhaps have taken longer in the SE Rauðfossafjöll veins relative to the Chaitén veins. This would potentially provide greater scope for diffusion-driven outgassing from the SE Rauðfossafjöll veins.

Gas venting during the Cordón Caulle eruption is thought to have been fed by permeable bubble networks, with gas-particle jetting fed by tuffisite veins (Schipper et al., 2013). However, it is probable that both types of vent activity were fed by internal tuffisite veins. In this framework, eruptions from any given vent commenced when bubbly magma failed (via shear or tension), connecting exsolved gas to the surface via tuffisite veins and generating jets of particles and gas. Following and perhaps simultaneous with this, particles were deposited within veins, with particle venting ceasing once the energy had sufficiently decreased, whilst intrusive deposition of particles and gas venting continued. Intrusive deposition of particles and welding acted to decrease vein permeability and increase vein strength, enabling pressure to build. This pressure was then relieved via fresh fracturing, or reactivation of pre-existing veins, depending on the degree of welding.

External tuffisite veins, emplaced at depths of ~300-500 m have previously been documented as existing at the margins of the rhyolitic Mule Creek vent (Stasiuk et al., 1996) and rhyodacitic conduit of Obsidian Dome (Heiken et al., 1988). The latter-mentioned veins were sampled using boreholes, but even with these size-limited samples it was recognised that the veins were important facilitators of particle and gas transport. The Mule Creek external veins extend sub-horizontally from the dyke interior into the country rock, weaving through pyroclastic breccia at the conduit margins, and are truncated by intact lava in the conduit interior (Stasiuk et al., 1996).

They thus formed after conduit opening, but before the latest stage of magma emplacement in the dyke interior. The veins are partially welded and crystal-rich (High Tuffen, pers. comm., 2016), and they may have been important outgassing pathways (Stasiuk et al., 1996). Of further significance in terms of outgassing is the pyroclastic breccia that lines the conduit margins, which is not welded next to the country rock. The significance of this material in terms of outgassing was not commented upon by Stasiuk et al. (1996), but it is significant, as it represents a large vertical external tuffisite vein, similar to the far smaller ones documented at Húsafell.

External veins such as these are thought to be important facilitators of outgassing because they may have a relatively long-lived permeability, as they may not weld as readily as internal tuffisite veins, due to their proximity to relatively cold, static country rock, and because they often incorporate significant amounts of cool, crystal-rich and frequently mafic country rock lithics. Furthermore, external tuffisite veins may extend vertically for tens or even hundreds of meters, thus providing a prolonged permeable connection between deep volatile-rich magma and the surface. Additionally, they may receive volatiles from dyke or conduit interiors via prolonged diffusion. During rhyolitic eruptions, persistent vent-marginal outgassing, which is punctuated by intermittent jets of particles and gas may be fed by external tuffisite veins.

To conclude, outgassing of rhyolitic magma is deemed most efficient when both internal and external tuffisite veins are operating, with direct outgassing from bubble networks being negligible compared with the role of tuffisite veins. In addition, the permeability and strength of the country rock/shallow conduit, which will evolve throughout eruptions, strongly governs the behaviour of rhyolitic

eruptions, and can similarly be important during basaltic eruptions (e.g., Kennedy et al., 2010).

References

Alidibirov, M., and Dingwell, D. B., 1996, Magma fragmentation by rapid decompression: Nature, v. 380, no. 6570, p. 146-148.

Almond, D. C., 1971, Ignimbrite vents in the Sabaloka cauldron, Sudan: Geological Magazine, v. 108, no. 2, p. 159-176.

Ambrose, S. H., 2003, Did the super-eruption of Toba cause a human population bottleneck? Reply to Gathorne-Hardy and Harcourt-Smith: Journal of Human Evolution, v. 45, no. 3, p. 231-237.

Bagdassarov, N., Dorfman, A., and Dingwell, D. B., 2000, Effect of alkalis, phosphorus, and water on the surface tension of haplogranite melt: American Mineralogist, v. 85, no. 1, p. 33-40.

Bédard, L. P., and Barnes, S. J., 2002, A comparison of N-type semi-planar and coaxial INAA detectors for 33 geochemical reference samples: Journal of Radioanalytical and Nuclear Chemistry, v. 254, no. 3, p. 485-497.

Behrens, H., and Nowak, M., 1997, The mechanisms of water diffusion in polymerized silicate melts: Contributions to Mineralogy and Petrology, v. 126, no. 4, p. 377-385.

Benson, P. M., Vinciguerra, S., Meredith, P. G., and Young, R. P., 2008, Laboratory simulation of volcano seismicity: Science, v. 322, no. 5899, p. 249-252.

Berlo, K., Tuffen, H., Smith, V. C., Castro, J. M., Pyle, D. M., Mather, T. A., and Geraki, K., 2013, Element variations in rhyolitic magma resulting from gas transport: Geochimica et Cosmochimica Acta, v. 121, p. 436-451.

Blake, S., 1981, Volcanism and the dynamics of open magma chambers: Nature, v. 289, no. 5800, p. 783-785.

-, 1984, Magma mixing and hydridization processes at the alkalic, silicic, Torfajökull central volcano triggered by tholeiitic Veidivötn fissuring, south Iceland: Journal of Volcanology and Geothermal Research, v. 22, p. 1-31.

Blower, J., 2001, Factors controlling permeability–porosity relationships in magma: Bulletin of Volcanology, v. 63, no. 7, p. 497-504.

Bluth, G. J. S., and Rose, W. I., 2004, Observations of eruptive activity at Santiaguito volcano, Guatemala: Journal of Volcanology and Geothermal Research, v. 136, no. 3–4, p. 297-302.

Bond, A., and Sparks, R. S. J., 1976, The Minoan eruption of Santorini, Greece: Journal of the Geological Society, v. 132, no. 1, p. 1-16.

Boudon, G., Villemant, B., Komorowski, J.-C., Ildefonse, P., and Semet, M. P., 1998, The hydrothermal system at Soufriere Hills Volcano, Montserrat (West Indies): Characterization and role in the on-going eruption: Geophysical Research Letters, v. 25, no. 19, p. 3693-3696.

Branney, M. J., and Kokelaar, P., 2002, Pyroclastic Density Currents and the Sedimentation of Ignimbrites, Geological Society, London, Memoirs.

Brendryen, J., Haflidason, H., and Sejrup, H. P., 2010, Norwegian Sea tephrostratigraphy of marine isotope stages 4 and 5: Prospects and problems for tephrochronology in the North Atlantic region: Quaternary Science Reviews, v. 29, no. 7–8, p. 847-864.

Brown, R. J., Buse, B., Sparks, R. S. J., and Field, M., 2008, On the Welding of Pyroclasts from Very Low-Viscosity Magmas: Examples from Kimberlite Volcanoes: The Journal of Geology, v. 116, no. 4, p. 354-374.

Brugger, C. R., and Hammer, J. E., 2010, Crystallization Kinetics in Continuous Decompression Experiments: Implications for Interpreting Natural Magma Ascent Processes: Journal of Petrology, p. 1941-1965.

Burgisser, A., and Gardner, J., 2004, Experimental constraints on degassing and permeability in volcanic conduit flow: Bulletin of Volcanology, v. 67, no. 1, p. 42-56.
Bushberg, J. T., Seibert, J. A., Leidholdt Jr., E. M., and Boone, J. M., 2011, The Essential Physics of Medical Imaging, Third Edition, LWW; Third, North American Edition edition.
Cabrera, A., Weinberg, R. F., and Wright, H. M. N., 2015, Magma fracturing and degassing associated with obsidian formation: The explosive–effusive transition: Journal of Volcanology and Geothermal Research, v. 298, p. 71-84.
Cabrera, A., Weinberg, R. F., Wright, H. M. N., Zlotnik, S., and Cas, R. A. F., 2011, Melt fracturing and healing: A mechanism for degassing and origin of silicic obsidian: Geology, v. 39, no. 1, p. 67-70.
Cabrera, A. P., 2013, Origin of silicic water-poor obsidian and non-explosive activity during the Mt Pilato-Rocche Rosse eruptions, Italy: Monash University.
Carn, S. A., Pallister, J. S., Lara, L., Ewert, J. W., Watt, S., Prata, A. J., Thomas, R. J., and Villarosa, G., 2009, The unexpected awakening of Chaitén volcano, Chile: Eos, Transactions American Geophysical Union, v. 90, no. 24, p. 205-206.
Cashman, K. V., and Sparks, R. S. J., 2013, How volcanoes work: A 25 year perspective: Geological Society of America Bulletin.
Cashman, K. V., Thornber, C. R., and Pallister, J. S., 2008, From dome to dust: shallow crystallization and fragmentation of conduit magma during the 2004-2006 dome extrusion of Mount St. Helens, Washington: Chapter 19 in A volcano rekindled: the renewed eruption of Mount St. Helens, 2004-2006, 1750-19.
Castro, J., Burgisser, A., Schipper, C. I., and Mancini, S., 2012a, Mechanisms of bubble coalescence in silicic magmas: Bulletin of Volcanology, v. 74, no. 10, p. 2339-2352.
Castro, J., Cashman, K., Joslin, N., and Olmsted, B., 2002a, Structural origin of large gas cavities in the Big Obsidian Flow, Newberry Volcano: Journal of Volcanology and Geothermal Research, v. 114, no. 3–4, p. 313-330.
Castro, J., and Cashman, K. V., 1999, Constraints on rheology of obsidian lavas based on mesoscopic folds: Journal of Structural Geology, v. 21, no. 7, p. 807-819.
Castro, J., Manga, M., and Cashman, K., 2002b, Dynamics of obsidian flows inferred from microstructures: insights from microlite preferred orientations: Earth and Planetary Science Letters, v. 199, no. 1–2, p. 211-226.
Castro, J. M., Beck, P., Tuffen, H., Nichols, A. R., Dingwell, D. B., and Martin, M. C., 2008, Timescales of spherulite crystallization in obsidian inferred from water concentration profiles: American Mineralogist, v. 93, no. 11-12, p. 1816-1822.
Castro, J. M., Bindeman, I. N., Tuffen, H., and Ian Schipper, C., 2014, Explosive origin of silicic lava: Textural and –H2O evidence for pyroclastic degassing during rhyolite effusion: Earth and Planetary Science Letters, v. 405, p. 52-61.
Castro, J. M., Cordonnier, B., Tuffen, H., Toblin, M. J., Pusker, L., Martin, M. C., and Bechtel, M. C., 2012b, The role of melt-fracture degassing in defusing explosive rhyolite eruptions at volcán Chaitén: Earth and Planetary Science Letters, v. 333-334, p. 63-69.
Castro, J. M., Cottrell, E., Tuffen, H., Logan, A. V., and Kelley, K. A., 2009, Spherulite crystallization induces Fe-redox redistribution in silicic melt: Chemical Geology, v. 268, no. 3–4, p. 272-280.
Castro, J. M., and Dingwell, D. B., 2009, Rapid ascent of rhyolitic magma at Chaiten volcano, Chile: Nature, v. 461, no. 7265, p. 780-783.
Castro, J. M., and Gardner, J. E., 2008, Did magma ascent rate control the explosive-effusive transition at the Inyo volcanic chain, California?: Geology, v. 36, no. 4, p. 279-282.
Castro, J. M., Manga, M., and Martin, M. C., 2005, Vesiculation rates of obsidian domes inferred from H2O concentration profiles: Geophysical Research Letters, v. 32, no. 21, L21307, p. 1-5.

Cerling, T. E., Brown, F. H., and Bowman, J. R., 1985, Low-temperature alteration of volcanic glass: Hydration, Na, K, 18O and Ar mobility: Chemical Geology: Isotope Geoscience section, v. 52, no. 3–4, p. 281-293.

Chadderton, A., Sammonds, P., Meredith, P., Smith, R., and Tuffen, H., 2015, Experimental permeability at volcanic temperatures and pressures: an insight into silicic magma degassing, IUGG abstract.

Chouet, B., 1988, Resonance of a Fluid-Driven Crack: Radiation Properties and Implications for the Source of Long-Period Events and Harmonic Tremor: J. Geophys. Res., v. 93, no. B5, p. 4375-4400.

Chouet, B. A., 1996, Long-period volcano seismicity: its source and use in eruption forecasting: Nature, v. 380, no. 6572, p. 309-316.

Clarke, A. B., Phillips, J. C., and Chojnicki, K. N., 2009, An investigation of Vulcanian eruption dynamics using laboratory analogue experiments, *in* Thordarson, T., Self, S., Larsen, G., Rowland, S. K., and Hoskuldsson, A., eds., Studies in Volcanology: the Legacy of George Walker: Bath, UK, The Geological Society.

Collier, L., and Neuberg, J., 2006, Incorporating seismic observations into 2D conduit flow modeling: Journal of Volcanology and Geothermal Research, v. 152, no. 3–4, p. 331-346.

Cordonnier, B., Caricchi, L., Pistone, M., Castro, J., Hess, K.-U., Gottschaller, S., Manga, M., Dingwell, D. B., and Burlini, L., 2012a, The viscous-brittle transition of crystal-bearing silicic melt: Direct observation of magma rupture and healing: Geology.

Cordonnier, B., Schmalholz, S., Hess, K. U., and Dingwell, D., 2012b, Viscous heating in silicate melts: An experimental and numerical comparison: Journal of Geophysical Research: Solid Earth (1978–2012), v. 117, no. B2.

Couch, S., Sparks, R. S. J., and Carroll, M. R., 2003, The Kinetics of Degassing-Induced Crystallization at Soufrière Hills Volcano, Montserrat: Journal of Petrology, v. 44, no. 8, p. 1477-1502.

D'Oriano, C., Pompilio, M., Bertagnini, A., Cioni, R., and Pichavant, M., 2013, Effects of experimental reheating of natural basaltic ash at different temperatures and redox conditions: Contributions to Mineralogy and Petrology, v. 165, no. 5, p. 863-883.

Degruyter, W., Bachmann, O., and Burgisser, A., 2010a, Controls on magma permeability in the volcanic conduit during the climactic phase of the Kos Plateau Tuff eruption (Aegean Arc): Bulletin of Volcanology, v. 72, no. 1, p. 63-74.

Degruyter, W., Burgisser, A., Bachmann, O., and Malaspinas, O., 2010b, Synchrotron X-ray microtomography and lattice Boltzmann simulations of gas flow through volcanic pumices: Geosphere, v. 6, no. 5, p. 470-481.

Denlinger, R. P., and Hoblitt, R. P., 1999, Cyclic eruptive behavior of silicic volcanoes: Geology, v. 27, no. 5, p. 459-462.

Denton, J. S., 2010, The post-emplacement hydration and alteration of subglaceially erupted obsidian to form perlite. PhD Thesis: Lancaster University, UK.

Denton, J. S., Tuffen, H., and Gilbert, J. S., 2012, Variations in hydration within perlitised rhyolitic lavas—evidence from Torfajökull, Iceland: Journal of Volcanology and Geothermal Research, v. 223–224, p. 64-73.

Denton, J. S., Tuffen, H., Gilbert, J. S., and Odling, N., 2009, The hydration and alteration of perlite and rhyolite: Journal of the Geological Society, v. 166, no. 5, p. 895-904.

Di Toro, G., Hirose, T., Nielsen, S., Pennacchioni, G., and Shimamoto, T., 2006, Natural and Experimental Evidence of Melt Lubrication of Faults During Earthquakes: Science, v. 311, no. 5761, p. 647-649.

Dingwell, D. B., 1996, Volcanic Dilemma--Flow or Blow?: Science, v. 273, no. 5278, p. 1054-1055.

Dingwell, D. B., and Webb, S. L., 1989, Structural relaxation in silicate melts and non-Newtonian melt rheology in geologic processes: Physics and Chemistry of Minerals, v. 16, no. 5, p. 508-516.
Dixon, J. E., 1997, Degassing of alkalic basalts: American Mineralogist, v. 82, no. 3-4, p. 368-378.
Dixon, J. E., and Stopler, E. M., 1995, An Experimental Study of Water and Carbon Dioxide Solubilities in Mid-Ocean Ridge Basaltic Liquids. Part II: Applications to Degassing: Journal of Petrology, v. 36, no. 6, p. 1633-1646.
Dixon, J. E., Stopler, E. M., and Holloway, J. R., 1995, An Experimental Study of Water and Carbon Dioxide Solubilities in Mid-Ocean Ridge Basaltic Liquids. Part I: Calibration and Solubility Models: Journal of Petrology, v. 36, no. 6, p. 1607-1631.
Dobson, P. F., Epstein, S., and Stolper, E. M., 1989, Hydrogen isotope fractionation between coexisting vapor and silicate glasses and melts at low pressure: Geochimica et Cosmochimica Acta, v. 53, no. 10, p. 2723-2730.
Donald, S. B., Swink, A. M., and Schreiber, H. D., 2006, High-iron ferric glass: Journal of Non-Crystalline Solids, v. 352, no. 6–7, p. 539-543.
Doremus, R. H., 2000, Water speciation in silicate glasses and melts: Langmuir limited site model: American Mineralogist, v. 85, no. 11-12, p. 1674-1680.
Echlin, P., Fiori, C., Goldstein, J., Joy, D. C., and Newbury, D. E., 2013, Advanced scanning electron microscopy and X-ray microanalysis, Springer Science & Business Media.
Eichelberger, J. C., 1995, Silicic Volcanism: Ascent of Viscous Magmas from Crustal Reservoirs: Annual Review of Earth and Planetary Sciences, v. 23, no. 1, p. 41-63.
Eichelberger, J. C., Carrigan, C. R., Westrich, H. R., and Price, R. H., 1986, Non-explosive silicic volcanism: Nature, v. 323, no. 6089, p. 598-602.
Eichelberger, J. C., and Westrich, H. R., 1981, Magmatic volatiles in explosive rhyolitic eruptions: Geophysical Research Letters, v. 8, no. 7, p. 757-760.
Ekren, E. B., and Byers, F. M., 1976, Ash-flow fissure vent in west-central Nevada: Geology, v. 4, no. 4, p. 247-251.
Elders, W. A., Friðleifsson, G. Ó., Zierenberg, R. A., Pope, E. C., Mortensen, A. K., Guðmundsson, Á., Lowenstern, J. B., Marks, N. E., Owens, L., Bird, D. K., Reed, M., Olsen, N. J., and Schiffman, P., 2011, Origin of a rhyolite that intruded a geothermal well while drilling at the Krafla volcano, Iceland: Geology, v. 39, no. 3, p. 231-234.
Farquharson, J. I., James, M. R., and Tuffen, H., 2015, Examining rhyolite lava flow dynamics through photo-based 3D reconstructions of the 2011–2012 lava flowfield at Cordón-Caulle, Chile: Journal of Volcanology and Geothermal Research, v. 304, p. 336-348.
Fenner, C. N., 1920, The Katmai Region, Alaska, and the Great Eruption of 1912: The Journal of Geology, v. 28, no. 7, p. 569-606.
Fink, J., 1980, Surface folding and viscosity of rhyolite flows: Geology, v. 8, no. 5, p. 250-254.
Fink, J. H., Anderson, S. W., and Manley, C. R., 1992, Textural Constraints on Effusive Silicic Volcanism: Beyond the Permeable Foam Model: J. Geophys. Res., v. 97, no. B6, p. 9073-9083.
Friedman, I., 1989, Are extrusive rhyolites produced from permeable foam eruptions?: Bulletin of Volcanology, v. 51, no. 1, p. 69-71.
Friedman, I., Long, W., and Smith, R. L., 1963, Viscosity and water content of rhyolite glass: Journal of Geophysical Research, v. 68, no. 24, p. 6523-6535.
Friedman, I., and Smith, R. L., 1958, The deuterium content of water in some volcanic glasses: Geochimica et Cosmochimica Acta, v. 15, no. 3, p. 218-228.
Fuller, R. E., 1927, The Mode of Origin of the Color of Certain Varicolored Obsidians: The Journal of Geology, v. 35, no. 6, p. 570-573.
Furukawa, Y., and Ponce, J., 2010, Accurate, Dense, and Robust Multiview Stereopsis: Pattern Analysis and Machine Intelligence, IEEE Transactions on, v. 32, no. 8, p. 1362-1376.

Gaillard, F., Scaillet, B., and Pichavant, M., 2002, Kinetics of iron oxidation-reduction in hydrous silicic melts: American Mineralogist, v. 87, no. 7, p. 829-837.
Gardner, J. E., Hilton, M., and Carroll, M. R., 1999, Experimental constraints on degassing of magma: isothermal bubble growth during continuous decompression from high pressure: Earth and Planetary Science Letters, v. 168, no. 1–2, p. 201-218.
Gardner, J. E., Thomas, R. M. E., Jaupart, C., and Tait, S., 1996, Fragmentation of magma during Plinian volcanic eruptions: Bulletin of Volcanology, v. 58, no. 2, p. 144-162.
Gathorne-Hardy, F. J., and Harcourt-Smith, W. E. H., 2003, The super-eruption of Toba, did it cause a human bottleneck?: Journal of Human Evolution, v. 45, no. 3, p. 227-230.
Gibson, I. L., and Walker, G. P. L., 1963, Some composite rhyolite/basalt lavas and related composite dykes in eastern Iceland: Proceedings of the Geologists' Association, v. 74, no. 3, p. 301-IN303.
Gil Cruz, F., and Chouet, B. A., 1997, Long-period events, the most characteristic seismicity accompanying the emplacement and extrusion of a lava dome in Galeras Volcano, Colombia, in 1991: Journal of Volcanology and Geothermal Research, v. 77, no. 1–4, p. 121-158.
Ginibre, C., Kronz, A., and WoÈrner, G., 2002, High-resolution quantitative imaging of plagioclase composition using accumulated backscattered electron images: new constraints on oscillatory zoning: Contributions to Mineralogy and Petrology, v. 142, no. 4, p. 436-448.
Giordano, D., Russell, J. K., and Dingwell, D. B., 2008a, Viscosity of magmatic liquids: A model: Earth and Planetary Science Letters, v. 271, no. 1–4, p. 123-134.
Giordano, D., Russell, J. K., and Dingwell, D. B., 2008b, Viscosity of magmatic liquids: a model: Earth and Planetary Science Letters, v. 271, no. 1, p. 123-134.
Girona, T., Costa, F., and Schubert, G., 2015, Degassing during quiescence as a trigger of magma ascent and volcanic eruptions: Scientific Reports, v. 5, p. 18212.
Gonnermann, H. M., and Manga, M., 2003, Explosive volcanism may not be an inevitable consequence of magma fragmentation: Nature, v. 426, no. 6965, p. 432-435.
-, 2005, Flow banding in obsidian: A record of evolving textural heterogeneity during magma deformation: Earth and Planetary Science Letters, v. 236, no. 1–2, p. 135-147.
Gonnermann, H. M., and Manga, M., 2007, The fluid mechanics inside a volcano: Annual Review of Fluid Mechanics, v. 39, p. 321-356.
Goranson, R. W., 1931, Solubility of water in granite magmas: Eos, Transactions American Geophysical Union, v. 12, no. 1, p. 183-183.
Goto, A., 1999, A new model for volcanic earthquake at Unzen Volcano: Melt Rupture Model: Geophys. Res. Lett., v. 26, no. 16, p. 2541-2544.
Govindaraju, K., 1994, Compilation of working values and sample description for 383 geostandards: Geostandards Newsletter, v. 18, p. 1-158.
Green, D. N., and Neuberg, J., 2006, Waveform classification of volcanic low-frequency earthquake swarms and its implication at Soufrière Hills Volcano, Montserrat: Journal of Volcanology and Geothermal Research, v. 153, no. 1–2, p. 51-63.
Gunnarsson, B., Marsh, B. D., and Taylor Jr, H. P., 1998, Generation of Icelandic rhyolites: silicic lavas from the Torfajökull central volcano: Journal of Volcanology and Geothermal Research, v. 83, no. 1–2, p. 1-45.
Guppy, E. M., and Hawkes, L., 1925, A composite dyke from eastern Iceland.
Hammer, J. E., and Rutherford, M. J., 2002, An experimental study of the kinetics of decompression-induced crystallization in silicic melt: Journal of Geophysical Research: Solid Earth, v. 107, no. B1, p. ECV 8-1-ECV 8-24.
Heap, M. J., Xu, T., Kushnir, A. R. L., Kennedy, B. M., and Chen, C.-f., 2015, Fracture of magma containing overpressurised pores: Journal of Volcanology and Geothermal Research, v. 301, p. 180-190.

Heiken, G., 1974, An atlas of volcanic ash, Washington, Smithsonian Inst., Smithsonian contributions to the earth science; no. 12.
Heiken, G., and McCoy, F., Jr., 1984, Caldera Development During the Minoan Eruption, Thira, Cyclades, Greece: J. Geophys. Res., v. 89, no. B10, p. 8441-8462.
Heiken, G., Wohletz, K., and Eichelberger, J., 1988, Fracture Fillings and Intrusive Pyroclasts, Inyo Domes, California: J. Geophys. Res., v. 93, no. B5, p. 4335-4350.
Hess, K.-U., Cordonnier, B., Lavallée, Y., and Dingwell, D. B., 2008, Viscous heating in rhyolite: An in situ experimental determination: Earth and Planetary Science Letters, v. 275, no. 1–2, p. 121-126.
Hess, K. U., and Dingwell, D. B., 1996, Viscosities of hydrous leucogranitic melts: a non-Arrhenian model: American Mineralogist, v. 81, no. 9-10, p. 1297-1300.
Hildreth, W., and Fierstein, J., 2012, The Novarupta-Katmai Eruption of 1912—Largest Eruption of the Twentieth Century: Centennial Perspectives: U.S. Geological Survey Professional Paper v. 1791.
Holland, A. S. P., Watson, I. M., Phillips, J. C., Caricchi, L., and Dalton, M. P., 2011, Degassing processes during lava dome growth: Insights from Santiaguito lava dome, Guatemala: Journal of Volcanology and Geothermal Research, v. 202, no. 1–2, p. 153-166.
Horwell, C., Williamson, B., Llewellin, E., Damby, D., and Le Blond, J., 2013, The nature and formation of cristobalite at the Soufrière Hills volcano, Montserrat: implications for the petrology and stability of silicic lava domes: Bulletin of Volcanology, v. 75, no. 3, p. 1-19.
Houghton, B. F., Carey, R. J., Cashman, K. V., Wilson, C. J. N., Hobden, B. J., and Hammer, J. E., 2010, Diverse patterns of ascent, degassing, and eruption of rhyolite magma during the 1.8 ka Taupo eruption, New Zealand: Evidence from clast vesicularity: Journal of Volcanology and Geothermal Research, v. 195, no. 1, p. 31-47.
Humphreys, M. C. S., Menand, T., Blundy, J. D., and Klimm, K., 2008, Magma ascent rates in explosive eruptions: Constraints from H2O diffusion in melt inclusions: Earth and Planetary Science Letters, v. 270, no. 1–2, p. 25-40.
Hurwitz, S., and Navon, O., 1994, Bubble nucleation in rhyolitic melts: Experiments at high pressure, temperature, and water content: Earth and Planetary Science Letters, v. 122, no. 3–4, p. 267-280.
Iddings, J. P., 1888, Obsidian Cliff, Yellowstone National Park, US Government Printing Office.
Iverson, R. M., Dzurisin, D., Gardner, C. A., Gerlach, T. M., LaHusen, R. G., Lisowski, M., Major, J. J., Malone, S. D., Messerich, J. A., and Moran, S. C., 2006, Dynamics of seismogenic volcanic extrusion at Mount St Helens in 2004–05: Nature, v. 444, no. 7118, p. 439-443.
James, M. R., and Robson, S., 2012, Straightforward reconstruction of 3D surfaces and topography with a camera: Accuracy and geoscience application: Journal of Geophysical Research, v. 117, p. 147-167.
Jaupart, C., and Allègre, C. J., 1991, Gas content, eruption rate and instabilities of eruption regime in silicic volcanoes: Earth and Planetary Science Letters, v. 102, no. 3-4, p. 413-429.
Jaupart, C., and Tait, S., 1990, Dynamics of eruptive phenomena: Reviews in Mineralogy and Geochemistry, v. 24, no. 1, p. 213-238.
Jezek, P. A., and Noble, D. C., 1978, Natural hydration and ion exchange of obsidian; an electron microprobe study: American Mineralogist, v. 63, no. 3-4, p. 266-273.
Jochum, K. P., Nohl, U., Herwig, K., Lammel, E., Stoll, B., and Hofmann, A. W., 2005, GeoReM: A New Geochemical Database for Reference Materials and Isotopic Standards: Geostandards and Geoanalytical Research, v. 29, no. 3, p. 333-338.

Kano, K., Matsuura, H., and Yamauchi, S., 1997, Miocene rhyolitic welded tuff infilling a funnel-shaped eruption conduit Shiotani, southeast of Matsue, SW Japan: Bulletin of Volcanology, v. 59, no. 2, p. 125-135.

Kendrick, J. E., Lavallée, Y., Ferk, A., Perugini, D., Leonhardt, R., and Dingwell, D. B., 2012, Extreme frictional processes in the volcanic conduit of Mount St. Helens (USA) during the 2004–2008 eruption: Journal of Structural Geology, v. 38, p. 61-76.

Kendrick, J. E., Lavallee, Y., Hirose, T., Di Toro, G., Hornby, A. J., De Angelis, S., and Dingwell, D. B., 2014, Volcanic drumbeat seismicity caused by stick-slip motion and magmatic frictional melting: Nature Geosci, v. 7, no. 6, p. 438-442.

Kendrick, M. A., Jackson, M. G., Hauri, E. H., and Phillips, D., 2015, The halogen (F, Cl, Br, I) and H2O systematics of Samoan lavas: Assimilated-seawater, EM2 and high-3He/4He components: Earth and Planetary Science Letters, v. 410, p. 197-209.

Kennedy, B. M., Jellinek, A. M., Russell, J. K., Nichols, A. R. L., and Vigouroux, N., 2010, Time- and temperature-dependent conduit wall porosity: A key control on degassing and explosivity at Tarawera volcano, New Zealand: Earth and Planetary Science Letters, v. 299, no. 1–2, p. 126-137.

Kennedy, L. A., and Russell, J. K., 2012, Cataclastic production of volcanic ash at Mount Saint Helens: Physics and Chemistry of the Earth, Parts A/B/C, v. 45–46, p. 40-49.

Keulen, N., Heilbronner, R., Stünitz, H., Boullier, A.-M., and Ito, H., 2007, Grain size distributions of fault rocks: A comparison between experimentally and naturally deformed granitoids: Journal of Structural Geology, v. 29, no. 8, p. 1282-1300.

Keulen, N., Stünitz, H., and Heilbronner, R., 2008, Healing microstructures of experimental and natural fault gouge: Journal of Geophysical Research: Solid Earth, v. 113, no. B6, p. B06205.

Klug, C., and Cashman, K. V., 1996, Permeability development in vesiculating magmas: implications for fragmentation: Bulletin of Volcanology, v. 58, no. 2, p. 87-100.

Klug, C. K., Cashman, K. C., and Bacon, C. B., 2002, Structure and physical characteristics of pumice from the climactic eruption of Mount Mazama (Crater Lake), Oregon: Bulletin of Volcanology, v. 64, no. 7, p. 486-501.

Kolzenberg, S., Heap, M. J., Lavallée, Y., Russell, J. K., Meredith, P. G., and Dingwell, D. B., 2012, The strength and permeability of tuffisite-bearing andesite in volcanic conduits: Solid Earth Discussions, v. 4, p. 459-473.

Komorowski, J.-C., Hoblitt, R. P., and Sheridan, M. F., 1997, Silicification and brecciation microtextures of the Mt. St. Helens 1980 cryptodome-country rock interface: Implications for hydrothermal fluid processes, precursory seismicity, and eruptive style, paper presented at IAVCEI General Assembly, Int, Assoc. of Volcanol. and Chem. of the Earth's Inter., Puerto Vallarta, Mexico, 19-25 Jan.

Lahr, J. C., Chouet, B. A., Stephens, C. D., Power, J. A., and Page, R. A., 1994, Earthquake classification, location, and error analysis in a volcanic environment: implications for the magmatic system of the 1989–1990 eruptions at redoubt volcano, Alaska: Journal of Volcanology and Geothermal Research, v. 62, no. 1–4, p. 137-151.

Lara, L. E., 2009, The 2008 eruption of the Chaitén Volcano, Chile: a preliminary report: Andean Geology.

Larsen, G., 1984, Recent volcanic history of the veidivötn fissure swarm, southern Iceland - an approach to volcanic risk assessment: Journal of Volcanology and Geothermal Research, v. 22, p. 33-58.

Lavallée, Y., Dingwell, D. B., Johnson, J. B., Cimarelli, C., Hornby, A. J., Kendrick, J. E., von Aulock, F. W., Kennedy, B. M., Andrews, B. J., Wadsworth, F. B., Rhodes, E., and Chigna, G., 2015, Thermal vesiculation during volcanic eruptions: Nature, v. 528, no. 7583, p. 544-547.

Lavallée, Y., Hirose, T., Kendrick, J. E., De Angelis, S., Petrakova, L., Hornby, A. J., and Dingwell, D. B., 2014, A frictional law for volcanic ash gouge: Earth and Planetary Science Letters, v. 400, p. 177-183.

Lejeune, A.-M., and Richet, P., 1995, Rheology of crystal-bearing silicate melts: An experimental study at high viscosities: Journal of Geophysical Research: Solid Earth, v. 100, no. B3, p. 4215-4229.

Lensky, N. G., Sparks, R. S. J., Navon, O., and Lyakhovsky, V., 2008, Cyclic activity at Soufrière Hills Volcano, Montserrat: degassing-induced pressurization and stick-slip extrusion: Geological Society, London, Special Publications, v. 307, no. 1, p. 169-188.

Leschik, M., Heide, G., Frischat, G. H., Behrens, H., Wiedenbeck, M., Wagner, N., Heide, K., Geißler, H., and Reinholz, U., 2004, Determination of H_2O and D_2O contents in rhyolitic glasses: Physics and Chemistry of Glasses, v. 45, no. 4, p. 238-251.

Lipman, P. W., and Mullineaux, D. R., 1981, The 1980 eruptions of Mount St. Helens, Washington, US Dept. of the Interior, US Geological Survey, v. 1250.

Liu, E. J., Cashman, K. V., Rust, A. C., and Gislason, S. R., 2015, The role of bubbles in generating fine ash during hydromagmatic eruptions: Geology, v. 43, no. 3, p. 239-242.

Llewellin, E. W., 2002, The rheology of bubble bearing magma: theory and experiments [PhD thesis: University of Bristol, UK.

Llewellin, E. W., Mader, H. M., and Wilson, S. D. R., 2002, The constitutive equation and flow dynamics of bubbly magmas: Geophysical Research Letters, v. 29, no. 24, p. 23-21-23-24.

Llewellin, E. W., and Manga, M., 2005, Bubble suspension rheology and implications for conduit flow: Journal of Volcanology and Geothermal Research, v. 143, no. 1–3, p. 205-217.

Manga, M., and Loewenberg, M., 2001, Viscosity of magmas containing highly deformable bubbles: Journal of Volcanology and Geothermal Research, v. 105, no. 1–2, p. 19-24.

Mangan, M., and Sisson, T., 2000, Delayed, disequilibrium degassing in rhyolite magma: decompression experiments and implications for explosive volcanism: Earth and Planetary Science Letters, v. 183, no. 3–4, p. 441-455.

Manley, C. R., 1995, How voluminous rhyolite lavas mimic rheomorphic ignimbrites: Eruptive style, emplacement conditions, and formation of tuff-like textures: Geology, v. 23, no. 4, p. 349-352.

Manley, C. R., 1996, In situ formation of welded tuff-like textures in the carapace of a voluminous silicic lava flow, Owyhee County, SW Idaho: Bulletin of Volcanology, v. 57, no. 8, p. 672-686.

Manley, C. R., and Fink, J. H., 1987, Internal textures of rhyolite flows as revealed by research drilling: Geology, v. 15, no. 6, p. 549-552.

Martel, C., 2012, Eruption Dynamics Inferred from Microlite Crystallization Experiments: Application to Plinian and Dome-forming Eruptions of Mt. Pelée (Martinique, Lesser Antilles): Journal of Petrology, p. 699-725.

Martel, C., and Schmidt, B., 2003, Decompression experiments as an insight into ascent rates of silicic magmas: Contributions to Mineralogy and Petrology, v. 144, no. 4, p. 397-415.

Marti, J., Soriano, C., and Dingwell, D. B., 1999, Tube pumices as strain markers of the ductile-brittle transition during magma fragmentation: Nature, v. 402, no. 6762, p. 650-653.

Mastin, L. G., and Witter, J. B., 2000, The hazards of eruptions through lakes and seawater: Journal of Volcanology and Geothermal Research, v. 97, no. 1–4, p. 195-214.

McBirney, A. R., and Murase, T., 1970, Factors governing the formation of pyroclastic rocks: Bulletin Volcanologique, v. 34, no. 2, p. 372-384.

McGarvie, D. W., 1984, Torfajökull: A volcano dominated by magma mixing: Geology, v. 12, no. 11, p. 685-688.
-, 1985, Volcanology and petrology of mixed magmas and rhyolites from the Torfajökull volcano, Iceland, PhD thesis: Lancaster University, UK.
McGarvie, D. W., Burgess, R., Tindle, A. G., Tuffen, H., and Stevenson, J. A., 2006, Pleistocene rhyolitic volcanism at Torfajökull, Iceland: eruption ages, glaciovolcanism, and geochemical evolution: Jökull, v. 56, p. 57-75.
McGowan, E. M., Tuffen, H., Castro, J. M., Berlo, K., James, M. R., Owen, J., Schipper, C. I., Wadsworth, F. B., Saubin, E., and Wehbe, K., 2015, Pressure changes before and after explosive rhyolitic bomb ejection at Chaiten, Chile recorded by water diffusion profiles around tuffisite veins, AGU abstract.
McIntosh, I. M., Llewellin, E. W., Humphreys, M. C. S., Nichols, A. R. L., Burgisser, A., Schipper, C. I., and Larsen, J. F., 2014a, Distribution of dissolved water in magmatic glass records growth and resorption of bubbles: Earth and Planetary Science Letters, v. 401, p. 1-11.
McIntosh, I. M., Tani, K., and Nichols, A., 2014b, H2O Contents of Submarine and Subaerial Silicic Pyroclasts from Oomurodashi Volcano, Northern Izu-Bonin Arc: AGU abstract V11B-4723.
Miller, A. D., Stewart, R. C., White, R. A., Luckett, R., Baptie, B. J., Aspinall, W. P., Latchman, J. L., Lynch, L. L., and Voight, B., 1998, Seismicity associated with dome growth and collapse at the Soufriere Hills Volcano, Montserrat: Geophysical Research Letters, v. 25, no. 18, p. 3401-3404.
Molina, I., Kumagai, H., and Yepes, H., 2004, Resonances of a volcanic conduit triggered by repetitive injections of an ash-laden gas: Geophysical Research Letters, v. 31, no. 3.
Moore, G., 2008, Interpreting H2O and CO2 contents in melt inclusions: constraints from solubility experiments and modeling: Reviews in Mineralogy and Geochemistry, v. 69, no. 1, p. 333-362.
Moore, G., Vennemann, T., and Carmichael, I., 1998, An empirical model for the solubility of H2O in magmas to 3 kilobars: American Mineralogist, v. 83, no. 1, p. 36-42.
Moriizumi, M., Nakashima, S., Okumura, S., and Yamanoi, Y., 2009, Color-change processes of a plinian pumice and experimental constraints of color-change kinetics in air of an obsidian: Bulletin of Volcanology, v. 71, no. 1, p. 1-13.
Mørk, M. B., E, 1984, Magma mixing in the post-glacial veidivötn fissure eruption, southeast Iceland: a microprobe study of mineral and glass variations: Lithos, v. 17, p. 55-75.
Morrissey, M. M., and Mastin, L. G., 2000, Vulcanian eruptions. , *in* Sigmundsson, H., Houghton, B., McNutt, S. R., Rymer, H., and Stix, J., eds., Encyclopedia of Volcanoes. Academic Press, New York, pp. 463-476.
Mott, N., 1987, The viscosity of vitreous silicon dioxide: Philosophical Magazine B, v. 56, no. 2, p. 257-262.
Mueller, S., Scheu, B., Spieler, O., and Dingwell, D. B., 2008, Permeability control on magma fragmentation: Geology, v. 36, no. 5, p. 399-402.
Müller, H., Strubel, C., and Bange, K., 2001, Characterization and identification of local defects in glass: Scanning, v. 23, no. 1, p. 14-23.
Murase, T., and McBirney, A. R., 1973, Properties of Some Common Igneous Rocks and Their Melts at High Temperatures: Geological Society of America Bulletin, v. 84, no. 11, p. 3563-3592.
Nakada, S., Shimizu, H., and Ohta, K., 1999, Overview of the 1990–1995 eruption at Unzen Volcano: Journal of Volcanology and Geothermal Research, v. 89, no. 1–4, p. 1-22.
Navon, O., and Lyakhovsky, V., 1998, Vesiculation processes in silicic magmas: Geological Society, London, Special Publications, v. 145, no. 1, p. 27-50.

Nelson, S. A., 1981, The possible role of thermal feedback in the eruption of siliceous magmas: Journal of Volcanology and Geothermal Research, v. 11, no. 2–4, p. 127-137.

Neuberg, J., 2000, Characteristics and causes of shallow seismicity in andesite volcanoes: Philosophical Transactions of the Royal Society of London A: Mathematical, Physical and Engineering Sciences, v. 358, no. 1770, p. 1533-1546.

Neuberg, J. W., Tuffen, H., Collier, L., Green, D., Powell, T., and Dingwell, D., 2006, The trigger mechanism of low-frequency earthquakes on Montserrat: Journal of Volcanology and Geothermal Research, v. 153, no. 1–2, p. 37-50.

Newhall, C. G., and Self, S., 1982, The volcanic explosivity index (VEI) an estimate of explosive magnitude for historical volcanism: Journal of Geophysical Research: Oceans, v. 87, no. C2, p. 1231-1238.

Newman, S., Epstein, S., and Stolper, E., 1988, Water, carbon dioxide, and hydrogen isotopes in glasses from the ca. 1340 A.D. eruption of the Mono Craters, California: Constraints on degassing phenomena and initial volatile content: Journal of Volcanology and Geothermal Research, v. 35, no. 1-2, p. 75-96.

Newman, S., and Lowenstern, J. B., 2002, VolatileCalc: a silicate melt–H2O–CO2 solution model written in Visual Basic for excel: Computers & Geosciences, v. 28, no. 5, p. 597-604.

Newman, S., Stolper, E., and Epstein, S., 1986, Measurement of water in rhyolitic glasses: Calibration of an infrared spectroscopic technique: American Mineralogist, v. 71, p. 1527-1541.

Ni, H., and Zhang, Y., 2008, H2O diffusion models in rhyolitic melt with new high pressure data: Chemical Geology, v. 250, no. 1–4, p. 68-78.

Ninkovich, D., Sparks, R., and Ledbetter, M., 1978, The exceptional magnitude and intensity of the Toba eruption, sumatra: An example of the use of deep-sea tephra layers as a geological tool: Bulletin of Volcanology, v. 41, no. 3, p. 286-298.

Nowak, M., and Behrens, H., 2001, Water in rhyolitic magmas: getting a grip on a slippery problem: Earth and Planetary Science Letters, v. 184, no. 2, p. 515-522.

Okumura, S., Nakamura, M., Nakano, T., Uesugi, K., and Tsuchiyama, A., 2010, Shear deformation experiments on vesicular rhyolite: Implications for brittle fracturing, degassing, and compaction of magmas in volcanic conduits: Journal of Geophysical Research: Solid Earth, v. 115, no. B6, p. B06201.

Okumura, S., Nakamura, M., Takeuchi, S., Tsuchiyama, A., Nakano, T., and Uesugi, K., 2009, Magma deformation may induce non-explosive volcanism via degassing through bubble networks: Earth and Planetary Science Letters, v. 281, no. 3-4, p. 267-274.

Okumura, S., Nakamura, M., Tsuchiyama, A., Nakano, T., and Uesugi, K., 2008, Evolution of bubble microstructure in sheared rhyolite: Formation of a channel-like bubble network: J. Geophys. Res., v. 113, no. B7, p. B07208.

Okumura, S., Nakamura, M., Uesugi, K., Nakano, T., and Fujioka, T., 2013, Coupled effect of magma degassing and rheology on silicic volcanism: Earth and Planetary Science Letters, v. 362, p. 163-170.

Oskarsson, N., Sigvaldason, G. E., and Steinthorsson, S., 1982, A dynamic-model of rift-zone petrogenesis and the regional petrology of Iceland: Journal of Petrology, v. 23, no. 1, p. 28-74.

Owen, J., 2013, Volatiles in Icelandic subglacial rhyolite, PhD thesis: Lancaster University, Lancaster, UK.

Owen, J., Tuffen, H., and McGarvie, D., 2012, Using dissolved H2O in rhyolitic glasses to estimate palaeo-ice thickness during a subglacial eruption at Bláhnúkur (Torfajökull, Iceland): Bulletin of Volcanology, v. 74, no. 6, p. 1355-1378.

Owen, J., Tuffen, H., and McGarvie, D. W., 2013a, Explosive subglacial rhyolitic eruptions in Iceland are fuelled by high magmatic H2O and closed-system degassing: Geology, v. 41, no. 2, p. 251-254.
-, 2013b, Pre-eruptive volatile content, degassing paths and depressurisation explaining the transition in style at the subglacial rhyolitic eruption of Dalakvísl, South Iceland: Journal of Volcanology and Geothermal Research, v. 258, p. 143-162.
Papale, P., 1999, Strain-induced magma fragmentation in explosive eruptions: Nature, v. 397, no. 6718, p. 425-428.
Papale, P., Moretti, R., and Barbato, D., 2006, The compositional dependence of the saturation surface of H2O + CO2 fluids in silicate melts: Chemical Geology, v. 229, no. 1–3, p. 78-95.
Parfitt, L., and Wilson, L., 2009, Fundamentals of physical volcanology, John Wiley & Sons.
Pinkerton, H., and Stevenson, R. J., 1992, Methods of determining the rheological properties of magmas at sub-liquidus temperatures: Journal of Volcanology and Geothermal Research, v. 53, no. 1–4, p. 47-66.
Plail, M., Edmonds, M., Humphreys, M. C. S., Barclay, J., and Herd, R. A., 2014, Geochemical evidence for relict degassing pathways preserved in andesite: Earth and Planetary Science Letters, v. 386, p. 21-33.
Proussevitch, A. A., and Sahagian, D. L., 1996, Dynamics of coupled diffusive and decompressive bubble growth in magmatic systems: Journal of Geophysical Research: Solid Earth, v. 101, no. B8, p. 17447-17455.
Proussevitch, A. A., Sahagian, D. L., and Kutolin, V. A., 1993, Stability of foams in silicate melts: Journal of Volcanology and Geothermal Research, v. 59, no. 1, p. 161-178.
Pyle, D. M., 2000, Sizes of volcanic eruptions, *in* Sigurdsson, H., ed., Encyclopedia of volcanoes: San Diego, Academic Press, p. 263-269
Reed, S. J. B., 2005, Electron microprobe analysis and scanning electron microscopy in geology, Cambridge University Press.
Reedman, A. J., Park, K. H., Merriman, R. J., and Kim, S. E., 1987, Welded tuff infilling a volcanic vent at Welseong, Republic of Korea Bulletin of Volcanology, v. 49, p. 541-546.
Ribeiro, J. M., Stern, R. J., Kelley, K. A., Shaw, A. M., Martinez, F., and Ohara, Y., 2015, Composition of the slab-derived fluids released beneath the Mariana forearc: Evidence for shallow dehydration of the subducting plate: Earth and Planetary Science Letters, v. 418, p. 136-148.
Romano, C., Mungall, J. E., Sharp, T., and Dingwell, D. B., 1996, Tensile strengths of hydrous vesicular glasses; an experimental study: American Mineralogist, v. 81, no. 9-10, p. 1148-1154.
Romine, W. L., Whittington, A. G., Nabelek, P. I., and Hofmeister, A. M., 2012, Thermal diffusivity of rhyolitic glasses and melts: effects of temperature, crystals and dissolved water: Bulletin of Volcanology, v. 74, no. 10, p. 2273-2287.
Ross, C. S., and Smith, R. L., 1961, Ash-flow tuffs, their origin, geological relations and identification: U.S. Geological Survey Professional Papers 354-F and 366, v. 9.
Roulia, M., Chassapis, K., Kapoutsis, J. A., Kamitsos, E. I., and Savvidis, T., 2006, Influence of thermal treatment on the water release and the glassy structure of perlite: Journal of Materials Science, v. 41, no. 18, p. 5870-5881.
Rust, A. C., and Cashman, K. V., 2011, Permeability controls on expansion and size distributions of pyroclasts: Journal of Geophysical Research: Solid Earth, v. 116, no. B11, p. B11202.
Rust, A. C., Cashman, K. V., and Wallace, P. J., 2004, Magma degassing buffered by vapor flow through brecciated conduit margins: Geology, v. 32, no. 4, p. 349-352.

Rust, A. C., Manga, M., and Cashman, K. V., 2003, Determining flow type, shear rate and shear stress in magmas from bubble shapes and orientations: Journal of Volcanology and Geothermal Research, v. 122, no. 1–2, p. 111-132.
Saar, M. O., and Manga, M., 1999, Permeability-porosity relationship in vesicular basalts: Geophysical Research Letters, v. 26, no. 1, p. 111-114.
Saemundsson, K., and Noll, H., 1974, K/Ar ages of rocks from Húsafell, Western Iceland, and the development of the Húsafell central volcano: Jökull, v. 24, p. 40-59.
Sato, M., and Wright, T. L., 1966, Oxygen Fugacities Directly Measured in Magmatic Gases: Science, v. 153, no. 3740, p. 1103-1105.
Schipper, C. I., Castro, J., Tuffen, H., Wadsworth, F., Chappell, D., Pantoja, A., Simpson, M., and Le Ru, E., 2015, Cristobalite in the 2011–2012 Cordón Caulle eruption (Chile): Bulletin of Volcanology, v. 77, no. 5, p. 1-19.
Schipper, C. I., Castro, J. M., Tuffen, H., James, M. R., and How, P., 2013, Shallow vent architecture during hybrid explosive–effusive activity at Cordón Caulle (Chile, 2011–12): Evidence from direct observations and pyroclast textures: Journal of Volcanology and Geothermal Research, v. 262, p. 25-37.
Schwarzkopf, L. M., Schmincke, H.-U., and Troll, V. R., 2002, Friction marks on blocks from pyroclastic flows at the Soufriere Hills volcano, Montserrat: Implications for flow mechanisms: Geology: comment, v. 30, no. 2, p. 190-190.
Selbekk, R. S., and Trønnes, R. G., 2007, The 1362 AD Öræfajökull eruption, Iceland: Petrology and geochemistry of large-volume homogeneous rhyolite: Journal of Volcanology and Geothermal Research, v. 160, no. 1–2, p. 42-58.
Self, S., Zhao, J., Holasek, R. E., Torres, R. C., and King, A. J., 2004, The Atmospheric Impact of the 1991 Mount Pinatubo Eruption, *in* Newhall, C. G., and Punongbayan, R. S., eds., Fire and mud: eruptions and lahars of Mount Pinatubo, Philippines: Hong Kong, University of Washington Press.
Sharma, K., Self, S., Blake, S., Thordarson, T., and Larsen, G., 2008, The AD 1362 Öræfajökull eruption, S.E. Iceland: Physical volcanology and volatile release: Journal of Volcanology and Geothermal Research, v. 178, no. 4, p. 719-739.
Shaw, H., 1972, Viscosities of magmatic silicate liquids; an empirical method of prediction: American Journal of Science, v. 272, no. 9, p. 870-893.
Shaw, H. R., 1963, Obsidian-H2O viscosities at 1000 and 2000 bars in the temperature range 700° to 900°C: Journal of Geophysical Research, v. 68, no. 23, p. 6337-6343.
Shepherd, J. B., and Aspinall, W. P., 1982, Seismological studies of the soufriere of St. Vincent, 1953-79: Implications for volcanic surveillance in the lesser antilles: Journal of Volcanology and Geothermal Research, v. 12, no. 1–2, p. 37-55.
Shields, J., Mader, H., Caricchi, L., Tuffen, H., Mueller, S., Pistone, M., and Baumgartner, L., 2016, Unravelling textural heterogeneity in obsidian: Shear-induced outgassing in the Rocche Rosse flow: Journal of Volcanology and Geothermal Research, v. 310, p. 137-158.
Silver, L., 1988, Water in silicate glasses [PhD: California Institute of Technology.
Silver, L., and Stolper, E., 1985, A Thermodynamic Model for Hydrous Silicate Melts: The Journal of Geology, v. 93, no. 2, p. 161-177.
Silver, L. A., Ihinger, P. D., and Stolper, E., 1990, The influence of bulk composition on the speciation of water in silicate glasses: Contributions to Mineralogy and Petrology, v. 104, no. 2, p. 142-162.
Smith, J. V., 1996, Ductile-brittle transition structures in the basal shear zone of a rhyolite lava flow, eastern Australia: Journal of Volcanology and Geothermal Research, v. 72, no. 3–4, p. 217-223.
Smith, R. L., 1960, Zones and zonal variations in welded ash flows, 354F.
Snavely, N., Garg, R., Seitz, S. M., and Szeliski, R., 2008a, Finding paths through the world's photos: ACM Trans. Graph., v. 27, no. 3, p. 1-11.

Snavely, N., Seitz, S. M., and Szeliski, R., 2006, Photo tourism: exploring photo collections in 3D, ACM SIGGRAPH 2006 Papers: Boston, Massachusetts, ACM, p. 835-846.
Snavely, N., Seitz, S. M., and Szeliski, R., 2008b, Modeling the World from Internet Photo Collections: Int. J. Comput. Vision, v. 80, no. 2, p. 189-210.
Soosalu, H., and Einarsson, P., 1997, Seismicity around the Hekla and Torfajökull volcanoes, Iceland, during a volcanically quiet period, 1991–1995: Bulletin of Volcanology, v. 59, no. 1, p. 36-48.
-, 2004, Seismic constraints on magma chambers at Hekla and Torfajökull volcanoes, Iceland: Bulletin of Volcanology, v. 66, no. 3, p. 276-286.
Soosalu, H., Lippitsch, R., and Einarsson, P., 2006, Low-frequency earthquakes at the Torfajökull volcano, south Iceland: Journal of Volcanology and Geothermal Research, v. 153, no. 3–4, p. 187-199.
Sparks, R. J. S., 1978, The dynamics of bubble formation and growth in magmas: A review and analysis: Journal of Volcanology and Geothermal Research, v. 3, no. 1–2, p. 1-37.
Sparks, R. S. J., Tait, S. R., and Yanev, Y., 1999, Dense welding caused by volatile resorption: Journal of the Geological Society, v. 156, no. 2, p. 217-225.
Sparks, S. R. J., Sigurdsson, H., and Wilson, L., 1977, Magma mixing: a mechanism for triggering acid explosive eruptions: Nature, v. 267, no. 5609, p. 315-318.
Spera, F. J., 2000, Physical properties of magma: Encyclopedia of volcanoes, p. 171-190.
Spieler, O., Kennedy, B., Kueppers, U., Dingwell, D. B., Scheu, B., and Taddeucci, J., 2004, The fragmentation threshold of pyroclastic rocks: Earth and Planetary Science Letters, v. 226, no. 1–2, p. 139-148.
Stasiuk, M. V., Barclay, J., Carroll, M. R., Jaupart, C., Ratté, J. C., Sparks, R. S. J., and Tait, S. R., 1996, Degassing during magma ascent in the Mule Creek vent (USA): Bulletin of Volcanology, v. 58, no. 2, p. 117-130.
Stein, D. J., and Spera, F. J., 2002, Shear viscosity of rhyolite-vapor emulsions at magmatic temperatures by concentric cylinder rheometry: Journal of Volcanology and Geothermal Research, v. 113, no. 1–2, p. 243-258.
Stevenson, J. A., 2005, Volcano-ice interaction at Öraefajökull and Kerlingarfjöll, Iceland, PhD thesis: The Open University, Milton Keynes.
Stix, J., Torres, R. C., Narváez, L., Raigosa, J. A., Gómez, D., and Castonguay, R., 1997, A model of vulcanian eruptions at Galeras volcano, Colombia: Journal of Volcanology and Geothermal Research, v. 77, no. 1, p. 285-303.
Stolper, E., 1982a, Water in silicate glasses: An infrared spectroscopic study: Contributions to Mineralogy and Petrology, v. 81, no. 1, p. 1-17.
-, 1982b, The speciation of water in silicate melts: Geochimica et Cosmochimica Acta, v. 46, no. 12, p. 2609-2620.
Tait, S., Jaupart, C., and Vergniolle, S., 1989, Pressure, gas content and eruption periodicity of a shallow, crystallising magma chamber: Earth and Planetary Science Letters, v. 92, no. 1, p. 107-123.
Tait, S., Thomas, R., Gardner, J., and Jaupart, C., 1998, Constraints on cooling rates and permeabilities of pumice in an explosive eruption jet from colour and magnetic mineralogy: Journal of Volcanology and Geothermal Research, v. 86, no. 1–4, p. 79-91.
Taylor, B. E., Eichelberger, J. C., and Westrich, H. R., 1983, Hydrogen isotopic evidence of rhyolitic magma degassing during shallow intrusion and eruption: Nature, v. 306, no. 5943, p. 541-545.
Taylor, H. P., O'Neil, J. R., and Kaplan, I. R., 1991, Stable Isotope Geochemistry: A Tribute to Samuel Epstein, Geochemical Society.
Thomas, N., Jaupart, C., and Vergniolle, S., 1994, On the vesicularity of pumice: J. Geophys. Res., v. 99, no. B8, p. 15633-15644.

Tuffen, H., 2001, Subglacial rhyolite volcanism at Torfajökull, PhD thesis: The Open University, Milton Keynes, UK.
Tuffen, H., and Castro, J. M., Brittle–ductile rheology, foam collapse and latent heat: the story of obsidian lava emplacement at Krafla volcano, Iceland. Abstract. IAVCEI General Assenbly, Reykjavik.2008.
Tuffen, H., and Castro, J. M., 2009, The emplacement of an obsidian dyke through thin ice: Hrafntinnuhryggur, Krafla Iceland: Journal of Volcanology and Geothermal Research, v. 185, no. 4, p. 352-366.
Tuffen, H., and Dingwell, D., 2005, Fault textures in volcanic conduits: evidence for seismic trigger mechanisms during silicic eruptions: Bulletin of Volcanology, v. 67, no. 4, p. 370-387.
Tuffen, H., Dingwell, D. B., and Pinkerton, H., 2003, Repeated fracture and healing of silicic magma generate flow banding and earthquakes?: Geology, v. 31, no. 12, p. 1089-1092.
Tuffen, H., Owen, J., and Denton, J., 2010, Magma degassing during subglacial eruptions and its use to reconstruct palaeo-ice thicknesses: Earth-Science Reviews, v. 99, no. 1–2, p. 1-18.
Tuffen, H., Pinkerton, H., McGarvie, D. W., and Gilbert, J. S., 2002, Physical volcanology of a subglacial-to-emergent rhyolitic tuya at Rauðufossafjöll, Torfajökull, Iceland, *in* Smellie, J. L., and Chapman, M. G., eds., Volcano-Ice interaction on Earth and Mars, Geological Society Special Publication, no. 202, p. 213-236.
Tuffen, H., Smith, R., and Sammonds, P. R., 2008, Evidence for seismogenic fracture of silicic magma: Nature, v. 453, no. 7194, p. 511-514.
Uhlmann, D. R., Klein, L., and Hopper, R. W., 1975, Sintering, crystallization, and breccia formation: The moon, v. 13, no. 1-3, p. 277-284.
Vasseur, J., Wadsworth, F. B., Lavallée, Y., Hess, K.-U., and Dingwell, D. B., 2013, Volcanic sintering: Timescales of viscous densification and strength recovery: Geophysical Research Letters, v. 40, no. 21, p. 5658-5664.
Voight, B., Hoblitt, R. P., Clarke, A. B., Lockhart, A. B., Miller, A. D., Lynch, L., and McMahon, J., 1998, Remarkable cyclic ground deformation monitored in real-time on Montserrat, and its use in eruption forecasting: Geophysical Research Letters, v. 25, no. 18, p. 3405-3408.
Voight, B., Linde, A. T., Sacks, I. S., Mattioli, G. S., Sparks, R. S. J., Elsworth, D., Hidayat, D., Malin, P. E., Shalev, E., Widiwijayanti, C., Young, S. R., Bass, V., Clarke, A., Dunkley, P., Johnston, W., McWhorter, N., Neuberg, J., and Williams, P., 2006, Unprecedented pressure increase in deep magma reservoir triggered by lava-dome collapse: Geophysical Research Letters, v. 33, no. 3, p. n/a-n/a.
Voight, B., Sparks, R. S. J., Miller, A. D., Stewart, R. C., Hoblitt, R. P., Clarke, A., Ewart, J., Aspinall, W. P., Baptie, B., Calder, E. S., Cole, P., Druitt, T. H., Hartford, C., Herd, R. A., Jackson, P., Lejeune, A. M., Lockhart, A. B., Loughlin, S. C., Luckett, R., and Lynch, L., 1999, Magma Flow Instability and Cyclic Activity at Soufriere Hills Volcano, Montserrat, British West Indies: Science, v. 283, no. 5405, p. 1138-1142.
von Aulock, F. W., Nichols, A. R. L., Kennedy, B. M., and Oze, C., 2013, Timescales of texture development in a cooling lava dome: Geochimica et Cosmochimica Acta, v. 114, p. 72-80.
Waite, G. P., Chouet, B. A., and Dawson, P. B., 2008, Eruption dynamics at Mount St. Helens imaged from broadband seismic waveforms: Interaction of the shallow magmatic and hydrothermal systems: Journal of Geophysical Research: Solid Earth, v. 113, no. B2, p. n/a-n/a.
Walker, G. P. L., 1969, Possible fissure vent for a Pliocene ash-flow tuff, Buzzard Creek area County, Oregaon, Geological Survey Research Chapter C, Volume 650, Geological Survey professional paper, p. C8-C17.

Walker, G. P. L., and Skelhorn, R. R., 1966, Some associations of acid and basic igneous rocks: Earth-Science Reviews, v. 2, no. 0, p. 93-109.
Watkins, J. M., Manga, M., and DePaolo, D. J., 2012, Bubble geobarometry: A record of pressure changes, degassing, and regassing at Mono Craters, California: Geology, v. 40, no. 8, p. 699-702.
Webb, S., and Dingwell, D., 1990a, Non-Newtonian Rheology of Igneous Melts at High Stresses and Strain Rates: Experimental Results for Rhyolite, Andesite, Basalt, and Nephelinite: Journal of Geophysical Research, v. 95, no. B10, p. 15,695-615,701.
Webb, S., and Dingwell, D., 1990b, The onset of non-Newtonian rheology of silicate melts: Physics and Chemistry of Minerals, v. 17, no. 2, p. 125-132.
Wells, O. C., 1974, Scanning electron microscopy, McGraw-Hill.
Westrich, H. R., and Eichelberger, J. C., 1994, Gas transport and bubble collapse in rhyolitic magma: an experimental approach: Bulletin of Volcanology, v. 56, no. 6, p. 447-458.
White, J. D. L., and Valentine, G. A., 2016, Magmatic versus phreatomagmatic fragmentation: Absence of evidence is not evidence of absence: Geosphere.
White, R. A., Miller, A. D., Lynch, L., and Power, J., 1998, Observations of hybrid seismic events at Soufriere Hills Volcano, Montserrat: July 1995 to September 1996: Geophysical Research Letters, v. 25, no. 19, p. 3657-3660.
Willmott, P., 2011, An Introduction to Synchrotron Radiation: Techniques and Applications, Wiley.
Wilson, C. J. N., 2001, The 26.5 ka Oruanui eruption, New Zealand: an introduction and overview: Journal of Volcanology and Geothermal Research, v. 112, no. 1–4, p. 133-174.
Wilson, C. J. N., Blake, S., Charlier, B. L. A., and Sutton, A. N., 2006, The 26·5 ka Oruanui Eruption, Taupo Volcano, New Zealand: Development, Characteristics and Evacuation of a Large Rhyolitic Magma Body: Journal of Petrology, v. 47, no. 1, p. 35-69.
Wilson, C. J. N., and Walker, G. P. L., 1985, The Taupo Eruption, New Zealand I. General Aspects: Philosophical Transactions of the Royal Society of London. Series A, Mathematical and Physical Sciences, v. 314, no. 1529, p. 199-228.
Wohletz, K., 2002, KWare Magma Software: University of California.
Wolff, J. A., 1986, Welded-tuff dykes, conduit closure, and lava dome growth at the end of explosive eruptions: Journal of Volcanology and Geothermal Research, v. 28, p. 379-384.
Wright, H. M. N., Roberts, J. J., and Cashman, K. V., 2006, Permeability of anisotropic tube pumice: Model calculations and measurements: Geophysical Research Letters, v. 33, no. 17, p. L17316.
Wright, H. M. N., and Weinberg, R. F., 2009, Strain localization in vesicular magma: Implications for rheology and fragmentation: Geology, v. 37, no. 11, p. 1023-1026.
Yoshimura, S., and Nakamura, M., 2008, Diffusive dehydration and bubble resorption during open-system degassing of rhyolitic melts: Journal of Volcanology and Geothermal Research, v. 178, no. 1, p. 72-80.
-, 2010, Fracture healing in a magma: An experimental approach and implications for volcanic seismicity and degassing: J. Geophys. Res., v. 115, no. B9, p. B09209.
Zhang, Y., 1999, H2O in rhyolitic glasses and melts: Measurement, speciation, solubility, and diffusion: Reviews of Geophysics, v. 37, no. 4, p. 493-516.
Zhang, Y., and Ni, H., 2010, Diffusion of H, C, and O components in silicate melts: Reviews in Mineralogy and Geochemistry, v. 72, no. 1, p. 171-225.
Zhang, Y., Stolper, E. M., and Ihinger, P. D., 1995, Kinetics of the reaction $H_20 + 0 = 20H$ in rhyolitic and albitic glasses: Preliminary results: American Mineralogist, v. 80, p. 593-612.

Zhang, Y., Stolper, E. M., and Wasserburg, G. J., 1991, Diffusion of water in rhyolitic glasses: Geochimica et Cosmochimica Acta, v. 55, no. 2, p. 441-456.
Zhang, Y., Xu, Z., and Behrens, H., 2000, Hydrous species geospeedometer in rhyolite: improved calibration and application: Geochimica et Cosmochimica Acta, v. 64, no. 19, p. 3347-3355.
Zhang, Y., Xu, Z., and Liu, Y., 2003, Viscosity of hydrous rhyolitic melts inferred from kinetic experiments, and a new viscosity model: American Mineralogist, v. 88, no. 11-12, p. 1741-1752.
Zierenberg, R. A., Schiffman, P., Barfod, G. H., Lesher, C. E., Marks, N. E., Lowenstern, J. B., Mortensen, A. K., Pope, E. C., Bird, D. K., Reed, M. H., Friðleifsson, G. Ó., and Elders, W. A., 2012, Composition and origin of rhyolite melt intersected by drilling in the Krafla geothermal field, Iceland: Contributions to Mineralogy and Petrology, v. 165, no. 2, p. 327-347.